Microphone arrays for imaging of aerospace noise sources

Merino Martinez, Roberto

DOI
10.4233/uuid:a3231ea9-1380-44f4-9a93-dbbd9a26f1d6

Publication date
2018

Document Version
Final published version

Citation (APA)
Merino Martinez, R. (2018). *Microphone arrays for imaging of aerospace noise sources*. [Dissertation (TU Delft), Delft University of Technology]. https://doi.org/10.4233/uuid:a3231ea9-1380-44f4-9a93-dbbd9a26f1d6

Microphone arrays for imaging of aerospace noise sources

Microphone arrays for imaging of aerospace noise sources

Proefschrift

ter verkrijging van de graad van doctor
aan de Technische Universiteit Delft,
op gezag van de Rector Magnificus prof. dr. ir. T.H.J.J. van der Hagen,
voorzitter van het College voor Promoties,
in het openbaar te verdedigen op maandag 10 december 2018 om 12:30 uur

door

Roberto MERINO–MARTÍNEZ

Master of Science in Aerospace Engineering,
Universidad Politécnica de Madrid, Spanje,
geboren te Burgos, Spanje.

Dit proefschrift is goedgekeurd door de

promotor: Prof. dr. D.G. Simons
copromotor: Dr. ir. M. Snellen

Samenstelling promotiecommissie bestaat uit:

Rector Magnificus,	voorzitter
Prof. dr. D.G. Simons,	Technische Universiteit Delft, promotor
Dr. ir. M. Snellen,	Technische Universiteit Delft, copromotor
Onafhankelijke leden:	
Prof. dr. ing. E. Sarradj,	Technische Universität Berlin
Prof. dr. ir. C.H. Venner,	Universiteit Twente
Prof. dr. ir. G.J.T. Leus,	Technische Universiteit Delft
Prof. dr. S.J. Watson,	Technische Universiteit Delft
Dr. ir. D.J. Verschuur,	Technische Universiteit Delft

Keywords: Phased Microphone Arrays, Beamforming, Acoustic Imaging, Aeroacoustics, Aircraft Noise, Wind Turbine Noise.

Printed by: IPSKAMP printing

Front & Back: Acoustic foam wedges of covering one of the walls of the anechoic vertical open–jet wind tunnel (A–tunnel) at Delft University of Technology.

ISBN 978–94–028–1301–2

An electronic version of this dissertation is available at
http://repository.tudelft.nl/.

Per ardua ad astra

Salud, fuerza y unión

Contents

Summary

With the continuous growth in demand for air traffic and wind turbines, the noise emissions they generate are becoming an increasingly important issue. To reduce their noise levels, it is essential to obtain accurate information about all the sound sources present.

Phased microphone arrays and acoustic imaging methods allow for the estimation of the location and strength of sound sources. Experiments with these devices are one of the main approaches in the current research in aeroacoustics, along with computational simulations or noise prediction models. This thesis presents a detailed literature review on the most common aerospace noise sources, challenges in aeroacoustic measurements, and the acoustic imaging methods typically used to overcome them. Practical recommendations are provided for selecting the appropriate imaging technique depending on the type of experiment.

New integration techniques for distributed sound sources, such as leading– or trailing–edge noise, are proposed in this thesis and are proven to provide the best performance in retrieving the source levels, compared to other well–known methods. In addition, the high–resolution version of the deconvolution method CLEAN–SC, HR–CLEAN–SC, is explained and applied to wind–tunnel measurements. It is confirmed that this method can resolve sound sources at half the frequency associated with the Rayleigh resolution limit, while keeping the inherent advantages of CLEAN–SC.

The most appropriate acoustic imaging methods (according to the recommendations from the literature study) were applied to aeroacoustic experiments and compared with other approaches, when possible.

Since the landing gear is considered as the dominant airframe noise source in commercial aircraft, this source was analyzed using four different approaches: aircraft flyover measurements under operational conditions, full–scale wind–tunnel experiments, computational simulations and noise prediction models. Strong tonal noise at certain frequencies was observed and suggested the presence of open cavities. Noise prediction models do not account for this behavior and seem to provide erroneous estimates. Eliminating the contribution of the cavity will reduce the noise levels considerably.

Trailing–edge noise is considered to be the dominant noise source for modern wind turbines. The performance of the two most promising noise reduction measures was investigated in wind–tunnel experiments. First, trailing–edge serrations featuring different geometries were studied and showed noise reductions of more than 10 dB. In case a serration–flow misalignment angle occurs, the performance of the serrations decreases and they even cause a noise increase after a crossover frequency. Similar results were found with computational simulations. Secondly, trailing–edge porous inserts showed noise reductions of approximately 10 dB at

low frequencies and a noise increase after a crossover frequency. It is argued that the reasons for these phenomena were, respectively, the cross–flow between the pressure and suction sides of the airfoil and the increased roughness of the porous material with respect to the solid case.

Lastly, the issue of the variability in aircraft noise levels was considered, since it is not properly taken into account by current best practice noise prediction models and hinders the enforcement of environmental laws. It was observed that variations in the fan rotational speed explain a large part of this variability. Two different approaches were proposed for estimating the fan rotational speed of aircraft flyovers based on audio recordings. Implementing these more accurate estimates of this parameter in the noise prediction model (rather than the default values as usual) considerably reduces the errors made and provide more accurate aircraft noise estimates.

In conclusion, phased microphone arrays have confirmed their importance for aeroacoustic studies, such as measuring aircraft noise emissions under operational conditions and assessing the performance of noise reduction measures.

Samenvatting

Door de toenemende groei van het vliegtuigverkeer en windturbines, is het geluid dat deze produceren van toenemend belang. Voor het verminderen van dit geluid, is het belangrijk om accuraat informatie te verzamelen van de aanwezige geluidsbronnen.

Met gerangschikte microfoons en akoestische beeldvormingsmethoden is het mogelijk om zowel de positie als de sterkte van de geluidsbronnen te bepalen. Het gebruik van deze systemen is één van de manieren voor hedendaags onderzoek op het gebied van aeroakoestiek. Andere methodieken zijn computationele simulaties of modellen voor het voorspellen van geluid. Dit proefschrift zal een uitgebreid overzicht geven uit de literatuur voor de typische geluidsbronnen in de luchtvaart en de bijbehorende beeldvormingsmethoden. Aanbevelingen zullen gegeven worden voor het bepalen van de geschikte afbeeldingsmethode op basis van het type experiment.

Nieuwe integratie technieken voor gedistribueerde geluidsbronnen, zoals een voorrand of achterrand, zullen in deze scriptie worden voorgelegd. De integratie technieken leveren het beste resultaat op om de bron niveaus te bepalen ten opzichte van andere gevestigde methodes. Daarnaast zal ook een hoge resolutie deconvolutie methode CLEAN–SC, ofwel HR–CLEAN–SC, worden uitgelegd en toegepast voor windtunnel metingen. Aangetoond zal worden dat deze methode gelijktijdig de geluidsbronnen kan onderscheiden bij de helft van de frequentie gerelateerd aan de Rayleigh resolutie limiet en de inherente voordelen behoudt van CLEAN–SC.

De meest geschikte akoestische afbeeldingsmethoden (aanbevolen uit de literatuur) zijn toegepast voor aeroakoestische experimenten en, zo mogelijk, vergeleken met andere methoden. Omdat het landingsgestel de dominantie geluidsbron is vanuit het casco, is deze bron geanalyseerd voor vier verschillende situaties: overvliegingen onder operationele condities, wind tunnel experimenten op ware grootte, computationele simulaties en modellen voor het voorspellen van geluid. Sterke tonale componenten waren te zien bij bepaalde frequenties die aanduidde op de aanwezigheid van een caviteit. Geluidsmodellen houden hier geen rekening mee en lijken foutieve schattingen te produceren. Verwijderen van deze bijdrage door de caviteit zal het geluidsniveau aanzienlijk verminderen.

Het achterrand geluid wordt aangenomen als de meest dominante geluidsbron voor moderne wind turbines. De prestatie van de twee meest veelbelovende geluidsverminderende maatregelen was onderzocht in windtunnel experimenten. Als eerste zijn achterrand vertandingen voor verschillende geometrieën onderzocht en is aangetoond dat deze het geluidsniveau kunnen verminderen tot 10 dB. In geval van een verkeerde uitlijning van de vertanding met de stroming neemt de prestatie van geluidsvermindering af en neemt het geluid zelfs toe na een kruisingsfrequentie.

Vergelijkbare resultaten zijn verkregen uit computationele simulaties. Ten tweede laten poreuze invoegingen in de achterrand zien dat het geluid ongeveer met 10 dB afneemt voor lage frequenties en toeneemt na een kruisingsfrequentie. Beargumenteerd kan worden dat de oorzaken voor deze fenomenen zijn, respectievelijk, de stroming tussen verhoogde en verlaagde druk vlakken en de toegenomen ruwheid van de poreuze invoeging ten opzichte van de massieve toestand.

Ten slotte wordt de kwestie van de variabiliteit van het geluidsniveau van vliegtuigen bekeken. Hier wordt geen rekening mee gehouden door huidige geluidsmodellen en kunnen zodoende de handhaving van milieuwetten belemmeren. Het was te zien dat de variaties in het toerental van de fan een grote invloed heeft op de variabiliteit. Twee verschillende benaderingen worden voorgesteld om het toerental van de fan te bepalen op basis van audio opnames. Het gebruik van deze meer accurate benadering in geluidsmodellen vermindert de fout aanzienlijk en geeft beter het geluidsniveau weer van vliegtuigen.

Concluderend hebben gerangschikte microfoons hun waarde kunnen laten zien voor aeroakoestisch onderzoek, zowel in het bepalen van vliegtuiggeluid in operationele condities als het bepalen van de effectiviteit van geluidsverminderende maatregelen.

Preface

This Ph.D. thesis studies the applications of phased microphone arrays for measuring aircraft and wind turbine noise. These devices allow for the application of acoustic imaging methods that estimate the location and strength of sound sources. In this way, the influence of unwanted sound sources on the measurements can be minimized.

One of the main aims of this thesis is to compare different approaches for aeroacoustic studies, such as aircraft flyover measurements, wind–tunnel experiments, computational simulations or noise prediction models.

First of all, a thorough literature review is presented about the typical aerospace noise sources, challenges in aeroacoustic measurements and acoustic imaging methods. Most of the contents of this review are published in the paper *A review of acoustic imaging methods using phased microphone arrays* in the CEAS Aeronautical Journal. I would like to kindly thank all of the many authors for their contributions and critical feedback. I feel really lucky to have counted with most of the experts in this field for the preparation of this manuscript.

For the wind–tunnel experiments, I had the opportunity to join experimental campaigns about trailing–edge serrations and trailing–edge porous inserts for reducing airfoil noise. Therefore, I would like to kindly thank Carlos Arce León and Alejandro Rubio Carpio, respectively, for their trust and patience. The technical expertise and support of Daniele Ragni and Francesco Avallone is also extremely appreciated.

For the comparison of the experimental results with computational simulations, the help and knowledge of Wouter van der Velden and Francesco Avallone was crucial.

Lastly, the experience and technical knowledge about aircraft noise prediction models of Lothar Bertsch, Abhishek K. Sahai, Dick H. T. Bergmans and Sander J. Heblij was very useful and kindly appreciated.

Special thanks to my promotor Dick G. Simons and my copromotor Mirjam Snellen for believing in me, for their support throughout all the Ph.D. project, and offering me the opportunity to continue my research as a postdoctoral researcher.

Roberto Merino–Martínez
Delft, December 2018

Nomenclature

Latin symbols

a	Array response to a plane wave
A	Source autopower
$\hat{A}$	Empirical parameter for Guo's method
$\tilde{A}$	Source power per unit strength
$\boldsymbol{A}$	Acoustic source map
$\tilde{\boldsymbol{A}}$	$J \times J$ Propagation matrix whose columns contain the PSF of each grid point
b	Wing span
$\hat{b}$	Empirical parameter for Guo's method
B	Number of fan blades
$\hat{B}$	Empirical parameter for Guo's method
$\boldsymbol{B}$	$J \times J$ Global source cross–spectral matrix for IBIA
BW	Array beamwidth of 3 dB down from beam peak maximum
c	Speed of sound
c_d	Drag coefficient
c_l	Local lift coefficient for two–dimensional airfoils
c_L	Lift coefficient
c_p	Pressure coefficient
c_P	Coefficient of power
$\hat{c}$	Wing chord
$\tilde{c}$	Propagation velocity
$\boldsymbol{c}$	$1 \times J$ propagation vector used in Linear Programming Deconvolution
$\boldsymbol{C}$	$N \times N$ cross–spectral matrix (CSM)
d	Diameter
$\tilde{d}$	$\sqrt{\tilde{D}}$
D	Diameter of a microphone array
$\hat{D}$	Directivity function
$\tilde{D}$	Individual source amplitude in SODIX method
$\mathrm{E}(\cdot)$	Expected value
E_0	Empirical parameter in Eq. (7.2)
f	Sound frequency
f_{sam}	Sampling frequency
F	Cost function in optimization problems
F_0	Empirical parameter in Eq. (7.2)
F_d	Drag force
F_L	Lift force
F_n	Thrust force per engine

$\frac{F_n}{\delta_0}$	Corrected thrust force per engine
$\hat{F}$	Spectrum function
$\mathcal{F}$	Fourier transform
$\boldsymbol{g}$	$N \times 1$ steering vector
G_A	Empirical parameter in Eq. (7.2)
G_B	Empirical parameter in Eq. (7.2)
G_{xx}	Actual value of the PSD
$\tilde{G}_{xx}$	One–sided PSD
$\tilde{G}_{yx}$	One–sided CSD
$\boldsymbol{G}$	$N \times K$ (unknown) matrix containing the steering vectors $\boldsymbol{g}$ to the unknown K source locations
$\tilde{\boldsymbol{G}}$	$N \times J$ (known) matrix containing the steering vectors $\boldsymbol{g}$ to all J grid points
h	Distance from the scan plane to the array
h_s	Serration semilength
$\hat{h}$	Empirical parameter for Guo's method
$\tilde{h}$	Aircraft altitude (in ft)
$\boldsymbol{h}$	Source component vector for CLEAN–SC
H	Number of FFT blocks in Welch's method
$\tilde{H}$	Empirical parameter in Eq. (7.2)
He	Helmholtz number
i^2	Imaginary unit, -1
$\boldsymbol{I}$	$N \times N$ identity matrix
J	Number of grid points
J_1	First order Bessel function
J_{prop}	Advance ratio of a propeller
k	Number of eigenvalues considered for Orthogonal Beamforming
k_0	Acoustic wavenumber
k_x, k_y	Wavenumbers in the x and y direction, respectively
$\boldsymbol{k}$	Wavevector (k_x, k_y)
K	Number of (incoherent) sound sources
K_1	Empirical parameter for Fink's method
K_2	Empirical parameter for Fink's method
K_3	Empirical parameter in Eq. (7.2)
K_4	Empirical parameter in Eq. (7.2)
$\hat{K}$	Permeability of a porous material
l	Characteristic length
l_y	Characteristic spanwise turbulence correlation scale
L_p	Sound Pressure Level (SPL)
$L_{p,A}$	A–weighted sound pressure level
$L_{p,A,e}$	Sound Exposure Level (SEL)
$\boldsymbol{L}$	Cross–spectral matrix due to a simulated line source for the SPIL method
$\mathcal{L}$	Acoustic transfer function for Amiet's method
M	Mach number

$\boldsymbol{M}$	Mach vector
n_{rot}	Rotational speed (in rpm)
$n_{\text{rot,max}}$	Maximum rotational speed (in rpm)
$\hat{n}$	Noise parameter for orthogonal beamforming
N	Number of microphones
N_{iter}	Number of iterations for DAMAS
N_{sam}	Number of samples
N_{speakers}	Number of speakers for acoustic GPS
N_{strut}	Number of struts in a landing gear
N_{wheel}	Number of wheels in a landing gear
$N1\%$	Engine fan settings (in $\%$)
p	Static acoustic pressure
p_{e}	Effective acoustic pressure
$p_{\text{e,0}}$	Threshold effective acoustic pressure (normally taken as 20 μPa)
p	Static acoustic pressure
$\tilde{p}$	Fourier transform of the recorded pressure at each microphone
$\boldsymbol{p}$	$N \times 1$ vector containing the Fourier transform recorded pressures at each microphone
P	Acoustic power
q	Dynamic pressure
$\hat{q}$	Empirical parameter for Guo's method
$\tilde{q}$	Sparsity parameter for IBIA
r	Distance between the sound source and the observer
r_0	Distance to the source (namely 1 m away from the source center)
$\bar{r}$	Mean distance between the sound source and the observer
$\boldsymbol{r}$	Source position vector
R	Spatial resolution according to Rayleigh resolution limit
R_0	Universal gas constant
$\tilde{R}_{xx}$	Autocorrelation function
Re	Reynolds number
$Re_{\hat{c}}$	Chord–based Reynolds number
s	Sound source amplitude
$\hat{s}$	Perimeter of the cross section of a landing gear strut
$\tilde{s}$	Standard deviation
S	Reference surface area
$\tilde{S}_{pp}$	Power spectral density of the far–field sound for Amiet's method
$\tilde{S}_{qq}$	Power spectral density of the spanwise cross–spectrum of the surface pressure for Amiet's method
$\tilde{S}_{xx}$	Power spectral density (PSD)
$\boldsymbol{S}$	Sound source amplitude vector
St	Strouhal number
t	Time
T	Time interval
T_0	Ambient temperature
T_{60}	Reverberation time

T_h	Duration of a time block for Welch's method
$\boldsymbol{u}$	Eigenvector of the cross–spectral matrix
$\tilde{\boldsymbol{u}}$	Left singular vector of $\boldsymbol{G}$
$\boldsymbol{U}$	Unitary matrix whose columns are eigenvectors of the cross–spectral matrix
v'	Mean turbulence velocity
$\boldsymbol{v}$	Parameter vector for the Global Optimization Method
V	Mean flow velocity
V_C	Calibrated airspeed (in kts) in Eq. (7.2)
V_Γ	Velocity generated due to the recirculation flow around the wing
V_∞	Inflow velocity
$\boldsymbol{V}$	Source velocity vector
w	Width
$\hat{w}$	Window function
$\boldsymbol{w}$	Weighted steering vector
W	Power generated by a wind turbine
$\boldsymbol{W}$	$J \times J$ diagonal matrix whose components are $\lvert s_j \rvert$ for a single microphone
x_0	Location of the simulated line source for the SPIL method
$\hat{x}$	Random signal in the time domain
$\bar{\hat{x}}$	Estimator of the mean value for $\hat{x}$
$\tilde{x}$	Source autopower
$\boldsymbol{x}$	Microphone position vector (x, y, z)
$\tilde{\boldsymbol{x}}$	$J \times 1$ vector containing the unknown source autopowers
X	Random signal in the frequency domain
$\hat{y}$	Random signal in the time domain
$\boldsymbol{y}$	$J \times 1$ vector containing the source autopowers obtained with CFDBF
Y	Random signal in the frequency domain
Z	Number of integration areas in the ISPI method

Greek symbols

α	Angle of attack
$\hat{\alpha}$	Atmospheric absorption coefficient
$\hat{\beta}$	Flow energy conversion efficiency parameter for Guo's method
γ	Ratio of a gas specific heats (≈ 1.4 for air)
Γ	Recirculation of the flow underneath the wing
$\hat{\gamma}^2_{y,x}$	Coherence function
δ	Noise parameter for compressive sensing beamforming
$\delta^\star$	Boundary layer displacement thickness
δ_0	Ratio between the ambient air pressure at the aircraft to the standard air pressure at mean sea level
δ_{95}	Boundary layer thickness where the velocity is 95% of the edge velocity

Δ	Difference
Δf	Frequency resolution
ΔL_p	Difference in sound pressure level
Δt	Time delay
Δx	Widthwise spacing of grid points
ϵ	Artificial diagonal loading factor for RAB and GIBF
ε	Error parameter
η^2	Regularization parameter used for IBIA
$\hat{\eta}$	Complexity factor for Guo's method
θ	Source emission angle
θ_scan	Scan angle of an array with respect to the normal direction
$\theta_\mathrm{scan,0}$	Scan angle associated to the Rayleigh resolution limit
θ_T	Ratio between the absolute total temperature at the engine inlet to the standard air temperature at mean sea level (288.15 K)
λ	Acoustic wavelength
λ_s	Serration width
μ	Dynamic viscosity of a fluid
μ_0	Artificial diagonal loading parameter for RAB
$\hat{\mu}$	Empirical parameter for Guo's method
$\tilde{\mu}$	Source marker constraint for HR–CLEAN–SC
ν	Functional beamforming exponent
$\boldsymbol{\xi}$	Grid point position vector
ρ	Correlation coefficient
ρ^2	Coefficient of determination
ρ_0	Density of a fluid
σ	Eigenvalue of the cross–spectral matrix
$\hat{\sigma}$	Empirical parameter for Guo's method
$\tilde{\sigma}$	Singular value of $\boldsymbol{G}$
$\boldsymbol{\Sigma}$	Diagonal matrix whose diagonal elements are eigenvalues of the cross–spectral matrix
τ	Time shift (for correlation functions)
ϕ	Azimuthal sideline emission angle
φ	Angle between two steering vectors in the N–dimensional space
φ_s	Serration–flow misalignment angle
$\hat{\varphi}$	Damping factor for CLEAN–SC
$\boldsymbol{\Psi}$	$J \times N$ regularized inverse of $\boldsymbol{G}$

Subscripts

array	Referring to a microphone array
bias	Referring to the bias error
c	Referring to the cell of a porous material
center	Referring to the center frequency in a frequency band
crossover	Referring to the crossover frequency
em	Referring to the sound emissions

eq	Referring to the equivalent number of averages
exact	Referring to the exact solution
exp	Experimental
h	h^{th} time block in Welch's method
high	High–frequency
i	i^{th} grid point
j	j^{th} grid point
jet	Referring to a jet
k	k^{th} sound source
l	l^{th} sound source
low	Low–frequency
lower	Referring to the lower frequency bound in a frequency band
m	m^{th} microphone
max	Maximum
mid	Mid–frequency
min	Minimum
n	n^{th} microphone
norm	Normalized
nozzle	Referring to a nozzle
overall	Overall (for L_{p} calculations)
porous	Referring to a porous trailing edge
prop	Referring to a propeller
rand	Referring to the random error
ref	Reference
rim	Referring to a landing gear rim
s	Referring to trailing–edge serrations
S	Referring to the signal subspace
sim	Simulated
solid	Referring to a solid trailing edge
strut	Referring to the strut of a landing gear
upper	Referring to the upper frequency bound in a frequency band
wheel	Referring to the wheel of the landing gear
z	z^{th} ROI for the ISPI method
∞	Free–field conditions

Superscripts

$''$	Second derivative with respect to the frequency
(4)	Fourth derivative with respect to the frequency
$*$	Complex conjugate transpose
$(\cdot)^{\intercal}$	Transpose
$\dagger\eta$	Pseudo–inverse using Tikhonov regularization with regularization parameter η
i	i^{th} iteration

Others

$\langle \cdot \rangle$	Time average of several snapshots
$\|\|\cdot\|\|$	Euclidean norm of a vector

Acronyms

ADC	Analog to Digital Converter
ADS–B	Automatic Dependent Surveillance–Broadcast
AEDT	Aviation Environmental Design Tool
AIAA	American Institute of Aeronautics and Astronautics
ALLEGRA	Advanced Low noise Landing (main and nose) Gear for Regional Aircraft
ANCE	Aircraft Noise and Climate Effects
ANOPP	Aircraft NOise Prediction Program
ANP	Aircraft Noise and Performance
Ap	Approach
BG	BackGround
BTU	Brandenburg University of Technology Cottbus – Senftenberg
BW	BeamWidth
CAA	Computational AeroAcoustics
CCP	Constant Current Power
CEAS	Council of European Aerospace Societies
CFD	Computational Fluid Dynamics
CFDBF	Conventional Frequency Domain BeamForming
CMF	Covariance Matrix Fitting
CNC	Computer Numerical Control
CROR	Counter–Rotating Open Rotor
CSD	Cross–Spectral Density
CSM	Cross–Spectral Matrix
DAMAS	Deconvolution Approach for the Mapping of Acoustic Sources
DAS	Data Acquisition System
Dep	Departure
DFT	Discrete Fourier Transform
DLR	Deutsches Zentrum für Luft– und Raumfahrt (German Aerospace Center)
DNB	Direct Numerical Beamforming
DNW	Deutsch Niederländischer Windkanal (German–Dutch Wind tunnels)
DR	Diagonal Removal
EMI	ElectroMagnetic Interference
EPNL	Effective Perceived Noise Level
ETW	European Transonic Wind Tunnel
FAA	Federal Aviation Administration
FFT	Fast Fourier Transform
FPGA	Field–Programmable Gate Array
FW–H	Ffowcs Williams–Hawkings
GE	General Electric
GIBF	Generalized Inverse BeamForming

GMF	Global Market Forecast
GPS	Global Positioning System
GSP	Gasturbine Simulation Program
HWA	Hot–Wire Anemometry
IAE	International Aero Engines
IBIA	Iterative Bayesian Inverse Approach
ICAO	International Civil Aviation Organization
IDFT	Inverse Discrete Fourier Transform
IDDES	Improved Delayed Detached Eddy Simulation
ILS	Instrument Landing System
INM	Integrated Noise Model
ISPI	Inverse Source Power Integration
KTH	Kungliga Tekniska Högskolan (Royal Institute of Technology (Sweden))
LAGOON	LAnding Gear nOise database and CAA validatiON
LBM	Lattice Boltzmann Method
LE	Leading Edge
LG	Landing Gear
LLF	Large Low–speed Facility (DNW)
LORE	Localization and Optimization of phased array REsults
LPD	Linear Programming Deconvolution
LST	Low–Speed Tunnel (DNW)
MEMS	Micro ElectroMechanical Systems
MIT	Massachusetts Institute of Technology
MLG	Main Landing Gear
MSL	Maximum Sidelobe Level
NACA	National Advisory Committee for Aeronautics
NASA	National Aeronautics and Space Administration
NG	Next Generation
NI	National Instruments
NLG	Nose Landing Gear
NLR	Nederlands Lucht– en Ruimtevaartcentrum (Netherlands Aerospace Center)
NMT	Noise Monitoring Terminal
NNLS	Non–Negative Least Squares
NOMOS	NOise MOnitoring System
NPD	Noise–Power–Distance
NWB	Niedergeschwindigkeits–Windkanal Braunschweig (Low–sped wind tunnel, DNW)
OASPL	Overall A–weighted Sound Pressure Level
OMP	Orthogonal Matching Pursuit
ONERA	Office National d'Etudes et de Recherches Aerospatiales (French Aerospace Lab)
OSPL	Overall Sound Pressure Level
PA	Psychoacoustic Annoyance
PANAM	Parametric Aircraft Noise Analysis Module

PIV	Particle Image Velocimetry
PNL	Perceived Noise Level
PNLT	Perceived Noise Level (Tone–corrected)
PSA3	Pieter Sijtsma Advanced AeroAcoustics
PSD	Power Spectral Density
PSF	Point Spread Function
PW	Pratt & Whitney
RMS	Root–Mean–Square
ROI	Region Of Integration
RPK	Revenue Passenger Kilometer
RR	Rolls–Royce
SEM	Spectral Estimation Method
SEMWAN	Spectral Estimation Method With Additive Noise
SNR	Signal–to–Noise Ratio
SODIX	SOurce DIrectivity modeling in the cross–spectral matriX
SPI	Source Power Integration
SPIL	Source Power Integration (Line extension)
SL	Sidelobe Level
SPL	Sound Pressure Level
STE	Straight Trailing Edge
sUAS	Small Unmanned Aerial System
TBL	Turbulent Boundary Layer
TE	Trailing Edge
TED	Trailing Edge Devices
TU Delft	Delft University of Technology (the Netherlands)
UniA	University of Adelaide (Australia)
UTwente	University of Twente (the Netherlands)
VKI	Von Karman Institute for Fluid Dynamics (Belgium)
VLES	Very Large Eddy Simulation

1

Introduction

If someone offers you an amazing opportunity
and you are not sure you can do it, say yes;
Then learn how to do it later.

Sir Richard Charles Nicholas Branson

The journey of a thousand miles begins with one step

Lao Tzu

This introduction explains the motivation for this thesis, namely the importance of the noise emissions by aircraft and wind turbines. A brief overview is provided about the current and most widely used approaches in the field aeroacoustics, with an special focus on the importance of phased microphone arrays.

1

1.1. Motivation

Sound is one of the most basic ways of communication and interaction for humans. In general, most animals can produce some kind of noise and have some sort of sensor to perceive the small pressure variations that define a sound wave. Sound can be pleasant to hear such as for (most) music types, but it can cause annoyance to the receiver as in the form of noise. Nowadays, several sources of noise pollution are common around us, especially in large cities. This thesis focuses on two main noise sources from the aerospace industry: aircraft noise and wind turbine noise.

First of all, the noise levels from individual aircraft have considerably decreased in the last decades due to a considerably amount of research which lead to noise reduction measures, such as the introduction of the high–bypass–ratio turbofan engines and acoustic liners [1, 2], which reduced the noise emissions with respect to the older turbojet engines. Despite this reduction in the noise levels per aircraft, the ever–increasing demand for flights (with an approximate growth of about 5% per year [3, 4]) causes the volume of air traffic to approximately double every 15 years, see Fig. 1.1, with more than $30,000$ new airliners expected to be required in the next 20 years [4]. Furthermore, stricter noise regulations [5, 6] make aircraft noise an increasingly important issue for the aeronautic industry, with a loss of revenue due to night curfews and limits in the amount of operations in airports [7]. It is also a social issue, especially for the population living close to airports. Airports are, especially in densely populated countries like the Netherlands[1], normally surrounded by urban areas [8] and more people are becoming affected due to the low flight altitudes and fixed traffic routing associated with typical approaches. Noise pollution can lead to severe health problems, such as hypertension, sleep deprivation, and harmful cognitive effects [9]. Obtaining accurate knowledge of aircraft noise levels is desired for reliably enforcing environmental laws in the vicinity of airports. Noise prediction models (see section 1.3.4) are typically employed for land–use planning and management worldwide. Thanks to the aforementioned reductions in engine noise, airframe noise is becoming increasingly important during approach, even reaching higher noise levels than the engines in some cases, and has been identified as a potential lower aircraft noise barrier [10]. The impact of aircraft noise on the population can be decreased in different ways, such as aircraft rerouting, installation of sound barriers around buildings, etc. The main aim in this thesis, however, is to (further) reduce the noise levels at the source itself. For this task, and to obtain accurate aircraft noise predictions, it is essential to accurately determine and analyze all possible noise sources on–board. Individual microphones only provide total noise levels, but do not offer information about the locations and strengths of the individual sound sources, such as engines, landing gears and high–lift devices.

The second object of study of this thesis are wind turbines. The growing demand of energy consumption and the global aim to search for sustainable energy sources have caused an increase in the number of wind turbines installed and the size of

[1] As an example, Lelystad Airport in the Netherlands is expected to be expanded due to the congestion of Amsterdam Airport Schiphol. This decision was received with considerable controversy and displeasure by the Dutch population because of the expected increase in the noise levels.

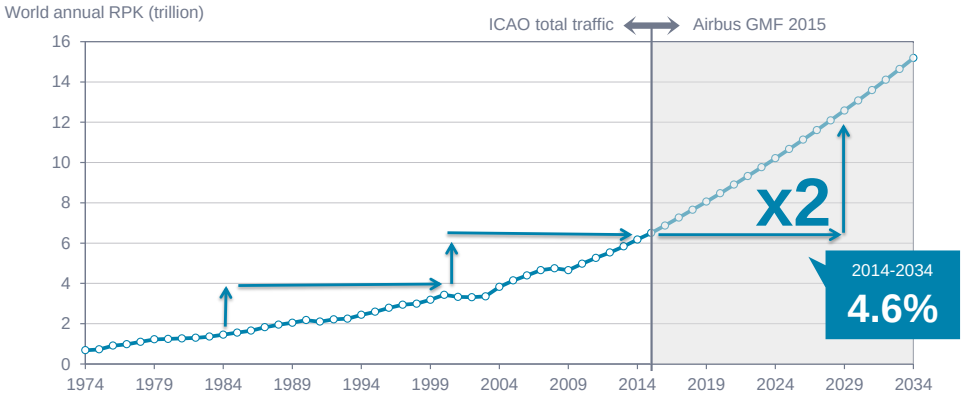

Figure 1.1: Annual world air traffic (in trillion Revenue Passenger Kilometer (RPK)): historical values by ICAO (International Civil Aviation Organization) and predictions by the Global Market Forecast (GMF) of Airbus S.A.S. Adapted from [4].

their blades, see Fig. 1.2. At the time this thesis was written, the largest operating wind turbine was the MHI Vestas V164 with a rotor diameter of 164 m and a nominal capacity of 9.5 MW. LM Wind Power has manufactured the longest blade with a length of 88.4 m, which will be installed on the Adwen wind turbine with a rotor diameter of 180 m and a nominal capacity of 8 MW [11]. Wind turbines can also be placed offshore, but installing wind turbines onshore is typically simpler in terms of installation and maintenance [12]. The placement of wind farms close to urban areas and strict noise regulations make noise emissions from wind turbines one of the main issues that the wind energy industry currently must deal with. For example, because of the noise, many wind turbines are required to operate at low power conditions during the night, with a consequent loss of energy production and revenue. It is estimated that a decrease of 1 dB of the sound pressure level (SPL or L_p, see Appendix A.1) is expected to allow an increase in energy production by 2 to 4% [13]. Given that the average expected lifetime of a typical modern wind turbine is approximately 20 years, these restrictions can cause losses of the order of millions of euros **per** wind turbine. As for the case of aircraft noise, the exposure of wind turbine noise also has harmful health effects for the population [14, 15]. The main noise source in modern wind turbines is the turbulent boundary layer trailing edge noise of the blades [16], especially at the tips since they move at a higher velocity, see Fig. 3.8 and Chapter 2.3. Therefore, for the case of wind turbines, it is of higher interest to assess the performance of noise reduction measures [17, 18], rather than investigating the already–known location of the noise sources. However, this task is also challenging with only the use of individual microphones.

In order to estimate the location and strength of sound sources, phased microphone arrays can be used. Section 1.2 provides a brief overview of the historical development of these tools.

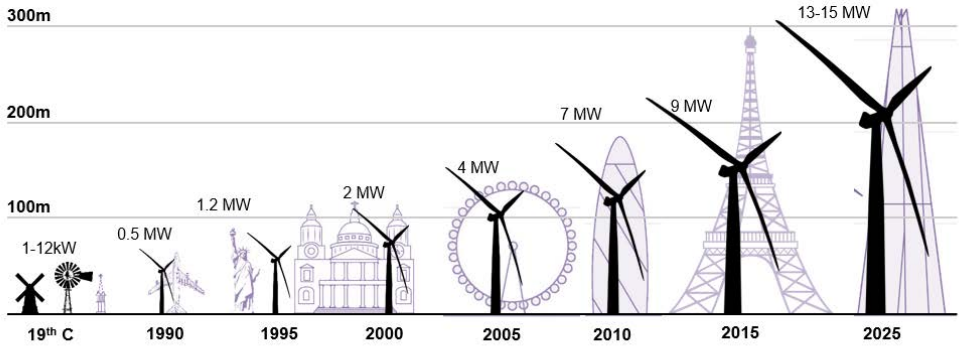

Figure 1.2: Historical evolution of wind turbine sizes and power output. Adapted from [19].

1.2. A brief historical overview of microphone arrays

The use of phased arrays dates back to World War II as radar antennas, later developed for applications such as the sonar, radioastronomy, seismology, mobile communication or ultrasound medical imaging [20]. The theory of electromagnetic antenna arrays was already applied in the field of acoustics for determining the direction of arrival of sound sources by Davids et al. in 1952 [21]. The phased microphone array (also known as microphone antenna, acoustic telescope, acoustic array or acoustic camera) was introduced by Billingsley in 1976 [22, 23] as an alternative to the acoustic mirror [24, 25]. An acoustic mirror is an elliptic mirror that focuses sound rays from a potential source location (at one of the focal points of the ellipse) to the other focal point, where a microphone is located [26]. Hence, the mirror requires to be displaced for each potential source location, which makes the measurements time–consuming and, therefore, expensive. By using several synchronized microphones in an array and a source localization algorithm [27, 28], the possibility to estimate the location and strength of sound sources was enabled. Since then, significant improvements have been made, for a large part by more powerful acquisition and computing systems [20], allowing higher sampling frequencies, longer acquisition times, larger numbers of microphones and even real–time sound source localization. Moreover, microphone arrays only require shorter measurement times than an acoustic mirror, because the scanning of potential source locations can be performed as postprocessing afterwards [26].

Acoustic imaging algorithms [28] are the essential link between the sound field measured at a number of microphone positions and the assessment of useful characteristics of noise sources, such as their locations and absolute sound levels. The main idea is to combine the data gathered by the microphone array with a sound propagation model to infer on the source parameters [29]. Conventional beamforming [27, 28] (see sections 4.1 and 4.2) is perhaps the most basic postprocessing approach for the signals recorded by the microphones, but it normally fails to provide satisfactory results for practical applications. The localization and quantification

of sound sources are limited by the geometry of the array. Most acoustic imaging methods are exhaustive search techniques, in which a selected grid containing the location of potential sound sources is scanned.

The development of advanced source localization algorithms has played a large role in recent years to further improve source identification and quantitative results [29]. These methods normally imply a higher computational cost due to the more sophisticated approaches considered. Two main categories can be considered: deconvolution techniques, which postprocess the results obtained using conventional beamforming, and inverse methods, which aim at solving a typically under–determined inverse problem accounting for the presence of all sound sources at once. Other classifications of acoustic imaging methods considering other criteria have been presented in the literature [29]. A description of several of these advanced methods is included in Chapter 4.

In general, measurements with phased microphone arrays provide certain advantages with respect to measurements with individual microphones when performing acoustic measurements [30]. For experiments in wind tunnels with open and closed test sections, as well as in engine test cells, the background noise suppression capability of the source localization algorithms is very useful [20, 31–33], as well as the removal of reflections from the walls [34, 35]. Acoustic imaging can also be applied to moving objects, such as flying aircraft or rotating blades, provided that the motion of the source is tracked accurately [20]. Moreover, microphone arrays are useful tools for studying the variability of the noise levels generated by different aircraft components, within the same aircraft type [6, 36–38] in order to improve the noise prediction models in the vicinity of airports. Nowadays, the microphone array has become the standard tool for analyzing noise sources on flying aircraft [39–44], trains [45–47], cars [48–50], snowmobiles [51], and other machinery, such as wind turbines [16, 52].

1.3. Current approaches in aeroacoustics

Several approaches can be distinguished in the field of aeroacoustics. In this thesis four categories are proposed: wind–tunnel experiments, field experiments, computational simulations and noise prediction models. A brief description of each approach is given below and the practical challenges associated with the experimental measurements (wind–tunnel experiments or field tests) are explained in detail in Chapter 3.

1.3.1. Wind–tunnel experiments

Measurements in wind tunnels are one of the main methods for aeroacoustic testing for several decades [53–55], as they offer a controlled environment. They typically feature scaled models in closed or open–jet test sections. The former provide better aerodynamic conditions but present challenges for placing the microphones outside of the flow, whereas the latter allow for easier acoustic measurements but have poorer aerodynamic properties [56].

Aeroacoustic measurements in wind tunnels allow for controllable conditions

(flow velocity, angle of attack, etc.), repeatability of the results, accurate knowledge of the model position, and, in general, cheaper experimental setups than for field measurements. One of the main challenges for wind–tunnel experiments is to replicate the exact conditions present at an aircraft in operational conditions [57] or in full–scale wind turbines in a field, because of the typically smaller scale and less–detailed geometry of the wind–tunnel models [58], the installation effects inside of the tunnel, or a discrepancy in the Reynolds number (see Appendix B.2) [30]. More information about the challenges in wind–tunnel measurements can be found in section 3.1.1.

In addition, a common non–intrusive flow visualization tool in wind tunnel measurements is Particle Image Velocimetry (PIV) [11, 59, 60], which can be used to resolve the flow characteristics (namely the velocity field) over the time and obtain data in a field of view of interest, such as close to the surface of the model. Far–field noise estimations can be obtained by applying an acoustic analogy [61] to the surface pressure data. Other methods, such as Hot–Wire Anemometry (HWA), require the placement of measurement instrumentation inside of the flow, but they can be used to obtain information downstream of the model, such as characteristics of the boundary layer at the trailing edge.

1.3.2. Field experiments

Since it is almost impossible to test full–scale models of aircraft or wind turbines in wind tunnels under similar conditions as in reality, it is essential to perform field measurements under operational conditions with full–size models. With this kind of experiments, the actual conditions found in practice are fully reproduced. However, there is lower or no controllability of the flow characteristics, typically higher distances between sound source and observer, less accurate knowledge about the exact model position and the fact that (at least for aircraft and wind turbines) the sound source is in constant movement [62]. In addition, these experimental campaigns are typically more costly than wind–tunnel tests. On the other hand, the fact that the sound sources are moving allows for a study of the sound emissions as a function of time [12] and, if the setup is appropriate, a sound radiation directivity analysis.

1.3.3. Computational simulations

Computational simulations for aeroacoustic purposes typically solve the equations for fluid motion [63] and the acoustic wave equation [64], which account for the aerodynamic sound source and the propagation of the acoustic waves, respectively [65]. These computations are normally quite time–consuming since they have to determine the noise source generation and its propagation [12], which normally limits the complexity of the shape of the model to be analyzed to simple geometries [65]. Hence, highly accurate tools are required. On the other hand, extensive wind–tunnel or flyover test campaigns usually have a large economic cost limiting the amount of configurations available to study. The field of Computational AeroAcoustics (CAA), which is a subfield of Computational Fluid Dynamics (CFD), has become of high interest after recent advances in computation allowed for solving

the source field accurately and obtaining time–resolved solutions [12].

Different CAA methods are available [12, 66, 67], but in this thesis only the Lattice Boltzmann Method (LBM) [68] is considered. The LBM method solves the kinetic equation in a mesoscopic scale to calculate the macroscopic fluid dynamic parameters on a Cartesian mesh, i.e., a lattice. It considers a collision modeling and explicit time–stepping, which makes the computational requirements for LBM simulations considerably shorter than other computational methods, such as implicit Navier–Stokes simulations [12].

After the flow field has been determined computationally, the noise emissions in the far–field can be estimated by propagating the pressure fluctuations around the model employing Lighthill's acoustic analogy [69]. Several solutions for Lighthill's analogy have been proposed in the past [69–71], but the Ffowcs Williams–Hawkings (FW–H) equation [61] is normally considered as the most general form of the wave equation which can consider sources in constant motion [12]. The accuracy of the far–field noise calculations mainly depends on the accuracy of the CFD simulations [12]. This method is employed for trailing–edge noise calculations in Chapter 6.

Recent studies [72, 73] employ simulated microphone arrays in the computational domain to apply acoustic imaging methods to the obtained far–field results to estimate the location and strength of the sound sources. This allows for the non–intrusive study of the noise emissions in directions that are impractical in wind–tunnel experiments, such as upwind from the model. Comparison with experimental measurements [72, 74] showed very similar results.

1.3.4. Noise prediction models

Instead of CAA simulations, use can be made of noise prediction models, which are relatively computationally cheaper, in case a large amount of estimations is required, such as for calculating noise contours or performing an iterative aircraft design loop. Hence, noise prediction models are of paramount importance for land–use planning and assessment of noise abatement procedures around airports [5]. These models are typically fully empirical (based only on interpolating or extrapolating measured experimental data) or semi–empirical (including some noise generation physics expected by the theory through certain design and operation parameters) [65]. These models normally estimate the sound spectra and directivity functions analytically, and use an empirical database for approximating the remaining noise characteristics. Several aircraft noise prediction models can be found [5] and they can be classified into two categories:

1. "*Best–practice*" methods which are developed to calculate the sound level at the receiver but are not accurate enough for assessing the performance of noise abatement procedures [5], since several aircraft configuration details are not accounted for in such methods.

2. More sophisticated, semi–empirical parametric prediction models, such as SIMUL [75], ANOPP [76] or PANAM [77] describe the sound emission and propagation separately and offer more detailed predictions. They model the noise emissions of selected aircraft elements and then superimpose them to

yield the overall aircraft noise signal, which is then propagated to selected arbitrary observer locations. Moving source effects can be applied. However, they require very detailed input data, which are not typically publicly available and their database is limited to a small number of aircraft [5]. In addition, these programs are not accessible to other users. The last two models (ANOPP and PANAM) are introduced in the following sections.

Empirical models can also be used for estimating far–field noise emissions of wind turbines [78] but they will not be treated in this thesis.

Best–practice methods

The current practice to estimate aircraft noise levels is typically based on legal compliance methods such as those described in Document 29 of the ECAC (European Civil Aviation Conference) [79]. When using such methods, noise contours around airports can be calculated to represent the noise impact of aircraft operations over a period of time. Hence, these contours are often employed to set noise limits, estimate future aircraft impact, and for law enforcement purposes. Scientifically, the methodology of ECAC's Document 29 can be called "*best–practice*": relatively large assumptions are made, either for practical reasons or due to the lack of detailed data. The noise levels are estimated for each operation using "*look–up*" tables, such as the Noise–Power–Distance (NPD) tables, whereby the aircraft thrust settings and distance to the observer are key inputs. After determining the noise levels from these tables for a specific observer position, corrections such as lateral attenuation, segment event level corrections, installation effects, and bank angle effects may apply [80]. In this practical calculation series, individual results can balance out unnoticed against each other. Therefore, it is highly recommended to validate each model element separately to ensure that future modifications actually improve the overall methodology. Comparisons between aircraft noise prediction models and experimental measurements have been done in the past [5, 80, 81] showing considerable differences. In chapter 7, the method described in Document 29 of the ECAC is further explained for a practical case in section 7.3.

Similar versions of the Document 29 of the ECAC method developed by the American Federal Aviation Administration (FAA) are the Integrated Noise Model (INM) [82–85] and the newer and extended version of it, the Aviation Environmental Design Tool (AEDT) [86]. These methods also make use of the NPD tables for their predictions. Other national models are used in practice [5].

ANOPP

The Aircraft NOise Prediction Program (ANOPP) [87–89] was introduced by NASA in the 1980s as a prediction tool for the noise generated by the many contributing sources depending on the aircraft flight conditions and atmospheric propagation conditions [90]. This tool is mainly based on semi–empirical methods for estimating the contributions of several aircraft noise sources, divided into airframe and engine noise [90]. ANOPP is relatively fast computationally and at the same time it offers good–quality predictions in terms of community noise metrics. ANOPP is employed by governmental agencies and stakeholders in the aircraft industry to assess the

noise emissions of currently existing aircraft, as well as to estimate the performance of new noise–reduction technologies [90]. The code is continuously updated and new noise source models are implemented [91].

Recently a new version of ANOPP, ANOPP2 [92] has been released, which integrates additional higher–fidelity noise prediction and propagation methods and can consider unconventional aircraft too, such as blended wing body configurations.

Some prediction tools inside of ANOPP for specific noise sources are explained in Chapter 2.

PANAM

The German Aerospace Center (DLR) has developed an aircraft system noise prediction tool called the Parametric Aircraft Noise Analysis Module (PANAM) [77, 91]. PANAM models the overall aircraft noise as a sum of individual noise components on–board and their interactions. Specific noise source models are applied to simulate the major noise sources, i.e., airframe and engine contributions, and ultimately to obtain the ground noise impact of the whole aircraft. These noise source models are parametrical, hence they allow to modify the underlying parameters of each source. As a consequence, the parameters which refer to the operational and geometrical data can be optimized for minimal noise contribution (within predefined limits). This tool is mainly used to assess the impact of low–noise modifications to individual components on–board of existing aircraft or for the design of new low–noise aircraft [93]. Therefore, this tool can be integrated within the conceptual aircraft design loop, allowing for the assessment of different noise reduction techniques at the beginning of the design chain [7]. In essence, PANAM is relatively similar to ANOPP in the noise generation mechanisms it considers and the way it estimates the aircraft noise levels.

A comparison between the estimations obtained by PANAM and experimental measurements for a landing Airbus A320 aircraft are presented in section 5.2.1.

1.3.5. Summary of all approaches

All the aforementioned approaches in aeroacoustics have their advantages and disadvantages and they all have their own purpose, accuracy and cost. A (very general) overview of all the considered approaches is included in Table 1.1.

1.4. Assumptions made in this thesis

Throughout this thesis, several assumptions are made and, unless explicitly stated, they apply to the whole manuscript:

- Only linear acoustics are considered. Therefore, the classical linear wave equation [64] applies:

$$\frac{1}{c^2}\frac{\partial^2 p}{\partial t^2} - \nabla^2 p = 0, \tag{1.1}$$

  where c is the speed of sound, p is the static acoustic pressure, t is the time and ∇ is the *nabla* operator [64].

Table 1.1: Summary of the main characteristics of the acoustic imaging methods introduced.

Approach	Advantages	Disadvantages	Typical applications
Wind-tunnel experiments	✓ Controlled flow conditions ✓ Easy repeatability of results ✓ Accurate knowledge of the model position ✓ Other techniques (PIV, HWA, etc.)	× Relatively expensive experimental setup × Reynolds and scaling effects (see Ch. 3) × Challenging measurement environment (see Ch. 3)	• Test scaled models of aircraft, aircraft components or wind turbine blades. • Assessment of noise reduction measures
Field experiments	✓ Actual operational conditions as found in practice ✓ Source motion considered ✓ Most reliable results	× Expensive experimental setup × Less controlled experimental conditions × Sound propagation considerations (see Ch. 3)	• Full-scale tests under real-life operational conditions • Assessment of noise reduction measures • Comparison with noise prediction models
Computational simulations	✓ Relatively cheap (compared to experiments) ✓ Controlled flow conditions ✓ Full knowledge of flow parameters	× Very high computational cost (short recording times) × Normally limited to simple geometries	• Test models of aircraft, aircraft components or wind turbine blades. • Assessment of noise reduction measures
"Best practice" noise prediction models	✓ Computationally cheap (multi-event calculations) ✓ Relatively easy to use (few inputs required)	× Relatively large assumptions are made × Not accurate enough for detailed noise studies	• Calculation of noise contours around airports • Enforcement of environmental laws
Advanced noise prediction models (PANAM, ANOPP)	✓ Individual source contributions controlled by parameters ✓ Able to predict future aircraft noise levels	× Very detailed input data is required × Limited accessibility × Small number of aircraft types	• Noise calculations within conceptual aircraft design (future aircraft) • Assessment of noise reduction measures

- Only subsonic flows (Mach numbers less than one, i.e., $M = V/c < 1$, where V is the mean flow velocity) are considered, see Appendix B.1.
- Sound sources are considered as incoherent, omnidirectional, point monopoles [64], especially for acoustic imaging methods, see Chapter 4. The extension to other source models, such as dipoles and quadrupoles [64] is normally simple.

1.5. Research objectives

In this chapter the motivations on reducing both aircraft and wind turbine noise have been clearly stated and the concept of phased microphone array has been introduced. From this point, four different research objectives can be formulated for the present thesis:

1. **Analyze the state–of–the–art acoustic imaging methods for microphone arrays and assess their performance and applicability to aeroacoustic measurements on typical aerospace noise sources.**
2. **Perform experiments with microphone arrays on typical airframe noise sources, such as landing gear noise, and, when possible, compare the results obtained with other aeroacoustic approaches, such as CAA or noise prediction models.**
3. **Evaluate the performance of noise reduction measures on airfoil noise for wind turbine applications using wind–tunnel measurements.**
4. **Assess the measured variability of aircraft noise flyovers under similar operational conditions, analyze potential causes for this variability, and compare the results with current noise prediction models.**

1.6. Thesis outline

This thesis is structured according to the research objectives defined in section 1.5.

In order to solve **objective 1** Chapters 2, 3 and 4 are included. Chapter 2 provides a description of the typical aerospace noise sources on both aircraft and modern wind turbines, as well as some insight on the noise generation mechanisms, current research and noise prediction models. Chapter 3 enumerates the most common challenges in aeroacoustic experiments, especially in open–jet and closed–section wind tunnels and in field measurements. Comparisons between these approaches are given, as well as some sound propagation considerations. Moreover, practical recommendations are provided for experiments with microphone arrays. Chapter 4 provides a thorough list of the most common and state–of–the–art acoustic imaging methods for microphone arrays (including deconvolution and inverse techniques) and recommendations on their use in aeroacoustic experiments. Several comparisons between different methods are presented.

With the aim to treat **objective 2**, Chapter 5 contains a complete study on landing gear noise emissions, including flyover measurements under operational

conditions, wind–tunnel experiments, CAA simulations and comparisons with the current noise prediction methods.

Research **objective 3** is treated in Chapter 6, where studies on the most promising airfoil trailing–edge noise reduction measures are presented. The performances of trailing–edge serrations and porous materials inserts are investigated in several wind–tunnel experimental campaigns. Several parameters are investigated, such as the angle of attack, serration geometry, serration–flow misalignment angle and the characteristics of the porous material inserts. This chapter contains comparisons between experimental results in different facilities, and with CAA simulations and noise prediction models.

Lastly, research **objective 4** is addressed in Chapter 7. A large number of aircraft flyover recordings under operational conditions are analyzed in order to assess the variability in the noise levels within the same aircraft type under similar conditions. Approaches for calculating the fan rotational speed of an aircraft flyover using only the audio signal are proposed and used. Comparisons of the results with the "*best–practice*" noise prediction models are included.

Finally, Chapter 8 gathers the main conclusions and recommendations for future work drawn from the whole thesis.

Bibliography

[1] G. Ruijgrok, *Elements of aviation acoustics*, Second ed. (VSSD, 2007) ISBN: 1090–6562–155–5.

[2] H. H. Hubbard, *Aeroacoustics of Flight Vehicles: Theory and Practice – Volume 1: Noise Sources*, Tech. Rep. NASA Technical Memorandum 1258 (NASA Reference Publication 1258, 1991).

[3] *Current Market Outlook 2013–2032*, Tech. Rep. (Boeing Commercial Airplanes, USA, 2013).

[4] *Global Market Forecast – Flying by Numbers 2015–2034*, Tech. Rep. D14029465 (Airbus S.A.S., Blagnac, France, 2015).

[5] C. Zellmann, B. Schäffer, J. M. Wunderli, U. Isermann, and C. O. Paschereit, *Aircraft Noise Emission Model Accounting for Aircraft Flight Parameters,* Journal of Aircraft (2017), 10.2514/1.C034275.

[6] M. Snellen, R. Merino-Martinez, and D. G. Simons, *Assessment of noise level variability on landing aircraft using a phased microphone array,* Journal of Aircraft **54**, 2173 (2017).

[7] L. Bertsch, *Noise Prediction within Conceptual Aircraft Design*, Ph.D. thesis, DLR (2013), DLR Forschungsbericht, ISRN DLR–FB–2013–20, ISSN 1434–8454.

[8] M. Arntzen, *Aircraft noise calculation and synthesis in a non–standard atmosphere*, Ph.D. thesis, Delft University of Technology (2014), ISBN: 978–94–62594–64–7.

[9] A. Hansell, M. Blangiardo, L. Fortunato, S. Floud, H. K. de, D. Fecht, R. Ghosh, H. Laszlo, C. Pearson, L. Beale, S. Beevers, J. Gulliver, N. Best, S. Richardson, and P. Elliott, *Aircraft noise and cardiovascular disease near Heathrow airport in London: small area study,* British Medical Journal **347** (2013), 10.1136/bmj.f5432.

[10] W. Dobrzynski, *Almost 40 Years of Airframe Noise Research: What Did We Achieve?* Journal of Aircraft **47**, 353 (2010).

[11] C. Arce León, *A Study on the Near–Surface Flow and Acoustic Emissions of Trailing Edge Serrations for the purpose of noise reduction of Wind Turbine Blades*, Ph.D. thesis, Delft University of Technology (2017), ISBN: 978–94–92516–68–8.

[12] W. C. P. van der Velden, *Computational aeroacoustic approaches for wind turbine blade noise prediction*, Ph.D. thesis, Delft University of Technology (2017), ISBN: 978–94–6186–756–8.

[13] S. Oerlemans, *Low–noise wind turbine design,* in *EWEA Workshop, December 11 – 12 2012. Oxford, United Kingdom* (2012).

[14] J. H. Schmidt and M. Klokker, *Health effects related to wind turbine noise exposure,* PLoS ONE **9**, 1 (2014).

[15] D. S. Michaud, K. Feder, S. E. Keith, and S. A. Voicescu, *Exposure to wind turbine noise: Perceptual responses and reported health effects,* Journal of the Acoustical Society of America **139**, 1443 (2016).

[16] S. Oerlemans, P. Sijtsma, and B. Méndez López, *Location and Quantification of Noise Sources on a Wind Turbine,* Journal of Sound and Vibration **299**, 869 (2007).

[17] S. Oerlemans, M. Fisher, T. Maeder, and K. Kögler, *Reduction of Wind Turbine Noise Using Optimized Airfoils and Trailing–Edge Serrations,* AIAA Journal **47**, 1470 (2009).

[18] S. Oerlemans, *Reduction of Wind Turbine Noise using Blade Trailing Edge Devices,* in *22nd AIAA/CEAS Aeroacoustics Conference. May 30 – June 1 2016. Lyon, France* (2016) AIAA paper 2016–3018.

[19] Bloomberg – Source for wind turbine evolution picture, *https://www.bloomberg.com/news/articles/2017-09-19/tipping-point-seen-for-clean-energy-as-monster-turbines-arrive,* Accessed in January 2018.

[20] U. Michel, *History of acoustic beamforming,* in *Proceedings on CD of the 1st Berlin Beamforming Conference, 22 – 23 November, 2006* (GFaI, e.V., Berlin, 2006).

[21] N. Davids, E. G. Thurston, and R. E. Mueser, *The Design of Optimum Directional Acoustic Arrays,* Journal of the Acoustical Society of America **24**, 50 (1952).

[22] J. Billingsley and R. Kinns, *The Acoustic Telescope,* Journal of Sound and Vibration **48**, 485 (1976).

[23] J. Billingsley, *A comparison of the source location techniques of the acoustic telescope and polar correlation,* Journal of Sound and Vibration **61**, 419 (1978).

[24] R. H. Schlinker, *Airfoil Trailing Edge Noise Measurements with a Directional Microphone,* in *4th AIAA Aeroacoustics Conference. October 3 – 5 1977. Atlanta, Georgia, USA* (1977) AIAA paper 1977–1269.

[25] F. R. Grosche, H. Stiewitt, and B. Binder, *Acoustic wind tunnel measurements with a highly directional microphone,* AIAA Journal **15**, 1590 (1977).

[26] S. Oerlemans, *Detection of aeroacoustic sound sources on aircraft and wind turbines*, Ph.D. thesis, University of Twente, Enschede, the Netherlands (2009).

[27] B. D. van Veen and K. M. Buckley, *Beamforming: A Versatile Approach to Spatial Filtering,* IEEE ASSP Magazine **5**, 4 (1988).

[28] D. H. Johnson and D. E. Dudgeon, *Array Signal Processing, Concepts and Techniques* (P T R Prentice Hall, Englewood Cliffs, 1993) ISBN: 978–0130485137.

[29] Q. Leclère, A. Pereira, C. Bailly, J. Antoni, and C. Picard, *A unified formalism for acoustic imaging based on microphone array measurements,* International Journal of Aeroacoustics **16**, 431 (2017), SAGE Publications Ltd. London, United Kingdom.

[30] R. Merino-Martinez, P. Sijtsma, M. Snellen, T. Ahlefeldt, J. Antoni, C. Bahr, D. Blacodon, D. Ernst, A. Finez, S. Funke, T. Geyer, S. Haxter, G. Herold, X. Huang, W. Humphreys, Q. Leclère, A. Malgoezar, U. Michel, T. Padois, A. Pereira, C. Picard, E. Sarradj, H. Siller, D. G. Simons, and C. Spehr, *Aircraft Noise Generation and Assessment: A review of acoustic imaging methods using phased microphone arrays, CEAS aeroacoustic journal*, CEAS Aeronautical Journal (2017), Accepted for publication.

[31] D. Blacodon, *Analysis of the Airframe Noise of an A320/A321 with a Parametric Method,* Journal of Aircraft **44**, 26 (2007).

[32] D. Blacodon, *Combustion–Noise Characterization of a Turbofan Engine with a Spectral Estimation Method,* Journal of Propulsion and Power 2009 **25**, 374 (2009).

[33] D. Blacodon, *Spectral estimation noisy data using a reference noise,* in *Proceedings on CD of the 3rd Berlin Beamforming Conference, 24 – 25 February, 2010, Berlin, Germany* (2010).

[34] S. Guidati, C. Brauer, and S. Wagner, *The reflection canceller – Phased array measurements in a reverberating environment,* in *8th AIAA/CEAS Aeroacoustics Conference and Exhibit, June 17-19, 2002, Breckenridge, Colorado, USA* (2002) AIAA paper 2002–2462.

[35] P. Sijtsma and H. Holthusen, *Corrections for Mirror Sources in Phased Array Processing Techniques,* in *9th AIAA/CEAS Aeroacoustics Conference, May 12 – 14, 2003, Hilton Head, South Carolina, USA* (2003) AIAA paper 2003–3196.

[36] D. G. Simons, M. Snellen, B. Midden, M. Arntzen, and D. H. T. Bergmans, *Assessment of noise level variations of aircraft fly–overs using acoustic arrays,* Journal of Aircraft **52**, 1625 (2015).

[37] M. Snellen, R. Merino-Martinez, and D. G. Simons, *Assessment of aircraft noise sources variability using an acoustic camera,* in *5th CEAS Air & Space Conference. Challenges in European Aerospace. September 7 – 11 2015, Delft, Netherlands*, Paper 2015–019 (Council of European Aerospace Societies, 2015).

[38] R. Merino-Martinez, M. Snellen, and D. G. Simons, *Determination of Aircraft Noise Variability Using an Acoustic Camera,* in *23rd International Congress on Sound and Vibration, July 10 – 14 2016, Athens, Greece* (International Inst. of Acoustics and Vibration (IIAV), Auburn, Alabama, USA., 2016).

[39] G. P. Howell, M. A. Bradley, M. A. McCormick, and J. D. Brown, *De–Dopplerization and acoustic imaging of aircraft flyover noise measurements,* Journal of Sound and Vibration **105**, 151 (1986).

[40] U. Michel, B. Barsikow, B. Haverich, and M. Schüttpelz, *Investigation of air–frame and jet noise in high–speed flight with a microphone array,* in *3rd AIAA/CEAS Aeroacoustics Conference, May 12-14, 1997, Atlanta, GA, USA* (1997) AIAA paper 1997–1596.

[41] U. Michel, B. Barsikow, J. Helbig, M. Hellmig, and M. Schüttpelz, *Flyover noise measurements on landing aircraft with a microphone array,* in *4th AIAA/CEAS Aeroacoustics Conference, June 2 – 4 1998, Toulouse, France* (1998) AIAA paper 1998–2336.

[42] J. F. Piet, G. Élias, and P. Lebigot, *Localization of acoustic source from a landing aircraft with a microphone array,* in *5th AIAA/CEAS Aeroacoustics Conference. Bellevue, WA, USA* (1999) AIAA paper 1999–1811.

[43] P. Sijtsma and R. Stoker, *Determination of Absolute Contributions of Aircraft Noise Components Using Fly–over Array Measurements,* in *10th AIAA/CEAS Aeroacoustics Conference, May 10 – 12 2004, Manchester, United Kingdom* (2004) AIAA paper 2004–2958.

[44] R. Merino-Martinez, M. Snellen, and D. G. Simons, *Functional beamforming applied to imaging of flyover noise on landing aircraft,* Journal of Aircraft **53**, 1830 (2016).

[45] B. Barsikow, W. F. King III, and E. Pfizenmaier, *Wheel/Rail Noise Generated by a High–Speed Train Investigated with a Line Array of Microphones,* Journal of Sound and Vibration **118**, 99 (1987).

[46] B. Barsikow and W. F. King III, *On Removing the Doppler Frequency Shift from Array Measurements of Railway Noise,* Journal of Sound and Vibration **120**, 190 (1988), letter to the editor.

[47] B. Barsikow, *Experiences with various configurations of microphone arrays used to locate sound sources on railway trains operated by the DB AG,* Journal of Sound and Vibration **193**, 283 (1996).

[48] U. Michel and B. Barsikow, *Localisation of sound sources on moving vehicles with microphone arrays,* in *Proceedings of EuroNoise 2003, May 19 – 21 2003, Naples, Italy*, paper ID 537 (2003).

[49] U. Michel, B. Barsikow, P. Böhning, and M. Hellmig, *Localisation of moving sound sources with phased microphone arrays,* in *Inter–Noise 2004, 22 – 25 August 2004, Prague, Czech Republic* (2004).

[50] S. N. Y. Gerges, W. D. Fonseca, and R. P. Dougherty, *State of the art beamforming software and hardware for application,* in 16^{th} *International Congress on Sound and Vibration, July 5 – 9 2009, Kraków, Poland* (2009).

[51] T. Padois and A. Berry, *Application of acoustic imaging techniques on snowmobile pass–by noise,* Journal of the Acoustical Society of America **141**, EL134 (2017).

[52] S. Oerlemans and B. Méndez López, *Acoustic Array Measurements on a Full Scale Wind Turbine,* in 11^{th} *AIAA/CEAS Aeroacoustics Conference, May 23 – 25, 2005, Monterey, California, USA* (2005) AIAA paper 2005–2963.

[53] R. K. Amiet, *Correction of Open Jet Wind Tunnel Measurements For Shear Layer Refraction,* in 2^{nd} *AIAA Aeroacoustics Conference, March 24 – 26, Hampton, VA, USA* (1975) AIAA paper 1975–532.

[54] H. H. Heller and W. M. Dobrzynski, *Sound Radiation from Aircraft Wheel–Well/Landing–Gear Configuration,* Journal of Aircraft **14**, 768 (1977).

[55] T. F. Brooks, M. A. Marcolini, and D. S. Pope, *A Directional Array Approach for the Measurement of Rotor Noise Source Distributions with Controlled Spatial Resolution,* Journal of Sound and Vibration **112**, 192 (1987).

[56] S. Kröber, *Comparability of Microphone Array Measurements in Open and Closed Wind Tunnels*, Ph.D. thesis, Technical University of Berlin (2014).

[57] R. Stoker, Y. Guo, C. Streett, and N. Burnside, *Airframe noise source locations of a 777 aircraft in flight and comparisons with past model–scale tests,* in *9th AIAA/CEAS Aeroacoustics Conference. May 12 – 14 2003. Hilton Head, South California, USA* (2003) AIAA paper 2003–3232.

[58] T. Mueller, *Aeroacoustic Measurements* (Springer Science & Business Media, 2002) p. 313, ISBN: 978–3–642–07514–8.

[59] S. Ghaemi, D. Ragni, and F. Scarano, *PIV–based pressure fluctuations in the turbulent boundary layer,* Experiments in Fluids **53**, 1823 (2012).

[60] S. Pröbsting, *Airfoil Self–Noise – Investigation with Particle Image Velocimetry*, Ph.D. thesis, Delft University of Technology (2015), ISBN: 978–94–61865–23–6.

[61] J. E. Ffowcs Williams and D. L. Hawkings, *Sound generation by turbulence and surfaces in arbitrary motion,* Philosophical Transactions of the Royal Society of London A – Mathematical, Physical and Engineering Sciences **264** (1969), 10.1098/rsta.1969.0031.

[62] R. Merino-Martinez, E. Neri, M. Snellen, J. Kennedy, D. Simons, and G. Bennett, *Comparing flyover noise measurements to full–scale nose landing gear wind–tunnel experiments for regional aircraft,* in *23rd AIAA/CEAS Aeroacoustics Conference. June 5 – 9 2017. Denver, Colorado, USA* (2017) AIAA paper 2017–3006.

[63] J. D. J. Anderson, *Fundamentals of Aerodynamics*, Third ed. (McGraw–Hill Series in Aeronautical and Aerospace Engineering, 2001) ISBN: 0–07–237335–0.

[64] S. Glegg and W. J. Devenport, *Aeroacoustics of Low Mach Number Flows – Fundamentals, Analysis, and Measurement* (Academic Press, 2017) p. 313, ISBN: 978–0–128–09651–2.

[65] A. K. Sahai, *Consideration of Aircraft Noise Annoyance during Conceptual Aircraft Design*, Ph.D. thesis, Rheinisch–Westfälische Technische Hochschule Aachen (2016).

[66] T. Colonius and S. K. Lele, *Computational aeroacoustics: progress on nonlinear problems of sound generation,* Progress in Aerospace Sciences **40**, 345 (2004).

[67] M. Wang, J. B. Freund, and S. K. Lele, *Computational prediction of flow–generated sound,* Annual Review of Fluid Mechanics **38**, 483 (2006).

[68] S. Succi, *The Lattice Boltzmann Equation For Fluid Dynamics and Beyond*, 1st ed. (Clarendon Press, 2001) ISBN: 9780198503989.

[69] M. J. Lighthill, *On sound generated aerodynamically, I: General theory,* Proceedings of the Royal Society of London. Series A, Mathematical and Physical Sciences **211**, 564 (1952).

[70] N. Curle, *The influence of solid boundaries upon aerodynamic sound,* Proceedings of Royal Society of London A **231**, 505 (1955).

[71] R. E. Musafir, *Sound generation by fluid flow,* in *23rd International Congress on Sound and Vibration, July 10 – 14 2016, Athens, Greece* (2016).

[72] D. P. Lockard, W. M. Humphreys, M. R. Khorrami, E. Fares, D. Casalino, and P. A. Ravetta, *Comparison of Computational and Experimental Microphone Array Results for an 18%–Scale Aircraft Model,* International Journal of Aeroacoustics **16**, 358 (2017), SAGE Publications Ltd. London, United Kingdom.

[73] H. Bouchouireb, N. J. Pignier, C. O'Reilly, S. Boij, and J. Dahan, *Identification of noise sources on a realistic landing gear using numerical phased array methods applied to computational data,* in *23rd AIAA/CEAS Aeroacoustics Conference. June 5 – 9 2017. Denver, Colorado, USA* (2017) AIAA paper 2017–3019.

[74] J. Bulté and S. Redonnet, *Landing Gear Noise Identification Using Phased Array with Experimental and Computational Data,* AIAA Journal **55**, 3839 (2017).

[75] U. Isermann, K. Matschat, and E. A. Mueller, *Prediction of Aircraft Noise Around Airports by a Simulation Procedure,* in *International Congress and Exposition of Noise Control Engineering, 21–23 July, 1986, Cambridge, Massachusetts, USA* (Institute of Noise Control Engineering, 11130 Sunrive Valley Drive, Suite 350 Reston, VA 20191, USA., 1986).

[76] K. B. Kontos, B. A. Janardan, and P. R. Gliebe, *Improved NASA–ANOPP Noise Prediction Computer Code for Advanced Subsonic Propulsion Systems. Volume 1: ANOPP Evaluation and Fan Noise Model*, Tech. Rep. NASA CR–195480 (NASA CR–195480, 1996).

[77] L. Bertsch, W. Dobrzynski, and S. Guérin, *Tool Development for Low–Noise Aircraft Design,* Journal of Aircraft **47**, 694 (2010).

[78] W. J. Zhu, *Aero–Acoustic Computations of Wind Turbines*, Ph.D. thesis, Technical Univeristy of Denmark (2007), ISBN: 978–87–7475–348–3.

[79] *CEAC Doc. 29. Report on Standard Method of Computing Noise Contours around Civil Airports. Volume 2: Technical Guide*, Tech. Rep. (European Civil Aviation Conference (ECAC), Neuilly sur Seine Cedex, France, 2016) 4th edition.

[80] R. Merino-Martinez, S. J. Heblij, D. H. T. Bergmans, M. Snellen, and D. G. Simons, *Improving Aircraft Noise Predictions by Considering the Fan Rotational Speed,* Journal of Aircraft (2018), 10.2514/1.C034849, Accepted for publication. DOI: 10.2514/1.C034849.

[81] R. Merino-Martinez, L. Bertsch, M. Snellen, and D. G. Simons, *Analysis of landing gear noise during approach,* in *22nd AIAA/CEAS Aeroacoustics Conference. May 30 – June 1 2016. Lyon, France* (2016) AIAA paper 2016–2769.

[82] *Procedure for the Calculation of Airplane Noise in the Vicinity of Airports, Aerospace Information Report AIR 1845*, Tech. Rep. 1845 (Society of Automotive Engineers, Inc. (SAE) - Committee on Aircraft Noise (SAE A-21), 400 Commonwealth Drive, Warrendale, PA 15096, 1986).

[83] *Recommended method for computing noise contours around airports (ICAO Circular 205–AN/1/25)*, Tech. Rep. 9911 (International Civil Aviation Organization (ICAO), Montreal, Canada., 1988).

[84] B. He, E. Dinges, J. Hemann, D. Rickel, L. Mirsky, C. Roof, E. Boeker, P. Gerbi, and D. Senzig, *Integrated Noise Model (INM) Version 7.0 User's Guide*, Tech. Rep. (Federal Aviation Administration (FAA) – U.S. Department of Transportation, Washington, DC, 2007) report No. FAA-AEE-07-04.

[85] E. Boeker, E. Dinges, B. He, G. Fleming, C. Roof, P. Gerbi, A. Rapoza, and J. Hemann, *Integrated Noise Model (INM) Version 7.0 User's Guide*, Tech. Rep. (Federal Aviation Administration (FAA) – U.S. Department of Transportation, Washington, DC, 2008) report No. FAA-AEE-08-01.

[86] Aviation Environmental Design Tool (AEDT) website, *https://aedt.faa.gov/,* Accessed in June 2017.

[87] W. E. Zorumski, *Aircraft Noise Prediction Program – Theoretical Manual – Part 1*, Tech. Rep. NASA Technical Memorandum 83199 (NASA Technical Memorandum 83199, 1982).

[88] W. E. Zorumski, *Aircraft Noise Prediction Program – Theoretical Manual – Part 2*, Tech. Rep. NASA Technical Memorandum 83199 (NASA Technical Memorandum 83199, 1982).

[89] H. H. Hubbard and J. C. Manning, *Aeroacoustic Research Facilities at NASA Langley Research Center*, Tech. Rep. NASA Technical Memorandum 84585 (NASA Technical Memorandum 84585, 1983).

[90] C. L. Burley, T. F. Brooks, W. M. Humphreys Jr., and R. J. J. W., *ANOPP Landing Gear Noise Prediction Comparisons to Model–Scale Data,* in *13th AIAA/CEAS Aeroacoustics Conference (28th AIAA Aeroacoustics Conference), May 21 – 23 2017, Rome, Italy* (2007) AIAA paper 2007–3459.

[91] L. Bertsch, S. Guérin, G. Looye, and M. Pott-Pollenske, *The Parametric Aircraft Noise Module – status overview and recent applications,* in *17th AIAA/CEAS Aeroacoustics Conference (32nd AIAA Aeroacoustics Conference), 5 – 8 June 2011, Portland, Oregon, USA* (2011) AIAA paper 2011–2855.

[92] L. V. Lopes and C. L. Burley, *ANOPP User's Manual*, Tech. Rep. NASA TM–2016–219342 (NASA, 2016).

[93] L. Bertsch, W. Heinze, and M. Lummer, *Application of an Aircraft Design–To–Noise Simulation Process,* in 14th AIAA Aviation Technology, Integration, and Operations Conference, June 16 – 20 2014, Atlanta, Georgia, USA (2014) AIAA paper 2014–2169.

2

Aerospace noise sources

Aeronautics was neither an industry nor a science.
It was a miracle.

Igor Ivanovich Sikorsky

A very friendly boom, like a pair of gleeful handclaps.

Sir Michael James Lighthill

No hay silencio en una ciudad y eso es muy duro,
tan duro como vivir con este miedo al futuro.

There is no silence in a city and that is very hard,
as hard as living with this fear of the future.

Javier Ibarra Ramos (*Javat y Kamel*)

This chapter provides a brief overview of the main noise sources present on flying aircraft and modern wind turbines. The research scope of this thesis is limited to the main noise sources according to literature: the turbofan engines, the landing gear system and airfoil noise. Explanations about their sound generation mechanisms, spectral shape, radiation pattern, noise prediction methods and potential noise reduction measures are included.

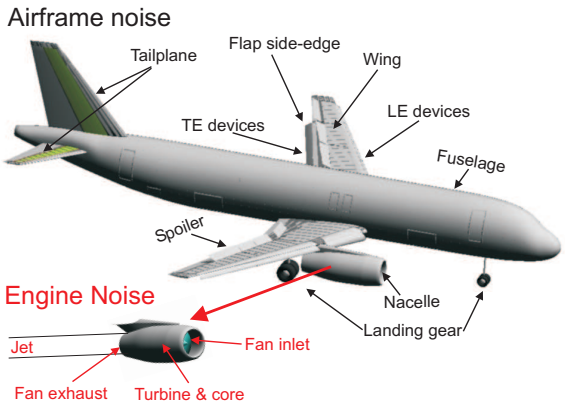

Figure 2.1: Major sources of aircraft noise. LE and TE stand for leading edge and trailing edge, respectively. Adapted from [6].

2.1. Introduction

2.1.1. Aircraft noise

There are several noise sources on–board of a typical commercial turbofan aircraft, which are illustrated in Fig. 2.1. These can be separated into airframe noise (generated by the interaction between the aerodynamic surfaces and the surrounding unsteady turbulent flow [1]) and engine noise (generated by the propulsion system). In the late 1970s, airframe noise was considered as the potential lower barrier for aircraft noise during approach [2], and due to advances in engine technology, such as high–bypass–ratio turbofan engines and acoustic liners [3], airframe noise currently presents similar noise contributions as engine noise in the approach stage [4].

Each source has a different noise generation mechanism, frequency components and sound directivity. In order to reduce aircraft noise levels accurate knowledge of each noise source is required. Extended research [5] has been performed in the past aiming at predicting the contributions of the major aircraft noise sources and assessing their relative importance, as it was mentioned in section 1.3.4.

Examples of such predictions are depicted in Fig. 2.2, where the breakdown of the major noise sources for an Airbus A319 aircraft is presented as overall A–weighted sound pressure levels ($L_{p,A}$ or OASPL, see Appendix A.2) for approach and departure operations, as experienced by an exemplary observer on the ground. For approach, the predictions indicate that the total airframe and total engine noise contributions present comparable values. A further breakdown of the airframe noise shows that the landing gear is the major airframe noise source, followed by the leading edge and trailing edge devices. This agrees with experimental results and theoretical predictions [4]. For departure operations, on the other hand, the engines are the dominant noise source, as expected. The total airframe noise contribution

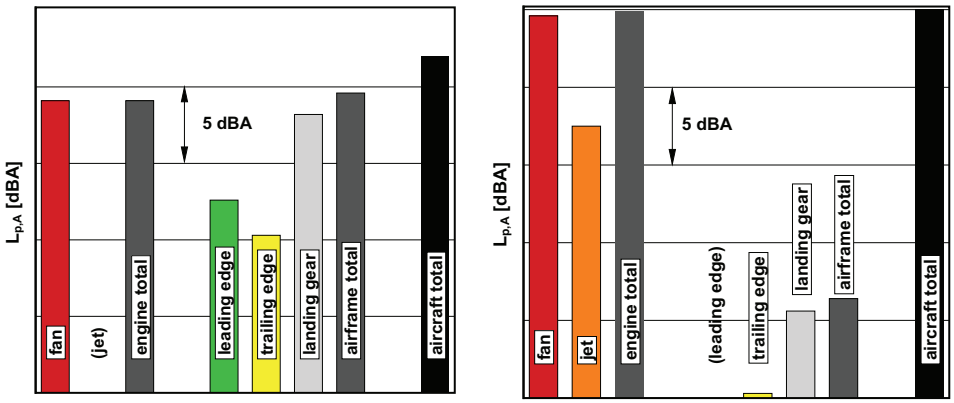

(a) Approach (b) Departure

Figure 2.2: Estimated aircraft noise source breakdown in overall $L_{p,A}$ for an Airbus A319 aircraft perceived by an observer on the ground during (a) approach and (b) departure. Adapted from [5].

is almost 20 dBA lower than that of the engines, becoming, therefore, negligible during departure.

In case the effective perceived noise level (EPNL, see Appendix A.4) metric is employed to assess the noise impact on the ground for the same aircraft approach, the total airframe noise contribution is around 3 EPNdB higher than the one from the engines, see Fig. 2.3. This could be due to the fact that almost idle conditions were considered for this estimation [5], and in this situation the tonal penalties of the EPNL metric due to the fan noise are considerably low because of the low fan rotational speed. These tonal penalties, however, dominate the EPNL metric for departures, see Fig. 2.2.

As mentioned before, the noise radiation pattern of each element of the aircraft is different. This can be observed in Figs. 2.5 and 2.6 where the estimated radiation patterns [7] of the main noise sources of a Boeing 747–400 aircraft with respect to the polar emission angle θ (see Fig. 2.4) are presented for an example approach and departure operation, respectively. These results were obtained with the noise prediction tool PANAM [6, 8] using the engine operating conditions estimated by the Gasturbine Simulation Program (GSP) [9]. The $L_{p,A}$ values correspond to a reference sphere with 1 m radius. The engine fan settings $N1\%$ (i.e., the relative fan rotational speed), the Mach number M and the deflection angles of the high–lift devices are specified for each figure in the captions. For the approach case (Fig. 2.5) the jet noise contribution is negligible and the airframe and fan noise are the main sources with comparable contributions. For the departure case (Fig. 2.6), however, the airframe contribution is negligible and fan noise is the dominant noise source (especially in the forward arc, i.e., $0° < \theta < 90°$) followed by the combustion noise. For both cases, the total noise directivity presents a maximum in the rearward arc, around $\theta = 120°$, with the difference that departure procedures present $L_{p,A}$ values around 10 dBA higher than approaches.

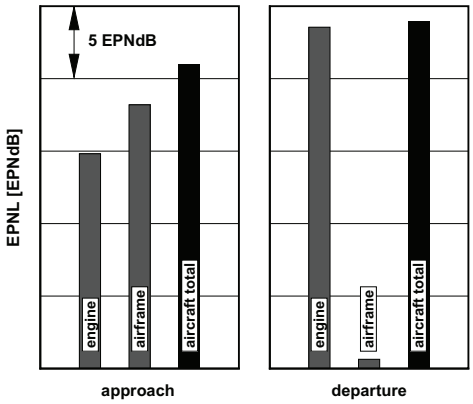

Figure 2.3: Estimated noise source ranking in EPNL for an observer on the ground and for an Airbus A319 aircraft during approach (left) and departure (right). Adapted from [5].

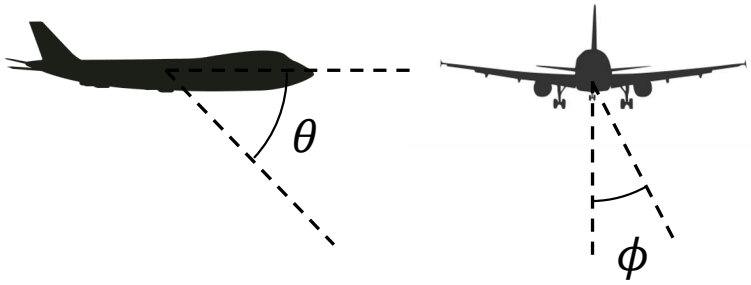

Figure 2.4: Diagram explaining the aircraft emission angles: (left) polar angle θ; (right) azimuthal sideline angle ϕ.

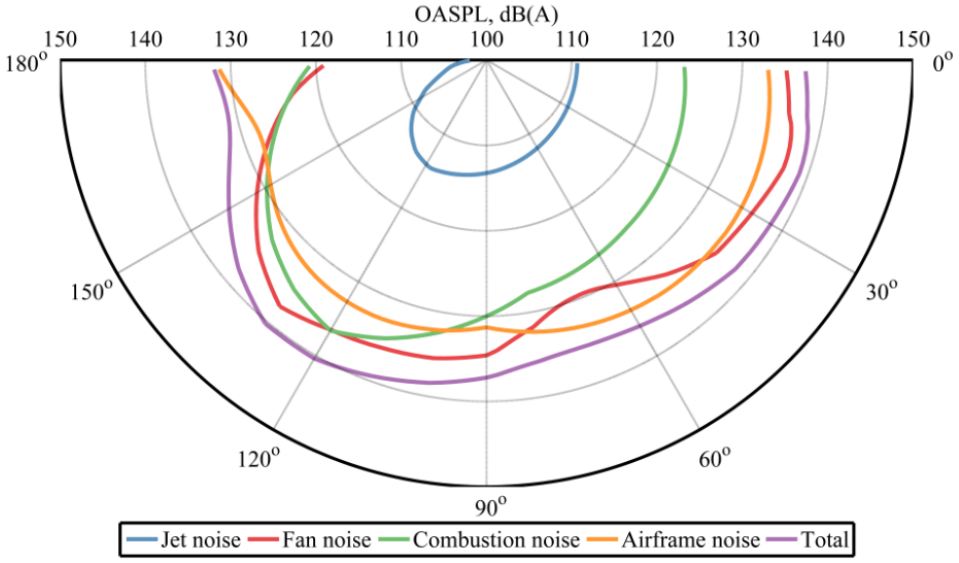

Figure 2.5: Predicted aircraft A–weighted noise levels for a Boeing 747–400 during approach with $N1 = 60\%$, $M = 0.22$, landing gear deployed and slats and flaps extended at $30°$ [7].

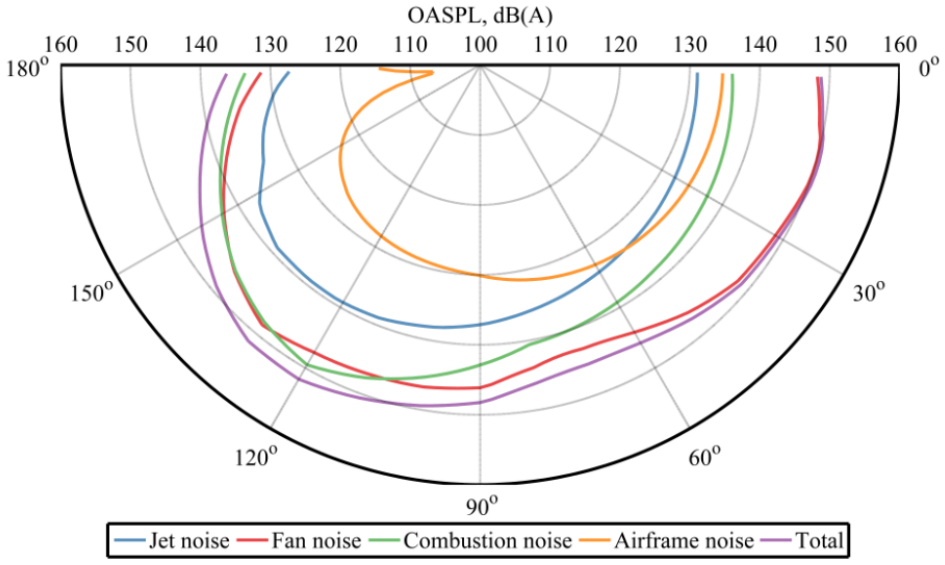

Figure 2.6: Predicted aircraft A–weighted noise levels for a Boeing 747–400 during departure with $N1 = 100\%$, $M = 0.25$ and slats and flaps extended at $10°$ [7].

2.1.2. Wind turbine noise

For the case of wind turbine noise [10, 11], a separation can be made between the noise generated mechanically in the hub (such as the gearbox, the generator or the cooling system inside the nacelle) and the noise generated aerodynamically due to the interaction between the incoming flow and the tower and the rotor blades [12], see Fig. 3.8a in Chapter 3. Whereas the first type of noise can be appropriately isolated by employing sound absorbing materials [13], it is difficult to isolate the aerodynamic noise because the sound sources are located on the rotor blades. Hence, aerodynamic noise is the dominant noise source for modern wind turbines. The generation mechanisms of aeroacoustic noise in wind turbine blades are further explained in section 2.3.

After having discussed the main noise sources responsible of aircraft and wind turbine noise, more detailed explanations of the sound generation mechanisms of some of the most important ones are included below: landing gear noise (section 2.2), airfoil noise (including high–lift devices, section 2.3) and engine noise (section 2.4).

2.2. Landing gear noise

2.2.1. Background and noise generation mechanism

The landing gear (LG) system is the main source of airframe noise for commercial aircraft [4, 14], which can generate approximately 30% of the whole aircraft noise during approach [5, 15], see Fig. 2.2. The LG system is typically a cluster of complicated structures of bluff bodies (struts, links, wheels, tires, fairings, etc.) of considerably different sizes, which are normally not optimized acoustically [16]. The usual components of a nose landing gear (NLG) system can be found in Fig. 5.7 in Chapter 5.

The same approaches explained in section 1.3 have been used in previous research to study LG noise [17]. The main methods are listed below, as well as their qualities and limitations:

1. **Wind–tunnel measurements** [18–22] offer controlled flow conditions but they require the LG model being tested to have a high level of geometric detail to represent the small–scale sound generating mechanisms [4, 14] and it is difficult to replicate the exact conditions present around a flying aircraft. The first scale models employed for studying LG noise in wind tunnels lacked design details and led to misleading results, underestimating the high–frequency noise [2, 4]. Only with tests featuring full–scale landing gears in high–quality acoustic wind tunnels in the 1990s [18], it was discovered that the maximum A–weighted sound pressure levels ($L_{p,A}$) in the frequency occur between 1 and 2 kHz [4], which is one of the most sensitive frequency ranges for the human ear [3].

2. **Flyover measurements** [14, 23–25] with aircraft under operational conditions present different challenges (see section 3.1.2), such as the inabil-

ity to control the aircraft position or less–controlled flow characteristics, but they fully represent the actual conditions experienced in reality [26, 27], such as crosswind. Differences between wind–tunnel and flyover measurements featuring a LG system normally occur, mostly due to lack of model fidelity, installation effects in the wind tunnel and discrepancies in the Reynolds number [28], see section 3.1.1. Hence, a comparison between the results of both experiments is of great interest [29].

3. **Computational simulations** [30–32] of a detailed LG geometry can be very time consuming due to its complex structure. In practice, for numerical simulations, the LG geometry is normally simplified to some extent, such that the computational cost becomes acceptable, such as the realistic NLG geometry from the ALLEGRA (Advanced Low noise Landing (main and nose) Gear for Regional Aircraft) project [30–32] or the more simplified geometry from the LAGOON (LAnding Gear nOise database and CAA validatiON) project from ONERA [33, 34].

4. **Noise prediction models** relying on semi–empirical data, such as Fink's [35] and Guo's [36, 37] models, provide one–third–octave–band noise spectra (see Appendix C.4) estimations for different directivity angles for simplified LG geometries. They require some geometrical parameters as input but they do not consider parasitic noise sources, such as cavities [23, 24]. Previous studies [23, 37, 38] showed that considerable differences exist between experimental measurements and the model predictions for LG noise. In addition, by their very nature, semi–empirical methods have a limited reliability in predicting the impact of noise reduction devices [30]. These models are further explained afterwards, in section 2.2.5.

2.2.2. Spectral shape

The frequency spectrum of LG noise can be separated into three components: the low–frequency component due to the large–scale elements such as the wheels, the mid–frequency component due to the main strut, and the high–frequency component due to all the small details and dressings, such as hydraulic lines [38]. This assumption was proposed by Guo [36, 37, 39]. A typical sound signal from a LG system is a complex combination of:

- **Broadband noise** caused by the turbulent flow separation off the bluff–body components of the LG and the interaction of the turbulent wake with other elements located downstream [2]. The turbulent flow interacts with the solid boundaries causing a small fraction of the turbulence energy to be radiated as sound waves modeled as compact acoustic dipoles with axes perpendicular to the strut axis and the inflow velocity vector [2, 36]. Thus, the acoustic intensity is expected to be proportional to the sixth power of the flow velocity V (i.e., $p^2 \propto V^6$) [40]. The main parameters governing the broadband noise radiation of the LG are the flow turbulence intensity, the average eddy length scale and the local flow velocity.

- **Tonal noise**, generated by:
  - Cavities [16, 41, 42] such as hollow pins in the numerous joints connecting different struts. The grazing turbulent flow over the orifices (either open on one or on both sides) can generate cavity resonances leading to tonal noise [2]. The excitation of such resonances depends on the cavity geometry and the local flow conditions (e.g., cross wind) [41, 42]. Hence, this phenomenon is considerably difficult to predict in aircraft operational conditions. The frequency of the tone depends on the cavity geometry [41]. This type of tones can be prominent and may govern the overall A–weighted LG noise level [2, 43].
  - Aeolian tones due to the flow separation and coherent periodic vortex shedding [19, 29] mainly from struts with smooth cross sections and for Reynolds numbers (based on the strut diameter d_{strut}, see Appendix B.2) below an approximate value of 5×10^5, i.e., in laminar flow separation conditions [2]. In these conditions, a so–called "Kármán vortex street" is developed and the periodic vortex separation causes periodic aerodynamic forces on the body, which in reaction with the fluid, generate sound radiation in the transverse direction of the mean flow [2]. Aeolian tones would correspond to a Strouhal number (see Appendix B.3) of $St = f\, d_{\text{strut}}/V \approx 0.2$ [2]. Thus, the frequency of the Aeolian tones depends on the source geometry as well as the flow velocity. There is little evidence, however, that this type of tonal noise is a major problem for current LG systems.

The size of the LG also influences the radiated noise levels. In general, the sound power is related linearly with the reference area of the LG components, see section 2.2.5.

2.2.3. Differences between main and nose landing gear

The noise emissions of the whole LG system are due to the contributions of the Nose Landing Gear (NLG) and the Main Landing Gear (MLG) systems. Even though the MLG structure is typically larger and more complicated than the NLG (i.e., it is expected to be noisier), the flow velocity impinging the MLG system V is lower than that upstream at the NLG (V_∞) because of the recirculation of the flow underneath the wings (Γ) [44], see Fig. 2.7a. In Fig. 2.7a, Δz is the distance of the sound source (the bogie) relative to the wing lower surface (i.e., Δz is approximately the length of the LG main leg). V_Γ is the velocity generated due to the recirculation flow [44] and can be approximated by

$$V_\Gamma \approx \frac{V_\infty c_L \hat{c}}{4\pi \Delta z}, \tag{2.1}$$

where c_L is the local lift coefficient (see Appendix B.6) and $\hat{c}$ is the local wing chord.

For typical landing approaches, V can be approximately 20% lower than V_∞ and, due to the strong dependence between the LG noise levels and the flow velocity

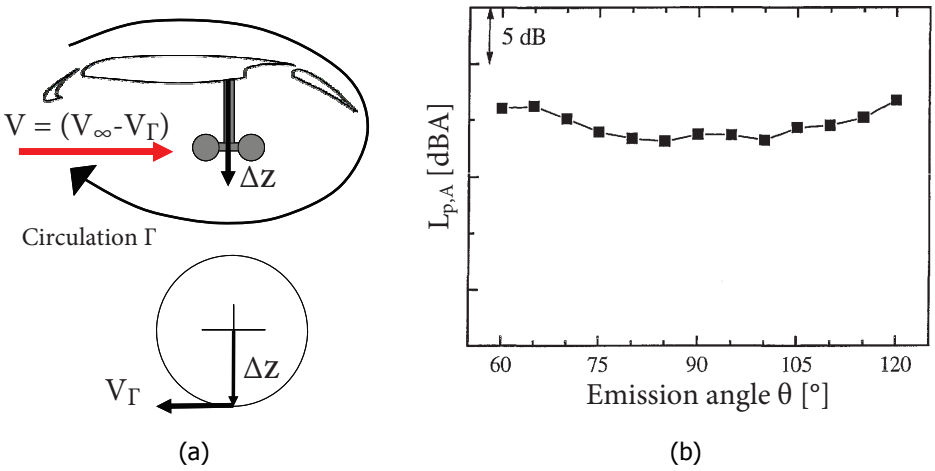

Figure 2.7: (a) Schematic representation of the installation effect for main landing gears installed under the wing. Adapted from [44]. (b) Measured polar radiation pattern of the $L_{p,A}$ of a NLG of a twin–aisle aircraft in the 280–3500 Hz band. Adapted from [14].

[40], the lower flow velocity can lead to reductions in the noise levels up to 5 dB [2]. Therefore, both LG systems usually present comparable noise levels [23].

2.2.4. Directivity

For low Strouhal numbers, it was found that the noise radiation pattern of LG systems is almost omnidirectional with slightly higher levels in the rearward arc (with polar emission angles $\theta > 90°$) [14, 18]. As the Strouhal number increases, a more pronounced minimum in the noise radiation occurs at $\theta \approx 90°$, i.e., overhead, see Fig. 2.7b.

2.2.5. Noise prediction models

Research on predicting the noise emissions of this source has been performed since the 1970s [16], although it was a challenging task due to the scarcity of acoustic measurements in wind–tunnel and flyover experiments. In this section two of the most widely–used prediction models for LG noise are explained: the methods by Fink [35] and Guo [36, 37]. Both methods are semi–empirical and implemented in ANOPP [45–47], see section 1.3.4. A comparison between the predictions of both methods and experimental data from a scaled model [48] has already been performed by Burley et al. [38].

Fink's method

Based on the two–wheel and four–wheel[1] LG noise data obtained by Heller and Dobrzynski [16], Fink [35] elaborated an empirical method which provided the predicted one–third–octave–band sound sound spectrum. The input parameters re-

[1]This method fails to calculate noise emissions of LG systems with more than 4 wheels [38].

quired for this method are just the inflow velocity V_∞, the number of wheels N_{wheel}, the wheel diameter d_{wheel} and the strut length l_{strut}. It is important to notice that this model uses imperial units, i.e., inches for lengths and knots for the velocity.

Fink's model assumes that the LG noise is generated by the interaction of the flow with the wheel assemblies and the main strut, i.e., the major LG components [35].

The far–field mean–square acoustic pressure can be estimated as

$$\langle p^2 \rangle = \frac{\rho_0 c P \hat{D} \hat{F}}{4\pi r^2 \left[1 - M\cos(\theta)\right]^4}, \tag{2.2}$$

where ρ_0 is the air density, c is the speed of sound, P is the sound power of each component (wheel and strut), $\hat{D}$ is the directivity function, $\hat{F}$ is the spectrum function, and r is the distance between source and observer. The term between brackets $\left[1 - M\cos(\theta)\right]^4$ is the convective amplification factor due to the Doppler effect, see section 3.1.2. M is the Mach number, see Appendix B.1.

The sound power for the wheel noise is defined as

$$P_{\text{wheel}} = K_1 M^6 N_{\text{wheel}} d_{\text{wheel}}^2, \tag{2.3}$$

where $K_1 = 4.349 \times 10^{-4}$ for two–wheel LG systems and $K_1 = 3.414 \times 10^{-4}$ for four–wheel LG systems.

The sound power for the strut noise is defined as

$$P_{\text{strut}} = K_2 M^6 d_{\text{wheel}} l_{\text{strut}}, \tag{2.4}$$

where $K_2 = 2.753 \times 10^{-4}$. The contributions of both components are typically of comparable order of magnitude.

The directivity functions for each component are calculated using

$$\hat{D}_{\text{wheel}} = \frac{3}{2}\sin^2(\theta), \tag{2.5}$$

$$\hat{D}_{\text{strut}} = 3\sin^2(\theta)\sin^2(\phi), \tag{2.6}$$

where ϕ is the azimuthal sideline noise emission angle (see Fig. 2.4) [35]. The case of $\phi = 0°$ corresponds to the direction directly under the landing gear and $\phi = 90°$ corresponds to the wheel axis pointing to the right. With this angle criteria, and according to Eq. (2.6), the strut does not contribute to the overall noise emissions directly under the landing gear ($\phi = 0°$).

The spectrum function $\hat{F}$ depends on the type of component and N_{wheel}, as well as on the Strouhal number based on the wheel diameter [35], $St = \frac{f d_{\text{wheel}}}{c}$. Equation (2.7) represents the spectrum function depending on several empirical parameters ($\hat{A}$, $\hat{B}$, $\hat{q}$, $\hat{\mu}$ and $\hat{\sigma}$), which can be found for each component in Table 2.1.

$$\hat{F} = \frac{\hat{A}\, St^{\hat{\sigma}}}{(\hat{B} + St^{\hat{\mu}})^{\hat{q}}}. \tag{2.7}$$

Table 2.1: Required empirical parameters for Fink's noise prediction method.

Component	$\hat{A}$	$\hat{B}$	$\hat{q}$	$\hat{\mu}$	$\hat{\sigma}$
Wheel ($N_{\text{wheel}} = 2$)	13.58	12.5	2.25	2	2
Wheel ($N_{\text{wheel}} = 4$)	0.0577	1	1.5	2	2
Strut ($N_{\text{wheel}} = 2$)	5.325	30	1	8	2
Strut ($N_{\text{wheel}} = 4$)	1.28	1.06	3	2	3

Hence, the total LG noise emissions can be calculated by summing the contributions of the wheel assembly and the strut introducing Eqs. (2.3) to (2.7) into Eq. 2.2.

Guo's method

Also known as the "Boeing" method, Guo's method [36, 37] is based on fundamental aerodynamic noise theory and scaling laws adjusted to fit full–scale LG aeroacoustic tests [38]. In order to include more physics than Fink's method, this technique considers three different types of LG components depending on their size, each of them contributing in a different frequency range:

1. **Large–scale structures** such as the wheels, contributing to the low–frequency noise.
2. **Mid–scale structures** such as the main struts, contributing to the mid–frequency noise.
3. **Small–scale structures** such as the hydraulic lines and LG dressings, contributing to the high–frequency noise.

Each of these three components are considered separately with a different spectral shape and directivity. For this purpose, more detailed geometrical inputs of the LG are required for this method, compared to Fink's method. Hence, Guo's method is expected to provide higher–fidelity noise predictions. In addition, this method provides the narrowband sound spectrum, which is converted to the one–third–octave–band sound spectrum afterwards. This model also uses imperial units, i.e., inches for lengths and knots for the velocity.

The far–field mean–square acoustic pressure can be estimated as

$$\langle p^2 \rangle = \frac{\rho_0^2 c^4 M^6 \hat{D}_{\text{overall}}}{r^2 \left[1 - M\cos(\theta)\right]^4} \left(P_{\text{low}} + P_{\text{mid}} + P_{\text{high}}\right), \tag{2.8}$$

where P_{low}, P_{mid}, and P_{high} represent the sound powers of the low, mid, and high frequency components, respectively. $\hat{D}_{\text{overall}}$ is the overall directivity function, in addition to the directivity function included in each P term, which accounts for the installation effects of the LG. The presence of the wing and fuselage of the aircraft causes reflection and diffraction [37], which will enhance the noise radiation,

especially in the overhead direction ($\theta = 90°$). This parameter can be estimated using the following empirical expression

$$\hat{D}_{\text{overall}} = 1.2(1 - 0.9\cos^2(\theta))^2. \tag{2.9}$$

Each of the P terms in Eq. (2.8) are defined as

$$P = \hat{\beta} S \hat{D} \hat{F}, \tag{2.10}$$

where $\hat{\beta}$ is the flow energy conversion efficiency parameter (see Table 2.2) and S is the aggregate surface integration effects [37], which depend on the geometry of the LG components:

$$S_{\text{low}} = \pi N_{\text{wheel}} w_{\text{wheel}} d_{\text{wheel}}, \tag{2.11}$$

$$S_{\text{mid}} = \sum_{k=1}^{N_{\text{strut}}} \hat{s}_{\text{strut},k} l_{\text{strut},k}, \tag{2.12}$$

$$S_{\text{high}} = \hat{\eta} l_{\text{high}}^2, \tag{2.13}$$

where w_{wheel} is the wheel width, N_{strut} is the number of main struts in the LG assembly, and $\hat{s}_{\text{strut},k}$ and $l_{\text{strut},k}$ are the perimeter of the cross section and the length of the k^{th} strut, respectively. The dimensionless parameter $\hat{\eta}$ is the complexity factor accounting for the geometric complexity of the small–scale components of the LG. This parameter has a complicated expression depending on the takeoff weight of the aircraft, but for NLG $\hat{\eta}$ can be approximated by a constant value of 0.1 [37], since a typical NLG is much simpler than a MLG and their complexity does not vary significantly within different aircraft types. The characteristic length of the small–scale components l_{high} can be approximated as

$$l_{\text{high}} = 0.15 \frac{S_{\text{mid}}}{\pi \sum_{k=1}^{N_{\text{strut}}} l_{\text{strut},k}}. \tag{2.14}$$

The Strouhal number is defined for each frequency range

$$St_{\text{low}} = \frac{f d_{\text{wheel}}}{V}, \tag{2.15}$$

$$St_{\text{mid}} = \frac{f S_{\text{mid}}}{\pi V \sum_{k=1}^{N_{\text{strut}}} l_{\text{strut},k}}, \tag{2.16}$$

$$St_{\text{high}} = \frac{f l_{\text{high}}}{V}. \tag{2.17}$$

The spectrum function $\hat{F}$ can be calculated in a similar way as for Fink's method, see Eq. (2.7) using the parameters gathered in Table 2.2.

The frequency–dependent directivity function $\hat{D}$ is defined as

Table 2.2: Required empirical parameters for Guo's noise prediction method.

Frequency	$\hat{A}$	$\hat{b}$	$\hat{B}$	$\hat{h}$	$\hat{q}$	$\hat{\beta}$	$\hat{\mu}$	$\hat{\sigma}$
Low	3.53	3	0.62	0.2	2.6	4.5×10^{-8}	2.5	4
Mid	0.42	2	0.18	0.6	4.2	1.5×10^{-8}	1.5	3
High	0.08	0.1	0.1	1	4.2	3.2×10^{-5}	1.1	2

$$\hat{D} = (1 + \hat{h}\cos^2(\theta))^2(1 + \hat{b}\sin^2(\phi))^2, \tag{2.18}$$

where $\hat{h}$ and $\hat{b}$ are empirical constants [38] whose values are listed in Table 2.2. This directivity pattern peaks at the upstream and downstream directions and shows a minimum near the overhead direction ($\theta \approx 90°$). Moreover, as the frequency increases, the radiation pattern becomes more directional in the polar direction [37]. In the azimuthal direction, the maximum emission direction corresponds to $\phi = 90°$.

The effect of the lower flow velocity impinging at the MLG compared to the NLG is also accounted for, see section 2.2.3. With all these equations, all the P terms in Eq. (2.8) can be calculated and the far–field noise emissions can be obtained.

The predictions of this method have been shown to compare well with experimental data from wind–tunnel and flight measurements [37, 38], both in parametric trends and absolute noise levels.

2.2.6. Potential noise reduction measures

It was found that for the NLG the steering system and the axle area are the major noise sources, whereas for the MLG the bogie area, the brakes, the articulation link and the leg–door arrangement are the most important noise sources [2, 49]. Potential noise reduction measures have been investigated, such as streamlined or perforated add–on fairings in order to cover complex gear structures. Noise reductions up to 3 dBA or 2 EPNdB were documented with such devices [2]. An increase in the local flow velocity due to flow displacement might be caused by the presence of fairings. Therefore, fairing designs featuring porous materials, meshes or elastic cloth have been proposed [50]. These devices offered reductions of approximately 2 dB, but coupled with a high–frequency noise increase.

Other measures, such as optimized bay door designs, ramp spoilers, wheel hub caps or flow–control techniques (such as air curtains, plasma actuators or boundary layer suction devices) have also been proposed [2, 20, 21, 51]. These measures need to fulfill operation, safety and cost constraints [2]. For example, pin–hole caps could be used to avoid tonal noise due to cavities, but manufacturers hesitate in employing this solution due to potential corrosion problems [2].

Chapter 5 focuses on this noise source and presents a comparison between experimental and computational acoustic results, as well as with noise prediction models.

2.3. Airfoil noise

2.3.1. Background and noise generation mechanism

Airfoil noise can have a non–negligible contribution to the overall noise emissions on landing aircraft in case the leading and trailing edge devices are deployed, see Fig. 2.2a. However, this noise source is especially important for wind turbines [12, 13, 52]. Similar approaches to study airfoil noise as those listed in section 2.2.1 for landing gear noise are typically employed [48, 53–57], although for this case field measurements on full–scale wind turbines [58, 59] are usually performed instead of aircraft flyover measurements.

According to Brooks et al. [60] the different sound generation mechanisms of airfoil noise can be divided into airfoil inflow turbulence noise and airfoil self–noise. The inflow turbulence noise is caused by the interaction between the incident eddies and the airfoil surface and, therefore, depends on the local atmospheric conditions. This mechanism typically has a marginal effect on the overall sound emission in wind turbines [12]. The main generation mechanisms for airfoil self–noise can be separated into five categories:

a **Laminar boundary layer instability noise:** If the flow is in the laminar regime ($Re < 10^6$), Tollmien–Schlichting waves can occur [12], which induce periodic surface pressure fluctuations as they convect over the airfoil surface. These waves scatter when they reach the trailing edge and can form a feedback mechanism with the Tollmien–Schlichting waves, amplifying them effectively and generating loud tonal (or narrowband) sound from the trailing edge, see Fig. 2.8a. This issue can be avoided by forcing the transition to the turbulent regime by smart airfoil designs or by using tripping devices [52, 62]. An example of the performance of these tripping devices is shown in Fig. 2.9 for a NACA 0018 airfoil at zero–lift angle of attack ($\alpha = 0°$) tested at Delft University of Technology. At a chord–based Reynolds number of 4.06×10^5 the airfoil is in the laminar regime and a strong tonal peak (almost 40 dB louder than the surrounding broadband noise) at 1274 Hz and its harmonics (at multiples of that frequency) appear. If transition to the turbulent regime (see item *b* in this list) is forced by using a tripping device (in this case carborundum elements of 0.6 mm nominal size placed on a trip tape of 10 mm width placed at 20% of the airfoil chord [62–64]) the tonal peaks disappear and the overall $L_{p,A}$ is reduced by 22 dBA. Additional information about the experimental setup used for this example is included afterwards in section 6.2.1 and Appendix E.

b **Turbulent boundary layer trailing edge (TBL–TE) noise:** If the flow is in the turbulent regime ($Re > 10^6$), eddies of different scales and energies convect within the turbulent boundary layer downstream. When these unsteady surface pressure fluctuations arrive at the trailing edge, they experience a sudden change in acoustic impedance. In addition, a difference exists between the pressure fluctuations acting on the pressure side and on the suction side [60]. The pressure fluctuations scatter as broadband noise,

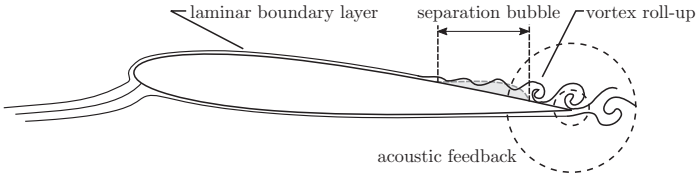

(a) Laminar boundary layer instability noise.

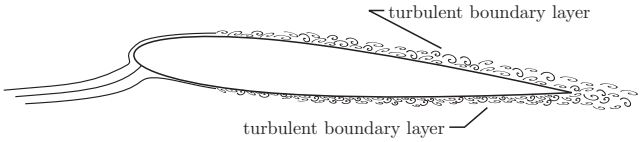

(b) Turbulent boundary layer trailing edge interaction noise.

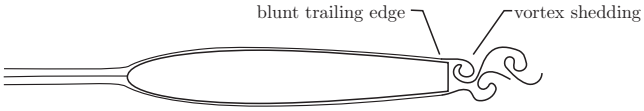

(c) Trailing edge bluntness vortex shedding noise.

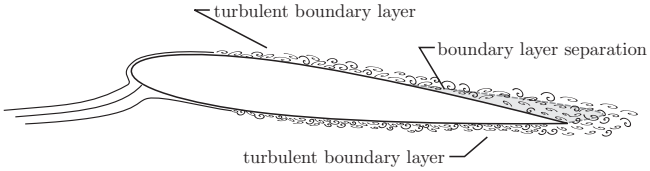

(d) Boundary layer separation noise.

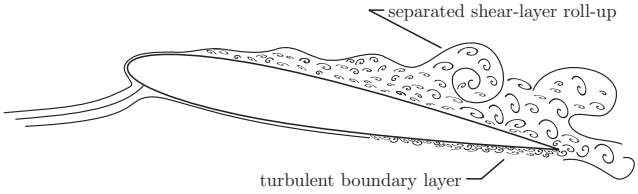

(e) Separation stall noise.

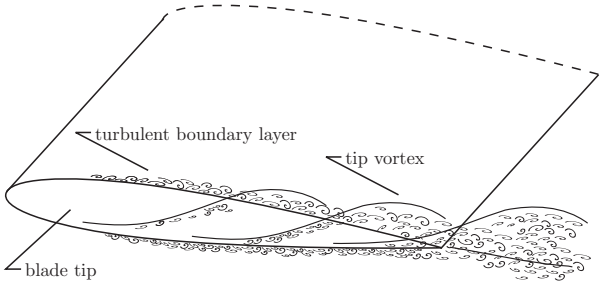

(f) Tip noise.

Figure 2.8: Mechanisms of airfoil noise generation [12] (previously adapted from [60, 61]).

see Fig. 2.8b, which is considered the dominant noise source of modern large wind turbines for most operating conditions [13, 65].

c **Trailing edge bluntness noise:** In case the trailing edge thickness exceeds a threshold value, von Kármán vortex streets can develop in the wake of the airfoil, generating periodic pressure fluctuations [12, 52], see Fig. 2.8c. Tonal (or narrowband) noise can be generated, whose frequency depends on the bluntness of the airfoil. This mechanism can be avoided by careful airfoil design or by using splitter plates [52].

d **Separation and stall noise:** For angles of attack α higher than a threshold value, flow separation occurs at the suction side with a large recirculation bubble of unsteady flow [52], which generates broadband noise due to the shedding of vorticity [12], see Fig. 2.8d. For even higher values of α, deep stall can occur (see Fig. 2.8e), generating large–scale vortex shedding which increases the low–frequency noise emissions [60]. Separation and stall can be avoided by selecting the operation conditions of the airfoil carefully or by the installation of vortex generators [52].

e **Tip noise:** Due to the finite length of the wings or blades, the pressure difference between the pressure and suction side can generate a strong vortex at the tip [52], potentially causing flow separation [12], see Fig. 2.8f. The contribution of this mechanism to the overall noise emissions is normally negligible for modern wind turbine blades [13].

According to the list above, TBL–TE noise is considered to be the most important noise contributor for most modern wind turbines operating within their design envelope [52, 65] and, henceforth, it will be the main airfoil noise generation mechanism studied in this thesis (see Chapter 6). More detailed explanations about airfoil noise and its generation mechanisms can be found in the papers of Howe [66, 67] and the Ph.D. theses of Pröbsting [61], van der Velden [12] and Arce León [52].

Scattering of sound

Some of the noise generation mechanisms for airfoil noise mentioned above refer to the term *scattering* of sound. Scattering occurs when a sound wave encounters an obstacle and part of the wave energy is deflected from its original course, spreading out from the obstacle in all directions [68]. Different scattering patterns occur depending on the ratio between the acoustic wavelength λ and the characteristic length of the obstacle l [68], see section 2.3.2. Analytical solutions for the scattered wave can be obtained for simple geometries [68], such as cylinders, spheres, etc. Scattering also occurs when a sound wave enters a region in which the acoustic properties (such as the acoustic impedance) are different, such as a region with turbulent flow. This is typically the case for trailing–edge noise, where the pressure fluctuations in the boundary layer meet a sharp impedance mismatch at the edge, which causes them to scatter as sound waves. This is further explained in the sections below. More information about scattering can be found in [68].

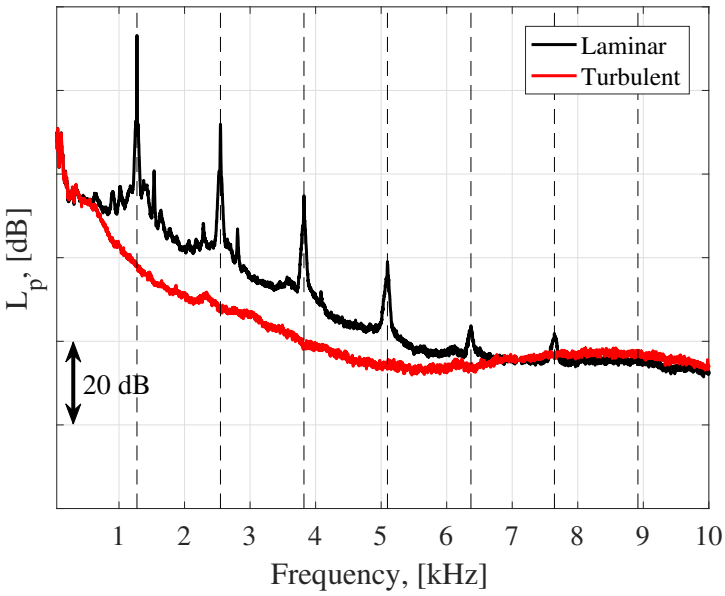

Figure 2.9: Integrated sound pressure levels of a NACA 0018 airfoil for a chord–based Reynolds number of 4.06×10^5, with (red) and without (black) tripping devices. The position of the tonal harmonics is indicated with vertical black dashed lines.

2.3.2. Spectral shape and directivity

In case the eddies are larger than the characteristic length of the sound source l (the airfoil chord for example), the acoustic wavelength λ will also be larger than l, i.e., $l/\lambda \ll 1$, and the source is considered as acoustically compact (see left part of the graph in Fig. 2.10). The eddies interact with the whole airfoil, radiating low–frequency noise as a compact dipole, i.e., as $p^2 \propto \sin^2(\theta_{\text{TE}})$, where θ_{TE} is the emission angle with respect to the trailing edge, see Fig. 2.10. As mentioned in section 2.2.2 this type of sources scales with the sixth power of the flow velocity [40], i.e., $p^2 \propto V^6$.

For most practical cases, the size of the eddies is considerably smaller than the airfoil chord [12], i.e., $l/\lambda \gg 1$, and the source is considered as acoustically non–compact. Hence, the eddies only generate local pressure fluctuations and the sound is scattered at the trailing edge. Ffowcs–Williams and Hall [69] provided an approximate solution of the acoustic intensity for a semi–infinite flat plate in the non–compact regime:

$$p^2 \propto \frac{V^5 b \delta^\star}{r^2} \sin^2(\theta_{\text{TE}}/2), \tag{2.19}$$

where b is the span of the wing or blade section and $\delta^\star$ is the boundary layer displacement thickness, which for turbulent boundary layers can be approximated as [70, 71]

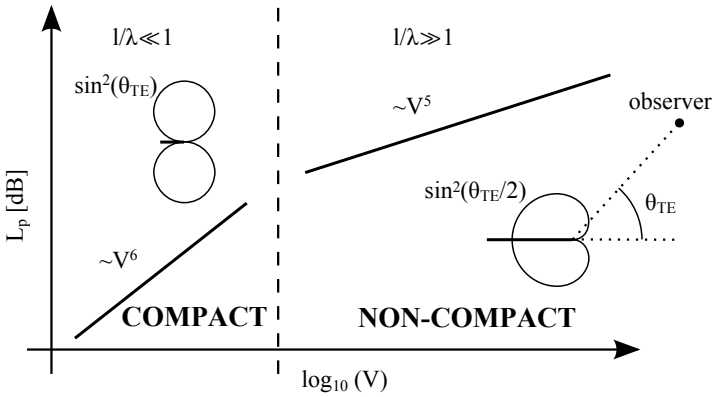

Figure 2.10: Noise radiation and flow velocity dependence for compact and non–compact trailing–edge noise sources for subsonic conditions. θ_{TE} is the emission angle with respect to the trailing edge, l is the characteristic length of the sound source, λ is the acoustic wavelength, and V is the flow velocity. Adapted from [72].

$$\frac{\delta^\star}{\hat{c}} \approx 0.047\, Re_{\hat{c}}^{\frac{-1}{5}}, \tag{2.20}$$

where $Re_{\hat{c}}$ is the chord–based Reynolds number.

According to Eq. (2.19), the radiation pattern for high–frequency noise can be modeled as a cardioid, i.e., as $p^2 \propto \sin^2(\theta_{TE}/2)$, see Fig. 2.10. Thus, the maximum radiation direction is towards the leading edge ($\theta_{TE} = 180°$). The sound power in this case, scales with the fifth power of the flow velocity [12], i.e., $p^2 \propto V^5$. This type of noise can be characterized using $\delta^\star$ as characteristic local length scale, providing a Strouhal number $St = f\delta^\star/V$. Modern wind turbines show a broadband spectrum around $St = 0.1$ [12].

For a fixed airfoil, transition from the compact to the non–compact regime can occur by a change in the characteristic length or in the flow velocity, because $f \approx V/l$. Both suction side and pressure side of the airfoil radiate in symmetry [12], but since $\delta^\star$ on the suction side is typically larger than on the pressure side, the noise generated by the suction side typically presents higher levels at lower frequencies, compared to the one generated the pressure side, see Fig. 2.11.

2.3.3. Noise prediction models

In this section one of the most widely–used prediction models for trailing–edge noise, Amiet's theory [71], is briefly explained to provide an overview of the main scaling laws. Additional models, such as Howe's method [66], the TNO–Blake [72, 73] method or the method by Brooks–Pope–Marcolini [60] can be found in the literature. Most of these models are based on the acoustic analogies by Lighthill [1], Curle [40] and Ffowcs Williams and Hall [69] and they normally require information

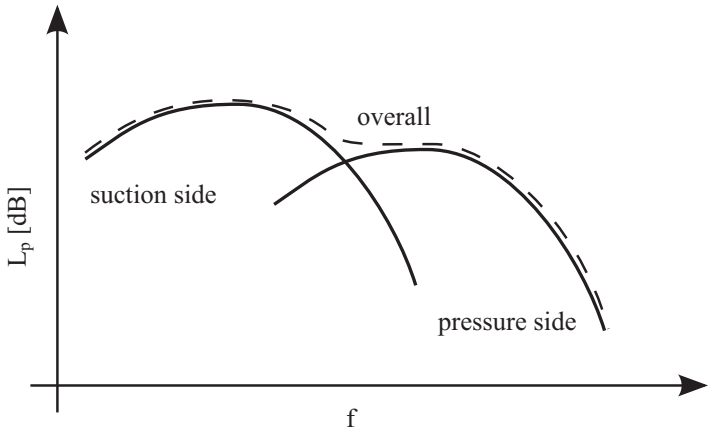

Figure 2.11: Contribution of the pressure and suction side boundary layers to the overall acoustic emissions. Adapted from [61].

about the flow field within the boundary layer. In addition, a brief description of the prediction model for clean airfoil noise by Lockard and Lilley [5, 74] is provided.

Amiet's method

Amiet [71] developed a theory for turbulent–trailing–edge noise of an airfoil in the 1970s which requires the convecting surface pressure spectrum upstream of the trailing edge as an input. This spectrum can be estimated using non–intrusive methods, such as PIV [52, 75].

This method considers that the TE noise is generated almost entirely by the induced non–compact surface dipoles near the trailing edge.This causes an equal and anticorrelated sound radiation on the pressure and suction sides of the airfoil. This theory assumes that the turbulence is stationary, in the statistical sense, as it moves past the trailing edge (i.e., it assumes frozen turbulence) [71]. Moreover it is assumed that the airfoil is semi–infinite with no leading edge, which is a good approximation for wavelengths smaller than the local airfoil chord $\hat{c}$ ($l/\lambda \gg 1$ in Fig. 2.10).

The system of reference for this theory considers the x axis in the streamwise direction, with $x = 0$ at the trailing edge location; the y axis in the spanwise direction and z in the wall–normal direction. The Power Spectral Density (PSD, see Appendix C.2.5) of the far–field sound spectrum $\tilde{S}_{pp}$ for an observer in the $y = 0$ plane can, therefore, be estimated as

$$\tilde{S}_{pp}(x, y = 0, z, f) = \left(\frac{\hat{c}zf}{2cr^2}\right)^2 |\mathcal{L}|^2 \tilde{S}_{qq}(y = 0, f) l_y(f), \tag{2.21}$$

where $\mathcal{L}$ is the acoustic transfer function, which depends on the surface pressure jump at the trailing edge [71]; $\tilde{S}_{qq}$ is the spanwise PSD of the surface pressure

[71], and l_y is the characteristic spanwise turbulence correlation scale defined as

$$l_y(f) = \frac{1}{\tilde{S}_{qq}(y=0,f)} \int_0^\infty \tilde{S}_{qq}(y,f)dy. \tag{2.22}$$

Roger and Moreau [76] made an extensive review of the characteristics and limitations of several airfoil self–noise prediction models and suggested a modification of the term $\mathcal{L}$ in Amiet's theory (see Eq. (2.21)), in order to describe low–frequency noise emissions more accurately by considering the back–scattered pressure from the leading edge [77, 78].

Lockard and Lilley's method

Lockard and Lilley [74] proposed a semi–empirical prediction model for clean airfoils under limited load conditions ($c_l \leq 0.5$), within turbulent flows that was later adapted by Dobrzynski [5]. This method was originally developed considering flat plates [5]. The far–field sound intensity for a wing without sweep angle of span b and mean chord $\hat{c}$ in the direction perpendicular to the trailing edge can be estimated as

$$p^2 \approx \frac{6.8}{\pi^3} \frac{V^5 \hat{c} b \rho_0 \delta^\star}{c^2 r^2} 0.046^5. \tag{2.23}$$

Further adjustments can be applied to account for the spectral, directivity, velocity and geometry characteristics [5]. This method is currently implemented in the noise prediction model PANAM [6, 79].

2.3.4. Potential noise reduction measures

According to Eq. (2.19) an obvious way to reduce the noise emissions of wind turbines is to lower the tip speed (and hence the rotational speed). Whereas this strategy is sometimes used during nighttime, it implies a loss in energy production [52] and, therefore, of revenue. Several noise–reduction measures have been proposed in the literature for reducing TBL–TE noise, such as flow injection [80, 81], quiet airfoil design [58], brushed trailing edges [82, 83], trailing–edge serrations [63, 64, 84–87] or porous materials [88–93]. A good overview of these measures is further explained in the Ph.D. thesis of Arce León [52], but in this thesis, only the last two measures are considered, see chapter 6.

Trailing–edge serrations

Ffowcs Williams and Hall [69] showed that trailing edge noise is scattered more efficiently when the turbulent eddies convect pass the trailing edge perpendicularly. Therefore, noise emissions can be reduced by modifying the edge shape with respect to the flow direction, such as with trailing–edge serrations. The use of serrated trailing edges for noise–reduction purposes was already studied by Howe [84] in 1991 and they are supposed to only alter the acoustic scattering efficiency of the trailing edge, while having a negligible effect on the aerodynamic performance of the airfoil [12].

The most common shape for trailing–edge serrations feature a sawtooth geometry (see Fig. 6.3 in Chapter 6). This type of serrations is already being used in the wind turbine industry [13, 52, 58, 65], although the noise reduction mechanism is not fully understood yet. Hence, additional knowledge on the underlying physics for this noise reduction is necessary for optimizing the performance of these devices.

Alternatives to the simple sawtooth geometry have also been proposed in the literature, such as slitted serrations [86], combed serrations that make the flow more aligned with the trailing edge [85, 86] or iron–shape concave serrations that reduce the noise more efficiently at the root of the serration [94]. Additional reductions with respect to the sawtooth configuration of up to 2 dB have been measured when using these alternative geometries with respect to the standard sawtooth serrations [12, 85, 94].

Section 6.1 contains the results of experimental campaigns studying the performance of different trailing–edge serrations for airfoil noise reduction, as well as comparisons with numerical simulations and noise prediction models.

Trailing–edge porous inserts

Previous studies using porous materials in airfoils [88–92] showed that they offered noise reduction at low and medium frequencies in exchange of a potential reduction in the aerodynamic efficiency. A noise increase at high frequency might also occur due to the higher surface roughness of the porous material [89]. One of the major challenges is to properly design the porous material, since there are several parameters to define [89–91], such as the porosity or the air flow resistivity. The exact physical mechanisms that provide this noise reduction are yet to be accurately defined, although previous literature [83, 89, 93, 95] suggested some potential causes:

- Modifications in the turbulent boundary layer mean flow field;
- Viscous damping of the pressure fluctuations within the porous material;
- Balance of the dynamic pressure (see Appendix B.6) difference between the pressure and suction sides at the trailing edge because of the cross–flow through the porous material;
- Reduction of the amplitude and spanwise coherence length of the pressure fluctuations.

The use of these devices in industrial applications might be limited by the durability and required maintenance of the porous materials.

Section 6.2 presents some experimental results of wind–tunnel tests on several porous materials applied to the trailing edge of an airfoil.

2.4. Engine noise

2.4.1. Background

One of the major reductions in aircraft engine noise in the last decades was due to the implementation of turbofan engines in the 1970s, compared to the louder tur-

bojet engines. Whereas turbojet engines produce thrust using a multistage system consisting of a compressor, a combustion chamber and a turbine (normally referred to as the core), turbofan engines add a large fan at the engine inlet which diverts and accelerates a portion of the incoming air that mixes with the jet exhaust, decreasing the net exhaust velocity. Since jet noise is strongly correlated with the exhaust velocity (see section 2.4.2), this technology considerably reduced jet noise levels.

Current trends in turbofan engines consist of increasing the fan diameter and bypass ratio (proportion of air mass diverted by the fan with respect to the air mass that goes trough the core), which increases the fuel efficiently significantly. Increasing the fan size, on the other hand, also increases fan noise levels considerably. Fan exhaust noise (see Fig. 2.1) can be partially reduced by using acoustic lining (a treatment of the engine inner nacelle with perforated materials that act as Helmholtz resonators that attenuate specific sound frequencies) [3, 7], but fan inlet noise is more difficult to treat and it is a dominant noise source for most modern aircraft, see Fig. 2.2, especially in the forward direction (i.e., $0° < \theta < 90°$), see Figs. 2.5 and 2.6. Fan noise is discussed more extensively in section 2.4.3.

A different approach to reduce engine noise is to place the engines over the wing or over the fuselage so the noise emissions can be shielded [96], such as for the case of the Fokker 70 aircraft (see Fig. 7.16b).

The noise generated by the engine core is briefly explained in section 2.4.4. A description of the noise generated by propeller engines, such as those typically used in regional aircraft, is included in section 2.4.5.

2.4.2. Jet noise

Jet noise is a major aircraft noise source during takeoff (see Fig. 2.2b) and it is the dominating noise source in aircraft equipped with turbojet engines (such as military fighters or old commercial airliners). This source features broadband noise especially strong below 500 Hz, with maximum values typically around 100 Hz [7, 43].

Jet noise is caused by the high–speed jet exhaust core intruding into the surrounding air (bypass flow and ambient air) which has a relatively much lower flow speed. This generates large and small scale turbulence and pressure fluctuations in the shear layer between both regions that propagate as acoustic waves. This sound source promoted the start of the field of aeroacoustics by Sir Michael James Lighthill [1, 97], who suggested the acoustic analogy most CAA methods are based on, by rearranging the fluid motion equations to account for pressure disturbances in the flow due to sound sources [43]. The derivation of this equation is out of the scope of this thesis but it can be found in the literature [1, 43, 97–99]. Lighthill's acoustic analogy provides an exact solution since no approximations are made in the derivation, but for solving it certain assumptions need to be made, which lead to several different approaches to solve this equation [98, 99].

If Lighthill's acoustic analogy is applied to a free, cold turbulent jet the noise generated can be approximated by the following equation:

$$p^2 \propto \frac{\rho_0 V_{\text{jet}}^8 d_{\text{jet}}^2}{c^5 r^2}, \tag{2.24}$$

where V_{jet} is the mean jet exhaust velocity, and d_{jet} is the diameter of the jet nozzle. Equation (2.24) shows the strong dependence of jet noise with the jet exhaust velocity ($p^2 \propto V_{\text{jet}}^8$), as mentioned in section 2.4.1. For jets with higher temperatures than the ambient one, the jet velocity exponent is reduced to a value between 6 and 8 due to entropy fluctuations [43]. The jet mixing noise will decrease in case the aircraft is in motion because the difference between the outflow and ambient speed is reduced [7]. Lighthill [1, 97] showed that, since turbulence is the main generation mechanism for jet noise, it presents a quadrupole–like radiation pattern [99], i.e., $p^2 \propto \sin(2\theta)$.

A noise prediction method for jet noise was developed by Stone [100], which provides frequency–dependent sound radiation patterns in one–third–octave bands. This method is implemented in ANOPP.

2.4.3. Fan noise

Fan noise can be divided into five components [101]:

1. Tonal noise from the inlet
2. "*Buzz–saw*" tones from the inlet
3. Broadband noise from the inlet
4. Tonal noise from the exhaust
5. Broadband noise from the exhaust

The interaction between the fan blades and the stator vanes every blade passage generates sound with a strong tonal component, which is specially noticeable in the forward direction [7, 102] (i.e., for $\theta < 90°$), as mentioned in section 2.4. The fundamental frequency of this sound, f_1, is called the blade passing frequency (BPF) and is calculated as:

$$\text{BPF} = f_1 = \frac{B\, n_{\text{rot}}}{60}, \tag{2.25}$$

where B is the number of fan blades and n_{rot} is the fan rotational speed in revolutions per minute. Typical BPF values for commercial turbofan aircraft during the landing stage range from 500 Hz to 2 kHz approximately [102], because this parameter strongly depends on the type of engine considered.

Higher harmonics of the BPF are usually found as well in the sound of aircraft flyovers. The frequencies of these harmonics, f_k, are multiples of the BPF (f_1):

$$f_k = k\, f_1, \;\; k = 1, 2, 3 \ldots . \tag{2.26}$$

The term *engine fan settings* typically refers to the ratio between the fan rotational speed, n_{rot}, and the maximum fan rotational speed, $n_{\text{rot,max}}$. This relative

fan percentage speed is normally denoted as $N1\% = 100\, n_{\text{rot}}/n_{\text{rot,max}}$ because it refers to the low–pressure shaft of the engine, on which the fan is mounted. In contrast to the thrust or the jet velocity of the engine, it can be directly measured during flight [103]. The expected value of $N1\%$ during approach is considerably lower than during takeoff because of the descent [104]. A method to estimate the $N1\%$ from audio recordings of aircraft flyovers will be introduced in section 7.4, [102, 104–106].

In addition, turbofan aircraft during takeoff can present the so–called *buzz–saw* noise produced at the tip of the fan blades when they reach supersonic speeds, thus, producing shock waves [7]. These waves gather in the inlet duct due to blade imperfections [7]. These tones are harmonics of the engine shaft rotation frequency, which is typically considerably lower than the BPF.

Broadband noise is generated due to the turbulence in the blade wakes, boundary layers and unsteady flow of the engine, which are related to different length scales, causing the emission of noise in a broad range of frequencies [7].

The fan noise model by Heidmann [101] is implemented in most aircraft noise prediction tools (such as ANOPP) and has been updated using data from modern engines.

2.4.4. Engine core noise

Although the noise emissions generated at the engine core are not dominant compared to other noise sources on the aircraft, it is expected to become increasingly important in the next decades as fan and jet noise levels are reduced [43, 107]. Engine core noise has two main components: combustion noise and turbine noise.

Combustion noise

Combustion noise is generated due to the expansion of the gas in the combustion chamber and the convection of non–uniformities through the pressure gradients in the turbine [7]. This type of noise is broadband, radiating mostly in the aft direction of the engine and having maximum values around 400 Hz to 500 Hz [108]. At low thrust settings, combustion noise can have a significant contribution to the overall aircraft noise levels [43].

Turbine noise

The noise generated at the turbine follows similar mechanisms as those for fan exhaust noise (see section 2.4.3): tonal noise due to the interaction between the blades wake and the vanes and broadband noise due to the unsteady flow around the turbine rotors and stators [43]. This kind of noise radiates mostly in the rear direction of the engine as well. A noise prediction model by Matta [109] for turbine noise is implemented in ANOPP.

2.4.5. Propeller noise

Even though the majority of this thesis considers the noise emissions of commercial aircraft equipped with turbofan engines, open–rotor propeller propulsion has gained resurgent interest in the last decades, due to its low fuel burn (up to 30% lower

than current turbofan engines [110]). This interest has been partly motivated by the high fuel prices in the last years. On the other hand, the commercial use of propeller–driven aircraft is limited by the high levels of cabin noise [99]. Therefore, in order to make open rotor engines competitive, they have to become acoustically acceptable too [110].

The concept of Counter–Rotating Open Rotor (CROR) [111] especially looks like a promising alternative to conventional aircraft engines, offering increased efficiency for the same disk loading compared to conventional open rotors, due to the reduction of swirl behind the engine because of the counter–rotating rotors [5, 112, 113]. However, they pose an even larger challenge with respect to noise emissions than conventional open rotors. They present stronger tones at lower frequencies than turbofan engines and also a higher number of tones [43]. This can cause higher levels of annoyance since low–frequency tones are damped by the atmosphere rather weakly [43], see section 3.1.2.

Rotating blades generate tonal noise due to phenomena repeated during each rotation and broadband noise due to turbulent flow over the blades [99]. This resembles the explanation given for fan noise in section 2.4.3 but the BPF for propeller engines is typically considerably lower than for fans, due to the lower number of blades.

Additional considerations that need to be taken into account with open rotors are the installation effects. Two main options for pylon–mounted propellers can be distinguished: a tractor configuration (where the propeller is set upstream of a pylon) or a pusher configuration (where the propeller is located downstream of a pylon). In the first option the slipstream of the propeller impinges on the pylon and vice versa for the second option [110, 114, 115]. These phenomena alter the performance of both the propeller and the pylon and can induce additional noise emissions and vibrations that can be perceived by the passengers inside the aircraft cabin [115].

Several theories and noise prediction models have been proposed to estimate the acoustic emissions of propellers [10, 116, 117], such as as the open–source software XROTOR [118] developed at the Massachusetts Institute of Technology (MIT). In most models, the geometry of the propeller blade is of great importance for the predictions.

Some reduction measures for propeller noise have been investigated in the past, such as optimized blade design [99, 110], active flow blowing [114, 119] or porous inserts in the pylon [115, 120, 121] to mitigate the installation effects of the propeller. A recent study [121] on the noise reduction provided by porous inserts compared the results obtained by wind–tunnel experiments and computational simulations, showing a very close agreement. Installing a duct around a propeller might provide acoustic shielding in certain emission directions [122].

Bibliography

[1] M. J. Lighthill, *On sound generated aerodynamically, I: General theory,* Proceedings of the Royal Society of London. Series A, Mathematical and Physical Sciences **211**, 564 (1952).

[2] W. M. Dobrzynski, *Airframe Noise: Landing Gear Noise,* Encyclopedia of Aerospace Engineering (2010), 10.1002/9780470686652.eae337.

[3] G. Ruijgrok, *Elements of aviation acoustics*, Second ed. (VSSD, 2007) ISBN: 1090–6562–155–5.

[4] W. Dobrzynski, *Almost 40 Years of Airframe Noise Research: What Did We Achieve?* Journal of Aircraft **47**, 353 (2010).

[5] L. Bertsch, *Noise Prediction within Conceptual Aircraft Design*, Ph.D. thesis, DLR (2013), DLR Forschungsbericht, ISRN DLR–FB–2013–20, ISSN 1434–8454.

[6] L. Bertsch, W. Dobrzynski, and S. Guérin, *Tool Development for Low–Noise Aircraft Design,* Journal of Aircraft **47**, 694 (2010).

[7] M. Arntzen, *Aircraft noise calculation and synthesis in a non–standard atmosphere*, Ph.D. thesis, Delft University of Technology (2014), ISBN: 978–94–62594–64–7.

[8] L. Bertsch, W. Heinze, and M. Lummer, *Application of an Aircraft Design–To–Noise Simulation Process,* in 14^{th} *AIAA Aviation Technology, Integration, and Operations Conference, June 16 – 20 2014, Atlanta, Georgia, USA* (2014) AIAA paper 2014–2169.

[9] W. P. J. Visser and M. J. Broomhead, *GSP – A generic object–oriented gas turbine simulation environment*, Tech. Rep. NLR–TP–2000–267 (National Aerospace Laboratory (NLR), Anthony Fokkerweg 2, 1059 CM Amsterdam, P.O. Box 90502, 1006 BM Amsterdam, The Netherlands, 2000).

[10] H. H. Hubbard, *Aeroacoustics of large wind turbines,* Journal of the Acoustical Society of America **89**, 2495 (1991).

[11] S. Guidati, J. Ostertag, and S. Wagner, *Prediction and Reduction of Wind Turbine Noise: An Overview of Research Activities in Europe,* in 18^{th} *ASME Wind Energy Symposium, January 10-13, 2000, Reno, Nevada, USA* (2000) AIAA paper 2000–0042.

[12] W. C. P. van der Velden, *Computational aeroacoustic approaches for wind turbine blade noise prediction*, Ph.D. thesis, Delft University of Technology (2017), ISBN: 978–94–6186–756–8.

[13] S. Oerlemans and B. Méndez López, *Acoustic Array Measurements on a Full Scale Wind Turbine,* in 11^{th} *AIAA/CEAS Aeroacoustics Conference, May 23 – 25, 2005, Monterey, California, USA* (2005) AIAA paper 2005–2963.

[14] U. Michel and W. Qiao, *Directivity of Landing–Gear Noise Based on Flyover Measurements,* in 5^{th} *AIAA/CEAS Aeroacoustics Conference, May 10 – 12 1999, Bellevue, Greater Seattle, WA, USA* (1998) AIAA paper 1999–1956.

[15] J. Piet, N. Molin, and C. Sandu, *Aircraft landing gear provided with at least one noise reducing means,* (U.S. Patent number 8,256,702. 2012).

[16] H. H. Heller and W. M. Dobrzynski, *Sound Radiation from Aircraft Wheel–Well/Landing–Gear Configuration,* Journal of Aircraft **14**, 768 (1977).

[17] R. Merino-Martinez, E. Neri, M. Snellen, J. Kennedy, D. Simons, and G. Bennett, *Analysis of nose landing gear noise comparing numerical computations, prediction models and flyover and wind–tunnel measurements,* in *24th AIAA/CEAS Aeroacoustics Conference. June 25 – 29 2018. Atlanta, Georgia, USA* (2018) AIAA paper 2018–3299.

[18] W. Dobrzynski and H. Buchholz, *Full–scale noise testing on Airbus landing gears in the German Dutch Wind Tunnel,* in *3rd AIAA/CEAS Aeroacoustics Conference. May 12 – 14 1997, Atlanta GA, USA* (1997) AIAA paper 1997–1597.

[19] W. Dobrzynski, L. C. Chow, P. Guion, and D. Shiells, *A European Study on Landing Gear Airframe Noise Sources,* in *6th AIAA/CEAS Aeroacoustics Conference. June 12 – 14 2000, Lahaina HI, USA* (2000) AIAA paper 2000–1971.

[20] E. Neri, J. Kennedy, and G. Bennett, *Characterization of low noise technologies applied to a full scale fuselage mounted nose landing gear,* in *Proceedings of the Internoise 2015/ASME NCAD Meeting, August 9 – 12 2015, San Francisco, CA, USA* (2015) NCAD2015–5911.

[21] E. Neri, J. Kennedy, and G. Bennett, *Aeroacoustic source separation on a full scale nose landing gear featuring combinations of low noise technologies,* in *Proceedings of the Internoise 2015/ASME NCAD Meeting, August 9 – 12 2015, San Francisco, CA, USA* (2015) NCAD2015–5912.

[22] J. Kennedy, E. Neri, and G. Bennett, *The reduction of main landing gear noise,* in *22nd AIAA/CEAS Aeroacoustics Conference. May 30 – June 1 2015. Lyon, France* (2016) AIAA paper 2016–2900.

[23] R. Merino-Martinez, L. Bertsch, M. Snellen, and D. G. Simons, *Analysis of landing gear noise during approach,* in *22nd AIAA/CEAS Aeroacoustics Conference. May 30 – June 1 2016. Lyon, France* (2016) AIAA paper 2016–2769.

[24] R. Merino-Martinez, E. Neri, M. Snellen, J. Kennedy, D. Simons, and G. Bennett, *Comparing flyover noise measurements to full–scale nose landing gear wind–tunnel experiments for regional aircraft,* in *23rd AIAA/CEAS Aeroacoustics Conference. June 5 – 9 2017. Denver, Colorado, USA* (2017) AIAA paper 2017–3006.

[25] T. Takaishi, H. Ura, K. Nagai, Y. Yokokawa, M. Muruyama, Y. Ito, R. Sakai, H. Shoji, and K. Yamamoto, *Airframe noise measurements on JAXA Jet Flying Test Bed "Hisho" using a phased microphone array,* International Journal of Aeroacoustics **16**, 255 (2017), SAGE Publications Ltd. London, United Kingdom.

[26] R. Merino-Martinez, M. Snellen, and D. G. Simons, *Functional beamforming applied to imaging of flyover noise on landing aircraft,* Journal of Aircraft **53**, 1830 (2016).

[27] D. G. Simons, M. Snellen, R. Merino-Martinez, and A. M. N. Malgoezar, *Noise breakdown of landing aircraft using a microphone array and an airframe noise model,* in *46th International Congress and Exposition of Noise Control Engineering, 27–30 August, 2017, Hong Kong* (2017).

[28] R. Stoker, Y. Guo, C. Streett, and N. Burnside, *Airframe noise source locations of a 777 aircraft in flight and comparisons with past model–scale tests,* in *9th AIAA/CEAS Aeroacoustics Conference. May 12 – 14 2003. Hilton Head, South California, USA* (2003) AIAA paper 2003–3232.

[29] I. Dedoussi, T. Hynes, and H. Siller, *Investigating landing gear noise using fly–over data: the case of a Boeing 747–400,* in *19th AIAA/CEAS Aeroacoustics Conference, May 27 – 29, 2013, Berlin, Germany* (2013) AIAA paper 2013–2115.

[30] H. Bouchouireb, N. J. Pignier, C. O'Reilly, S. Boij, and J. Dahan, *Identification of noise sources on a realistic landing gear using numerical phased array methods applied to computational data,* in *23rd AIAA/CEAS Aeroacoustics Conference. June 5 – 9 2017. Denver, Colorado, USA* (2017) AIAA paper 2017–3019.

[31] J. A. Dahan, C. O'Reilly, and G. Efraimsson, *Numerical Investigation of a Realistic Nose Landing Gear,* in *20th AIAA/CEAS Aeroacoustics Conference, June 16 – 20 2014, Atlanta, GA, USA* (2014) AIAA paper 2014–2077.

[32] J. Dahan, R. Futrzynski, C. O'Reilly, and G. Efraimsson, *Aero–acoustic source analysis of landing gear noise via dynamic mode decomposition,* in *21st International Congress on Sound and Vibration, July 13 – 17 2014, Beijing, China*, Vol. 2 (2014) pp. 1245–1252.

[33] S. Redonnet and J. Bulté, *Landing Gear Noise Sources Identification through an Application of Array Methods to Experimental and Computational Data,* in *22nd AIAA/CEAS Aeroacoustics Conference. May 30 – June 1 2016. Lyon, France* (2016) AIAA paper 2016–2844.

[34] J. Bulté and S. Redonnet, *Landing Gear Noise Identification Using Phased Array with Experimental and Computational Data,* AIAA Journal **55**, 3839 (2017).

[35] M. R. Fink, *Noise component method for airframe noise,* in *4th AIAA Aeroacoustics Conference. October 3 – 5 1977, Atlanta, Georgia, USA* (1977) AIAA paper 1977–1271.

[36] Y. Guo, *Empirical Prediction of Aircraft Landing Gear Noise*, Tech. Rep. NASA TM–2005–213780 (NASA, 2005).

[37] Y. Guo, *A Semi–Empirical Model for Aircraft Landing Gear Noise Prediction,* in 12th *AIAA/CEAS Aeroacoustics Conference. May 8 – 10 2006, Cambridge, Massachusetts, USA* (2006) AIAA paper 2006–2627.

[38] C. L. Burley, T. F. Brooks, W. M. Humphreys Jr., and R. J. J. W., *ANOPP Landing Gear Noise Prediction Comparisons to Model–Scale Data,* in 13th *AIAA/CEAS Aeroacoustics Conference (28th AIAA Aeroacoustics Conference), May 21 – 23 2017, Rome, Italy* (2007) AIAA paper 2007–3459.

[39] Y. Guo, *A component–based model for aircraft landing gear noise prediction,* Journal of Sound and Vibration **312**, 801 (2008), retracted from the journal.

[40] N. Curle, *The influence of solid boundaries upon aerodynamic sound,* Proceedings of Royal Society of London A **231**, 505 (1955).

[41] F. C. De Metz and T. M. Farabee, *Laminar and Turbulent Shear Flow Induced Cavity Resonances,* in 4th *AIAA Aeroacoustics Conference. October 3 – 5 1977, Atlanta, Georgia, USA* (1977) AIAA paper 1977–1293.

[42] S. A. Elder, T. M. Farabee, and F. C. De Metz, *Mechanisms of flow–excited cavity tones at low Mach number,* Journal of the Acoustical Society of America **72**, 532 (1982).

[43] A. K. Sahai, *Consideration of Aircraft Noise Annoyance during Conceptual Aircraft Design*, Ph.D. thesis, Rheinisch–Westfälische Technische Hochschule Aachen (2016).

[44] M. Pott-Pollenske, W. Dobrzynski, H. Buchholz, S. Guérin, G. Saueressig, and U. Finke, *Airframe Noise Characteristics from Flyover Measurements and Predictions,* in 12th *AIAA/CEAS Aeroacoustics Conference. May 8 – 10 2006. Cambridge, Massachusetts, USA* (2006) AIAA paper 2006–2567.

[45] W. E. Zorumski, *Aircraft Noise Prediction Program – Theoretical Manual – Part 1*, Tech. Rep. NASA Technical Memorandum 83199 (NASA Technical Memorandum 83199, 1982).

[46] W. E. Zorumski, *Aircraft Noise Prediction Program – Theoretical Manual – Part 2*, Tech. Rep. NASA Technical Memorandum 83199 (NASA Technical Memorandum 83199, 1982).

[47] H. H. Hubbard and J. C. Manning, *Aeroacoustic Research Facilities at NASA Langley Research Center*, Tech. Rep. NASA Technical Memorandum 84585 (NASA Technical Memorandum 84585, 1983).

[48] W. M. Humphreys and T. F. Brooks, *Noise Spectra and Directivity for a Scale–Model Landing Gear,* International Journal of Aeroacoustics **8**, 409 (2009), SAGE Publications Ltd. London, United Kingdom.

[49] W. M. Dobrzynski, L. C. Chow, P. Guion, and D. Shiells, *Research into landing gear airframe noise reduction,* in *8th AIAA/CEAS Aeroacoustics Conference and Exhibit, June 17-19, 2002, Breckenridge, Colorado, USA* (2002) AIAA paper 2002–2409.

[50] P. A. Ravetta, R. A. Burdisso, and W. F. Ng, *Noise constrol of landing gears using elastic membrane–based fairings,* in *13th AIAA/CEAS Aeroacoustics Conference (28th AIAA Aeroacoustics Conference), May 21 – 23 2017, Rome, Italy* (2007) AIAA paper 2007–3466.

[51] E. Neri, *Characterisation and Reduction of Aircraft Landing Gear Noise*, Ph.D. thesis, Trinity College Dublin (2017).

[52] C. Arce León, *A Study on the Near–Surface Flow and Acoustic Emissions of Trailing Edge Serrations for the purpose of noise reduction of Wind Turbine Blades*, Ph.D. thesis, Delft University of Technology (2017), ISBN: 978–94–92516–68–8.

[53] T. F. Brooks and W. M. Humphreys, *Effect of Directional Array Size on the Measurement of Airframe Noise Components,* in *5th AIAA/CEAS Aeroacoustics Conference. Bellevue, WA, USA* (1999) AIAA paper 1999–1958.

[54] W. M. Humphreys and T. F. Brooks, *Design and Use of Microphone Directional Arrays for Aeroacoustic Measurements,* in *36th AIAA Aerospace Sciences Meeting and Exhibit, Reno, NV, USA* (1998) AIAA paper 1998–0471.

[55] F. Hutcheson and T. F. Brooks, *Measurement of Trailing Edge Noise Using Directional Array and Coherent Output Power Methods,* International Journal of Aeroacoustics **1**, 329 (2002), SAGE Publications Ltd. London, United Kingdom.

[56] T. F. Brooks and W. M. Humphreys, *Flap Edge Aeroacoustic Measurements and Predictions,* in *6th AIAA/CEAS Aeroacoustics Conference. Lahaina, HI, USA* (2000) AIAA paper 2000–1975.

[57] J. M. Mendoza, T. F. Brooks, and W. M. Humphreys, *An Aerodynamic Study of a Leading Edge Slat Configuration,* International Journal of Aeroacoustics **1**, 241 (2002), SAGE Publications Ltd. London, United Kingdom.

[58] S. Oerlemans, M. Fisher, T. Maeder, and K. Kögler, *Reduction of Wind Turbine Noise Using Optimized Airfoils and Trailing–Edge Serrations,* AIAA Journal **47**, 1470 (2009).

[59] S. Oerlemans, *Detection of aeroacoustic sound sources on aircraft and wind turbines*, Ph.D. thesis, University of Twente, Enschede, the Netherlands (2009).

[60] T. F. Brooks, D. S. Pope, and M. A. Marcolini, *Airfoil Self–Noise and Prediction*, Tech. Rep. NASA Reference Publication 1218 (NASA Reference Publication 1218, 1989).

[61] S. Pröbsting, *Airfoil Self–Noise – Investigation with Particle Image Velocimetry*, Ph.D. thesis, Delft University of Technology (2015), ISBN: 978–94–61865–23–6.

[62] A. L. Braslow, R. M. Hicks, and R. V. Harris Jr., *Use of grit–type boundary–layer transition trips on wind–tunnel models*, Tech. Rep. NASA–TN–D–3579 (NASA Technical Note (D–3579), 1966).

[63] C. Arce León, R. Merino-Martinez, D. Ragni, F. Avallone, and M. Snellen, *Boundary layer characterization and acoustic measurements of flow–aligned trailing edge serrations,* Experiments in Fluids **57**, 1 (2016).

[64] C. Arce León, R. Merino-Martinez, D. Ragni, F. Avallone, F. Scarano, S. Pröbsting, M. Snellen, D. G. Simons, and J. Madsen, *Effect of trailing edge serration–flow misalignment on airfoil noise emission,* Journal of Sound and Vibration **405**, 19 (2017).

[65] S. Oerlemans, P. Sijtsma, and B. Méndez López, *Location and Quantification of Noise Sources on a Wind Turbine,* Journal of Sound and Vibration **299**, 869 (2007).

[66] M. S. Howe, *A review of the theory of trailing edge noise,* Journal of Sound and Vibration **61**, 437 (1978).

[67] M. S. Howe, *Trailing edge noise at low Mach numbers, Part 2: Attached and separated edge flows,* Journal of Sound and Vibration **234**, 761 (2000).

[68] P. M. Morse and K. U. Ingard, *Theoretical Acoustics*, Second ed. (McGraw Hill, 1987) ISBN: 978–0691024011.

[69] J. E. Ffowcs Williams and L. H. Hall, *Aerodynamic sound generation by turbulent flow in the vicinity of a scattering half plane,* Journal of Fluid Mechanics **40**, 657 (1970).

[70] J. D. J. Anderson, *Fundamentals of Aerodynamics*, Third ed. (McGraw–Hill Series in Aeronautical and Aerospace Engineering, 2001) ISBN: 0–07–237335–0.

[71] R. K. Amiet, *Noise due to Turbulent Flow Past a Trailing Edge,* Journal of Sound and Vibration **47**, 387 (1976).

[72] W. K. Blake, *Mechanics of Flow–Induced Sound and Vibration* (Academic Press, 1986) p. 313, ISBN: 978–0–128–09273–6.

[73] O. Stalnov, P. Chaitanya, and P. F. Joseph, *Prediction of Broadband Trailing–Edge Noise Based on Blake Model and Amiet Theory,* in *21st AIAA/CEAS Aeroacoustics Conference, June 22 – 26 2015, Dallas, TX, USA* (2015) AIAA paper 2015–2526.

[74] D. P. Lockard and G. M. Lilley, *The Airframe Noise Reduction Challenge*, Tech. Rep. NASA TM–2004–213013 (NASA TM–2004–213013, 2004).

[75] S. Ghaemi, D. Ragni, and F. Scarano, *PIV–based pressure fluctuations in the turbulent boundary layer,* Experiments in Fluids **53**, 1823 (2012).

[76] M. Roger and S. Moreau, *Extensions and limitations of analytical airfoil broadband noise models,* International Journal of Aeroacoustics **9**, 273 (2010), SAGE Publications Ltd. London, United Kingdom.

[77] M. Roger and S. Moreau, *Back–scattering correction and further extensions of Amiet's trailing–edge noise model. Part 1: theory,* Journal of Sound and Vibration **286**, 477 (2005).

[78] S. Moreau and M. Roger, *Back–scattering correction and further extensions of Amiet's trailing–edge noise model. Part II: Application,* Journal of Sound and Vibration **323**, 397 (2009).

[79] L. Bertsch, S. Guérin, G. Looye, and M. Pott-Pollenske, *The Parametric Aircraft Noise Module – status overview and recent applications,* in *17th AIAA/CEAS Aeroacoustics Conference (32nd AIAA Aeroacoustics Conference), 5 – 8 June 2011, Portland, Oregon, USA* (2011) AIAA paper 2011–2855.

[80] D. L. Sutliff, D. L. Tweedt, E. B. Fite, and E. Envia, *Low–speed fan noise reduction with trailing edge blowing,* International Journal of Aeroacoustics **1**, 275 (2002), SAGE Publications Ltd. London, United Kingdom.

[81] J. Yu, S. R. Koh, M. Meinke, and W. Schröder, *Noise Reduction via Jet Injection near the Trailing Edge,* in *22nd AIAA/CEAS Aeroacoustics Conference. May 30 – June 1 2016. Lyon, France* (2016) AIAA paper 2016–2831.

[82] A. Finez, E. Jondeau, M. Roger, and M. C. Jacob, *Broadband Noise Reduction with Trailing Edge Brushes,* in *16th AIAA/CEAS Aeroacoustics Conference. Stockholm, Sweden* (2010) AIAA paper 2010–3980.

[83] M. Herr and W. Dobrzynski, *Experimental Investigations in Low–Noise Trailing–Edge Design,* AIAA Journal **43**, 1167 (2005).

[84] M. S. Howe, *Aerodynamic noise of a serrated trailing edge,* Journal of Fluids and Structures **5**, 33 (1991).

[85] S. Oerlemans, *Reduction of Wind Turbine Noise using Blade Trailing Edge Devices,* in *22nd AIAA/CEAS Aeroacoustics Conference. May 30 – June 1 2016. Lyon, France* (2016) AIAA paper 2016–3018.

[86] C. Arce León, R. Merino-Martinez, S. Pröbsting, D. Ragni, and F. Avallone, *Acoustic Emissions of Semi–Permeable Trailing Edge Serrations,* Acoustics Australia **46**, 111 (2017).

[87] C. Arce León, R. Merino-Martinez, D. Ragni, S. Pröbsting, F. Avallone, A. Singh, and J. Madsen, *Trailing Edge Serrations – Effect of Their Flap Angle on Flow and Acoustics,* in *7th International Meeting on Wind Turbine Noise, May 2 – 5 2017, Rotterdam, the Netherlands* (2017).

[88] M. R. Khorrami and M. M. Choudhari, *Application of passive porous treatment to slat trailing edge noise*, Tech. Rep. NASA TM–2003–212416 (2003).

[89] E. Sarradj and T. Geyer, *Noise Generation by Porous Airfoils,* in *13th AIAA/CEAS Aeroacoustics Conference (28th AIA Aeroacoustics Conference), May 21 – 23 2017, Rome, Italy* (2007) AIAA paper 2007–3719.

[90] T. Geyer, E. Sarradj, and C. Fritzsche, *Measurement of the noise generation at the trailing edge of porous airfoils,* Experiments in Fluids **48**, 291 (2010).

[91] T. Geyer, E. Sarradj, and C. Fritzsche, *Porous Airfoils: Noise Reduction and Boundary Layer Effects,* International Journal of Aeroacoustics **9**, 787 (2010), SAGE Publications Ltd. London, United Kingdom.

[92] M. Herr, K. S. Rossignol, J. Delfs, N. Lippitz, and M. Mößner, *Specification of Porous Materials for Low–Noise Trailing–Edge Application,* in *20th AIAA/CEAS Aeroacoustics Conference, June 16 – 20 2014, Atlanta, GA, USA* (2014) AIAA paper 2014–3041.

[93] A. Rubio Carpio, R. Merino-Martinez, F. Avallone, D. Ragni, M. Snellen, and S. van der Zwaag, *Broadband Trailing Edge Noise Reduction Using Permeable Metal Foams,* in *46th International Congress and Exposition of Noise Control Engineering, 27–30 August, 2017, Hong Kong* (2017).

[94] D. Ragni, F. Avallone, and W. C. P. van der Velden, *Concave serrations on broadband trailing–edge noise reduction,* in *23rd AIAA/CEAS Aeroacoustics Conference. June 5 – 9 2017. Denver, Colorado, USA* (2017) AIAA paper 2017–4174.

[95] M. Herr, *Design Criteria for Low–Noise Trailing–Edge,* in *13th AIAA/CEAS Aeroacoustics Conference (28th AIAA Aeroacoustics Conference), May 21 – 23 2017, Rome, Italy* (2007) AIAA paper 2007–3470.

[96] A. Vieira, M. Snellen, and D. G. Simons, *Assessing the shielding of engine noise by the wings for current aircraft using model predictions and measurements,* Journal of the Acoustical Society of America **143**, 388 (2018).

[97] M. J. Lighthill, *On sound generated aerodynamically, II: Turbulence as a Source of Sound,* Proceedings of the Royal Society of London. Series A, Mathematical and Physical Sciences **222**, 1 (1954).

[98] R. E. Musafir, *Sound generation by fluid flow,* in *23rd International Congress on Sound and Vibration, July 10 – 14 2016, Athens, Greece* (2016).

[99] S. Glegg and W. J. Devenport, *Aeroacoustics of Low Mach Number Flows – Fundamentals, Analysis, and Measurement* (Academic Press, 2017) p. 313, ISBN: 978–0–128–09651–2.

[100] J. R. Stone, *Interim Prediction Method for Jet Noise*, Tech. Rep. NASA–TM–X–71618 (1974).

[101] M. F. Heidmann, *Interim Prediction Method for Fan and Compressor Source Noise*, Tech. Rep. NASA–TM–X–71763 (1979).

[102] M. Snellen, R. Merino-Martinez, and D. G. Simons, *Assessment of noise level variability on landing aircraft using a phased microphone array,* Journal of Aircraft **54**, 2173 (2017).

[103] C. Zellmann, B. Schäffer, J. M. Wunderli, U. Isermann, and C. O. Paschereit, *Aircraft Noise Emission Model Accounting for Aircraft Flight Parameters,* Journal of Aircraft (2017), 10.2514/1.C034275.

[104] R. Merino-Martinez, S. J. Heblij, D. H. T. Bergmans, M. Snellen, and D. G. Simons, *Improving Aircraft Noise Predictions by Considering the Fan Rotational Speed,* Journal of Aircraft (2018), 10.2514/1.C034849, Accepted for publication. DOI: 10.2514/1.C034849.

[105] M. Snellen, R. Merino-Martinez, and D. G. Simons, *Assessment of aircraft noise sources variability using an acoustic camera,* in 5^{th} *CEAS Air & Space Conference. Challenges in European Aerospace. September 7 – 11 2015, Delft, Netherlands*, Paper 2015–019 (Council of European Aerospace Societies, 2015).

[106] R. Merino-Martinez, M. Snellen, and D. G. Simons, *Determination of Aircraft Noise Variability Using an Acoustic Camera,* in 23^{rd} *International Congress on Sound and Vibration, July 10 – 14 2016, Athens, Greece* (International Inst. of Acoustics and Vibration (IIAV), Auburn, Alabama, USA., 2016).

[107] L. S. Hultgren, *A Comparison of Combustor–Noise Models,* in 18^{th} *AIAA/CEAS Aeroacoustics Conference. June 4 – 6 2012. Colorado Springs, Colorado, USA* (2012) AIAA paper 2012–2087.

[108] P. Y. Ho and V. L. Doyle, *Combustion noise prediction update,* in 5^{th} *AIAA/CEAS Aeroacoustics Conference. March 12 – 14 1979. Seattle, WA, USA* (1979) AIAA paper 1979–588.

[109] R. K. Matta, G. T. Sandusky, and V. L. Doyle, *GE Core Engine Noise Investigation – Low Emission Engines*, Tech. Rep. (Federal Aviation Administration (FAA), Washington D.C., 1977) FAA–RD–77–4.

[110] E. Envia, *NASA Open Rotor Research,* in 14^{th} *CEAS–ASC Workshop, October 7 – 8, 2010, Warsaw, Poland* (2010).

[111] M. E. Quaglia, S. Moreau, M. Roger, and R. Fernando, *A preliminary semi–analytical approach for CROR noise modeling,* in *22nd AIAA/CEAS Aeroacoustics Conference. May 30 – June 1 2016. Lyon, France* (2016) AIAA paper 2016–2743.

[112] C. Horváth, E. Envia, and G. G. Podboy, *Limitations of Phased Array Beamforming in Open Rotor Noise Source Imaging,* AIAA Journal **52**, 1810 (2014).

[113] C. Horváth, *Beamforming Investigation of Dominant Counter–Rotating Open Rotor Tonal and Broadband Noise Sources,* AIAA Journal **53**, 1602 (2015).

[114] T. Sinnige, A. M. N. Malgoezar, D. Ragni, K. Y. W. Scheper, M. Snellen, G. Eitelberg, and L. L. M. Veldhuis, *APIAN-INF: a Low–Speed Aerodynamic and Aeroacoustic Investigation of Pylon–Pusher Propeller Interaction Effects,* in *5th CEAS Air & Space Conference. Challenges in European Aerospace. September 7 – 11 2015, Delft, Netherlands* (2015).

[115] T. Sinnige, B. Della Corte, R. de Vries, F. Avallone, R. Merino-Martinez, D. Ragni, G. Eitelberg, and L. L. M. Veldhuis, *Alleviation of Propeller–Slipstream–Induced Unsteady Pylon Loading by a Flow–Permeable Leading Edge,* Journal of Aircraft (2018), Accepted for publication.

[116] F. Farassat, S. L. Padula, and M. H. Dunn, *Advanced Turboprop Noise Prediction Based on Recent Theoretical Results,* Journal of Sound and Vibration **119**, 53 (1987).

[117] M. Nallasamy, B. J. Clark, and J. F. Groeneweg, *High–Speed Propeller Noise Predictions: Effects of Boundary Conditions Used in Blade Loading Calculations*, Tech. Rep. NASA TM–88913 (NASA, 1987).

[118] XROTOR website, *http://web.mit.edu/drela/public/web/xrotor/,* Accessed in January 2017.

[119] T. Sinnige, K. P. Lynch, D. Ragni, G. Eitelberg, and L. L. M. Veldhuis, *Aerodynamic and Aeroacoustic Effects of Pylon Trailing Edge Blowing on Pusher Propeller Installation,* in *21st AIAA/CEAS Aeroacoustics Conference, June 22 – 26 2015, Dallas, TX, USA* (2015) AIAA paper 2015–2356.

[120] B. Della Corte, T. Sinnige, R. de Vries, F. Avallone, D. Ragni, G. Eitelberg, and L. L. M. Veldhuis, *Tractor Propeller–Pylon Interaction, Part II: Mitigation of Unsteady Pylon Loading by Application of Leading–Edge Porosity,* in *55th AIAA Aerospace Sciences Meeting, January 9 – 13 2017, Grapevine, Texas, USA* (2017) AIAA paper 2017–1176.

[121] F. Avallone, D. Casalino, and D. Ragni, *Impingement of a propeller–slipstream on a leading edge with a flow–permeable insert: a computational aeroacoustic study,* International Journal of Aeroacoustics (2018), 10.1177/1475472X18788961, SAGE Publications Ltd. London, United Kingdom. Accepted for publication.

[122] A. M. N. Malgoezar, A. Vieira, M. Snellen, D. G. Simons, and L. L. M. Veldhuis, *Experimental characterization of noise shielding of a propeller in a hard wall duct,* Journal of Sound and Vibration (2018), Under review process.

3

Challenges in aeroacoustic experiments

If the challenge we face does not scare us,
then it is probably not that important.

Tim Ferriss

The greater the obstacle, the more glory in overcoming it.

Jean-Baptiste Poquelin (Molière)

The major challenges involved in aeroacoustic experiments are gathered in the present chapter. These are divided depending on the type of test to be applied: wind–tunnel experiments (both in closed and open–jet test sections), field measurements (featuring aircraft flyovers and full–scale wind turbines) or engine noise tests. Considerations about the sound propagation that should be accounted for are listed. Additional recommendations about the experimental setup and hardware use are also included[1].

[1] Some of the contents of this chapter are included in [1].

3.1. Types of aeroacoustic experiments

The aerospace noise sources described in chapter 2 can be studied using three main types of aeroacoustic experiments:

1. Wind–tunnel measurements (closed test sections and open jets)
2. Field measurements (aircraft flyovers and full–scale wind turbines)
3. Engine noise tests

The three of them are described in this section, but the main focus of the present research is placed on the first two, for which advantages and limitations are listed below.

3.1.1. Wind–tunnel measurements

As in the field of aerodynamics, wind–tunnel measurements offer a controlled environment to perform acoustic measurements on scaled models of aircraft, aircraft components and other test objects of interest, such as wind turbine blades or automobiles. It is, however, difficult to replicate the exact conditions present at an aircraft in flight. As shown by Stoker et al. [2], differences occur when results from a standard aeroacoustic wind–tunnel measurement with a closed test section are compared to results obtained from flight tests. These differences can be explained by lack of model fidelity, installation effects, a discrepancy in the Reynolds number, and the applicability of the assumptions made in the acoustic processing. Depending on the size of the model, scale effects need to be taken into account for the sound generation mechanisms [3]. Wind–tunnel acoustic measurements feature the convection of sound waves, which can be corrected for [3, 4] but they lack the important feature of the relative motion between source and receiver [5]. A major issue is the high background noise levels, but mitigation techniques are available [6–9], as will be explained in Chapter 4.

Wind–tunnel measurements can be performed in closed test sections or open jets, each of these options having different challenges:

Closed test sections

Closed test sections offer well–controlled aerodynamic properties. Acoustic measurements can be performed non–intrusively by mounting microphones flush in the floor, ceiling or walls of the wind tunnel. However, the amplitudes of the near–field pressure fluctuations inside the turbulent boundary layer (TBL) of the wind tunnel are generally much larger than the acoustic signal from the model, see Fig. 3.1. Mitigation of these near–field pressure fluctuations can be realized by mounting the microphones in cavities covered by a perforated plate or wire mesh at some distance from the TBL [10–12]. This solution takes advantage of the fact that TBL pressure fluctuations decay exponentially with distance. Microphones recessed in a cavity are offered commercially too [13]. A more *radical* solution for the TBL issues is to replace the wind–tunnel walls by Kevlar sheets and to place the microphones behind the sheets, outside of the flow, as in the stability "hybrid" wind tunnel of

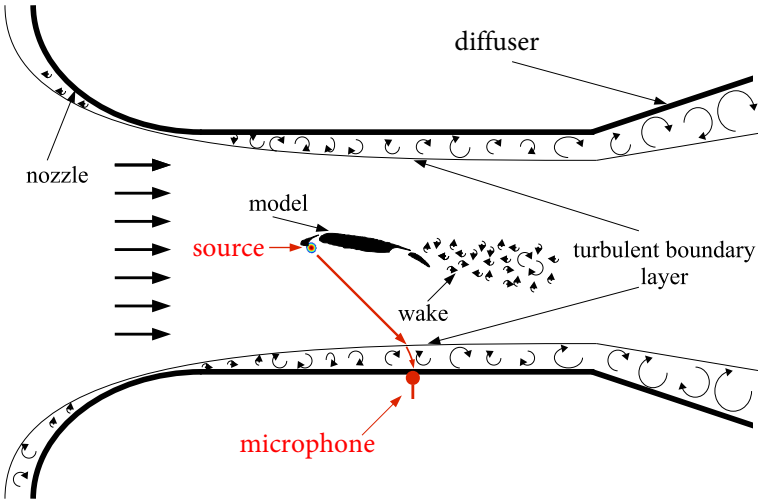

Figure 3.1: Schematic experimental setup for aeroacoustic testing in a closed–section wind tunnel. Adapted from [20].

Virginia Polytechnic Institute and State University [14]. In addition, acoustic measurements are hampered by reflections by the test section walls [15–18] and by the noise from the wind–tunnel circuit [6, 8, 19].

Open jets

The test chamber surrounding the jet is typically acoustically treated, so that most reflections are suppressed. Moreover, the background noise levels are lower than in a closed test section and the microphones can be placed outside of the flow, not being subject to turbulence. However, the aerodynamic conditions are less well–controlled and corrections are required to account for the refraction through the shear layer, which produces some disturbances (distortion in phase) that need to be taken into account [4, 21–23], see Fig. 3.2. Furthermore, the turbulence in the shear layer causes spectral broadening [24, 25] and decorrelation [26, 27]. Decorrelation is especially important for high frequencies and is further explained later in this section.

Comparability of wind–tunnel measurements

The comparability of measurements conducted with a similar model in different wind tunnels (either of the same type of test section but conducted at a different facility [28], or with different types of test sections at the same facility [20, 29, 30]) is still an open issue. In the work by Oerlemans et al. [30], the comparability of absolute and relative source levels obtained from microphone–array measurements in open and closed test sections on a scaled Airbus A340 model has been addressed.

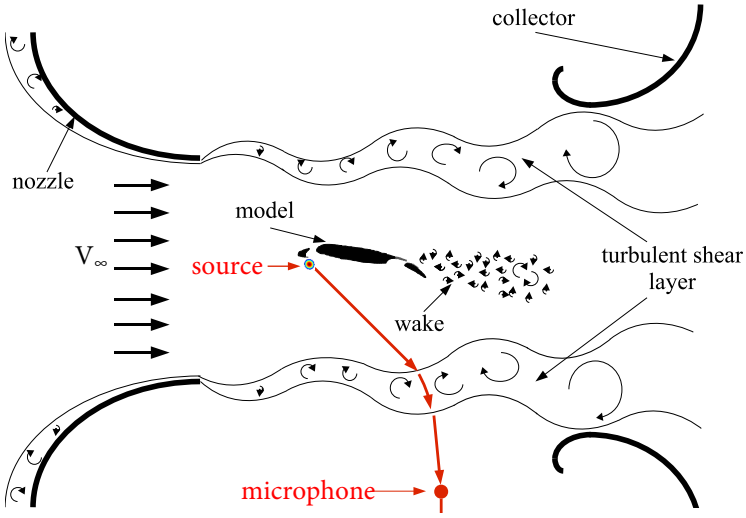

Figure 3.2: Schematic experimental setup for aeroacoustic testing in an open–jet wind tunnel. Adapted from [20].

Both measurements were conducted in the DNW–LLF[2] wind tunnel and both the open and the closed test sections were used for comparison. The source maps of both measurements by Oerlemans showed a comparable source distribution. The spatial resolution [31] in the open test section was higher than the resolution in the closed test section, because of the higher ratio between array diameter and distance to the scan plane. Some sources only appeared in one of the test sections and were not present in the other. The difference in the source occurrence can most likely be explained by the different flow conditions in each of the test sections, even though the overall lift forces on the models were equal. In order to compare test models with different sizes and operational conditions, the use of dimensionless data representation is recommended, such as the Strouhal number, see Appendix B.3. A systematic comparison between microphone measurements in both open and closed test sections was performed by Kröber [20] who studied several types of sound sources by evaluating comparable measurements. In Fig. 3.3 an overview of the advantages and disadvantages of both types of test sections is outlined. In general, background noise is a low–frequency issue for both cases. The importance of the reflections and the TBL influence is higher at low frequencies for closed–section wind tunnels, whereas the influence of scattering and refraction through the shear layer is more dominant at high frequencies for open–jet wind tunnels [20].

Therefore, open–jet wind tunnels are recommended for measuring models emitting low frequency noise with a low source strength, whereas closed–section wind tunnels are preferred for measuring high–frequency noise sources [20]. For middle

[2]Large low–speed facility at the German–Dutch wind tunnels in Marknesse, Netherlands.

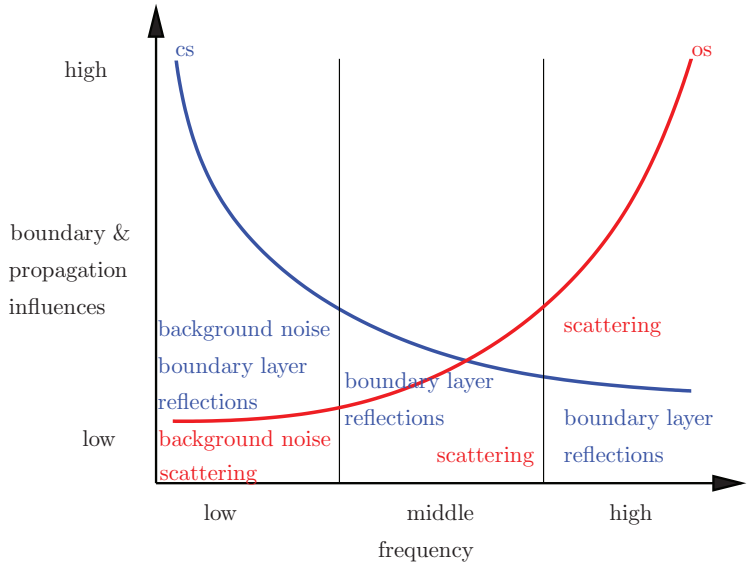

Figure 3.3: Illustration of the frequency–dependent influences on acoustic imaging results caused by boundary–layer and propagation effects in the open (os, in red) and closed test sections (cs, in blue) [20].

frequencies both test sections provide comparable acoustic performance. In practice, far–field noise measurements can almost only be performed in open–jet wind tunnels, since it is typically possible to place the microphone array further away from the source than in closed–section wind tunnels.

Reynolds number dependence

In standard wind–tunnel measurements a sole discrepancy in Reynolds number at otherwise similar conditions can lead to a difference in results (as aforementioned in this section). The effect of a varying Reynolds number on the noise generated was investigated by Ahlefeldt [32]. Acoustic measurements were performed on a small–scale aircraft model in high–lift configuration at both, a real–flight Reynolds number ($Re = 20.1 \times 10^6$) and a lower Reynolds number corresponding to standard wind–tunnel conditions ($Re = 1.4 \times 10^6$). Measurements were performed in the European Transonic Wind tunnel (ETW) which, due to its pressurized and cryogenic environment, enabled a variation of Reynolds number up to real–flight Reynolds numbers. Other parameters were kept unchanged. Thus, Reynolds number effects on aeroacoustic behavior were separated from effects of model fidelity and Mach number.

Several noise sources with significant Reynolds number dependency were found and exemplary differences at selected Strouhal numbers are shown in Fig. 3.4. Several dominant sources can be found at real–flight Reynolds number but are not present at standard conditions. Contrary to that, sources are present in the

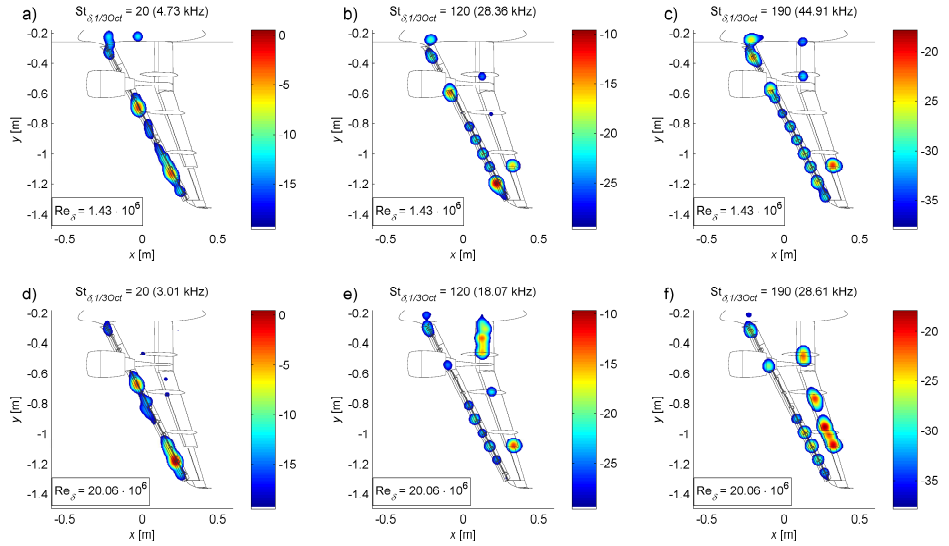

Figure 3.4: Beamforming source plots (using CLEAN–SC, see section 4.5) of an Airbus A320 model for a Reynolds number of 1.4×10^6 (top, standard wind–tunnel conditions) and 20.1×10^6 (bottom, real–flight conditions) in the ETW [32].

standard measurement but not at real–flight Reynolds number, as can be seen for example in the slat region.

The locally–integrated sound spectra of sources from the slat and the flap are shown in Fig. 3.5. The strong tonal components in the spectrum in the slat region measured at standard wind–tunnel conditions (lower Reynolds number) disappeared at real–flight Reynolds numbers. In standard wind–tunnel measurements these so–called "slat tones" are avoided using different transition forcing concepts as mentioned in section 2.3. For the flap, the real–flight Reynolds number flap sources show their dominant character.

An example of the influence of the flow regime (laminar or turbulent) for the same Reynolds number was mentioned when airfoil noise was explained in Fig. 2.9 in section 2.3. The noise emissions of a symmetric airfoil remarkably varied when a tripping device was applied in order to force the transition to the turbulent regime.

Coherence loss

The impact of decorrelation of acoustic waves when passing through the shear layer in open–jet wind tunnels or through the boundary layer in closed–section wind tunnels is usually neglected. Decorrelation, however, results in both a loss of image resolution and a corruption of the sound pressure levels in the source map. The influence of decorrelation can be estimated by means of an analytical model where the shear (or boundary) layer is modeled as a random medium with a single length scale [26, 27, 33]. In Fig. 3.6 a comparison between the theoretical predictions

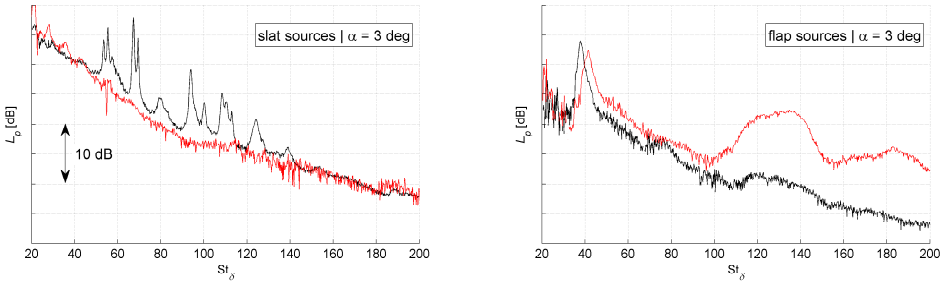

Figure 3.5: CLEAN–SC (see section 4.5) locally (slat and flap) integrated sound pressure levels of an Airbus A320 model with respect to the Strouhal number for a Reynolds number of 1.4×10^6 (black, standard wind–tunnel conditions) and 20.1×10^6 (red, real–flight conditions) in the ETW [32].

[26, 34, 35] assuming a Gaussian turbulence model and the measured coherence in the DNW–NWB[3] open–jet wind tunnel [27] is shown. It can be seen that, as expected, the coherence loss increases with the freestream velocity, the sound frequency and the streamwise distance of the microphone. The agreement between measurements and theoretical predictions is deemed as acceptable in most cases for microphone positions within a common distance range used in practice (below 2 m). It seems like the theoretical models overpredict the coherence values for distances close to the source and then, after a threshold distance, they underpredict the coherence with respect to the experimental measurements.

3.1.2. Field measurements

Aircraft flyovers

Measurements on flying aircraft provide the most reliable results of engine and airframe noise emissions of a certain aircraft type [36], especially if the measurements are taken under operational conditions [37, 38]. However, less controlled experimental conditions, like propagation effects [39],larger distances between the sound source and the observer, and the accurate tracing of the source movement [40, 41] need to be considered.

Michel et al. [42] from DLR Berlin were the pioneers in the use of ground microphone arrays for aircraft flyover measurements in 1998 by employing 96 microphones distributed in a 8 m × 8 m array for airframe noise analysis. Since then, a large amount of studies have been performed using larger arrays with a higher number of microphones [37, 43–49]. The Boeing Company used an elliptical array shape for their aircraft flyover tests in the Quiet Technology Demonstrator II program [50] consisting of 614 microphones in five subarrays with an overall size of approximately 91 m by 76 m, likely the largest array ever used in aircraft flyover tests. Sijtsma and Stoker [51, 52] showed in 2002 that the absolute noise contributions of different aircraft components could be determined and ranked. Researchers from NASA Langley have developed field–deployable microphone phased arrays for

[3]Low–speed wind tunnel at the German Aerospace Center facilities in Braunschweig, Germany.

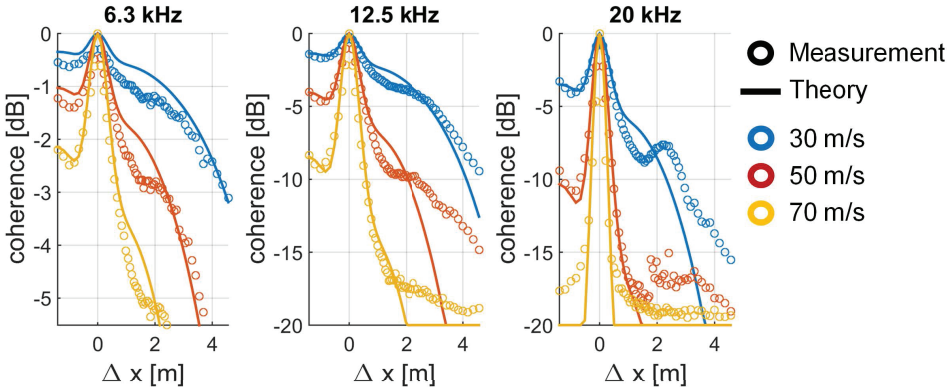

Figure 3.6: Comparison of the predicted and measured coherence loss with respect to the microphone spacing at one–third–octave bands (6.3 kHz, 12.5 kHz, 20 kHz) and different freestream velocities (30 m/s, 50 m/s, 70 m/s) in the DNW–NWB open–jet wind tunnel [27]. Note the different scales in the vertical axes.

flight tests [47], including acoustic measurements of small Unmanned Aerial System (sUAS) vehicles [53]. Investigations of the use of array processing techniques to cross–validate computational and experimental results of airframe noise analysis have also been performed [54, 55] with satisfactory results.

Some acoustic imaging results by Sijtsma et al. [41] for flyover measurements are illustrated in Fig. 3.7, where typical one–third–octave band source plots for MD82, Fokker 100, Airbus A340, and Boeing 777 aircraft are included. An acoustic array with 243 microphones and a diameter of 12 m was employed. The average aircraft height overhead was approximately 43 m. The large aperture and relatively short distance between the array and the aircraft allow for the separation of different noise sources, such as the landing gear system, the slat, the flap–side–edge and the engine inlet and exhaust. The algorithm used for Fig. 3.7 is an adapted time–domain version of conventional beamforming for moving sources [41], see Chapter 4.

Full–scale wind turbines

Aeroacoustic field measurements with full–scale wind turbines provide valuable information, since they represent the real blade geometries and operational conditions, compared to wind–tunnel experiments that only deal with airfoil sections. Moreover, the time dependency of the noise levels, such as amplitude modulation at the blade passing frequency, can also be studied in this kind of experiments [56].

Some of the challenges of this type of measurements are the typically large dimensions of the wind turbine (with rotor diameters of about 100 m) and the fact that the sound sources (i.e., the blades) are in rotating motion with tip speeds as high as 80 m/s. Moreover, the microphone array is typically located on the ground whereas the rotating plane of the sources is approximately vertical. These issues make the

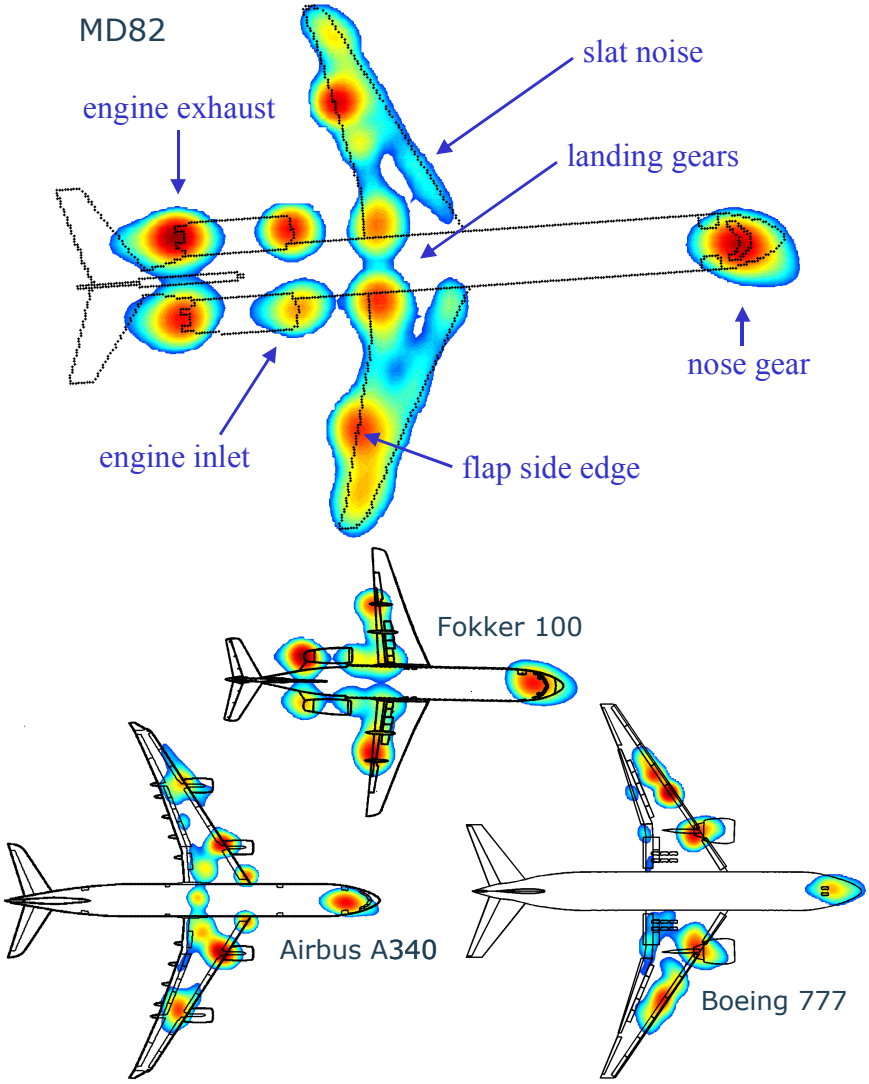

Figure 3.7: Conventional beamforming source plots for flyover measurements of MD82, Fokker 100, Airbus A340m and Boeing 777 aircraft. Adapted from [41].

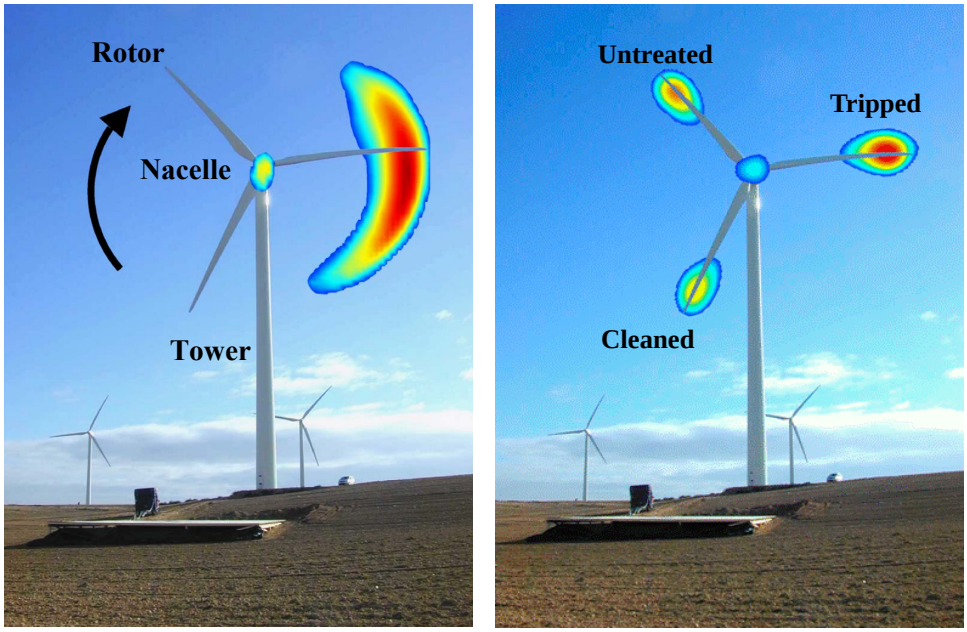

(a) (b)

Figure 3.8: Beamforming results of field measurements on a full–scale G58 wind turbine: (a) Using conventional beamforming [57]. (b) Using the Rotating Source Identifier technique ROSI [41], adapted from [59].

imaging and analysis of the noise sources more complicated, requiring large aperture microphone arrays and the use of acoustic imaging algorithms that account for the source motion [41, 57], see Chapter 4. An example of this phenomenon is illustrated in Fig. 3.8, where the acoustic images of a full–scale G58 wind turbine from Gamesa rotating clockwise are depicted. In Fig. 3.8a conventional beamforming (see Chapter 4) was employed, whereas in Fig. 3.8b the Rotating Source Identifier technique (ROSI) [41] was used. In both cases, the rotor hub is identified as a secondary noise source and the outer part of the blade is the main noise source. Conventional beamforming only localizes the downstroke going blade since TBL–TE noise scatters more efficiently towards the leading edge for non–compact sources, as mentioned in section 2.3.2. ROSI, on the other hand, is able to successfully localize the noise sources on each blade, which allowed for a detailed study of a different type of treatments (tripping or cleaning) on each blade at the same time [58].

Sound propagation considerations

Due to the typically large distances between sound source and observer in field tests, additional sound propagation considerations need to be taken into account. These physical phenomena may also be present in other types of experiments (wind–tunnel or engine noise tests) but their effect is often negligible. Therefore,

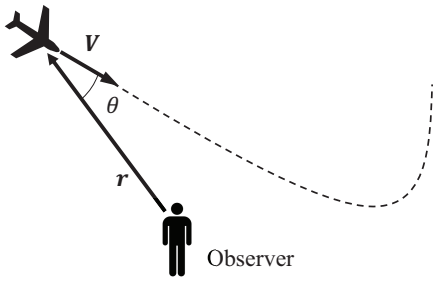

Figure 3.9: Diagram explaining the relative movement of an aircraft with respect to the observer [62].

they are explained in this section, although it is recommended to evaluate their influence in every type of experiment. These considerations can be grouped in four points:

- **Motion of the sound source:** The relative motion of a sound source (such as an aircraft or a wind turbine) with respect to the observer causes the well–known Doppler effect. This affects the perceived sound by the observer in terms of frequency and amplitude.

  The expression for the Doppler–shifted frequency, f', is

$$f' = \frac{f}{1 - \|\boldsymbol{M}\| \cos(\theta)}, \tag{3.1}$$

  where $\|\cdot\|$ is the Euclidean norm of the vector, f' is the observed frequency, f is the emitted frequency, $\boldsymbol{M}$ is the Mach number vector, $\boldsymbol{M} = \left(M_x, M_y, M_z\right) = \left(\frac{V_x}{c}, \frac{V_y}{c}, \frac{V_z}{c}\right) = \frac{\boldsymbol{V}}{c}$, $\boldsymbol{V}$ is the source velocity vector, and θ is the emission angle, i.e., the angle between the relative position vector of the source with respect to the observer, $\boldsymbol{r}$, and the source velocity vector, $\boldsymbol{V}$, see Fig. 3.9. The parameter f'/f is normally referred to as Doppler shift. This frequency shift can be corrected by de–Dopplerizing the microphone signals by re–sampling the original time series by interpolation [40]. Interpolation errors were shown to be small if the maximum frequency of analysis is restricted to one tenth of the sampling frequency and for flight Mach numbers up to 0.81 and flyover altitudes as low as 30 m [60]. Upsampling can be performed numerically before interpolation to alleviate this requirement [61].

  The amplitude of the perceived sound pressure at the observer position is also affected by the motion of the sound source [63], and multiplied by the convective amplification factor $1/\left[1 - \|\boldsymbol{M}\| \cos(\theta)\right]^2$. Thus, when the sound source is moving towards the observer, the perceived frequency and amplitude

are higher than those emitted, and vice versa. A detailed derivation of these formulae can be found in the Ph.D. thesis of Arntzen [63].

More general expressions for Eq. (3.1) can be derived in case the propagation medium is also in motion (i.e., the effect of wind) or if the observer is also moving [64, 65]. For aeroacoustic measurements, the observer is typically stationary and the sound speed can be considered as constant in the propagation medium if the distance between the source and the observer is not too large [66] (below 100 m). For relatively short recording times (as usual for flyover measurements), the source velocity vector $\boldsymbol{V}$ and the medium velocity vector $\boldsymbol{V}_\infty$ can be approximated as constant. With these assumptions, a modified version of Eq. (3.1) is derived

$$\frac{f'}{f} = \frac{\left\|\boldsymbol{x} - \boldsymbol{\xi}(\tau_{\text{em}})\right\| + \boldsymbol{M}_\infty \cdot [\boldsymbol{x} - \boldsymbol{\xi}(\tau_{\text{em}})]}{\left\|\boldsymbol{x} - \boldsymbol{\xi}(\tau_{\text{em}})\right\| - (\boldsymbol{M} - \boldsymbol{M}_\infty) \cdot [\boldsymbol{x} - \boldsymbol{\xi}(\tau_{\text{em}})]}, \tag{3.2}$$

where $\boldsymbol{x}$ is the observer position vector, $\boldsymbol{\xi}(\tau_{\text{em}})$ is the source position vector at the emission time τ_{em}, and $\boldsymbol{M}_\infty$ is the Mach number vector of the moving medium $\boldsymbol{M}_\infty = \frac{\boldsymbol{V}_\infty}{c}$. From Eq. (3.2) it can be derived that, if both the source and the observer are stationary, there is no change in frequency, despite the motion of the medium [64].

The effect of the motion of the sound source should also be accounted for in the steering vector formulation when applying acoustic imaging methods in the frequency domain [31, 67] or use imaging methods in the time domain [41], see Chapter 4. Strictly speaking, the Doppler shift should be calculated for every single grid point and microphone combination, which is computationally expensive [68–70]. For aircraft flyovers at low Mach numbers measured with microphone arrays of small aperture and for emission angles close to the vertical ($\theta \approx 90°$), an approximation can be made of considering a single Doppler shift value for the whole scan grid and for each time block, which considerably speeds up the processing. This is not applicable, however, for rotating sources, such as wind turbines, since each grid point has a different velocity vector $\boldsymbol{V}$, and hence a considerably different Doppler shift. Additional considerations need to be taken when applying deconvolution algorithms to moving sources [68, 69, 71].

- **Spreading losses:** If monopole sound sources are considered, the acoustic energy will spread in spherical wavefronts. As the distance to the source r increases, this results in a larger wavefront area, decreasing the sound intensity as $1/r^2$. This phenomenon is normally referred to as spherical spreading [39, 72].

  Sound is also absorbed by the atmosphere due to viscous and molecular relaxation effects [39, 63]. Hence, the L_p at the source position, namely at a distance of one meter from the source center ($r_0 = 1$ m), is estimated by adding the transmission losses due to the geometrical spreading and the

atmospheric absorption to the sound recorded at the observer position at a distance r as

$$L_\mathrm{p}\left(r_0, f\right) = L_\mathrm{p}\left(r, f\right) + 20\log\left(\frac{r}{r_0}\right) + \hat{\alpha}\left(f\right) r. \tag{3.3}$$

The atmospheric absorption coefficient (in dB/m), $\hat{\alpha}$, depends on the sound frequency f, and the temperature, relative humidity and static pressure of the atmosphere. More information about how to estimate this coefficient can be found in the literature [39, 72].

A potential risk when applying Eq. (3.3) is to amplify the background noise (such as the noise generated by the microphone electronics and the ambient noise), especially at higher frequencies, since α increases with frequency. Hence, a common practice is to neglect L_p values in the spectrogram under a threshold value (30 dB for example) before using Eq. (3.3) [73, 74].

Spherical spreading can be considered when applying beamforming by using the $1/r$ term in the steering vector formulation, see Eq. (4.2). The atmospheric absorption per frequency can also be easily accounted for [67].

- **Ground reflection:** When an acoustic wave arrives to a surface it is reflected and/or absorbed. In practical cases, most surfaces present some roughness so the reflected wave is scattered in many different directions as diffuse reflection. This is normally the case for field measurements taken outdoors, but also for wind–tunnel measurements, although there the walls can be normally treated with acoustically absorbent materials, as mentioned in section 3.1.1. As a consequence, a microphone situated over the ground records the direct wave coming from the source, as well as that reflected by the ground. This may create interference patterns in the recording depending on the sound frequency, ground impedance [75] and the relative position of the observer with respect to the source. If both waves arrive in phase a maximum coherent amplification of 6 dB can occur [63], whereas if both waves arrive with opposite phase destructive interference takes place. Therefore, the manner in which microphones are placed for field measurements condition the influence of the ground reflection effects [76]. Siller [70] recommended placing the microphones near the ground on flat and acoustically hard surfaces (such as concrete) and to avoid placing them near surfaces with impedance changes or where they can be easily reached by reflected sound waves. The application of sound absorbing materials [77] or optimized shapes for the mounting structure [76] can also mitigate the interference effects from ground reflections.

- **Atmospheric inhomogeneities:** A common assumption in acoustics is to consider a uniform propagation medium with homogeneous and constant properties, which leads to the consideration that the sound travels along

a straight–line path between source and observer [63]. In practice, however, temperature gradients (and their effects on sound speed) and non–uniform wind speeds lead to curved sound propagation paths due to refraction [72, 75]. This phenomenon leads to differences in the spreading losses and ground reflection effects, which are normally negligible for relatively small vertical distances between source and observer (less than 100 m) [66].

For larger source heights, calculation methods, such as ray tracing [63, 75], can be used. Ray tracing is frequency independent and considers refraction using Snell's law for fast propagation computations. If the gradient of sound speed is positive (i.e., if c increases with height) the rays will bend downwards and vice versa. Depending on the sound speed profiles and source position, areas with higher (caustics) or with lower sound pressure levels (shadow zones), with respect to the expected spherical spreading, can occur relatively far away from the source position (for horizontal distances in the order of kilometers) [63]. Diffraction phenomena should also be considered per frequency for large–distance propagation. For typical field measurements featuring microphone arrays, however, the distances to the sound source are considerably small in both the vertical and horizontal direction [31, 42, 67, 78], so these considerations can be neglected. Recent publications consider the application of ray tracing methods applied to measurements with microphone arrays in wind tunnels [23] or field measurements featuring full–size wind turbines [79]. The convection of sound waves [80] due to the wind has to be taken into account in the same way as for wind–tunnel measurements, see section 3.1.1.

Additionally, coherence loss can also occur in case that high turbulence levels are present in the atmosphere, as explained for the case of wind tunnels in section 3.1.1.

As an example, the result of first two corrections (source motion and spreading losses) is depicted in Fig. 3.10 in the form of two spectrograms corresponding to an Airbus A321 flyover: the picture on the left represents the spectrogram recorded at the ground before any correction and the picture on the right the spectrogram at the source position after correcting the data. Notice the different decibel color scales and the change in the Doppler shifted fan tones to straight lines. Whereas the spectrograms provide an overview on the time–varying frequency content of a sound signal, acoustic imaging methods offer information in the spatial domain, i.e., the location of the sound sources, see Chapter 4.

3.1.3. Engine noise tests

As aforementioned in section 2.4, engines are still one of the major noise sources on aircraft. Therefore, several studies focusing only on the noise emitted by the engines have been performed. Acoustic imaging techniques have been applied to engine indoor tests [81], ground tests with an aircraft model [82–84], measurements of a CROR model in an open–jet wind tunnel [85, 86], measurements of

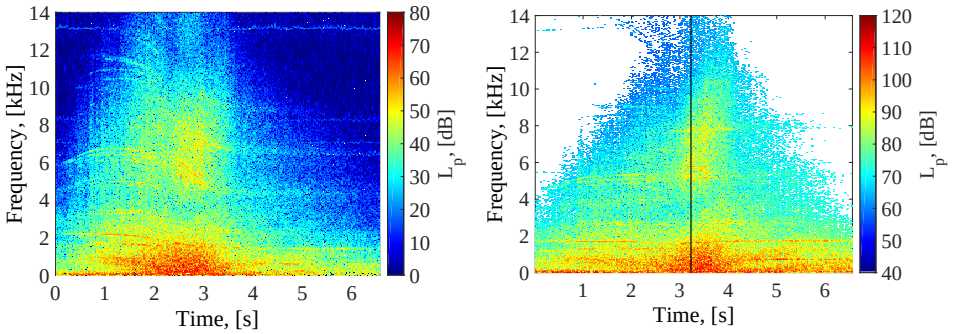

Figure 3.10: (a) Spectrogram recorded on the ground during an Airbus A321 flyover. (b) Spectrogram at the source position (r_0 = 1 m) after applying the propagation and source motion corrections. The white part represents the background noise deletion and the solid black line represents the time overhead [74].

scale turbofan–nozzles in an open–jet wind tunnel [87] and to ducted rotating machinery [88–90].

The acoustic imaging method SODIX [91, 92] was specifically developed for studying the noise emissions and directivity of turbofan engine noise tests, see section 4.11.

3.2. Experimental and hardware considerations

The main challenges regarding the use of phased microphone arrays for the aeroacoustic measurements explained in section 3.1 are:

- **Limited spatial resolution**, especially at low frequencies, i.e., the capability to separate two different sound sources placed at a small distance from each other. This is related to the beamwidth BW of the main lobe (normally defined as the (maximum) width 3 dB below the peak) in the source map [3, 93], see Fig. 3.11. Therefore, it is desirable to have a BW as narrow as possible. The spatial resolution for a circular array can be approximated using the Rayleigh resolution limit [94], which provides the angular resolution $\theta_{\text{scan},0}$ for an array of diameter D, see Eq. (3.4).

$$\theta_{\text{scan},0} \approx 1.2196\frac{c}{Df} = 1.2196\frac{\lambda}{D}. \tag{3.4}$$

  The spatial resolution for planar arrays in the direction perpendicular to the array plane is much lower than the lateral resolution. This phenomenon can be an advantage, as it makes the acoustic results of the array rather insensitive to small errors in the distance to the array plane [95]. More information about the spatial resolution limits can be found in Appendix D.

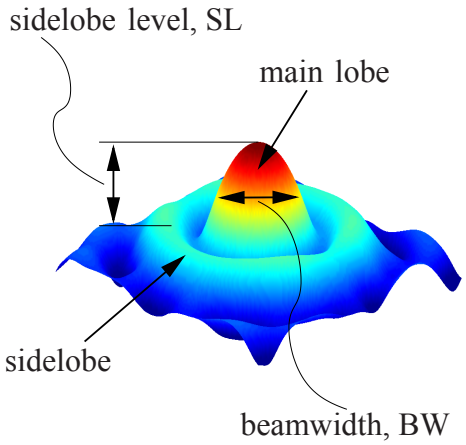

Figure 3.11: Schematic illustration of an example Point Spread Function (PSF). Adapted from [20].

- **The presence of sidelobes or "spurious sources"**, due to the array response function, which can be misidentified as real sources. This phenomenon, as well as the spatial resolution, is characterized by the array Point Spread Function (PSF), see Fig. 3.11, which is the array response (beam pattern) to a unitary–strength point source [3], and it is the consequence of the finite number of microphones in the array. The sidelobe level SL (also known as dynamic range [3]) is defined as the difference in dB between the main lobe peak and the highest sidelobe, see Fig. 3.11. It is, thus, desirable to have the largest dynamic range as possible. The number of microphones N in the array and its distribution (see section 3.2.2) are the dominant parameters influencing the SL [3, 96]. The theoretical SL in decibels for a random planar array can be approximated by $10\log_{10}(1/N) + 3$ [96]. The SL can also be estimated by empirical formulae [97]. One characteristic of the sidelobes is that they are coherent with their main lobe [98]. In case the spacing between microphones is larger than half the wavelength ($\lambda/2$), spatial aliasing occurs, causing an increase of the amplitude of some sidelobes, which can reach similar peak levels as that of the main lobe. These lobes are called "grating lobes" [99]. Avoiding this phenomenon can require very small spacings between microphones in case the study of very high frequencies is of interest.

- **High background noise levels**. This is especially the case for noisy environments, such as closed–section wind tunnels.

- **Reliability** of both the estimated location and strength of the sound sources.

The influence of each of these four factors (and hence the quality of the acoustic results) is determined by the experimental and hardware characteristics as well as

by the acoustic imaging method employed. This section (3.2) provides some recommendations and guidelines to improve the quality of the acoustic results obtained by microphone arrays regarding the experimental and hardware conditions, whereas the discussion about the most appropriate acoustic imaging methods depending on the intended application is included later in Chapter 4.

3.2.1. Hardware requirements

Processing multiple microphone signals increases the Signal–to–Noise Ratio (SNR) and the spatial resolution compared to a measurement with only one microphone [3]. The choice of the microphones highly depends on the particular experiment to be performed. Characteristics such as the dynamic range, frequency range and sensitivity have to be selected with care. In general, smaller microphones can measure up to higher frequencies and larger microphones have higher sensitivities. The directivity of the microphones has to be taken into account as well, especially for higher frequencies. Most of these specifications are provided by the manufacturer.

A microphone array comprises a set of microphones, an electronic amplifier with signal conditioning and an Analog to Digital Converter (ADC) together with frequency filters (typically low–pass). All the channels are connected by cables to the Data Acquisition System (DAS), which simultaneously samples all the microphone signals, typically using 24–bit resolution for signal recording. The sampling frequency should be at least twice the maximum frequency of interest, according to the sampling theorem [93]. As mentioned in section 3.1.2, the sampling frequency is recommended to be ten times the maximum frequency of interest in the case of moving sources. Monitoring the data acquisition during the experiment is recommended, in order to check that the frequency spectra obtained are valid.

Typical microphone arrays are equipped with high–accuracy analog microphones. For analog systems, the DAS normally contains all the necessary circuitry for the analog–to–digital conversion. In this configuration, the cables connecting the microphones to the DAS should have good electromagnetic shielding properties, otherwise electromagnetic interference (EMI) will degrade the data, as the signal inside the cable is analog. In general, this results in a rather complicated and expensive system [100].

Recent technological advances in digital microphones, such as micro electromechanical systems (MEMS), offer a less expensive and simpler alternative with respect to conventional analog microphones for phased array applications. These microphones are normally found in modern cellphones and are, therefore, usually optimized for the human speech frequency range (approximately from 300 Hz to 3 kHz) [100]. Digital sensors are more complex as they have the filtering and ADC embedded. A positive feature of this type of systems is that cables transporting digital data are less sensitive to EMI. Another important aspect is the quality of the ADC embedded in each sensor. ADC systems are usually expensive especially if precision (> 16–bits) and simultaneous sampling are required. Therefore, having this feature embedded in a cheap sensor can save a reasonable amount of the budget. On the other hand, it is difficult to ensure the precision of this data conversion [100].

The results of a recent study [101] comparing the performance of two microphone arrays (one equipped with digital MEMS microphones and the other with analog condenser microphones) for aeroacoustic measurements are presented later in section 6.1.2 in Chapter 6.

Lastly, for microphone arrays installed in small plates, the sound waves diffract and scatter at the edges of the plate. Reflections from walls in wind tunnels and from the ground in field measurements should also be taken into account, as it was mentioned in section 3.1.2. These phenomena produce phase and amplitude changes on the measured signal [76, 102, 103]. Thus, it is recommended to either use hard plates (for complete reflection) or on an acoustically *transparent* structure, by using sound absorbing materials, for example.

3.2.2. Microphone distribution guidelines

A detailed study of the optimization of the array microphone distribution is out of the scope of this thesis since it is a whole research topic in its own, but few basic guidelines are listed in this subsection.

In general, lower sidelobe levels are obtained by having microphones densely distributed around the center of the array and lower beamwidths are achieved when placing the microphones close to the edges of the array [104, 105]. Therefore, a compromise solution has to be found between the BW and the SL [106]. In general, periodicities in the microphone locations should be avoided [96].

Microphone arrays consisting of spirals or of several circles with an odd number of regularly spaced microphones seem to perform best [3, 36]. In addition, the microphone density close to the center of the array is normally higher than in the periphery to minimize coherence loss and to simultaneously have both good spatial resolution at low frequencies and low sidelobe levels at high frequencies, see sections 3.1.1 and 3.2.4. Interesting studies using optimization methods [104, 107–109], iterative microphone removal [110] and thorough parametric approaches leading to Paretto–optimal arrangements [105] can be found in the literature.

The microphone positions in the first large test campaign of aircraft flyovers [111] were optimized with a genetic algorithm. To study moving sources, such as aircraft flyovers, the array shape can be elongated in the flight direction [50, 112] to compensate for the loss of resolution due to emission angles other than $90°$.

An alternative to the optimization of the microphone positions is to repeat the measurements with different array positions and perform an average of the source maps [113]. This can be an approach for stationary sources in wind–tunnel measurements that do not present strong sound radiation directivities, but ensuring an accurate knowledge of all the relative array positions may be a cumbersome procedure.

In case a very large number of microphones is available, the use of subarrays can lead to improved results, providing adaptable aperture with a high dynamic range over a large range of emission angles [114].

3.2.3. Microphone array calibration

Amplitude and phase calibration of individual microphones

All the microphones in a phased array should be individually calibrated in both amplitude and phase. Normally, the microphone manufacturer provides some initial calibration data sheets per frequency. Additional calibrations can be performed employing a calibration pistonphone which generates a sinusoidal signal of known amplitude at a certain frequency, typically 250 Hz or 1000 Hz.

Metrological determination of the microphone positions

A precise calibration of the microphone positions is crucial for accurate aeroacoustic measurements [3]. Small sound sources with omni–directional radiation patterns and with known sound pressure levels are recommended for the calibration of the microphone array in both source location and quantification [20].

The acoustic GPS is a tool to determine the positions of an arbitrary number of microphones, especially for large–aperture and three–dimensional arrays. Similar to the satellite Global Positioning System (GPS), microphone positions are calculated based on the time delays between known reference positions and the microphones. The procedure requires that the pathway of acoustic waves propagating from the acoustic GPS to each microphone is not obstructed by any obstacle. However, perfect free–field conditions are not required. The basic acoustic GPS consists of N_{speakers} speakers and one reference microphone. They are mounted at known positions on a plate, see Fig. 3.12. The speakers are then driven with a noise signal, one speaker at a time, and the time delays between the reference microphone and all the array microphones are calculated. The sampling frequency is chosen as high as possible. Using these time delays, a set of N_{speakers} non–linear equations can be set up for every microphone.

$$\|\boldsymbol{x}_n - \boldsymbol{\xi}_j\| - \|\boldsymbol{x}_{\text{ref}} - \boldsymbol{\xi}_j\| = c\Delta t_{n,\text{ref},j}, \quad j = 1, ..., N_{\text{speakers}}, \tag{3.5}$$

where $\boldsymbol{x}_n$ is the n^{th} unknown microphone position, $\boldsymbol{\xi}_j$ are the known speaker positions, $\boldsymbol{x}_{\text{ref}}$ is the known reference microphone position, and $\Delta t_{n,\text{ref},j}$ is the measured time delay between the array microphone and reference microphone for the j^{th} speaker. Since there are three coordinates to calculate, the number of speakers should be at least three. Lauterbach et al. [115] chose $N_{\text{speakers}} = 8$, whereas Ernst et al. [116] chose $N_{\text{speakers}} = 6$ and used two reference microphones to calculate the speed of sound and a more advanced algorithm to account for errors of the known speaker and reference microphone geometrical positions. The positioning accuracy decreases with increasing distance between the acoustic GPS and the array microphones. Usually the positioning error is smaller than 1 mm. Moreover, this method is capable of compensating small individual phase errors of each array microphone and accounts for these by providing a more suitable "acoustic position" rather than just a geometric position. More details about how to solve the system of equations and process the data can be found in the literature [115, 116].

3.2.4. Microphone weighting

Different weighting or "shading" functions can be applied to the signals of each microphone to obtain acoustic imaging results of higher quality [31, 48, 95, 117,

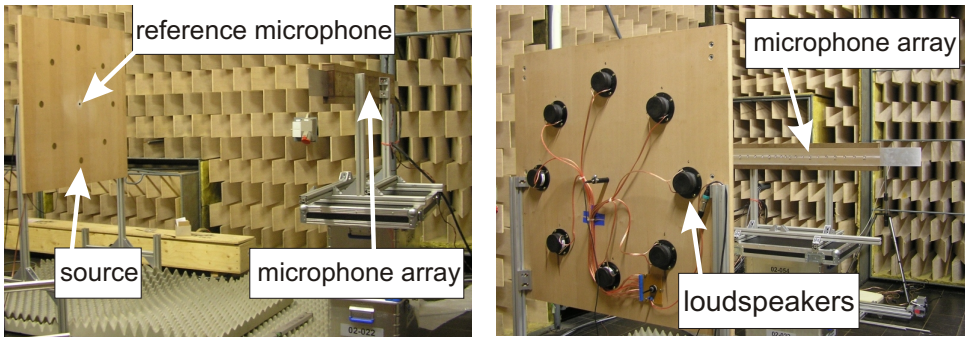

Figure 3.12: Experimental setup for an array calibration with calibration unit and line array in the anechoic chamber at DLR Göttingen [115].

118].

As explained in section 3.1.1, coherence loss increases with the frequency and with the distance between microphones. Thus, for high frequencies, the outer microphones of the array have low or no correlation with the inner microphones, and therefore, they do not contribute to the source L_p and this leads to an underestimation of the noise levels. To overcome this issue, the aperture of the array can be reduced for increasing frequency by neglecting the signals from all microphones further away from the array center than a threshold frequency–dependent distance [95]. This way, the width of the main lobe can be kept roughly constant by selecting smaller sub–arrays for higher frequencies [119].

For this reason, the inner part of most arrays present a higher microphone density than the outer part, as mentioned in section 3.2.2. This can be an issue when analyzing low frequencies because the inner part is more heavily weighted than the outer part, leading to a lower spatial resolution [95]. Hence, to compensate for the non–uniform microphone density, a weighting can be applied so that the weight per unit area *covered* by a microphone is roughly constant over the surface of the array. Thus, sparsely spaced microphones will be weighted more than clustered microphones. This correction only depends on the array distribution.

Acknowledgements

The author would like to express his profound gratitude to all the authors of the paper "*A review of acoustic imaging methods using phased microphone arrays*" [1], as well as to Takao Suzuki from the Boeing Company, for their constructive feedback and useful comments.

Bibliography

[1] R. Merino-Martinez, P. Sijtsma, M. Snellen, T. Ahlefeldt, J. Antoni, C. Bahr, D. Blacodon, D. Ernst, A. Finez, S. Funke, T. Geyer, S. Haxter, G. Herold, X. Huang, W. Humphreys, Q. Leclère, A. Malgoezar, U. Michel, T. Padois,

A. Pereira, C. Picard, E. Sarradj, H. Siller, D. G. Simons, and C. Spehr, *Aircraft Noise Generation and Assessment: A review of acoustic imaging methods using phased microphone arrays, CEAS aeroacoustic journal*, CEAS Aeronautical Journal (2017), Accepted for publication.

[2] R. Stoker, Y. Guo, C. Streett, and N. Burnside, *Airframe noise source locations of a 777 aircraft in flight and comparisons with past model–scale tests,* in *9^{th} AIAA/CEAS Aeroacoustics Conference. May 12 – 14 2003. Hilton Head, South California, USA* (2003) AIAA paper 2003–3232.

[3] T. Mueller, *Aeroacoustic Measurements* (Springer Science & Business Media, 2002) p. 313, ISBN: 978–3–642–07514–8.

[4] T. Padois, C. Prax, and V. Valeau, *Numerical validation of shear flow corrections for beamforming acoustic source localisation in open wind–tunnels,* Applied Acoustics **74**, 591 (2013).

[5] H. H. Heller and W. M. Dobrzynski, *Sound Radiation from Aircraft Wheel–Well/Landing–Gear Configuration,* Journal of Aircraft **14**, 768 (1977).

[6] C. J. Bahr and W. C. Horne, *Subspace–based background noise subtraction applied to aeroacoustic wind tunnel testing,* International Journal of Aeroacoustics **16**, 299 (2017), SAGE Publications Ltd. London, United Kingdom.

[7] R. P. Dougherty, *Advanced Time–domain Beamforming Techniques,* in *10^{th} AIAA/CEAS Aeroacoustics Conference. May 10 – 12 2004, Manchester, United Kingdom* (2004) AIAA paper 2004–2955.

[8] D. Blacodon, *Array Processing for Noisy Data: Application for Open and Closed Wind Tunnels,* AIAA Journal **49**, 55 (2011).

[9] D. Blacodon and J. Bulté, *Reverberation cancellation in a closed test section of a wind tunnel using a multi-microphone cepstral method,* Journal of Sound and Vibration **333**, 26 (2014).

[10] P. Sijtsma and H. Holthusen, *Source Location by Phased Array Measurements in Closed Wind Tunnel Test Sections,* in *5^{th} AIAA/CEAS Aeroacoustics Conference, Bellevue, WA, USA* (1999) AIAA paper 1999–1814.

[11] S. M. Jaeger, W. Horne, and C. Allen, *Effect of surface treatment on array microphone self–noise,* in *6^{th} AIAA/CEAS Aeroacoustics Conference. June 12–14 2016, Lahaina, HI, USA* (2000) AIAA paper 2000-1937.

[12] V. Fleury, L. Coste, R. Davy, and A. Mignosi, *Optimization of Microphone Array Wall-Mountings in Closed-Section Wind Tunnels,* in *16^{th} AIAA/CEAS Aeroacoustics Conference. Stockholm, Sweden* (2010) AIAA paper 2010–3738.

[13] G.R.A.S. Sound & Vibration – Turbulence screen microphones, *https://www.gras.dk/products/special-microphone/turbulence-screen-microphones,* Accessed in March 2017.

[14] B. S. Smith, H. E. Camargo, R. A. Burdisso, and W. J. Devenport, *Development of a Novel Acoustic Wind Tunnel Concept,* in *11th AIAA/CEAS Aeroacoustics Conference. May 23 – 25 2005. Monterey, California, USA* (2005) AIAA paper 2005–3053.

[15] S. Guidati, C. Brauer, and S. Wagner, *The reflection canceller – Phased array measurements in a reverberating environment,* in *8th AIAA/CEAS Aeroacoustics Conference and Exhibit, June 17-19, 2002, Breckenridge, Colorado, USA* (2002) AIAA paper 2002–2462.

[16] P. Sijtsma and H. Holthusen, *Corrections for Mirror Sources in Phased Array Processing Techniques,* in *9th AIAA/CEAS Aeroacoustics Conference, May 12 – 14, 2003, Hilton Head, South Carolina, USA* (2003) AIAA paper 2003–3196.

[17] M. Pelz, D. Döbler, and J. Ocker, *Microphone Arrays in a Wind Tunnel Environment with a Reverberating Floor,* in *7th Berlin Beamforming Conference, March 5 – 6 2018, Berlin, Germany* (GFaI, e.V., Berlin, 2018) BeBeC–2018–D05.

[18] J. Fischer and C. J. Doolan, *The Evaluation of Methods for Improving Beamforming Maps in Noisy Environment,* in *7th Berlin Beamforming Conference, March 5 – 6 2018, Berlin, Germany* (GFaI, e.V., Berlin, 2018) BeBeC–2018–D13.

[19] L. Koop and K. Ehrenfried, *Microphone–array processing for wind–tunnel measurements with strong background noise,* in *14th AIAA/CEAS Aeroacoustics Conference (29th AIAA Aeroacoustics Conference), May 5–7, 2008, Vancouver, British Columbia, Canada* (2008) AIAA paper 2008–2907.

[20] S. Kröber, *Comparability of Microphone Array Measurements in Open and Closed Wind Tunnels*, Ph.D. thesis, Technical University of Berlin (2014).

[21] R. K. Amiet, *Correction of Open Jet Wind Tunnel Measurements For Shear Layer Refraction,* in *2nd AIAA Aeroacoustics Conference, March 24 – 26, Hampton, VA, USA* (1975) AIAA paper 1975–532.

[22] R. K. Amiet, *Refraction of sound by a shear layer,* Journal of Sound and Vibration **58**, 467 (1978).

[23] E. Sarradj, *A fast ray casting method for sound refraction at shear layers,* International Journal of Aeroacoustics **16**, 65 (2017), SAGE Publications Ltd. London, United Kingdom.

[24] P. Sijtsma, S. Oerlemans, T. Tibbe, T. Berkefeld, and C. Spehr, *Spectral broadening by shear layers of open jet wind tunnels,* in *20th AIAA/CEAS*

Aeroacoustics Conference, June 16 – 20 2014, Atlanta, GA, USA (2014) AIAA paper 2014–3178.

[25] B. J. Tester and P. Sijtsma, *Measurement and analysis of phased array data on haystacked tones from a source located in a free jet,* in 23^{rd} *AIAA/CEAS Aeroacoustics Conference. June 5 – 9 2017. Denver, Colorado, USA* (2017) AIAA paper 2017–3864.

[26] R. P. Dougherty, *Turbulent decorrelation of aeroacoustic phased arrays: lessons from atmospheric science and astronomy,* in 9^{th} *AIAA/CEAS Aeroacoustics Conference. May 12 – 14 2003, Hilton Head, South California, USA* (2003) AIAA paper 2003–3200.

[27] D. Ernst, C. Spehr, and T. Berkefeld, *Decorrelation of acoustic wave propagation through the shear layer in open jet wind tunnel,* in 21^{st} *AIAA/CEAS Aeroacoustics Conference, June 22 – 26 2015, Dallas, TX, USA* (2015) AIAA paper 2015–2976.

[28] C. Spehr and T. Ahlefeldt, *Aircraft Noise Generation and Assessment: Comparison of Microphone Array Measurements in the Closed Test Section of LSWT and ETW, CEAS aeroacoustic journal*, CEAS Aeronautical Journal (2018), Under review process.

[29] S. Oerlemans and P. Sijtsma, *Acoustic Array Measurements of a 1:10.6 Scaled Airbus A340 Model,* in 10^{th} *AIAA/CEAS Aeroacoustics Conference, May 10 – 12, 2004, Manchester, United Kingdom* (2004) AIAA paper 2004–2924.

[30] S. Oerlemans, L. Broersma, and P. Sijtsma, *Quantification of Airframe Noise Using Microphone Arrays in Open and Closed Wind Tunnels,* International Journal of Aeroacoustics **6**, 309 (2007), SAGE Publications Ltd. London, United Kingdom.

[31] P. Sijtsma, *Phased array beamforming applied to wind tunnel and fly–over tests*, Tech. Rep. NLR–TP–2010–549 (National Aerospace Laboratory (NLR), Anthony Fokkerweg 2, 1059 CM Amsterdam, P.O. Box 90502, 1006 BM Amsterdam, The Netherlands, 2010).

[32] T. Ahlefeldt, *Microphone Array Measurement in European Transonic Wind Tunnel at Flight Reynolds Numbers,* AIAA Journal **55**, 36 (2016).

[33] L. Pires, R. Dougherty, S. Gerges, and F. Catalano, *Predicting Turbulent Decorrelation in Acoustic Phased Arrays,* in 18^{th} *AIAA/CEAS Aeroacoustics Conference. January 9 – 12 2012, Nashville, Tennessee, USA* (2012) AIAA paper 2012–0387.

[34] F. Grosche, H. Stiewitt, and B. Binder, *On aero–acoustic measurements in wind tunnels by means of a highly directional microphone system,* in 3^{rd} *AIAA/CEAS Aeroacoustics Conference. July 20 – 23 1976. Palo Alto, California, USA* (1976) AIAA paper 1976–535.

[35] T. F. Brooks and W. M. Humphreys, *Effect of Directional Array Size on the Measurement of Airframe Noise Components,* in *5th AIAA/CEAS Aeroacoustics Conference. Bellevue, WA, USA* (1999) AIAA paper 1999–1958.

[36] U. Michel, *History of acoustic beamforming,* in *Proceedings on CD of the 1st Berlin Beamforming Conference, 22 – 23 November, 2006* (GFaI, e.V., Berlin, 2006).

[37] C. Camier, T. Padois, J. Provencher, P.-A. Gauthier, A. Berry, J. F. Blais, M. Patenaude-Dufour, and R. Lapointe, *Fly–over source localization on civil aircraft,* in *19th AIAA/CEAS Aeroacoustics Conference. May 27 – 29 2013. Berlin, Germany* (2013) AIAA paper 2013–2261.

[38] D. G. Simons, M. Snellen, R. Merino-Martinez, and A. M. N. Malgoezar, *Noise breakdown of landing aircraft using a microphone array and an airframe noise model,* in *46th International Congress and Exposition of Noise Control Engineering, 27–30 August, 2017, Hong Kong* (2017).

[39] G. Ruijgrok, *Elements of aviation acoustics*, Second ed. (VSSD, 2007) ISBN: 1090–6562–155–5.

[40] G. P. Howell, M. A. Bradley, M. A. McCormick, and J. D. Brown, *De–Dopplerization and acoustic imaging of aircraft flyover noise measurements,* Journal of Sound and Vibration **105**, 151 (1986).

[41] P. Sijtsma, *Beamforming on moving sources*, Tech. Rep. NLR–TP–2006–733 (National Aerospace Laboratory (NLR), Anthony Fokkerweg 2, 1059 CM Amsterdam, P.O. Box 90502, 1006 BM Amsterdam, The Netherlands, 2006).

[42] U. Michel, B. Barsikow, J. Helbig, M. Hellmig, and M. Schüttpelz, *Flyover noise measurements on landing aircraft with a microphone array,* in *4th AIAA/CEAS Aeroacoustics Conference, June 2 – 4 1998, Toulouse, France* (1998) AIAA paper 1998–2336.

[43] J. F. Piet, G. Élias, and P. Lebigot, *Localization of acoustic source from a landing aircraft with a microphone array,* in *5th AIAA/CEAS Aeroacoustics Conference. Bellevue, WA, USA* (1999) AIAA paper 1999–1811.

[44] J. Piet, U. Michel, and P. Böhning, *Localization of the Acoustic Sources of the A340 with a Large Phased Microphone Array During Flight Tests,* in *8rd AIAA/CEAS Aeroacoustics Conference, Breckenridge, Colorado, USA* (2002) AIAA paper 2002–2506.

[45] H. A. Siller and U. Michel, *Buzz–saw noise spectra and directivity from flyover tests,* in *8th AIAA/CEAS Aeroacoustics Conference and Exhibit, June 17-19, 2002, Breckenridge, Colorado, USA* (2002) AIAA paper 2002–2562.

[46] J. F. Piet, R. Davy, G. Elias, H. A. Siller, L. C. Chow, C. Seror, and F. Laporte, *Flight Test Investigation of Add–On Treatments to Reduce Aircraft Airframe*

Noise, in 11th *AIAA/CEAS Aeroacoustics Conference, May 23 – 25, 2005, Monterey, California, USA* (2005) AIAA paper 2005–3007.

[47] M. R. Khorrami, D. P. Lockard, W. M. Humphreys, M. M. Choudhari, and T. Van de Ven, *Preliminary Analysis of Acoustic Measurements from the NASA–Gulfstream Airframe Noise Flight Test,* in 14th *AIAA/CEAS Aeroacoustics Conference. Vancouver, Canada* (2008) AIAA paper 2008–2814.

[48] T. Takaishi, H. Ura, K. Nagai, Y. Yokokawa, M. Muruyama, Y. Ito, R. Sakai, H. Shoji, and K. Yamamoto, *Airframe noise measurements on JAXA Jet Flying Test Bed "Hisho" using a phased microphone array,* International Journal of Aeroacoustics **16**, 255 (2017), SAGE Publications Ltd. London, United Kingdom.

[49] H. Siller, W. Hage, and T. Schumacher, *Source Localisation on Aircraft in Flight – New Measurements with the DLR Research Aircraft Airbus 320 ATRA,* in 7th *Berlin Beamforming Conference, March 5 – 6 2018, Berlin, Germany* (GFaI, e.V., Berlin, 2018) BeBeC–2018–D01.

[50] D. Reed, W. Herkes, and B. Shivashankara, *The Boeing Quiet Technology Demonstrator Program,* in 25th *International Congress of the Aeronautical Sciences (ICAS)* (2006).

[51] P. Sijtsma and R. Stoker, *Determination of Absolute Contributions of Aircraft Noise Components Using Fly–over Array Measurements,* in 10th *AIAA/CEAS Aeroacoustics Conference, May 10 – 12 2004, Manchester, United Kingdom* (2004) AIAA paper 2004–2958.

[52] P. Sijtsma, *Acoustic beamforming for the ranking of aircraft noise*, Tech. Rep. NLR–TP–2012–137 (National Aerospace Laboratory (NLR), Anthony Fokkerweg 2, 1059 CM Amsterdam, P.O. Box 90502, 1006 BM Amsterdam, The Netherlands, 2012).

[53] W. M. Humphreys, D. P. Lockard, M. R. Khorrami, W. G. Culliton, R. G. McSwain, P. A. Ravetta, and Z. Johns, *Development and Calibration of a Field–Deployable Microphone Phased Array for Propulsion and Airframe Noise Flyover Measurements,* in 22nd *AIAA/CEAS Aeroacoustics Conference. May 30 – June 1 2016. Lyon, France* (2016) AIAA paper 2016–2898.

[54] D. P. Lockard, W. M. Humphreys, M. R. Khorrami, E. Fares, D. Casalino, and P. A. Ravetta, *Comparison of Computational and Experimental Microphone Array Results for an 18%–Scale Aircraft Model,* International Journal of Aeroacoustics **16**, 358 (2017), SAGE Publications Ltd. London, United Kingdom.

[55] M. M. Choudhari, C. J. Bahr, M. R. Khorrami, D. P. Lockard, L. V. Lopes, N. S. Zawodny, M. Herr, M. Pott-Pollenske, M. Kamruzzaman, T. Van de Ven, E. Manoha, S. Redonnet, K. Yamamoto, T. Ikeda, and T. Imamura, *Simulations & Measurements of Airframe Noise: A BANC Workshops Perspective*, Tech. Rep. Progress and Challenges in Validation Testing for Computational

Fluid Dynamics, AVT–246 (NATO Applied Vehicle Technology Specialists Meeting, Avila, Spain, 2016).

[56] W. C. P. van der Velden, *Computational aeroacoustic approaches for wind turbine blade noise prediction*, Ph.D. thesis, Delft University of Technology (2017), ISBN: 978–94–6186–756–8.

[57] S. Oerlemans, P. Sijtsma, and B. Méndez López, *Location and Quantification of Noise Sources on a Wind Turbine,* Journal of Sound and Vibration **299**, 869 (2007).

[58] P. Sijtsma, S. Oerlemans, and H. Holthusen, *Location of rotating sources by phased array measurements,* in *7th AIAA/CEAS Aeroacoustics Conference, May 28-30, 2001, Maastricht, the Netherlands* (2001) AIAA paper 2001–2167.

[59] P. Sijtsma, *Challenges in acoustic measurements of airfoil noise,* in *Workshop on Serration Technology on Airfoil – Unsteady Aerodynamic and Aeroacoustics. October 17 – 21 2016. Leiden, the Netherlands* (2016) Presentation in the workshop.

[60] U. Michel, B. Barsikow, B. Haverich, and M. Schüttpelz, *Investigation of air–frame and jet noise in high–speed flight with a microphone array,* in *3rd AIAA/CEAS Aeroacoustics Conference, May 12-14, 1997, Atlanta, GA, USA* (1997) AIAA paper 1997–1596.

[61] J. Antoni and M. Eltabach, *A KIS solution for high fidelity interpolation and resampling of signals,* Mechanical Systems and Signal Processing **35**, 85 (2013).

[62] R. Merino-Martinez, S. J. Heblij, D. H. T. Bergmans, M. Snellen, and D. G. Simons, *Improving Aircraft Noise Predictions by Considering the Fan Rotational Speed,* Journal of Aircraft (2018), 10.2514/1.C034849, Accepted for publication. DOI: 10.2514/1.C034849.

[63] M. Arntzen, *Aircraft noise calculation and synthesis in a non–standard atmosphere*, Ph.D. thesis, Delft University of Technology (2014), ISBN: 978–94–62594–64–7.

[64] R. W. Young, *The Doppler Effect for Sound in a Moving Medium,* Journal of the Acoustical Society of America **6**, 112 (1934).

[65] R. N. Ghosh, *Doppler Effect in a Moving Medium,* American Journal of Physics **14**, 132 (1946), notes and Discussion.

[66] D. Bergmans, M. Arntzen, and W. Lammen, *Noise attenuation in varying atmospheric conditions*, Tech. Rep. NLR–TP–2011–262 (National Aerospace Laboratory (NLR), Anthony Fokkerweg 2, 1059 CM Amsterdam, P.O. Box 90502, 1006 BM Amsterdam, The Netherlands, 2011).

[67] R. Merino-Martinez, M. Snellen, and D. G. Simons, *Functional beamforming applied to imaging of flyover noise on landing aircraft,* Journal of Aircraft **53**, 1830 (2016).

[68] S. Guérin and C. Weckmüller, *Frequency–domain reconstruction of the point–spread–function for moving sources,* in *Proceedings on CD of the 2nd Berlin Beamforming Conference, 19 – 20 February, 2008* (GFaI, e.V., Berlin, 2008).

[69] S. Guérin and H. Siller, *A Hybrid Time-Frequency Apprach for the Noise Localization Analysis of Aircraft Fly–overs,* in *14th AIAA/CEAS Aeroacoustics Conference (29th AIAA Aeroacoustics Conference), May 5 – 7, 2008, Vancouver, British Columbia, Canada* (2008) AIAA paper 2008–2955.

[70] H. Siller, *Localisation of sound sources on aircraft in flight,* in *4th Berlin Beamforming Conference, February 22 – 23 2012, Berlin, Germany* (GFaI, e.V., Berlin, 2012).

[71] P. Böhning and H. Siller, *Study of a de–convolution method for aircraft flyover measurements,* in *8th AIAA/CEAS Aeroacoustics Conference, 17 – 19 June 2007, Breckenridge, Co, USA* (2007) AIAA paper 2007–3474.

[72] T. D. Rossing, *Handbook of Acoustics*, Second ed. (Springer Science & Business Media, 2007) ISBN: 987–0–387–30446–5.

[73] M. Snellen, R. Merino-Martinez, and D. G. Simons, *Assessment of aircraft noise sources variability using an acoustic camera,* in *5th CEAS Air & Space Conference. Challenges in European Aerospace. September 7 – 11 2015, Delft, Netherlands*, Paper 2015–019 (Council of European Aerospace Societies, 2015).

[74] M. Snellen, R. Merino-Martinez, and D. G. Simons, *Assessment of noise level variability on landing aircraft using a phased microphone array,* Journal of Aircraft **54**, 2173 (2017).

[75] K. Attenborough, K. M. Li, and K. Horoshenkov, *Predicting Outdoor Sound*, 1st ed. (CRC Press, 2006) ISBN: 978–0–419–23510–1.

[76] M. Albert, P. Bousquet, and D. Lizarazu, *Ground Effects for Aircraft Noise Cerfitication,* in *23rd AIAA/CEAS Aeroacoustics Conference. June 5 – 9 2017. Denver, Colorado, USA* (2017) AIAA paper 2017–3845.

[77] R. van der Goot, J. Hendriks, K. Y. W. Scheper, W. Hermans, G.and van der Wal, and D. G. Simons, *A low cost, high resolution acoustic camera with a flexible microphone configuration,* in *4th Berlin Beamforming Conference, February 22 – 23 2012, Berlin, Germany* (GFaI, e.V., Berlin, 2012).

[78] R. Merino-Martinez, E. Neri, M. Snellen, J. Kennedy, D. Simons, and G. Bennett, *Comparing flyover noise measurements to full–scale nose landing gear*

wind–tunnel experiments for regional aircraft, in 23rd AIAA/CEAS Aeroacoustics Conference. June 5 – 9 2017. Denver, Colorado, USA (2017) AIAA paper 2017–3006.

[79] P. Sijtsma, *Fast Calculation of Microphone Array Steering Vectors with Shear Flow,* in 7th Berlin Beamforming Conference, March 5 – 6 2018, Berlin, Germany (GFaI, e.V., Berlin, 2018) BeBeC–2018–S03.

[80] S. Glegg and W. J. Devenport, *Aeroacoustics of Low Mach Number Flows – Fundamentals, Analysis, and Measurement* (Academic Press, 2017) p. 313, ISBN: 978–0–128–09651–2.

[81] S. Funke, H. A. Siller, W. Hage, and O. Lemke, *Microphone–array measurements of a Rolls–Royce BR700 series aeroengine in an indoor test–bed and comparison with free–field data,* in 20th AIAA/CEAS Aeroacoustics Conference, 16 – 20 Jun 2014, Atlanta, Georgia, USA (2014) AIAA paper 2014–3070.

[82] H. Siller, A. Bassetti, S. Davies, and S. Funke, *Investigation of the noise emission of the V2500 engine of an A320 aircraft during ground tests with a line array and SODIX,* in 5th Berlin Beamforming Conference, February 19 – 20 2014, Berlin, Germany (2014) BeBeC–2014–18.

[83] H. Siller, A. Bassetti, and S. Funke, *Investigation of Turbo Machinery and Jet Noise of the V2500 Engine During Ground Tests with an A320 Aircraft,* in 11th European Turbomachinery Conference, 23 – 27 Mar 2015, Madrid, Spain (2015) ETC2015–216.

[84] H. Siller, A. Bassetti, and S. Funke, *SAMURAI – jet noise source analysis of a V2500 engine,* in AIAA SciTech 2016, 4 – 8 January 2016, San Diego, California, USA (2016) AIAA paper 2016–0110.

[85] S. Funke, L. Kim, and H. Siller, *Microphone–Array Measurements of a Model Scale Contra–Rotating Open Rotor in a Reverberant Open Wind–Tunnel,* in 17th AIAA/CEAS Aeroacoustics Conference (32nd AIAA Aeroacoustics Conference), 5 – 8 June 2011, Portland, Oregon, USA (2011) AIAA paper 2011–2766.

[86] S. Funke, L. Kim, and H. Siller, *Acoustic measurements of a contra–rotating open rotor in an open jet wind–tunnel,* International Journal of Aeroacoustics **11**, 197 (2012), SAGE Publications Ltd. London, United Kingdom.

[87] H. Siller, J. König, S. Funke, S. Oertwig, and L. Hritsevskyy, *Acoustic source localization on a model engine jet with different nozzle configurations and wing installation,* International Journal of Aeroacoustics **16**, 403 (2017), SAGE Publications Ltd. London, United Kingdom.

[88] G. Herold and E. Sarradj, *Microphone array method for the characterization of rotating sound sources in axial fans,* Noise Control Engineering Journal **63**, 546 (2015).

[89] R. P. Dougherty, *Mutual Incoherence of Broadband Duct Acoustic Modes,* in *22nd AIAA/CEAS Aeroacoustics Conference. May 30 – June 1 2015. Lyon, France* (2016) AIAA paper 2016–3032.

[90] L. C. Caldas, P. C. Greco, C. C. J. Pagani, and L. A. Baccalá, *Comparison of different techniques for rotating beamforming at the university of São Paulo fan rig test facility,* in *6th Berlin Beamforming Conference, February 29 – March 1 2016, Berlin, Germany* (GFaI, e.V., Berlin, 2016) BeBeC–2016–D14.

[91] U. Michel and S. Funke, *Noise Source Analysis of an Aeroengine with a New Inverse Method SODIX,* in *14th AIAA/CEAS Aeroacoustics Conference, May 5 – 7, 2008, Vancouver, BC, Canada* (2008) AIAA paper 2008–2860.

[92] U. Michel and S. Funke, *Inverse method for the acoustic source analysis of an aeroengine,* in *Proceedings on CD of the 2nd Berlin Beamforming Conference, 19 – 20 February, 2008* (GFaI, e.V., Berlin, 2008).

[93] A. Brandt, *Noise and vibration analysis: signal analysis and experimental procedures*, Second (John Wiley & Sons, 2011) ISBN: 978-0-470-74644-8.

[94] F. R. S. Lord Rayleigh, *XXXI. Investigations in Optics with special reference to the Spectroscope,* The London, Edinburgh and Dublin Philosophical Magazine and Journal of Science **8**, 261 (1879).

[95] S. Oerlemans, *Detection of aeroacoustic sound sources on aircraft and wind turbines*, Ph.D. thesis, University of Twente, Enschede, the Netherlands (2009).

[96] B. D. Steinberg, *Principles of Aperture and Array System Design: Including Random and Adaptive Arrays*, Second ed. (John Wiley & Sons, 1976) ISBN: 978–0471821021.

[97] J. J. Christensen and J. Hald, *Beamforming*, Tech. Rep. 1 (Brüel & Kjær, DK–2850 Nærum, Denmark, 2004) technical Review.

[98] P. Sijtsma, *CLEAN based on spatial source coherence,* International Journal of Aeroacoustics **6**, 357 (2007), SAGE Publications Ltd. London, United Kingdom.

[99] J. Benesty, J. Chen, and H. Yiteng, *Microphone Array Signal Processing* (Springer Science & Business Media, 2008) ISBN: 978-3-540-78611-5.

[100] A. Alexandridis, S. Papadakis, D. Pavlidi, and A. Mouchtaris, *Development and evaluation of a digital MEMS microphone array for spatial audio,* in *24th Signal Porcessing Conference (EUSIPCO). August 29 – September 2 2016. Budapest, Hungary* (2016).

[101] R. Merino-Martinez, M. P. J. Sanders, L. C. Caldas, F. Avallone, D. Ragni, L. D. de Santana, M. Snellen, and D. G. Simons, *Comparison between analog and digital microphone phased arrays for aeroacoustic measurements,* in *24th*

AIAA/CEAS Aeroacoustics Conference. June 25 – 29 2018. Atlanta, Georgia, USA (2018) AIAA paper 2018–2809.

[102] M. Pott-Pollenske, W. Dobrzynski, H. Buchholz, S. Guérin, G. Saueressig, and U. Finke, *Airframe Noise Characteristics from Flyover Measurements and Predictions,* in 12^{th} *AIAA/CEAS Aeroacoustics Conference. May 8 – 10 2006. Cambridge, Massachusetts, USA* (2006) AIAA paper 2006–2567.

[103] S. Funke, R. P. Dougherty, and U. Michel, *SODIX in comparison with various deconvolution methods,* in 5^{th} *Berlin Beamforming Conference, February 19 – 20 2014, Berlin, Germany* (2014) BeBeC–2014–11.

[104] S. Luesutthiviboon, A. Malgoezar, M. Snellen, P. Sijtsma, and D. G. Simons, *Improving Source Discrimination Performance by Using an Optimized Acoustic Array and Adaptive High–Resolution CLEAN–SC Beamforming,* in 7^{th} *Berlin Beamforming Conference, March 5 – 6 2018, Berlin, Germany* (GFaI, e.V., Berlin, 2018) BeBeC–2018–D07.

[105] E. Sarradj, *A generic approach to synthesize optimal array microphone arrangements,* in 6^{th} *Berlin Beamforming Conference, February 29 – March 1 2016, Berlin, Germany* (GFaI, e.V., Berlin, 2016) BeBeC–2016–S4.

[106] Z. Prime and C. J. Doolan, *A comparison of popular beamforming arrays,* in *Proceedings of ACOUSTICS November 17 – 20 2013. Victor Harbor, Australia*, edited by A. A. Society (2013).

[107] A. M. N. Malgoezar, M. Snellen, P. Sijtsma, and D. G. Simons, *Improving beamforming by optimization of acoustic array microphone positions,* in 6^{th} *Berlin Beamforming Conference, February 29– March 1 2016, Berlin, Germany* (2016).

[108] S. Luesutthiviboon, *Design of an Optimized Acoustic Array for Aero–acoustic Research in an Open–jet Anechoic Wind Tunnel*, Master's thesis, Delft University of Technology (2017).

[109] L. Carneiro, A. Berry, and T. Padois, *Optimization Methodology of Microphone Arrays for Environmental Source Localization Using the Generalized Cross–Correlation,* in 7^{th} *Berlin Beamforming Conference, March 5 – 6 2018, Berlin, Germany* (GFaI, e.V., Berlin, 2018) BeBeC–2018–D06.

[110] E. Arcondoulis and Y. Liu, *Beamforming array design via iterative microphone removal,* in 24^{th} *AIAA/CEAS Aeroacoustics Conference. June 25 – 29 2018. Atlanta, Georgia, USA* (2018) AIAA paper 2018–2807.

[111] U. Michel and W. Qiao, *Directivity of Landing–Gear Noise Based on Flyover Measurements,* in 5^{th} *AIAA/CEAS Aeroacoustics Conference, May 10 – 12 1999, Bellevue, Greater Seattle, WA, USA* (1998) AIAA paper 1999–1956.

[112] I. Dedoussi, T. Hynes, and H. Siller, *Investigating landing gear noise using fly–over data: the case of a Boeing 747–400,* in *19th AIAA/CEAS Aeroacoustics Conference, May 27 – 29, 2013, Berlin, Germany* (2013) AIAA paper 2013–2115.

[113] L. K. Wächter, J. Ocker, D. Döbler, C. Puhle, and G. Herold, *Investigations on Beamforming in the Wind Tunnel Using Multiple Microphone Array Measurements,* in *7th Berlin Beamforming Conference, March 5 – 6 2018, Berlin, Germany* (GFaI, e.V., Berlin, 2018) BeBeC–2018–S09.

[114] J. R. Underbrink, *Pletharrays for aeroacoustic phased array applications,* International Journal of Aeroacoustics **16**, 202 (2017), SAGE Publications Ltd. London, United Kingdom.

[115] A. Lauterbach, K. Ehrenfried, L. Koop, and S. Loose, *Procedure for the Accurate Phase Calibration of a Microphone Array,* in *15th AIAA/CEAS Aeroacoustics Conference. May 11-13 2009. Miami, Florida, USA* (2009) AIAA paper 2009–3122.

[116] D. Ernst, T. Ahlefeldt, S. Haxter, and C. Spehr, *Microphone localization with self calibrating acoustic GPS,* in *23rd AIAA/CEAS Aeroacoustics Conference. June 5 – 9 2017. Denver, CO, USA* (2017) AIAA paper 2017–3842.

[117] T. F. Brooks, M. A. Marcolini, and D. S. Pope, *A Directional Array Approach for the Measurement of Rotor Noise Source Distributions with Controlled Spatial Resolution,* Journal of Sound and Vibration **112**, 192 (1987).

[118] M. A. Marcolini and T. F. Brooks, *Rotor Noise Measurements Using a Directional Microphone Array,* in *11th AIAA/CEAS Aeroacoustics Conference. Palo Alto, CA, USA* (1987) AIAA paper 1987–2746.

[119] U. Michel, B. Barsikow, P. Böhning, and M. Hellmig, *Localisation of moving sound sources with phased microphone arrays,* in *Inter–Noise 2004, 22 – 25 August 2004, Prague, Czech Republic* (2004).

4

Acoustic imaging methods in aeroacoustics

Give us the tools and we will finish the job.

Sir Winston Leonard Spencer–Churchill

An ounce of algebra is worth a ton of verbal argument.

John Burdon Sanderson Haldane

A vast list of acoustic imaging algorithms exists in the literature. In this chapter, a brief explanation of the basics of acoustic beamforming is given. Some advanced methods are based on the deconvolution of the sound sources, i.e., the removal of the effect of the Point Spread Function (PSF) of the microphone array, such as CLEAN–SC, DAMAS, etc. These methods aim at enhancing the results of conventional beamforming, but their computation time is considerably larger. This chapter aims to summarize the most widely–used acoustic imaging methods and their applicability for aeroacoustic experiments. An illustrative benchmark case for simulated trailing–edge noise is included, comparing the performance of several methods[1].

[1] Some of the contents of this chapter are included in [1–7].

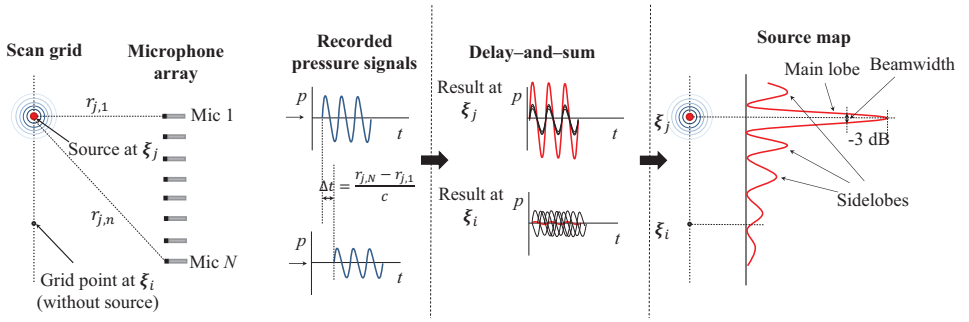

Figure 4.1: Diagram explaining the performance of delay–and–sum beamforming in the time domain.

4

4.1. Basics of beamforming

To provide an introductory understanding to acoustic imaging algorithms, the delay–and–sum method [8–10] is explained in this section as an illustrative technique. This algorithm works in the time domain and is based on the time delays and pressure amplitudes recorded by the microphones in an array.

In practice, the locations of the sound sources are not known *a priori*, so a scan grid covering all the potential expected source locations is defined. Figure 4.1 illustrates an example application case of delay–and–sum beamforming. Consider a single sound source located in the scan point $\boldsymbol{\xi}_j$ and a linear array of N microphones[2]. Due to the relative position of the microphones with respect to the sound source, the sound will arrive earlier at the nearest microphones. In this case, microphone 1 will be the first to receive the sound signal and microphone N will be the last ($r_{j,1} < r_{j,N}$, where $r_{j,n}$ is the distance between the j^{th} grid point and the n^{th} microphone). The time delay between both microphones depends on the travel distances from the source to each microphone $\Delta t = (r_{j,1} - r_{j,N})/c$. Moreover, the pressure amplitude recorded by microphone N will also be slightly lower than the one recorded by microphone 1, due to the larger travel distance, see section 3.1.2.

An exhaustive search process is performed by evaluating each point of the scan grid, for which the microphone time signals are shifted to account for the different relative time delays Δt and the amplitude losses due to the sound spreading [11]. Afterwards, the corrected time signals from all microphones are summed for that grid point. In case there is actually a sound source at the considered location (such as for $\boldsymbol{\xi}_j$ in Fig. 4.1), the summed signals will be in phase and their sum will provide a high amplitude. On the other hand, if no sound source is present in the considered grid point (such as for $\boldsymbol{\xi}_i$ in Fig. 4.1), the summed signals will present random phase and their sum will have a low amplitude. Therefore, the phased microphone array amplifies the sound from the grid point considered with respect to the sound coming from other directions [11].

[2]For simplicity a linear array is considered here, but the explanation can be easily extended to a planar array.

If the squared pressures of each grid point are plotted (normally in logarithmic scale in dB, i.e., L_p, see Appendix A.1), a source map (also known as beamform plot) is obtained, see right part of Fig. 4.1. In this plot, the beamwidth (BW), main lobe and sidelobes introduced in Fig. 3.11 can also be observed, which determine the concepts of spatial resolution and sidelobe level (SL) introduced in section 3.2. For quantifying the strength of the sound source, the summed signal needs to be averaged by the number of microphones N.

More advanced time–domain methods have been developed in the past [12–15], some of them are especially tailored for moving sources [16], with special focus on rotating sources, such as wind turbines or propellers.

4.2. Conventional Frequency Domain Beamforming (CFDBF)

If we transfer the delay–and–sum beamforming method explained in section 4.1 to the frequency domain, we obtain the so–called Conventional Frequency Domain Beamforming (CFDBF) [8, 9]. CFDBF is a very popular method, since it is robust, fast and intuitive. However, this algorithm (as well as its time–domain version) suffers from the Sparrow resolution limit [17] (see Appendix D) and presents a high sidelobe level, especially at high frequencies, see Fig. 3.11.

The CFDBF algorithm considers the Fourier transforms (see Appendix C.1) of the recorded pressures in each of the N microphones of the array ($\tilde{p}_n$) as an N–dimensional vector $\boldsymbol{p}(f) \in \mathbb{C}^{N\times 1}$, with frequency (f) dependence

$$\boldsymbol{p}(f) = \begin{pmatrix} \tilde{p}_1(f) \\ \vdots \\ \tilde{p}_N(f) \end{pmatrix}. \tag{4.1}$$

Assuming a single sound source in the scan point $\boldsymbol{\xi}_j$, the received signal is modeled as $s_j \boldsymbol{g}_j$, where s_j is the source strength and $\boldsymbol{g}_j \in \mathbb{C}^{N\times 1}$ is the so–called steering vector. The steering vector has N components, $g_{j,n}, n \in [1, \dots, N]$, which are the modeled pressure amplitudes at the microphone locations for a sound source with unit strength at that grid point [18].

There are several possible steering vector formulations in the literature [19, 20], each of them with different advantages and limitations. For simplicity, monopole sources are normally considered, although it is possible to consider other sources, such as dipoles [21, 22]. For a stationary point source, the steering vector is the free–field Green's function of the Helmholtz equation [23]

$$g_{j,n} = \frac{\exp\left(-2\pi i f \Delta t_{j,n}\right)}{4\pi \left\|\boldsymbol{x}_n - \boldsymbol{\xi}_j\right\|} = \frac{\exp\left[\frac{-2\pi i f \left\|\boldsymbol{x}_n - \boldsymbol{\xi}_j\right\|}{c}\right]}{4\pi \left\|\boldsymbol{x}_n - \boldsymbol{\xi}_j\right\|}, \tag{4.2}$$

where $i^2 = -1$, $\boldsymbol{x}_n = (x_n, y_n, z_n) \in \mathbb{R}^{N\times 3}$, $n = 1, \dots, N$ are the locations of the N microphones, and $\Delta t_{j,n}$ is the time delay between the emission at $\boldsymbol{\xi}_j$ and the

reception of the signal by the observer at $\boldsymbol{x}_n$. The distance between the j^{th} grid point and the n^{th} microphone $\|\boldsymbol{x}_n - \boldsymbol{\xi}_j\|$ is sometimes referred to as $r_{j,n}$.

For the case of moving sources (see section 3.1.2), a more complex expression of Eq. 4.2 can be derived [1, 11, 16] that accounts for the source movement [24]. An example of the application of the time–domain algorithm Rotating Source Identifier (ROSI) [16] was shown in Fig. 3.8.

An estimate for the source autopower, A, at a source located at grid point $\boldsymbol{\xi}_j$ is obtained by minimizing (in a least–squares sense [11]) the difference between the recorded pressure vector, $\boldsymbol{p}$, and the modeled pressures for a source at that grid point $\boldsymbol{\xi}_j$, $s_j \boldsymbol{g}_j$

$$A(\boldsymbol{\xi}_j) = \frac{1}{2} \frac{\boldsymbol{g}_j^* \langle \boldsymbol{p}\boldsymbol{p}^* \rangle \boldsymbol{g}_j}{\|\boldsymbol{g}_j\|^4} = \boldsymbol{w}_j^* \boldsymbol{C} \boldsymbol{w}_j. \tag{4.3}$$

In Eq. (4.3), an asterisk, $(\cdot)^*$, denotes the complex conjugate transpose, $\langle \cdot \rangle$ denotes the time average of several snapshots and $\boldsymbol{w}_j$ is the weighted steering vector (once again, several different formulations for the weighted steering vector exist in the literature [19]):

$$\boldsymbol{w}_j = \frac{\boldsymbol{g}_j}{\boldsymbol{g}_j^* \boldsymbol{g}_j} = \frac{\boldsymbol{g}_j}{\|\boldsymbol{g}_j\|^2}, \tag{4.4}$$

and $\boldsymbol{C}$ is the $N \times N$ Cross–Spectral Matrix (CSM) of the measured pressures, generated by averaging the Fourier–transformed sample blocks over time (see Appendix C.3). The CSM is Hermitian (i.e., conjugate symmetric) and positive–semidefinite:

$$\boldsymbol{C} = \langle \boldsymbol{p}\boldsymbol{p}^* \rangle. \tag{4.5}$$

A source map (also known as beamform plot or acoustic image) obtained with CFDBF is the summation of the PSFs of the actual sound sources, and since the strengths of the sources are always positive because $\boldsymbol{C}$ is positive–definite, (and due to the fact that noise is present in practice) the source plot represents, in practice, an overestimation of the actual source levels when multiple sound sources are present.

4.2.1. Background noise suppression

For measurements featuring strong wind noise or TBL noise, such as in closed–section wind tunnels [10, 18], the flow–noise signals can be approximated as independent stationary stochastic processes [25]. If the averaging time is sufficiently long, then the flow noise will contribute almost exclusively to the main diagonal of the averaged CSM (see Appendix C.2.6), which does not include any phase information and is, therefore, not critical for the array performance [11]. The elements of the main diagonal of $\boldsymbol{C}$ normally have much higher levels than the cross–powers and they contribute to the beamforming results at each grid point, because there is no phase cancellation [11] and, therefore, impose a noise floor in the source plots that hampers the source identification process, see the left plot in Fig. 4.2.

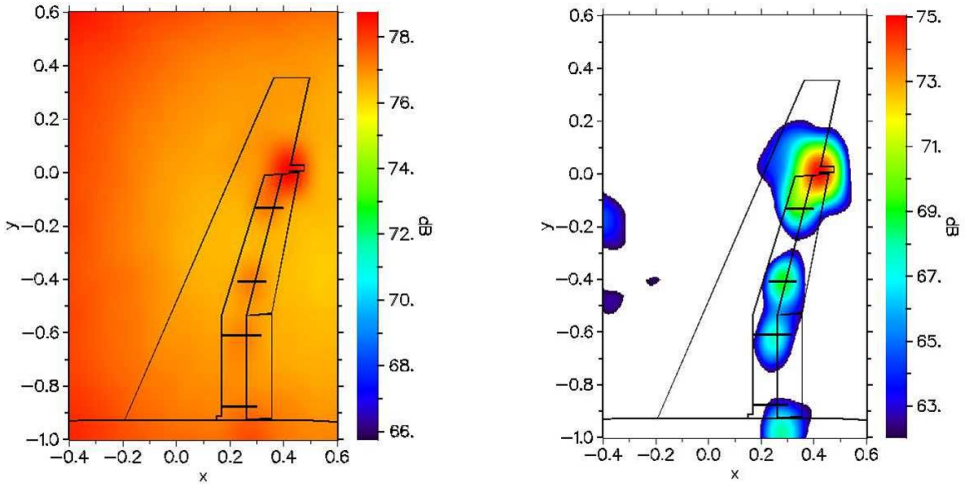

Figure 4.2: CFDBF source plots of a Fokker 100 half–model in a closed–section wind tunnel without diagonal removal (left) and with diagonal removal (right) [18].

Thus, the main diagonal of $\boldsymbol{C}$ can be removed (converted to zeros) in order to neglect the contribution of the noise which is incoherent for all the array microphones. However, precaution has to be taken when removing the main diagonal of $\boldsymbol{C}$, because, after that, $\boldsymbol{C}$ is no longer positive–definite and the PSF can present negative values (which are not physical) and the negative sidelobes of strong sources can eliminate weaker sources in some situations. This is explained by the appearance of negative eigenvalues in $\boldsymbol{C}$ when the main diagonal is removed, since the sum of the eigenvalues of a square matrix is always equal to the sum of its diagonal elements (zero, in this case). Hence, all the methods based on the CFDBF algorithm will suffer from this issue with the Diagonal Removal (DR) process.

An example of the application of this technique can be observed in Fig. 4.2 for a half–model of a Fokker 100 aircraft tested in the DNW–LST[3] closed–section wind tunnel [18]. A 96–microphone array was used, flush–mounted on one of the walls of the wind tunnel.

4.2.2. Integration methods

For well–separated monopole sources, CFDBF provides the correct source sound pressure levels L_p as the peak levels in the source map[11]. In practice, this situation rarely occurs. Main lobes of closely–spaced sound sources can overlap, sidelobes can deteriorate the source map, and the sound sources can be spatially distributed, such as for trailing–edge noise. In these cases, the peak levels obtained from CFDBF correspond to erroneous source levels. In addition, if coherence loss [26] applies, the main lobe becomes broader and gets reduced in strength [11].

Different integration methods have been proposed [6, 7], to overcome all these

[3]Low–speed facility at the German–Dutch wind tunnels in Marknesse, Netherlands.

issues. Three of them are described below, in increasing order of sophistication.

Source Power Integration (SPI)

In order to limit the effect of the array's PSF, the Source Power Integration (SPI) technique [18, 27] was proposed. The idea of the SPI method is to *integrate* the source power within a predefined Region Of Integration (ROI), and suppose that the integrated source power is represented by a simulated unit monopole. The integrated source power needs to be scaled by determining a certain scaling factor to normalize the total source power to a unit monopole source. This scaling factor, therefore, represents the total sound power within the ROI.

Figure 4.3a shows an arbitrarily distributed sound source obtained from an experiment. At the j^{th} grid point, the source power estimate is $A_{j,\text{exp}}$ (with $j \in J$). By applying the SPI method, the source powers from J grid points within a predefined ROI (framed by the dashed lines) are integrated and represented by a simulated monopole source indicated by the k^{th} grid point, as shown in Fig. 4.3b. The location of the simulated monopole is usually defined in the center of the ROI. Instead of $A_{j,\text{exp}}$ in Fig. 4.3a, $A_{j,\text{sim}}$ in Fig. 4.3b provides the source power of the simulated monopole's PSF at the j^{th} grid point in the ROI. Normally, the maximum value of $A_{j,\text{sim}}$, i.e., the peak of the simulated monopole's PSF at the k^{th} grid point, is considered as one. Thus, the integrated source power from the experiment needs to be scaled to match with the integrated source power of the monopole within the ROI by dividing it by the sound power P_{exp} as

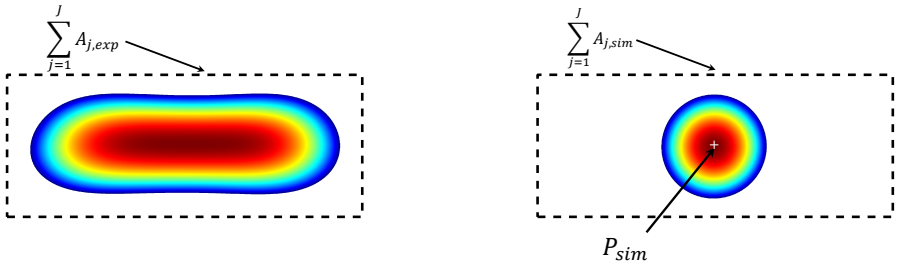

Figure 4.3: (a) Example of the application of the SPI technique: Experimental distributed sound source and (b) simulated point source. The dashed black rectangle denotes the ROI, and the white + marker the location of the simulated point source [6].

$$\frac{\sum_{j=1}^{J} A_{j,\text{exp}}}{P_{\text{exp}}} = \frac{\sum_{j=1}^{J} A_{j,\text{sim}}}{P_{\text{sim}}}, \tag{4.6}$$

where P_{sim} is typically taken as one. In order to correctly scale the integrated source power from the experiment, the sound power P_{exp} should represent the total sound power within the ROI. The value of P_{exp} can be solved from Eq. (4.6) as

$$P_{\text{exp}} = \frac{P_{\text{sim}} \sum_{j=1}^{J} A_{j,\text{exp}}}{\sum_{j=1}^{J} A_{j,\text{sim}}} = \frac{P_{\text{sim}} \sum_{j=1}^{J} \left(\boldsymbol{w}_j^* \boldsymbol{C} \boldsymbol{w}_j \right)}{\sum_{j=1}^{J} \left[\boldsymbol{w}_j^* \left(\boldsymbol{g}_k \boldsymbol{g}_k^* \right) \boldsymbol{w}_j \right]}, \tag{4.7}$$

where $\boldsymbol{g}_k$ is the steering vector to the k^{th} grid point, and $\boldsymbol{w}_j = \boldsymbol{g}_j / \left\| \boldsymbol{g}_j \right\|^2$ is the weighted steering vector [18].

The ROI should encompass the complete sound source (see Fig. 4.3a) and be large enough to capture the potential main–lobe broadening due to coherence loss [11]. However, it should be ensured that the variation of the main lobe width is always captured in the ROI for all considered frequencies. Furthermore, the choice of the ROI should also avoid the contributions and sidelobes from other sound sources and the noise floor from the source map [11].

This integration technique has been successfully applied to several wind–tunnel experiments [18, 28–34] and aircraft flyover measurements[35–37], yielding accurate sound pressure levels, even in the cases when coherence loss is present [11].

Extension to line sources (SPIL)

In aeroacoustic measurements of leading– and/or trailing–edge noise, the presence of a line source can be expected. When a certain source distribution is known beforehand, the simulated monopole source in the SPI method can be replaced by another predefined source distribution to better represent the physical characteristics of the source. In this case, the simulated monopole is replaced by a set of linearly–arranged incoherent monopoles.

In practice, a large number K of simulated incoherent point sources of equal power level are placed along the expected location of the experimental line source with steering vectors $\boldsymbol{g}_k$, $k \in 1, 2, \ldots, K$. To obtain the line source level, a minimization problem can be solved for the difference between the measured CSM ($\boldsymbol{C}$) and the CSM corresponding to the line source, $\boldsymbol{L}$. This can be formulated as

$$\min \left\| \boldsymbol{C} - P_{\text{exp}} \boldsymbol{L} \right\|^2, \tag{4.8}$$

where $\boldsymbol{L}$ is the CSM due to the simulated line source. By solving Eq. (4.8) for P_{exp} using a least–squares approach, Eq. (4.7) is updated as

$$P_{\text{exp}} = \frac{P_{\text{sim}} \sum_{j=1}^{J} \left(\boldsymbol{g}_j^* \boldsymbol{C} \boldsymbol{g}_j \right)}{\sum_{j=1}^{J} \left[\boldsymbol{g}_j^* \left(\sum_{k=1}^{K} \boldsymbol{g}_k \boldsymbol{g}_k^* \right) \boldsymbol{g}_j \right]} = \frac{P_{\text{sim}} \sum_{j=1}^{J} \left(\boldsymbol{g}_j^* \boldsymbol{C} \boldsymbol{g}_j \right)}{\sum_{j=1}^{J} \left(\boldsymbol{g}_j^* \boldsymbol{L} \boldsymbol{g}_j \right)}. \tag{4.9}$$

where P_{sim} now is due to *all* K simulated sources.

For distributed sound sources, the source coherence should be taken into account. However, the coherence length of a source is typically much smaller than the main lobe width, so the assumption of distributed incoherent monopoles is, in essence, valid [11].

This integration technique (SPIL) has proven to provide very accurate results on synthetic data simulating trailing–edge noise in a closed–section wind–tunnel

measurement, heavily contaminated by background noise, within the Array Methods Benchmark [6, 32], see section 4.17. This technique even surpassed other more sophisticated methods such as DAMAS or CLEAN–SC, see sections 4.6 and 4.5, respectively. A sensitivity analysis of the choice of the ROI for this method has been performed [6], see section 4.17. It has been recently applied to trailing–edge–noise measurements in closed–section [38] and open–jet [7, 39] wind tunnels.

Inverse SPI (ISPI)

The SPI method can be extended to include multiple ROIs for which the simulated sources are allowed to differ in power. This extension is known as Inverse SPI (ISPI). It addresses a similar minimization problem as the one presented in Eq. (4.8) considering Z different ROIs simultaneously (each of them with different sound powers $P_{\text{exp},z}$). It is, therefore, assumed that the CSM results from Z line sources. The minimization problem can be formulated as

$$\min \left\| \boldsymbol{C} - \sum_{z=1}^{Z} P_{\text{exp},z} \boldsymbol{L}_z \right\|^2 . \tag{4.10}$$

where the Z ROIs can have different sizes. This problem needs to be solved under non–negative constraints of $P_{\text{exp},z} \geq 0$. A standard Non–Negative Least Squares (NNLS) solver can be used [40].

This integration technique is especially useful for wind–tunnel measurements featuring mounting plates for the test model, which can cause extraneous noise sources on the junction between the test model and the mounting plates, also known as "corner" sources [41]. These sources can contaminate the results of the ROI of interest in experiments [30, 31, 33, 34, 42]. The aim of the ISPI technique is to exclude their influence on the actual results by defining dedicated ROIs at the expected locations of the "corner" sources.

If this method is taken to the limit of considering each single grid point as an integration area (i.e., $Z = J$), the obtained method is in essence DAMAS [43], explained later in section 4.6.

To demonstrate the added value of the ISPI method, a simulated line–source benchmark similar to the one presented in section 4.17.1 was considered, but two additional incoherent point sources were placed at both ends of the line, representing "corner sources" [6].

Figure 4.4 shows the ISPI and the SPI results of the mid–span integration area. Results obtained with CLEAN–SC [44] (see section 4.5) are included as well. It is observed that both SPI and CLEAN–SC fail at low frequencies, say below 700 Hz. The ISPI results, however, show very small errors (with maximum differences of 0.18 dB) for the whole frequency range.

The absolute errors made by each method averaged over the whole frequency range $\varepsilon = |\Delta \bar{L}_{\text{p}}|$ are indicated in Table 4.1. The three methods show relatively small errors, although, for frequencies lower than 700 Hz, SPI considerably overpredicts the results and CLEAN–SC shows an oscillating behavior. The results obtained with the ISPI technique collapse almost perfectly with the exact solution.

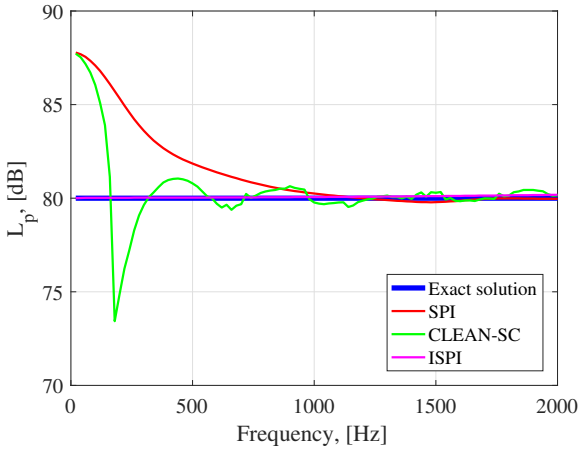

Figure 4.4: Results of the line–source with corner sources benchmark for the SPI, CLEAN–SC and ISPI methods with $w = 0.04$ m. The exact solution is a constant level of 80 dB per frequency (depicted in blue) [6].

Table 4.1: Average absolute errors made by each method with respect to the exact solution.

Method	ε, [dB]
SPI	1.4031
CLEAN–SC	0.9266
ISPI	0.0754

4.3. Functional beamforming

Functional beamforming is a method developed by Dougherty [45, 46] which is a modification of the CFDBF algorithm. A similar formulation was first proposed by Pisarenko [47]. Since the CSM is Hermitian and positive semidefinite, it can be expressed as its eigenvalue decomposition

$$\boldsymbol{C} = \boldsymbol{U}\boldsymbol{\Sigma}\boldsymbol{U}^* = \sum_{n=1}^{N} \sigma_n \boldsymbol{u}_n \boldsymbol{u}_n^*, \tag{4.11}$$

where $\boldsymbol{U}$ is a unitary matrix whose columns are the eigenvectors $(\boldsymbol{u}_1, \ldots, \boldsymbol{u}_N)$ of $\boldsymbol{C}$, and $\boldsymbol{\Sigma}$ is a diagonal matrix whose diagonal elements are the real–valued eigenvalues $(\sigma_1, \ldots, \sigma_N)$ of $\boldsymbol{C}$. In general, the number K of non–zero eigenvalues is equal to the number of incoherent sound sources that can be distinguished by the array [25].

The expression for the functional beamformer is

$$A_\nu(\boldsymbol{\xi}) = \left(\boldsymbol{w}^* \boldsymbol{C}^{\frac{1}{\nu}} \boldsymbol{w}\right)^\nu = \left(\boldsymbol{w}^* \boldsymbol{U}\boldsymbol{\Sigma}^{\frac{1}{\nu}}\boldsymbol{U}^* \boldsymbol{w}\right)^\nu, \tag{4.12}$$

with $\nu \geq 1$ a parameter which needs to be set by the user. It can be easily proven that for the case of $\nu = 1$ the CFDBF method is obtained and that $\nu = -1$ provides the adaptive beamforming formula, see section 4.9.

For single sound sources, the PSF, which has a value of one at the correct source locations (and alias points) and a value less than one elsewhere, is powered to the exponent ν. Therefore, powering the PSF at a sidelobe will lower its level, leaving the true source value virtually identical [45] if an adequate grid is used [1]. For ideal conditions, the dynamic range of functional beamforming should increase linearly with the exponent value, ν. Thus, for an appropriate exponent value the dynamic range is significantly increased. The beamwidth of the main lobe decreases rapidly with increasing ν approaching an asymptotic value of about 20% of the beamwidth of the main lobe obtained with CFDBF [1]. In general, values higher than $\nu = 100$ barely show further decrease.

In practice, the position vectors for the considered grid may not exactly coincide with the actual position vector of the sound source $(\boldsymbol{\xi}_j)$. In that case, the closest scan point to the actual sound source $(\boldsymbol{\xi}_i)$ will be treated in the same way as a sidelobe since the PSF will have a value less than one there. Around the true source location, the shape of the PSF can be approximated as $\cos^2(\varphi)$, where φ is the angle between $\boldsymbol{g}_j$ and $\boldsymbol{g}_i$ in the N–dimensional steering vector space [45]. After applying functional beamforming with an exponent ν (employing Bernoulli's inequality and considering small values of φ), the PSF at $\boldsymbol{\xi}_i$ can be approximated as

$$\cos^{2\nu}(\varphi) \approx \left(1 - \frac{\varphi^2}{2}\right)^{2\nu} \geq 1 - \nu\varphi^2. \tag{4.13}$$

Therefore, any potential difference between the source position $\boldsymbol{\xi}_j$ and the closest grid point $\boldsymbol{\xi}_i$ would imply an approximate autopower reduction given by the

factor $\left(1-\nu\varphi^2\right)$. Therefore, finer grids and accurate array calibration are recommended, because they imply lower values of φ, with the limitation of their higher computational demand [1]. Additionally, a careful study of the influence of ν on the source levels is recommended in experimental applications [48]. In case significant L_p reductions are observed, the value of the main lobe provided by the CFDBF method should be taken as a reference. A solution for this issue is to scale the whole source map so that the maximum L_p coincides with that obtained with the CFDBF method, which is assumed to provide the correct value [2].

The application of the diagonal removal technique aforementioned (Sec. 4.2) to functional beamforming is even more prone to errors, since this algorithm is based on the eigenvalue decomposition of the CSM. Mitigation of the diagonal removal issue is possible with CSM diagonal reconstruction methods (also known as diagonal denoising) [25, 49, 50] that reduce the autopower elements on the CSM diagonal as much as possible, while maintaining the matrix positive semidefinite. This problem can be solved efficiently and with guaranteed convergence using convex optimization [25]. This technique performs more efficiently if the number of incoherent noise sources K is smaller than the number of microphones N.

In previous work, functional beamforming has been applied to numerical simulations [1, 45, 46], controlled experiments with components in a laboratory [45, 46] and to full–scale aircraft flyover measurements under operational conditions [1, 2, 35, 37, 51]. More details about the experimental setup can be found in section 5.1.1. Figures 4.5 and 4.6 present the results of different acoustic imaging methods (CFDBF, functional beamforming, CLEAN–SC (see section 4.5) and robust adaptive beamforming (see section 4.9)) applied to two aircraft flyovers which belong to a measurement campaign in Amsterdam Airport Schiphol, where 115 landing aircraft were recorded with a 32–microphone array [1, 2, 35, 36, 51] and a diameter of 1.7 m (i.e., about seven times fewer microphones and seven times smaller than for the array used in Fig. 3.7). A more detailed description of the experimental setup is included later in section 5.1.1. These flyovers were selected because they presented a strong tonal component at the presented frequencies: 1630 Hz and 7140 Hz, respectively [1].

Figure 4.5 shows the source plots for an Airbus A321 flyover at 1630 Hz, where the main noise source seems to be the nose landing gear (see Chapter 5 for more details). Functional beamforming (with $\nu = 100$) and CLEAN–SC present the highest dynamic ranges. Figure 4.6 shows the source plots for a Fokker 70 flyover at 7140 Hz, where the main noise sources appear to be located at the MLG wheels. Once again, functional beamforming (with $\nu = 100$) and CLEAN–SC present the highest dynamic ranges, but CLEAN–SC only shows one of the two sources (left). Figures 4.5 and 4.6 show that even with a relatively *cheap* and small experimental setup, satisfactory results can be obtained for aircraft flyover measurements.

The computation time for the functional beamforming is basically identical to the CFDBF one, since the only relevant operation added is the eigenvalue decomposition of $\boldsymbol{C}$ [1], which is typically a fast process.

A similar integration method as the SPI technique explained in section 4.2.2 was used for quantifying noise sources in flyover measurements [38, 52]. A somewhat

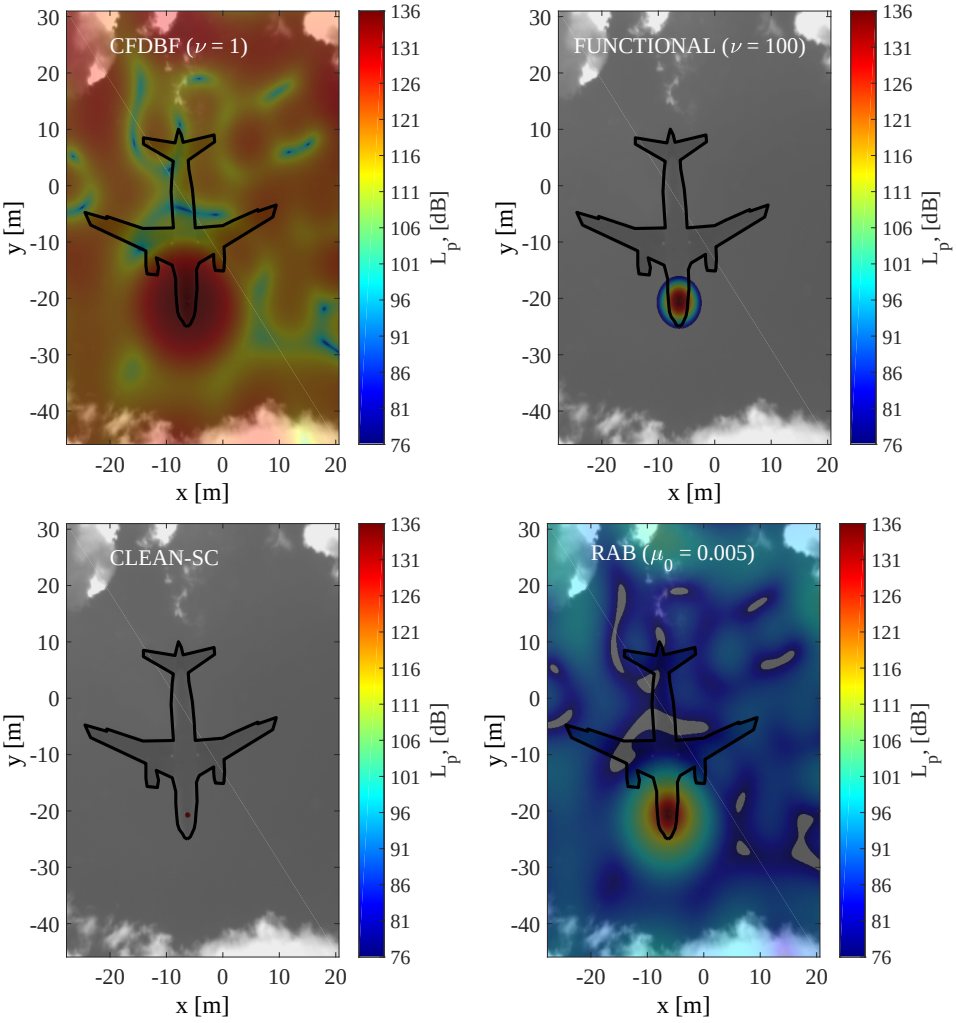

Figure 4.5: Acoustic source plots for an Airbus A321 flyover at 1630 Hz. From left to right and from top to bottom: CFDBF, functional beamforming with $\nu = 100$, CLEAN–SC and RAB $\mu_0 = 0.005$. The outline of the aircraft has been added for clarity reasons. Adapted from [1].

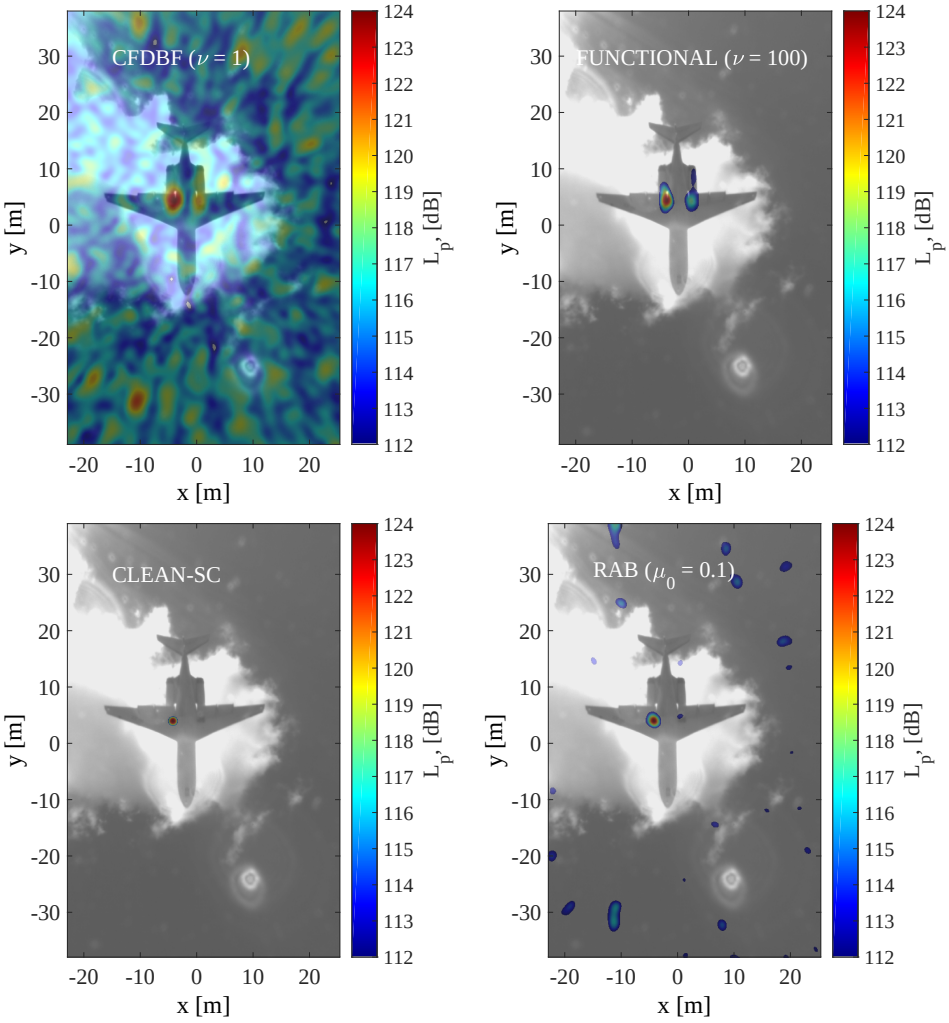

Figure 4.6: Acoustic source plots for a Fokker 70 flyover at 7140 Hz. From left to right and from top to bottom: CFDBF, functional beamforming with $\nu = 100$, CLEAN–SC and RAB with $\mu_0 = 0.1$. Adapted from [1].

similar time domain technique based on the generalized mean of the generalized cross correlation has been developed recently [53, 54].

4.4. Orthogonal beamforming

Orthogonal beamforming [55–57], similarly to functional beamforming, is also based on the eigenvalue decomposition of the CSM. It builds on the idea of separating the signal and the noise subspace [58]. In a setup with K incoherent sources and $K < N$, it is reasonable to assume that the $(N - K)$ smallest eigenvalues are attributed to noise and are all equal to $\hat{n}^2$. The CSM eigenvalue decomposition can be written as

$$\boldsymbol{C} = \boldsymbol{U}_S \boldsymbol{\Sigma}_S \boldsymbol{U}_S^* + \hat{n}^2 \boldsymbol{I}, \tag{4.14}$$

where $\hat{n}^2$ contains the power from uncorrelated sound sources (e.g., generated by non–acoustic pressure fluctuations, the microphone electronics and data acquisition hardware). Hence, the eigenvectors in $\boldsymbol{U}_S$ span the signal subspace of $\boldsymbol{U}$, whereas the remaining eigenvectors span the noise subspace.

Let the $N \times K$ matrix $\boldsymbol{G}$ contain the transfer functions (i.e., the steering vectors) between the K sources and N microphones $[\boldsymbol{g}_1, \ldots, \boldsymbol{g}_K]$ (see Eq. (4.2)). As shown in [57], the matrix $\boldsymbol{\Sigma}_S$ is mathematically similar to $(\boldsymbol{G}^* \boldsymbol{G}) \boldsymbol{C}_S$ and, therefore, it has the same eigenvalues. Here $\boldsymbol{C}_S$ is the CSM of the source signals. The main idea behind orthogonal beamforming is that each eigenvalue of $\boldsymbol{\Sigma}_S$ can be used to estimate the absolute source level of one source, from the strongest sound source within the map to the weakest, assuming orthogonality between steering vectors.

In a second step, these sources are mapped to specific locations. This is done by assigning the eigenvalues to the location of the highest peak in a special beamforming sound map, which is purposely constructed from a rank–one CSM that is synthesized only from the corresponding eigenvector. Hence, the map is the output of the spatial beamforming filter for only one single source and the highest peak in this map is an estimate of the source location. The main diagonal of the reduced CSM for each eigenvalue may be removed to reduce uncorrelated noise. The beamforming map can be constructed on the basis of vector–vector products and is, therefore, computationally very fast.

An important parameter in the eigenvalue decomposition, which has to be adjusted by the user, is the number of eigenvalues k that span the signal subspace $\boldsymbol{U}_S$. In a practical measurement, a reliable approach is to estimate the number of sources K and choose a value $k > K$. If the last eigenvalues represent sources that only marginally contribute to the overall sound level, the most important sound sources will be correctly estimated by using a value of k considerably smaller than N. The influence of the number of eigenvalues k considered for orthogonal beamforming can be observed in Fig. 4.7 for trailing–edge noise measurements of a tripped NACA 0012 airfoil with a span of 0.15 m with a freestream velocity of 81.5 m/s and zero angle of attack. As expected, the results converge to a final solution when the value of k is increased. The results obtained with DAMAS with 500 iterations are also plotted for comparison purposes. Ray tracing was applied to

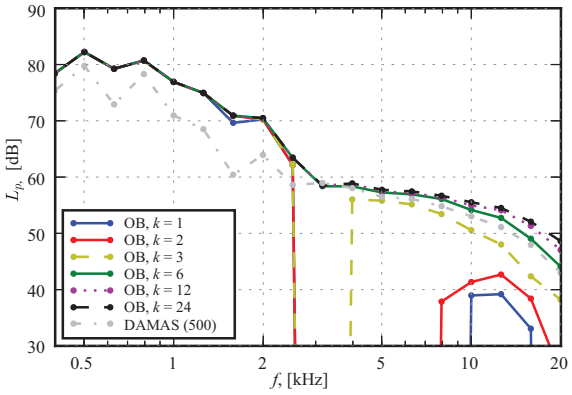

Figure 4.7: Trailing–edge noise spectra for a NACA 0012 airfoil using orthogonal beamforming considering different number k of eigenvalues [5].

the results to account for refraction at the shear layer and diagonal removal was applied for both methods. The results in Fig. 4.7 represent the integrated source maps over a region covering a part of the trailing edge. Further comparisons of orthogonal beamforming with other acoustic imaging methods can be found in the literature [59–62].

Since the eigenvalue decomposition of the CSM results in a reduced number of point sources in the map, which is always less than or equal to the number of microphones, the sum of all source strengths within the map is never greater than the sum of the microphone auto spectral densities. Hence, the sum of the acoustic source strengths is never overestimated.

4.5. CLEAN–SC

CLEAN–SC [44] is a frequency domain deconvolution technique developed by Sijtsma and based on the radio–astronomy method CLEAN–PSF [63]. Dougherty and Stoker [64] already applied CLEAN–PSF to aeroacoustic measurements for the first time in 1998. CLEAN–SC uses the fact that the sidelobes are spatially coherent with the main lobe [44].

CLEAN–SC assumes that the CSM can be written as a summation of contributions from K incoherent sources:

$$\boldsymbol{C} = \sum_{k=1}^{K} \langle \boldsymbol{p}_k \boldsymbol{p}_k^* \rangle. \tag{4.15}$$

Herein, $\boldsymbol{p}_k$ are the N–dimensional acoustic "source vectors" representing the Fourier components of the signals from the k^{th} source. The assumption of Eq. (4.15) is valid under the following conditions:

- The CSM is calculated from a large number of time blocks, so that the ensemble averages of the cross–products $\boldsymbol{p}_k \boldsymbol{p}_l^*$, $k \neq l$, can be neglected, see Appendix C.
- There is no decorrelation of signals from the same source between different microphones (e.g., due to sound propagation through turbulence, see section 3.1.1).
- All sound sources present are incoherent.
- There is no additional incoherent noise.

The CLEAN–SC algorithm starts by finding the steering vector yielding the maximum value of the beamforming source plot (Eq. (4.3)), say at scan point $\boldsymbol{\xi}_j$:

$$\max(A) = A\left(\boldsymbol{\xi}_j\right) = \boldsymbol{w}_j^* \boldsymbol{C} \boldsymbol{w}_j. \tag{4.16}$$

The corresponding "source component" $\boldsymbol{h}_j$ representing the identified source's contribution to the CSM is defined by

$$\boldsymbol{h}_j = \frac{\boldsymbol{C}\boldsymbol{w}_j}{A\left(\boldsymbol{\xi}_j\right)}. \tag{4.17}$$

Insertion of Eq. (4.15) yields

$$\boldsymbol{h}_j = \frac{\sum_{k=1}^{K} \left(\boldsymbol{p}_k^* \boldsymbol{w}_j\right) \boldsymbol{p}_k}{A\left(\boldsymbol{\xi}_j\right)}. \tag{4.18}$$

The source component $\boldsymbol{h}_j$ can be considered as an improved version of the steering vector $\boldsymbol{g}_j$ because it is more proportional to the unknown source vector $\boldsymbol{p}_j$. Thus, CLEAN–SC has low sensitivity to errors made in the source model that describe the sound propagation, i.e., if the steering vectors considered do not exactly match with the source vectors [3].

If the sources are well separated, then the term between parentheses in Eq. (4.18) is large when there is a close match between $\boldsymbol{w}_j$ and the peak source and small for the other sources. Then, the source component $\boldsymbol{h}_j$ provides a good estimate of the loudest source vector, even if this vector is not exactly proportional to the corresponding steering vector.

Thus, the following estimate is obtained:

$$\boldsymbol{p}_k \boldsymbol{p}_k^* = \frac{\left[A\left(\boldsymbol{\xi}_j\right)\right]^2 \boldsymbol{h}_j \boldsymbol{h}_j^*}{|\boldsymbol{p}_k^* \boldsymbol{w}_j|^2} \approx A\left(\boldsymbol{\xi}_j\right) \boldsymbol{h}_j \boldsymbol{h}_j^*. \tag{4.19}$$

This expression is subtracted from the CSM and the source is given an amplitude which is related to the average autopower of the microphone array. This quantity is often multiplied by a so–called loop gain or damping factor $\tilde{\varphi}$, with $0 < \tilde{\varphi} \leq 1$ [44]. This is done to take into account the contributions of other sound sources, which are normally small [65]. Hence, the CSM for the i^{th} iteration of CLEAN–SC is calculated as

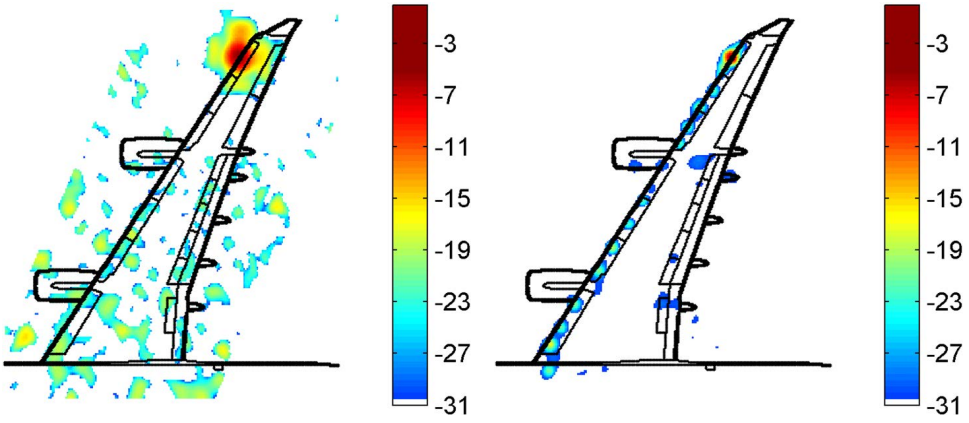

Figure 4.8: Acoustic source plots of an Airbus A340 half–model in a closed–section wind tunnel at 12360 Hz for CFDBF (left) and CLEAN–SC (right) [16].

$$\boldsymbol{C}^{(i)} = \boldsymbol{C}^{(i-1)} - \tilde{\varphi} A\left(\boldsymbol{\xi}_j\right) \boldsymbol{h}_j \boldsymbol{h}_j^*. \tag{4.20}$$

Then, the same procedure is repeated for the remaining CSM, until a certain stop criterion is fulfilled [44]. Ideally, the remaining CSM is "empty" after the iteration process. In other words, its norm should be small compared to the one from the original CSM. The new source map is obtained by the summation of the clean beams of the K identified sound sources and the remaining degraded CSM [65]. This method can also be applied after applying diagonal removal to the CSM [3].

This method works well for the case of a well–located source and it is especially suitable for closed–section wind–tunnel measurements. A successful example of CLEAN–SC is presented in Fig. 4.8 for a scale model of an Airbus A340 in the closed test section of the DNW–LLF[4] wind tunnel [44]. The application of the CFDBF algorithm at a frequency of 12360 Hz shows a dominant outer–wing slat noise source (which was found to be due to the low Reynolds number of the flow) but its sidelobes mask useful information about other noise sources. CLEAN–SC reveals additional leading–edge noise sources between the main source and the outer engine, which are not visible with CFDBF. An application of this method for aircraft flyover measurements [1] can be found in Figures 4.5 and 4.6. CLEAN–SC has also been applied to turbofan engine noise tests [66].

Another algorithm called TIDY [67] is similar to CLEAN–SC but works in the time domain, using the cross–correlation matrix instead of the CSM. TIDY has been used for the imaging of jet noise [67, 68] and motor vehicle pass–by tests [69]. An implementation of CLEAN–PSF in the time domain called CLEANT was proposed by Cousson et al. [70] and applied to rotating sound sources in a laboratory.

[4]Large Low–speed facility at the German–Dutch wind tunnels in Marknesse, Netherlands.

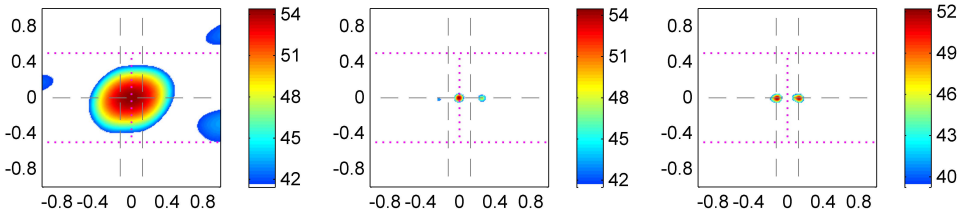

Figure 4.9: One–third–octave band (2 kHz) acoustic source plots for two sound sources in an anechoic chamber separated 0.25 m and located at the intersections of the dashed lines. Each source plot corresponds to a different method: CFDBF (left), CLEAN–SC (center) and HR–CLEAN–SC (right). Adapted from [3]

4

4.5.1. High–Resolution CLEAN–SC

A disadvantage of CLEAN–SC is that it does not provide a spatial resolution beyond the Rayleigh limit (see Appendix D), i.e., if two sources are too close to each other, the CFDBF peak is somewhere in between both sources (the "source marker") and the corresponding CLEAN–SC source component is a linear combination of the two individual sources [3]. In these cases, an alternative source marker can be considered, away from the actual peak position in a location within the main lobe of the PSF where the CFDBF source map is dominated by either one of the sources, so that the relative influence of the PSFs of the other $(K-1)$ sources is minimized. The location of the source markers can be restricted to a predefined set of grid points determined by the source marker constraint $\tilde{\mu}$, which limits how far the source marker is allowed to move from the main lobe's peak [65]. It is desirable to remain on the main lobe because other sources might have different PSFs [3, 4] and also to have $\tilde{\mu}$ larger than the Maximum Sidelobe Level (MSL) [65]. The source components obtained this way are considerably better estimates of the microphone array data from the true sources. To determine the best source marker positions, an iterative procedure starting with the standard CLEAN–SC solution can be performed. The improved sources locations can be calculated by applying CFDBF to the improved source components. These steps constitute the basis of the high–resolution version of CLEAN–SC (HR–CLEAN–SC) [3, 4, 71]. The additional required computation time with respect to the standard version of CLEAN–SC is limited as long as the number of incoherent sound sources K is limited. Normally, the solution converges in less than 20 steps [3, 4].

HR–CLEAN–SC has been applied successfully to simulated data [71], to experimental data using two speakers in an anechoic chamber [3, 4], see Fig. 4.9, and to aeroacoustic measurements of a nose landing gear in an open–jet wind tunnel [52]. The spatial resolution in these cases was increased by, typically, a factor of two with respect to the standard CLEAN–SC method. Therefore, the Rayleigh resolution limit can be surpassed because the method considers additional information, such as the number of sound sources present. This parameter is normally not known *a priori*, but a simple iterative process can be performed, where different number of sources can be considered until the solution converges. A first guess for the number of sound sources present may be the number of non–zero eigenvalues

of the CSM [57], which is at most the rank of the matrix.

An adaptive version of HR–CLEAN–SC was recently proposed by Luesutthiviboon et al. [65, 72], which considers a frequency–dependent source marker constraint $\tilde{\mu} = \tilde{\mu}(f)$ because the sidelobe level strongly depends on the frequency considered [10]. This value can be obtained by calculating the MSL per frequency and choosing $\tilde{\mu}$ accordingly or by approximating it through empirical formulae [73] to ease the computational effort. The adaptive HR–CLEAN–SC method was applied to an experiment with several speakers in an anechoic chamber showing that even better results than with the simple HR–CLEAN–SC can be obtained.

4.6. DAMAS

The Deconvolution Approach for the Mapping of Acoustic Sources (DAMAS) is a tool for quantitative analysis of beamforming results that was developed in the NASA Langley Research Center by Brooks and Humphreys [43, 74, 75]. This method solves the following inverse problem in an attempt to remove the influence of the array geometry and aperture from the output of CFDBF:

$$\boldsymbol{y} = \tilde{\boldsymbol{A}}\tilde{\boldsymbol{x}}, \tag{4.21}$$

where $\boldsymbol{y} \in \mathbb{R}^{J\times 1}$ is a column vector whose elements are the source autopowers of the J grid points of the source map obtained with CFDBF, $\tilde{\boldsymbol{A}} \in \mathbb{R}^{J\times J}$ is the propagation matrix whose columns contain the PSF at each of the J grid points, and $\tilde{\boldsymbol{x}} \in \mathbb{R}^{J\times 1}$ is a column vector containing the actual unknown source autopowers. Due to the finite resolution and the presence of sidelobes $\tilde{\boldsymbol{x}} \neq \boldsymbol{y}$. For practical cases, the number of grid points J is high and much larger than the number of actual sources K.

DAMAS considers distributions of incoherent point sources located at the grid points and attempts to determine each source power by solving the inverse problem of Eq. (4.21), subject to the constraint that source powers are non–negative. The problem is commonly solved using a Gauss–Seidel iterative method, which typically requires thousands of iterations to provide a "clean" source map. For practical grids, the large size of $\tilde{\boldsymbol{A}}$ can become an issue. The computation time of DAMAS employed this way is proportional to the third power of the number of grid points, J^3. In most applications $\tilde{\boldsymbol{A}}$ is singular and not diagonal dominant [76] and the convergence towards the exact solution is not guaranteed. DAMAS has no mechanism to let the iteration converge towards a well–defined result and the solution may depend on how the grid points and the initial values are ordered [76].

The inverse problem in Eq. (4.21) can also be evaluated using efficient NNLS solvers [40, 76, 77]. In case the sparsity of the vector $\tilde{\boldsymbol{x}}$ is considered, the inverse problem can also be solved with greedy algorithms, such as the Orthogonal Matching Pursuit (OMP), which approximates the solution in a considerably lower computation time, proportional to J^2 instead of J^3. The different steps of OMP are summarized in [78]. The Least Angle Regression Lasso algorithm (LarsLasso) also benefits of the sparsity of $\tilde{\boldsymbol{x}}$ but requires the choice of a regularization factor by the user, which can be quite complicated for non–experienced users [77]. Herold et al. [77] compared the NNLS, OMP and LarsLasso approaches on an aeroacoustic exper-

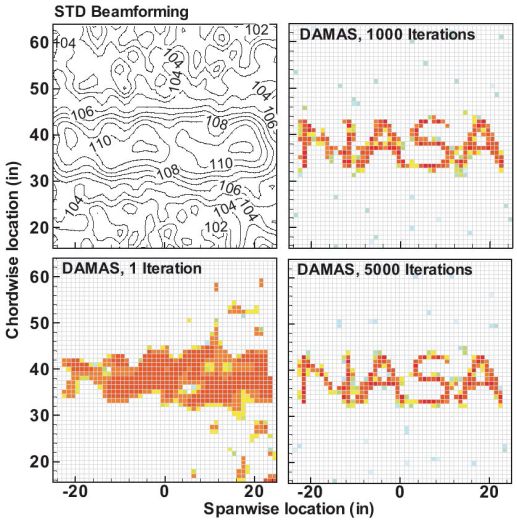

Figure 4.10: NASA image source for $f = 30$ kHz and $\Delta x/BW = 0.25$ [74].

iment and found that only NNLS and LarsLasso (using an appropriate regularization factor) surpass the classic DAMAS algorithm in terms of overall performance.

One of the most famous results of DAMAS is depicted in Fig. 4.10, where simulated incoherent monopoles were distributed to form the word *NASA* [74]. The grid spacing Δx was chosen to be 25.4 mm (1 inch), which normalized by the array beamwidth BW provides $\Delta x/BW = 0.25$. Apart from considerably improving the results of CFDBF (top left), the integrated sound levels rapidly converged to the correct value (within 0.05 dB after 100 iterations) [74].

DAMAS was later extended to allow for source coherence (DAMAS–C) [79]. Whereas the computational challenges in the use of DAMAS–C have limited its widespread application, conventional DAMAS has shown its potential with coherent source distributions in jet–noise analyses [80]. This jet–noise study also demonstrated the use of in–situ point source measurements for the calibration of array results. Slat–noise measurements in a wind tunnel [42] showed that DAMAS provides very similar results as CFDBF.

A similar method to DAMAS–C called noise source Localization and Optimization of Phased Array Results (LORE) was proposed by Ravetta et al. [81, 82]. LORE first solves an equivalent linear problem as DAMAS using a NNLS solver, but considering the complex PSF [81, 82], which contains information about the relative source phase. The output obtained is optimized solving a non–linear problem. Satisfactory results were obtained in simulated and experimental cases in a laboratory featuring incoherent and coherent sound sources [81, 82]. Whereas this method is faster than DAMAS–C, it does not provide accurate results when using diagonal removal and when calibration errors are present in the microphone array [81, 82].

4.6.1. DAMAS2

Further versions of DAMAS have been proposed in the literature [83–85], especially for reducing the high computational cost that it implies. For example, DAMAS2 assumes that the array's PSF is shift–invariant. The term shift–invariant describes the property that the characteristics of the PSF do not vary relative to the source position even if the absolute position of that source in the steering grid is changed. Thus, if a source is translated by a certain offset, the entire PSF will also translate with it. The error involved in this assumption is small in astronomy applications [63] where the distance between the source and the observer is huge compared to the size of the array or of the source itself, but in aeroacoustic measurements the PSF can vary significantly within the source region [76]. The distortion of the PSF away from the center of the scanning domain can be alleviated by including spatial–differentiation terms [86]. When applied, the size of the PSF has to be chosen large enough to prohibit wrapping, which has been implemented in DAMAS2.1 [87]. Also, a fast implementation of DAMAS–C based on similar techniques to reduce computational costs as DAMAS2 has been introduced [88], exploiting the benefits of convolution using Fourier transforms. Embedded versions of DAMAS2 and a Fourier–based NNLS approach of DAMAS were proposed by Ehrenfried and Koop [76] which do account for the shift variation of the PSF and are potential faster alternatives compared to the original DAMAS algorithm.

4.7. Wavenumber beamforming

A different steering vector representation can be used to display the sources in terms of propagation characteristic, rather than source position (as in Eq. (4.2)). The uniformly weighted steering vector can be written as

$$g_{j,n} = \exp\left[-i\left(k_{x,j}x_n + k_{y,j}y_n\right)\right], \tag{4.22}$$

which is the representation of a planar wave. In contrast to monopole sources, which cast a near–field–like pressure pattern on the array, the sources used for wavenumber beamforming are located at infinite distance and can, therefore, conveniently be characterized by their wavenumbers k_x and k_y as a plane wave [89]. This type of beamforming is particularly useful when mechanisms resulting in different propagation speeds and directions are present, provided that far–field conditions apply. This technique has been used to distinguish between the noise from a model and duct modes in a closed–section wind tunnel [90] and to characterize the TBL propagation and the acoustic disturbances of a high–speed wind–tunnel flow [91–93] and of an aircraft boundary–layer flow [94].

The planar wave approach produces beamforming maps based on a shift–invariant PSF which makes them very suitable for further processing with DAMAS2.1 [87], see section 4.6.

Exemplary plots of the wavenumber domain for $f = 1480$ Hz are shown in Fig. 4.11. Due to the relation $\tilde{c} = 2\pi f / \|\boldsymbol{k}\|$ with $\tilde{c}$ being the propagation velocity, and $\boldsymbol{k} = (k_x, k_y)$ the wavevector of a source, each position in the map represents a different propagation velocity. Sources with a propagation speed equal to or higher

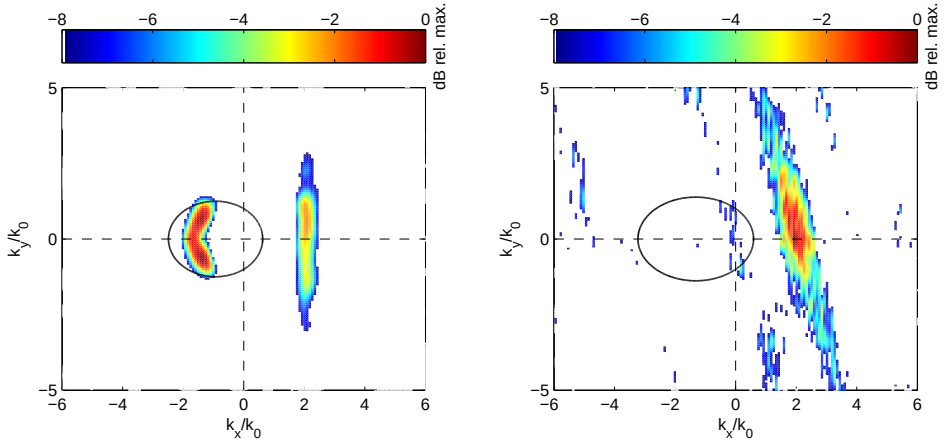

Figure 4.11: Wavenumber representation of the pressure fluctuations over a flat plate in: a closed–section wind tunnel at $f = 1480$ Hz and $M = 0.6$ (left) and on an aircraft fuselage in a flight test at $f = 1630$ Hz and $M = 0.69$ (right). The x and y axes have been normalized by the acoustic wavenumber $k_0 = 2\pi/c$ [94].

than the speed of sound are located in the elliptic–shaped acoustic domain shown in both plots in Fig. 4.11 with a solid black line. In the closed–section wind–tunnel test of Fig. 4.11 (left), acoustic sources are present while the flight test data of Fig. 4.11 (right) appear to be free of dominant acoustic content at the frequency shown. The elongated spot on the right hand side outside the acoustic domain is a representation of the pressure fluctuations caused by the subsonic TBL flow. In the wind–tunnel data, this elongated spot is seen to be parallel to the k_y–axis, indicating a flow component only in the x–direction. In the flight test plot, the elongated shape is rotated slightly about the origin, which indicates a flow direction that is not aligned with the array's x– and y–axes. The wavenumber domain can be used to easily separate between different propagation mechanisms.

4.8. Linear programming deconvolution (LPD)

Linear Programming Deconvolution (LPD) [95] is basically a faster alternative than DAMAS to solve the inverse problem introduced in Eq. (4.21). It considers the additional constraint that no correct model of the beamform map $\tilde{\boldsymbol{A}}\tilde{\boldsymbol{x}}$ would exceed the beamform source map obtained by CFDBF $\boldsymbol{y}$ anywhere. This difference ($\boldsymbol{y} - \tilde{\boldsymbol{A}}\tilde{\boldsymbol{x}}$) represents the effect of uncorrelated sound sources that were present in the measurement but not in the model, such as background noise, microphone self noise and long–range reflections [95].

Hence, an approach to obtain $\tilde{\boldsymbol{x}}$ is to maximize the model $\tilde{\boldsymbol{A}}\tilde{\boldsymbol{x}}$, subject to the constraint that it nowhere exceeds $\boldsymbol{y}$. Defining the $1 \times J$ propagation vector $\boldsymbol{c}$ as

$$c_{j'} = \sum_{j=1}^{J} A_{j,j'}, \text{ with } j' = 1, \ldots, J. \tag{4.23}$$

Therefore, the proposed problem is to maximize the product $\boldsymbol{c}\cdot\tilde{\boldsymbol{x}}$, subject to $\tilde{\boldsymbol{A}}\tilde{\boldsymbol{x}} \leq \boldsymbol{y}$ and $\tilde{\boldsymbol{x}} \geq 0$. This linear programming problem can be solved, for example, by the simplex algorithm, which guarantees finding an optimal solution in a finite number of steps, provided that a feasible vector exists, and that the objective function is bounded. Unlike DAMAS (see section 4.6), LPD has a definite result with no uncertainty about whether a sufficient number of iterations has been performed [95].

However, a disadvantage of LPD is that is does not work well with diagonal removal [95]. An alternative approach is to add an extra element to $\tilde{\boldsymbol{x}}$ which represents the incoherent noise level. The matrix $\tilde{\boldsymbol{A}}$ would now be $J \times (J+1)$ and the extra column is filled with ones.

This method has been applied to a distribution of aeroacoustic point sources in a laboratory [95] and was shown to provide better resolution than the Sparrow resolution limit.

A combination of LPD and functional beamforming has been proposed by Dougherty [46] showing even better results due to the higher dynamic range offered by functional beamforming.

The application of LPD, however, breaks up continuous source distributions into spots. This method is, thus, appropriate for discrete sources and for situations where the spatial resolution is more important than the dynamic range.

4.9. Robust adaptive beamforming (RAB)

Adaptive beamforming [96, 97], also known as Capon or minimum variance distortionless response beamforming, can produce acoustic images with a higher spatial resolution than CFDBF and has been used in array signal processing for sonar and radar applications. This method uses a weighted steering vector formulation that maximizes the SNR

$$\boldsymbol{w}_{\text{Capon},j} = \frac{\boldsymbol{C}^{-1}\boldsymbol{g}_j}{\boldsymbol{g}_j^{*}\boldsymbol{C}^{-1}\boldsymbol{g}_j}. \tag{4.24}$$

It is natural to expect that adaptive beamforming could be helpful to locate aeroacoustic noise sources more accurately and better minimize the convolution effects, [98] which, in turn, could produce array outputs of higher quality saving the computational efforts of deconvolution methods. However, Huang et al. [99] showed that adaptive beamforming is quite sensitive to any perturbations and its performance quickly deteriorates below an acceptable level, preventing the direct application of present adaptive beamforming methods for aeroacoustic measurements. A new derivation for the adaptive beamforming formula has been recently proposed by Dougherty [100].

To improve the performance, a robust adaptive beamforming (RAB) method has been proposed [99] specifically for aeroacoustic applications. To mitigate any potential ill–conditioning of the CSM, diagonal loading [99] is applied as

$$\boldsymbol{w}_{\mathrm{RAB},j} = \frac{(\boldsymbol{C} + \epsilon \boldsymbol{I})^{-1} \boldsymbol{g}_j}{\boldsymbol{g}_j^* (\boldsymbol{C} + \epsilon \boldsymbol{I})^{-1} \boldsymbol{g}_j}, \tag{4.25}$$

where $\boldsymbol{I}$ is the $N \times N$ identity matrix. The value of the diagonal loading factor ϵ is usually determined empirically. One method proposed by Huang et al. [99] consists of calculating the maximum eigenvalue σ of the CSM and multiplying it by a diagonal loading parameter μ_0:

$$\epsilon = \mu_0 \max(\sigma). \tag{4.26}$$

The value of μ_0 is typically between 0.001 and 0.5 but needs to be iteratively determined considering a quality threshold in the difference between the obtained results and the CFDBF results, usually 3 dB. In general, smaller values of μ_0 provide acoustic images with better array resolution but the computation can fail due to numerical instability. On the other hand, a larger value of μ_0 generates results more similar to the CFDBF. RAB can save significant amounts of postprocessing time compared with deconvolution methods [99].

A different approach to calculate ϵ, based on the white noise gain constraint idea from Cox et al. [96], can be found in [101]. In this approach, however, a different value of ϵ is calculated for each grid point, consequently increasing the computational cost considerably.

An application of this method for aircraft flyover measurements [1] can be found in Figs. 4.5 and 4.6.

Capon beamforming can be extended to treat potentially coherent sources [102].

4.10. Spectral Estimation Method (SEM)

The Spectral Estimation Method (SEM) [103] is intended for the location of distributed sound sources. It is based on the idea of describing the sound sources by mathematical models that depend on several unknown parameters. It is assumed that the PSD (see Appendix C.2.5) of the sources can then be expressed in terms of these parameters. This method is also known in the literature as Covariance Matrix Fitting (CMF) [61, 104–106].

The choice of the source model is based on the fact that an extended sound source may only be viewed as an equivalence class between source functions radiating the same pressure field on a phased microphone array. In many applications, a majority of sound sources have smooth directivity patterns. This means that if the aperture angle of a microphone array seen from the overall source region is not too large, the directivity pattern of each region may be considered as isotropic within this aperture, neglecting its directivity.

Therefore, SEM models the array CSM $C_{m,n}$ with a set of J uncorrelated monopoles with unknown autopowers $\tilde{x}_j$ (see section 4.6), which is a quite appropriate model

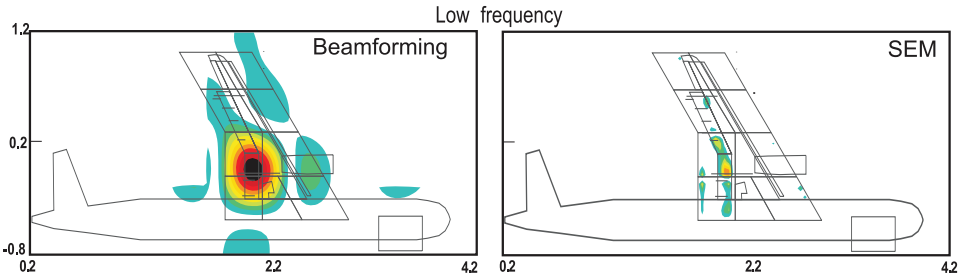

Figure 4.12: CFDBF (left) and SEM (right) source maps of an Airbus A320/A321 half–aircraft model tested in the CEPRA 19 anechoic open–jet wind tunnel. [107]

to study airframe noise, by minimizing the following cost function (mean least–squares error between the array and modeled matrices)

$$F(\boldsymbol{S}) = \sum_{m,n=1}^{M} \left| C_{m,n} - \sum_{j=1}^{J} g_{j,m} \tilde{x}_j g_{j,n}^{*} \right|^2 . \tag{4.27}$$

The constraint of a non–negative PSD is satisfied by introducing a new unknown s_j defined by $\tilde{x} = s^2$. This allows the use of efficient optimization methods for solving unconstrained problems. The resulting non–linear minimization problem is solved using an iterative procedure based on a conjugate gradient method algorithm. The solution generally converges fast with only a few hundred iterations.

SEM has shown its efficiency in noiseless environments, on numerical simulations [103] and on data measured during experiments performed with an Airbus A320 half–aircraft model in the open–jet anechoic wind tunnel CEPRA 19 (see Fig. 4.12) at ONERA in France, where the microphone array was located outside of the flow in the medium at rest [103, 107, 108]. An improved spatial resolution and a reduction of the sidelobe level are observed by using SEM.

One big advantage of SEM over deconvolution methods using beamforming is that the main diagonal of the CSM can be excluded from the optimization without violating any assumptions. SEM can even be used to reconstruct the diagonal without the influence of the spurious contributions. The resulting source distribution is relatively independent on the array pattern and the assumed source positions can be restricted to known regions on an aircraft.

In order to take into account the inevitable background noise in practical applications, an extension of SEM has been proposed: the Spectral Estimation Method With Additive Noise (SEMWAN) [109]. This method is based on a prior knowledge of the noise signal and it has the advantage of being able to reduce the smearing effect due to the array response and, at the same time, the inaccuracy of the results caused by noise sources, which can be coherent as well as incoherent, with high or low sound pressure levels. This technique is well suited for applications in wind tunnels since, for example, a noise reference or record of the environmen-

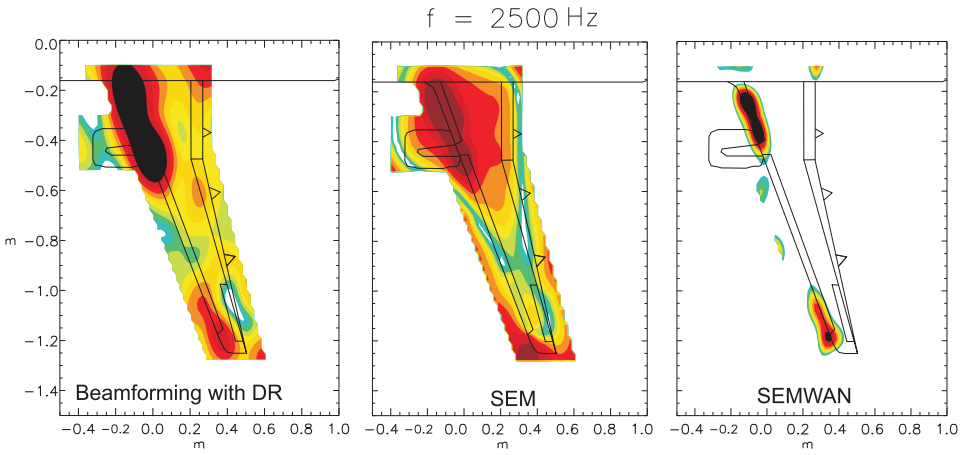

Figure 4.13: CFDBF with diagonal removal (left), SEM without diagonal removal (center), and SEMWAN (right) source plots of a typical Airbus half–model tested in the closed test section of Bremen wind tunnel at a frequency of 2500 Hz [5].

tal noise can be obtained prior to the installation of the model in the test section [109, 110]. The performances of SEM and SEMWAN are evaluated in Fig. 4.13 for an Airbus half–model for a one–third–octave frequency band centered at 2500 Hz in a closed–section wind tunnel in Bremen compared to CFDBF with diagonal removal. SEMWAN offers even better results than SEM compared to CFDBF, reducing the influence of the background noise of the closed wind tunnel and showing two main noise sources at the leading edges of the wing root and the wing tip. Additional results for the same model for a one–third–octave frequency band centered at 3150 Hz are shown in Fig. 4.14, where results for CFDBF (with diagonal removal), DAMAS (with diagonal removal) and SEMWAN are presented. Once again, SEMWAN improves the results with respect to CFDBF and renders distributed sound sources, in comparison with DAMAS, which only shows discrete point sources. The integration area and the integrated spectra using SPI on the results obtained by DAMAS and SEMWAN for an area covering the whole aircraft half–model are depicted in the bottom part of Fig. 4.14. The measured spectrum by the microphone array is also plotted for reference. The SEMWAN spectrum presents a peak at around 4 kHz which is also shown in the measured spectrum by the array but is not captured by DAMAS. Moreover, SEMWAN provides higher noise reduction capabilities than DAMAS, especially at low frequencies. Overall, both spectra (DAMAS and SEMWAN) show comparable trends.

Another important issue arises when the acoustic measurements are performed in a non–anechoic closed–section wind tunnel. In this situation, the pressures collected by the microphones are not only due to the direct paths of the acoustic sources but are also due to their unwanted reflections on the unlined walls, thereby losing accuracy when calculating the power spectra. In order to remove this drawback, a multi–microphone cepstrum method, aiming at removing spurious echoes

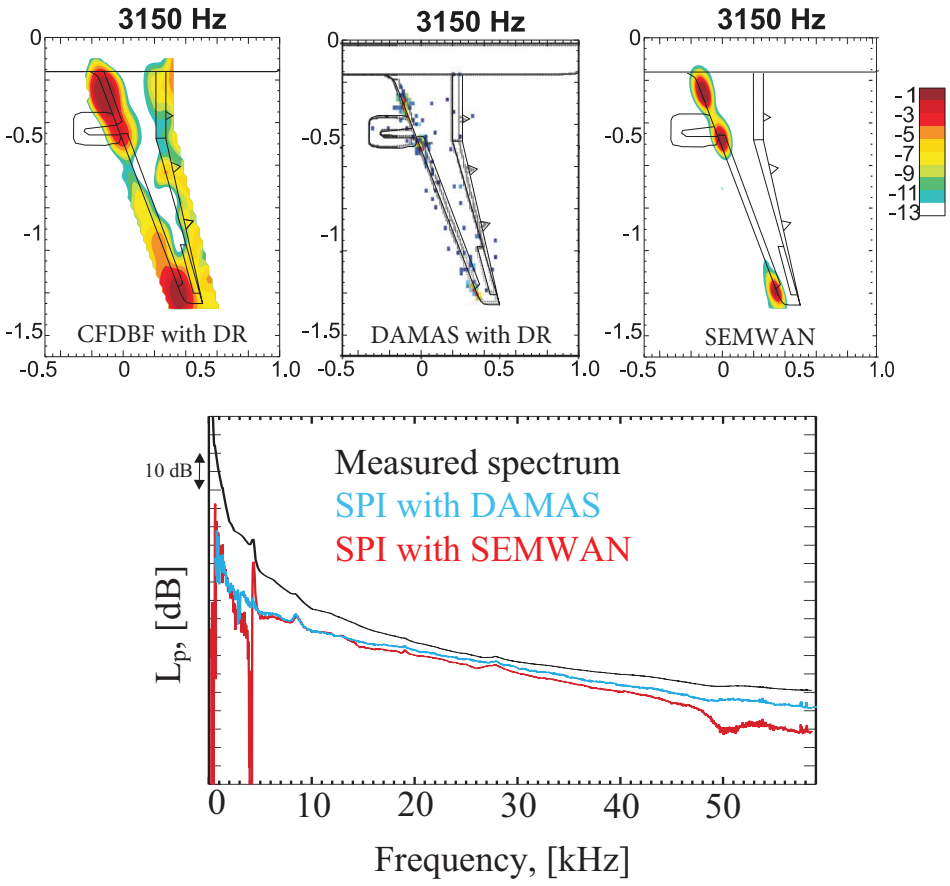

Figure 4.14: Top: Source plots with CFDBF with diagonal removal (left), DAMAS with diagonal removal (center), and SEMWAN (right) of a typical Airbus half–model in landing configuration tested in the closed test section of Bremen wind tunnel at 60 m/s and at a frequency of 3150 Hz. Bottom: Integrated spectra using SPI on the results of DAMAS and SEMWAN. The measured spectrum by the microphone array is also plotted (in black) for reference [5].

in the power spectra has been developed and tested successfully with numerical and experimental data [111].

4.11. SODIX

SODIX (Source Directivity Modeling in the Cross–Spectral Matrix) is an extension of SEM that can model sound sources with arbitrary directivities. The method was initially developed for noise tests with engines in open static test beds to separate the various broadband sound sources of turbofan engines, which are known to have sizable directivities. However, the method can be applied to any problem where the directivities of the sound sources are of interest.

The source model of SODIX extends the point–source model of SEM by replacing the omnidirectional source amplitudes s_j with individual source amplitudes $\tilde{D}_{j,m}$, which are proportional to the sound pressure radiated from a source j to a microphone m. The least–squares optimization problem features the cost function

$$F(D) = \sum_{m,n=1}^{N} \left| C_{m,n} - \sum_{j=1}^{J} g_{j,m} \tilde{D}_{j,m} \tilde{D}_{j,n} g_{j,n}^{*} \right|^2 . \tag{4.28}$$

A conjugate gradient method is used to determine the source amplitudes that minimize the cost function in Eq. (4.28). Equation (4.28) was first published by Michel and Funke [112, 113] in 2008. The constraint of positive source amplitudes was considered similarly as in SEM (see section 4.10) by using $\tilde{D} = \tilde{d}^2$ and solving for $\tilde{d}$ [114]. This modification also increases the robustness of SODIX and makes it converge from simple starting solutions, e.g., an energy–equivalent, constant source distribution that can be directly derived from the microphone signals.

In order to reduce the number of possible solutions and to support physical results, smoothing terms can be added to the cost function [112–114]. The smoothing terms prevent spurious peaks in the source amplitudes and can, therefore, also improve the dynamic range of the results.

The source model of SODIX is based on two assumptions:

1. The amplitudes $\tilde{d}_{j,m}^2$ of each point source may have different values for every microphone.

2. The phase of a sound wave radiated by a point source spreads spherically, i.e., according to the complex argument in the steering vector $g_{j,m}$.

Both assumptions are valid for the sound propagation within a single lobe in the acoustic far–field of a multipole source.

As in the case of SEM (see section 4.10), the main diagonal of the CSM can be removed from the calculations without violating any assumptions. This makes SODIX, like SEMWAN (see section 4.10), suitable for closed–section wind–tunnel applications.

The spatial resolution of SODIX was compared to that of CFDBF and various deconvolution methods in [115]. The results showed that SODIX overcomes the

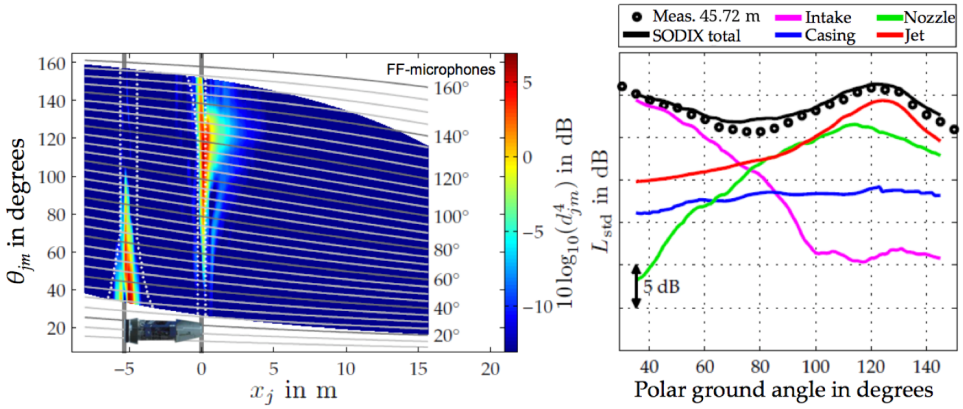

Figure 4.15: SODIX results for the broadband noise in the 800 Hz one–third–octave band during static engine tests [5].

Sparrow resolution limit and, therefore, provides super–resolution. However, the computational effort for SODIX is rather high, because the number of unknowns to be determined, i.e., $J \times N$, can be very large.

The analysis of broadband noise during static engine tests with large linear microphone arrays demonstrated that SODIX can calculate reliable results over a wide range of angles around the engine [114, 116]. Phase jumps between different radiation lobes become a problem mainly for tonal noise. They violate the second assumption in the source model and, therefore, lead to source distributions and directivities that are not representative. However, the main capability of SODIX is the *free* modeling of the directivities of the sound sources: SODIX can not only account for the multipole characteristics of the sound sources, but also for directivities due to source interference within coherent sources, such as jet mixing noise.

SODIX was also successfully applied to engine indoor tests [116], ground tests with an Airbus A320 aircraft [117–119], measurements of a CROR model in an open–jet wind tunnel [120, 121] and measurements of model–scale turbofan–nozzles in an open–jet wind tunnel [122]. Oertwig et al. [123] recently applied SODIX using a relatively sparse microphone array showing good results. Exemplary SODIX results from static tests with a long–cowl turbofan engine at low engine speed using a linear array with 248 microphones [116] are shown in Fig. 4.15. The microphones were aligned parallel to the engine axis on the test–bed floor at a distance of approximately 11.2 m to the engine axis. A linear grid of point sources with a spacing of $\Delta x \approx 0.25\lambda$ between grid points is placed on the engine axis.

The source map on the left of Fig. 4.15 shows the source directivities as a function of the source emission angle θ_{jm} that is defined between the engine axis and the connection from a source j to a microphone m with $\theta_{jm} = 0°$ in flight direction, see Fig. 3.9. SODIX models strong sources at the axial positions of the intake and the nozzle. Jet sources appear close to the nozzle exit, which is reasonable for a Strouhal number of $St = 4.6$. All sources present strong directivities

with peak radiation angles in the forward arc for the intake and in the rear arc for the nozzle and the jet. The dynamic range of these results is greater than 20 dB.

In order to evaluate the contributions of the single sources in the far–field, the source amplitudes were extrapolated to the positions of microphones at a distance of 150 ft = 45.72 m which are commonly used for noise certification purposes. With the assumption of an axisymmetric sound radiation of the engine, the source amplitudes, $\tilde{d}^2$, at emission angles corresponding to the far–field microphones (grey lines in Fig. 4.15 (left)) are scaled according to the $1/r$ distance law, where r is the distance between the source and the observer. Dotted white lines around the positions of the intake and the nozzle indicate the parts of the source grid that are used for the calculation of the far–field contributions from the intake ($x = -5.4$ m) and the nozzle ($x = 0$ m) in Fig. 4.15 (left). The far–field contribution of the jet is calculated from all sources downstream of the nozzle region.

The far–field results of each component are shown in the right plot in Fig. 4.15. The intake dominates in the forward arc up to $\theta \approx 75°$. The sound field radiated from the nozzle shows a maximum at $\theta \approx 115°$ and the jet noise peaks at $\theta \approx 125°$. The sum of all sources (SODIX total) agrees very well with the measured data of the far–field microphones. The trends also agree with those obtained by aircraft noise prediction tools, see Figs 2.5 and 2.6.

The capability to model the directive sound sources of a turbofan engine makes SODIX a useful tool for the development and the validation of new engine technologies. Other methods, which often consider monopole sources, would average the sound field over the aperture of the array and therefore lead to inaccurate results.

4.12. Compressive sensing beamforming

Compressive sensing [124, 125] is a new paradigm of signal processing used in the field of information technology which reduces sampling efforts extensively by conducting L_1 optimization. Huang [126] provides a tutorial example to demonstrate this method for potential aeroacoustic applications. A compressive sensing based beamforming method has been developed recently for aeroacoustic applications [127], by assuming a spatially–sparse distribution of flow–induced sound sources, $\boldsymbol{S}$. In particular, a narrowband compressive sensing beamforming can be performed by using a non–linear optimization algorithm, such as

$$\arg\min ||\hat{\boldsymbol{S}}||_1, \text{subject to } ||\boldsymbol{p} - \boldsymbol{G}\hat{\boldsymbol{S}}||_2 \leq \delta, \delta \geq 0, \tag{4.29}$$

where here $\hat{(\cdot)}$ denotes the estimation and δ is a noise parameter for which $\delta = 0$ if the measurements are free of noise. A more robust (but more complicated) form can be found in reference [127].

This method has been adopted in the identification of spinning modes for turbofan noise using microphone–array measurements. The required number of sensors can be much less than the number required by the sampling theorem, as long as the incident fan noise is sparse in spinning modes [128–131].

It should be noted that compressive sensing, unlike the beamforming methods discussed, is an inverse method that aims to determine the phase and amplitude of

the source distribution. The linear algebra problems at the core of inverse methods are often severely underdetermined. Selecting a particular solution to display requires that the undetermined components of the solution be established somehow. The conventional approach of minimizing the L_2 norm of the solution can give solutions that look incorrect because they have many small non–zero elements. Compressive sensing can be considered as a cosmetic improvement that tends to cluster the non–zero sources. If there is a reason to believe that the true sources have this kind of distribution, then the compressive sensing result may be more accurate than the conventional inverse solution. Several of the techniques discussed below are also inverse methods that handle the ill conditioned problem in slightly different ways.

4.13. Generalized inverse beamforming (GIBF)

The idea behind Generalized Inverse Beamforming (GIBF) [132] is to reconstruct the CSM by a collection of partially coherent sources. Although a method exists which directly recovers the entire CSM [133], its computational cost drastically increases with the number of microphones. To reduce the computation time substantially, use of an eigenvalue decomposition can be made, see Eq. (4.11). This decomposition breaks the problem into N decoupled equations as

$$\tilde{\boldsymbol{G}}\boldsymbol{S}_n = \sqrt{\sigma_n}\boldsymbol{u}_n, \tag{4.30}$$

where $\tilde{\boldsymbol{G}} \in \mathbb{C}^{N\times J}$ denotes an $N \times J$ matrix consisting of steering vectors $[\boldsymbol{g}_1 \ldots, \boldsymbol{g}_J]$ and $\boldsymbol{S}_n$ represents a column vector of the complex source–amplitude distribution $(s_1, \ldots, s_J)^{\mathsf{T}}_n$ corresponding to the n^{th} eigenvector. Here $(\cdot)^{\mathsf{T}}$ represents the transpose.

In general, the number of grid points J is considerably larger than the number of microphones N. Therefore, Eq. (4.30) can be solved as an underdetermined problem using generalized inverse techniques. The simplest method is to minimize an L_2 norm, and to generate a source map for each eigenvector by solving

$$\boldsymbol{S}_n \approx \tilde{\boldsymbol{G}}^*\left(\tilde{\boldsymbol{G}}\tilde{\boldsymbol{G}}^* + \epsilon\boldsymbol{I}\right)^{-1}\left(\sqrt{\sigma_n}\boldsymbol{u}_n\right), \tag{4.31}$$

where ϵ generally ranges from 0.1% to 10% of the maximum eigenvalue of $\boldsymbol{\Sigma}$ to numerically stabilize the matrix inversion (a systematic optimization method was proposed in [134]). This solution actually serves as an initial condition for the iterative method given below.

The resolution of source maps generated by Eq. (4.31) is, however, still comparable to CFDBF [135]. To increase the resolution, it is crucial to minimize an L_1 norm by iteratively solving

$$\boldsymbol{S}_n^{i+1} \approx \boldsymbol{W}_n^i\tilde{\boldsymbol{G}}^*\left(\tilde{\boldsymbol{G}}\boldsymbol{W}_n^i\tilde{\boldsymbol{G}}^* + \epsilon\boldsymbol{I}\right)^{-1}\left(\sqrt{\sigma_n}\boldsymbol{u}_n\right), \tag{4.32}$$

where the superscript i denotes the iteration counter, and $\boldsymbol{W}_n$ is a $J \times J$ diagonal matrix whose components are $\left|s_{j,n}^i\right|$. The convergence can be accelerated by re-

ducing the number of grid points through the iteration. Likewise, overdetermined cases can be solved using an analogous generalized inverse technique [132].

Benefits of this algorithm are not only the treatment of the source coherence, but also to include any types of prescribed sources in $\tilde{\boldsymbol{G}}$. Hence, in principle, multipoles in an arbitrary orientation can be detected and different types of sources can be collocated at the same grid point. An application to duct acoustics, in which overdetermined problems are typically solved, was studied in [136]. Several regularization methods for GIBF were recently applied to airfoil–noise measurements in open–jet wind tunnels [137, 138].

4.14. Iterative Bayesian Inverse Approach (IBIA)

Inverse methods are based on a global formulation and are used to identify the source strength at all points of the scan grid at once. The output of the inverse formulation is no longer described as single source autopowers $A(\boldsymbol{\xi}_j)$ at each point $\boldsymbol{\xi}_j$ of the grid, as in Eq. (4.3), but rather as a global source CSM, noted $\boldsymbol{B} \in \mathbb{C}^{J\times J}$, obtained as follows

$$\boldsymbol{B} = \boldsymbol{\Psi}\boldsymbol{C}\boldsymbol{\Psi}^*. \tag{4.33}$$

The matrix $\boldsymbol{\Psi}(\in \mathbb{C}^{J\times N})$ is a regularized inverse of $\tilde{\boldsymbol{G}}$, $\boldsymbol{C}$ is the CSM of the signals at the microphones, and the diagonal terms of $\boldsymbol{B}$ represent the actual source autopowers $\tilde{x}_j$ for $j \in [1, \ldots, J]$. The difficulty in applying inverse methods is to correctly build the matrix $\boldsymbol{\Psi}$. This is not an easy task because the problem is often underdetermined ($J \gg N$), and ill–conditioned (steering vectors $\boldsymbol{g}_j$ are far from being orthogonal to each other, especially at low frequencies). Iterative Bayesian Inverse Approaches (IBIA) are based on a Bayesian regularization process assuming a user–defined level of sparsity. The first step of the iterative process is to calculate the pseudo–inverse of $\tilde{\boldsymbol{G}}$ with Tikhonov regularization:

$$\boldsymbol{\Psi}^0 = \tilde{\boldsymbol{G}}^{\dagger\eta} = \tilde{\boldsymbol{G}}^* \left(\tilde{\boldsymbol{G}}\tilde{\boldsymbol{G}}^* + \eta^2\boldsymbol{I}\right)^{-1}, \tag{4.34}$$

where the regularization parameter η^2 is estimated using a Bayesian criterion [139–141]. The optimal value of η^2 is defined as the one minimizing the following cost function:

$$\hat{\eta}^2 = \operatorname{argmin}\left[\sum_{n=1}^{N} \ln(\tilde{\sigma}_n^2 + \eta^2) + (N-2)\ln\left(\sum_{n=1}^{N} \frac{\tilde{\boldsymbol{u}}_n^* \boldsymbol{C} \tilde{\boldsymbol{u}}_n}{\tilde{\sigma}_n^2 + \eta^2}\right)\right], \tag{4.35}$$

where $\tilde{\sigma}_n$ and $\tilde{\boldsymbol{u}}_n (n \in [1, \ldots, N])$ are singular values and left singular vectors of $\tilde{\boldsymbol{G}}$, respectively. The sparsity constraint is then enforced through an iterative estimation of $\boldsymbol{\Psi}$:

$$\boldsymbol{\Psi}^{i+1} = \boldsymbol{R}^i \left(\tilde{\boldsymbol{G}}\boldsymbol{R}^i\right)^{\dagger\eta} = (\boldsymbol{R}^i)^2 \tilde{\boldsymbol{G}}^* \left[\tilde{\boldsymbol{G}}(\boldsymbol{R}^i)^2 \tilde{\boldsymbol{G}}^* + \eta^2\boldsymbol{I}\right]^{-1}, \tag{4.36}$$

where $\boldsymbol{R}^i$ is a right diagonal weighting matrix balancing the weight of each source in the regularization process (for the i^{th} iteration), whose j^{th} diagonal entry is calculated as follows:

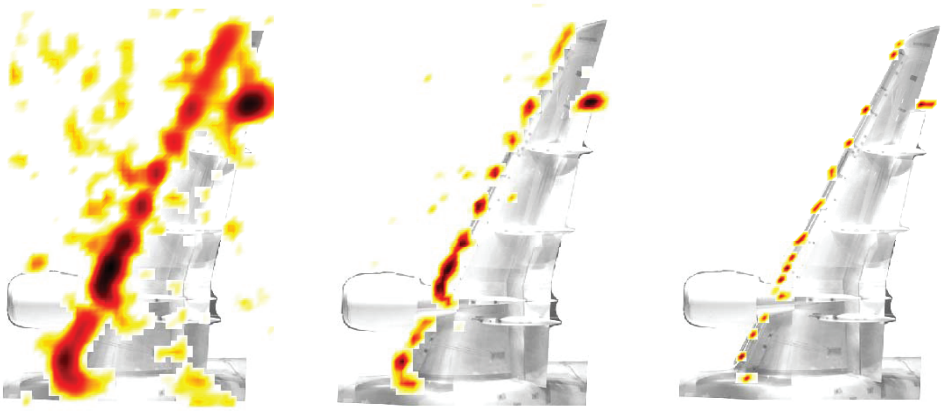

Figure 4.16: Source maps using IBIA on a scaled half–model of a Dornier–728 in a closed–section wind tunnel at 8500 Hz ($M = 0.2$), color range of 20 dB. Left: $\tilde{q} = 2$; center: $\tilde{q} = 1.2$; right: $\tilde{q} = 0$. Experimental database from DLR [143].

$$\left(\boldsymbol{R}^i_{j,j}\right)^2 = \left([\boldsymbol{B}^i]_{j,j}\right)^{1-\tilde{q}/2}, \text{ with } \boldsymbol{B}^i = \boldsymbol{\Psi}^i \boldsymbol{C} (\boldsymbol{\Psi}^i)^*, \tag{4.37}$$

where $\tilde{q}$ is the parameter defined by the user controlling the sparsity with $0 \leq \tilde{q} \leq 2$ defined by the user. In Eq. (4.36), η^2 is estimated during each iteration using Eq. (4.35), in which $\tilde{\sigma}_n$ and $\tilde{\boldsymbol{u}}_n$ are now the singular values and left singular vectors of $(\tilde{\boldsymbol{G}}\boldsymbol{R}^i)$, respectively. Several conditions can be used as a stopping criterion, like a maximum number of iterations or a distance between $\boldsymbol{B}^{i+1}$ and $\boldsymbol{B}^i$.

The parameter $\tilde{q}$, defining the shape of the *a priori* probability density function of sources, determines the power of the solution norm used in the regularization process. A value of $\tilde{q} = 2$ keeps the initial value $\boldsymbol{\Psi}^0$ (Eq. (4.34)), which means no sparsity. Thus, the amount of sparsity increases as $\tilde{q}$ decreases, down to $\tilde{q} = 0$, for which a strong sparsity is requested.

Figure 4.16 presents some results of the IBIA applied to a scaled half–model of a Dornier–728 at $M = 0.2$ in a closed–section wind tunnel at the DLR Cologne site. Full details of this experimental application are available in [142]. This dataset has been studied in the frame of the AIAA benchmark on array methods [143]. Figure 4.16 shows the effect of the sparsity parameter q in Eq. (4.37) on the source map at 8500 Hz: for $\tilde{q} = 2$ (no sparsity, left), $\tilde{q} = 1.2$ (soft sparsity, center), and $\tilde{q} = 0$ (strong sparsity, right). The main sources are identified on the whole wing leading edge, and on the flap side edge. The source map presents an almost continuous source along the leading edge for $\tilde{q} = 2$, while point sources clearly appear when $\tilde{q}$ decreases (precisely on the slat tracks). An interesting remark is that the result for $\tilde{q} = 2$ and $\tilde{q} = 0$ are very similar to results obtained with CFDBF and CLEAN–SC, respectively [143].

4.15. Global optimization methods

In reference [144] a method was presented by Malgoezar et al. where the search for the locations and amplitudes of sound sources is treated as a global optimization problem. The search can be easily extended to more unknowns, such as additional geometrical parameters, and more complex situations with, for example, multiple sound sources or reflections being present. The method is essentially grid–free and can overcome the Sparrow resolution limit.

The presence of sidelobes will, however, hamper the optimization as they act as local optima against which the global optimum needs to be found. In the literature, a number of mathematical methods are presented which allow for optimization problems with many unknowns and with the capability to escape from local optima, in contrast to local search techniques, e.g., gradient methods. These methods are generally denoted as global optimization methods. Well–known examples are genetic algorithms [145], simulated annealing [146], and ant colony optimization [147].

In [144] a variation of the genetic algorithm, called differential evolution [148], was proposed as a global optimization method. These optimization methods mimic natural evolution. They use populations of solutions, where promising solutions are given a high probability to reproduce and worse solutions have a lower probability to reproduce.

This work can be seen as an alternative approach to DAMAS and SEM. Whereas DAMAS assesses the performance of a solution based on the agreement between modeled and measured beamformed outputs, SEM is based on the comparison between the modeled and measured pressure fields. In contrast, in this technique, the locations of the sources are sought by using a global optimization method, instead of considering a predefined grid of potential source locations. This way, estimates for source positions and source strengths are obtained as a solution of the optimization and do not need to be obtained from a source plot. This allows for an estimation of the location of the sound sources in the perpendicular direction to the array plane [144, 149], which is a cumbersome procedure with other acoustic imaging methods [150]. The number of sound sources presents is not known *a priori*, but a simple iterative process can be performed using as first guess the number of non–zero eigenvalues of the CSM, as mentioned in section 4.5.1.

In order to use global optimization methods, a cost function F has to be defined. This can be done by constructing a CSM from a signal model, $\boldsymbol{C}_{\text{model}}$, and comparing it to the *measured* CSM, $\boldsymbol{C}_{\text{meas}}$. For example, the objective function can have the following form

$$F_{\text{CSM}}(\mathbf{v}) = \sum_{\text{elements of CSM}} \Big\{ \left[\text{Re}(\boldsymbol{C}_{\text{meas}}) - \text{Re}(\boldsymbol{C}_{\text{model},\mathbf{v}})\right]^2 + \left[\text{Im}(\boldsymbol{C}_{\text{meas}}) - \text{Im}(\boldsymbol{C}_{\text{model},\mathbf{v}})\right]^2 \Big\}, \tag{4.38}$$

where $\boldsymbol{v}$ is the parameter vector for the optimization method containing the spatial positions and strengths of the sources. This objective function can then in turn

be used in an optimizer, such as differential evolution. By minimizing the objective function over many generations, the parameter vector v will converge to the actual source positions and strengths.

Some first results of this technique applied to simulated data and to experimental data featuring a single speaker in an anechoic room are presented in [144, 151].

4.16. Main applications

A short summary of the aforementioned acoustic imaging methods and their most suitable applications is presented in the following list:

- **Conventional Beamforming (CFDBF)** [8, 9] should be a standard procedure in all cases, since it provides a fast overview of the sound sources characteristics. However, its spatial resolution and dynamic range are usually not suitable for several applications. Integration methods can be applied for distributed sources [6].

- **Functional Beamforming** [45, 46] greatly increases the dynamic range compared with CFDBF in a comparable computation time. It works well in wind–tunnel (both in open–jet and closed–section) and in aircraft flyover measurements [1, 35, 37]. However, diagonal removal produces considerable errors and diagonal denoising methods are recommended [49].

- **Orthogonal Beamforming** [55–58] is based on the eigenvalue decomposition of the CSM, has a low computational cost and never overestimates the strength of the acoustic sources. This method has been applied in trailing–edge noise measurements in an open–jet wind–tunnel [59–62].

- **CLEAN–SC** [44] is a widely–used deconvolution technique that *cleans* the source map obtained with CFDBF iteratively, removing the parts of it that are coherent with the real sources. Thus, the dynamic range is greatly improved. The spatial resolution can be increased beyond the Rayleigh resolution limit using the new high–resolution version HR–CLEAN–SC [3]. This technique has been applied to wind–tunnel [44, 52] and aircraft flyover experiments [1, 2].

- **DAMAS** [43, 74, 75] is a deconvolution method that solves an inverse problem iteratively to remove the influence of the array geometry from the obtained results. Enhancements in the dynamic range and the spatial resolution are obtained but it has a high computational cost. The extension DAMAS–C [79] is suitable for analyzing source coherence, but it requires even higher computational resources. Further and similar versions of DAMAS have been proposed [76, 81–88] in order to reduce the computation time. This technique is normally used in jet–noise analyses [80] and in wind tunnel–tests [43, 74, 75].

- **Wavenumber beamforming** [90–94] is a useful technique when mechanisms resulting in different propagation speeds and directions are present,

provided that far–field conditions apply. This method has been used in wind–tunnel experiments [90–93] and to characterize an aircraft boundary–layer flow [94].

- **Linear Programming Deconvolution (LPD)** [95] is a faster alternative to DAMAS. It has been applied to aeroacoustic point sources in a laboratory [95], showing better resolution than the Sparrow resolution limit. It can be combined with functional beamforming providing even better results [46].
- **Robust Adaptive Beamforming** [99] attempts to maximize the SNR. It works well for *clean* data, but it is quite sensitive to noise and errors in the data. It has been used for aeroacoustic sources [99] and flyover measurements [1]. This method can be extended to treat potentially coherent sources [102].
- **Spectral Estimation Method (SEM)** [103] is intended for the analysis of distributed sound sources. It offers better dynamic range and spatial resolution than CFDBF. Removing the main diagonal of the CSM does not violate any assumption for this method. The effect of background noise and reflections can also be taken into account using SEMWAN [109] or cepstrum [111], respectively. This method has been applied in open–jet and closed–section wind–tunnel experiments [103, 107, 108].
- **SODIX** [112–114] is an extension of SEM for experiments where the directivities of the sound sources are of interest. It provides better resolution than the Sparrow resolution limit. SODIX has been mostly applied to static engine tests on free–field and indoor test–beds, [112, 114, 116] and measurements in open–jet wind tunnels [120–122].
- **Compressive Sensing Beamforming** [124–126] assumes spatially–sparse distributions of sound sources and requires a lower number of microphones. This inverse technique has been used to identify spinning modes of turbofan engines [128, 129].
- **Generalized Inverse Beamforming (GIBF)** [132] considers partially–coherent sound sources using inversion techniques. Multipoles in an arbitrary direction can be considered as well. An application to duct acoustics was studied in [136] and to airfoil noise in [137, 138].
- **Iterative Bayesian Inverse Approach (IBIA)** [139–141] is based on a user–defined level of sparsity of the sound sources. The results are somewhat between those of CFDBF (no sparsity) and CLEAN–SC (strong sparsity). It has been applied to measurements in closed–section wind tunnels [143].
- **Global Optimization Methods** [144] can be used for searching the locations and amplitudes of sound sources without using a scan grid. Other parameters, such as the sound speed, can be added to the optimization problem to obtain more information about the sound field. Differential evolution was applied to a experiment with a speaker in an anechoic room [144].

A summary of the required parameters and typical applications of all the methods described in this thesis is presented in Table 4.2, as well as additional comments if needed. Except when explicitly stated, a scan grid is also required for most of the acoustic imaging methods listed. The reader is warned to consider that the information indicated in Table 4.2 is just indicative and not at all restrictive.

The beamforming methods that determine only the incoherent source strengths are conventional, functional, orthogonal, wavenumber and robust adaptive beamforming, as well as CLEAN–SC, DAMAS, LPD, and SEM. SODIX adds source directivity to the results, and DAMAS–C adds source coherence as an output (CLEAN–SC considers it implicitly). The remaining methods attempt to find the amplitude, phase, and, in some cases, the partial coherence of sources using different regularization schemes.

In general, more complex methods require considerably more computation time than CFDBF. Hence, depending on the experiment requirements, this can pose some constraints when selecting the most suitable method.

Other benchmark cases analyzing the performance of some of these methods for specific acoustic applications can be found in the literature [1, 105, 106, 152, 153]. Moreover, a broad effort in the aeroacoustics community was started by NASA Langley researchers to establish a common set of benchmark problems for the purpose of testing and validation of new analysis techniques, coordinated by Bahr [154–157]. This ongoing working group has met at several forums, shared initial results for the chosen test cases, and has recently presented the results from the first release of benchmark problems [32, 143, 156–158]. Some illustrative results for the benchmark case consisting of a simulated line source are included in section 4.17.

4.17. Benchmark case: Trailing–edge noise

This synthetic case is obtained from the Phased–Array Methods Benchmark[5] [154–157]. The case consists of recorded microphone array data from a simulated acoustic line source. The measurement data was subject to severe incoherent noise. This representation is typical for measuring trailing–edge noise in a closed–section wind tunnel for which the microphones are flush–mounted in the wall of the tunnel. For recordings in this setup, noise is introduced due to wall–boundary–layer turbulence [32]. An experimental example of a similar setup is presented later in section 6.1.3 in Chapter 6.

This benchmark case was proposed by Pieter Sijtsma (PSA3) [159] and the preliminary results obtained by several researchers using different acoustic imaging methods have been published recently by Sarradj et al. [32].

4.17.1. Setup description

The considered coordinate system is shown in Fig. 4.17, with the x axis in the streamwise direction, the y axis perpendicular to the line source pointing away

[5]The acoustic data and more details of this benchmark case (B1) are currently available online in the following website: https://www-fs.tu-cottbus.de/aeroakustik/analytical/.

Table 4.2: Summary of the main characteristics of the acoustic imaging methods introduced.

Method	Parameters to be set	Typical use	Other characteristics
Conventional Beamforming	None	General purpose	-Integration techniques for extended sources -Time-domain version
Functional Beamforming	-Power parameter v	Aircraft flyover measurements	-Sensitive to diagonal removal
Orthogonal Beamforming	-Number of eigenvalues k	Limited use, see text	-The sum of the acoustic source strengths is not overestimated
CLEAN–SC	-Damping parameter -Number of iterations	Airframe noise measurements	-Allows diagonal removal -Super-resolution version
DAMAS	-Number of iterations	Airframe noise measurements	-Super-resolution -Allows diagonal removal -Faster versions
Wavenumber Beamforming	None	Measurements featuring different wave propagation speeds	-Far field formulation
Linear Programming Deconvolution	-Same as DAMAS	Same as DAMAS	-Super-resolution -Does not work with diagonal removal -Can be combined with functional beamforming
RAB	-Diagonal loading parameter μ_0	Limited use, see text	-Very sensitive to the uncorrelation assumption
SEM	-Number of iterations or the maximum error in solutions	Airframe noise measurements	-High resolution with positivity constrained -Allows diagonal removal -Distributed sound sources
SODIX	-Optional regularization function (smoothness constraint of directivity) with 2 parameters	Engine noise measurements (directional sources)	-Super-resolution -Robust also for ill-posed problems -Allows diagonal removal
Compressive Sensing Beamforming	-Regularization parameter δ	Duct acoustics	-Imposed sparsity degree (L_1–norm)
GIBF	-Requires SNR to set up regularization	Wind-tunnel experiments and duct acoustics	-Imposed sparsity degree (L_1–norm)
IBIA	-Degree of sparsity $\tilde{q}$	General purpose	-Fully automatic regularization -Possibility to tune the degree of sparsity (L_q–norm)
Global Optimization Methods	-Number of unknowns to search -Settings for the optimization algorithm	General purpose	This method does not require a predefined scan grid

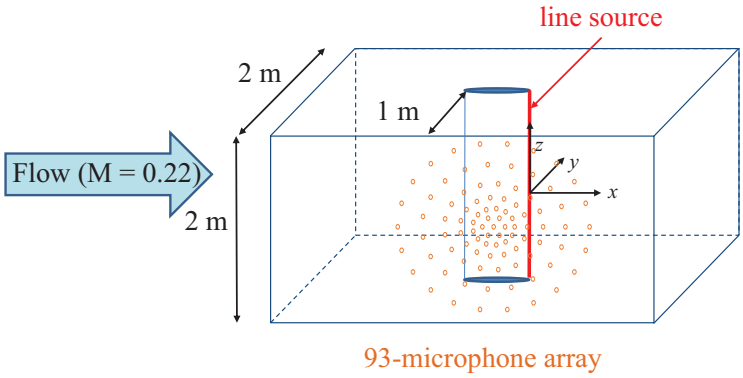

Figure 4.17: Diagram explaining the computational setup for the line source benchmark case. Adapted from [32].

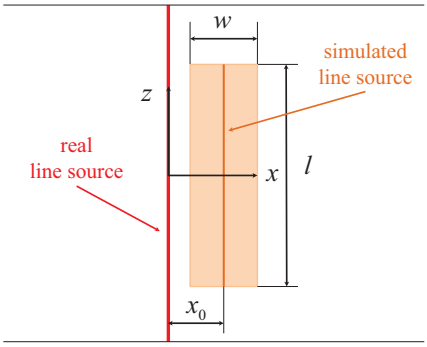

Figure 4.18: Diagram explaining the parameters that define the ROI (shaded in orange) [6].

from the array plane, the z axis in the spanwise direction of the line source pointing upwards, and the center in the middle of the line source.

The setup for this case can be seen in Fig. 4.17. A 2–m–long line source with short correlation length was simulated between $z = -1$ m and $z = 1$ m located at $x = y = 0$ m, inside of a 2 m $\times$ 2 m cross section of a wind tunnel. Henceforth, this line source is referred to as "real" line source, see Fig. 4.18. The line source was subject to a uniform flow with a Mach number of $M = 0.22$ in the positive x–direction. A 93–microphone array distributed in concentric circles and located at the $y = -1$ m plane with an aperture of 1.8 m was considered, see Fig. 4.17. The presence of hard wind–tunnel walls was neglected for the simulations, i.e., no reflections are present.

A detailed explanation of the signal generation process can be found in[32]. The line source was synthesized as a large number of incoherent monopoles at

equal spacing and equal strengths. This results in a source strength distribution per unit length denoted as $\tilde{A}$ in Pa^2/m. The resulting source strength per frequency f for this benchmark case expressed as the sound pressure level (L_p) at the center microphone of the array, $(x, y, z) = (0, -1, 0)$ m, in dB and 50 Hz steps (resulting in a total of 200 frequencies from 50 Hz to 10 kHz) was:

$$L_p = 61.16 + 0.34127f + 0.87242f^2 - 0.163f^3 + 0.0082341f^4, \tag{4.39}$$

where f here is the frequency expressed in kHz.

On top of the signal generated by the line source, Gaussian white noise, incoherent from microphone to microphone, was added with an L_p of 86.89 dB per frequency considered. This provides negative SNR values for the whole frequency range (between -25.7 dB at 50 Hz to -15.7 dB at 10 kHz), due to the varying source strength with frequency.

The challenge of this benchmark is to obtain the value of $\tilde{A}$ per frequency, expressed as the L_p at the center of the array $(x, y, z) = (0, -1, 0)$ m using the following expression [32, 159]

$$L_p = 10\log_{10}\left\{\frac{\tilde{A}}{8\pi^2(1-M^2)p_{e,0}^2 h}\left[\arctan\left(\frac{l}{2h}\right)\right]\right\}, \tag{4.40}$$

where h represents the distance between the array plane and the scan plane, l is the length of the ROI in the spanwise direction (symmetric with respect to the $z = 0$ plane), see Fig. 4.18, and $p_{e,0}$ is the reference effective pressure of 20μPa. This way of expressing the results was selected in order to compare the different contributions to the benchmark. It represents the L_p observed at the center of the array if only the line source would be present.

For this case, $h = 1$ m and $l = 2$ m, so Eq. (4.40) can be simplified to

$$L_p = 10\log_{10}\left[\frac{\tilde{A}}{32\pi(1-M^2)p_{e,0}^2}\right]. \tag{4.41}$$

4.17.2. Results comparison and discussion

A preliminary study of the acoustic data using CFDBF confirmed that removing the main diagonal of the CSM (see section 4.2.1) is necessary since the SNR values are very low and the influence of incoherent noise is very strong. The convection of the sound waves due to the flow inside the wind tunnel also needs to be taken into account for obtaining valid results [18]. Four CFDBF source plot examples for the whole frequency range (50 Hz to 10 kHz) are presented in Fig. 4.19 to illustrate these phenomena. The overall sound pressure levels ($L_{p,overall}$) are presented, see Eq. (A.3) in Appendix A.1.

Figure 4.19a shows the CFDBF results without applying the DR or convective effects; Figure 4.19b includes convective effects but no DR; Figure 4.19c includes DR but no convective effects and Figure 4.19d includes both effects. In Figs. 4.19a and 4.19b, the incoherent noise hinders any useful interpretation of the source plot

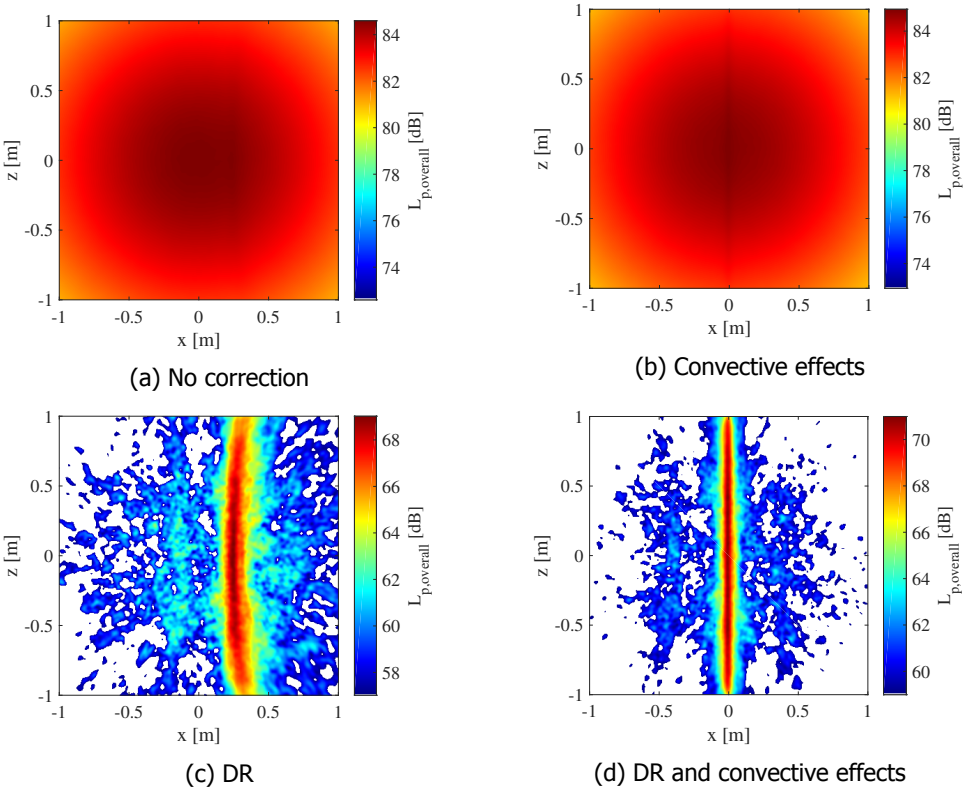

Figure 4.19: CFDBF source maps for the whole frequency range (50 Hz to 10 kHz): (a) Without DR or considering convective effects. (b) Without DR of the CSM, but considering convective effects. (c) DR without considering convective effects. (d) DR and considering convective effects [6].

and the presence of the line can barely be detected. Moreover, the $L_{\text{p,overall}}$ values in these figures are considerably higher than the true ones due to the line source. After applying DR (see Fig. 4.19c) the line source is clearly visible, and located at the correct position if the convective effects are accounted for (see Fig. 4.19d).

Several well–known acoustic imaging methods (orthogonal beamforming, CMF, functional beamforming, SPI, SPIL, DAMAS, CLEAN–SC and GIBF) were applied by different researchers using the parameters specified in Table 4.3. Most of the solutions obtained were extracted from Sarradj et al. [32] and Merino–Martínez et al. [7]. Only one solution per method is considered, but significant differences were found when different contributors applied the same method, such as DAMAS or CLEAN–SC [32], which is not a desired feature.

In the second column of Table 4.3, BTU corresponds to the Brandenburg University of Technology Cottbus–Senftenberg and TU Berlin in Germany, NASA to the NASA Langley Research Center in the United States, PSA3 to Pieter Sijstma Advanced AeroAcoustics in the Netherlands, TU Delft to Delft University of Technology in the Netherlands, UniA to the University of Adelaide in Australia [32], and

VKI to the von Karman Institute for Fluid Dynamics in Belgium [137, 158]. In the third column of Table 4.3, the relevant parameters of each method are specified: k is the number of eigenvalues considered for orthogonal beamforming, ν is the functional beamforming exponent, N_{iter} is the number of iterations for DAMAS, $\tilde{\varphi}$ is the damping factor (or loop gain) for CLEAN–SC, and L_1 norm is the type of regularization chosen for GIBF. The ROI employed by each contributor is stated in the fourth column of Table 4.3 in terms of width (w) × length (l), see Fig. 4.18. The spacing between grid points Δx is included in the last column. All the contributors used ROIs centered at $x = 0$ and from $y = -1$ m to $y = 1$ m, i.e., the whole span.

The frequency spectra obtained by these methods for the line–source benchmark are presented in Fig. 4.20a, as well as the exact solution given by Eq. (4.39). The relative errors made by each method with respect to the exact solution, $\Delta L_{\text{p}} = L_{\text{p}} - L_{\text{p,exact}}$, are included in Fig. 4.20b. This way, a positive value of ΔL_{p} means that the method overpredicts the solution. Moreover, the absolute errors made by each method averaged over the whole frequency range (i.e., over the 200 frequencies) $\varepsilon = \overline{|\Delta L_{\text{p}}|}$ are indicated in Table 4.4. In general, most methods tend to overpredict the spectrum (with the exception of functional beamforming below 2 kHz). Orthogonal beamforming seems to considerably overpredict the results, especially at low frequencies, with errors up to about 15 dB. CMF and DAMAS present a similar behavior, but with increasing errors (up to 15 dB) for high frequencies. CLEAN–SC shows a similar trend as orthogonal beamforming but with errors about 5 dB lower. GIBF presents a comparable trend as CLEAN–SC but even closer to the exact solution, especially for lower frequencies, and it shows a good overall performance with average errors of about 1.7 dB. Surprisingly, in spite of underpredicting the results below 2 kHz, functional beamforming provides values that are in agreement with the exact solution, even though DR was not applied [32]. Optimizing the diagonal of the CSM [25, 49], instead of removing it, is of interest for future research. The SPIL method (with a ROI width of $w = 0.04$ m) provides the best results for this case in the whole spectrum, with an average error lower than 0.3 dB and maximum errors for single frequencies of 1.2 dB. In addition, the computation time required by the SPIL method is considerably lower (in the order of seconds) than other methods, especially DAMAS.

For clarity reasons, the solutions obtained by UniA and PSA3 using the SPI method were not included in Fig. 4.20 but instead, a separate plot is presented in Fig. 4.21 comparing the performance of SPI and SPIL. In order to have a fair comparison all the ROI parameters were kept constant: $w = 0.08$ m, $l = 2$ m, $x_0 = 0$ and $\Delta x = 0.02$ m. Figure 4.21a presents the absolute spectra of both SPI and the SPIL contributions. It can be observed that the results collapse almost perfectly with the exact solution. In addition, there seems to be almost no difference between the results by TU Delft, PSA3 and UniA, suggesting that this method is more robust than other more complex methods [32]. The relative errors made by each method are depicted in Fig. 4.21b, with a considerably smaller scale in the y axis than in Fig. 4.20b. The three contributions provide similar results, with maximum errors for single frequencies of ± 1.5 dB. However, the average absolute error made by the SPI method ($\varepsilon \approx 0.65$ dB) is approximately double than the one

Table 4.3: Overview of the contributors and parameters for each method. Adapted from [32].

Method	Contributor	Parameters	ROI	Δx
Orthogonal	BTU	DR, $k = 16$	0.2 m × 2 m	0.025 m
CMF	BTU	DR, NNLS solver	0.2 m × 2 m	0.025 m
SPI	PSA3 and UniA	DR	0.08 m × 2 m	0.02 m
SPIL	TU Delft	DR	0.08 m × 2 m	0.02 m
SPIL	TU Delft	DR	0.04 m × 2 m	0.01 m
Functional	TU Delft	no DR, $\nu = 16$	0.1 m × 2 m	0.01 m
DAMAS	NASA	DR, $N_{\text{iter}} = 200$	0.12 m × 2 m	0.02 m
CLEAN–SC	UniA	DR, $\bar{\varphi} = 0.99$	0.08 m × 2 m	0.02 m
GIBF	VKI	DR, L_1 norm	0.04 m × 2 m	0.02 m

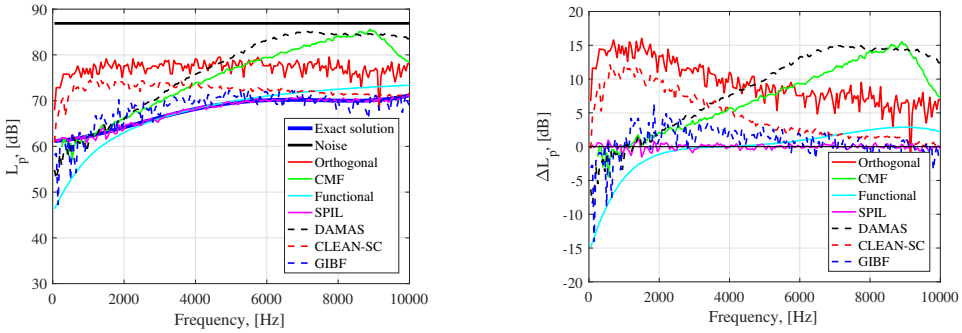

(a) (b)

Figure 4.20: (a) Results of the line–source benchmark for different acoustic imaging methods. Adapted from [32]. (b) Relative errors ΔL_{p} with respect to the exact solution for each method [6].

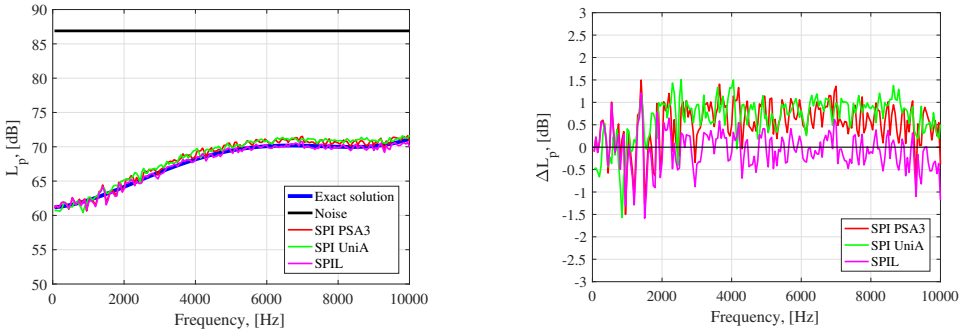

(a) (b)

Figure 4.21: (a) Results of the line–source benchmark for the SPI and SPIL methods with $w = 0.08$ m. (b) Relative errors ΔL_{p} with respect to the exact solution for each method [6].

made by the SPIL technique ($\varepsilon \approx 0.33$ dB), see Table 4.4. Therefore, the use of the SPIL method is recommended for this type of experiments, since it approximates the physics of the sound source in a better way.

The ISPI technique was not used in this benchmark case because all the incoherent monopoles had the same strength, and in this situation the ISPI technique is essentially the same as the SPIL method. A separate benchmark case to test the ISPI method can be found in [6, 7], whose results have already been presented in Fig. 4.4.

Table 4.4: Average absolute errors made by each method with respect to the exact solution.

Method	ε, [dB]
Orthogonal ($k = 16$)	9.4034
CMF	7.2963
SPI PSA3 ($w = 0.08$ m)	0.6314
SPI UniA ($w = 0.08$ m)	0.7414
SPIL ($w = 0.08$ m)	0.3281
SPIL ($w = 0.04$ m)	0.2881
Functional ($\nu = 50$)	2.1741
DAMAS ($N_{\text{iter}} = 200$)	9.0901
CLEAN–SC	4.5769
GIBF	1.6624

4.17.3. Sensitivity analysis for SPIL

A sensitivity analysis was performed for the SPIL method to investigate the influence of the parameters defining the ROI. Only the SPIL method is studied here for brevity reasons, but sensitivity analyses for the SPI and ISPI techniques are expected to provide similar results. The ROI in Fig. 4.18 (shaded in orange) has four main parameters:

1. The width in the chordwise direction w.
2. The length in the spanwise direction l.
3. The spacing between grid points Δx.
4. The location of the simulated line source chosen by the user x_0.

For simplicity's sake, only integration lines parallel to the "real" line source are considered. This assumption is easily fulfilled in practical experiments where, even though the exact locations of the noise sources are not known *a priori*, the orientation of the model (such as an airfoil) with respect to the microphone array can be accurately determined. Moreover, all the ROIs considered here are symmetric with respect to the $z = 0$ plane and are contained in the $y = 0$ plane, i.e., the correct

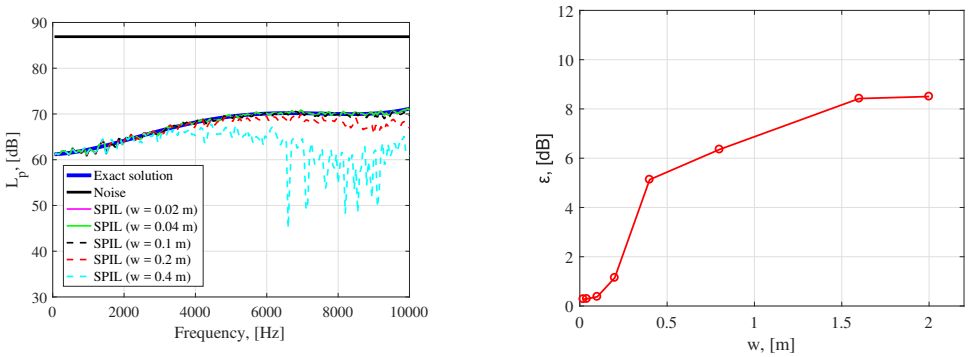

(a) (b)

Figure 4.22: (a) Results of the sensitivity analysis performed for the SPIL method with respect to the ROI width w. Adapted from [32]. (b) Average absolute errors ε made for each width case [6].

source distance to the array. The influence of the distance of the scan plane to the array was not investigated here, but it has been previously addressed in the literature [19].

Chordwise extension

Different ROI widths w were tested (considering $x_0 = 0$, $l = 2$ m and $\Delta x = 0.01$ m) and plotted in Fig. 4.22a. The average absolute errors ε made for each width case are presented in Fig. 4.22b. Acceptable results are obtained with widths up to 0.1 m (with $\varepsilon \approx 1$ dB). After that threshold value, the error rapidly increases due to the inclusion of sidelobes in the ROI, until what looks like an asymptotic value of about 9 dB at around $w = 2$ m, which is comparable to the errors presented in Table 4.4 for DAMAS and orthogonal beamforming for narrower ROIs. The improvement of the results by reducing w also seems to have an asymptotic behavior. For example, reducing $w = 0.04$ m to $w = 0.02$ m only reduces ε by less than 0.01 dB. Therefore, there seems to be an acceptable range of integration widths for which the SPIL method works well.

Spanwise extension

Due to the fact that L_p explicitly depends on the length of the ROI l, see Eq. (4.40), a correction factor needs to be applied to the obtained solutions. If the whole length of the experimental line source is selected for normalizing the results (i.e., $l = 2$ m), the L_p obtained with the reduced integration area of length l ($L_{\mathrm{p},l}$) can be corrected to full span by

$$L_\mathrm{p} = L_{\mathrm{p},l} + 10\log_{10}\left[\frac{\frac{\pi}{4}}{\arctan\left(\frac{l}{2}\right)}\right], \tag{4.42}$$

where l is the length of the reduced integration area and the term $\pi/4$ comes from the solution of the $\arctan$ term in Eq. (4.40) for the full span ($l = 2$ m and $h = 1$ m), and consequently, $\arctan(1) = \pi/4$.

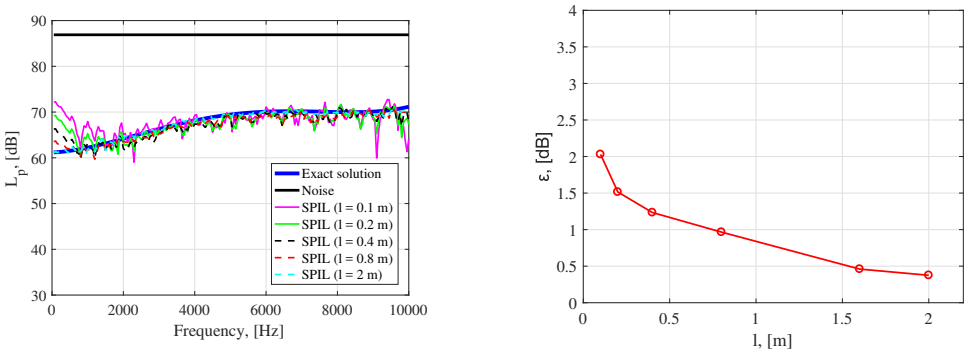

Figure 4.23: (a) Results of the sensitivity analysis performed for the SPIL method with respect to the ROI length l, corrected using Eq. (4.42). (b) Average absolute errors ε made for each length case [6].

To investigate the influence of the choice of the ROI length, several tests were performed using different values of l (considering $x_0 = 0$, $w = 0.1$ m and $\Delta x = 0.01$ m). The results are gathered in Fig. 4.23a. The average absolute errors ε made for each length case are presented in Fig. 4.23b. It seems that the error decreases when l is increased. The results for considerably short integration lengths still present relatively good results, with $\varepsilon \leq 2$ dB. It seems that an increasing error occurs when reducing the value of l, especially for frequencies below 2000 Hz. The influence of the spanwise extension seems to have a lower impact in the results than the chordwise extension, see Fig. 4.22. Hence, the SPIL method is considered as robust with respect to the choice of the ROI length.

Mesh fineness

Tests were performed using several spacings between grid points Δx (considering $x_0 = 0$ m, $w = 0.04$ m and $l = 2$ m) and plotted in Fig. 4.24a. The average absolute errors ε made for each width case are presented in Fig. 4.24b. The mesh fineness seems to hardly influence the results. Only very coarse grids ($\Delta x = 0.5$ m, i.e., only 5 grid points in the z direction) seem to diverge from the exact solution, especially after 9 kHz. In practice, there is normally no need for using such coarse grids. Grids with $\Delta x \leq 0.2$ m show values of ε lower than 1 dB, which is deemed as acceptable. The improvement of the results by reducing Δx seems to have an asymptotic behavior once again. For example, reducing $\Delta x = 0.01$ m to $\Delta x = 0.001$ m only reduces ε by around 0.003 dB, but increases the computation time by 100 times. Hence, the SPIL method seems to be quite robust with respect to the choice of the mesh fineness and offers acceptable results for relatively coarse grids.

Line source location

One of the unknowns when measuring trailing–edge noise in aeroacoustic experiments is the exact location of the line source. To analyze the robustness of the SPIL method with respect to this variable, several tests were performed considering

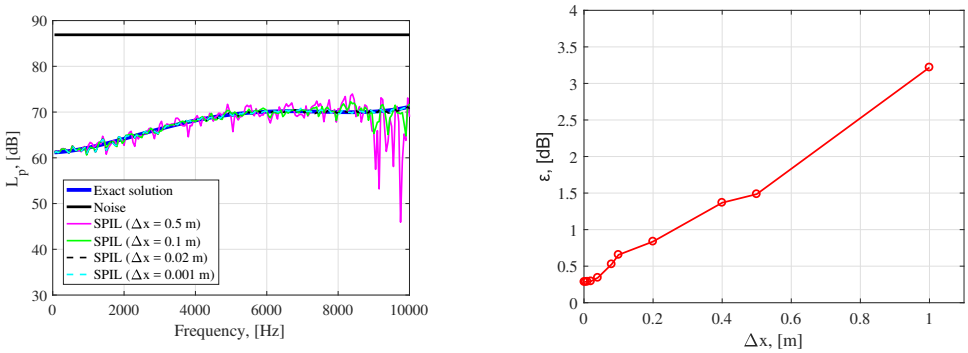

(a) (b)

Figure 4.24: (a) Results of the sensitivity analysis performed for the SPIL method with respect to the spacing between grid points Δx. (b) Average absolute errors ε made for each Δx case [6].

different locations of the simulated line source x_0, see Fig. 4.18. The length of the ROI and mesh fineness were kept constant as $l = 2$ m and $\Delta x = 0.01$ m. Two different ROI widths were tested $w = 0.04$ m and $w = 0.1$ m, and the obtained frequency spectra are presented in Fig. 4.25a and Fig. 4.25b, respectively. It can be observed that the differences with the exact solution rapidly increase after a threshold value of $x_0 = 0.02$ m with errors of about 20 dB for certain frequencies. This phenomenon is even more pronounced for the narrow width case ($w = 0.04$ m).

Figure 4.25c depicts the values of ε for different values of x_0 for both cases of w. An almost–symmetric behavior with respect to $x_0 = 0$ is observed, which fits the relatively simple geometry of the benchmark. A sharp minimum of ε is found for $x_0 = 0$ for both cases, but the narrower width ($w = 0.04$ m) presents an even sharper minimum.

Figure 4.25d presents the $L_{\text{p,overall}}$ (see Eq. A.3) values with respect to x_0 for both cases of w. A similar behavior as in Fig. 4.25c is observed, with the difference that, in this case, a maximum is observed for $x_0 = 0$, instead of a minimum. Once again, the narrower ROI shows a sharper peak, with still an almost–symmetric behavior with respect to $x_0 = 0$. This is an important finding in order to search for the correct location of a line source in practical cases. A fast sweep can be performed for different x_0 values using small values of w and select the x_0 value that provides a maximum for $L_{\text{p,overall}}$. In practice, the expected range of x_0 is typically in the order of centimeters, so the computational demand of this procedure is not high.

Since this parameter seems to be the most sensitive for the performance of the SPIL method, it is further investigated in section 6.2 with an actual trailing–edge noise experiment featuring porous material inserts at the trailing edge as a noise reduction measure, see section 2.3.4. The application of porous material inserts is expected to change the location of the line source causing trailing–edge noise [160].

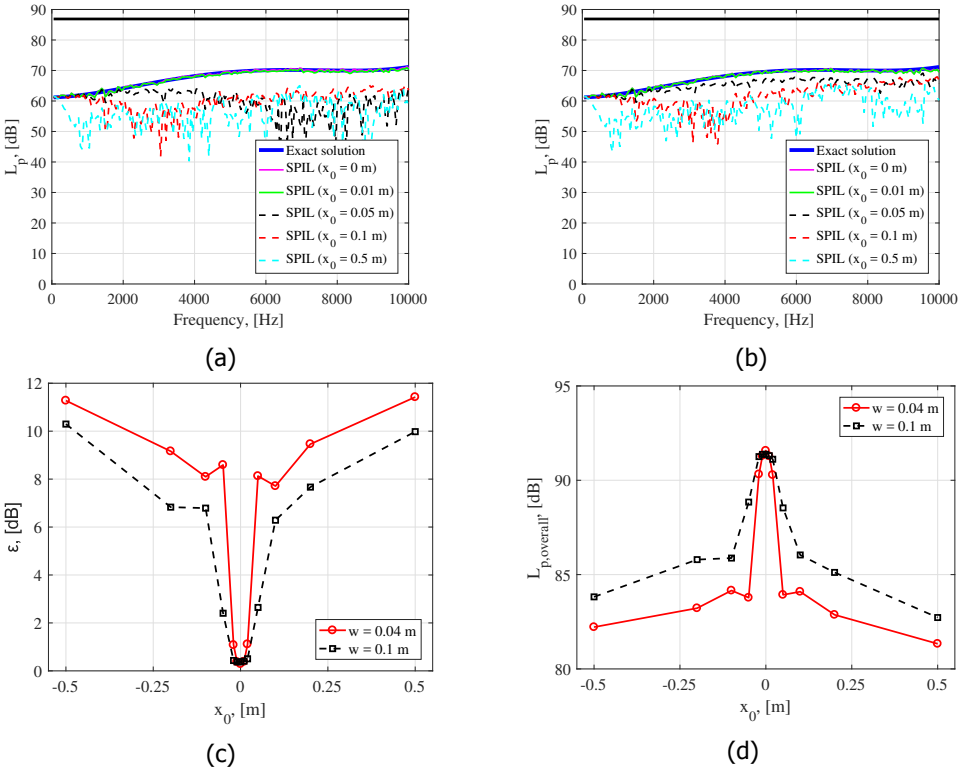

Figure 4.25: Results of the sensitivity analysis performed for the SPIL method with respect to the error in the line location x_0 for (a) $w = 0.04$ m and (b) $w = 0.1$ m. (c) Average absolute errors ε and (d) $L_{\text{p,overall}}$ for each x_0 case [6].

4.18. Conclusions

Phased microphone arrays are useful tools for estimating the location and strength of sound sources. Aeroacoustic experiments present important challenges, such as noisy environments like wind tunnels or moving sources like flying aircraft. A wide variety of 14 acoustic imaging methods is presented in this chapter and the performance of each method for aeroacoustic applications is assessed. This selection spans from the simple conventional beamforming algorithm to deconvolution and inversion methods, which normally imply higher computational cost. Although there is no such thing as a *perfect method*, recommendations are given for non–experienced users in order to obtain the best results, depending on the desired application.

Acknowledgements

The author would like to express his profound gratitude to all the authors of the paper "*A review of acoustic imaging methods using phased microphone arrays*" [5], as well as to Takao Suzuki from the Boeing Company, for their constructive feedback and useful comments.

Bibliography

[1] R. Merino-Martinez, M. Snellen, and D. G. Simons, *Functional beamforming applied to imaging of flyover noise on landing aircraft,* Journal of Aircraft **53**, 1830 (2016).

[2] R. Merino-Martinez, M. Snellen, and D. G. Simons, *Functional Beamforming Applied to Full Scale Landing Aircraft,* in *6th Berlin Beamforming Conference, February 29 – March 1 2016, Berlin, Germany* (GFaI, e.V., Berlin, 2016) BeBeC–2016–D12.

[3] P. Sijtsma, R. Merino-Martinez, A. M. N. Malgoezar, and M. Snellen, *High–Resolution CLEAN–SC: Theory and Experimental Validation,* International Journal of Aeroacoustics **16**, 274 (2017), SAGE Publications Ltd. London, United Kingdom.

[4] P. Sijtsma, R. Merino-Martinez, A. M. N. Malgoezar, and M. Snellen, *High–Resolution CLEAN–SC: Theory and Experimental Validation,* in *23rd AIAA/CEAS Aeroacoustics Conference. June 5 – 9 2017. Denver, Colorado, USA* (2017) AIAA paper 2017–3841.

[5] R. Merino-Martinez, P. Sijtsma, M. Snellen, T. Ahlefeldt, J. Antoni, C. Bahr, D. Blacodon, D. Ernst, A. Finez, S. Funke, T. Geyer, S. Haxter, G. Herold, X. Huang, W. Humphreys, Q. Leclère, A. Malgoezar, U. Michel, T. Padois, A. Pereira, C. Picard, E. Sarradj, H. Siller, D. G. Simons, and C. Spehr, *Aircraft Noise Generation and Assessment: A review of acoustic imaging methods using phased microphone arrays, CEAS aeroacoustic journal*, CEAS Aeronautical Journal (2017), Accepted for publication.

[6] R. Merino-Martinez, P. Sijtsma, and M. Snellen, *Inverse Integration Method for Distributed Sound Sources,* in *7th Berlin Beamforming Conference, March 5 – 6 2018, Berlin, Germany* (GFaI, e.V., Berlin, 2018) BeBeC–2018–S07.

[7] R. Merino-Martinez, P. Sijtsma, A. Rubio Carpio, R. Zamponi, S. Luesutthiviboon, A. M. N. Malgoezar, M. Snellen, N. Van de Wyer, C. Schram, and D. G. Simons, *Integration methods for distributed sound sources,* International Journal of Aeroacoustics (2018), Under review process.

[8] B. D. van Veen and K. M. Buckley, *Beamforming: A Versatile Approach to Spatial Filtering,* IEEE ASSP Magazine **5**, 4 (1988).

[9] D. H. Johnson and D. E. Dudgeon, *Array Signal Processing, Concepts and Techniques* (P T R Prentice Hall, Englewood Cliffs, 1993) ISBN: 978–0130485137.

[10] T. Mueller, *Aeroacoustic Measurements* (Springer Science & Business Media, 2002) p. 313, ISBN: 978–3–642–07514–8.

[11] S. Oerlemans, *Detection of aeroacoustic sound sources on aircraft and wind turbines*, Ph.D. thesis, University of Twente, Enschede, the Netherlands (2009).

[12] R. P. Dougherty, *Advanced Time–domain Beamforming Techniques,* in *10th AIAA/CEAS Aeroacoustics Conference. May 10 – 12 2004, Manchester, United Kingdom* (2004) AIAA paper 2004–2955.

[13] T. Padois, F. Sgard, O. Doutres, and A. Berry, *Acoustic source localization using a polyhedral microphone array and an improved generalized cross–correlation technique,* Journal of Sound and Vibration **386**, 82 (2016).

[14] T. Padois, O. Doutres, F. Sgard, and A. Berry, *Time domain localization technique with sparsity constraint for imaging acoustic sources,* Mechanical Systems and Signal Processing **94**, 85 (2017).

[15] N. Quagebeur, T. Padois, P.-A. Gauthier, and P. Masson, *Enhancement of time–domain acoustic imaging based on generalized cross-correlation and spatial weighting,* Mechanical Systems and Signal Processing **75**, 515 (2015).

[16] P. Sijtsma, *Beamforming on moving sources*, Tech. Rep. NLR–TP–2006–733 (National Aerospace Laboratory (NLR), Anthony Fokkerweg 2, 1059 CM Amsterdam, P.O. Box 90502, 1006 BM Amsterdam, The Netherlands, 2006).

[17] C. Sparrow, *On spectroscopic resolving power,* The Astrophysical Journal **44**, 76 (1916).

[18] P. Sijtsma, *Phased array beamforming applied to wind tunnel and fly–over tests*, Tech. Rep. NLR–TP–2010–549 (National Aerospace Laboratory (NLR), Anthony Fokkerweg 2, 1059 CM Amsterdam, P.O. Box 90502, 1006 BM Amsterdam, The Netherlands, 2010).

[19] E. Sarradj, *Three–Dimensional Acoustic Source Mapping with Different Beamforming Steering Vector Formulations,* Advances in Acoustics and Vibration **2012**, 1 (2012).

[20] T. Ahlefeldt, C. Spehr, T. Berkefeld, A. Di Marco, and L. Burghignoli, *A Tomographic Directivity Approach for Frequency Domain Beamforming,* in *24th AIAA/CEAS Aeroacoustics Conference. June 25 – 29 2018. Atlanta, Georgia, USA* (2018) AIAA paper 2018–2808.

[21] Y. Liu, A. R. Quayle, A. P. Dowling, and P. Sijtsma, *Beamforming correction for dipole measurement using two–dimensional microphone arrays,* Journal of the Acoustical Society of America **124**, 182 (2008).

[22] M. Demyanov, O. Bychkov, G. Faranosov, and M. Zaytsev, *Development of Beamforming Methods for Uncorrelated Dipole Sources,* in *7th Berlin Beamforming Conference, March 5 – 6 2018, Berlin, Germany* (GFaI, e.V., Berlin, 2018) BeBeC–2018–D16.

[23] S. Glegg and W. J. Devenport, *Aeroacoustics of Low Mach Number Flows – Fundamentals, Analysis, and Measurement* (Academic Press, 2017) p. 313, ISBN: 978–0–128–09651–2.

[24] G. P. Howell, M. A. Bradley, M. A. McCormick, and J. D. Brown, *De–Dopplerization and acoustic imaging of aircraft flyover noise measurements,* Journal of Sound and Vibration **105**, 151 (1986).

[25] J. Hald, *Removal of incoherent noise from an averaged cross–spectral matrix,* Journal of the Acoustical Society of America **142**, 846 (2017).

[26] D. Ernst, C. Spehr, and T. Berkefeld, *Decorrelation of acoustic wave propagation through the shear layer in open jet wind tunnel,* in *21st AIAA/CEAS Aeroacoustics Conference, June 22 – 26 2015, Dallas, TX, USA* (2015) AIAA paper 2015–2976.

[27] T. F. Brooks and W. M. Humphreys, *Effect of Directional Array Size on the Measurement of Airframe Noise Components,* in *5th AIAA/CEAS Aeroacoustics Conference. Bellevue, WA, USA* (1999) AIAA paper 1999–1958.

[28] S. Oerlemans and P. Sijtsma, *Acoustic Array Measurements of a 1:10.6 Scaled Airbus A340 Model,* in *10th AIAA/CEAS Aeroacoustics Conference, May 10 – 12, 2004, Manchester, United Kingdom* (2004) AIAA paper 2004–2924.

[29] P. Sijtsma and R. Stoker, *Determination of Absolute Contributions of Aircraft Noise Components Using Fly–over Array Measurements,* in *10th AIAA/CEAS Aeroacoustics Conference, May 10 – 12 2004, Manchester, United Kingdom* (2004) AIAA paper 2004–2958.

[30] C. Arce León, R. Merino-Martinez, D. Ragni, F. Avallone, and M. Snellen, *Boundary layer characterization and acoustic measurements of flow–aligned trailing edge serrations,* Experiments in Fluids **57**, 1 (2016).

[31] C. Arce León, R. Merino-Martinez, D. Ragni, F. Avallone, F. Scarano, S. Pröbsting, M. Snellen, D. G. Simons, and J. Madsen, *Effect of trailing edge serration–flow misalignment on airfoil noise emission,* Journal of Sound and Vibration **405**, 19 (2017).

[32] E. Sarradj, G. Herold, P. Sijtsma, R. Merino-Martinez, A. M. N. Malgoezar, M. Snellen, T. F. Geyer, C. J. Bahr, R. Porteous, D. J. Moreau, and C. J. Doolan, *A microphone array method benchmarking exercise using synthesized input data,* in *23rd AIAA/CEAS Aeroacoustics Conference. June 5 – 9 2017. Denver, CO, USA* (2017) AIAA paper 2017–3719.

[33] C. Arce León, R. Merino-Martinez, S. Pröbsting, D. Ragni, and F. Avallone, *Acoustic Emissions of Semi–Permeable Trailing Edge Serrations,* Acoustics Australia **46**, 111 (2017).

[34] C. Arce León, R. Merino-Martinez, D. Ragni, S. Pröbsting, F. Avallone, A. Singh, and J. Madsen, *Trailing Edge Serrations – Effect of Their Flap Angle on Flow and Acoustics,* in *7th International Meeting on Wind Turbine Noise, May 2 – 5 2017, Rotterdam, the Netherlands* (2017).

[35] R. Merino-Martinez, L. Bertsch, M. Snellen, and D. G. Simons, *Analysis of landing gear noise during approach,* in *22nd AIAA/CEAS Aeroacoustics Conference. May 30 – June 1 2016. Lyon, France* (2016) AIAA paper 2016–2769.

[36] M. Snellen, R. Merino-Martinez, and D. G. Simons, *Assessment of noise level variability on landing aircraft using a phased microphone array,* Journal of Aircraft **54**, 2173 (2017).

[37] R. Merino-Martinez, E. Neri, M. Snellen, J. Kennedy, D. Simons, and G. Bennett, *Comparing flyover noise measurements to full–scale nose landing gear wind–tunnel experiments for regional aircraft,* in *23rd AIAA/CEAS Aeroacoustics Conference. June 5 – 9 2017. Denver, Colorado, USA* (2017) AIAA paper 2017–3006.

[38] R. Merino-Martinez, W. C. P. van der Velden, F. Avallone, and D. Ragni, *Acoustic measurements of a DU96–W–180 airfoil with flow–misaligned serrations at a high Reynolds number in a closed–section wind tunnel,* in *7th International Meeting on Wind Turbine Noise, May 2 – 5 2017, Rotterdam, the Netherlands* (2017).

[39] A. Rubio Carpio, R. Merino-Martinez, F. Avallone, D. Ragni, M. Snellen, and S. van der Zwaag, *Broadband Trailing Edge Noise Reduction Using Permeable Metal Foams,* in *46th International Congress and Exposition of Noise Control Engineering, 27–30 August, 2017, Hong Kong* (2017).

[40] C. L. Lawson and R. J. Hanson, *Solving least squares problems*, edited by S. for Industrial and A. Mathematics (Prentice–Hall, Inc., Englewood Cliffs, New Jersey, 1974) ISBN: 0–89871–356–0.

[41] M. Tuinstra and P. Sijtsma, *Suppression of spurious noise sources in airfoil self–noise measurements,* in 21^{st} *AIAA/CEAS Aeroacoustics Conference. June 22 – 26 2015. Dallas, TX, USA* (2015) AIAA paper 2015–2689.

[42] C. C. J. Pagani, D. S. Souza, and M. A. F. Medeiros, *Slat Noise: Aeroacoustic Beamforming in Closed–Section Wind Tunnel with Numerical Comparison,* AIAA Journal **54**, 2100 (2016).

[43] T. F. Brooks and W. M. Humphreys, *A Deconvolution Approach for the Mapping of Acoustic Sources (DAMAS) determined from phased microphone arrays,* in 10^{th} *AIAA/CEAS Aeroacoustics Conference. May 10 – 12 2004. Manchester, UK* (2004) AIAA paper 2004–2954.

[44] P. Sijtsma, *CLEAN based on spatial source coherence,* International Journal of Aeroacoustics **6**, 357 (2007), SAGE Publications Ltd. London, United Kingdom.

[45] R. P. Dougherty, *Functional Beamforming,* in 5^{th} *Berlin Beamforming Conference, February 19 – 20 2014, Berlin, Germany* (GFaI, e.V., Berlin, 2014).

[46] R. P. Dougherty, *Functional Beamforming for Aeroacoustic Source Distributions,* in 20^{th} *AIAA/CEAS Aeroacoustics Conference. June 16 – 20 2014. Atlanta GA, USA* (2014) AIAA paper 2014–3066.

[47] V. F. Pisarenko, *On the estimation of Spectra by Means of Non–linear Functions of the Covariance Matrix,* Geophysical Journal of the Royal Astronomical Society **28**, 511 (1972).

[48] V. Baron, A. Finez, and B. Nicolas, *Numerical and Experimental Assessment of Functional Beamforming for Source Quantification,* in 7^{th} *Berlin Beamforming Conference, March 5 – 6 2018, Berlin, Germany* (GFaI, e.V., Berlin, 2018) BeBeC–2018–S08.

[49] R. P. Dougherty, *Cross Spectral Matrix Diagonal Optimization,* in 6^{th} *Berlin Beamforming Conference, February 29 – March 1, 2016, Berlin, Germany* (GFaI, e.V., Berlin, 2016).

[50] A. Dinsenmeyer, J. Antoni, Q. Leclère, and A. Pereira, *On the Denoising of Cross–Spectral Matrices for (Aero)Acoustic Applications,* in 7^{th} *Berlin Beamforming Conference, March 5 – 6 2018, Berlin, Germany* (GFaI, e.V., Berlin, 2018) BeBeC–2018–S02.

[51] R. Merino-Martinez, M. Snellen, and D. G. Simons, *Determination of Aircraft Noise Variability Using an Acoustic Camera,* in 23^{rd} *International Congress on Sound and Vibration, July 10 – 14 2016, Athens, Greece* (International Inst. of Acoustics and Vibration (IIAV), Auburn, Alabama, USA., 2016).

[52] R. Merino-Martinez, E. Neri, M. Snellen, J. Kennedy, D. Simons, and G. Bennett, *Analysis of nose landing gear noise comparing numerical computations, prediction models and flyover and wind–tunnel measurements,* in 24^{th}

AIAA/CEAS Aeroacoustics Conference. June 25 – 29 2018. Atlanta, Georgia, USA (2018) AIAA paper 2018–3299.

[53] T. Padois, O. Doutres, F. Sgard, and A. Berry, *On the use of geometric and harmonic means with the generalized cross–correlation in the time domain to improve noise source maps,* Journal of the Acoustical Society of America **140**, EL56 (2016).

[54] T. Padois, O. Doutres, F. Sgard, and A. Berry, *Time Domain Source Localization Technique Based on Generalized Cross Correlation and Generalized Mean,* in *Acoustic week in Canada, Vancouver.*, Vol. 44 (2016).

[55] E. Sarradj, C. Schulze, and A. Zeibig, *Identification of Noise Source Mechanisms using Orthogonal Beamforming,* in *Noise and Vibration: Emerging Methods* (2005).

[56] E. Sarradj and C. Schulze, *Practical Application of Orthogonal Beamforming,* in *Proceedings Euronoise 2006, 30 May – 1 June, 2006, Tampere, Finland* (2006).

[57] E. Sarradj, *A fast signal subspace approach for the determination of absolute levels from phased microphone array measurements,* Journal of Sound and Vibration **329**, 1553 (2010).

[58] S. U. Pillai, *Array Signal Processing*, edited by C. S. Burrus (Springer, 1989) p. 313, ISBN: 978–3–540–96951–8.

[59] T. Geyer, E. Sarradj, and C. Fritzsche, *Measurement of the noise generation at the trailing edge of porous airfoils,* Experiments in Fluids **48**, 291 (2010).

[60] T. Geyer, E. Sarradj, and C. Fritzsche, *Porous Airfoils: Noise Reduction and Boundary Layer Effects,* International Journal of Aeroacoustics **9**, 787 (2010), SAGE Publications Ltd. London, United Kingdom.

[61] G. Herold, E. Sarradj, and T. Geyer, *Covariance Matrix Fitting for Aeroacoustic Application,* in *Fortschritte der Akustik AIA - DAGA Merano* (2013) pp. 325–326.

[62] G. Herold and E. Sarradj, *Performance analysis of microphone array methods,* Journal of Sound and Vibration **401**, 152 (2017).

[63] J. A. Högbom, *Aperture synthesis with a non–regular distribution of interferometer baselines,* Astronomy and Astrophysics Supplement Series **15**, 417 (1974).

[64] R. P. Dougherty and R. W. Stoker, *Sidelobe Suppresion for Phased Array Aeroacoustic Measurements,* in 4^{th} *AIAA/CEAS Aeroacoustics Conference, June 2 – 4 1998, Toulouse, France* (1998) AIAA paper 1998–2242.

[65] S. Luesutthiviboon, A. M. N. Malgoezar, R. Merino-Martinez, M. Snellen, P. Sijtsma, and D. G. Simons, *Adaptive HR–CLEAN–SC for resolving multiple closely–spaced sound sources,* International Journal of Aeroacoustics (2018), Under review process.

[66] T. Ishii, Y. Ishii, J. Hald, K. Nagai, and H. Oinuma, *Application of Sound Source Identification Using CLEAN–SC to a Turbofan Engine,* in *7^{th} Berlin Beamforming Conference, March 5 – 6 2018, Berlin, Germany* (GFaI, e.V., Berlin, 2018) BeBeC–2018–D25.

[67] R. P. Dougherty and G. Podboy, *Improved Phased Array Imaging of a Model Jet,* in *15^{th} AIAA/CEAS Aeroacoustics Conference. May 11 – 13 2009. Miami, Florida, USA* (2009) AIAA paper 2004–2955.

[68] R. P. Dougherty, *Jet noise beamforming with several techniques,* in *3^{th} Berlin Beamforming Conference, February 24 – 25 2010, Berlin, Germany* (GFaI, e.V., Berlin, 2010).

[69] S. N. Y. Gerges, W. D. Fonseca, and R. P. Dougherty, *State of the art beamforming software and hardware for application,* in *16^{th} International Congress on Sound and Vibration, July 5 – 9 2009, Kraków, Poland* (2009).

[70] R. Cousson, Q. Leclère, M. Pallas, and M. Bérengier, *Identification of Acoustic Moving Sources Using a Time–Domain Method,* in *7^{th} Berlin Beamforming Conference, March 5 – 6 2018, Berlin, Germany* (GFaI, e.V., Berlin, 2018) BeBeC–2018–D17.

[71] P. Sijtsma and M. Snellen, *High–Resolution CLEAN–SC,* in *6^{th} Berlin Beamforming Conference, February 29 – March 1 2016, Berlin, Germany* (GFaI, e.V., Berlin, 2016) BeBeC–2016–S1.

[72] S. Luesutthiviboon, A. Malgoezar, M. Snellen, P. Sijtsma, and D. G. Simons, *Improving Source Discrimination Performance by Using an Optimized Acoustic Array and Adaptive High–Resolution CLEAN–SC Beamforming,* in *7^{th} Berlin Beamforming Conference, March 5 – 6 2018, Berlin, Germany* (GFaI, e.V., Berlin, 2018) BeBeC–2018–D07.

[73] J. J. Christensen and J. Hald, *Beamforming*, Tech. Rep. 1 (Brüel & Kjær, DK–2850 Nærum, Denmark, 2004) technical Review.

[74] T. F. Brooks and W. M. Humphreys, *A Deconvolution Approach for the Mapping of Acoustic Sources (DAMAS) determined from phased microphone arrays,* Journal of Sound and Vibration **294**, 856 (2006).

[75] T. F. Brooks and W. M. Humphreys, *Three–Dimensional Application of DAMAS Methodology for Aeroacoustic Noise Source Definition,* in *11^{th} AIAA/CEAS Aeroacoustics Conference. May 23 – 25 2005. Monterey, California, USA* (2005) AIAA paper 2005–2960.

[76] K. Ehrenfried and L. Koop, *A comparison of iterative deconvolution algorithms for the mapping of acoustic sources,* in 12^{th} *AIAA/CEAS Aeroacoustics Conference. May 8 – 10 2006. Cambridge, Massachusetts, USA* (2006) AIAA paper 2006–2711.

[77] G. Herold, T. F. Geyer, and E. Sarradj, *Comparison of Inverse Deconvolution Algorithms for High–Resolution Aeroacoustic Source Characterization,* in 23^{rd} *AIAA/CEAS Aeroacoustics Conference. June 5 – 9 2017. Denver, Colorado, USA* (2017) AIAA paper 2017–4177.

[78] T. Padois and A. Berry, *Orthogonal matching pursuit applied to the deconvolution approach for the mapping of acoustic sources inverse problem,* Journal of the Acoustical Society of America **138**, 3678 (2015).

[79] T. F. Brooks and W. M. Humphreys, *Extension of DAMAS Phased Array Processing for Spatial Coherence Determination (DAMAS–C),* in 12^{th} *AIAA/CEAS Aeroacoustics Conference. May 8 – 10 2006. Cambridge, Massachusetts, USA* (2006) AIAA paper 2006–2654.

[80] T. F. Brooks, W. M. Humphreys, and G. E. Plassman, *DAMAS Processing for a Phased Array Study in the NASA Langley Jet Noise Laboratory,* in 16^{th} *AIAA/CEAS Aeroacoustics Conference. Stockholm, Sweden* (2010) AIAA paper 2010–3780.

[81] P. A. Ravetta, R. A. Burdisso, and W. F. Ng, *Noise Source Localization and Optimization of Phased Array Results (LORE),* in 12^{th} *AIAA/CEAS Aeroacoustics Conference. May 8 – 10 2006. Cambridge, Massachusetts, USA* (2006) AIAA paper 2006–2713.

[82] P. A. Ravetta, R. A. Burdisso, and W. F. Ng, *Noise Source Localization and Optimization of Phased–Array Results,* AIAA Journal **47**, 2520 (2009).

[83] R. P. Dougherty, *Extensions of DAMAS and Benefits and Limitations of Deconvolution in Beamforming,* in 11^{th} *AIAA/CEAS Aeroacoustics Conference. May 23 – 25 2005. Monterey, California, USA* (2005) AIAA paper 2005–2961.

[84] T. Padois, P.-A. Gauthier, and A. Berry, *Inverse problem with beamforming regularization matrix applied to sound source localization in closed wind–tunnel using microphone array,* Journal of Sound and Vibration **333**, 6858 (2014).

[85] W. Ma and X. Liu, *Compression computational grid based on functional beamforming for acoustic source localization,* Applied Acoustics **134**, 75 (2018).

[86] T. Suzuki, *DAMAS2 using a point–spread function weakly varying in space,* AIAA Journal **48**, 2165 (2010).

[87] S. Haxter, *Extended Version: Improving the DAMAS 2 Results for Wavenumber–Space Beamforming,* in 6^{th} *Berlin Beamforming Conference, February 29 – March 1 2016, Berlin, Germany* (2016).

[88] C. J. Bahr and L. N. Cattafesta, *Wavenumber–frequency deconvolution of aeroacoustic microphone phased array data of arbitrary coherence,* Journal of Sound and Vibration **382**, 13 (2016).

[89] F. Casagrande Hirono, P. F. Joseph, and F. M. Fazi, *Wavenumber–Domain Method for Source Reconstruction from Far–Field Array Measurements in Flow,* in *7th Berlin Beamforming Conference, March 5 – 6 2018, Berlin, Germany* (GFaI, e.V., Berlin, 2018) BeBeC–2018–D10.

[90] L. Koop and K. Ehrenfried, *Microphone–array processing for wind–tunnel measurements with strong background noise,* in *14th AIAA/CEAS Aeroacoustics Conference (29th AIAA Aeroacoustics Conference), May 5–7, 2008, Vancouver, British Columbia, Canada* (2008) AIAA paper 2008–2907.

[91] K. Ehrenfried and L. Koop, *Experimental study of pressure fluctuations beneath a compressible turbulent boundary layer,* in *14th AIAA/CEAS Aeroacoustics Conference (29th AIAA Aeroacoustics Conference), May 5 – 7, 2008, Vancouver, British Columbia, Canada* (2008) AIAA paper 2008–2800.

[92] S. Haxter, J. Brouwer, J. Sesterhenn, and C. Spehr, *Obtaining Phase Velocity of Turbulent Boundary Layer Pressure Fluctuations at High Subsonic Mach Number from Wind Tunnel Data Affected by Strong Background Noise,* Journal of Sound and Vibration **402**, 85 (2017).

[93] O. Robin, S. Moreau, T. Padois, and A. Berry, *Measurement of the wavenumber–frequency spectrum of wall pressure fluctuations: spiral–shaped rotative arrays with pinhole–mounted quarter inch microphones,* in *19th AIAA/CEAS Aeroacoustics Conference. May 27 – 29 2013. Berlin, Germany* (2013) AIAA paper 2013–2058.

[94] S. Haxter and C. Spehr, *Infinite Beamforming: Wavenumber Decomposition of Surface Pressure Fluctuations,* in *5th Berlin Beamforming Conference, February 19 – 20 2014, Berlin, Germany* (2014).

[95] R. P. Dougherty, R. C. Ramachandran, and G. Raman, *Deconvolution of Sources in Aeroacoustic Images from Phased Microphone Arrays Using Linear Programming,* in *19th AIAA/CEAS Aeroacoustics Conference, May 27 – 29 2013, Berlin, Germany* (2013) AIAA paper 2013–2210.

[96] H. Cox, R. Zeskind, and M. Owen, *Robust adaptive beamforming,* IEEE Transactions on Acoustics Speech and Signal Processing **ASSP–35**, 1365 (1987).

[97] O. L. Frost, *An algorithm for linearly constrained adaptive array processing,* Proceedings of the IEEE **60**, 926 (1972).

[98] R. A. Gramann and J. W. Mocio, *Aeroacoustic measurements in wind tunnels using adaptive beamforming methods,* Journal of the Acoustical Society of America **97**, 3694 (1995).

[99] X. Huang, L. Bai, I. Vinogradov, and E. Peers, *Adaptive beamforming for array signal processing in aeroacoustic measurements,* Journal of the Acoustical Society of America **131**, 2152 (2012).

[100] R. P. Dougherty, *A New Derivation of the Adaptive Beamforming Formula,* in *7th Berlin Beamforming Conference, March 5 – 6 2018, Berlin, Germany* (GFaI, e.V., Berlin, 2018) BeBeC–2018–S06.

[101] P. Sijtsma, *Experimental techniques for identification and characterisation of noise sources*, Tech. Rep. NLR–TP–2004–165 (National Aerospace Laboratory (NLR), Anthony Fokkerweg 2, 1059 CM Amsterdam, P.O. Box 90502, 1006 BM Amsterdam, The Netherlands, 2004).

[102] Y. Jiang, P. Stoica, Z. Wang, and J. Li, *Capon beamforming in the presence of steering vector errors and coherent signals,* in *15th AIAA/CEAS Aeroacoustics Conference. May 11 – 13 2009. Miami, Florida, USA* (2003).

[103] D. Blacodon and G. Élias, *Level Estimation of Extended Acoustic Sources Using a Parametric Method,* Journal of Aircraft **41**, 1360 (2004).

[104] T. Yardibi, J. Li, P. Stoica, N. S. Zawodny, and L. N. Cattafesta III, *A covariance fitting approach for correlated acoustic source mapping,* Journal of the Acoustical Society of America **127**, 2920 (2010).

[105] T. Yardibi, N. S. Zawodny, C. J. Bahr, F. Liu, L. N. Cattafesta III, and J. Li, *Comparison of microphone array processing techniques for aeroacoustic measurements,* International Journal of Aeroacoustics **9**, 733 (2010), SAGE Publications Ltd. London, United Kingdom.

[106] E. Sarradj, G. Herold, and S. Jekosch, *Array methods: Which one is the best?* in *7th Berlin Beamforming Conference, March 5 – 6 2018, Berlin, Germany* (GFaI, e.V., Berlin, 2018) BeBeC–2018–S01.

[107] D. Blacodon, *Analysis of the Airframe Noise of an A320/A321 with a Parametric Method,* Journal of Aircraft **44**, 26 (2007).

[108] D. Blacodon, *Combustion–Noise Characterization of a Turbofan Engine with a Spectral Estimation Method,* Journal of Propulsion and Power 2009 **25**, 374 (2009).

[109] D. Blacodon, *Spectral estimation noisy data using a reference noise,* in *Proceedings on CD of the 3rd Berlin Beamforming Conference, 24 – 25 February, 2010, Berlin, Germany* (2010).

[110] D. Blacodon, *Array Processing for Noisy Data: Application for Open and Closed Wind Tunnels,* AIAA Journal **49**, 55 (2011).

[111] D. Blacodon and J. Bulté, *Reverberation cancellation in a closed test section of a wind tunnel using a multi-microphone cepstral method,* Journal of Sound and Vibration **333**, 26 (2014).

[112] U. Michel and S. Funke, *Noise Source Analysis of an Aeroengine with a New Inverse Method SODIX,* in *14th AIAA/CEAS Aeroacoustics Conference, May 5 – 7, 2008, Vancouver, BC, Canada* (2008) AIAA paper 2008–2860.

[113] U. Michel and S. Funke, *Inverse method for the acoustic source analysis of an aeroengine,* in *Proceedings on CD of the 2nd Berlin Beamforming Conference, 19 – 20 February, 2008* (GFaI, e.V., Berlin, 2008).

[114] S. Funke, A. Skorpel, and U. Michel, *An extended formulation of the SODIX method with application to aeroengine broadband noise,* in *18th AIAA/CEAS Aeroacoustics Conference, 4 – 6 June 2012, Colorado Springs, USA* (2012) AIAA paper 2012–2276.

[115] S. Funke, R. P. Dougherty, and U. Michel, *SODIX in comparison with various deconvolution methods,* in *5th Berlin Beamforming Conference, February 19 – 20 2014, Berlin, Germany* (2014) BeBeC–2014–11.

[116] S. Funke, H. A. Siller, W. Hage, and O. Lemke, *Microphone–array measurements of a Rolls–Royce BR700 series aeroengine in an indoor test–bed and comparison with free–field data,* in *20th AIAA/CEAS Aeroacoustics Conference, 16 – 20 Jun 2014, Atlanta, Georgia, USA* (2014) AIAA paper 2014–3070.

[117] H. Siller, A. Bassetti, S. Davies, and S. Funke, *Investigation of the noise emission of the V2500 engine of an A320 aircraft during ground tests with a line array and SODIX,* in *5th Berlin Beamforming Conference, February 19 – 20 2014, Berlin, Germany* (2014) BeBeC–2014–18.

[118] H. Siller, A. Bassetti, and S. Funke, *Investigation of Turbo Machinery and Jet Noise of the V2500 Engine During Ground Tests with an A320 Aircraft,* in *11th European Turbomachinery Conference, 23 – 27 Mar 2015, Madrid, Spain* (2015) ETC2015–216.

[119] H. Siller, A. Bassetti, and S. Funke, *SAMURAI – jet noise source analysis of a V2500 engine,* in *AIAA SciTech 2016, 4 – 8 January 2016, San Diego, California, USA* (2016) AIAA paper 2016–0110.

[120] S. Funke, L. Kim, and H. Siller, *Microphone–Array Measurements of a Model Scale Contra–Rotating Open Rotor in a Reverberant Open Wind–Tunnel,* in *17th AIAA/CEAS Aeroacoustics Conference (32nd AIAA Aeroacoustics Conference), 5 – 8 June 2011, Portland, Oregon, USA* (2011) AIAA paper 2011–2766.

[121] S. Funke, L. Kim, and H. Siller, *Acoustic measurements of a contra–rotating open rotor in an open jet wind–tunnel,* International Journal of Aeroacoustics **11**, 197 (2012), SAGE Publications Ltd. London, United Kingdom.

[122] H. Siller, J. König, S. Funke, S. Oertwig, and L. Hritsevskyy, *Acoustic source localization on a model engine jet with different nozzle configurations and*

wing installation, International Journal of Aeroacoustics **16**, 403 (2017), SAGE Publications Ltd. London, United Kingdom.

[123] S. Oertwig, S. Funke, and H. Siller, *Improving Source Localisation with SODIX for a Sparse Microphone Array,* in *7th Berlin Beamforming Conference, March 5 – 6 2018, Berlin, Germany* (GFaI, e.V., Berlin, 2018) BeBeC–2018–S05.

[124] E. J. Candes and M. B. Wakin, *An introduction to compressive sampling,* IEEE Signal Processing Magazine **25**, 21 (2008).

[125] J. Romberg, *Imaging via compressive sampling,* IEEE Signal Processing Magazine **25**, 14 (2008).

[126] X. Huang, *Compressive sensing and reconstruction in measurements with an aerospace application,* AIAA Journal **51**, 1011 (2013).

[127] S. Y. Zhong, Q. K. Wei, and X. Huang, *Compressive sensing beamforming based on covariance for acoustic imaging with noisy measurements,* Journal of the Acoustical Society of America **134**, EL445 (2013).

[128] W. J. Yu and X. Huang, *Compressive sensing based spinning mode detections by in–duct microphone arrays,* Measurement Science and Technology **27**, 1 (2016).

[129] M. Behn, R. Kisler, and U. Tapken, *Efficient Azimuthal Mode Analysis using Compressed Sensing,* in *22nd AIAA/CEAS Aeroacoustics Conference. May 30 – June 1 2016. Lyon, France* (2016) AIAA paper 2016–3038.

[130] M. Behn, B. Pardowitz, and U. Tapken, *Compressed Sensing Based Radial Mode Analysis of the Broadband Sound Field in a Low–Speed Fan Test Rig,* in *7th Berlin Beamforming Conference, March 5 – 6 2018, Berlin, Germany* (GFaI, e.V., Berlin, 2018) BeBeC–2018–D26.

[131] W. J. Yu and X. Huang, *Reconstruction of Aircraft Engine Noise Source Using Beamforming and Compressive Sensing,* IEEE Access **6**, 11716 (2018).

[132] T. Suzuki, L_1 *generalized inverse beam–forming algorithm resolving coherent/incoherent, distributed and multipole sources,* Journal of Sound and Vibration **330**, 5835 (2011).

[133] V. Fleury, J. Bulté, and R. Davy, *Determination of acoustic directivity from microphone array measurements using correlated monopoles,* in *14th AIAA/CEAS Aeroacoustics Conference. October 5 – 7 2008, Vancouver, British Columbia, Canada* (2008) AIAA paper 2008–2855.

[134] P. A. G. Zavala, W. De Roeck, K. Jassens, J. R. F. Arruda, A. Sas, and W. Desmet, *An algorithm for linearly constrained adaptive array processing,* Mechanical Systems and Signal Processing **25**, 928 (1972).

[135] R. P. Dougherty, *Improved generalized inverse beamforming for jet noise,* International Journal of Aeroacoustics **11**, 259 (2012), SAGE Publications Ltd. London, United Kingdom.

[136] T. Suzuki and B. Day, *Comparative study on mode–identification algorithms using a phased–array system in a rectangular duct,* Journal of Sound and Vibration **347**, 27 (2015).

[137] R. Zamponi, N. van de Wyer, and C. Schram, *An Improved Regularization of the Generalized Inverse Beamforming Applied to a Benchmark Database,* in *7th Berlin Beamforming Conference, March 5 – 6 2018, Berlin, Germany* (GFaI, e.V., Berlin, 2018) BeBeC–2018–D09.

[138] S. Jekosch, E. Sarradj, G. Herold, and T. F. Geyer, *Comparison of Different Solvers for General Inverse Beamforming Algorithms for High Resolution Aeroacoustic Source Characterization,* in *7th Berlin Beamforming Conference, March 5 – 6 2018, Berlin, Germany* (GFaI, e.V., Berlin, 2018) BeBeC–2018–D08.

[139] J. Antoni, *A Bayesian approach to sound source reconstruction: Optimal basis, regularization, and focusing,* Journal of the Acoustical Society of America **131**, 2873 (2012).

[140] A. Pereira, J. Antoni, and Q. Leclère, *Empirical Bayesian regularization of the inverse acoustic problem,* Applied Acoustics **97**, 11 (2015).

[141] Q. Leclère, A. Pereira, C. Bailly, J. Antoni, and C. Picard, *A unified formalism for acoustic imaging based on microphone array measurements,* International Journal of Aeroacoustics **16**, 431 (2017), SAGE Publications Ltd. London, United Kingdom.

[142] T. Ahlefeldt, *Aeroacoustic measurements of a scaled half–model at high Reynolds numbers,* AIAA Journal **51**, 2783 (2013).

[143] C. J. Bahr, W. M. Humphreys, D. Ernst, T. Ahlefeldt, C. Spehr, A. Pereira, Q. Leclère, C. Picard, R. Porteus, D. J. Moreau, J. Fischer, and C. J. Doolan, *A comparison of microphone phased array methods applied to the study of airframe noise in wind tunnel testing,* in *23rd AIAA/CEAS Aeroacoustics Conference. June 5 – 9 2017. Denver, CO, USA* (2017) AIAA paper 2017–3718.

[144] A. M. N. Malgoezar, M. Snellen, R. Merino-Martinez, D. G. Simons, and P. Sijtsma, *On the use of global optimization methods for acoustic source mapping,* Journal of the Acoustical Society of America **141**, 453 (2017).

[145] D. G. Simons and M. Snellen, *Multi–frequency matched field inversion of benchmark data using a genetic algorithm,* Journal of Computational Acoustics **6**, 135 (1998).

[146] C. E. Lindsay and C. N. R., *Matched–field inversion for geoacoustic model parameters using simulated annealing,* IEEE Journal of Oceanic Engineering **18**, 224 (1993).

[147] M. Dorigo, G. Di Caro, and L. M. Gambardella, *Ant algorithms for discrete optimization,* Artificial Life **5**, 137 (1999).

[148] M. Snellen and D. G. Simons, *An assessment of the performance of global optimisation methods for geo–acoustic inversion,* Journal of Computational Acoustics **16**, 199 (2008).

[149] G. Battista, P. Chiarotti, G. Herold, E. Sarradj, and P. Castellini, *Inverse Methods for Three–Dimensional Acoustic Mapping with a Single Planar Array,* in *7^{th} Berlin Beamforming Conference, March 5 – 6 2018, Berlin, Germany* (GFaI, e.V., Berlin, 2018) BeBeC–2018–S04.

[150] E. Sarradj, *Three-Dimensional Acoustic Source Mapping,* in *4^{th} Berlin Beamforming Conference, February 2012, Berlin, Germany.* (2012).

[151] D. Nijhof, *Assessing the performance of two new acoustic imaging techniques*, Master's thesis, Delft University of Technology (2018).

[152] G. Herold and E. Sarradj, *An approach to estimate the reliability of microphone array methods,* in *21^{st} AIAA/CEAS Aeroacoustics Conference, June 22 – 26 2015, Dallas, TX, USA* (2015) AIAA paper 2015–2977.

[153] G. Herold, C. Ocker, E. Sarradj, and W. Pannert, *A Comparison of Microphone Array Methods for the Characterization of Rotating Sound Sources,* in *7^{th} Berlin Beamforming Conference, March 5 – 6 2018, Berlin, Germany* (GFaI, e.V., Berlin, 2018) BeBeC–2018–D22.

[154] C. J. Bahr, T. F. Brooks, L. Brusniak, R. P. Dougherty, W. M. Humphreys, R. Schröder, and J. R. Underbrink, *Array Analysis Methods Benchmarking – Initial Planning Meeting,* in *20^{th} AIAA/CEAS Aeroacoustics Conference, June 16 – 20 2014, Atlanta, GA, USA* (2014) array Analysis Methods Meeting.

[155] C. J. Bahr, *Phased Array Methods Panel Session: Introduction, Moving Forward, and Discussion,* in *21^{st} AIAA/CEAS Aeroacoustics Conference, June 22 – 26 2015, Dallas, TX, USA* (2015) array Analysis Methods Meeting.

[156] C. J. Bahr, *Phased Array Methods Panel Session: Introduction, Year 2 Progress, and Discussion,* in *6^{th} Berlin Beamforming Conference, February 29 – March 1 2016, Berlin, Germany* (2016).

[157] C. J. Bahr, *Phased Array Methods Panel Session: Introduction, Year 2 Summary, and Discussion,* in *22^{nd} AIAA/CEAS Aeroacoustics Conference. May 30 – June 1 2016. Lyon, France* (2016) array Methods Panel Session.

[158] R. Zamponi, N. van de Wyer, and C. Schram, *Benchmark Assessment of an Improved Regularization Technique for Generalized Inverse Beamforming,* in 24^{th} *AIAA/CEAS Aeroacoustics Conference. June 25 – 29 2018. Atlanta, Georgia, USA* (2018) AIAA paper 2018–4106.

[159] P. Sijtsma, *Analytical Benchmark 1,* in 22^{nd} *AIAA/CEAS Aeroacoustics Conference. May 30 – June 1 2016. Lyon, France* (2016) Presentation in Microphone Array Methods Discussion Panel.

[160] A. Kisil and L. J. Ayton, *Aerodynamic noise from rigid trailing edges with finite porous extensions,* Journal of Fluid Mechanics **836**, 117 (2017).

5

Landing–gear noise

Todo el mundo sueña con volar
hasta que vive junto al aeropuerto
y acaba odiando a los aviones.

Everyone dreams about flying
until you live close to an airport
and end up hating airplanes.

Juan Ignacio Guerrero Moreno (*Sol sale cada día*)

Whereas in the previous chapters the focus was placed in understanding the theory and the acoustic imaging methods, the chapters ahead deal with the application of these to actual aeroacoustic cases. This chapter analyzes the noise emissions of the nose landing gear for two aircraft types: the Airbus A320 and different regional aircraft. Flyover measurements under operational conditions are compared with wind–tunnel experiments, computational simulations and several noise prediction models (PANAM and Guo's and Fink's methods). The use of microphone arrays and acoustic imaging algorithms allows for the separation of the sound signal coming from the landing gear system. Furthermore, the potential presence of open cavities in the gear causing loud tonal noise is discussed. Lastly, recommendations to improve the noise prediction models are provided[1].

[1] Some of the contents of this chapter are included in [1–5].

As discussed in Chapter 2, the landing gear system is the dominant airframe noise source for most commercial aircraft. The relatively complicated sound generation mechanisms for this noise source were already explained in section 2.2. This chapter presents experimental flyover results for two aircraft types: the Airbus A320 (section 5.2.1) and different regional aircraft (section 5.2.2). In addition, comparisons of the flyover measurements with other approaches, such as wind–tunnel measurements, CAA simulations or noise prediction models are also included. An important aspect here is that landing gear noise is a complex sound source that normally presents discrepancies within different study approaches [2, 6], such as the presence of cavity noise or the misrepresentation of small–scale details.

5.1. Experimental and numerical setups

This section briefly explains the two experimental setups (field tests for flyover measurements and wind–tunnel experiments) and the numerical setup considered for the comparison.

5.1.1. Flyover measurements

A total of 115 landing aircraft flyovers were recorded at Amsterdam Airport Schiphol using a phased microphone array. The array consisted of 32 PUI Audio POM–2735P–R analog condenser microphones [7] with a sensitivity of -35 ± 2 dB (ref. 1 V/Pa) and a frequency range of 20 Hz to 25 kHz. The array structure allows for different microphone configurations. A spiral distribution was selected for this experiment, see Fig. 5.1, due to its proven good performance within a wide frequency range [8]. The array diameter was 1.7 m and the data were band–filtered in the frequency range from 45 Hz to 11,200 Hz. The sampling frequency employed was 40 kHz. Moreover, an optical camera (Datavision UI-1220LE [9] with a Kowa LM4NCL lens recording with a sampling frequency of 30 Hz) was integrated into the center of the array at a fixed angle facing straight up from the ground. Additional details about the array structure can be found in [8].

The flight trajectories during the landing approach are typically less variable than the ones for takeoff, since all aircraft follow the Instrument Landing System (ILS) approach. Moreover, the main reason for recording landing aircraft is because the engines are usually operating at approach idle, so engine noise is less dominant, and thus other noise sources, such as airframe noise, are more likely to be identified [1], see section 2.1.1. Hence, the microphone array was placed 1240 m to the south of the threshold of the Aalsmeerbaan airport runway (36R), used for landing, as illustrated in Fig. 5.1c. Henceforth, the data will be referred to the relative distances to the array, with the y axis in the direction of the runway and the x axis perpendicular to it and pointing right.

The measurements were taken on two different days with similar weather conditions and low wind speeds. Table 5.1 contains the most relevant meteorological data for those days at 12 : 00 A.M., as provided by the Royal Netherlands Meteorological Institute, KNMI [10]. The values for the same parameters are available every hour. The sound speed, c, and the atmospheric absorption coefficient, α,

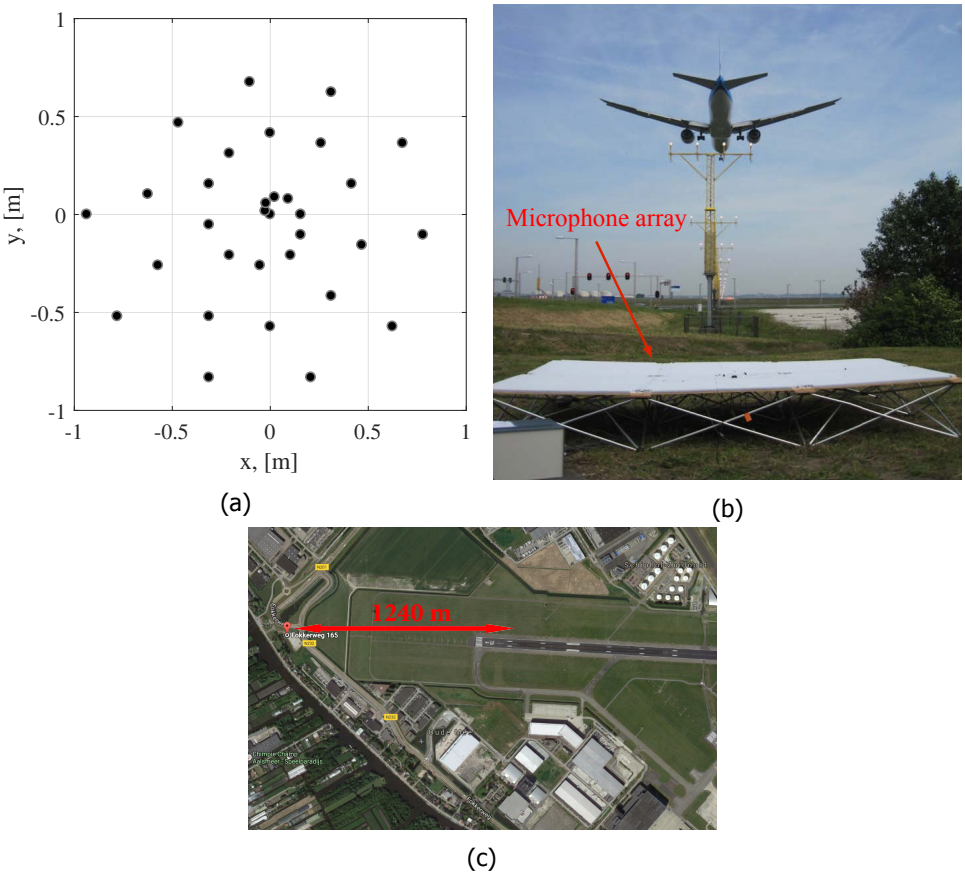

Figure 5.1: (a) Microphone distribution for the flyover measurements. (b) Experimental setup at Amsterdam Airport Schiphol [1]. (c) Location of the microphone array with respect to the Aalsmeerbaan (36R) airport runway. The North is pointing to the right of the picture [3].

depend on these meteorological conditions and, therefore, require to have their variations taken into account.

Table 5.1: Meteorological conditions at Amsterdam Airport Schiphol at 12:00 A.M. [10].

Variable	June 18^{th} 2013	August 8^{th} 2013
Temperature	27.2°C	20.3°C
Relative Humidity	56%	61%
Air pressure	101,500 Pa	101,890 Pa
Precipitation	0 mm	0 mm
Wind speed (at 10 m height)	2 m/s	5 m/s
Wind direction (at 10 m height)	160°	340°

The measurements taken correspond to 13 different aircraft families depending on their turbofan engine [11], see Table 5.2. The Boeing 737 "Next Generation (*NG*)" (700, 800 and 900 series) is the most frequently occurring, with 50 flyover measurements available. This set of series was considered as a collective since they have the same engine, wing area, wing span and nose landing gear geometries, which are the objects of study in this chapter. Table 5.2 also contains the number of fan blades B and maximum rotational speed $n_{\text{rot,max}}$ of each turbofan engine.

Out of all the aircraft types recorded (see Table 5.2), only flyovers featuring Airbus A320 aircraft (narrow–body, twin–engine commercial jet airliner) and three narrow–body, twin–engine aircraft regional types (referred to as Aircraft Types A, B and C for confidentiality issues) are studied in this thesis in terms of NLG emissions in sections 5.2.1 and 5.2.2, respectively. The Airbus A320 type was separated into two categories because they were equipped with different engines, but for the study of NLG noise, both categories were analyzed together [2].

The flight paths of the aircraft have to be precisely estimated and recorded together with a reference time signal that can later be used for the synchronization with the acoustic data. The trajectories need to be determined in order to properly take into account the propagation, moving source, and Doppler effects explained in section 3.1.2. For such close distances to the threshold, small variations of velocity and altitude can be expected along the standard ILS approach. Three different methods were employed for calculating the aircraft position and velocity, each of them using data from a different source:

1. With the **ADS–B** (Automatic Dependent Surveillance–Broadcast) aircraft determine their own position and attitude using the Global Navigation Satellite System in combination with the on–board Inertial Navigation System. For surveillance purposes, this information is actively sent to the ground approximately twice per second. However, the ADS–B is a rather new system and not all the aircraft are currently equipped with this transponder. In this research, only 59 out of the 115 recorded flyovers had this information.

Table 5.2: Aircraft types with their correspondent engine [11] and the number of recorded measurements for each type. Here $n_{\text{rot,max}}$ corresponds to the maximum fan rotational speed (at 100% engine fan settings) in rpm [11, 12].

Aircraft type	Amount	Engine type	B	$n_{\text{rot,max}}$ [rpm]
Airbus A300	1	CF6–80C2A5	38	3320
Airbus A320 (CFM)	4	CFM56–5B5/P	36	5000
Airbus A320 (IAE)	3	IAE V2500–A1	22	5465
Airbus A380	1	GP7270	24	2467
Boeing 737 *Classic*	9	CFM56–3C1	38	5175
Boeing 737 *NG*	50	CFM56–7B	24	5175
Boeing 747	4	CF6–80C2B1F	38	3280
Boeing 767	1	PW 4060	38	3600
Boeing 777	6	GE90–94B	22	2262
Embraer 145	1	RR AE3007A1	24	8700
Embraer 190	11	GE CF34–10E5	24	5954
Fokker 70	23	RR TAY 620	22	8100
McDonnell Douglas 81	1	PW JT8D–217C	24	8219

2. When the **ground radar** is used, air traffic control uses position, altitude, and identity data for aircraft surveillance in the departure and approach phases. Nowadays, all commercial aircraft are equipped with a Mode C transponder to transmit this information. However, the aircraft position is only detected every 4 s due to the rotation time of the radar. Furthermore, there is a minimum height (around 65 m) below which no position data are recorded by the radar, but because the approach is expected to be a straight line, for this research, the final part of the trajectories is linearly extrapolated using a least–squares fit applied to the last 11 data points.

3. With the **extrapolation of optical camera images** method, when the aircraft comes overhead, it flies through the camera's field of view, as depicted in Figs. 4.5 and 4.6. The recordings from the optical camera are used to determine the aircraft height and ground speed when above the array, which can be extrapolated to estimate its full trajectory during the flyover.

All three methods were used and were found to provide very similar results (with variations up to 6%). The extrapolation of the optical camera images is preferred due to its versatility and availability, and because it is easier to overlay the beamforming results on to the optical frames. The average flight height and average aircraft velocity overhead were determined to be 67 m and 75.3 m/s, respectively. The estimated overhead time was confirmed by checking the Doppler–shifted lines in the spectrograms. Henceforth, true air speeds (considering the wind speeds) are presented.

For each measurement, 0.1024 s of data was considered for which the NLG is

approximately overhead of the microphone array center (emission angle of $\theta = 90°$, corrected for the source motion). The averaged CSM is computed using data blocks of 2048 samples and Hanning windowing with 50% data overlap, providing a frequency resolution of approximately 20 Hz, see section C.3. Functional beamforming was applied to the acoustic data. Removing the main diagonal of the CSM for this algorithm is prone to significant errors, since the method relies on the eigenvalue decomposition of the CSM [13]. For this experiment, however, it was not considered to be necessary to remove the main diagonal of the CSM, due to the low wind speeds and low background noise levels [1]. Henceforth, all the presented results refer to an emission angle of $\theta = 90°$ and an azimuthal angle of $\phi = 0°$, i.e., within the aircraft symmetry plane, see Fig. 2.4.

The frequency range of interest considered ranges from 1 kHz to 10 kHz. The lower bound was chosen for having enough spatial resolution to separate the sound coming from the NLG position from other noise sources on–board, such as the turbofan engines. For the aircraft types selected, the minimum distance between NLG and engines ranged from 12 m to 20 m, approximately. The fact that Aircraft Types A and C had rear–mounted engines was favorable to separate the contribution of the NLG, see Fig. 5.15. Aliasing and the amount of sidelobes determined the highest frequency of study [3].

5.1.2. Open–jet wind–tunnel measurements

This experimental campaign (as well as the computational simulations explained below) were performed under the European Clean Sky funded ALLEGRA (Advanced Low noise Landing (main and nose) Gear for Regional Aircraft) project. The ALLEGRA project was developed to assess low–noise technologies applied to a full–scale NLG model [14, 15] and a half–scale MLG model [16] of an advanced regional turboprop aircraft design. ALLEGRA consisted of a consortium of universities (Trinity College Dublin and the Royal Institute of Technology (KTH)), an aeroacoustic wind–tunnel company (Pininfarina SPA), and European SME manufacturing and design partners (Eurotech and Teknosud) supported by a landing gear manufacturer (Magnaghi Aeronautica).

The wind–tunnel experiments were coordinated by Trinity College Dublin and performed in the Pininfarina open–jet semi–cylindrical wind–tunnel facility in Turin, Italy, which has a test section of 8 m (length) $\times$ 9.60 m (width) $\times$ 4.20 m (height). The facility contains a low–noise, high–speed fan–driven system of 13 fans, which provides wind speeds up to 72.2 m/s and presents a background noise level of 68 dBA at 27.8 m/s. The background noise for the ALLEGRA NLG tests was considered as a combination of the wind–tunnel noise and the noise produced by the belly fuselage itself. Both are mostly low frequency noise sources, below 100 Hz and outside of the frequency range of interest [3]. The flow velocity produced by the wind tunnel is very uniform, since it varies by only 0.5% over the test area. The turbulence level had a value of 0.3% in these experiments.

Figure 5.2 depicts the relative position of the NLG model in the wind tunnel, as well as the coordinate system employed, where the xz plane is the symmetry plane of the test model, the yz plane corresponds to the wind–tunnel nozzle exit and the

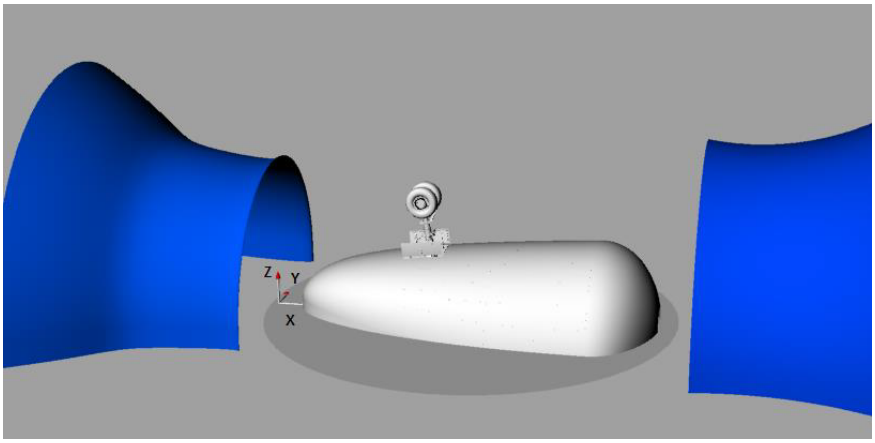

Figure 5.2: ALLEGRA NLG model and coordinate system inside the Pininfarina wind tunnel [3].

origin is situated on the floor of the testing platform. The full–scale NLG complete model, including a full representation of the NLG details and associated structures (e.g., bay cavity, bay doors, belly fuselage and hydraulic dressings) was placed in the wind tunnel so that the distance between the wind–tunnel nozzle and the NLG wheel axis was 2.8 m. Therefore, the coordinates of the middle point of the wheel axis were:

$$x = 2.8 \text{ m}; \quad y = 0 \text{ m}; \quad z = 2.175 \text{ m}.$$

Figure 5.3 shows a picture of the model inside the wind tunnel, whereas Fig. 5.4 presents the overall dimensions (in mm) of the wind–tunnel test model.

The wind–tunnel model had a fixed, built–in angle of attack of 4°. Each model configuration was tested at a variety of flow speeds and yaw settings, allowing the analysis of conditions equivalent to landing with a crosswind. In this thesis, only the yaw angle of 0° (no crosswind) is considered. Flow velocities V of 40, 50, 60 and 65 m/s were employed for the experiment.

Four different planar microphone arrays were installed in the top, side and front of the wind tunnel. For the present study, only the data from two arrays were used:

1. For considering the acoustic results radiated in the *flyover* direction (i.e., for polar emission angles $\theta \approx 90^\circ$) the top array was employed (illustrated in Fig. 5.5a). The array consisted of 78 microphones in a multi–spiral arrangement of approximately 3 m diameter. This array was located in the $z = 4$ m plane, i.e., at a distance to the NLG axis of 1.825 m.

2. To study the lateral or *side* emission pattern of the NLG (i.e., for azimuthal angles $\phi \approx 90^\circ$) the side array was used (see Fig. 5.5b). The array was positioned in the $y = -4.22$ m plane, i.e., parallel to the plane of symmetry of the model and consisted of 66 microphones arranged in a half–wheel distribution with a diameter of approximately 3 m.

Figure 5.3: ALLEGRA NLG model inside the wind tunnel with the top array visible [17].

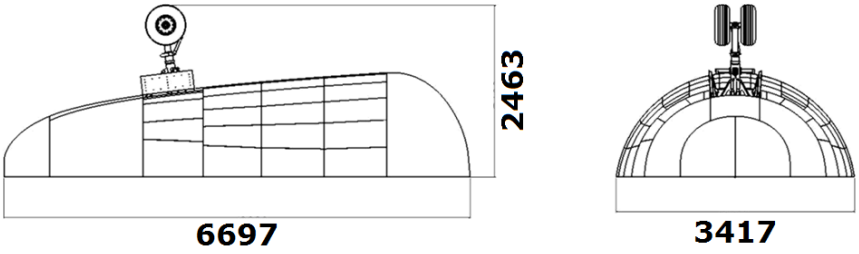

Figure 5.4: Main dimensions of the ALLEGRA wind–tunnel test model in mm [3].

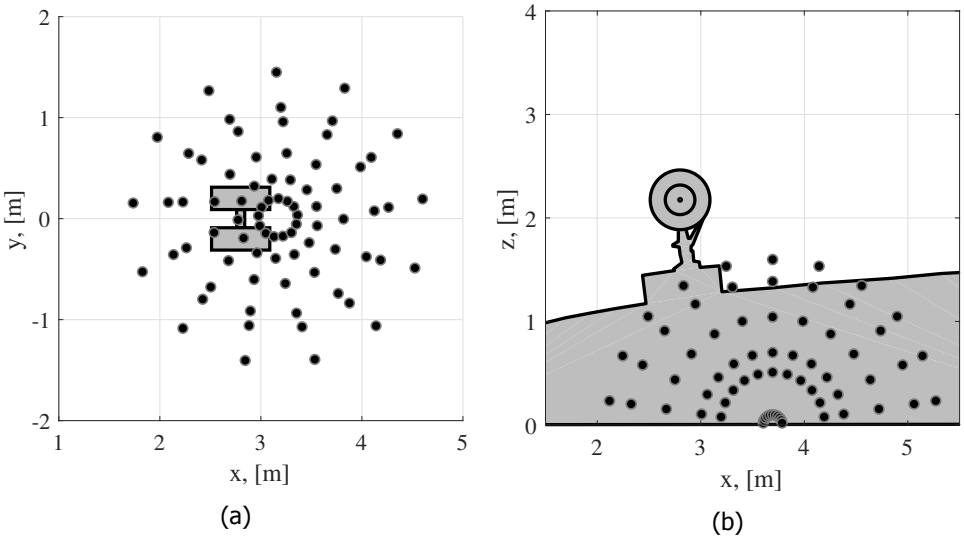

Figure 5.5: Microphone distribution for (a) the top array (b) the side array. A sketch of the ALLEGRA NLG model is plotted in gray for clarity reasons [5].

More details about the experimental setup can be found in the Ph.D. thesis of Neri [17].

The data of both arrays were acquired simultaneously at a sampling frequency of $32,768$ Hz for 10 s per measurement. The time–averaged CSM was obtained by using frequency spectra processed with a block length of 8192 samples, Hanning windowing and 50% data overlap, providing a frequency resolution Δf of 4 Hz. The main diagonal of the CSM was removed in order to eliminate the influence of noise incoherent for all the microphones [18], such as wind noise. The convection of the sound waves due to the flow velocity was considered. A standard shear layer correction, as outlined by Amiet [19], was applied.

The frequency range of interest considered for postprocessing ranges from 200 Hz to 4000 Hz. The lower limit was defined by the background noise and the spatial resolution of the array in order to properly separate the sound coming from the NLG model from other noise sources. The higher frequency limit was imposed by the minimum distance between microphones to prevent aliasing, the amount of sidelobes, and the SNR.

5.1.3. Computational simulations

Compressible flow simulations were performed using the commercial flow-solver STAR–CCM+ with an Improved Delayed Detached Eddy Simulation (IDDES) model [20]. A computational domain spanning 30 times the wheel diameter (d_{wheel}) in the streamwise direction, $18d_{\text{wheel}}$ in the horizontal direction and $10d_{\text{wheel}}$ in the vertical direction was used. Different mesh refinements were employed, with a higher grid density for meshes closer to the NLG smaller components [21]. The domain

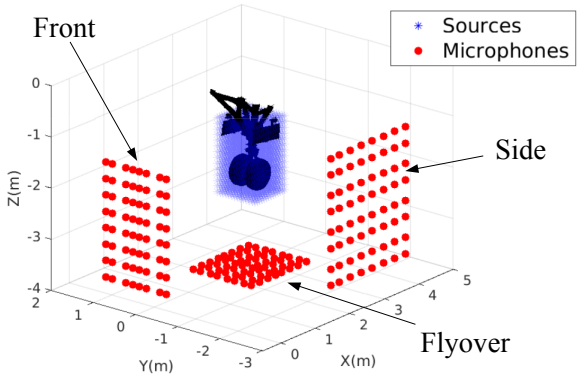

Figure 5.6: Position of the simulated ALLEGRA NLG model and the three virtual microphone arrays considered. Adapted from [21].

is discretized using an unstructured mesh with a total of 97 million hexahedral cells. The resolution of the mesh was sufficient to propagate the acoustic waves up to about 5000 Hz [21]. Volumetric quadrupole sources were neglected as it is commonly done for simulations featuring low Mach numbers. A detailed explanation about the computational setup and simulations is out of the scope of this thesis. More information about the computational setup and the propagation analysis can be found in [21–24].

The NLG geometry employed in the numerical simulations has been slightly simplified compared to the one used in the ALLEGRA wind–tunnel measurements: the bolts, nuts and air valves were removed from the wheels, since they included details that were deemed too small to be resolved correctly by the computational grid and were replaced with coarser versions [21]. Moreover, small gaps between parts were filled, in particular the gap at the center of the rim was filled to approximate the wheel bearings. Lastly, the position of the whole model considered was flipped upside down in the z direction compared to the wind–tunnel tests, see Fig. 5.6, although this change has no influence in the results. Henceforth, only positive z coordinates are considered, even if the figures referring to the computational simulations display negative values of z. The fuselage belly was also included in the simulations, but is not illustrated in Fig. 5.6 for clarity reasons.

A uniform velocity field of $V = 50$ m/s was imposed at the inlet plane, a Dirichlet condition imposed the atmospheric pressure at the outlet plane and a no–slip condition was applied on the top plane of the computational domain, since it corresponds to the floor of the wind tunnel [21].

Five simulated acoustic arrays of 225 microphones (distributed in square grids of 15×15) were considered in the computational domain, see Fig. 5.6. The microphone coordinates were approximated to the nearest cell center available. These arrays were placed in the direct sound computation region, outside the unsteady region close to the NLG surface, where hydrodynamical waves were dominant. Hence,

it was considered that at the arrays' positions, the acoustic field was the dominating fluctuating field [21]. The relative positions of each array with respect to the NLG model were:

1. *Flyover array*: Located at $z = 2.75$ m, i.e., 0.575 m away from the NLG axis, where the mesh spacing is 0.01 m.
2. *Side array* 1: Located at $y = -1$ m, i.e., 1 m away from the center of the NLG axis, where the mesh spacing is 0.02 m.
3. *Side array* 2: Located at $y = -0.4$ m, i.e., 0.4 m away from the center of the NLG axis, where the mesh spacing is 0.003 m.
4. *Front array* 1: Located at $x = 1.75$ m, i.e., 1.05 m away from the NLG axis, where the mesh spacing is 0.02 m.
5. *Front array* 2: Located at $x = 2.25$ m, i.e., 0.55 m away from the NLG axis, where the mesh spacing is 0.0025 m.

Different scan planes (parallel to the considered array) were used, and will be specified when presenting the results. All the scan grids consisted of 961 scan points disposed in a square fashion (31×31).

Apart from the signals recorded at the microphones arrays, the propagated far–field signals using the FW–H analogy [25] at different observer positions located 1.5 m from the model are also considered.

The acoustic pressure data were extracted at all the microphone positions from 2500 samples at a sampling frequency of 20 kHz during 0.125 s (or 10 wheel convection cycles) [21]. The results were weighted using a Hanning windowing function and averaged using Welch's method (see Appendix C.3), providing a frequency resolution of approximately 39 Hz.

The acoustic data extracted from the flow computations were propagated to the simulated microphone arrays and processed using several beamforming approaches [21]. In this chapter only results obtained with an adapted version of Linear Programming Deconvolution (LPD) (see section 4.8), called dual–LPD [24], are presented. Unfortunately, the absolute spectra obtained by the simulated microphone–array measurements were not available for confidentiality reasons. Hence, only source maps depicting the location of the identified sound sources and two far–field sound spectra are presented for comparison purposes.

5.1.4. NLG geometries

In this section, the geometries of NLG of the Airbus A320, the ALLEGRA full–scale NLG model tested in the Pininfarina wind tunnel and the computational simulations, and those of the three regional aircraft types selected are presented. All the considered NLG geometries consist of a bogie structure with a single axis and two wheels. Table 5.3 contains the dimensions of the wheel diameter d_{wheel}, tire width w_{wheel} and rim diameter d_{rim} for the five NLG geometries, as well as the technical denomination of the NLG (following the ISO metric tire code for flotation sizes) in

Table 5.3: NLG geometry parameters [3, 28].

Case	NLG type	d_{wheel}, [m]	w_{wheel}, [m]	d_{rim}, [m]
Airbus A320	30×8.8 R15	0.762	0.223	0.381
Aircraft Type A	24×7.7 10 12 PR	0.610	0.196	0.286
Aircraft Type B	24×7.7 16 PR	0.610	0.196	0.406
Aircraft Type C	$19.5 \times 6.75 - 8$	0.495	0.172	0.203
ALLEGRA	$22 \times 8.0 - 10$	0.577	0.221	0.286

each case. Except for the NLG of the Airbus A320, all the dimensions listed in Table 5.3 present similar values. Such small differences in the size of the NLG are not expected to cause considerable changes in the L_p values radiated (less than 1 dB) [26, 27], see section 2.2.5.

The landing gear geometry designed within ALLEGRA, displayed schematically in Fig. 5.7, features a part of the fuselage, the gear bay, the doors and the gear assembly. The main elements of the NLG structure of the ALLEGRA model are depicted in Fig. 5.7 and listed with their names in Table 5.4.

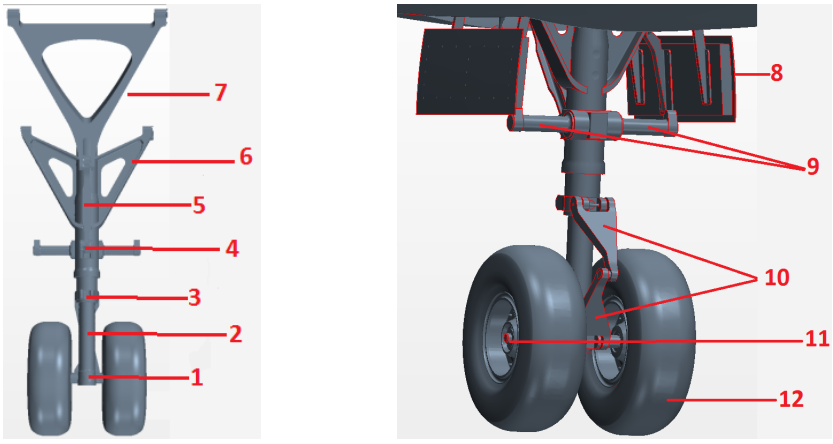

(a) (b)

Figure 5.7: (a) View of the bare ALLEGRA NLG assembly; (b) View of the back of the NLG assembly with bay doors and fuselage. Extracted from [21].

5.2. Results comparison

As it was mentioned at the beginning of this chapter, the obtained NLG noise results can be separated into two categories: Airbus A320 and regional aircraft. These types of aircraft were selected because of their considerable market share (out of the 115 flyovers recorded, 36 correspond to regional airliners, i.e., 31% of the total) and for the significant contribution of their landing gears to the total noise levels.

Table 5.4: Main elements of the landing gear. Extracted from [21].

Part Number	Part Name
1	Wheel axle
2	Main strut
3	Tow fitting
4	Lower arm joint
5	Drag stay Lower arm
6	Main fitting
7	Drag stay upper panel
8	Bay door
9	Steering pinions
10	Torque link
11	Wheel hub
12	Wheel

5.2.1. Analysis of the Airbus A320 NLG noise

Beamforming results

After analyzing the acoustic spectra of each flyover, it was observed that all the measurements from the Airbus A320 family presented a strong tonal peak in a frequency range between 1530 and 1720 Hz protruding about 10 dB over the surrounding broadband noise, see Fig. 5.8a. Moreover, this aircraft type has an important market share [29] and, hence, impact in community noise [2]. The beamforming source plots at those peak frequencies showed that the tonal noise is generated at the NLG position, see Fig. 5.8b. Additional results were already shown in Fig. 4.5 for a frequency of 1630 Hz. Interestingly, analogous frequency peaks and source location were found by Michel and Qiao [30] for a single–aisle aircraft during flyover measurements with a microphone array. Similar tones at the NLG of a Boeing 747–400 aircraft were identified by Dedoussi et al. [31] but at lower frequencies (around 400 Hz), which could be related to the considerably larger size (and, hence, wavelength) of this aircraft type compared to the Airbus A320.

It is interesting to notice that the frequencies of the aforementioned tonal peaks for all the seven Airbus A320 flyovers in this research do not have a significant correlation with the aircraft velocity [2] because the correlation coefficient (see Appendix C.2.4), $\rho \approx 0.16$, is considerably low and the p–value ≈ 0.73 is much larger than the 0.05 threshold typically used for determining whether a correlation is significant or not [12], see Appendix C.2.4. The lack of a clear correlation indicates that these tones are likely to be caused by a flow–induced cavity resonance in the LG system and not by Aeolian tones, as suggested by Michel and Qiao [30], Dobrzynski [6], Dedoussi et al. [31], and Bulté and Redonnet [32]. For the case of [26], it was determined that one of the main sources of tonal noise was the cavity of the pin that links the brakes and the brake–rods. As explained in section 2.2.2, cavity noise depends on both the geometry of the orifice and the local flow conditions [6]. For

sound waves with a frequency of around 1700 Hz and a sound speed of $c = 343$ m/s, the approximate value of the half–wavelength is 10 cm. This length is of the same order of magnitude as the dimensions of some of the many components of the NLG for this aircraft type [28], such as the towing fitting width (see Fig. 5.9), which would explain the presence of the tonal peaks found in the spectra.

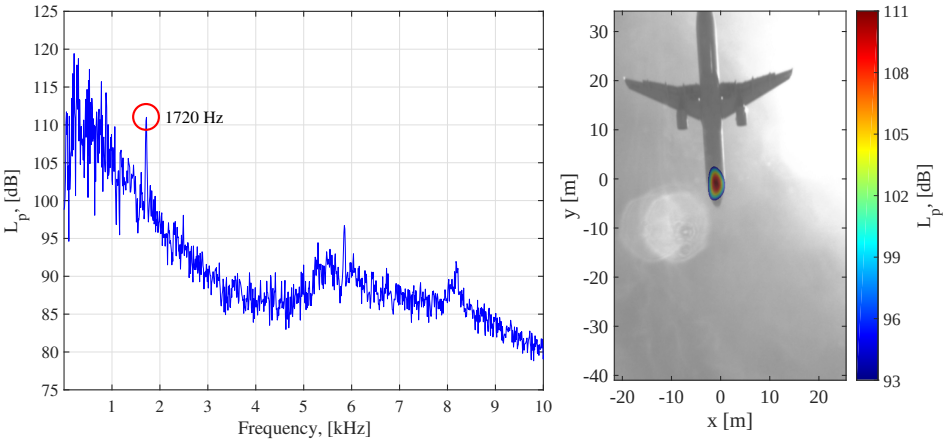

Figure 5.8: (a) Frequency spectrum at the source position for an Airbus A320 flyover; (b) Functional beamforming source plot (with $\nu = 100$) for the same Airbus A320 flyover at the peak frequency of 1720 Hz. Adapted from [2].

An additional confirmation that the NLG system is an important noise source for the Airbus A320 is presented in Fig. 5.10b, where the functional beamforming (with $\nu = 100$) source plot for the same aircraft flyover as in Fig. 5.8 is presented, this time for the whole frequency range considered (1 kHz to 10 kHz). Notice that A–weighting (see Appendix A.2) is applied to the results in order not to obscure the results with the poorer resolution at low frequencies. Other noise sources located at the flaps (with possible contributions of the MLG and the engine exhausts) can be observed in Fig. 5.10b. Unfortunately, the current experimental setup does not allow for a correct separation of these noise sources at the lower frequencies. The noise contribution of the NLG was obtained by integrating the area denoted with a dashed rectangle using a similar technique as SPI (see section 4.2.2) but considering the functional beamforming PSF [3].

Correlation with the aircraft velocity

A correlation analysis was performed between the NLG noise levels and the aircraft velocity to confirm the expected 6^{th} power law [34] for this type of noise source, see section 2.2.2. Previous studies [35, 36] showed that the effect of the variable atmosphere on the sound propagation causes a negligible noise level variability for distances up to 100 m. Therefore, the variability in the noise levels is assumed to be mainly caused by changes in the sound source itself, i.e., the aircraft [2]. Figure

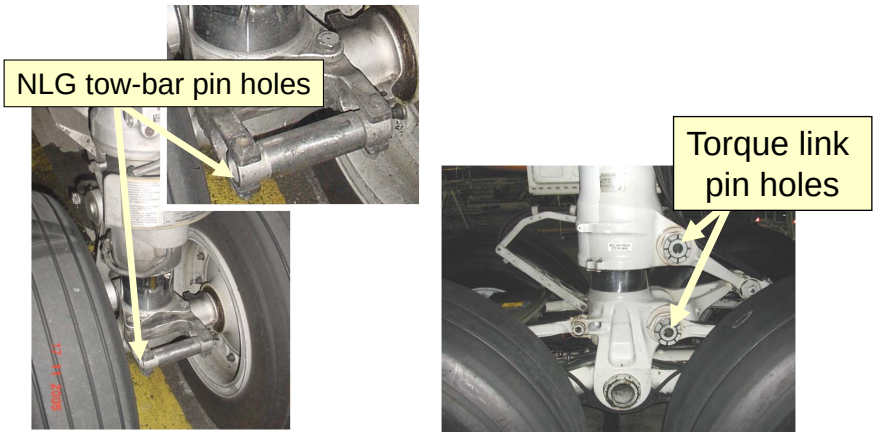

Figure 5.9: Examples of potential cavities in the LG system. Adapted from [33].

5.10a depicts the variability of the NLG L_p values for the whole frequency range (1 kHz to 10 kHz) obtained from the integration of the source plots around the NLG as aforementioned (see Fig. 5.10b). The least–squares fit to the seven flyovers is also plotted in Fig. 5.10a and provides an exponent for the power law of approximately 6.3, which is slightly higher than the expected value of 6 by Curle's theory [34]. Similar behaviors were observed by Michel and Qiao [30] and Dedoussi et al. [31] in their flyover experiments. A coefficient of determination ρ^2 (see Appendix C.2.4) of around 0.7 is obtained, meaning that approximately 70% of the variability in the noise levels from the NLG can be explained by changes in the aircraft velocity.

Comparison with noise prediction model

For the current research, prediction results were generated with the noise prediction tool PANAM [37–39] (see section 1.3.4) for the Airbus A320 experimental test cases aforementioned. For the different flights, the frequency spectra for the NLG and for the whole aircraft on a reference sphere of 1 m were predicted and compared to the measured spectra after applying functional beamforming. For illustration purposes, only the two cases with lowest (70 m/s) and highest (81 m/s) aircraft velocities available are presented here. The same analysis was repeated for measurements with different velocities, showing similar results. The comparisons of the experimental and predicted one–third–octave frequency band spectra for the NLG noise are presented in Fig. 5.11. The maximum A–weighted noise levels are present in the frequency range between 500 Hz and 3000 Hz, as observed by Dobrzynski [6, 40] in wind–tunnel tests with full–scale landing gears. However, a considerable difference between the experimental and the predicted spectra is observed for both cases. The measured data using beamforming consistently indicate higher noise values with L_p values approximately 7 dB higher than those predicted by PANAM.

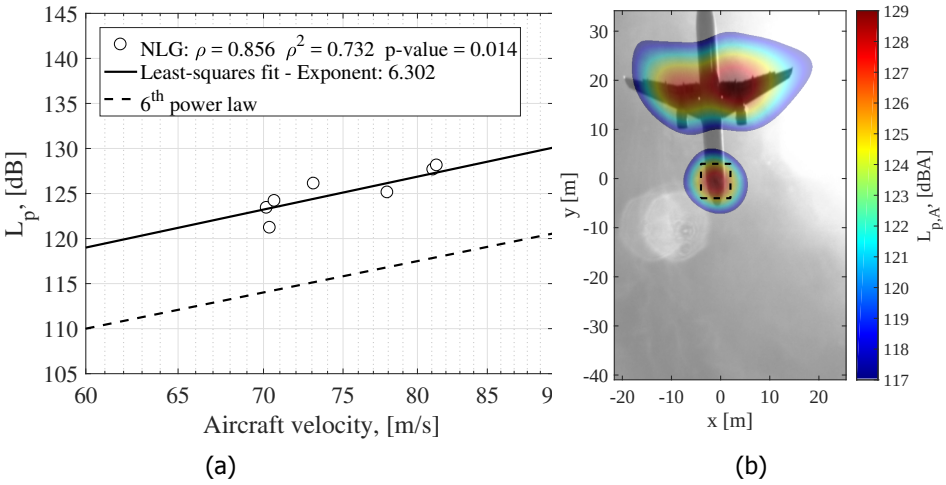

Figure 5.10: (a) Correlation analysis between the L_p at the NLG and the aircraft velocity. Notice the logarithmic scale of the velocity axis; (b) Functional beamforming source plot (with $\nu = 100$) for the same Airbus A320 flyover for the whole A–weighted frequency range (1 kHz to 10 kHz). The integration area is denoted with a dashed rectangle. Adapted from [2].

One of the main causes for this difference is the presence of the tonal peak around 1600 Hz mentioned before in Fig. 5.8. The spectra predicted by PANAM do not present such peaks. This is an additional indicator that the measured tonal peaks do indeed originate from a cavity on the NLG, since PANAM (as well as other noise prediction methods) does not account for parasitic noise sources, such as cavities [2]. In case the tonal peaks were not present, the observed L_p values for the NLG would be approximately 2 dB lower, obtaining a closer agreement with the modeled results.

The frequency spectra for the whole aircraft were also compared for both flyovers, as depicted in Fig. 5.12. In this case, the experimental data considered refer to the sound signal of the array center microphone corrected for the propagation effects mentioned in section 3.1.2. Because the whole aircraft is considered now, the noise contribution from the engines and all other modeled airframe sources is also included in the calculations of PANAM [2]. The corresponding engine fan settings ($N1\%$, see section 2.4.3) of each flyover were calculated from the spectrograms with the method that will be explained in section 7.4. For the cases shown in Fig. 5.12 they were found to be 48% for the flyover with $V = 70$ m/s and 43% for the one with $V = 81$ m/s. Furthermore, the geometric parameters for airframe and engines, and, most importantly, the engine performance data are required. All these necessary input data were not directly recorded during the experiments, and, therefore, had to be derived from the sound signals [4, 12, 41, 42] and additional simulation results.

In general, it seems that the experimental data in Fig. 5.12 present higher noise levels for frequencies between 150 and 1000 Hz and lower levels for higher frequencies. The graphs for both velocities present similar trends in frequency.

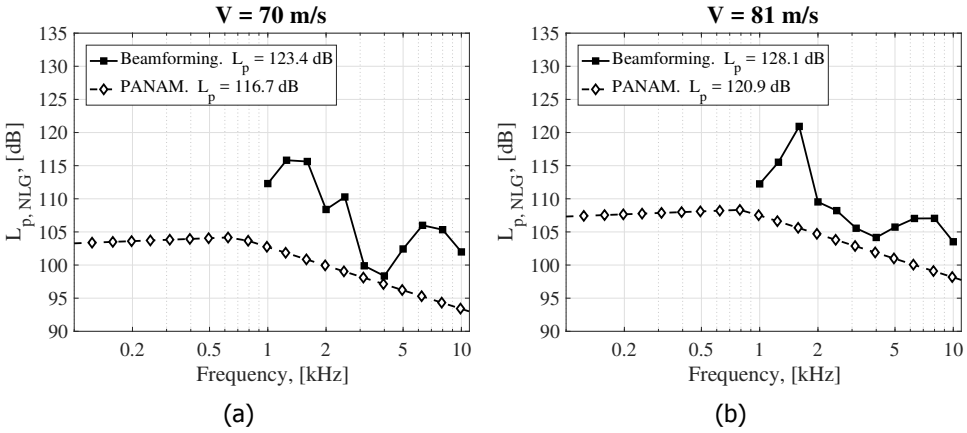

Figure 5.11: Comparison between the experimental beamforming spectrum and the predicted frequency spectrum by PANAM for the NLG for two Airbus A320 flyovers with: (a) $V = 70$ m/s and (b) $V = 81$ m/s. Adapted from [2].

The $L_{\text{p,overall}}$ difference between the predicted and experimental results in this case is less than 1 dB. Even though there was a considerable difference in the NLG predictions, the predicted total noise levels at the source are in very close agreement with the experimental data. The observed differences between the experiment and the model can be partially attributed to one or a combination of the following facts [2]:

1. The experimental results for the NLG sound spectra (see Fig. 5.11) are obtained after applying beamforming, whereas the ones for the whole aircraft (see Fig. 5.12) are obtained using data from a single microphone.

2. Beamforming considers separated sound sources, whereas prediction models, such as PANAM, consider all the noise sources on an aircraft as a point source.

3. Apart from the inherent uncertainties of the experiments and models, the input data employed for the predictions (such as the trajectories and engine settings) were not directly recorded and had to be estimated or derived from additional data sources.

Finally, the observed ranking of the most dominant noise sources for these operational conditions (which can be found in [2]) was found to be the same as that predicted by the model, see Fig. 2.2a.

5.2.2. Analysis of NLG noise of regional aircraft

Beamforming results

The acoustic imaging results obtained can be divided in three categories depending on the emission direction considered, see Fig. 5.6: flyover (in the z direction, as

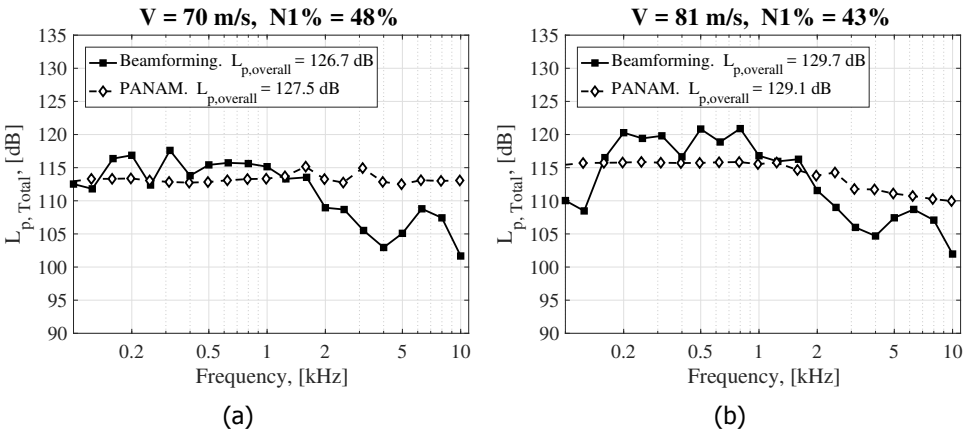

Figure 5.12: Comparison between the experimental spectrum and the predicted frequency spectrum by PANAM for the total aircraft for two Airbus A320 flyovers with: (a) $V = 70$ m/s, $N1\% = 48\%$ and (b) $V = 81$ m/s, $N1\% = 43\%$. Adapted from [2].

5

considered for the flyover measurements), side (in the y direction) and front (in the x direction).

Flyover direction

Figure 5.13 depicts three CFDBF source plots of the ALLEGRA NLG corresponding to the wind–tunnel measurements with a flow speed of 50 m/s and to the one–third–octave bands with center frequencies of 630 Hz, 1250 Hz and 2000 Hz, respectively. The scan plane used was parallel to the top microphone array, at a distance of 1.825 m from it (i.e., at $z = 2.175$ m, containing the wheel axis). The beamforming results were integrated over a ROI (depicted as a dashed rectangle in Fig. 5.13) covering the NLG position using the SPI technique, see section 4.2.2.

Figure 5.14 contains the results corresponding to the same conditions as in Fig. 5.13 after applying the high–resolution deconvolution method HR–CLEAN–SC (see section 4.5.1), which offers clearer source plots. In both figures, it seems that the dominant noise source for all frequency cases is at the center of the wheel axis, between both wheels. The dashed rectangle denotes the ROI. However, sound sources could be located anywhere along the vertical line passing through the middle point of the axis, since the resolution of the microphone array in the normal direction (z direction) is not so accurate to localize the source within the axis. Thus, it is also possible that the main sound source is located on the strut of the NLG or thereabouts.

For the frequency range considered in the wind–tunnel measurements (200 Hz to 4 kHz), the differences between the obtained spectra by the SPI technique and HR–CLEAN–SC were small. Henceforth, the spectra obtained with HR–CLEAN–SC are presented.

Additional acoustic imaging results of the ALLEGRA NLG in different configurations featuring the removal of some of the NLG components (such as the doors,

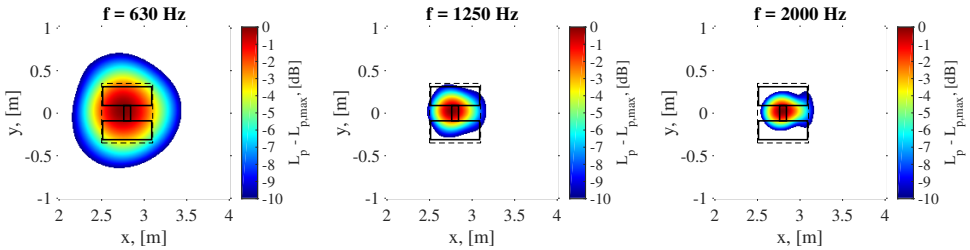

Figure 5.13: One–third–octave band CFDBF source plots for the ALLEGRA NLG model (*flyover* view) at a flow velocity of $V = 50$ m/s and a center frequency of (a) 630 Hz; (b) 1250 Hz; (c) 2000 Hz. The schematic position of the ALLEGRA NLG model is depicted as solid black lines and the dashed rectangle denotes the ROI [5].

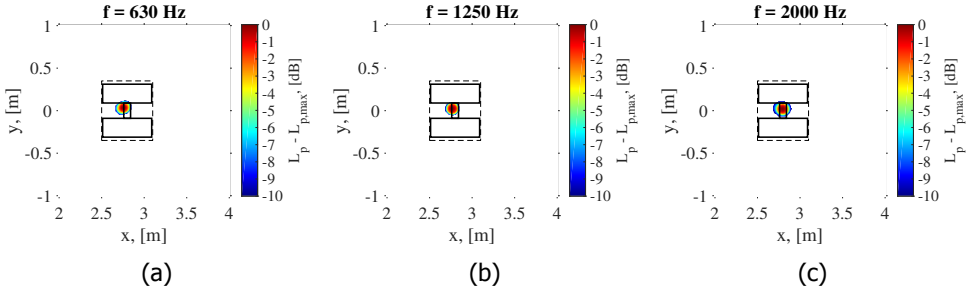

Figure 5.14: One–third–octave band HR–CLEAN–SC source plots for the ALLEGRA NLG model (*flyover* view) in the wind tunnel at a flow velocity of $V = 50$ m/s and a center frequency of (a) 630 Hz; (b) 1250 Hz; (c) 2000 Hz. The schematic position of the ALLEGRA NLG model is depicted as solid black lines and the dashed rectangle denotes the ROI [5].

torque link, steering pinion, etc.) can be found in [17].

Figure 5.15 illustrates an example functional beamforming source plot for a fly-over measurement of each of the three aircraft types aforementioned. It is observed that the NLG is always the dominant noise source for the frequency range selected (one–third–octave band centered at 2 kHz). This frequency band was selected due to the presence of strong tonal noise for all three regional aircraft types. The dashed rectangles again denote the ROIs. For Aircraft Type B (Fig. 5.15 (b)) an additional sound source is localized at what appears to be the flap side edge of the left wing. For this example the outline of the aircraft has been manually added for clarity, because the sunshine blurred the picture.

Additionally, an integration of the results over the ROI located at the NLG position for each case was performed (see Fig. 5.15) in the same way as in section 5.2.1.

Two source plots obtained from the computational simulations in the flyover direction with the *Flyover* array are depicted in Fig. 5.16 for the one–twelfth–octave band with center frequencies of 1200 Hz and 2300 Hz, respectively. The scan plane was located at $z = 2.5$ m. Although the source plots obtained by dual–LPD present a more *discontinuous* distribution, the locations of the dominant sound sources agree

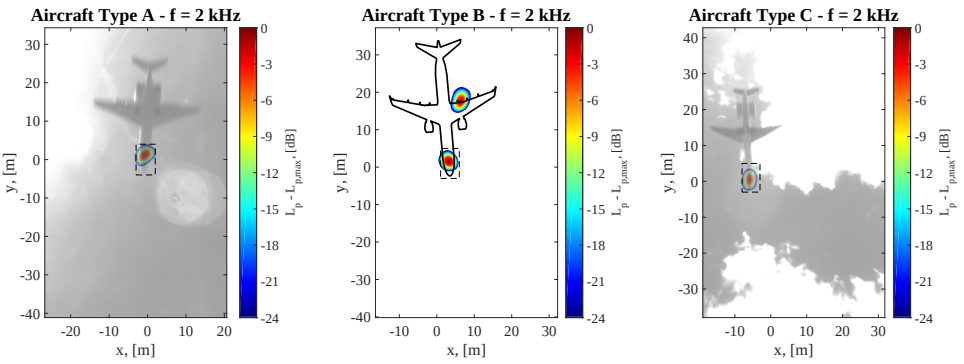

Figure 5.15: One–third–octave band (2 kHz) functional beamforming source plots for each aircraft type using $\nu = 32$. (a) Type A; (b) Type B (aircraft outline has been added for clarity); (c) Type C. The dashed rectangles denote the respective ROIs [3].

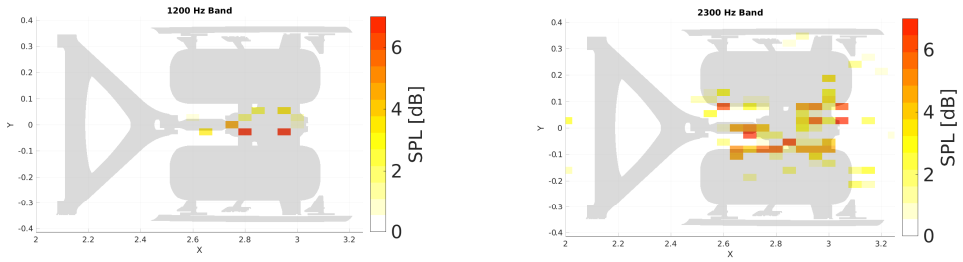

Figure 5.16: One–twelfth–octave band dual–LPD source plots for the ALLEGRA NLG model (*flyover* view) in the computational simulations at a flow velocity of $V = 50$ m/s and a center frequency of (a) 1200 Hz and (b) 2300 Hz. Extracted from [21].

with those found in the wind–tunnel experiments, i.e., between both wheels, see Figs. 5.13 and 5.14. Once again, for the highest frequency (2300 Hz), the sound sources seem to be more distributed, including some areas of the downwind side of the wheels.

Similar source distributions and trends were observed for open–jet wind–tunnel experiments and computational simulations on a simplified NLG geometry within the LAGOON project [32]. Ravetta et al. [43] also compared wind–tunnel experiments in the hybrid wind tunnel of Virginia Polytechnic Institute and State University [44] with computational simulations for a 26%–scale MLG model and both approaches showed comparable source locations as in the present research. Additionally, the research of Ravetta et al. [43] attempted to perform sound source localization in a three–dimensional manner.

Side direction

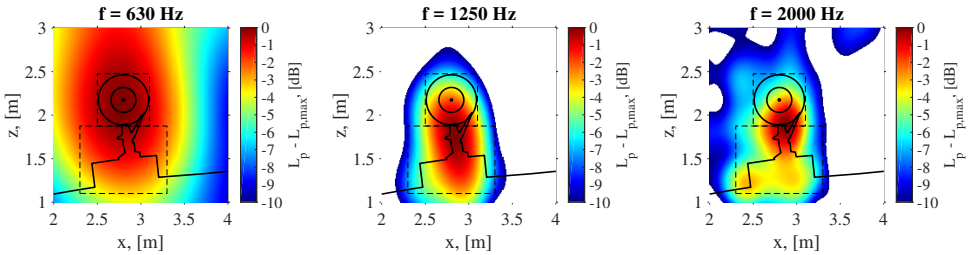

Figure 5.17: One–third–octave band CFDBF source plots for the ALLEGRA NLG model (*side* view) at a flow velocity of $V = 50$ m/s and a center frequency of (a) 630 Hz; (b) 1250 Hz; (c) 2000 Hz. The position of the ALLEGRA NLG model is depicted as solid black lines and the dashed rectangles denote the respective ROIs [5].

The source plots corresponding to the side array in the ALLEGRA wind–tunnel experiments are presented in Figs. 5.17 and 5.18, for CFDBF and HR–CLEAN–SC, respectively. The same conditions as in Figs. 5.13 and 5.14 are considered (a flow speed of 50 m/s and one–third–octave bands with center frequencies of 630 Hz, 1250 Hz and 2000 Hz). The scan plane used was parallel to the side microphone array, at a distance of 4.2 m from it (i.e., at $y = 0$ containing the center of the wheel axis).

Once again, HR–CLEAN–SC provides clearer source plots, which are used to determine the location of the dominant sound sources. For the 630 Hz frequency band, it seems that the dominant sound source is located along the wheel vertical diameter, close to the rim of the wheel, next to the wheel axle. The presence of the wheels might shield potential sources located exactly at the axle in the *side* direction. For the frequency bands centered at 1250 Hz and 2000 Hz, the main noise sources seem to be located near the tow fitting and near the torque link, respectively, see Fig. 5.7. For this emission direction, two different ROIs were defined (denoted as dashed rectangles in Figs. 5.17 and 5.18), one covering the wheel and the other covering the main strut and the bay door. This way, the contributions of each region can be separated using HR–CLEAN–SC.

Figure 5.19 contains two source plots obtained from the computational simulations in the side direction for the one–twelfth–octave band with center frequencies of 1200 Hz and 2400 Hz, obtained by the *Side array* 1 and the *Side array* 2, respectively. The scan plane was located at $y = -0.3$ m. For the band centered at 1200 Hz, the sound sources seem to be clustered along the tow fitting, the lower arm joint and the torque link, which agrees with the wind–tunnel results. For the case of 2400 Hz, on the other hand, the dominant sound source is located at the upwind part of the bay door.

Front direction

Computational simulations allow for the non–intrusive placement of virtual microphone arrays to study emission directions that would be impractical to measure

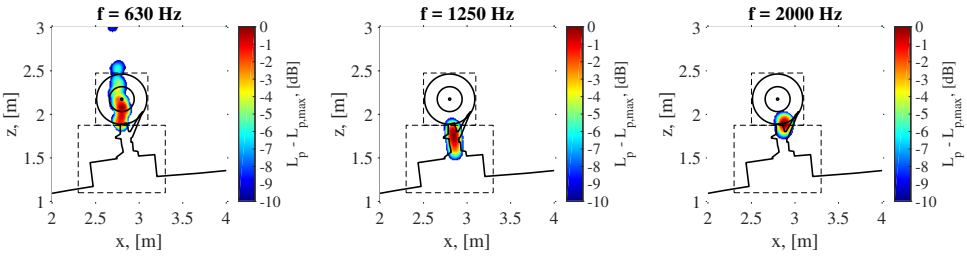

Figure 5.18: One–third–octave band HR–CLEAN–SC source plots for the ALLEGRA NLG model (*side* view) at a flow velocity of $V = 50$ m/s and a center frequency of (a) 630 Hz; (b) 1250 Hz; (c) 2000 Hz. The position of the ALLEGRA NLG model is depicted as solid black lines and the dashed rectangles denote the respective ROIs [5].

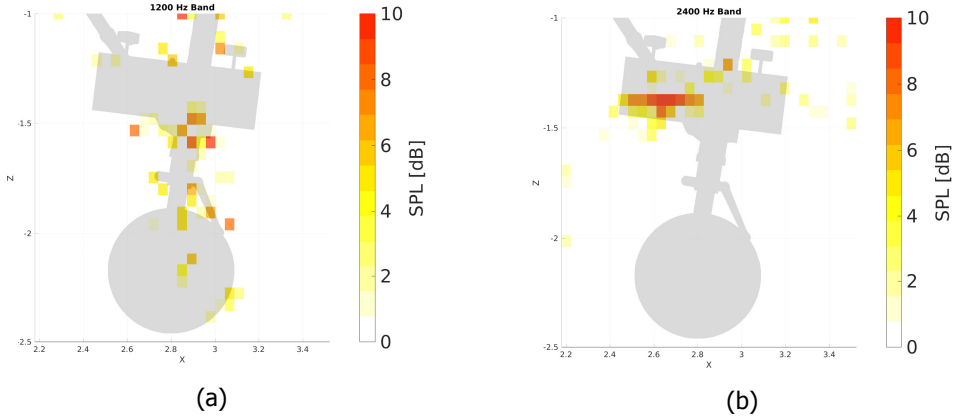

Figure 5.19: One–twelfth–octave band dual–LPD source plots for the ALLEGRA NLG model (*side* view) in the computational simulations at a velocity of $V = 50$ m/s and a center frequency of (a) 1200 Hz obtained with *Side array* 1, and (b) 2400 Hz obtained with *Side array* 2. Extracted from [21].

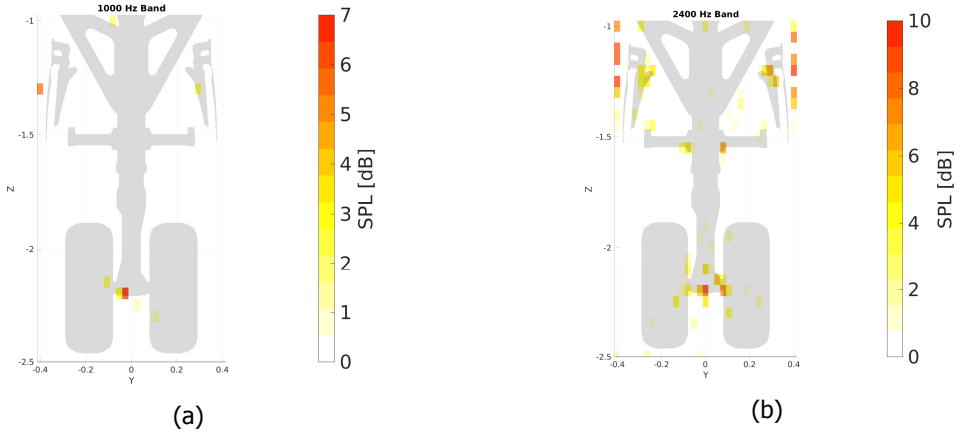

Figure 5.20: One–twelfth–octave band dual–LPD source plots for the ALLEGRA NLG model (*front* view) in the computational simulations at a flow velocity of $V = 50$ m/s and a center frequency of (a) 1000 Hz obtained with *Front array* 1, and (b) 2400 Hz obtained with *Front array* 2. Extracted from [21].

in wind tunnels. Figure 5.20 shows the simulated source plots in the front direction for one–twelfth–octave band with center frequencies of 1000 Hz and 2400 Hz obtained by the *Front array* 1 and *Front array* 2, respectively. The scan plane was located at $x = 2.826$ m. For the first case, the strongest noise source is located at the center of the wheel axle, whereas for the second band, the sources are more spread around the center of the wheel axle, the lower arm joint and the bay doors. The bay door was also a dominant noise source for the side direction at that frequency, see Fig. 5.19b.

Correlation with flow velocity

Since the experimental datasets considered contain measurements at different flow velocities (or aircraft velocities, for the case of the flyovers), a correlation study was performed to investigate the dependence between the sound pressure level L_p and the flow or aircraft velocity in the flyover direction, respectively, as done before in section 5.2.1.

Figure 5.21 presents the overall integrated L_p values for the available frequency spectra (200 Hz to 4 kHz for the wind–tunnel experiment, and 1 kHz to 10 kHz for the flyover measurements) as a function of the velocity V, using a logarithmic scale for the velocity axis. Results for the ALLEGRA model for the four flow velocities and for the measurements of the Aircraft Type A are presented. This aircraft type was selected due to its higher number of occurrences. A very satisfactory agreement is found between both cases.

The power laws found with respect to the velocity have exponents of 5.90 for the ALLEGRA model and of 5.93 for the Aircraft Type A, see Eq. (5.1). The variable V_{ref} denotes an arbitrary reference velocity. These values match the 6^{th} power law with velocity expected for NLG noise [6, 26, 30, 34, 45], see section 2.2.2. The small differences between both cases are not considered to be statistically significant and

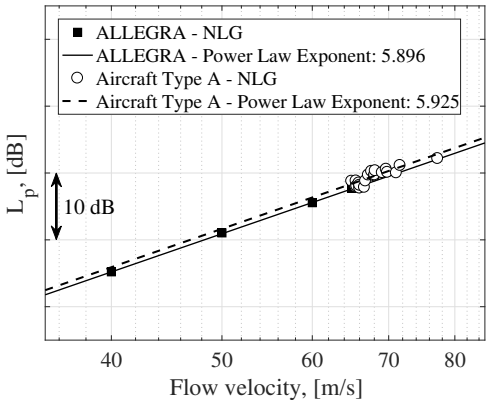

Figure 5.21: Correlation analysis for the NLG noise of the ALLEGRA model and Aircraft Type A with respect to the velocity. The least–squares fits are also included. Note the logarithmic scale of the velocity axis. Adapted from [3].

5

Table 5.5: Statistical coefficients for the velocity dependence.

Case	Power law exponent	ρ	ρ^2	p–value
ALLEGRA	5.896	0.9999	0.9999	7.19×10^{-5}
Aircraft Type A	5.925	0.8777	0.7704	3.69×10^{-7}

are probably explained by the slightly different NLG geometries, the consideration of different parts of the frequency spectrum, and by the different flow conditions in each test case.

$$L_{p,V} - L_{p,V_{\text{ref}}} \approx \begin{cases} 58.96 \log \frac{V}{V_{\text{ref}}} & \text{for ALLEGRA model.} \\ 59.25 \log \frac{V}{V_{\text{ref}}} & \text{for Aircraft Type A.} \end{cases} \tag{5.1}$$

Moreover, the statistical coefficients of the correlations (see Appendix C.2.4) are gathered in Table 5.5, where the correlation coefficient ρ, the coefficient of determination ρ^2 and the p–value are presented for each case. An almost perfect fit ($\rho^2 = 0.9999$) is found for the ALLEGRA model, whereas a lower correlation is found for the flyover case ($\rho^2 = 0.7704$). The higher spread of the results for the flyover experiments can be explained due to the less–controlled flow conditions and by possible errors when calculating the true air speeds. Another significant cause of variability is that the measurements correspond to different aircraft, rather than to the same aircraft measured several times. In general, both cases present significant correlations if the typical p–value threshold of 0.05 is considered.

Henceforth, the 6^{th} power law is considered for both datasets for simplicity reasons.

An illustrative example that confirms the considered power law is presented in Fig. 5.22a, where the HR–CLEAN–SC narrow–band frequency spectra (obtained

by integrating over the ROI defined in Fig. 5.13) for the ALLEGRA model in the flyover direction for the four flow velocities are presented. When the spectra are corrected following the 6^{th} power law and taking 40 m/s as the reference velocity V_{ref}, all the spectra collapse in one single line with only small differences at around 2500 Hz, see Fig. 5.22b. All the spectra are mostly broadband with just few tonal components below 500 Hz, but they do not protrude a lot over the broadband levels around them.

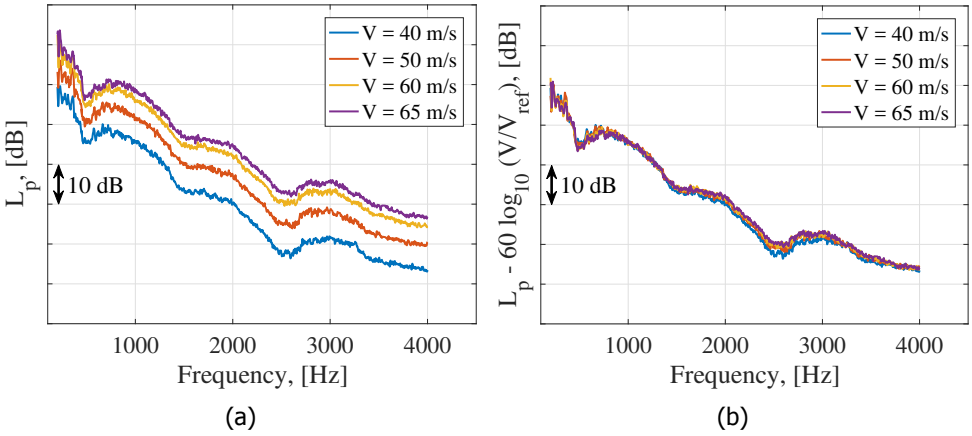

Figure 5.22: (a) Integrated NLG sound frequency spectra for each velocity of the ALLEGRA model in the *flyover* direction. (b) Idem for the spectra converted to $V_{ref} = 40$ m/s using the obtained velocity power law [3].

For high frequencies, the LG cannot be considered as compact with respect to the sound wavelength anymore and more sophisticated power laws can be derived [46], featuring an exponent of 7 instead of 6, because the noise generation is considered to be due to the turbulent flow surrounding the small components of the LG. Since the effective frequency range for comparison in this study (1 kHz to 4 kHz) is relatively low–frequency, this aspect could not be considered.

Frequency spectra comparison (flyover direction)

This section compares the noise emissions of the NLG in the flyover direction. Figure 5.23a presents the A–weighted sound pressure levels ($L_{p,A}$) of the integrated narrow–band frequency spectra (corrected for the velocity influence taking $V_{ref} = 65$ m/s) of an example flyover of each aircraft type, as well as the spectrum for the ALLEGRA model in the wind tunnel at $V = 65$ m/s. Similar trends are observed between the wind–tunnel and the flyover results. Unfortunately, the portion of the spectrum where both wind–tunnel and flyover results overlap is limited (1 kHz to 4 kHz). Other flyover measurements of these aircraft types were similar to the ones presented here, but are not included for the sake of simplicity. Since the aircraft velocities are of the same order of magnitude for the four cases shown in Fig. 5.23a, as well as the NLG geometries, differences in the Reynolds number are expected to be negligible. The differences between the wind–tunnel results and the

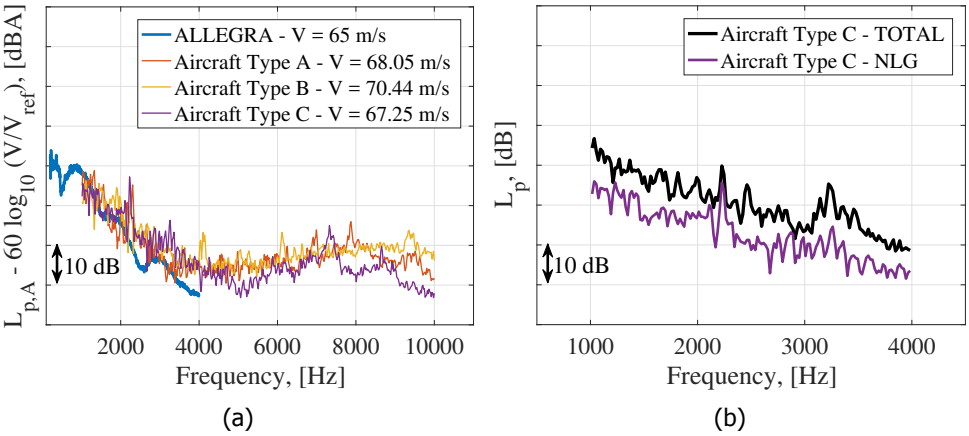

Figure 5.23: (a) Integrated A–weighted narrow–band frequency spectra of the NLG for an example flyover of each aircraft type. The spectrum of the ALLEGRA model with $V_{ref} = 65$ m/s is also plotted for comparison. (b) Zoomed–in spectra comparison for an Aircraft Type C flyover between the NLG and the total aircraft ($V = 67.25$ m/s) [3].

5

flyover measurements could be due to several reasons, such as installation effects or different propagation conditions [47].

It can be noticed that strong tonal noise is present for the three aircraft types at approximately 2200 Hz. This is especially the case for Aircraft Type C, for which a tone, protruding more than 12 dB over the broadband noise around it, is found. This phenomenon was already discussed in section 5.2.1, where it was suggested that the cause for these tonal peaks could be the presence of open pin–cavities [26, 30–32, 48] in the LG system, see Fig. 5.9. As in section 5.2.1, the fact that no dependency was found between the tone frequency and the aircraft velocity (unlike with Aeolian tones) confirms the likelihood that these tones originate from a cavity [30, 31]. Since the geometries of the NLG for the three aircraft are similar, it is possible that they have cavities of similar dimensions as well, generating tones with comparable wavelengths. The flyover measurements of section 5.2.1, featured Airbus A320 aircraft with larger NLG geometries [2] and presented tonal noise at lower frequencies (approximately 1700 Hz, see Fig. 5.8a) and hence, larger wavelengths. The ratio between the wavelengths of the tonal noise of the experiment in section 5.2.1 with Airbus A320 aircraft and the one of the present section (with regional aircraft) agrees with the ratio between the axle lengths, providing more evidence that the tonal noise is likely to be due to a cavity. On the other hand, no significant tones were present in the ALLEGRA model in this frequency range. This may be because cavities were intentionally designed out of the model.

For the measured flyovers, the aforementioned tones were also present in the overall spectra of the whole aircraft, indicating the importance of NLG noise at around 2200 Hz. This is illustrated in Fig. 5.23b for the same flyover measurement of an Aircraft Type C as in Fig. 5.23a, where the NLG spectrum is compared to the total aircraft sound spectrum obtained using a single microphone and correcting

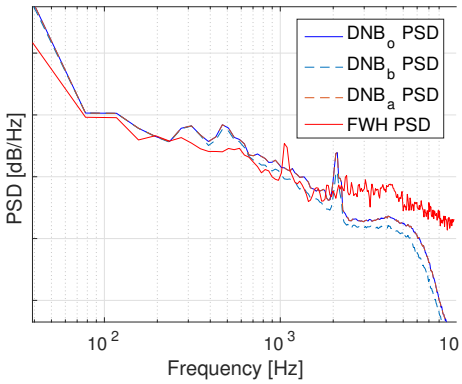

Figure 5.24: Far–field acoustic spectra obtained by the *Flyover array* in the computational simulations with DNB and the FW–H analogy. The grid step in the ordinate axis is 20 dB. The observer for the FW–H analogy is located at (2.826 m, 0 m, 3 m). Extracted from [21].

for the propagation effects [4]. The tone at 2200 Hz is also present in the total aircraft spectrum. Removing the tone at that frequency would cause overall L_p reductions up to 1 dB (up to 2 dB if A–weighting is considered) for the frequency range considered. In addition, tonality (see Appendix A.5) is of high importance when assessing aircraft noise around airports, since it has been shown that tonal noise causes significantly more annoyance than broadband noise with the same $L_{p,A}$ [49–51].

The far–field acoustic spectra obtained by the *Flyover array* in the computational simulations are presented in Fig. 5.24, where the Direct Numerical Beamforming (DNB) results using dual–LPD are shown, as well as the propagated signal using the FW–H analogy. The three different lines for DNB refer to how the deconvolution approach is performed: from below (DNB$_b$), from above (DNB$_a$) or in the optimal way (DNB$_o$). For further explanations, the reader can refer to [21].

It can be observed that the three DNB approaches present a strong tonal peak (protruding about 20 dB over the surrounding broadband noise) approximately at 2100 Hz, which agrees with the tonal peaks found in the flyover measurements displayed in Fig. 5.23. The FW–H results, however, only present a tonal peak at about 1050 Hz, which is coincidentally half of the tonal frequency for DNB. The reason for this difference remains unknown and is subject for future research.

Figure 5.25a presents the comparison between the one–third–octave band spectra of the NLG emissions of three aircraft types, the ALLEGRA NLG from the wind–tunnel experiments (as presented in Fig. 5.23a) and the estimations of the two noise prediction models considered (Fink and Guo, see section 2.2.5) using the geometry inputs of the ALLEGRA NLG model and a flow velocity $V = 65$ m/s. A first observation in the frequency range of common comparison (1 kHz to 4 kHz) indicates that Guo's model has a better fit with the experimental data (especially with the flyover measurements) and that Fink's model tends to overpredict the noise

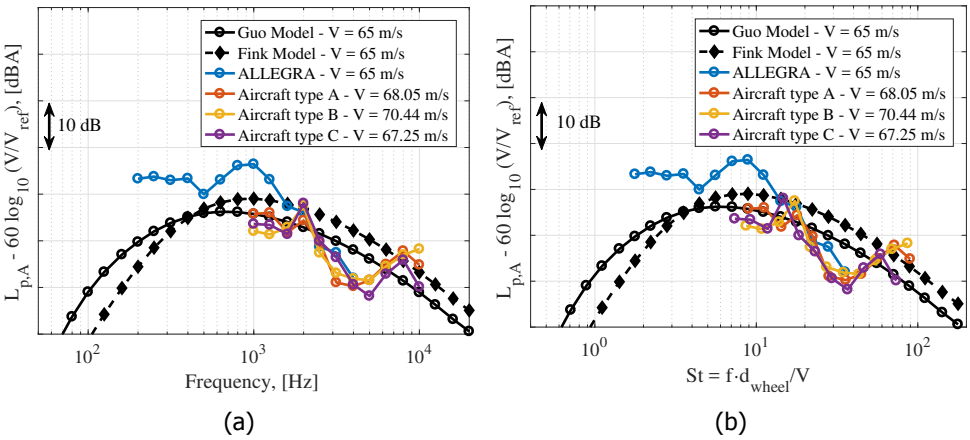

Figure 5.25: Spectra comparison of the NLG noise emissions in the flyover direction ($\theta \approx 90°$, $\phi = 0°$) between both noise prediction models, the ALLEGRA wind–tunnel experiments model with $V_{ref} = 65$ m/s and an example flyover measurement for each aircraft type: (a) Absolute frequencies. (b) Normalized frequencies with the Strouhal number ($St = f\, d_{wheel}/V$) [5].

5

emissions in this case by several decibels. Neither of the two noise prediction models seem to include the tonal peak at around 2 kHz as expected, but they also do not consider the noise decrease at around 4 kHz. The wind–tunnel results present a *hump* between 500 Hz and 1600 Hz that is not captured by the noise prediction models either. Moreover, the relatively high noise levels at low frequencies observed for the ALLEGRA NLG could be explained by the higher background noise levels at the wind–tunnel facility at that frequency range, which could be coherent for all the microphones and, hence, not efficiently mitigated by the diagonal removal of the CSM.

The integrated noise values in the frequency range between 1 kHz to 4 kHz predicted by Guo are considerably closer to those measured in the flyover experiments (within approximately a 1.5 dB difference), while the predictions by Fink are approximately 4 dB higher than the flyover experiments.

Figure 5.25b depicts the same results as Fig. 5.25a but using the normalized frequency axis with the Strouhal number based on the wheel diameter ($St = f\, d_{wheel}/V$). In this case, the broadband frequency components after $St > 20$ of the three aircraft types seem to collapse in a better way, but the tonal peaks are now slightly more spread in different Strouhal numbers.

Frequency spectra comparison (side direction)

The integrated frequency spectra in the side direction for each of the ROIs defined in Figs. 5.17 and 5.18 (namely the wheel and the strut and bay door of the ALLEGRA NLG, respectively) are presented in Fig. 5.26a, as well as the total NLG emissions. The spectrum of the ALLEGRA NLG in the flyover direction from Fig. 5.25a is also displayed for reference. It can be observed that the noise contribution of the strut and bay door is slightly higher than that from the wheel, except for the one–third–

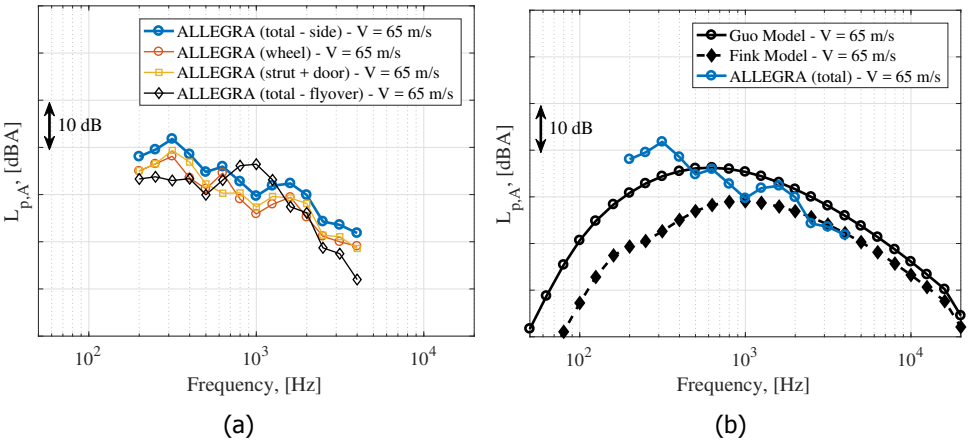

Figure 5.26: (a) Spectral breakdown for the noise emissions of the ALLEGRA NLG in the side direction ($\theta \approx 90°$, $\phi \approx 90°$) in the wind–tunnel tests. (b) Spectra comparison of the NLG noise emissions in the side direction between both noise prediction models and the ALLEGRA wind tunnel experiments model with $V_{\text{ref}} = 65$ m/s [5].

octave band centered at 630 Hz, where the wheel presents considerably higher levels. Interestingly, the noise levels in the flyover direction are considerably lower than in the side direction for the whole frequency range, except between 800 Hz and 1200 Hz, where the aforementioned *hump* in the previous section causes an increase in the noise levels, even over the noise emissions in the side direction. Once again, no important tonal peaks were observed in the narrow–band spectra of the wind–tunnel experiments, which are not shown here for brevity reasons.

Figure 5.26b presents the comparison of the total noise emissions of the ALLEGRA NLG in the wind–tunnel tests in the side direction and the predictions of Fink's and Guo's models with $\phi = 90°$. Once again, the wind–tunnel data present higher noise levels at low frequencies (below 400 Hz), which could be due to the higher background noise levels in the facility in that range. For frequencies higher than 400 Hz, the experimental data are bounded between the predictions of both noise prediction models, with a closer agreement to the results of Fink's model in this case. For this emission direction, the wind–tunnel data show another hump (smaller than for the flyover direction) between 1 kHz and 2.5 kHz. None of the noise prediction models captures this trend.

The far–field acoustic spectra obtained by the *Side array* 2 in the computational simulations are presented in Fig. 5.27, which shows the DNB results using the three dual–LPD approaches aforementioned and the propagated signal using the FW–H analogy. In this case, only the DNB_a spectrum shows a small peak at 2100 Hz (protruding about 5 dB over the broadband noise), whereas the other two DNB spectra present no important tonal peaks in the whole frequency range. The FW–H results contain several tonal peaks at about 1050 Hz and higher frequencies up to 2500 Hz. These peaks are not observed in the experimental data from the ALLEGRA wind–tunnel campaign.

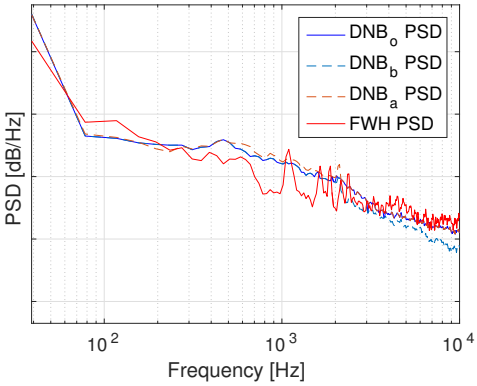

Figure 5.27: Far–field acoustic spectra obtained by the *Side array* 2 in the computational simulations with DNB and the FW–H analogy. The grid step in the ordinate axis is 20 dB. The observer for the FW–H analogy is located at (2.826 m, 2 m, 1.8 m). Extracted from [21].

Observing the source plots presented in Figs. 5.16 and 5.20, it could be proposed that the emissions of the main noise sources found between the NLG wheels, and around the axle, are perhaps shielded by the presence of the wheels themselves, which would explain the lack of tonal peaks in the spectra presented in Fig. 5.27. Once again, a more detailed numerical analysis is suggested.

5.3. Conclusions and outlook

This chapter analyzed the noise emissions of landing gear systems, more precisely those from the nose landing gear (NLG), due to its high contribution to the total aircraft noise levels during the approach stage. Comparisons between aircraft flyover measurements under operational conditions, full–scale wind–tunnel tests, computational simulations and noise prediction models (PANAM and Fink's and Guo's methods) were performed. All the NLG models considered had similar geometries.

Microphone arrays and acoustic imaging methods were employed in the experimental and computational setups for isolating the sound signals generated by the landing gear. For the frequencies considered, the wind–tunnel tests and the computational simulations indicate that the main noise sources are located around the center of the wheel axle, followed by the main strut and bay doors.

The experimental results follow the expected 6^{th} power law with the flow velocity. A good agreement is found between the wind–tunnel experiments and the flyover measurements, except for the presence of strong tonal peaks in all the flyover recordings considered. Such tones are considered to be of high annoyance for the population living near airports. The acoustic source plots confirmed that the sound source emitting these tones was the NLG in all cases. The frequencies of these tones (about 1600 Hz for the Airbus A320 and 2200 Hz for the regional aircraft) do not scale with the flow velocity, which indicates that the cause of these

tones might be the presence of open cavities in the NLG systems. Removing these tones would cause overall noise reductions up to 2 dB in the frequency range examined. Interestingly, the computational simulations also showed a strong tonal peak around 2200 Hz for the regional aircraft NLG but the wind–tunnel results do not show such behavior for neither the flyover or side emission directions.

The noise prediction tool PANAM seems to considerably underestimate the noise emissions of the NLG when applied to an Airbus A320 aircraft, whereas it is able to predict the total aircraft noise emissions with an accuracy of less than 1 dB. The predictions by Fink's and Guo's methods present comparable trends as the experimental results, but do not consider the tonal peaks either. Guo's method provides a closer agreement in the flyover emission direction, whereas Fink's method seems to offer a better match in the side emission direction. These differences in noise levels are partially caused by the presence of the strong tonal peaks aforementioned, which are not considered by the noise prediction models because they do not include parasitic noise sources, such as cavities.

Including cavity–noise estimations in the models would improve the noise predictions around airports. However, cavity noise is considerably difficult to predict since the intensity of the excitation of the cavity resonant mode depends on the velocity, turbulence levels and direction of the flow. Moreover, the tones due to cavity noise must be considered individually and cannot be represented in a convenient nondimensional form [48]. The use of cavity caps might be an effective and easy noise–reduction treatment [26] (keeping in mind practical and safety constraints). Other noise–reduction devices [17] can also help to reduce the LG emissions. In addition, due to the strong dependence between the noise emissions of the NLG (and most airframe noise sources, in general) and the flow velocity, an obvious recommendation would be to reduce the approach speed as much as possible, keeping in mind that the high–lift devices would then generate more noise due to the additional lift requirement.

In conclusion, the importance of the use of phased microphone arrays in aeroacoustic experiments and simulations has been confirmed, as well as the advantages and limitations of different approaches in aeroacoustic studies. Hybrid studies as the one presented in this chapter are, thus, of high interest, whenever possible. Furthermore, to ensure the validity of the results, full–scale tests under operational conditions are essential.

Future work is recommended, especially a more detailed computational study with higher resolution. Flyover measurements featuring larger microphone arrays and wind–tunnel tests with microphone arrays suitable for higher–frequency recordings are of high interest to extend the comparison over a larger frequency range. Further research involving different aircraft types under a wider variety of operational conditions is recommended, allowing a more detailed comparison with the current prediction models.

Acknowledgements

The research leading to the ALLEGRA wind–tunnel results has received funding from the European Union's Seventh Framework Programme (FP7/2007–2013) for

the Clean Sky Joint Technology Initiative under grant agreements n° [308225] (ALLEGRA) and n° [620188] (ARTIC). The author acknowledges all the partners that took part in the ALLEGRA and ARTIC projects.

The author also acknowledges Dr. Lothar Bertsch from DLR Göttingen for his feedback and help with the use of PANAM and Hamza Bouchouireb from KTH in Stockholm, Sweden, for his constructive discussions about the computational results.

Bibliography

[1] R. Merino-Martinez, M. Snellen, and D. G. Simons, *Functional beamforming applied to imaging of flyover noise on landing aircraft,* Journal of Aircraft **53**, 1830 (2016).

[2] R. Merino-Martinez, L. Bertsch, M. Snellen, and D. G. Simons, *Analysis of landing gear noise during approach,* in *22nd AIAA/CEAS Aeroacoustics Conference. May 30 – June 1 2016. Lyon, France* (2016) AIAA paper 2016–2769.

[3] R. Merino-Martinez, E. Neri, M. Snellen, J. Kennedy, D. Simons, and G. Bennett, *Comparing flyover noise measurements to full–scale nose landing gear wind–tunnel experiments for regional aircraft,* in *23rd AIAA/CEAS Aeroacoustics Conference. June 5 – 9 2017. Denver, Colorado, USA* (2017) AIAA paper 2017–3006.

[4] M. Snellen, R. Merino-Martinez, and D. G. Simons, *Assessment of aircraft noise sources variability using an acoustic camera,* in *5th CEAS Air & Space Conference. Challenges in European Aerospace. September 7 – 11 2015, Delft, Netherlands*, Paper 2015–019 (Council of European Aerospace Societies, 2015).

[5] R. Merino-Martinez, E. Neri, M. Snellen, J. Kennedy, D. Simons, and G. Bennett, *Analysis of nose landing gear noise comparing numerical computations, prediction models and flyover and wind–tunnel measurements,* in *24th AIAA/CEAS Aeroacoustics Conference. June 25 – 29 2018. Atlanta, Georgia, USA* (2018) AIAA paper 2018–3299.

[6] W. Dobrzynski, *Almost 40 Years of Airframe Noise Research: What Did We Achieve?* Journal of Aircraft **47**, 353 (2010).

[7] PUI Audio POM–2735P–R microphone website, *http://www.puiaudio.com/product-detail.aspx?categoryid=4&partnumber=pom-2735p-r,* Accessed in January 2017.

[8] R. van der Goot, J. Hendriks, K. Y. W. Scheper, W. Hermans, G.and van der Wal, and D. G. Simons, *A low cost, high resolution acoustic camera with a flexible microphone configuration,* in *4th Berlin Beamforming Conference, February 22 – 23 2012, Berlin, Germany* (GFaI, e.V., Berlin, 2012).

[9] Datavision UI-1220LE optical camera website, *https://en.ids-imaging.com/store/ui-1220le.html,* Accessed in January 2015.

[10] Royal Netherlands Meteorological Institute (KNMI) website, *https://www.knmi.nl/nederland-nu/klimatologie/uurgegeven,* Accessed in August 2013.

[11] European Aviation Safety Agency (EASA) website, *http://www.easa.europa.eu,* Accessed in August 2013.

[12] M. Snellen, R. Merino-Martinez, and D. G. Simons, *Assessment of noise level variability on landing aircraft using a phased microphone array,* Journal of Aircraft **54**, 2173 (2017).

[13] R. P. Dougherty, *Cross Spectral Matrix Diagonal Optimization,* in *6th Berlin Beamforming Conference, February 29 – March 1, 2016, Berlin, Germany* (GFaI, e.V., Berlin, 2016).

[14] E. Neri, J. Kennedy, and G. Bennett, *Characterization of low noise technologies applied to a full scale fuselage mounted nose landing gear,* in *Proceedings of the Internoise 2015/ASME NCAD Meeting, August 9 – 12 2015, San Francisco, CA, USA* (2015) NCAD2015–5911.

[15] E. Neri, J. Kennedy, and G. Bennett, *Aeroacoustic source separation on a full scale nose landing gear featuring combinations of low noise technologies,* in *Proceedings of the Internoise 2015/ASME NCAD Meeting, August 9 – 12 2015, San Francisco, CA, USA* (2015) NCAD2015–5912.

[16] J. Kennedy, E. Neri, and G. Bennett, *The reduction of main landing gear noise,* in *22nd AIAA/CEAS Aeroacoustics Conference. May 30 – June 1 2015. Lyon, France* (2016) AIAA paper 2016–2900.

[17] E. Neri, *Characterisation and Reduction of Aircraft Landing Gear Noise*, Ph.D. thesis, Trinity College Dublin (2017).

[18] P. Sijtsma, *Phased array beamforming applied to wind tunnel and fly–over tests*, Tech. Rep. NLR–TP–2010–549 (National Aerospace Laboratory (NLR), Anthony Fokkerweg 2, 1059 CM Amsterdam, P.O. Box 90502, 1006 BM Amsterdam, The Netherlands, 2010).

[19] R. K. Amiet, *Refraction of sound by a shear layer,* Journal of Sound and Vibration **58**, 467 (1978).

[20] M. L. Shur, P. R. Spalart, M. K. Strelets, and A. K. Travin, *A hybrid RANS–LES approach with delayed–DES and wall–modelled LES capabilities,* International Journal of Heat and Fluid Flow **29**, 1638 (2008).

[21] H. Bouchouireb, N. J. Pignier, C. O'Reilly, S. Boij, and J. Dahan, *Identification of noise sources on a realistic landing gear using numerical phased array methods applied to computational data,* in *23rd AIAA/CEAS Aeroacoustics Conference. June 5 – 9 2017. Denver, Colorado, USA* (2017) AIAA paper 2017–3019.

[22] J. A. Dahan, C. O'Reilly, and G. Efraimsson, *Numerical Investigation of a Realistic Nose Landing Gear,* in *20th AIAA/CEAS Aeroacoustics Conference, June 16 – 20 2014, Atlanta, GA, USA* (2014) AIAA paper 2014–2077.

[23] J. Dahan, R. Futrzynski, C. O'Reilly, and G. Efraimsson, *Aero–acoustic source analysis of landing gear noise via dynamic mode decomposition,* in *21st International Congress on Sound and Vibration, July 13 – 17 2014, Beijing, China*, Vol. 2 (2014) pp. 1245–1252.

[24] N. J. Pignier, C. O'Reilly, and S. Boij, *Identifying equivalent sound sources from aeroacoustic simulations using a numerical phased array,* Journal of Sound and Vibration **394**, 203 (2017).

[25] J. E. Ffowcs Williams and D. L. Hawkings, *Sound generation by turbulence and surfaces in arbitrary motion,* Philosophical Transactions of the Royal Society of London A – Mathematical, Physical and Engineering Sciences **264** (1969), 10.1098/rsta.1969.0031.

[26] W. Dobrzynski, L. C. Chow, P. Guion, and D. Shiells, *A European Study on Landing Gear Airframe Noise Sources,* in *6th AIAA/CEAS Aeroacoustics Conference. June 12 – 14 2000, Lahaina HI, USA* (2000) AIAA paper 2000–1971.

[27] Y. Guo, *A Semi–Empirical Model for Aircraft Landing Gear Noise Prediction,* in *12th AIAA/CEAS Aeroacoustics Conference. May 8 – 10 2006, Cambridge, Massachusetts, USA* (2006) AIAA paper 2006–2627.

[28] *Airbus A320 Aircraft Characteristics. Airport and Maintenance Planning*, Tech. Rep. (Airbus S.A.S., Blagnac, France., 2005).

[29] *Global Market Forecast – Flying by Numbers 2015–2034*, Tech. Rep. D14029465 (Airbus S.A.S., Blagnac, France, 2015).

[30] U. Michel and W. Qiao, *Directivity of Landing–Gear Noise Based on Flyover Measurements,* in *5th AIAA/CEAS Aeroacoustics Conference, May 10 – 12 1999, Bellevue, Greater Seattle, WA, USA* (1998) AIAA paper 1999–1956.

[31] I. Dedoussi, T. Hynes, and H. Siller, *Investigating landing gear noise using fly–over data: the case of a Boeing 747–400,* in *19th AIAA/CEAS Aeroacoustics Conference, May 27 – 29, 2013, Berlin, Germany* (2013) AIAA paper 2013–2115.

[32] J. Bulté and S. Redonnet, *Landing Gear Noise Identification Using Phased Array with Experimental and Computational Data,* AIAA Journal **55**, 3839 (2017).

[33] L. Bertsch, *Noise sources on–board,* in *Presentation at the course Advanced Aircraft Noise Modeling (AE–4463)* (Delft University of Technology, 2015).

[34] N. Curle, *The influence of solid boundaries upon aerodynamic sound,* Proceedings of Royal Society of London A **231**, 505 (1955).

[35] D. Bergmans, M. Arntzen, and W. Lammen, *Noise attenuation in varying atmospheric conditions*, Tech. Rep. NLR–TP–2011–262 (National Aerospace Laboratory (NLR), Anthony Fokkerweg 2, 1059 CM Amsterdam, P.O. Box 90502, 1006 BM Amsterdam, The Netherlands, 2011).

[36] D. G. Simons, M. Snellen, B. Midden, M. Arntzen, and D. H. T. Bergmans, *Assessment of noise level variations of aircraft fly–overs using acoustic arrays,* Journal of Aircraft **52**, 1625 (2015).

[37] L. Bertsch, W. Dobrzynski, and S. Guérin, *Tool Development for Low–Noise Aircraft Design,* Journal of Aircraft **47**, 694 (2010).

[38] L. Bertsch, *Noise Prediction within Conceptual Aircraft Design*, Ph.D. thesis, DLR (2013), DLR Forschungsbericht, ISRN DLR–FB–2013–20, ISSN 1434–8454.

[39] L. Bertsch, W. Heinze, and M. Lummer, *Application of an Aircraft Design–To–Noise Simulation Process,* in *14^{th} AIAA Aviation Technology, Integration, and Operations Conference, June 16 – 20 2014, Atlanta, Georgia, USA* (2014) AIAA paper 2014–2169.

[40] W. Dobrzynski and H. Buchholz, *Full–scale noise testing on Airbus landing gears in the German Dutch Wind Tunnel,* in *3^{rd} AIAA/CEAS Aeroacoustics Conference. May 12 – 14 1997, Atlanta GA, USA* (1997) AIAA paper 1997–1597.

[41] R. Merino-Martinez, M. Snellen, and D. G. Simons, *Determination of Aircraft Noise Variability Using an Acoustic Camera,* in *23^{rd} International Congress on Sound and Vibration, July 10 – 14 2016, Athens, Greece* (International Inst. of Acoustics and Vibration (IIAV), Auburn, Alabama, USA., 2016).

[42] R. Merino-Martinez, S. J. Heblij, D. H. T. Bergmans, M. Snellen, and D. G. Simons, *Improving Aircraft Noise Predictions by Considering the Fan Rotational Speed,* Journal of Aircraft (2018), 10.2514/1.C034849, Accepted for publication. DOI: 10.2514/1.C034849.

[43] P. A. Ravetta, M. R. Khorrami, B. König, and E. Fares, *Analysis of Simulated and Experimental Noise Sources of the Boeing 777 Main Gear Model via CLEAN in 3D,* in *24^{th} AIAA/CEAS Aeroacoustics Conference. June 25 – 29 2018. Atlanta, Georgia, USA* (2018) AIAA paper 2018–3470.

[44] B. S. Smith, H. E. Camargo, R. A. Burdisso, and W. J. Devenport, *Development of a Novel Acoustic Wind Tunnel Concept,* in *11^{th} AIAA/CEAS Aeroacoustics Conference. May 23 – 25 2005. Monterey, California, USA* (2005) AIAA paper 2005–3053.

[45] M. R. Fink, *Noise component method for airframe noise,* in *4^{th} AIAA Aeroacoustics Conference. October 3 – 5 1977, Atlanta, Georgia, USA* (1977) AIAA paper 1977–1271.

[46] Y. Guo, K. J. Yamamoto, and R. W. Stoker, *Experimental Study on Aircraft Landing Gear Noise,* Journal of Aircraft **43**, 306 (2006).

[47] R. Stoker, Y. Guo, C. Streett, and N. Burnside, *Airframe noise source locations of a 777 aircraft in flight and comparisons with past model–scale tests,* in *9th AIAA/CEAS Aeroacoustics Conference. May 12 – 14 2003. Hilton Head, South California, USA* (2003) AIAA paper 2003–3232.

[48] H. H. Heller and W. M. Dobrzynski, *Sound Radiation from Aircraft Wheel–Well/Landing–Gear Configuration,* Journal of Aircraft **14**, 768 (1977).

[49] W. Aures, *Procedure for calculating the sensory euphony of arbitrary sound signal,* Acustica **59**, 130 (1985).

[50] A. K. Sahai and E. Stumpf, *Incorporating and Minimizing Aircraft Noise Annoyance during Conceptual Aircraft Design,* in *20th AIAA/CEAS Aeroacoustics Conference, June 16 – 20 2014, Atlanta, GA, USA* (2014) AIAA paper 2014–2078.

[51] A. K. Sahai, *Consideration of Aircraft Noise Annoyance during Conceptual Aircraft Design*, Ph.D. thesis, Rheinisch–Westfälische Technische Hochschule Aachen (2016).

6

Trailing–edge noise

Profound study of nature is the most fertile source of mathematical discoveries.

Jean–Baptiste–Joseph Fourier

Con todos mis sentidos en activo escribo
estas palabras que me libren del olvido,
entre molinos y campos de olivo.

With all my senses active I write
these words to free me from oblivion,
within windmills and olive fields.

Rafael Lechowski (*Entre molinos y campos de olivo*)

As aforementioned in Chapter 2, TBL–TE noise is the dominant noise source for modern wind turbines. The physical concepts behind the noise generation mechanisms involved in trailing–edge noise and brief descriptions about potential broadband noise reduction measures have already been given in section 2.3. This chapter contains the results of experimental campaigns aimed at studying the noise–reduction performance of trailing–edge serrations (section 6.1) and trailing–edge porous inserts (section 6.2)[1].

[1] Some of the contents of this chapter are included in [1–9].

In order to measure the TBL–TE noise emissions with a microphone array, the integration methods introduced in section 4.2.2 were employed, since they are considered the best technique available for this type of measurements [7, 10, 11]. Whereas obtaining accurate estimations of the sound spectra can be an issue in wind–tunnel measurements due to their multiple challenges (see section 3.1.1), measuring the differences in sound levels between different configurations is typically easier [12]. These *delta* values are of great interest for the assessment of the performance of noise reduction measures.

6.1. Trailing–edge serrations

Previous research [13–16] on trailing–edge serrations showed that a crucial factor to reduce the broadband TBL–TE noise is the alleviation of the acoustic impedance discontinuity at the trailing edge provided by the serrations, instead of a straight trailing edge design perpendicular to the streamwise direction. Further benefits may be obtained from beneficially modifying the flow properties near the trailing edge [16].

Several trailing–edge serration geometries have been proposed in the literature [3, 13, 14, 17, 18], but the typical design features solid sawtooth triangles (see Fig. 6.2) with an aspect ratio between their length $2\,h_s$ and their width λ_s of $2\,h_s/\lambda_s = 2$, since it has shown to provide the best noise reduction results in previous research [13]. Thus, only serrations with this aspect ratio were tested for this research, although different sizes and permeabilities are considered.

The solid serrations have been found to reduce noise, but are known to increase it beyond a certain frequency ([1, 13]), especially if there is a serration–flow misalignment angle φ_s (see Fig. 6.2). This unwanted effect can lead to the degradation of the overall noise reduction performance in industrial applications, or constrain the application of serrations to a limited range of conditions. The slitted serrations tested in [19], however, seem to avoid this issue.

In order to study the different aspects influencing the performance of trailing–edge serrations, three experimental campaigns were performed in different wind tunnels, each of them with a different purpose:

1. Measurements of a NACA 0018 airfoil at an open–jet vertical wind tunnel at Delft University of Technology (TU Delft) to investigate the influence of the serration geometry, angle of attack α and serration–flow misalignment angle φ_s (see Fig. 6.2). The performance of semi–permeable serrations was also analyzed. The setup and results of this campaign are included in section 6.1.1.

2. Measurements of two airfoils (NACA 0012 and NACA 0018) at an open–jet anechoic wind tunnel at the University of Twente (UTwente) featuring flow–aligned serrations. In this experiment, the performance of two different microphone arrays (consisting of digital and analog microphones, respectively) was compared. Moreover, the effect of the airfoil thickness on the performance of the serrations was investigated. This research is the result of a collaboration between UTwente and TU Delft. The setup and results of this campaign are included in section 6.1.2

3. Measurements of a cambered DU96–W–180 airfoil with flow–misaligned serrations at the closed–section, low–turbulence wind tunnel (LTT) at Delft University of Technology. This wind tunnel allowed for measurements at chord–based Reynolds numbers as high as 1.5×10^6. The setup and results of this campaign are included in section 6.1.3.

6.1.1. Effect of serration geometry, angle of attack and serration–flow misalignment angle

Experimental setup

The measurements were performed at the vertical wind tunnel (V–tunnel) at Delft University of Technology, which has a contraction ratio of approximately $60:1$. For this experiment, a square nozzle of 0.4 m $\times$ 0.4 m was used with a turbulence intensity below 1% [1].

A symmetric NACA 0018 airfoil was manufactured into an aluminum wing of chord $\hat{c} = 0.2$ m and span of $b = 0.4$ m, equal to the test section width. The model was installed in an open test section with two long wooden side plates terminating 0.7 m downstream of the airfoil trailing edge to approximate the two-dimensional flow condition over most of the wing span [20]. The airfoil leading edge was located 0.5 m from the nozzle exit to separate the extraneous noise sources (e.g., from the nozzle) from the airfoil trailing–edge noise source.

To ensure that the noise source observed was TBL–TE noise, the boundary layer Was forced to turbulent transition (see section 2.3) with randomly distributed carborundum roughness elements with a nominal size of 0.6 mm, placed on a tape of 10 mm width, following the recommendations in [21]. The tape was centered at 20% of the chord ($0.2\,\hat{c}$) and covered the whole span on both sides of the airfoil. A stethoscope probe was used to verify that the boundary layer was tripped and that it remains turbulent downstream until the trailing edge [2]. This system is composed by a Brüel & Kjær 4134 microphone [22], a Brüel & Kjær 2619 preamplifier [23] and a Brüel & Kjær 2801 power supply [24].

Four serration geometries were tested in this experimental campaign defined by their width λ_s and length $2\,h_s$, see Fig. 6.2. All of them had a sawtooth geometry of 1 mm thickness throughout all the airfoil span and the same aspect ratio ($2\,h_s/\lambda_s = 2$), but presented different characteristics, see Fig. 6.3:

- **Short solid serrations** with $\lambda_s = 10$ mm and $2\,h_s = 0.1\,\hat{c} = 20$ mm. Henceforth these serrations are referred to as *Sr10*, since their length is 10% of the airfoil chord.
- **Long solid serrations** with $\lambda_s = 20$ mm and $2\,h_s = 0.2\,\hat{c} = 40$ mm. These dimensions follow the recommendations for serration design of Gruber *et al.* [13]. Henceforth these serrations are referred to as *Sr20*.
- **Long slitted serrations** with the same dimensions as the *Sr20* but with semi–permeable area. Henceforth these serrations are referred to as *Slitted*.
- **Hybrid serrations** with the same geometry as the *Slitted*, but including solid

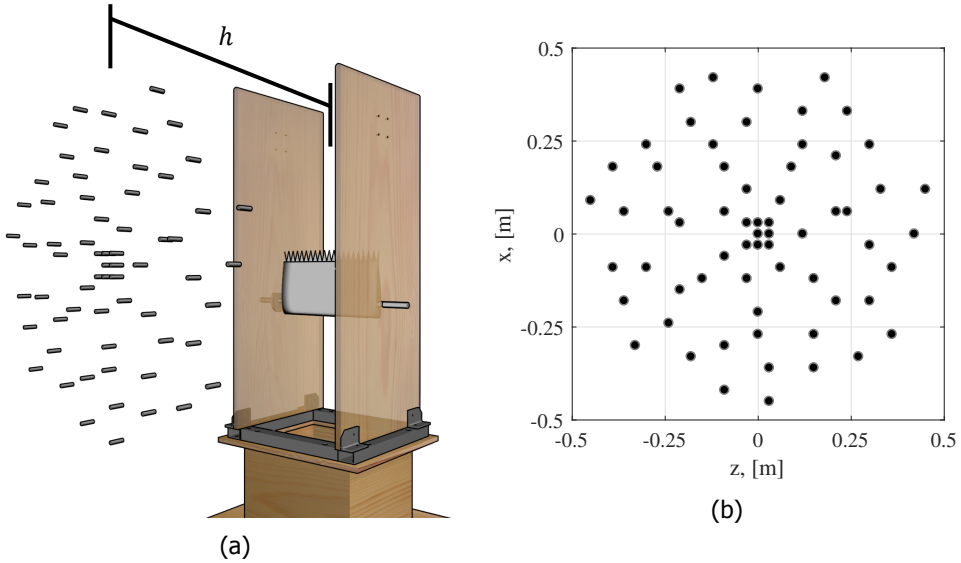

Figure 6.1: (a) Illustration of the experimental setup in the V–tunnel showing the position of the microphone array with respect to the test section and airfoil. Adapted from [3]. (b) Microphone distribution for the V–tunnel measurements. Adapted from [3].

serrations with the same geometry as *Sr10*. Henceforth these serrations are referred to as *Hybrid*.

A modular trailing–edge design in the airfoil allowed the serration inserts to be retrofitted while keeping the surface free from irregularities. All the serration geometries were mounted aligned with the flow, i.e., the misalignment angle $\varphi_s = 0°$, see Fig. 6.2. Only the *Sr20* case was tested with $\varphi_s = 6°$ to study the effect of the serration–flow misalignment angle (or flap angle) on the noise emissions [2]. All these configurations were compared with respect to the straight trailing edge baseline case.

The coordinate system for this experimental campaign is illustrated in Fig. 6.2, with the x axis in the streamwise direction, the y axis normal to the mean camber plane of the airfoil pointing at the microphone array, the z axis in the spanwise direction, and the origin located in the center of the straight trailing edge. The noise emissions were studied at three freestream velocities V_∞ (30, 35 and 40 m/s) and three geometric angles of attack α: 0°, 6° and 12°. The maximum velocity corresponds to a chord–based Reynolds number of 5.26×10^5 and a Mach number of 0.118, approximately.

A 64–microphone array with a diameter of 0.9 m was used, arranged in a multi–arm logarithmic spiral configuration ([25, 26]), as shown in figure 6.1b. The microphones used were of the same type as for the flyover measurements described in section 5.1.1, and had been previously calibrated using a pistonphone [27] [1]. The array was placed at a distance h away from the airfoil in the y direction, as illus-

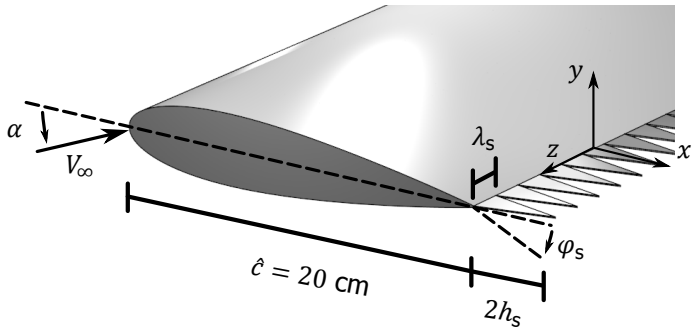

Figure 6.2: Convention used for the coordinate system and serration–misalignment angle φ_s. Adapted from [3].

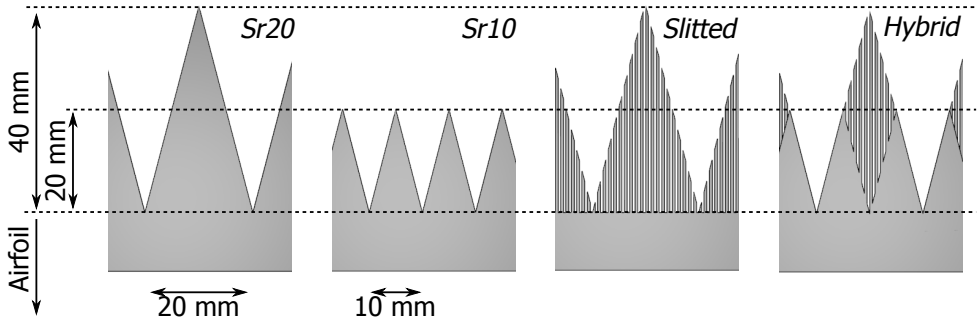

Figure 6.3: Explanation of the geometries of the four serration types tested. Adapted from [2].

trated in Fig. 6.1a. This distance had a value of 1.26 m when testing flow–aligned serrations and of 1.05 m when studying flow–misaligned serrations. The center of the array ($x = z = 0$) was aligned in the streamwise direction with the root of the serrations at the trailing edge.

The sampling frequency employed was 50 kHz and the selected sound frequency range of interest extended from 1 kHz to 5 kHz. For each measurement, 60 s of data were recorded. The acoustic data were averaged using time blocks of 2048 samples ($T_h = 40.96$ ms) and windowed using a Hanning weighting function with 50% data overlap following Welch's method, see Appendix C.3. With these values, the frequency resolution is $\Delta f \approx 24.41$ Hz. The expected random error in the estimate (see Appendix C.3.1) is approximately 1.9%. The SNR of this setup was found to be between 10 and 24 dB for the frequency range of interest (1 kHz to 5 kHz) for all cases [3]. Moreover, the main diagonal of the CSM was deleted to reduce the influence of incoherent background noise, see section 4.2.1.

The effect of the shear layer in the acoustic measurements ([28]) was neglected due to the small angle ($< 10°$) between the center of the array and the scan area of interest and the considerably low flow velocities employed in this experiment ([29]).

In addition to the acoustic measurements with the phased microphone array, time–resolved stereoscopic PIV measurements [16, 30] (see section 1.3.1) were performed to obtain the boundary layer flow characteristics in the vicinity of the trailing edge [1, 2].

Results and discussion

A clear example of the noise–reduction performance of the serrations is illustrated in Fig. 6.4, where the CFDBF source plots obtained for the straight–trailing–edge baseline case and the *Sr20* serrations are presented for the three freestream velocities 30, 35 and 40 m/s for $\alpha = 0°$ (i.e., at zero lift). The frequency range of the source plots corresponds to the whole frequency range of interest (1 kHz to 5 kHz). It can be observed that the strongest noise sources are located at the trailing edge, as expected [1] and that the presence of the *Sr20* serrations reduce the peak beamform levels, as observed in [13], by approximately 6 dB for the three velocities. In Fig. 6.4 it can also be observed that higher freestream velocities generate higher noise levels, as expected (see section 2.3.2).

The frequency spectrum of the TBL–TE noise emissions can be calculated by integrating the CFDBF source plots in a ROI using the SPIL technique, as explained in sections 4.2.2 and 4.17. For this experiment a spacing between grid points Δx of 1 mm was used and a ROI extending from $z = -0.1$ m to $z = 0.1$ m and from $x = -0.06$ m to $x = 0.06$ m was selected for all the trailing–edge geometries (depicted as a dashed rectangle in Figs. 6.4 and 6.9), in order to avoid the influence of potential corner sources in the junctions of the airfoil with the side plates [31, 32], following the recommendations mentioned in section 4.17. A simulated line source was considered at the trailing edge position ($x = 0$ m and from $z = -0.1$ m to $z = 0.1$ m). Figure 6.5 shows the integrated overall L_p values for the frequency range of interest (1 kHz to 5 kHz) for the straight trailing edge and the *Sr20* serration with

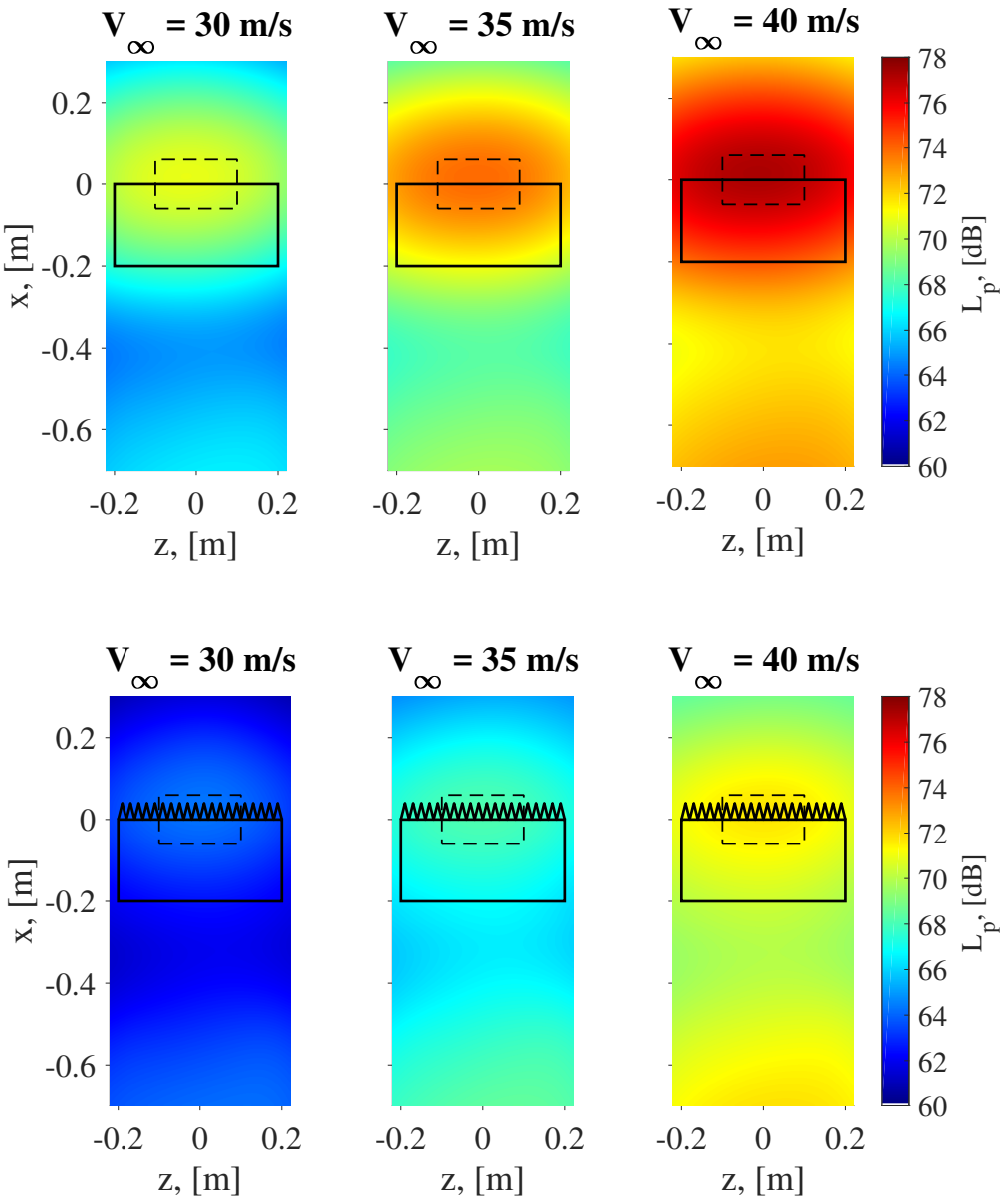

Figure 6.4: CFDBF source maps obtained for the straight trailing edge (top) and the *Sr20* serrations (bottom) at the freestream velocities indicated on top of each figure, for $\alpha = 0°$, and for the frequency range between 1 kHz and 5 kHz. The airfoil location is denoted by a solid rectangle and the ROI by a dashed rectangle. Adapted from [1].

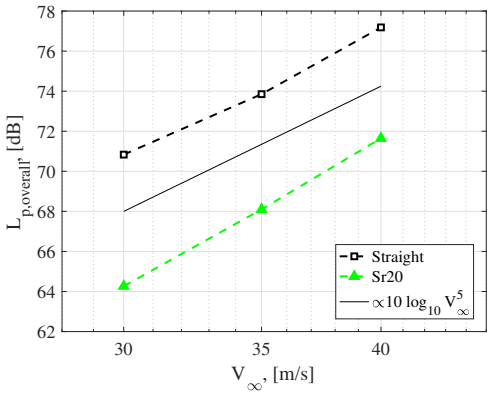

Figure 6.5: Velocity dependence law (straight line) for trailing–edge noise emissions compared to the measured noise from the straight and *Sr20* edges for a frequency range between 1 kHz and 5 kHz and $\alpha = 0°$. Note the logarithmic scale for the velocity axis. Adapted from [1].

respect to the freestream velocity V_∞. An approximately constant L_p difference of 6 dB is present in all cases [1], as observed in Fig. 6.4. The expected 5^{th} power law dependence of the acoustic power with the freestream velocity [33, 34] is also plotted in Fig. 6.5, showing a close agreement with both cases. Similar behaviors were found when studying the noise emissions of trailing–edge devices on aircraft flyovers [35].

The integrated one–third–octave–band sound spectra for each flow–aligned, trailing–edge serration and for the straight trailing edge are presented in Fig. 6.6 for $\alpha = 0°$ and the three freestream velocities. The background (BG) noise spectra are also plotted as reference. The noise reduction achieved by the four serration geometries is evident [3]. To better show the noise reduction levels obtained, the same spectra as in Fig. 6.6 are depicted in Fig. 6.7 relative to the straight trailing–edge spectrum in terms of $\Delta L_p = L_{p,\,STE} - L_{p,\,s}$, where $L_{p,\,STE}$ and $L_{p,\,s}$ refer to the straight and serrated trailing edge cases, respectively. Therefore, a positive value of ΔL_p represents a noise reduction.

The noise reductions vary moderately when increasing the flow velocity, showing some slight degradation especially at lower frequencies [3]. Noise reductions up to 8 dB are achieved by the *Hybrid* serrations. The *Sr20* perform in a similar way with slightly lower noise reduction levels. The *Sr10* perform about 2 dB worse across the considered frequency spectrum. The *Slitted* serration geometry seems to be the most inefficient, especially for frequencies below 2.5 kHz. This result disagrees with the findings by Gruber et al. [19] where this serration design performed in a similar or even better way than the solid serration design, but it was tested on a non–symmetric airfoil with serrations manufactured in a different material. The worse noise reduction achieved by the *Slitted* serrations compared to the *Sr20* is probably explained regarding the modified trailing edge because 50% of the wetted edge of the *Slitted* serration is still perpendicular to the streamwise direction (at

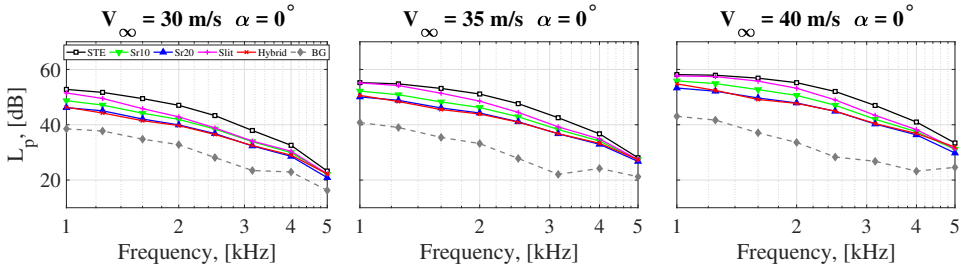

Figure 6.6: Integrated sound spectra for the four serration geometries and the straight trailing edge at $\alpha = 0°$ and freestream velocities of 30, 35 and 40 m/s (from left to right). Adapted from [3].

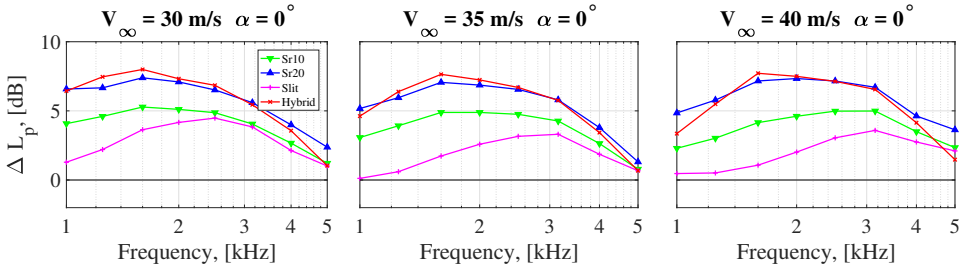

Figure 6.7: Relative integrated sound spectra for the four serration geometries with respect to the straight trailing edge at $\alpha = 0°$ and freestream velocities of 30, 35 and 40 m/s (from left to right). Adapted from [3].

the root) causing a strong acoustic impedance change there [3, 33] in the same way as the straight trailing edge. The *Hybrid* serrations, on the other hand, achieve considerably higher noise reductions than the *Sr10* serrations while having the same solid serration contour, i.e., with a lower wetted surface than the *Sr20* design, which is likely to have a lower impact to the aerodynamic performance of the airfoil [3]. This fact suggests that slits need to be carefully integrated into a proper design [3].

The ΔL_p results for the case with $\alpha = 12°$ are included in Fig. 6.8 and exhibit a weakened noise reduction performance for all the serration designs [3] compared to the case with $\alpha = 0°$. The *Hybrid* and *Sr20* serrations remain as the most efficient designs, reaching reductions of almost 6 dB. Negligible trend differences are again observed when increasing the flow velocity, suggesting that the noise reduction performance is only weakly affected by the flow velocity [3].

The PIV measurements showed that, at the root of the serrations and upstream, the flow remains practicably unmodified, whereas considerable changes are experienced as it convects downstream, leading to lower intensities in the unsteady pressure fluctuations [1]. This way, the local pressure waves might vary along the serration edges, leading to the observed TBL–TE noise reductions [1].

The effect of the serration–flow misalignment angle φ_s is observed in the CFDBF source maps illustrated in Fig. 6.9, which represents the noise emissions of the straight–trailing–edge case and the *Sr20* serrated trailing edges with $\varphi_s = 0°$ and

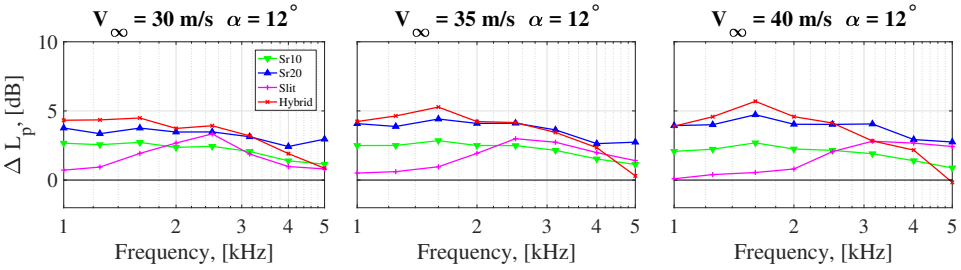

Figure 6.8: Relative integrated sound spectra for the four serration geometries with respect to the straight trailing edge at $\alpha = 12°$ and freestream velocities of 30, 35 and 40 m/s (from left to right). Adapted from [3].

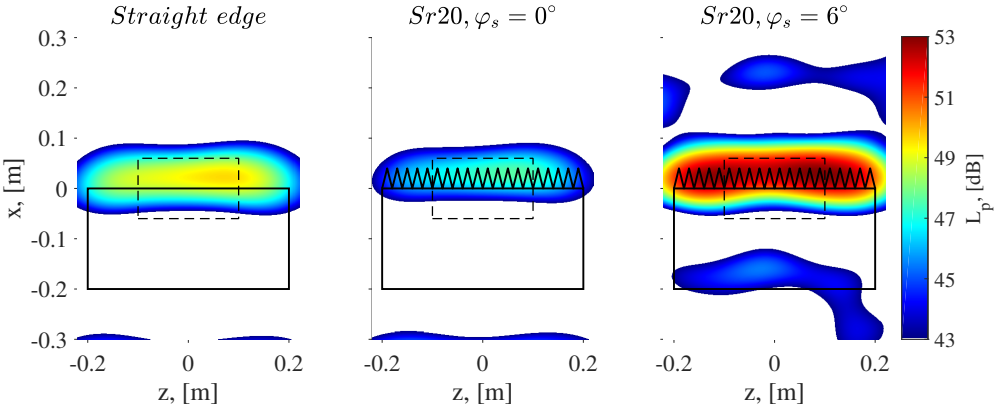

Figure 6.9: CFDBF source maps obtained for the straight trailing edge (left), the *Sr20* serrations with $\varphi_s = 0°$ (center), and the *Sr20* serrations with $\varphi_s = 6°$ (right). The results correspond to a freestream velocity of 35 m/s and $\alpha = 0°$, and a one–third–octave frequency band centered at 4 kHz. The airfoil location is denoted by a solid rectangle and the ROI by a dashed rectangle. Adapted from [2].

$\varphi_s = 6°$ for a one–third–octave frequency band centered at 4 kHz. The results depicted correspond to a freestream velocity of $V_\infty = 35$ m/s and $\alpha = 0°$. As it was observed in Fig. 6.4, the trailing edge is the primary sound source in all three cases [2]. The flow–aligned serrations ($\varphi_s = 0°$) provide a noise reduction of approximately 2 dB, whereas the flow–misaligned serrations ($\varphi_s = 6°$) have an adverse effect [2].

To further investigate this phenomenon, the integrated one–third–octave–band spectra in the ROI for the *Sr20* serrated trailing edge with $\varphi_s = 6°$ relative to the straight–trailing–edge baseline (i.e., the ΔL_p) are presented in Fig. 6.10 for α values of $0°$, $6°$ and $12°$. A crossover frequency $f_{crossover}$ is observed for all the freestream velocities and angles of attack, after which the flow–misaligned serrations generate an increase in noise, instead of a reduction. The serration flap angle φ_s induces a localized deflection of the flow field which causes a change of the local pressure gradient, an increase in the turbulence levels near the edge and the formation of streamwise coherent structures, which causes a noise increase [2].

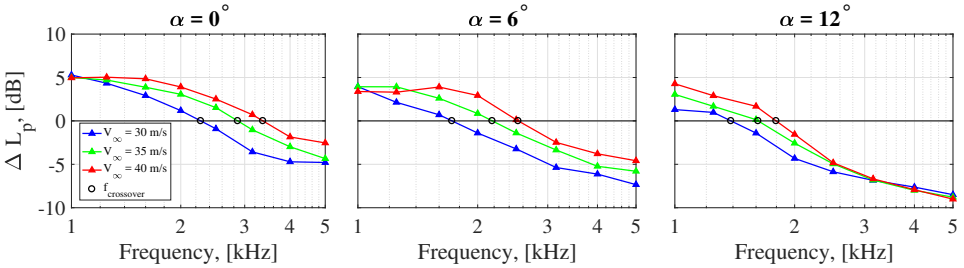

Figure 6.10: Relative integrated sound spectra for the *Sr20* serration with $\varphi = 6°$ with respect to the straight trailing edge at different V_∞ values and α values of $0°$, $6°$ and $12°$ (from left to right). The crossover frequency $f_{\text{crossover}}$ is indicated for each V_∞ case with a black circle. Adapted from [2].

The crossover frequencies (estimated by linear interpolation of the one–third–octave–band spectra) are depicted with black circles in Fig. 6.10. The flow–misaligned serrations provide a noise reduction of about 5 dB at around 1 kHz, but this amount quickly decreases as the frequency increases. This phenomenon occurs earlier for lower velocities and for increasing angles of attack. For $\alpha = 0°$, $f_{\text{crossover}}$ is between 2.2 kHz and 3.4 kHz and the maximum noise increase is about 5 dB. For $\alpha = 6°$, $f_{\text{crossover}}$ is observed between 1.7 kHz and 2.6 kHz and the noise increase reaches 7.5 dB. Finally, for $\alpha = 12°$, $f_{\text{crossover}}$ is between 1.3 kHz and 1.8 kHz and noise increases up to 8 dB are obtained. It was found that $f_{\text{crossover}}$ scales with the Strouhal number based upon the boundary layer displacement thickness (measured with PIV) and the freestream velocity $St = f\delta^*/V_\infty$, [2]. Moreover, instead of a single value for the Strouhal number, a linear relation is found between St and α [2]. The consideration of the boundary layer of the pressure side is preferred since it was found to be more representative [2]. An increase in the energy of turbulent fluctuations is also observed at the expected crossover frequency and the dominant cause for the noise increase is identified at the pressure side of the flow–misaligned serrations [2].

A comparison between the data obtained in this experimental campaign and LBM computational results (see section 1.3.3) was performed by van der Velden [15] and Avallone et al. [36], see Fig. 6.11. The frequency spectra of the straight trailing edge and the *Sr20* geometry obtained experimentally (with $V_\infty = 30$ m/s and $\alpha = 0°$) are compared to the far–field computational results propagated using the FW–H analogy. More information about the computational simulations can be found in the original publications [15, 36].

In Fig. 6.11 the axis of abscissas is expressed as the Strouhal number based on the airfoil chord $St = f\hat{c}/V_\infty$ and the L_p values are normalized considering a Mach number $M = 1$, the distance between the source and the observer $r = 1$ m and the airfoil span $b = 1$ m in order to enable a proper comparison [15]:

$$L_{p,\text{norm}} = L_p + 10\log_{10}\left(\frac{r^2}{bM^5}\right), \tag{6.1}$$

where $L_{p,\text{norm}}$ denotes the normalized L_p values.

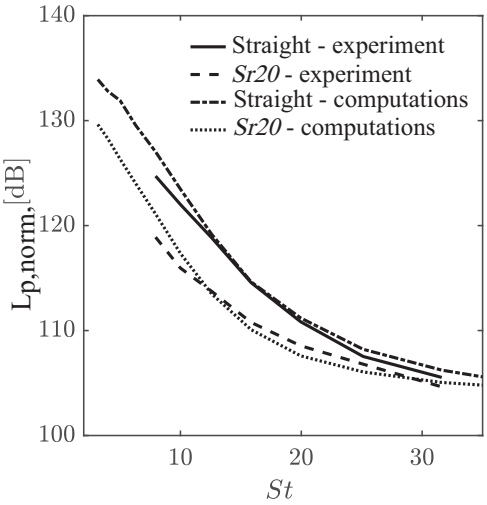

Figure 6.11: Computational and experimental (with $V_\infty = 30$ m/s and $\alpha = 0°$) normalized far–field sound spectra for the straight trailing edge and *Sr20* serrated edge. Adapted from [15, 36].

The agreement between the experimental and computational spectra is very close for both trailing edge cases (straight and *Sr20*). The noise reduction provided by the serrations is maximal around $St \approx 8$ and becomes negligible after $St = 32$. The spectra from other freestream velocities showed very similar results [15].

6.1.2. Microphone array comparison and effect of airfoil thickness

Experimental setup

Aeroacoustic measurements were performed in the Silent Wind–Tunnel facility of the UTwente. The facility is a closed–circuit wind tunnel with an open–jet test section located inside an anechoic chamber of dimensions 6 m (length) $\times$ 6 m (width) $\times$ 4 m (height). In this facility, aeroacoustic measurements can be performed in an anechoic environment (i.e., free–field conditions) for frequencies above 200 Hz. The open–jet test section has rectangular dimensions of 0.9 m (width) $\times$ 0.7 m (height), see Fig. 6.12. The freestream velocities V_∞ considered were 20, 30 and 40 m/s with turbulence intensity levels below 0.2%. The maximum freestream velocity corresponds to a chord–based Reynolds number of 5.26×10^5 and a Mach number of 0.118, approximately, as in the experiments explained in section 6.1.1.

Two airfoils (NACA 0012 and NACA 0018) with a chord of $\hat{c} = 0.2$ m and a span of $b = 0.7$ m (i.e., equal to the test section height) and manufactured in aluminum were tested in this experiment. Boundary–layer tripping was applied using the same method as in section 6.1.1 and centered at $0.2\,\hat{c}$ on both sides of the airfoil, see Fig. 6.13. The turbulent feature of the flow was confirmed using a remote microphone probe. A remote microphone was used to verify that the boundary layer was tripped

Table 6.1: Boundary layer thickness at the trailing edge (δ_{95}) for both airfoils at different flow velocities.

Flow velocity V_∞, [m/s]	δ_{95} for NACA 0012, [mm]	δ_{95} for NACA 0018, [mm]
20	7.5	8.5
30	7	8
40	6.5	7.5

and that it remains turbulent downstream until the trailing edge.

Two types of solid sawtooth serrations were measured, both manufactured in aluminum and aligned with the flow, retrofitted inside a slot in the trailing edge of each airfoil and with a thickness of 1 mm. The aspect ratio between the serration length $2\,h_s$ and the serration width λ_s was $2\,h_s/\lambda_s = 2$ (the same as in section 6.1.1). The two serration geometries considered were:

- **Long solid serrations** with $\lambda_s = 30$ mm and $2\,h_s = 0.3\,\hat{c} = 60$ mm. These serrations are referred to as *Sr30*.
- **Short solid serrations** with $\lambda_s = 15$ mm and $2\,h_s = 0.15\,\hat{c} = 30$ mm. These serrations are referred to as *Sr15*.

HWA measurements were performed on both airfoils (for the straight trailing edge configuration) to determine the boundary layer thickness at the trailing edge based on the 95% of the edge velocity (δ_{95}). The average results of these measurements for the three considered flow velocities (20, 30 and 40 m/s) are gathered in Table 6.1. For a flow velocity of 30 m/s, δ_{95} was measured to be 7 mm for the NACA 0012 and 8 mm for the NACA 0018, approximately. The length of the serrations is about 8 and 4 times δ_{95} for the *Sr30* and the *Sr15* geometries, respectively. Thus, these serrations are considerably longer than the ones tested by Arce León et al. [1] (see section 6.1.1) for the same airfoil and flow conditions, and, hence, are expected to provide higher noise reductions [13].

The coordinate system employed for the experiment is illustrated in Fig. 6.13, with the x axis in the downwind streamwise direction, the z axis in the spanwise direction pointing upwards, the y axis perpendicular to the other two axes pointing at the digital microphone array (see Fig. 6.12), and the origin placed at the center of the straight trailing edge.

Since both airfoils are symmetric (i.e., they have no camber), the radiated far–field noise is expected to inhibit similar properties on both the pressure and suction sides under no angle of attack. Therefore, only measurements with zero angle of attack ($\alpha = 0°$) are used for comparison.

Two phased microphone arrays were employed to analyze the TBL–TE noise emissions and placed at opposite side of the airfoil, as shown in Fig. 6.12, and at a distance of $h = 1.2$ m from the airfoil trailing edge:

- A CAE Systems M–112 Bionic Array [37] (Fig. 6.12 left) consisting of 112 Invensense INMP441 digital MEMS microphones with an integrated DAS inside

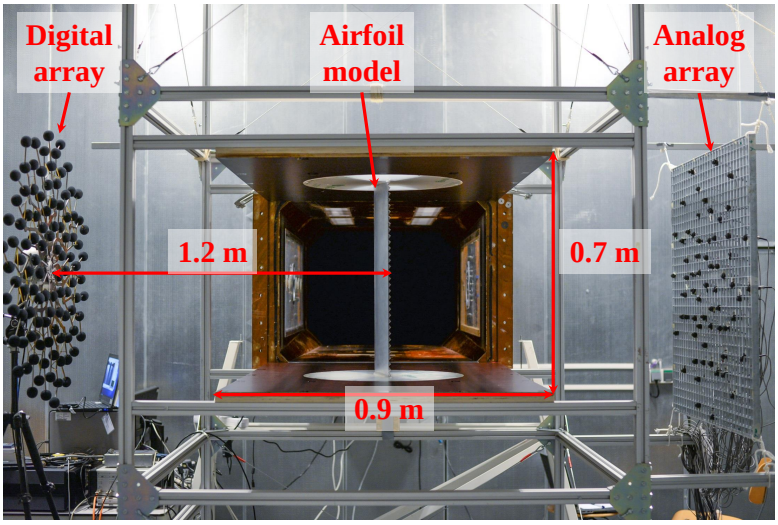

Figure 6.12: NACA 0012 airfoil installed in the open–jet test section (front view) with both microphone arrays (*Digital* on the left and *Analog* on the right) [6].

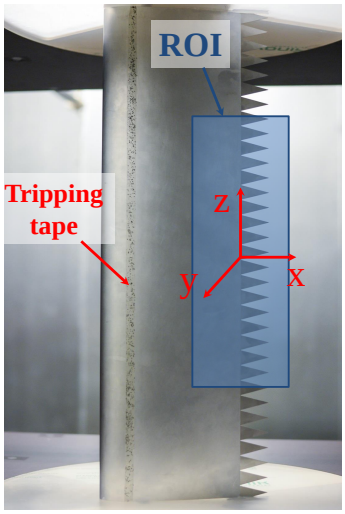

Figure 6.13: Coordinate system adopted and representation of the region of integration (ROI) size and location (shaded in blue). The location of the tripping tape is also indicated for this example of the NACA 0012 airfoil with *Sr30* serrations [6].

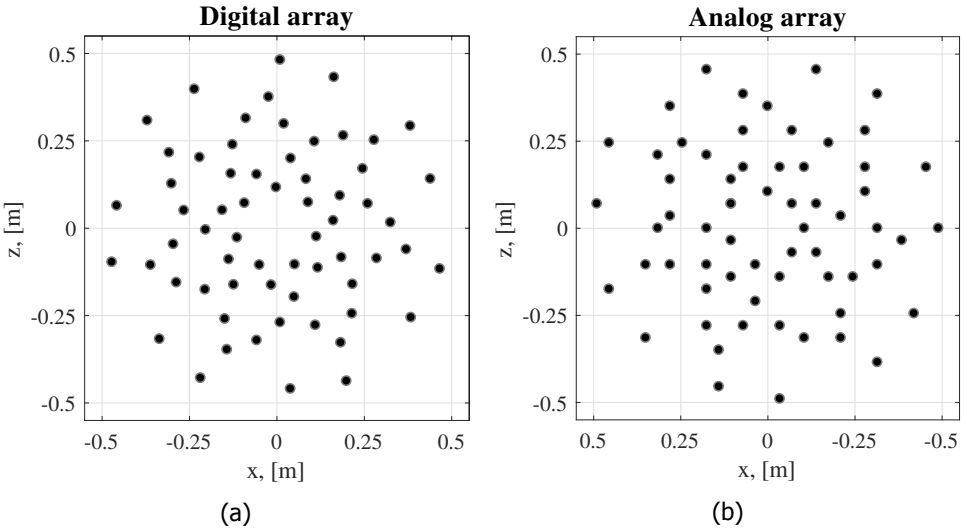

Figure 6.14: Microphone distribution for (a) The *Digital* phased microphone array. (b) The *Analog* phased microphone array. Note that the x axis is reversed for better comparison [6].

the hub of the array. The frequency range of the microphones spans from 10 Hz to 24 kHz. Digital time data are directly saved to a laptop computer at a sampling frequency of 48 kHz using the array's integrated FPGA (Field–Programmable Gate Array) system. The microphones are recessed inside small cavities, flush–mounted with the array mounting structure. Thus, sound reflections from the array structure can be expected at the microphones. From the total of 112 microphones, 63 were selected to compare the results with the other array, see Fig. 6.14a. Henceforth, this array is referred to as *Digital* array.

- A reconfigurable microphone array (Fig. 6.12 right) consisting of 63 PUI Audio POM–2735P–R analog condenser microphones [38] (see section 5.1.1 for the specifications of the microphones) with a DAS developed at TU Delft, as in sections 5.1.1 and 6.1.1. The microphone distribution approximated the selected undersampled geometry of the *Digital* array, see Fig. 6.14b. The sampling frequency employed was 50 kHz. Each microphone was previously calibrated using a calibrated pistonphone [27] emitting sound at 250 Hz. The performance of this array has already been compared with computational aeroacoustic methods, with successful results [5, 15]. Henceforth, this array is referred to as *Analog* array.

Both arrays have an approximate diameter of $D = 1$ m, see Fig. 6.14. The approximate costs of both microphone types are similar and in the order of 1 euro per piece. Therefore, the comparison between both systems is considered as representative.

The centers of both arrays were aligned with the center of the trailing edge of the airfoil ($x = z = 0$ m). Both microphone distributions were almost identical, but the *Analog* array presented a small rotation with respect to the *Digital* array. The effect of this small difference, however, is expected to be negligible.

Raw time signals were simultaneously acquired by both arrays. For each measurement, 60 s of data were recorded. The acoustic data were averaged using time blocks of 4096 samples (corresponding to a time interval of $T_h = 85.33$ ms for the *Digital* array and $T_h = 81.92$ ms for the *Analog* array) and windowed using a Hanning weighting function with 50% data overlap following Welch's method, see Appendix C.3. With these values, the frequency resolution for both arrays is approximately $\Delta f \approx 12$ Hz. The frequency range of interest was selected to be between 1 kHz and 5 kHz as in previous experiments [1–4], see section 6.1.1.

Mean flow convection of the sound was taken into account in the steering vector formulation using an average Mach number of the flow following the approach proposed by Amiet [39]. Moreover, the main diagonal of the CSM was removed in order to mitigate the effect of the incoherent background noise from the wind tunnel, see section 4.2.1.

Results and discussion

As it was done in section 6.1.1, the TBL–TE noise emissions were calculated by integrating the CFDBF source plots in a ROI using the SPIL technique explained in sections 4.2.2 and 4.17. A scan grid covering a range from $x = -0.3$ m to $x = 0.3$ m and from $z = -0.45$ m to $z = 0.45$ m, i.e., covering the whole airfoil, was defined for both arrays. A constant spacing between grid points Δx of 10 mm was selected. Both datasets were processed with the same software developed in–house.

Following the guidelines specified in [11], a ROI was defined in order to apply the SPIL method ranging from $x = -0.07$ m to $x = 0.07$ m and from $z = -0.2$ m to $z = 0.2$ m, see Fig. 6.13a. A simulated line source was considered at the trailing edge position ($x = 0$ m and from $z = -0.2$ m to $z = 0.2$ m). The corners of the airfoil's trailing edge were excluded from the ROI in order to mitigate the influence of any potential "corner" sources due to interaction of the airfoil with the boundary layers of the wind–tunnel walls [7, 31, 32].

As an illustrative example, the CFDBF source plots obtained by both arrays for the NACA 0012 airfoil with straight trailing edge at $\alpha = 0°$ and $V_\infty = 30$ m/s and a one–third–octave frequency band centered at 2 kHz are presented in Fig. 6.15. Whereas both beamforming plots present a similar source distribution (a vertical line source located at the trailing edge of the airfoil, $x = 0$ m) and comparable peak values, the beamform map provided by the *Digital* array (Fig. 6.15a) has higher sidelobes (i.e., spurious sources) than the one by the *Analog* array (Fig. 6.15b). Results for the same configuration but at a one–third–octave frequency band centered at 4 kHz are presented in Fig. 6.16. Once again the results from the *Analog* array present less sidelobes than those from the *Digital* array. Slightly lower peak levels (about 1.5 dB lower) are observed in the source plot by the *Analog* array compared to the *Digital* one. Similar behaviors were found for other frequency ranges and airfoil configurations.

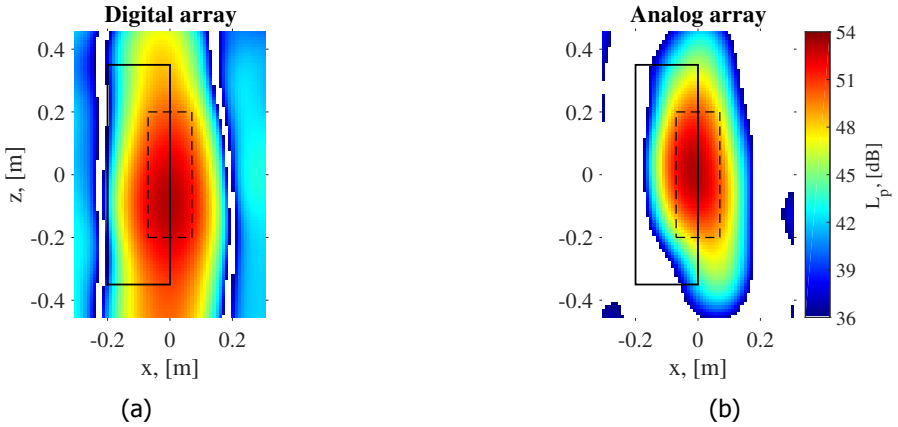

Figure 6.15: CFDBF source plots obtained for the NACA 0012 airfoil with straight trailing edge at $\alpha = 0°$ and $V_\infty = 30$ m/s for: (a) the *Digital* array and (b) the *Analog* array. The results correspond to a one–third–octave frequency band centered at 2 kHz. The airfoil location is denoted by a solid rectangle and the ROI by a dashed rectangle using the same orientation as depicted in Fig. 6.13. The results for the *Analog* array have been mirrored with respect to the z axis for an easier comparison [6].

The spatial resolution of an array follows the Rayleigh resolution limit [40], see Eqs. (D.3) and (D.4) in Appendix D. Both arrays show similar spatial resolutions, since this parameter mostly depends on the array aperture and the microphone distribution [41], and these features are almost identical for both arrays, see Fig. 6.14.

To further investigate the dynamic range (or sidelobe level) of both arrays, this parameter was calculated for both arrays when analyzing the NACA 0012 airfoil with straight trailing edge at $\alpha = 0°$ and $V_\infty = 30$ m/s. Since the spatial resolution of an array improves with increasing frequency, see Eq. (D.4), only the results further away than a distance $R(f)$ from the trailing edge of the airfoil ($x = 0$ m) and within a scan grid going from $x = -0.6$ m to $x = 0.6$ m are considered, i.e., for $x \in -0.6$ m $\leq x \leq -R(f) \cup R(f) \leq x \leq 0.6$ m (see Fig. 6.17a) and for $z \in -0.35$ m $\leq z \leq 0.35$ m. The dynamic range is, thus, defined as the difference between the peak level found in the trailing–edge region $x \in -R(f) \leq x \leq -R(f)$ and the peak sidelobe level in the sidelobe search area defined in Fig. 6.17a (colored in orange). Thus, different search areas are considered for each frequency. These boundaries were selected in order to include potential sidelobes, but to exclude extraneous noise sources from the wind–tunnel facility located further away as much as possible.

The dynamic ranges obtained for both arrays for these conditions are presented in Fig. 6.17b. Both microphone arrays show similar behaviors between 1 kHz and 1.6 kHz and for frequencies higher than 8 kHz. Between 2 kHz and 6 kHz, however, the dynamic range of the *Analog* array is considerably higher (approximately 4.8 dB in that range) than the one of the *Digital* array. The exact reason for this difference is unknown, but could be caused by the different microphone electronics as well as different DAS used.

The relatively low dynamic range for frequencies below 1.6 kHz can be explained

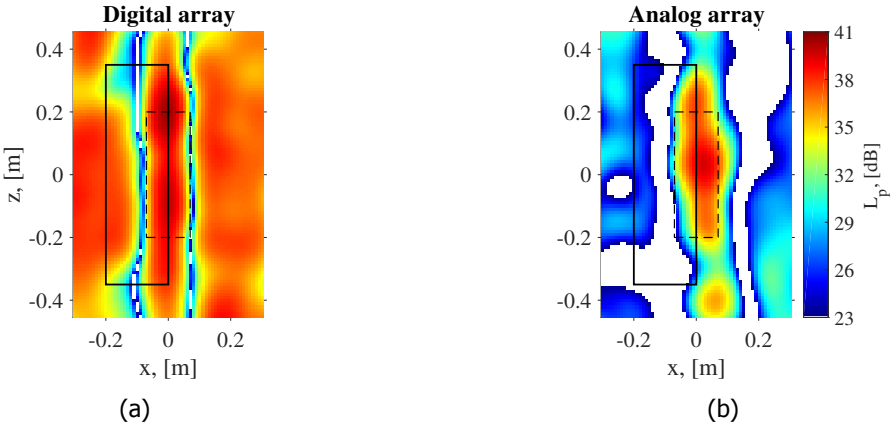

Figure 6.16: CFDBF source plots obtained for the NACA 0012 airfoil with straight trailing edge at $\alpha = 0°$ and $V_\infty = 30$ m/s for: (a) the *Digital* array and (b) the *Analog* array. The results correspond to a one–third–octave frequency band centered at 4 kHz. The airfoil location is denoted by a solid rectangle and the ROI by a dashed rectangle using the same orientation as depicted in Fig. 6.13. The results for the *Analog* array have been mirrored with respect to the z axis for an easier comparison [6].

6

because of the limited sidelobe search area for low frequencies since $R \approx 0.53$ m for 1 kHz. In general, higher frequencies present higher sidelobes [25], and hence lower dynamic ranges. The fact that both arrays present very similar values for the 8 kHz and 10 kHz one–third–octave bands may be due to the lower SNR at those frequencies for trailing–edge noise [1]. Therefore, those two frequency bands probably correspond to background noise.

A comparison of the integrated sound spectra in the ROI defined in Fig. 6.15 is presented in Fig. 6.18 for the *Digital* array (left) and for the *Analog* array (right). Both plots correspond to the NACA 0018 airfoil at $\alpha = 0°$ and $V_\infty = 40$ m/s and the three trailing–edge geometries (straight, *Sr15* and *Sr30*). The absolute values of the three spectra for both arrays are comparable. This confirms that, despite the higher presence of sidelobes for the *Digital* array results (see Figs. 6.15 and 6.16), the SPIL method reduces their influence by integrating the results in a ROI. The main difference observed in Fig. 6.18 is that the *Digital* array shows a crossover frequency around 3.5 kHz after which the spectra from both serrated cases show higher noise emissions than the straight trailing–edge baseline case. A noise increase of about 5 dB is measured for the 4 kHz one–third–octave band and about 2 dB for the 5 kHz band. This phenomenon does not occur for the *Analog* array, where only a noise increase of about 2 dB is observed for the band centered at 5 kHz. Such noise increase after a crossover frequency was not observed in the analogous experiment in section 6.1.1 with the same airfoil and flow conditions. A noise increase was only observed when a serration–flow misalignment angle was present [2], see section 6.1.1. This phenomenon might be related to the fact that digital microphones are normally optimized for the human speech frequency range (300 Hz to 3 kHz), as aforementioned.

In order to investigate this phenomenon in more detail, the calculated noise

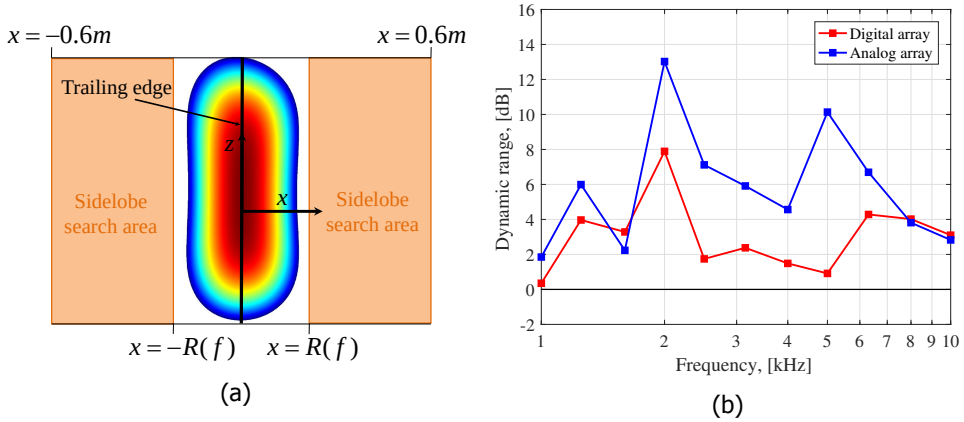

Figure 6.17: (a) Diagram explaining the search areas for sidelobes (colored in orange). (b) Dynamic range of both microphone arrays for the NACA 0012 airfoil with straight trailing edge at $\alpha = 0°$ and $V_\infty = 30$ m/s [6].

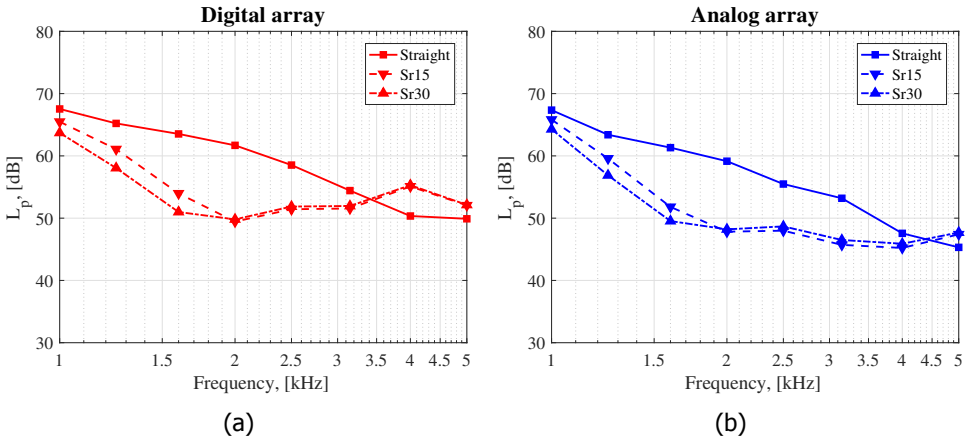

Figure 6.18: Integrated sound spectra for the three trailing–edge geometries for the NACA 0018 airfoil at $\alpha = 0°$ and $V_\infty = 40$ m/s for: (a) the *Digital* array and (b) the *Analog* array [6].

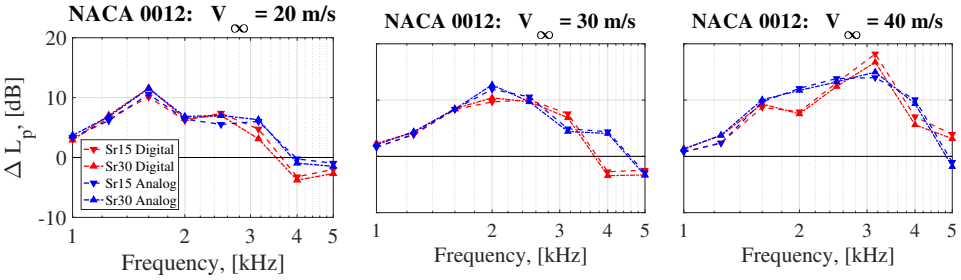

Figure 6.19: Relative integrated sound spectra with respect to the straight trailing edge for both serration geometries and both microphone arrays for the NACA 0012 airfoil at $\alpha = 0°$ and freestream velocities of 20, 30 and 40 m/s (from left to right) [6].

reduction levels ΔL_p are presented. As in section 6.1.1, $\Delta L_p > 0$ corresponds to a noise reduction and vice versa.

Figure 6.19 depicts the ΔL_p values for the NACA 0012 airfoil at $\alpha = 0°$ and freestream velocities V_∞ of 20, 30 and 40 m/s (from left to right). It can be observed that when the freestream velocity increases, the frequency at which the maximum noise reduction is obtained increases. This behavior agrees with the theory [13] and with the trends observed in Fig. 6.7 for similar serrations. The maximum ΔL_p also increases with V_∞, up to a maximum of about 16 dB at 40 m/s. Both microphone arrays show similar results for the whole frequency range of interest, except at 2 kHz, where the *Digital* array presents a lower noise reduction. Another interesting difference is that for $V_\infty = 20$ m/s and $V_\infty = 30$ m/s, the results from the *Digital* array show negative values of ΔL_p for 4 kHz and 5 kHz, i.e., a noise increase. The *Analog* array only presents minor noise increases at 5 kHz which can be due to accuracy reasons and the poorer SNR at that frequency. Both serration geometries seem to provide similar noise–reduction performances, with the *Sr30* configuration performing slightly better than the *Sr15* in most cases up to 3 kHz.

Figure 6.20 illustrates the ΔL_p values for the NACA 0018 airfoil at $\alpha = 0°$ and freestream velocities of 20, 30 and 40 m/s (from left to right). Once again, when the freestream velocity increases, the frequency at which the maximum noise reduction is obtained increases. This time, a maximum ΔL_p value of about 12 dB is obtained. For this configuration, larger differences are present between the results of both arrays, especially at 1.6 kHz and $V_\infty = 20$ m/s and for frequencies higher than 2.5 kHz in the case with $V_\infty = 40$ m/s. In general, the *Digital* array shows higher noise reductions for frequencies between 1.2 kHz and 2 kHz but lower (and even negative) ΔL_p values for frequencies higher than 3 kHz. In this case, the *Sr30* geometry also shows slightly better performance than the *Sr15*, especially at low frequencies.

The higher noise reduction levels obtained by the NACA 0012 airfoil compared with the NACA 0018 airfoil are probably because of the different pressure gradient (due to the lower thickness of the first) and, therefore, a closer resemblance to a flat plate [13, 17] for the NACA 0012 airfoil.

Figures 6.21 and 6.22 present the noise reductions ΔL_p obtained by the *Sr30* serrations measured by both microphone arrays for the NACA 0012 and NACA 0018

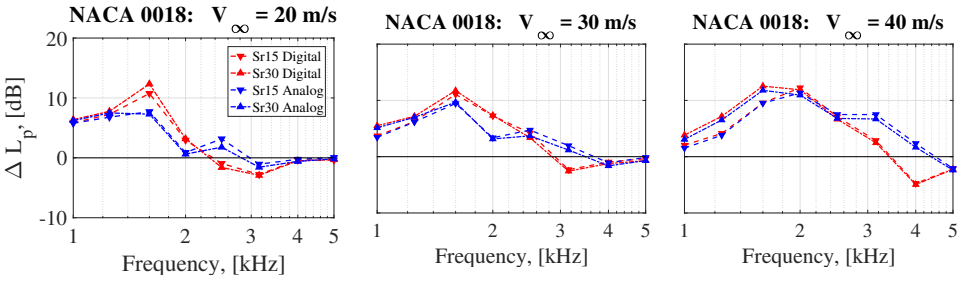

Figure 6.20: Relative integrated sound spectra with respect to the straight trailing edge for both serration geometries and both microphone arrays for the NACA 0018 airfoil at $\alpha = 0°$ and freestream velocities of 20, 30 and 40 m/s (from left to right) [6].

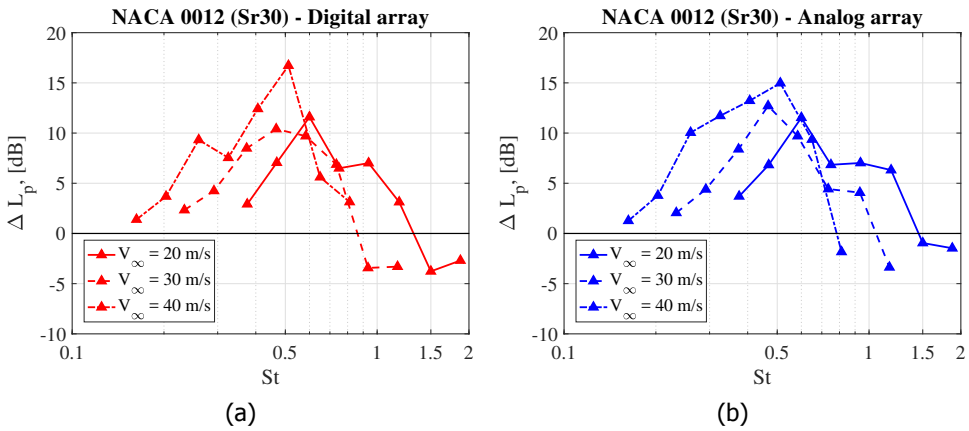

Figure 6.21: Relative integrated sound spectra for the *Sr30* serrations with respect to the straight trailing edge for the NACA 0012 airfoil at $\alpha = 0°$ with respect to the Strouhal number St based on δ_{95} for: (a) the *Digital* array. (b) the *Analog* array [6].

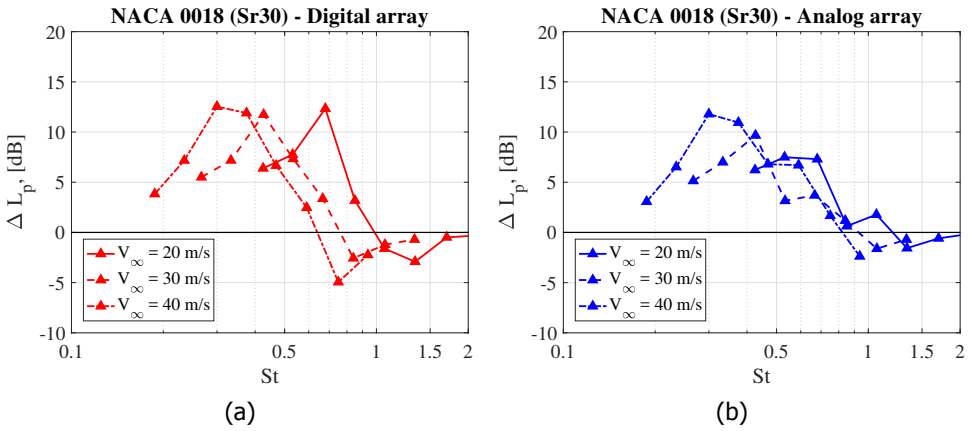

Figure 6.22: Relative integrated sound spectra for the *Sr30* serrations with respect to the straight trailing edge for the NACA 0018 airfoil at $\alpha = 0°$ with respect to the Strouhal number St based on δ_{95} for: (a) the *Digital* array. (b) the *Analog* array [6].

airfoils, respectively. In this case, the frequency axes are expressed in terms of the Strouhal number based on the boundary layer thickness (see Table 6.1) $St = f\delta_{95}/V_\infty$. Only the *Sr30* geometry was considered for simplicity reasons and because similar results were obtained for the *Sr15* case, see Figs. 6.19 and 6.20.

For both airfoils, the maximum noise reductions are obtained for a Strouhal number of about $St \approx 0.5$ for both microphone arrays. This Strouhal number agrees well with the findings by Arce León et al. [1, 2]. In general, higher freestream velocities lead to higher noise reductions. For the NACA 0018 airfoil, the spectrum for the case of $V_\infty = 20$ m/s measured by the *Digital* array (Fig. 6.22a) does not seem to collapse well with the spectra corresponding to the other two freestream velocities. Thus, there is a considerable spread in the values of the crossover Strouhal number. A slightly better collapse is found for the *Analog* array results (Fig. 6.22b). The crossover Strouhal numbers in this case show a somewhat better agreement with the expected value of $St \approx 1$ found by Gruber [14].

The frequency spectra measured by both arrays for the NACA 0018 airfoil with straight trailing–edge at $\alpha = 0°$ and $V_\infty = 40$ m/s were compared with the experimental results by Arce León et al. [1] (see section 6.1.1) and computational results by Avallone et al. [36] for the same airfoil and conditions, see Fig. 6.23. These computational results were already presented in Fig. 6.11 using a scale factor. The results from literature were scaled to consider the same airfoil span $b = 0.7$ m. The computational data were obtained by applying the LBM [15, 42] (see section 1.3.3) and propagating the far–field solution using the FW–H [43] analogy.

It can be observed that the *Analog* array presents a closer agreement to the results from literature, especially to those from Arce León et al., with differences up to 3 dB. The *Digital* array, on the other hand, presents a similar trend but with slightly higher values (about 4 dB) with respect to the literature cases, especially at higher frequencies. The cause of this offset might be the higher presence of

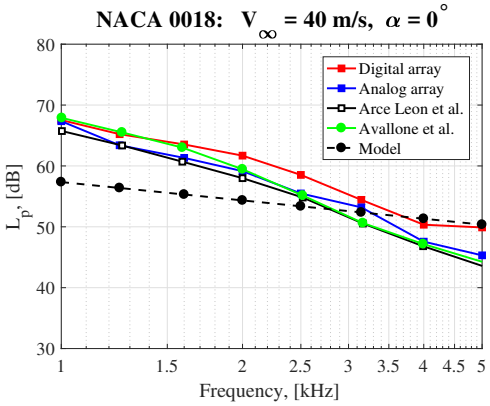

Figure 6.23: Integrated sound spectra for the NACA 0018 airfoil with straight trailing–edge at $\alpha = 0°$ and $V_\infty = 40$ m/s measured by both arrays, experimental results by Arce León et al. [1], computational results by Avallone et al. [36] and predictions using the model by Lockard and Lilley [44] for the same airfoil and conditions [6].

sidelobes for the *Digital* array results (see Fig. 6.17b) which causes an increase in the numerator in Eq. (4.9), whereas the denominator remains constant.

Moreover, the predicted sound spectrum by the model for clean airfoils within turbulent flows developed by Lockard and Lilley [44, 45] (see section 2.3.3) for a straight wing of the same dimensions and at $\alpha = 0°$ and $V_\infty = 40$ m/s, and same observer position, is also included in Fig. 6.23 for comparison. Similar orders of magnitude in the noise levels with respect to the experimental data are observed, but the predicted spectrum presents a lower decrease in levels for increasing frequencies. These differences can be explained because no information about the airfoil cross section is used by the method by Lockard and Lilley, which was originally developed considering flat plates [45].

The ΔL_p values obtained with the *Analog* array show a better agreement with those obtained by Arce León et al. [1] (see section 6.1.1) and Avallone et al. [36], but, in general, higher noise reduction values are measured in the current experiment. This is likely to be due to the considerably longer serration lengths used in this experiment, compared to the ones found in [1] and in [36], which were 10% and 20% of the airfoil chord (i.e., 20 mm and 40 mm), respectively. As aforementioned, in general, longer serrations are expected to provide higher noise reductions [13].

As a last comparison between the results obtained by both microphone arrays, the correlation between the measured trailing–edge noise levels and the flow velocity V_∞ is investigated for both airfoils. Figure 6.24 presents the measured overall L_p values ($L_{p,overall}$) values for the frequency range of interest and for the straight–trailing–edge baseline with respect to the flow velocity, as well as the expected 5^{th} power law dependence of the acoustic power with the flow velocity for this type of sound sources [33, 34], see section 2.3.2.

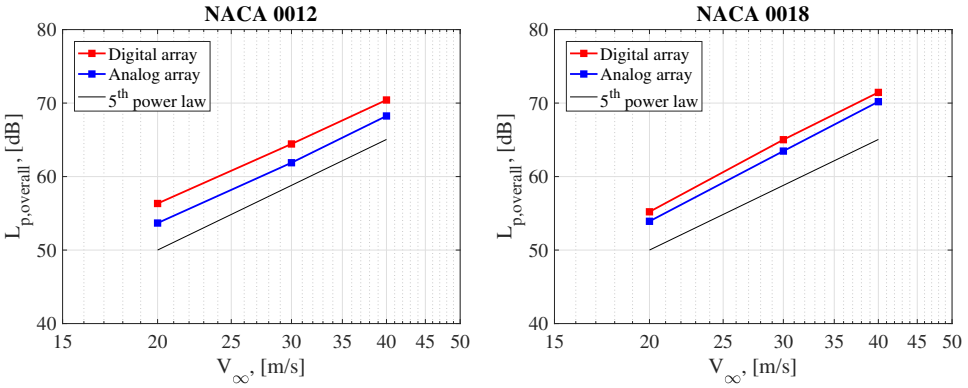

Figure 6.24: $L_{\text{p,overall}}$ trailing–edge noise values measured by both arrays for the straight–trailing–edge case at $\alpha = 0°$ with respect to the flow velocity for: (a) NACA 0012 and (b) NACA 0018 airfoils [6].

The $L_{\text{p,overall}}$ results of both arrays are similar (with the *Digital* array results slightly about 2 dB higher) and agree very well with the 5^{th} power law. The results of the NACA 0018 present a constant positive offset of approximately 2 dB with respect to those of the NACA 0012, which is explained by its higher thickness.

6

6.1.3. Study of a cambered airfoil in a closed test section at high Reynolds number

Experimental setup

The measurements were conducted at the low–turbulence wind tunnel (LTT) at Delft University of Technology, which has a contraction ratio of approximately 17.8:1 and a turbulence intensity between 0.04% at 20 m/s and 0.1% at 75 m/s [5]. The tunnel has an octagonal closed test section of 1.8 m width, 1.25 m height and 2.6 m length, see Fig. 6.25a. This test setup resembles the one of the simulated benchmark case treated in section 4.17.

The test model consisted of a DU96–W–180 airfoil with a span $b = 1.25$ m and a chord $\hat{c} = 0.6$ m installed vertically and flush mounted to the tunnel section, see Fig. 6.25a. Two different serration geometries were tested in this experiment:

- **Short solid serrations** with $\lambda_s = 15$ mm and $2\,h_s = 0.05\,\hat{c} = 30$ mm. Henceforth these serrations are referred to as *Sr05*.
- **Long solid serrations** with $\lambda_s = 45$ mm and $2\,h_s = 0.15\,\hat{c} = 90$ mm. Henceforth these serrations are referred to as *Sr15*. This serration design has a length approximately equal to five times the boundary layer thickness, and according to Gruber et al. [13], minor improvements in the noise reductions achieved by the *Sr05* design are to be expected.

Both serrations were manufactured in steel, had the same aspect ratio as considered before in sections 6.1.1 and 6.1.2 ($2\,h_s/\lambda_s = 2$), see Fig. 6.25b, a thickness

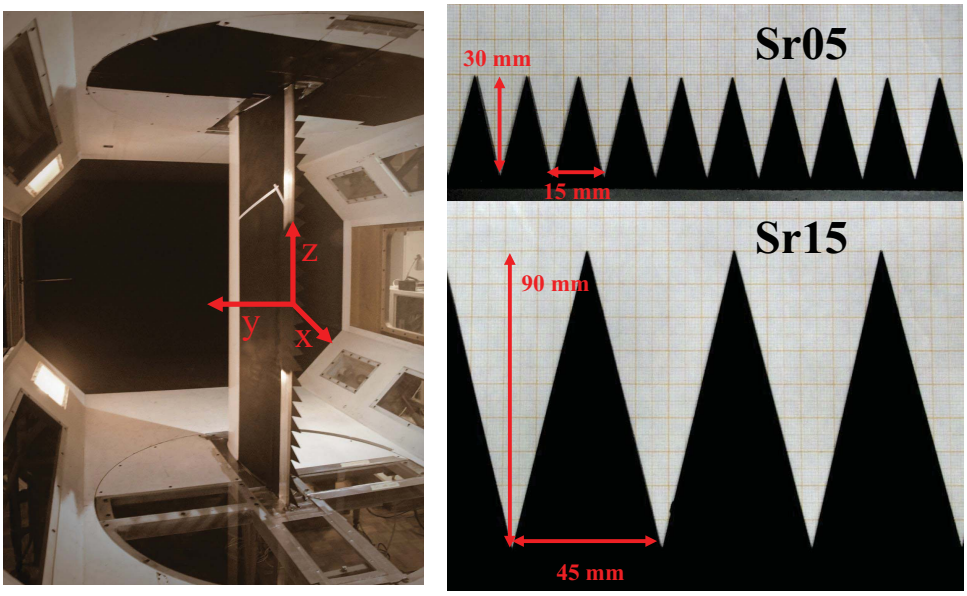

(a) (b)

Figure 6.25: (a) Experimental setup showing the airfoil in the LTT and the coordinate system used. (b) Serration geometries employed [5].

of 1.5 mm and a misalignment angle of $\varphi_s = 6°$.

The coordinate system employed for the experiment is illustrated in Fig. 6.25a, with the x axis in the downwind streamwise direction, the z axis in the spanwise direction pointing up, the y axis perpendicular to both pointing at the microphone array, and the origin in the center of the straight trailing edge.

Several freestream velocities and angles of attack were tested [5], but in this chapter only results corresponding to $V_\infty = 37.4$ m/s, $\alpha = -2°$ (zero–lift angle) and $\alpha = 6°$ are presented. These conditions correspond to a Reynolds number of 1.5×10^6 and a Mach number of 0.11. Transition from laminar to turbulent regime in these conditions occurs in a natural way [5, 20].

The same phased microphone array employed in the experiments of sections 6.1.1 and 6.1.2 was rearranged in a multi–arm logarithmic spiral configuration with an elliptical shape [46], with a major axis of 0.93 m, see Fig. 6.26. The array was located at a distance of $h = 0.9$ m away from the trailing edge (facing the suction side of the airfoil) in the y direction. The center of the array ($x = z = 0$) was aligned in the streamwise direction with the root of the serrations at the trailing edge. The microphones were recessed 20 mm deep along one of the walls of the wind tunnel behind an acoustically–transparent flat Kevlar window in order to alleviate the effect of the turbulent boundary layer convecting along the wall [5], see section 3.1.1.

For each measurement, data were acquired for 30 s at a sampling frequency of 50 kHz and averaged using time blocks of 2048 samples ($T_h = 40.96$ ms) and

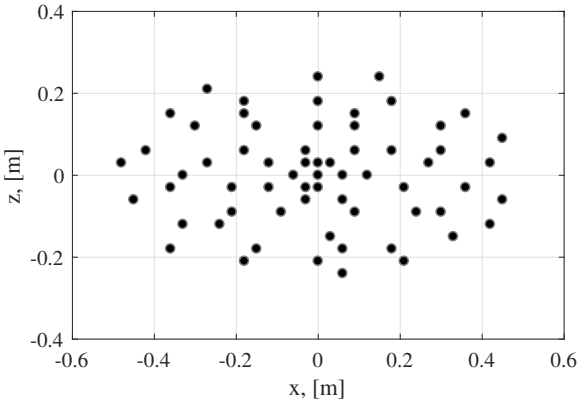

Figure 6.26: Microphone distribution for the LTT measurements. Adapted from [5].

windowed using a Hanning weighting function with 50% data overlap. With these values, the frequency resolution is $\Delta f \approx 24.41$ Hz. The selected sound frequency range of interest was again from 1 kHz to 5 kHz. The main diagonal of the CSM was removed in order to mitigate the effect of the incoherent background noise from the wind tunnel.

In addition to the acoustic measurements with the phased microphone array, stereoscopic PIV measurements were performed to obtain the boundary layer flow characteristics in the vicinity of the trailing edge. The specific parameters used can be found in [5].

Computational simulations

Computational simulations on the same model geometry under similar flow characteristics and employing the LBM, see section 1.3.3, were performed using the commercial software package Exa PowerFLOW 5.3c. A discretization consisting in 19 discrete velocities in three dimensions (D3Q19) was employed and a Very Large Eddy Simulation (VLES) was implemented as viscosity model. A turbulent wall–model was used to resolve the near–wall region [5] and to obtain estimates of the boundary layer parameters. The sound pressure field was obtained directly from the computational domain and propagated using the FW–H analogy, see section 1.3.3. In total, the grid used in this study contained 60 million voxels, with 8 different refinement regions around the airfoil and a minimum size (around the trailing edge) of 3.52×10^{-4} m. Simulations were run for a physical time of 0.3 s (approximately 20 flow passes). A total of 10 flow passes were used for this analysis and data were recorded at a sampling frequency of 26 kHz. A total of 1350 CPU hours were necessary on a Linux Xeon E5–2690 2.9 GHz platform with 20 cores. More information about the computational method used and the simulation parameters can be found in [5].

Transition from laminar to turbulent regime occurs naturally as in the experiments. The boundary layer characteristics calculated computationally were similar

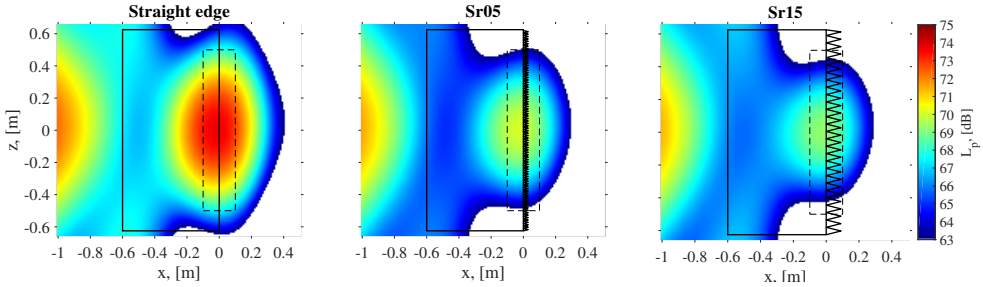

Figure 6.27: CFDBF source maps obtained for the straight trailing edge (left), the *Sr05* serrations (center), and the *Sr15* serrations (right). The results correspond to a freestream velocity of 37.4 m/s and $\alpha = 6°$, $Re = 1.5 \times 10^6$, and a one–third–octave frequency band centered at 2 kHz. The airfoil location is denoted by a solid rectangle and the ROI by a dashed rectangle. Adapted from [5].

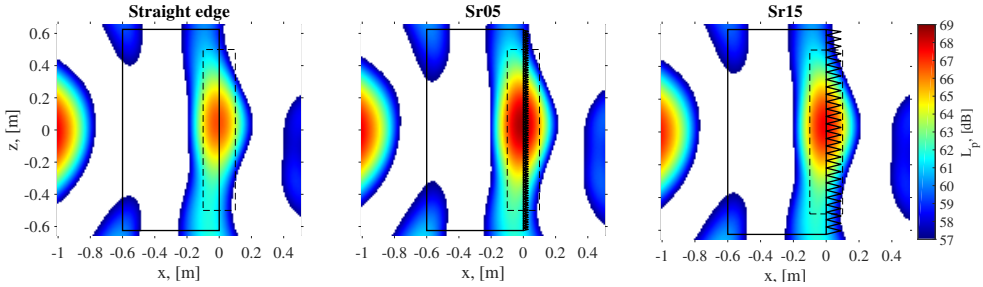

Figure 6.28: CFDBF source maps obtained for the straight trailing edge (left), the *Sr05* serrations (center), and the *Sr15* serrations (right). The results correspond to a freestream velocity of 37.4 m/s and $\alpha = 6°$, $Re = 1.5 \times 10^6$, and a one–third–octave frequency band centered at 4 kHz. The airfoil location is denoted by a solid rectangle and the ROI by a dashed rectangle. Adapted from [5].

to those obtained by PIV measurements, with a better agreement for the case of $\alpha = -2°$ [5].

Results and discussion

Two examples of the CFDBF source plots obtained for the three trailing edge configurations (straight trailing edge, *Sr05* and *Sr15*) at the one–third–octave frequency bands centered at 2 kHz and 4 kHz are presented in Figs. 6.27 and 6.28, respectively. Both figures correspond to $\alpha = 6°$ and $V_\infty = 37.4$ m/s (i.e., $Re = 1.5 \times 10^6$). If the peak values in the beamforming maps are considered, noise reductions (with respect to the straight–edge baseline) of approximately 3 dB and 4 dB are observed for the *Sr05* and *Sr15*, respectively for 2 kHz (Fig. 6.27). For the case of 4 kHz (Fig. 6.28), on the other hand, noise increases of around 3 dB and 2 dB are measured for the *Sr05* and *Sr15*, respectively. These values agree with those observed by Oerlemans et al. [47] in field measurements on full–scale wind turbines, where the serrated trailing edge caused a noise increase after a crossover frequency.

As in the previous sections in this chapter, the frequency spectra of the TBL–TE noise emissions were calculated by integrating the CFDBF source plots in a

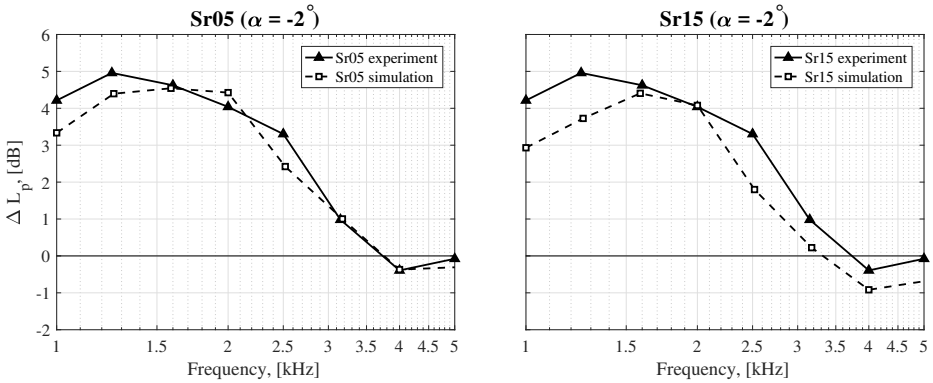

Figure 6.29: Relative integrated sound spectra for both serration geometries (*Sr05* and *Sr15*) with respect to the straight trailing edge for $V_\infty = 37.4$ m/s and $\alpha = -2°$. Adapted from [5].

ROI using the SPIL technique, see sections 4.2.2 and 4.17. For this experiment a spacing between grid points of $\Delta x = 1$ mm and a ROI extending from $x = -0.1$ m to $x = 0.1$ m and from $z = -0.5$ m to $z = 0.5$ m was selected for all the trailing–edge configurations (depicted as a dashed rectangle in Figs. 6.27 and 6.28). This ROI covered the whole serration length for both geometries and prevented the influence of potential corner sources in the junctions of the airfoil due to the interaction of the boundary layer of the wind tunnel with the airfoil side edges [31, 32]. This type of unwanted noise sources can be seen in Fig. 6.28 on the junctions of the leading edge with the tunnel wall. A simulated line source was considered at the trailing edge position ($x = 0$ m and from $z = -0.5$ m to $z = 0.5$ m).

The noise reductions ΔL_p for the frequency range of interest (with respect to the straight–trailing–edge baseline) obtained by the two serration geometries are presented in Figs. 6.29 and 6.30 for $\alpha = -2°$ and $\alpha = 6°$, respectively. As in the previous sections in this chapter, positive values indicate noise reduction and vice versa. Both the results obtained from the integrated CFDBF source plots and the LBM simulations are shown in the same plot.

In Fig. 6.29 (corresponding to $\alpha = -2°$) noise reductions up to approximately 5 dB and 4 dB are achieved between 1 kHz and 2 kHz by the *Sr05* and *Sr15* serrations, respectively. The agreement between the simulated and experimental results is very close for both serration designs, showing a decay in the noise reduction performance for increasing frequency, leading even to some noise increase after a crossover frequency of approximately $f_{crossover} \approx 3800$ Hz. This noise increase is supposed to be due to the flap angle of the serrations $\varphi_s = 6°$, as it was mentioned in section 6.1.1. Similar noise reduction values were observed in [13] for a similar experiment.

In Fig. 6.30 (corresponding to $\alpha = 6°$) similar trends are observed as in Fig. 6.29 but with lower noise reduction values for the whole spectrum, reaching maximums of approximately 3 dB for both serration geometries. Once again, a noise increase of around 1 dB is observed after a crossover frequency (this time $f_{crossover} \approx 3$ kHz).

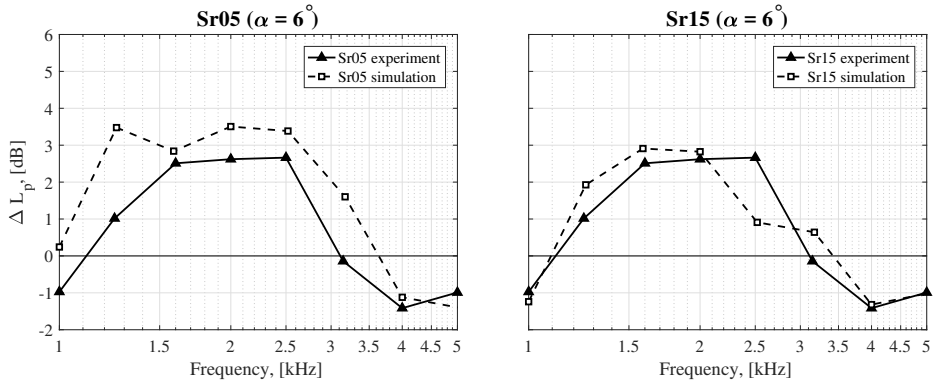

Figure 6.30: Relative integrated sound spectra for both serration geometries (*Sr05* and *Sr15*) with respect to the straight trailing edge for $V_\infty = 37.4$ m/s and $\alpha = 6°$. Adapted from [5].

In general, the agreement between experimental and simulated results is worse in this case, which could be explained by the larger differences found between the boundary–layer characteristics measured with PIV and those calculated with the LBM method [5].

The LBM simulations provide the sound radiation directivity pattern of the TBL–TE noise with respect to the emission angle with respect to the trailing edge θ_{TE}, see Fig. 2.10 in Chapter 2. Figure 6.31 illustrates the radiation directivity plots for the three trailing–edge geometries at a distance of 10 airfoil chords ($10\hat{c}$) for the case with $\alpha = -2°$ and $Re = 1.5 \times 10^6$ banded in three frequency ranges: 500 Hz to 1 kHz, 1 kHz to 2 kHz, and 2 kHz to 5 kHz. The radial magnitude in Fig. 6.31 is the raw far–field pressure normalized by the straight–trailing–edge baseline configuration [5]. In general, both serration designs provide considerable noise reductions at all angles, especially in the upstream direction ($120° \leq \theta_{TE} \leq 150°$). The directivity pattern exhibits a convective dipole oriented towards the leading edge, which agrees with the expected diffraction pattern for these cases [48], see section 2.3.2.

6.2. Trailing–edge porous inserts

The use of inserts made of porous materials (see Fig. 6.32) for reducing TBL–TE noise has already been addressed in the literature [18, 49–53]. Promising noise–reduction results were obtained with different porous materials, especially at low frequencies. However, a noise increase was also observed for high frequencies [50, 51].

The results presented in this section belong to a recent extensive experimental campaign performed at Delft University of Technology which featured a full characterization of the porous material properties [8], a detailed analysis of the flow parameters around the porous inserts [9] (obtained using PIV) and a parametric study including different porous materials, flow velocities and angles of attack. One of the main physical features analyzed in the aforementioned campaign was the ef-

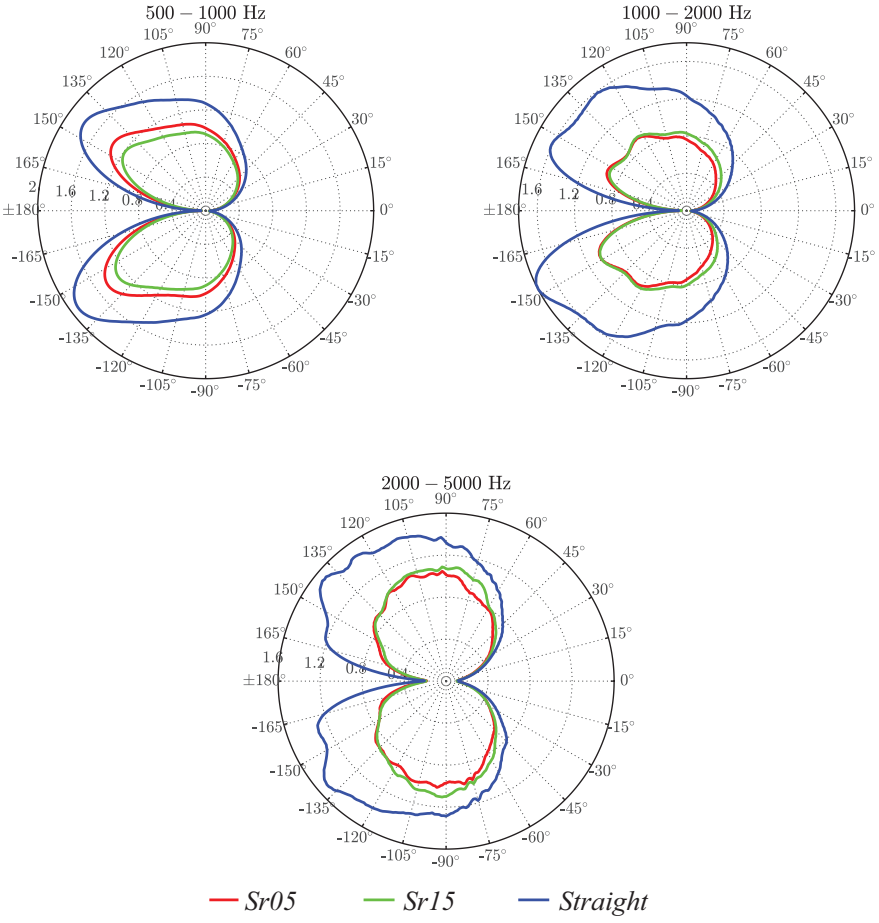

Figure 6.31: Sound radiation directivity plots for 500 Hz to 1 kHz (left), 1 kHz to 2 kHz (right), and 2 kHz to 5 kHz (bottom) for the three trailing–edge geometries and $\alpha = -2°$ and $Re = 1.5 \times 10^6$. Adapted from [5].

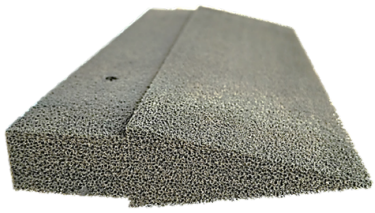

Figure 6.32: Metal foam trailing–edge insert used in the experiment. The total length of the insert is 60 mm. Extracted from [54].

fect of the cross–flow (or permeability) in the obtained noise reductions [54], in order to obtain more information about the noise generation mechanisms.

Discussing all these aspects is certainly out of the scope of this thesis. Therefore, only a small portion of the gathered experimental data was selected for further analysis in this chapter, featuring a single porous material, angle of attack and flow velocity. The other main purpose of this section is to evaluate the performance of the SPIL method (see section 4.2.2) by applying it to experimental data. A validation using synthetic data was already presented in section 4.17 and showed that the SPIL method provided the best results compared to other well–known acoustic imaging methods.

6.2.1. Experimental setup

The measurements were performed at the anechoic vertical wind tunnel (A–tunnel) at Delft University of Technology, which is the refurbished version of the V–tunnel employed for the experiments explained in section 6.1.1. For information about the aeroacoustic characterization of the A–tunnel, see Appendix E. The new tunnel has a contraction ratio of approximately $15:1$. For this experiment, a rectangular test section of 0.4 m $\times$ 0.7 m was used with a freestream velocity uniform within 0.5% and a turbulence intensity below 0.1% for the entire velocity range [8].

A similar NACA 0018 airfoil as the one tested in section 6.1.1 was employed, manufactured in aluminum and with a chord $\hat{c} = 0.2$ m and a span of $b = 0.4$ m, equal to the test section width. The model was manufactured in aluminum using Computer Numerical Control (CNC) machining, ensuring that the surface roughness was below 0.05 mm. The airfoil was installed in an open test section between two wooden plates of 1.2 m length, to ensure the two–dimensionality of the flow over most of the wing span [20]. The airfoil leading edge was located 0.5 m away from the outlet of the wind–tunnel nozzle, see Fig. 6.33a.

The transition to turbulent boundary layer was forced using a similar tripping tape as in section 6.1.1, but with carborundum elements with a nominal size of 0.84 mm, placed on a tape of 10 mm width centered at $0.2\,\hat{c}$ that covered the whole airfoil span on both sides of the airfoil. The turbulent nature of the boundary layer was assessed using a remote wall–pressure probe.

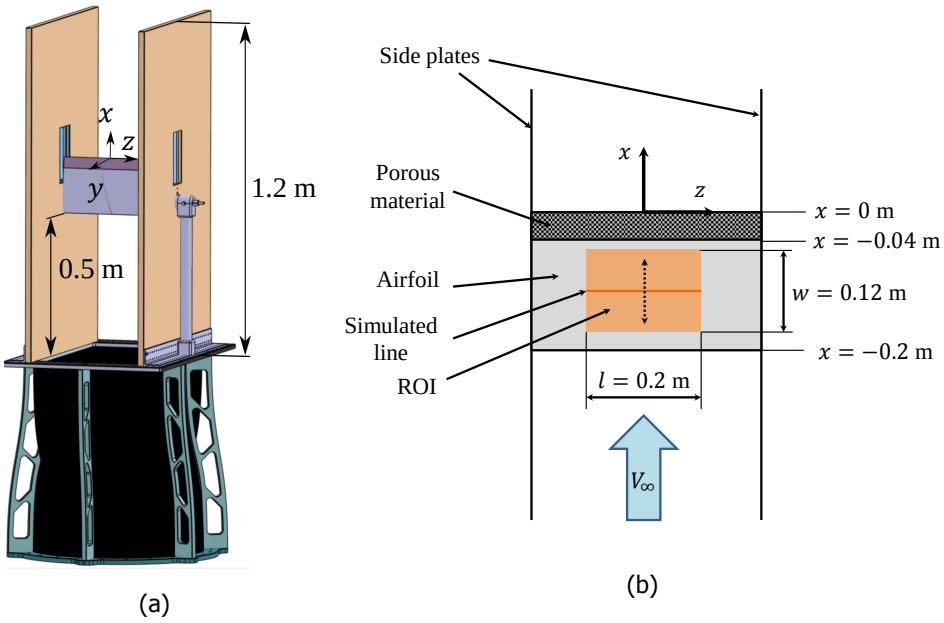

Figure 6.33: (a) Illustration of the experimental setup in the A–-tunnel indicating the coordinate system. (b) Schematic view of the experimental setup and the location of the ROI (shaded in orange) for the trailing–edge noise measurements. Extracted from [7].

The airfoil allowed the installation of exchangeable inserts at the trailing edge with an extent of 20% of the airfoil chord (40 mm), see Fig. 6.32. The insert employed in the present experiment was fabricated with *Alantum* NiCrAl metal foam, with cell diameter $d_c = 800\mu$m and permeability $\hat{K} = 27 \times 10^{-10}$ m^2. This material was selected since it provided the highest noise reductions in the experiment performed by Rubio Carpio et al. [8]. The reader is referred to Rubio Carpio et al. [9] for a detailed description of the topology and characterization of this material and for additional results featuring other porous materials.

The coordinate system for this experimental campaign was the same as in section 6.1.1 and is depicted in Fig. 6.33a, with the x axis in the streamwise direction, the y axis normal to the mean camber plane of the airfoil pointing at the microphone array, the z axis in the spanwise direction, and the origin located in the center of the trailing edge.

The freestream velocity analyzed in this section corresponded to 30 m/s, providing a Mach number of 0.088 and a chord–based Reynolds number of 3.95×10^5. The airfoil was set at a geometric angle of attack of $\alpha = 0°$ using a digital angle meter [54].

An acoustic array consisting of 64 microphones was used for measuring the far–field noise emissions of the airfoil, see Fig. E.1b. The diameter of the array is approximately 2 m and the distance from the array plane to the trailing edge (for $\alpha = 0°$) was 1.43 m, in a similar configuration as illustrated before in Fig. 6.1a. The

center microphone was approximately aligned with the center of the trailing edge of the airfoil, with coordinates $(x, y, z) = (-0.1, 1.43, 0.014)$ m. More information about the microphone array can be found in Appendix E.1.

For each measurement a sampling frequency of 50 kHz and 60 s of recording time were used. The acoustic data were averaged in time blocks of 8192 samples ($T_h = 163.84$ ms) and windowed using a Hanning weighting function with 50% data overlap, again following Welch's method (see Appendix C.3). With these parameters, the frequency resolution is $\Delta f \approx 6.1$ Hz. The frequency range of interest for this research extended from 500 Hz to 4 kHz.

For beamforming, a scan grid covering a region ranging from $z = -0.4$ m to $z = 0.4$ m and from $x = -0.4$ m to $x = 0.4$ m was used with a spacing between grid points of $\Delta x = 1$ mm. The results with a grid spacing of 10 mm were also analyzed and presented negligible differences (see section 4.17.3). The diagram in Fig. 6.33 shows the position of the airfoil and the porous insert, as well as the coordinate system. The shape of the ROI is also depicted as an orange rectangle with $w = 0.12$ m and $l = 0.2$ m, placed symmetrically with respect to the x axis and located at a random x position.

6.2.2. Results and discussion

Figure 6.34 depicts two CFDBF source plots for the trailing–edge noise measurements in the wind tunnel: one for the solid trailing edge (Fig. 6.34a) and one for the porous trailing edge (Fig. 6.34b). Both plots correspond to a flow velocity of $V_\infty = 30$ m/s, an angle of attack of $\alpha = 0°$ and a one–third–octave band with center frequency of 1600 Hz. It can be observed that the trailing edge is indeed the dominant noise source in both cases and that the application of the porous insert in the trailing edge causes a noise reduction in the peak values of about 3 dB for this frequency band. It can be observed that the source plots in Fig. 6.34 present lower sidelobe levels than those in Fig. 4.19, since the SNR in the experiment was considerably higher than in the simulated line–source benchmark case.

Following the guidelines proposed in section 4.17.3, Fig. 6.35a shows the $L_{\text{p,overall}}$ values corresponding to the frequency range of interest (500 Hz to 4 kHz) obtained with the SPIL technique plotted with respect to the selected value of the location of the simulated line source (x_0) for both the solid and the porous trailing edges. The location of the maximum $L_{\text{p,overall}}$ value is denoted with a red asterisk in each case. Compared with the analogous results shown in Fig. 4.25d, the curves in Fig. 6.35a present a considerably less sharp shape, probably due to the lower frequency range considered. For illustration purposes, the beginning of the porous material insert and the trailing edge are denoted as dashed vertical black lines. It can be observed that the application of the porous insert causes a reduction in the noise emissions of about 5 dB for the frequency range and for the range of x_0 values considered. Interestingly, the location of the maximum $L_{\text{p,overall}}$ value, and hence the most likely position of the line source, also moves upwind several centimeters, approximately to the beginning of the porous material insert ($x \approx -0.04$ m $= 0.2\hat{c}$). This might be due to the acoustic impedance change caused by the presence of the porous insert instead of a solid trailing edge. In other words, the

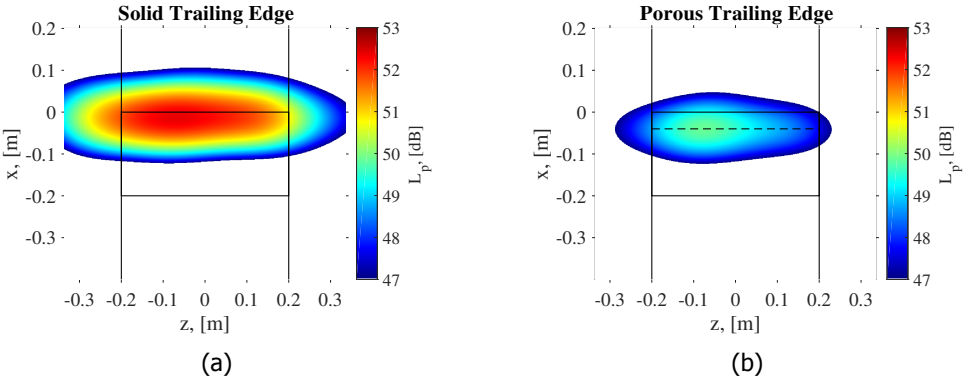

Figure 6.34: CFDBF source plots for a one–third–octave band with center frequency of 1600 Hz for $V_\infty = 30$ m/s and $\alpha = 0°$ for (a) the solid trailing edge baseline (b) the porous trailing edge. The dashed line indicates the beginning of the porous material insert. Extracted from [7].

permeable–impermeable junction would act as a trailing edge, i.e., as a contributor to the noise generated, as described by Kisil and Ayton [55].

In order to study this phenomenon in detail, the x_0 values for which the maximum $L_{\text{p,overall}}$ is observed are plotted in Fig. 6.35b with respect to the frequency for both trailing edges. The aforementioned offset in x_0 when applying the porous material insert is also observed throughout all the frequency range considered. Moreover, it can be observed that for the lower frequencies (below 1200 Hz) the estimated location of the line source in the x direction moves upwind up to about 0.08 m ($\approx 0.4\hat{c}$). The porous trailing edge presents a sudden increase of the x_0 values around 800 Hz. The cause for this behavior remains unknown and will be subject of future research.

With the calculated values of x_0 presented in Fig. 6.35b, the trailing–edge noise emissions can be estimated using Eq. (4.9) and scaled to decibels using Eq. (4.40). Figure 6.36 depicts the estimated noise emissions for both trailing–edge cases using the chord–based Strouhal number, $St = f\hat{c}/V_\infty$. Noise reductions due to the porous material insert are observed until a crossover Strouhal number of $St \approx 14$, which corresponds to a frequency of about 2100 Hz. After that frequency, the porous trailing edge seems to cause a noise increase. Similar behaviors were observed in previous studies in the literature [8, 9, 50, 51, 54].

Figure 6.37 shows the relative noise reductions $\Delta L_\text{p} = L_{\text{p,solid}} - L_{\text{p,porous}}$ achieved by the application of the porous material insert with respect to the solid baseline. As in previous sections, positive values of ΔL_p correspond to noise reductions and vice versa. The narrow–band results with respect to the chord–based Strouhal number are presented in Fig. 6.37a and the ΔL_p values for each one–third–octave band considered are depicted in Fig. 6.37b. Maximum noise reductions, up to approximately 10 dB, are obtained at a frequency of about 800 Hz ($St \approx 5$). After the crossover frequency of about 2100 Hz ($St \approx 14$), the porous insert causes a noise increase that becomes larger for higher frequencies, up to a 4 dB noise increase at 4 kHz ($St \approx 27$). The cause of this noise increase was suggested

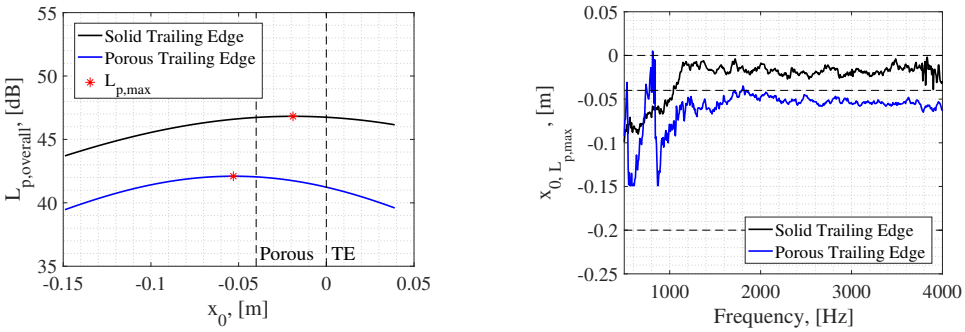

Figure 6.35: (a) $L_{\text{p,overall}}$ values obtained with respect to the considered location of the line source x_0 for both trailing edges. (b) Estimated locations of the line source (x_0) per frequency and for both trailing edges. The dashed black lines indicate the positions of the leading edge ($x = -0.2$ m), the beginning of the porous material ($x = -0.04$ m) and the trailing edge ($x = 0$ m). Extracted from [7].

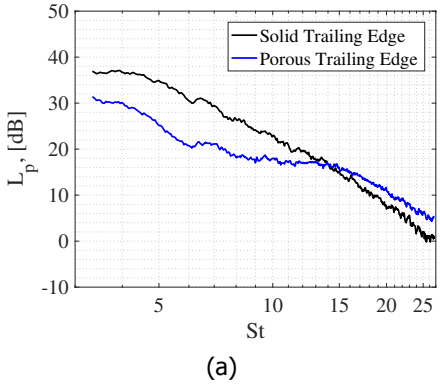

Figure 6.36: Integrated (using the SPIL technique) narrow–band spectra of the trailing–edge noise for both cases at $V_\infty = 30$ m/s and $\alpha = 0°$. The results are presented with respect to the chord–based Strouhal number. Extracted from [7].

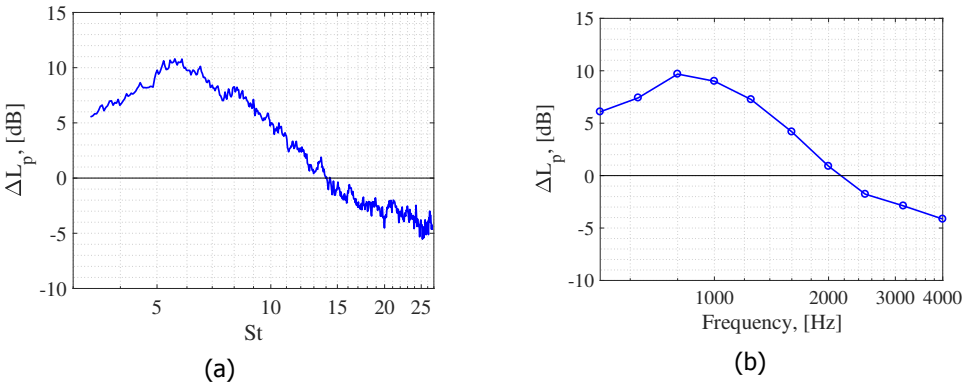

Figure 6.37: Relative noise reductions achieved by the porous trailing edge at $V_\infty = 30$ m/s and $\alpha = 0°$. Results presented in (a) narrow–band frequencies with respect to the Strouhal number and (b) one–third–octave bands. Extracted from [7].

to be due to the additional roughness present in the porous material, which is expected to generate high–frequency noise [50, 51]. This fact was confirmed by the experimental campaign by Rubio Carpio et al. [54].

Lastly, the effect of the cross–flow (or permeability) through the porous material insert was investigated by testing a similar porous trailing edge (i.e., same material, cell diameter, etc.) that had an adhesive layer applied in the symmetry plane ($y = 0$) to avoid the cross–flow through the pressure and suction sides. Figure 6.38 shows the ΔL_p values obtained by both porous inserts (analogously to Fig. 6.37a). Interestingly, the non–permeable porous insert barely offers any noise reduction at low frequencies, whereas the noise increase after the crossover frequency is still observed. This seems to indicate that the cross–flow through the insert is indeed the mechanism that causes the noise reductions and supports the hypothesis that the roughness of the porous insert is the cause of high–frequency noise. On the other hand, negligible changes were observed in the characteristics of the boundary layer at the porous trailing edge or in the upstream pressure distribution [8, 54]. Additional results and more detailed explanations can be found in [54].

6.3. Conclusions and outlook

6.3.1. Trailing–edge serrations

According to the findings of the three experimental campaigns analyzing the performance of trailing–edge serrations for the reduction of TBL–TE noise, some conclusions can be drawn about the influence of certain design parameters:

- **Serration geometry**: As a rule of thumb, longer serrations provide higher noise reductions. The *Slit* geometry tested did not perform as well as in the literature, but the *Hybrid* serration design worked similarly and even outperformed the solid serrations of the same wetted area. Noise reductions of more than 10 dB were observed for the *Sr30* geometry. The maximum noise

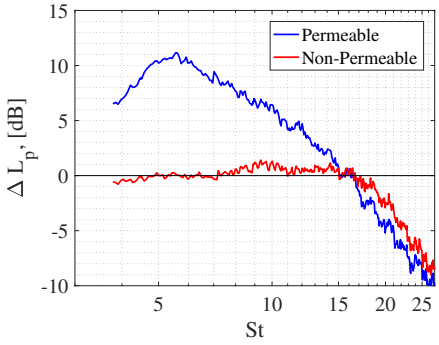

(a)

Figure 6.38: Relative noise reductions achieved by the porous trailing edges (permeable and non–permeable) at $V_\infty = 20$ m/s and $\alpha = 0°$. Results presented in narrow–band frequencies with respect to the chord–based Strouhal number. Adapted from [54].

reductions in these experiments were obtained for $St \approx 0.5$.

- **Serration–flow misalignment angle**: In case a serration–flow misalignment angle occurs, the noise reductions provided by the trailing–edge serrations decrease, even reaching noise increases of several decibels after a certain crossover frequency, whose value increases for increasing flow velocity and decreases for increasing angle of attack. The crossover frequencies seem to correspond to a Strouhal number (based on the TBL thickness) of approximately 1. Thus, special care should be taken when installing serrations on wind turbine blades to avoid this phenomenon.

- **Airfoil shape**: The highest noise reductions were obtained with the thinnest symmetric airfoil tested (the NACA 0012), since it was the model that resembled the pressure gradients of a flat plate the most. In general, it seems that increasing the camber or the thickness of an airfoil reduces the performance of the trailing–edge serrations.

- **Angle of attack**: In general, the presence of an angle of attack causes a loss in performance for all serration geometries of several decibels. Therefore, the serration designs tested in this thesis showed the best performance at $\alpha = 0°$.

- **Flow velocity**: Increasing the flow velocity increases the noise reductions achieved by trailing–edge serrations and displaces the maximum noise reduction towards higher frequencies, corresponding to Strouhal numbers of about 0.5. The expected 5^{th} power law between the noise levels and the flow velocity was also confirmed.

Overall, the comparisons performed with computational simulations show a very close agreement, both in terms of absolute levels and relative noise reductions.

The comparison between the *Analog* and *Digital* microphone arrays in section 6.1.2 showed that they provide similar results, but the *Analog* array presented considerably less sidelobes (i.e., about 5 dB higher dynamic range). Another difference between both arrays is that, according to the *Digital* array, the flow–aligned trailing–edge serrations seem to cause a noise increase after a threshold frequency of about 3.5 kHz, which is not expected from the theory or observed in similar experiments. The *Analog* array does not present such behavior. The differences in performance by the *Digital* array for frequencies higher than 3 kHz might be explained by the fact that digital MEMS microphones are usually optimized for the frequency range in human speech (300 Hz to 3 kHz). The overall cost of a digital array system is typically lower than an analog one. Therefore, the hardware choice mostly depends on the frequency range of interest and the budget available.

Testing trailing–edge serrations in a closed–section wind tunnel allows for the analysis at higher Reynolds numbers (up to 1.5×10^6 in this case) and more controlled aerodynamic conditions, as mentioned in section 3.1.1. However, measuring the absolute noise emissions of a noise source as quiet as serrated–trailing–edge noise becomes a challenge, due to the higher background noise levels present. Despite of that, differences between configurations can still be retrieved in a satisfactory manner.

6.3.2. Trailing–edge porous inserts

The experimental results analyzed in this chapter confirmed the performance of porous materials as noise–reduction measures, especially at low frequencies. Maximum noise reductions of about 10 dB are observed for a chord–based Strouhal number of 5. In general, materials with higher porosities (or cell diameters d_c) seem to provide higher noise reductions [8]. It was argued that the reason for this noise reduction is the cross–flow between the pressure and suction sides of the airfoil (i.e., a reduction in the acoustic impedance) and not by the acoustically absorbent properties of the foam used [54]. It was also observed that the porous inserts do not affect significantly the mean flow field characteristics [54]. However, previous research [56] showed that materials with a higher permeability (i.e., with a lower flow resistivity) presented lower lift and higher drag, and, therefore, a worse overall aerodynamic performance with respect to the solid baseline case.

A noise increase after a certain crossover frequency ($St \approx 14$) is observed and considered to be due to the higher surface roughness of the porous inserts compared to the solid airfoil. The increased roughness is also believed to cause an increase in the boundary layer thickness [54]. Additional results featuring different porous materials, freestream velocities, insert chordwise extensions and angles of attack can be found in [8].

Moreover the performance of the SPIL method was validated experimentally and showed that, when porous inserts are employed, the location of the line source causing the trailing–edge noise moves upwind towards the permeable–impermeable junction. This fact supports the hypothesis that the noise reductions achieved are due to the acoustic impedance change due to the porous insert.

6.3.3. Outlook

Recent research [36, 57] investigated the performance of novel serration geometries, such as combed–sawtooth serrations or concave curved (or *iron–shaped*) serrations, and showed that they can lead to even larger noise reductions than the conventional solid sawtooth serrations analyzed in this chapter. The recent work of several researchers [14–16, 36] provided insight about the physical mechanisms that allow serrations to reduce the trailing–edge noise emissions. However, additional work is recommended such as parametric studies to study the influence of certain design parameters and, especially, the installation effects when placing these devices on full–scale wind turbines under operational conditions [47, 58].

The use of different porous materials featuring different pore sizes, porosities and roughness properties is encouraged since the accurate details about the complex physical mechanisms leading to a noise reduction (or increase) when employing porous inserts in trailing edges are not fully understood yet. Hybrid studies featuring acoustic and aerodynamic measurements, as those presented in [9, 54], are of great interest for simultaneously investigating the acoustic and flow mechanisms that can lead to noise reductions. The practical applicability and aerodynamic performance of porous materials in full–scale wind turbines should also be confirmed carefully, since environmental and weather factors may alter the performance of these devices.

A combination of both concepts, i.e., porous serrations or a porous trailing edge with variable porosity in the spanwise direction is certainly an interesting and promising topic for future research. Some recent publications [59, 60] reported the added value of poro–serrated trailing edges in further reducing the broadband noise levels. Researchers at Delft University of Technology are currently working on this idea (at the time this thesis was written). Moreover, it would be of interest to repeat the experiments performed in an open–jet wind tunnel presented here in a closed–section wind tunnel at higher Reynolds numbers to investigate whether the findings obtained still hold.

Bibliography

[1] C. Arce León, R. Merino-Martinez, D. Ragni, F. Avallone, and M. Snellen, *Boundary layer characterization and acoustic measurements of flow–aligned trailing edge serrations,* Experiments in Fluids **57**, 1 (2016).

[2] C. Arce León, R. Merino-Martinez, D. Ragni, F. Avallone, F. Scarano, S. Pröbsting, M. Snellen, D. G. Simons, and J. Madsen, *Effect of trailing edge serration–flow misalignment on airfoil noise emission,* Journal of Sound and Vibration **405**, 19 (2017).

[3] C. Arce León, R. Merino-Martinez, S. Pröbsting, D. Ragni, and F. Avallone, *Acoustic Emissions of Semi–Permeable Trailing Edge Serrations,* Acoustics Australia **46**, 111 (2017).

[4] C. Arce León, R. Merino-Martinez, D. Ragni, S. Pröbsting, F. Avallone, A. Singh, and J. Madsen, *Trailing Edge Serrations – Effect of Their Flap Angle on Flow*

and Acoustics, in 7th *International Meeting on Wind Turbine Noise, May 2 – 5 2017, Rotterdam, the Netherlands* (2017).

[5] R. Merino-Martinez, W. C. P. van der Velden, F. Avallone, and D. Ragni, *Acoustic measurements of a DU96–W–180 airfoil with flow–misaligned serrations at a high Reynolds number in a closed–section wind tunnel,* in 7th *International Meeting on Wind Turbine Noise, May 2 – 5 2017, Rotterdam, the Netherlands* (2017).

[6] R. Merino-Martinez, M. P. J. Sanders, L. C. Caldas, F. Avallone, D. Ragni, L. D. de Santana, M. Snellen, and D. G. Simons, *Comparison between analog and digital microphone phased arrays for aeroacoustic measurements,* in 24th *AIAA/CEAS Aeroacoustics Conference. June 25 – 29 2018. Atlanta, Georgia, USA* (2018) AIAA paper 2018–2809.

[7] R. Merino-Martinez, P. Sijtsma, A. Rubio Carpio, R. Zamponi, S. Luesutthiviboon, A. M. N. Malgoezar, M. Snellen, N. Van de Wyer, C. Schram, and D. G. Simons, *Integration methods for distributed sound sources,* International Journal of Aeroacoustics (2018), Under review process.

[8] A. Rubio Carpio, R. Merino-Martinez, F. Avallone, D. Ragni, M. Snellen, and S. van der Zwaag, *Broadband Trailing Edge Noise Reduction Using Permeable Metal Foams,* in 46th *International Congress and Exposition of Noise Control Engineering, 27–30 August, 2017, Hong Kong* (2017).

[9] A. Rubio Carpio, R. Merino-Martinez, F. Avallone, D. Ragni, M. Snellen, and S. van der Zwaag, *Experimental characterization of the turbulent boundary layer over a porous trailing edge for noise abatement,* Journal of Sound and Vibration (2018), Accepted for publication.

[10] E. Sarradj, G. Herold, P. Sijtsma, R. Merino-Martinez, A. M. N. Malgoezar, M. Snellen, T. F. Geyer, C. J. Bahr, R. Porteous, D. J. Moreau, and C. J. Doolan, *A microphone array method benchmarking exercise using synthesized input data,* in 23rd *AIAA/CEAS Aeroacoustics Conference. June 5 – 9 2017. Denver, CO, USA* (2017) AIAA paper 2017–3719.

[11] R. Merino-Martinez, P. Sijtsma, and M. Snellen, *Inverse Integration Method for Distributed Sound Sources,* in 7th *Berlin Beamforming Conference, March 5 – 6 2018, Berlin, Germany* (GFaI, e.V., Berlin, 2018) BeBeC–2018–S07.

[12] S. Oerlemans and P. Sijtsma, *Acoustic Array Measurements of a 1:10.6 Scaled Airbus A340 Model,* in 10th *AIAA/CEAS Aeroacoustics Conference, May 10 – 12, 2004, Manchester, United Kingdom* (2004) AIAA paper 2004–2924.

[13] M. Gruber, P. Joseph, and T. Chong, *On the mechanisms of serrated airfoil trailing edge noise reduction,* in 17th *AIAA/CEAS Aeroacoustics Conference (32nd AIAA Aeroacoustics Conference), 5 – 8 June 2011, Portland, Oregon, USA* (2011) AIAA paper 2011–2781.

[14] M. Gruber, *Airfoil noise reduction by edge treatments*, Ph.D. thesis, University of Southampton (2012).

[15] W. C. P. van der Velden, *Computational aeroacoustic approaches for wind turbine blade noise prediction*, Ph.D. thesis, Delft University of Technology (2017), ISBN: 978–94–6186–756–8.

[16] C. Arce León, *A Study on the Near–Surface Flow and Acoustic Emissions of Trailing Edge Serrations for the purpose of noise reduction of Wind Turbine Blades*, Ph.D. thesis, Delft University of Technology (2017), ISBN: 978–94–92516–68–8.

[17] M. S. Howe, *Aerodynamic noise of a serrated trailing edge,* Journal of Fluids and Structures **5**, 33 (1991).

[18] M. Herr, *Design Criteria for Low–Noise Trailing–Edge,* in 13^{th} *AIAA/CEAS Aeroacoustics Conference (28^{th} AIAA Aeroacoustics Conference), May 21 – 23 2017, Rome, Italy* (2007) AIAA paper 2007–3470.

[19] M. Gruber, P. F. Joseph, and M. Azerpeyvand, *An experimental investigation of novel trailing edge geometries on airfoil trailing edge noise reduction,* in 19^{th} *AIAA/CEAS Aeroacoustics Conference , 27 – 29 May 2013, Berlin, Germany* (2013) AIAA paper 2013–2011.

[20] J. D. J. Anderson, *Fundamentals of Aerodynamics*, Third ed. (McGraw–Hill Series in Aeronautical and Aerospace Engineering, 2001) ISBN: 0–07–237335–0.

[21] A. L. Braslow, R. M. Hicks, and R. V. Harris Jr., *Use of grit–type boundary–layer transition trips on wind–tunnel models*, Tech. Rep. NASA–TN–D–3579 (NASA Technical Note (D–3579), 1966).

[22] Brüel & Kjær – condenser microphone type 4134, *https://www.bksv.com/media/doc/bp0100.pdf,* Accessed in March 2015.

[23] Brüel & Kjær – preamplifier type 2619, *https://www.bksv.com/media/doc/be0089.pdf,* Accessed in March 2015.

[24] Brüel & Kjær – power supply type 2801, *https://www.bksv.com/media/doc/bp0218.pdf,* Accessed in March 2015.

[25] T. Mueller, *Aeroacoustic Measurements* (Springer Science & Business Media, 2002) p. 313, ISBN: 978–3–642–07514–8.

[26] S. Pröbsting, M. Zamponi, S. Ronconi, Y. Guan, S. C. Morris, and F. Scarano, *Vortex shedding noise from a beveled trailing edge,* International Journal of Aeroacoustics **15**, 712 (2016).

[27] G.R.A.S. Sound & Vibration – 42AA Pistonphone class 1, *https://www.gras.dk/products/calibration-equipment/reference-calibrator/product/255-42aa,* Accessed in March 2017.

[28] R. K. Amiet, *Correction of Open Jet Wind Tunnel Measurements For Shear Layer Refraction,* in *2nd AIAA Aeroacoustics Conference, March 24 – 26, Hampton, VA, USA* (1975) AIAA paper 1975–532.

[29] P. Salas and S. Moreau, *Noise prediction of a simplified high–lift device,* in *22nd AIAA/CEAS Aeroacoustics Conference. May 30 – June 1 2016. Lyon, France* (2016) AIAA paper 2016–2962.

[30] S. Ghaemi, D. Ragni, and F. Scarano, *PIV–based pressure fluctuations in the turbulent boundary layer,* Experiments in Fluids **53**, 1823 (2012).

[31] M. Tuinstra and P. Sijtsma, *Suppression of spurious noise sources in airfoil self–noise measurements,* in *21st AIAA/CEAS Aeroacoustics Conference. June 22 – 26 2015. Dallas, TX, USA* (2015) AIAA paper 2015–2689.

[32] C. C. J. Pagani, D. S. Souza, and M. A. F. Medeiros, *Slat Noise: Aeroacoustic Beamforming in Closed–Section Wind Tunnel with Numerical Comparison,* AIAA Journal **54**, 2100 (2016).

[33] J. E. Ffowcs Williams and L. H. Hall, *Aerodynamic sound generation by turbulent flow in the vicinity of a scattering half plane,* Journal of Fluid Mechanics **40**, 657 (1970).

[34] M. R. Fink, *Noise component method for airframe noise,* in *4th AIAA Aeroacoustics Conference. October 3 – 5 1977, Atlanta, Georgia, USA* (1977) AIAA paper 1977–1271.

[35] M. Snellen, R. Merino-Martinez, and D. G. Simons, *Assessment of noise level variability on landing aircraft using a phased microphone array,* Journal of Aircraft **54**, 2173 (2017).

[36] F. Avallone, W. C. P. van der Velden, D. Ragni, and D. Casalino, *Noise reduction mechanisms of sawtooth and combed–sawtooth trailing–edge serrations,* Journal of Fluid Mechanics **848**, 560 (2018).

[37] CAE Systems website, *https://www.cae-systems.de/en/products/acoustic-camera-sound-source-localization/bionic-m-112.html,* Accessed in January 2017.

[38] PUI Audio POM–2735P–R microphone website, *http://www.puiaudio.com/product-detail.aspx?categoryid=4&partnumber=pom-2735p-r,* Accessed in January 2017.

[39] R. K. Amiet, *Refraction of sound by a shear layer,* Journal of Sound and Vibration **58**, 467 (1978).

[40] F. R. S. Lord Rayleigh, *XXXI. Investigations in Optics with special reference to the Spectroscope,* The London, Edinburgh and Dublin Philosophical Magazine and Journal of Science **8**, 261 (1879).

[41] E. Sarradj, *A generic approach to synthesize optimal array microphone arrangements,* in *6th Berlin Beamforming Conference, February 29 – March 1 2016, Berlin, Germany* (GFaI, e.V., Berlin, 2016) BeBeC–2016–S4.

[42] S. Succi, *The Lattice Boltzmann Equation For Fluid Dynamics and Beyond*, 1st ed. (Clarendon Press, 2001) ISBN: 9780198503989.

[43] J. E. Ffowcs Williams and D. L. Hawkings, *Sound generation by turbulence and surfaces in arbitrary motion,* Philosophical Transactions of the Royal Society of London A – Mathematical, Physical and Engineering Sciences **264** (1969), 10.1098/rsta.1969.0031.

[44] D. P. Lockard and G. M. Lilley, *The Airframe Noise Reduction Challenge*, Tech. Rep. NASA TM–2004–213013 (NASA TM–2004–213013, 2004).

[45] L. Bertsch, *Noise Prediction within Conceptual Aircraft Design*, Ph.D. thesis, DLR (2013), DLR Forschungsbericht, ISRN DLR–FB–2013–20, ISSN 1434–8454.

[46] T. Sinnige, B. Della Corte, R. de Vries, F. Avallone, R. Merino-Martinez, D. Ragni, G. Eitelberg, and L. L. M. Veldhuis, *Alleviation of Propeller–Slipstream–Induced Unsteady Pylon Loading by a Flow–Permeable Leading Edge,* Journal of Aircraft (2018), Accepted for publication.

[47] S. Oerlemans, M. Fisher, T. Maeder, and K. Kögler, *Reduction of Wind Turbine Noise Using Optimized Airfoils and Trailing–Edge Serrations,* AIAA Journal **47**, 1470 (2009).

[48] T. F. Brooks, D. S. Pope, and M. A. Marcolini, *Airfoil Self–Noise and Prediction*, Tech. Rep. NASA Reference Publication 1218 (NASA Reference Publication 1218, 1989).

[49] T. Geyer, E. Sarradj, and C. Fritzsche, *Porous Airfoils: Noise Reduction and Boundary Layer Effects,* in *15th AIAA/CEAS Aeroacoustics Conference (30th AIAA Aeroacoustics Conference)* (2009) AIAA paper 2009–3392.

[50] T. Geyer, E. Sarradj, and C. Fritzsche, *Measurement of the noise generation at the trailing edge of porous airfoils,* Experiments in Fluids **48**, 291 (2010).

[51] T. Geyer, E. Sarradj, and C. Fritzsche, *Porous Airfoils: Noise Reduction and Boundary Layer Effects,* International Journal of Aeroacoustics **9**, 787 (2010), SAGE Publications Ltd. London, United Kingdom.

[52] E. Sarradj, C. Fritzsche, and T. Geyer, *Silent Owl Flight: Bird Flyover Noise Measurements,* AIAA Journal **49**, 769 (2011).

[53] M. Herr, K. S. Rossignol, J. Delfs, N. Lippitz, and M. Mößner, *Specification of Porous Materials for Low–Noise Trailing–Edge Application,* in *20th AIAA/CEAS Aeroacoustics Conference, June 16 – 20 2014, Atlanta, GA, USA* (2014) AIAA paper 2014–3041.

[54] A. Rubio Carpio, F. Avallone, and D. Ragni, *On the Role of the Flow Permeability of Metal Foams on Trailing Edge Noise Reduction,* in 24^{th} *AIAA/CEAS Aeroacoustics Conference. June 25 – 29 2018. Atlanta, Georgia, USA* (2018) AIAA paper 2018–2964.

[55] A. Kisil and L. J. Ayton, *Aerodynamic noise from rigid trailing edges with finite porous extensions,* Journal of Fluid Mechanics **836**, 117 (2017).

[56] E. Sarradj and T. Geyer, *Noise Generation by Porous Airfoils,* in 13^{th} *AIAA/CEAS Aeroacoustics Conference (28^{th} AIAA Aeroacoustics Conference), May 21 – 23 2017, Rome, Italy* (2007) AIAA paper 2007–3719.

[57] F. Avallone, W. C. P. van der Velden, and D. Ragni, *Benefits of curved serrations on broadband trailing–edge noise reduction,* Journal of Sound and Vibration **400**, 167 (2017).

[58] S. Oerlemans, *Reduction of Wind Turbine Noise using Blade Trailing Edge Devices,* in 22^{nd} *AIAA/CEAS Aeroacoustics Conference. May 30 – June 1 2016. Lyon, France* (2016) AIAA paper 2016–3018.

[59] A. Vathylakis, T. P. Chong, and P. F. Joseph, *Poro–Serrated Trailing–Edge Devices for Airfoil Self–Noise Reduction,* AIAA Journal **53**, 3379 (2015).

[60] T. P. Chong and E. Dubois, *Optimization of the poro–serrated trailing edges for airfoil broadband noise reduction,* Journal of the Acoustical Society of America **140**, 1361 (2016).

7

Assessment of aircraft noise variability

It doesn't matter how beautiful your theory is,
it doesn't matter how smart you are.
If it doesn't agree with experiment, it's wrong

Richard Phillips Feynman

The last two chapters focused on localizing and analyzing individual noise sources in the spatial domain. The current chapter mainly considers the whole aircraft as a source and analyzes its sound signal in the frequency domain to study the large variability observed in the noise levels of flying aircraft within the same aircraft type. This variability hinders the accurate calculation of noise contours employing best–practice noise prediction models, because they do not account for it properly. Two experimental campaigns (one featuring a microphone array and one single microphones) were performed on a large number of aircraft flyovers under operational conditions. Two approaches are proposed for estimating the engine fan rotational speed using the audio signals recorded. Strong and significant correlations are found between the engine fan settings (N1%) and the emitted noise levels. Moreover, the expected dependency between airframe noise levels and the flow velocity is confirmed. Lastly, suggestions are provided to improve the current best–practice noise prediction models[1].

[1] Some of the contents of this chapter are included in [1–4].

Table 7.1: (Part of an) NPD table for the A333 and B772 aircraft types. "Ap" denotes approach and "Dep" denotes departure. The third block of columns represent the $L_{p,A,max}$ values in dBA for each distance r in ft. Adapted from [4, 13].

Type	$\frac{F_n}{\delta_0}$, [lbf]	r, [ft]						
		200	400	630	1000	2000	4000	6300
A333 Ap	6000	93.8	86.6	82	77.2	69.6	61.4	55.4
A333 Ap	12000	96.7	89.2	84.3	79.1	71	62.4	56.2
A333 Dep	34000	105.5	97.4	92	86.3	77.7	68.4	61.8
A333 Dep	42000	106	98.2	93.2	88	79.8	70.7	64.2
A333 Dep	52000	107.5	100.1	95.2	90.2	82.3	73.8	67.6
A333 Dep	62000	111.7	104.4	99.6	94.5	86.6	78.4	72.4
B772 Ap	12000	94.2	86.8	81.8	76.8	68.9	60.3	54.1
B772 Ap	17000	95.3	87.9	82.9	77.9	69.9	61.2	55
B772 Ap	22000	96.6	89	84	78.9	70.7	62	55.6
B772 Ap	27000	97.9	90	84.9	79.7	71.4	62.5	56.2
B772 Dep	31000	97.5	90.7	86	80.8	72.8	63.8	57.5
B772 Dep	41000	98.8	92	87.3	82.2	74.2	65.3	59
B772 Dep	51000	100.6	93.8	89.2	84.1	76.2	67.3	61.1
B772 Dep	61000	102.8	96	91.4	86.4	78.5	69.7	63.6
B772 Dep	71000	105	98.3	93.7	88.7	80.8	72.1	66.1
B772 Dep	81000	109	102.4	97.8	92.9	85.2	76.7	70.8

7.1. Introduction

The *best–practice* aircraft noise prediction tools introduced in section 1.3.4, such as the NPD tables, provide a single noise level for a certain aircraft type and at a specific distance from the observer [5–9]. Nevertheless, previous research [1–3, 10, 11] showed that changes in certain aircraft settings (especially the fan rotational speed) produce variations in the noise levels of several decibels. This fact can considerably hamper an accurate calculation of noise contours. Zellmann et al. [12] showed that the dependency between the noise levels and the fan rotational speed can be modeled using second–order polynomials, depending on the frequency and the emission direction. The *best–practice* noise prediction models employ estimations for the net engine thrust, which are normally provided as input by the user via a standard thrust profile (i.e., for different flight phases). As an example, the noise levels predicted for the Boeing 777–200 aircraft type equipped with GE90–76B engines are depicted in Fig. 7.1a. The curves corresponding to different net engine thrusts are presented, for which the noise levels are plotted against the distance. The data from Fig. 7.1a were obtained from the international Aircraft Noise and Performance (ANP) database [13], see Table 7.1.

In order to assess the assumptions of the noise contour models, the actual engine fan settings and the distance between the aircraft and the observer need to be determined. Whereas the actual aircraft engine fan settings are recorded

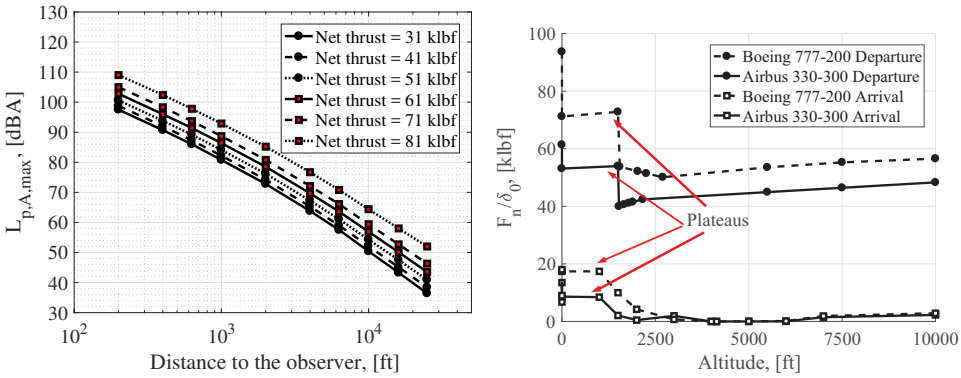

Figure 7.1: (a) NPD noise level estimations for B772 departures. (b) Corrected net thrust per engine estimations for example flight profiles [13].

by airlines using the aircraft flight movement system, these data are not publicly available for reasons such as pilot privacy and to ensure the operation business strategies of the airlines. To counteract this lack of information, different methods to determine the engine fan settings based solely on audio files are proposed and described in section 7.4. Other configuration parameters, such as the flap and slat deflection angles, are typically not publicly available either and need to be approximated to calculate the airframe noise [14].

The focus of this chapter is, therefore, on assessing the variability of the aircraft noise levels, investigating the causes for this variability, and comparing the experimental results with the current noise prediction models when possible. The variability in the noise levels was assumed to depend mostly on the emitted noise at the source, i.e., the aircraft itself, neglecting the effects of a variable atmosphere, which is normally negligible for experiments as the ones presented here [10, 11]. In order to achieve this aim, two different experimental campaigns of aircraft flyovers under operational conditions are considered:

1. Acoustic measurements of landing aircraft featuring a microphone array located next to an airport runway (see section 5.1.1). The distances to the aircraft were about 70 m and the audio recordings have an effective frequency content up to 11.2 kHz. Moreover, the use of the microphone array allows for the application of acoustic imaging algorithms see section 7.5.1.

2. Acoustic measurements featuring individual microphones of the Noise Monitoring System (NOMOS) around Amsterdam Airport Schiphol (see section 7.2.2). Both arrivals and departures were recorded. The average minimum distance to the aircraft was about 790 m and the maximum frequency available for the audio recordings was limited to 3500 Hz.

Both experimental setups are further explained in section 7.2. The noise prediction model considered for comparison is briefly introduced in section 7.3. The

Table 7.2: NMT locations.

NMT number	Latitude, [°]	Longitude, [°]	Altitude, [m]
01	52.3784122	4.7400112	−2
10	52.2631668	4.7732408	−3
14	52.2353764	4.5937646	−3

different methods for estimating the flight–phase–dependent engine fan settings ($N1\%$) based on the audio recordings are described in section 7.4. The experimental results, correlation analyses between the noise levels and the measured $N1\%$ and the aircraft velocity, and the comparison with the prediction models are gathered in section 7.5 for both experimental campaigns. Finally, the conclusions are presented in section 7.6.

7.2. Experimental setup

7.2.1. Microphone array setup

All the details of the experimental setup used for the aircraft noise variability analysis featuring a microphone array were already explained in section 5.1.1.

7.2.2. NOMOS setup

The present experimental campaign only considers the total aircraft noise levels recorded by individual microphones from the Noise Monitoring Terminals (NMT) of NOMOS around Amsterdam Airport Schiphol in the Netherlands in 2016. This system provides the recorded noise levels on–line to the public [15] and the raw data upon request. Naturally, the recorded noise metrics, e.g. the maximum Overall A–weighted Sound Pressure Level ($L_{p,A,max}$ or $OASPL_{max}$, see Appendix A.2) or the Sound Exposure Level ($L_{p,A,e}$ or SEL, see Appendix A.3), of a specific event can also be traced back to the recorded audio files.

The study is based on 1121 audio files recorded by three different NMTs. These flyovers correspond to arrivals and departures of two aircraft types: Airbus A330–300 (henceforth Airbus 333) and Boeing 777–200 (henceforth Boeing 772). Both aircraft are wide–body twin–engine jet airliners of comparable size, but the Airbus 333 is designed for medium– to long–range operations, whereas the Boeing 772, with higher takeoff weight and thrust, is intended for long–range purposes. It can be observed in Fig. 7.1b that the Boeing 772 normally has indeed higher corrected net thrust values (F_n/δ_0) than the Airbus 333.

The locations of the selected three NMTs (out of the 31 NMTs available) used for this research (01, 10 and 14) are highlighted with red pins in Fig. 7.2 and their coordinates are presented in Table 7.2. The airport runways are denoted as black lines. The positions of the NMTs have been selected in order to include a representative number of both arrival and departure operations.

The NOMOS system has been active since 1993 in residential areas around this airport. Each of the NMT has a calibrated microphone which continuously

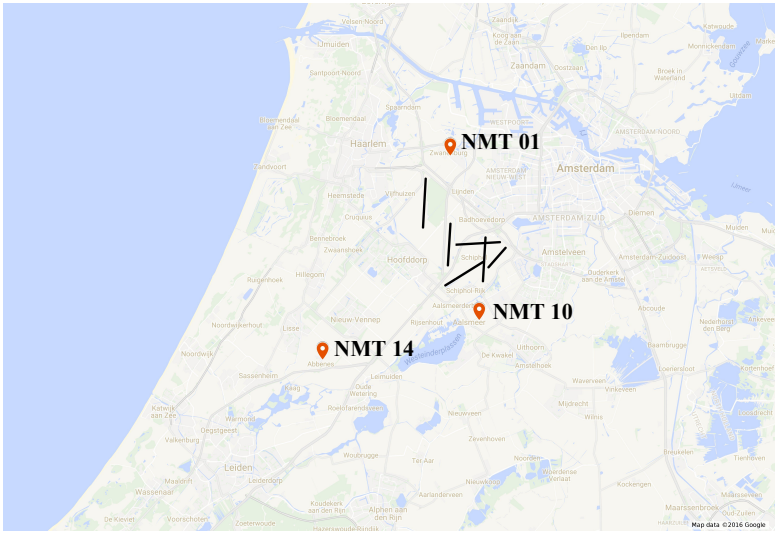

Figure 7.2: NMTs 01, 10 and 14 and airport runways (black lines). Map obtained using Google Maps [4].

measures the noise in the area. The microphones employed are part of the Brüel & Kjær airport noise monitoring and management system [16]. The microphones start recording whenever a certain threshold sound pressure level (L_p) is exceeded and measured. Normally, the trigger cause corresponds to an aircraft flyover, but sometimes other sound sources, such as birds tweeting nearby or a church bell ringing, also trigger the recording, and need to be rejected.

Unfortunately, to reduce data storage, the NOMOS audio files are filtered and resampled with a sampling frequency of 8 kHz when stored. This causes a loss of information [17] and errors when calculating the noise metrics with the audio files available, since all the spectral information is lost for frequencies higher than 3500 Hz. Therefore, it was decided to only consider the recorded noise metrics by NOMOS (before the data compression) as a reference. Henceforth, the $L_{p,A,max}$ metric is considered in this study. Additional metrics recorded by NOMOS, such as the $L_{p,A,e}$ and the Effective Perceived Noise Level (EPNL, see Appendix A.4), showed a very strong and significant correlation (with correlation coefficients $\rho > 0.9$) with the $L_{p,A,max}$. Therefore, the conclusions presented afterwards in the correlation analysis with $L_{p,A,max}$ (see section 7.5.2) can be extended to these other metrics.

Table 7.3 divides the total number of flyovers depending on the aircraft type, the NMT that recorded the measurement and whether the operation mode was an approach or a departure. A total of 623 Airbus 333 and 498 Boeing 772 flyovers were recorded. The number of approaches (565) was similar to the number of departures (556).

Since not all the aircraft recorded had the same engine type, Table 7.4 contains an overview of the number of aircraft equipped with each engine type, as well as the number of fan blades, B, and the maximum fan rotational speed at 100%

Table 7.3: Number of flyovers selected for each NMT and each aircraft type [4].

NMT number	Airbus 333 flyovers	Boeing 772 flyovers	Subtotal per NMT
01 (Approach)	96	63	159
10 (Departure)	94	133	227
14 (Approach)	221	185	406
14 (Departure)	212	117	329
TOTAL	623	498	1121

Table 7.4: Aircraft types with their corresponding engine and number of recorded measurements for each type. The minimum and maximum EPNL certification values in EPNdB for approach for each engine type are also indicated [4].

Aircraft type	Engine type	Amount	B	$n_{\text{rot,max}}$	$\Delta\text{EPNL}_{\text{Ap}}$
Airbus 333	CF6–80E1A3	169	38	3320	[99.1 – 99.6]
	CF6–80E1A4	79	38	3320	[99.1 – 99.6]
	CF6–80E1A4B	139	38	3320	[99.1 – 99.6]
	PW4168A	179	34	3600	[97.9 – 98.7]
	PW4170	17	34	3680	[98.1 – 98.7]
	TRENT 772	21	26	3900	[96.7 – 97]
	TRENT 772B–60	19	26	3900	[96.7 – 97]
Boeing 772	GE90–90B DAC I	23	22	2262	[97.6 – 98.8]
	GE90–92B	2	22	2262	Not found
	GE90–92B DAC I	3	22	2262	Not found
	GE90–94B	468	22	2262	[98.4 – 98.8]
	RB211 TRENT 892	2	24	3300	[99.9 - 100.1]

engine fan settings ($n_{\text{rot,max}}$) in rpm. The minimum and maximum EPNL certification values in EPNdB for approach for each engine type (obtained from [18]) are also indicated in the last column for illustration purposes. Variabilities in the EPNL metric between 0.2 and 1.2 EPNdB are observed within the same engine type, due to small modifications by the manufacturers [18]. These differences are deemed to be negligible compared to the variability ranges found in practice [2, 11]. Different engine types from the same family can be grouped in a same category, provided that they have the same values for B and $n_{\text{rot,max}}$ (see Table 7.4). The EPNL certification values for each category are practically identical. Thus, the Airbus 333 flyovers are divided into four categories: CF6–80E1A (387 cases), PW4168A (179 cases), PW4170 (17 cases) and TRENT 772 (40 cases); whereas the Boeing 772 flyovers are divided into two categories: GE90 (496 cases) and TRENT 892 (2 cases).

The trajectories of the aircraft flyovers were determined using radar data from air traffic control and referenced to the coordinates of the respective NMT. The position data are recorded every 4 seconds and interpolated linearly in between. Hence, the aircraft velocities and the distances to the observer over time are approximately

known. The x, y and z coordinates considered in this study are relative to the respective NMT coordinates. Figure 7.3a shows an example of the aircraft flyover trajectories for the approaches recorded by the NMT 01 (denoted by a red dot), confirming that the flight paths during approach are relatively uniform, since all aircraft follow the ILS approach. Figure 7.3b contains a box plot of the minimum distances of each flyover to each of the four NMT cases, where a distinction is made between approaches (Ap) and departures (Dep). On each box, the central mark is the median, the edges of the box are the 25^{th} and the 75^{th} percentiles and the whiskers extend to the most extreme data points. It can be observed that the minimum distances for departure maneuvers are indeed more variable than landings. The average minimum distance to the observer (NMT station) for all measurements was 790 m.

Since the (minimum) distances from each aircraft to the respective NMT show differences, a correction in the measured noise levels was performed to correct for the varying effect of sound spreadings (see section 3.1.2), in order to study all aircraft in similar conditions. For each of the four NMT cases the mean minimum distance ($\bar{r}_{\text{min}}$) to each NMT for all the recorded flyovers was calculated. A correction value ΔL_{p} was added to the noise metrics from the measurements of all flyovers depending on their respective minimum distance to the NMT (r_{min}), given by the following formula

$$\Delta L_{\text{p}} = 20 \log\left(\frac{r_{\text{min}}}{\bar{r}_{\text{min}}}\right). \tag{7.1}$$

Note that ΔL_{p} is negative for $r_{\text{min}} < \bar{r}_{\text{min}}$ and positive for $r_{\text{min}} > \bar{r}_{\text{min}}$. This means that for aircraft flying further away than the $\bar{r}_{\text{min}}$ will increase the values of their noise levels and vice versa. Hence, the effect of having different measuring distances is at least partially accounted for.

Due to the limited frequency range available in the audio recordings (only up to 3500 Hz), the effect of the atmospheric absorption on sound (see section 3.1.2) was not accounted for, since the effect of the atmospheric absorption is specially notable for high frequencies. Hence, the relative effect of the atmospheric absorption on each flyover with respect to the effect at the mean distance $\bar{r}_{\text{min}}$ is expected to be small for the frequency range available. However, the full frequency range was used when calculating the $L_{\text{p,A,max}}$ values by NOMOS. The NPD tables do account for an average effect of the atmospheric absorption, depending on the distance to the observer.

The experimental data was continuously recorded during a two–month period, with relatively similar weather conditions. The weather data were recorded hourly by the Royal Netherlands Meteorological Institute (KNMI) [19]. The local temperatures were used for estimating the sound speed c and for the parameters for the noise predictions. The recorded wind speeds were taken into account to determine the true airspeeds of the aircraft, which are presented henceforth.

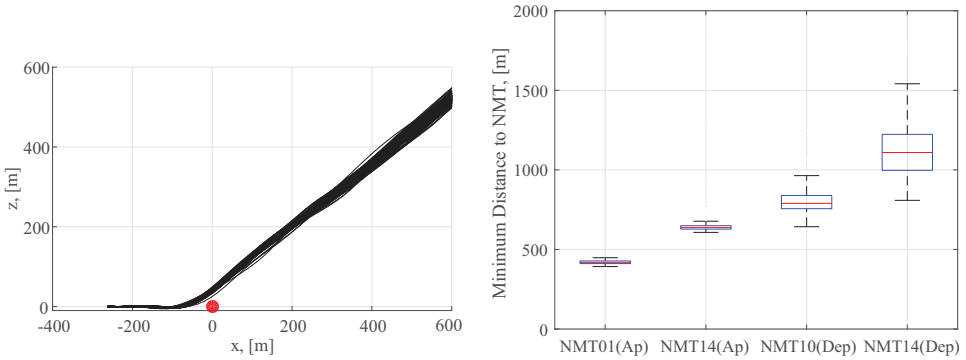

Figure 7.3: (a) Recorded approaches trajectories at NMT 01. (b) Box plot of the minimum distances to each NMT [4].

7.3. Noise prediction model

As it was mentioned in section 1.3.4, the *best–practice* or simpler legal compliance prediction tools are the models normally employed in practice for noise contour calculations around airports. Therefore, the comparison with the experimental data is performed with respect to the predictions of the method of ECAC's Document 29 [7] introduced in section 1.3.4.

The aim of this research [4] is to investigate the effects of considering the instantaneous thrust setting on the noise level predictions by the noise contour models, rather than employing tabulated values as in practice. These models predict the noise levels perceived at a certain distance from the aircraft, depending on the thrust setting employed. In particular, NPD tables usually require the corrected net thrust per engine $\frac{F_n}{\delta_0}$ as an input, which can be calculated using the following equation

$$\frac{F_n}{\delta_0} = E_0 + F_0 V_C + G_A \tilde{h} + G_B \tilde{h}^2 + \tilde{H} T_0 + K_3 \left(\frac{N1\%}{\sqrt{\theta_T}} \right) + K_4 \left(\frac{N1\%}{\sqrt{\theta_T}} \right)^2, \tag{7.2}$$

where F_n is the net thrust per engine in lbf, δ_0 is the ratio between the ambient air pressure at the aircraft to the standard air pressure at mean sea level ($101,325$ Pa), V_C is the calibrated airspeed in kts, $\tilde{h}$ is the aircraft altitude in ft and T_0 is the ambient air temperature in which the aircraft is operating in °C. The parameter $N1\%$ refers to the engine fan rotational speed (as explained in section 2.4.3) and θ_T is the ratio between the absolute total temperature at the engine inlet to the standard air temperature at mean sea level (288.15 K). The constants K_3 and K_4 are derived from the installed engine data encompassing the $N1\%$ values of interest. The variables E_0, F_0, G_A, G_B and $\tilde{H}$ are engine constants for temperatures below the engine flat rating temperature at the thrust rating in use, obtainable from the

ANP database [13] for most aircraft types (except turbojet aircraft). The unit of the corrected net thrust obtained with Eq. (7.2) is lbf.

Once the corrected net thrust per engine $\frac{F_n}{\delta_0}$ is known, it is introduced in the NPD tables, where it is interpolated (or extrapolated) linearly within the available data. Afterwards, the selected distance is introduced in the table and interpolated (or extrapolated) logarithmically to obtain the estimated noise level at that distance from the aircraft. An example of (part of) an NPD table is depicted in Table 7.1, which contains the available data used in this research for the Airbus 333 (equipped with CF6–80E1A engines) and Boeing 772 (equipped with GE90–76B engines) aircraft types. The first column denotes the aircraft type and operation mode (approach (Ap) or departure (Dep)), the second column contains the corrected net thrust per engine $\frac{F_n}{\delta_0}$ and the last block of columns represents the $L_{\text{p,A,max}}$ values in dBA for each distance r in ft, as specified in the first row. The graphical representation of these values for departures of the Boeing 772 type equipped with GE90 engines (last 6 rows in Table 7.1) is depicted in Fig. 7.1a. In Fig. 7.1 one klbf is equivalent to 4.448 kN.

As aforementioned, one of the main issues of the noise prediction models is that the actual value of $N1\%$ (and hence the net thrust) is not disclosed in practice and estimations need to be made. Figure 7.1b depicts typical corrected net thrust profiles (per engine) for both aircraft types during departure and arrival, depending on the altitude [13]. The respective engine fan rotational speed values can be calculated solving Eq. (7.2) for $N1\%$. It should be noted that several thrust profiles are used for departures in practice, depending on the assumed takeoff weight of the flight, typically categorized in so–called stage lengths, but for the altitudes considered in this research, the differences between thrust profiles were negligible for all stage lengths considered (third to eighth) [4]. On the other hand, a single approach thrust profile per aircraft type is normally employed. The altitudes of the flyovers considered in this study are located in the *plateaus* in Fig. 7.1b before (on the left of) the cutback points, which correspond to altitudes of 1500 ft for departures and of 1000 ft for arrivals. Therefore, the estimated thrust values are practically constant for the whole altitude range, within each aircraft type and operation mode. However, previous studies [1–3, 10, 11] confirmed that, in practice, large variations in $N1\%$ occur at the same distance to the observer. The operational reasons why $N1\%$ varies are because pilots and airlines make use of reduced thrust to extend maintenance intervals and that automatic thrust settings control the aircraft to follow the glide path under the influence of wind gust and to maintain constant landing velocity. Hence, there is a clear interest in obtaining the actual $N1\%$ values of the aircraft.

An additional consideration and premise about this prediction model that should be noted is that, according to the Document 29 of the ECAC [7], "*this methodology applies only to long–term average noise exposure; it cannot be relied upon to predict with any accuracy the absolute level of noise from a single aircraft movement and should not be used for that purpose*". Thus, the aim of this research is to extend the model capabilities for predicting the noise levels of single events and to account for the inherent variability in the noise levels observed. This is done

because the aforementioned variability can lead to important errors when assessing the annoyance experience by the population living around airports.

7.4. Determination of the engine fan settings

The physical generation mechanisms of fan noise were previously described in section 2.4.3. In this section, two comparable approaches are proposed for calculating the engine fan settings of aircraft flyovers depending on the available frequency range of the audio recordings. Section 7.4.1 contains the approach for audio signals with high–frequency content (several BPF harmonics present, see Eq. (2.26)) and section 7.4.2 includes the approach for audio signals without high–frequency content available (few BPF harmonics present). Similar methods can be found in the literature, in which frequency filtering can also be applied as preprocessing to improve the search process [20].

7.4.1. Method for the microphone array setup

In case the audio signal has relatively high–frequency content (about 10 kHz), it is likely to find several BPF harmonics (because typical BPF values for turbofan aircraft during landing range from 500 Hz to 2 kHz). For this study, the forward arc spectra, i.e., the sound when the aircraft is approaching the array, are extracted from the signal's spectrogram and used for the calculations. The spectrograms are calculated following the signal processing parameters specified in section 5.1.1. After extracting a time interval (from 1.5 to 1 s before the time overhead, corresponding to emission angles between $\theta \approx 37°$ to $63°$, respectively) of the forward arc from the spectrogram (see Fig. 7.4a), the Doppler–corrected spectra (see section 3.1.2) are averaged over time and a polynomial fit is applied to the averaged spectrum, representing the broadband noise as presented in Fig. 7.4b. This polynomial is then subtracted from the spectrum and the difference is squared to observe the tonal peaks of the engine noise in a better way (only positive differences are considered). This magnitude is called squared residual and it is used to estimate the BPF and its harmonics.

After selecting all the peaks of interest (higher than a threshold amplitude) from the squared residual vector, three different methods [1, 2] are employed to determine the engine fan settings of each flyover:

1. **Method 1** considers all the possible combinations of three peaks for all the selected peaks as candidates for being the BPF or its harmonics. It uses a least–squares regression to estimate a BPF value and its corresponding harmonics for each combination. The four values with the smallest deviation between the modeled and the measured peaks are selected as candidates for being harmonics of the BPF.

2. **Method 2** uses the three considered peaks with lowest frequency and the differences between them as potential candidates for being the BPF. The selected BPF value is the one whose harmonics coincide with the largest number of peaks, as long as it provides a realistic value for $N1\%$.

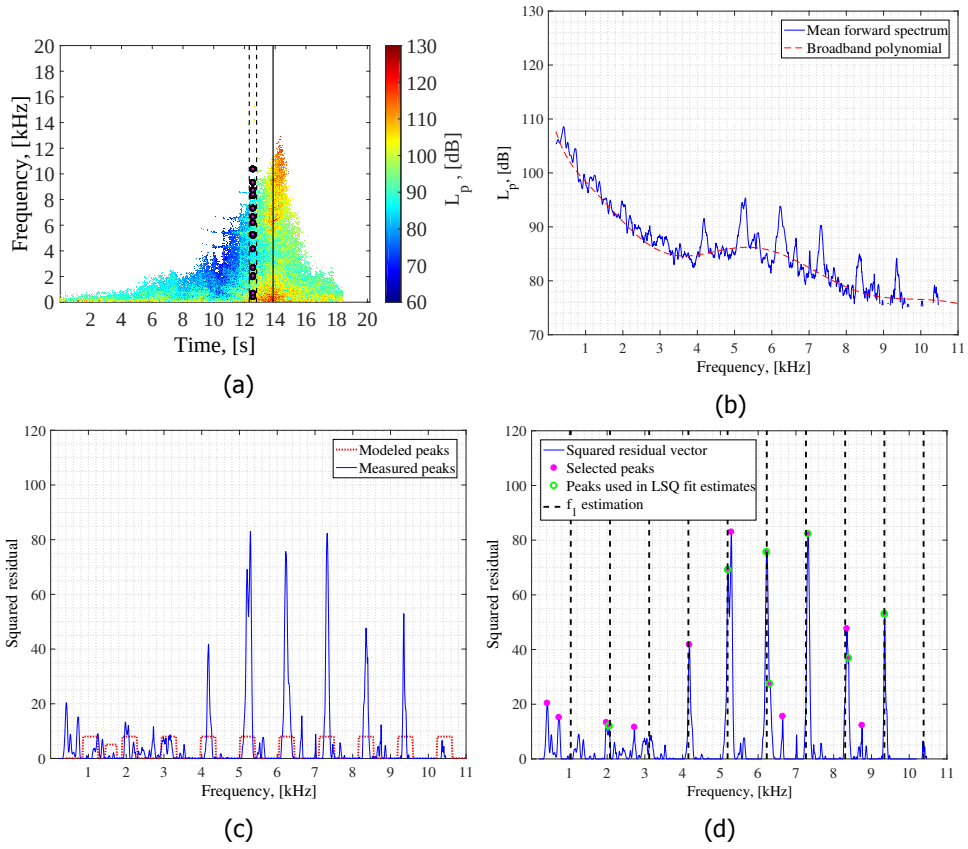

Figure 7.4: (a) Spectrogram at the source of a Boeing 737–800 flyover. The solid black line represents the time overhead and the black dashed lines the selected time window. The circles show the peaks considered. (b) Mean forward spectrum and the 10^{th} degree broadband polynomial fit. (c) Comparison between the modeled and measured peaks for method 3. (d) BPF estimation results for method 1 [2].

3. **Method 3** employs a synthetic noise model for the full expected spectrum. An iterative process is performed varying the engine fan settings $N1\%$, i.e., the BPF value, within a realistic range. The engine fan settings value resulting in the maximum correlation between the modeled and the experimental data is selected as the candidate, as shown in Fig. 7.4c.

Figure 7.5 explains the process for estimating the BPF value using the aforementioned methods. The inputs necessary are the Doppler–corrected spectrogram (see Fig. 3.10), a time interval selected by the user and the engine characteristics of the aircraft (Table 5.2). An example of the results obtained by the first method is depicted in Fig. 7.4d. The spectrograms need to be individually studied with care and the outcomes of the three methods evaluated depending on their fit with the spectra. Even if the three methods normally provide similar results, it is required to confirm whether the solution has a realistic value and whether it explains as many harmonics as possible. In case the value obtained for $N1\%$ is not realistic, a different time interval is chosen until this condition is fulfilled.

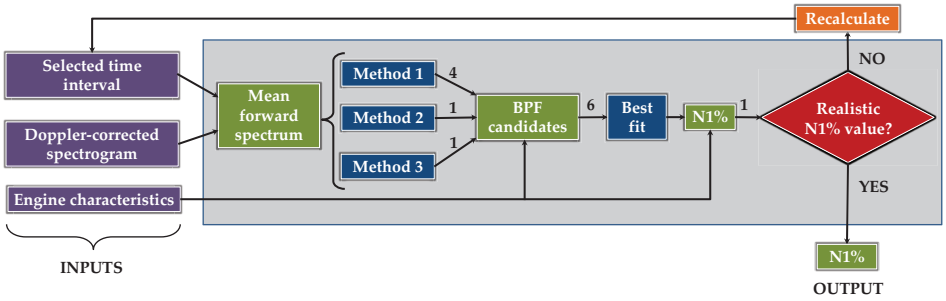

Figure 7.5: Flowchart showing the process for estimating the $N1\%$ value using the three different methods for the microphone array setup [2].

Normally, the three methods provided similar results, with methods 1 and 3 showing the best performance. The $N1\%$ range in this research varies from 40% to 70%, which are typical values for commercial planes during the landing phase [2].

7.4.2. Method for the NOMOS setup

Unfortunately, due to the resampling of the available audio data for the NOMOS setup mentioned in section 7.2.2 and the consequent low maximum frequency (3500 Hz), few higher harmonics are found in the spectrograms in practice, in this case.

The flowchart presented in Fig. 7.6 shows the inputs necessary for this method: the trajectory and engine characteristics of the aircraft (Table 7.4) and the audio recording of the flyover. The expected Doppler shift can be estimated using the aircraft trajectory and Eq. (3.1). Afterwards, a least–squares curve–fitting process [21] is performed in order to find narrow–band engine fan tones in the signal spectrogram that agree with the calculated Doppler shift. The spectrograms are

calculated by using 2048 samples per time block with Hanning windowing and a 50% data overlap. For each time step, peaks over a certain threshold are considered. Afterwards, the characteristic Doppler–shifted curves corresponding to the fan tonal noise were searched for using these peaks, considering the expected Doppler shift as calculated from the aircraft trajectory, according to Eq. (3.1) and shown in Fig. 7.7c. First, the BPF is searched for in the spectrogram within a predefined search frequency band over time, depending on the operation mode and engine characteristics. A least–square fitting process [21] was performed to match the detected peaks to the expected continuous and monotonically decreasing Doppler–shift curve. Changes in the engine fan settings performed by the pilot during the recording time or due to the turbulence in the atmosphere can also cause "bumps" in the curves representing the engine fan tones, which are expected to be monotonically decreasing otherwise, see Fig. 7.8b. These irregularities can be accounted for by allowing a small increase in the Doppler–shifted tone frequency. The presence of higher harmonics is also evaluated by searching for multiples of the estimated BPF and serves as a further confirmation that the obtained BPF value is correct. This process provides a (Doppler–corrected) BPF value (for the instant when $r = r_{\text{min}}$) and, therefore, an $N1\%$ value for that instant. The obtained $N1\%$ needs to be checked to confirm that it falls within the typical range of values depending on the aircraft operation (approach or departure). In case the provided $N1\%$ value is not realistic, the whole process is repeated using a different search frequency band for the BPF. Henceforth, for consistency, the selected instant for studying the value of $N1\%$ was chosen to be when the aircraft is located at the minimum distance r_{min} to the NMT.

The results for an example Airbus 333 approach flyover recorded by NMT 01 are presented in Fig. 7.7. Figure 7.7a illustrates the flight path with respect to the NMT (situated at the origin and represented by a red dot). The thick black line corresponds to the period where the audio recording is available. The calculated emission angle θ between the relative aircraft position vector, $\boldsymbol{r}$, and the source velocity vector, $\boldsymbol{V}$, over that period is presented in Fig. 7.7b. The $90°$ angle is shown as a dashed line for reference. Figure 7.7c contains the calculated Doppler shift during the same period. The spectrogram of the audio signal is shown in Fig. 7.8. The vertical solid black line represents the time with $r = r_{\text{min}}$. Figure 7.8a presents with a thick black line the curve fitted to the calculated Doppler shift (from Fig. 7.7c). Figure 7.8b depicts the obtained estimates for the locations of the detected Doppler–shifted engine fan tones. Double dashed lines around the real solution are plotted to show the curves in the spectrogram. This case is especially illustrative, since not only the BPF but also the next four harmonics are clearly detected and marked with dashed lines in Fig. 7.8b. The time when $r = r_{\text{min}}$ is marked with a solid black vertical line. Unfortunately, due to the limited maximum frequency and the higher atmospheric absorption at higher sound frequencies, harmonics higher than the fifth are rarely found in these measurements. The presence of "bumps" in the tones can also be observed in Fig. 7.8, as explained before, most probably due to changes in the engine fan settings by the pilot or to the atmospheric turbulence, which are successfully detected by the search method.

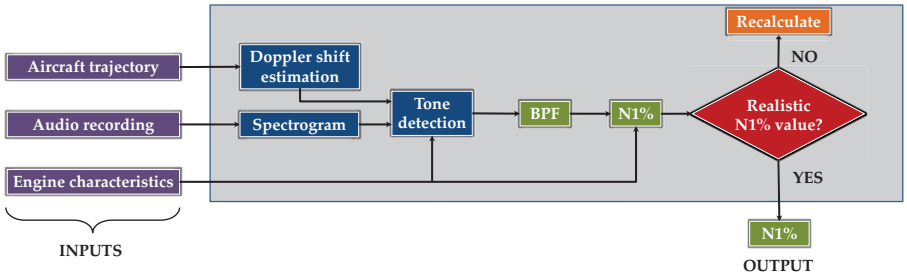

Figure 7.6: Flowchart showing the process for estimating the engine fan settings ($N1\%$) for the NOMOS setup [4].

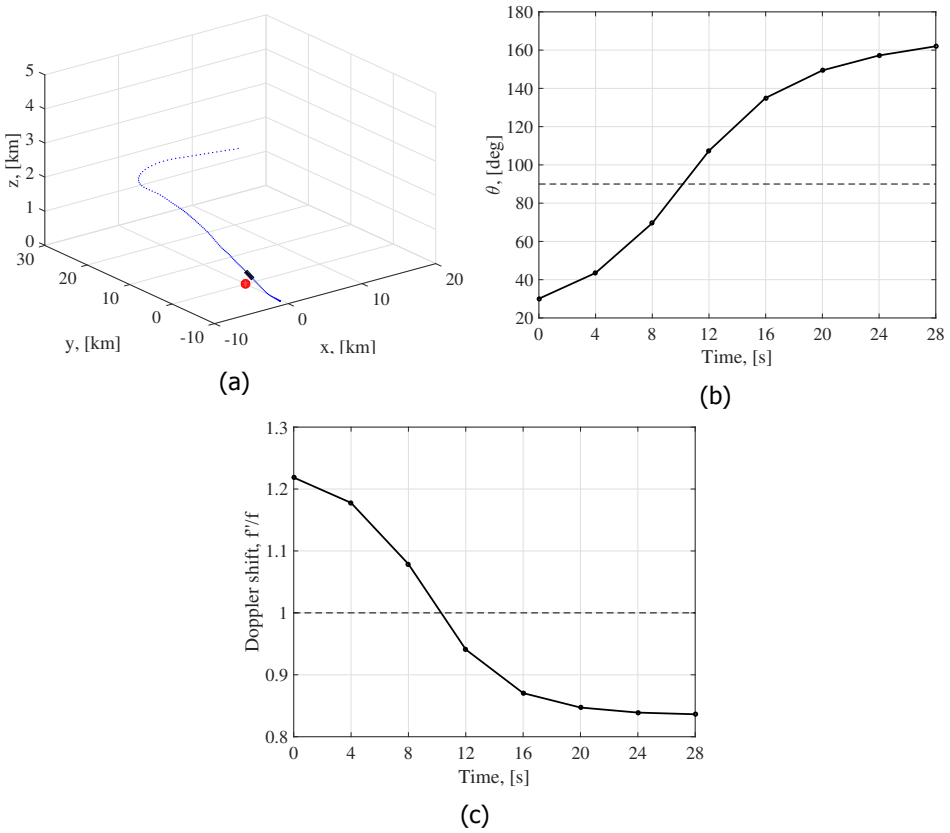

Figure 7.7: (a) A333 trajectory. Note the different axes scales. (b) Angle θ and (c) Doppler shift during the recording [4].

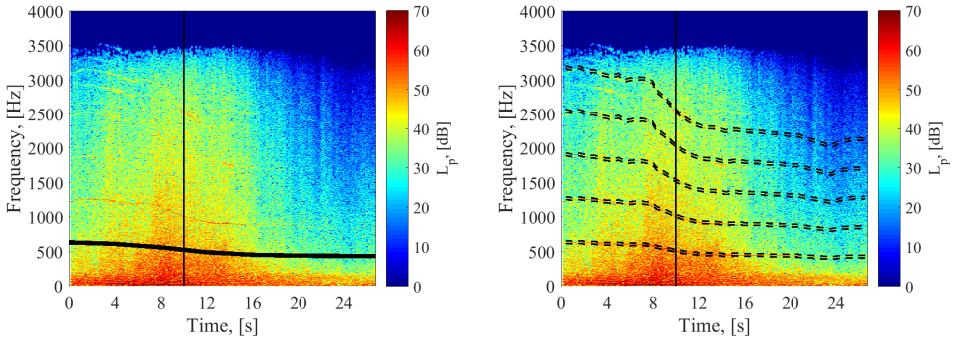

Figure 7.8: Spectrograms of the audio signal with: (a) Curve fitted to the Doppler shift. (b) Detected engine tones [4].

Since the NOMOS data also include departure operations, the presence of *buzz–saw* tones is also expected, see section 2.4.3. These tones are harmonics of the engine shaft rotation frequency, which is typically considerably lower than the BPF. Therefore, additional care needs to be taken when analyzing aircraft tonal noise during departure to only consider fan tones and not *buzz–saw* tones.

7.5. Results

7.5.1. Microphone array results

Assessment of noise variations using a single microphone

The maximum overall $L_{p,A}$ (see Appendix A.2) at the source location ($r_0 = 1$ m) and the Sound Exposure Level ($L_{p,A,e}$, see Appendix A.3) were calculated for each flyover. Both metrics are obtained from the spectrograms.

The obtained results for both metrics are gathered in the box plots in Fig. 7.9, where the aircraft types are presented at the abscissa axis in order of increasing size. It can be noticed that the Boeing 747 and Boeing 777 generate the highest noise metrics in both cases, as it could be expected, due to their considerably larger size. The differences between the values of both box plots are due to the fact that the $L_{p,A,e}$ considers the sound perceived at the array (and not at the source position) and also the duration of the sound, but, in general, the tendencies between aircraft types are similar in both figures. Variations for the same aircraft type as large as 7 dBA for the $L_{p,A,max}$ and 6 dBA for the $L_{p,A,e}$ can be observed.

This variability is also present in the flyover sound frequency spectra and is even larger for single frequencies, as it can be seen in the examples depicted in Fig. 7.10 for the Boeing 737 "Next Generation (*NG*)" (series 700, 800 and 900) and Fokker 70 cases. The frequency axis for each spectrum was normalized by the corresponding BPF obtained in section 7.4. The time interval chosen for this spectral analysis was 1.5 to 1 s before the time overhead (forward arc). The relatively large contribution of the BPF harmonics can be observed in a clear way for the Boeing 737 *NG* in Fig.

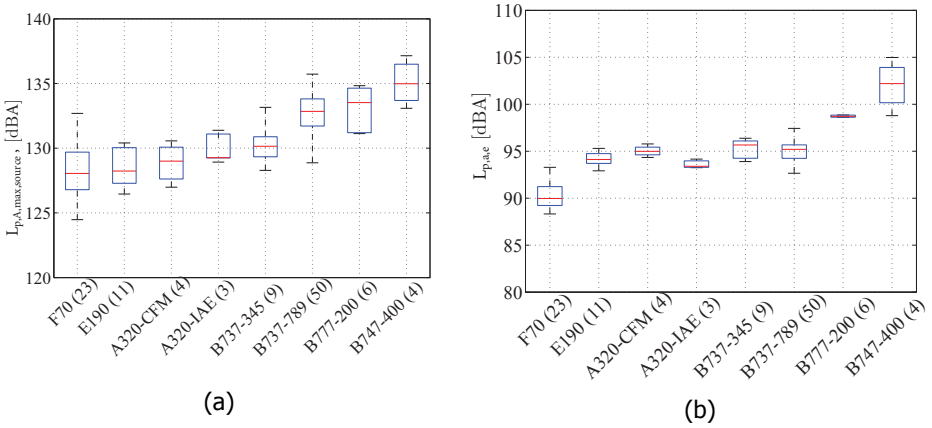

Figure 7.9: Box plot of the (a) $L_{p,A,max}$ at the source position (b) $L_{p,A,e}$ for the different aircraft types [2].

7.10a, where the peaks from the third to the eighth harmonic align in a satisfactory manner. On the other hand, the harmonic tones are not so distinguishable for the Fokker 70 case, see Fig. 7.10b. However, the fan tones were clearly detected in all cases.

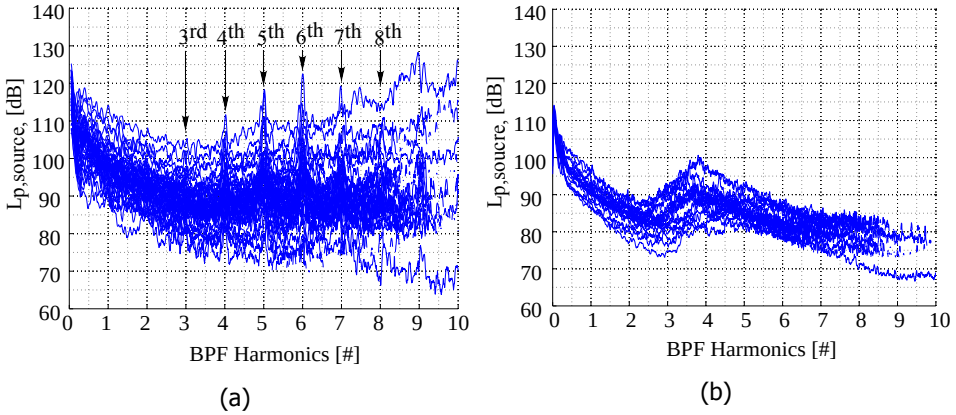

Figure 7.10: Flyover spectra at the source position with the frequencies normalized with respect to the BPF harmonics for (a) the Boeing 737 *NG* and (b) Fokker 70. The time interval selected was 1.5 s before the time overhead to 1 s before the time overhead [2].

As an attempt to explain these variations of the noise levels, a correlation study was performed with respect to the engine fan settings $N1\%$ (calculated in section 7.4) and the aircraft velocity, which was estimated as explained in section 5.1.1. As a first approach, the $L_{p,A,max}$ at the source was used, without any beamforming method applied and without focusing on any specific frequency.

The results presented in Figs. 7.11 and 7.12 correspond to the Boeing 737 *NG*

and the Fokker 70 cases, respectively, because they are the two most numerous aircraft types in this research, see Table 5.2. The correlation coefficient, ρ, the coefficient of determination, ρ^2, and the p–value are calculated and depicted in each plot, see Appendix C.2.4. The linear least–squares fit is also included. It can be observed that there is a significant correlation in all cases (considering the typical p–value threshold value of 0.05), especially with $N1\%$. Also interesting is the relatively large correlation ($\rho \approx 0.55$) found between the maximum overall $L_{p,A}$ and the aircraft velocity for the Fokker 70 case.

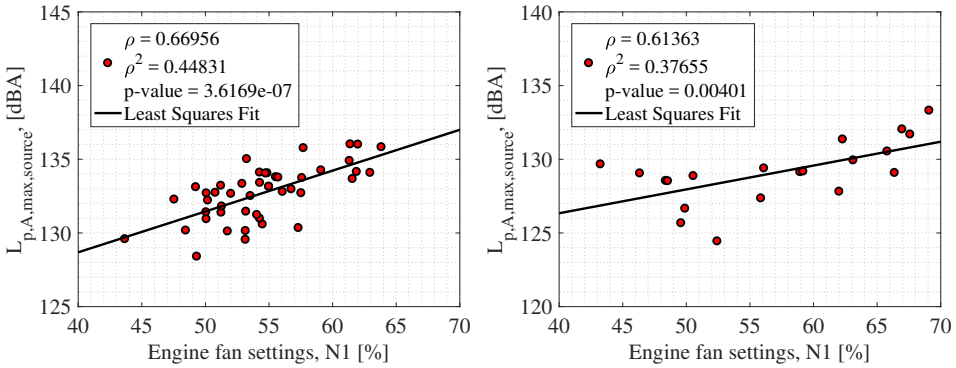

Figure 7.11: Correlation analysis results (without beamforming) between the $L_{p,A,max}$ and the engine fan settings ($N1\%$) for: (a) the Boeing 737 *NG* and (b) the Fokker 70. Adapted from [2].

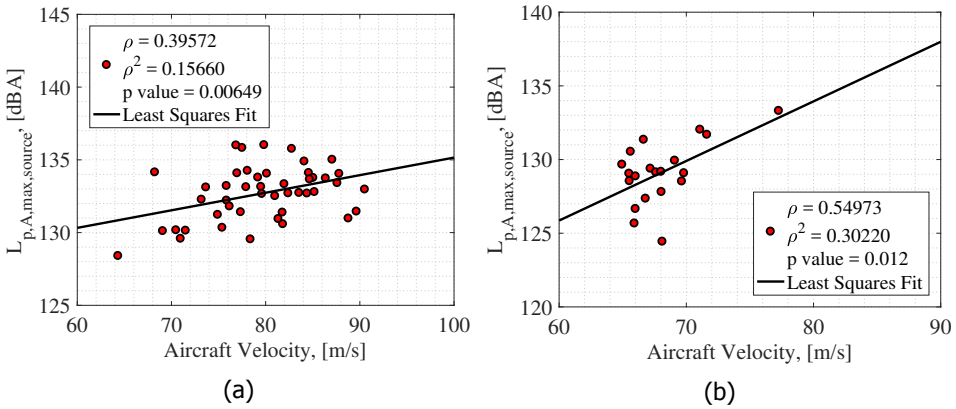

Figure 7.12: Correlation analysis results (without beamforming) between the $L_{p,A,max}$ and the aircraft velocity for: (a) the Boeing 737 *NG* and (b) the Fokker 70. Adapted from [2].

For the Boeing 737 *NG* case, the $L_{p,A,max}$ vs. the $N1\%$ presents $\rho^2 \approx 0.45$, i.e., almost 45% of the total variance observed in the $L_{p,A,max}$ can be explained by the changes in the fan rotational speed, and 16% is explained by variations in

the aircraft velocity. For the Fokker 70 these numbers amount to 37% and 30%, respectively.

However, since $N1\%$ and the aircraft speed are also correlated ($\rho \approx 0.80$), conclusions about the exact contribution of these parameters to the variability cannot be drawn. Therefore, in the next section, functional beamforming (see section 4.3) will be applied to the flyover data. This allows for investigating the noise from the different aircraft components separately. In this chapter, the focus is placed on the noise from the engines, which is expected to be influenced by the engine fan settings, and the noise from the airframe, which is expected to be determined by the aircraft speed.

Assessment of noise level variations using beamforming

Engine noise

For studying the variation of the noise levels at an aircraft component level, a correlation analysis was also performed after applying functional beamforming to the acoustic data. This section focuses on the sound generated by the engines. The times selected for this analysis span from 0.2 s before the time overhead to 0.1 s before the time overhead. Figure 7.13 contains one representative example of the beamforming source plots for both aircraft types. A–weighting (see Appendix A.2) was applied to the results to reduce the influence of low–frequency noise, for which the microphone array has a lower spatial resolution, see Appendix D. The rest of the signal processing parameters were same as in section 5.1.1. Also, indicated in the plots as black rectangles are the ROIs covering the engines, see section 4.2.2. It can be clearly observed that the engines are the dominant noise source for the Boeing 737–800 case. For the Fokker 70 this is less clear.

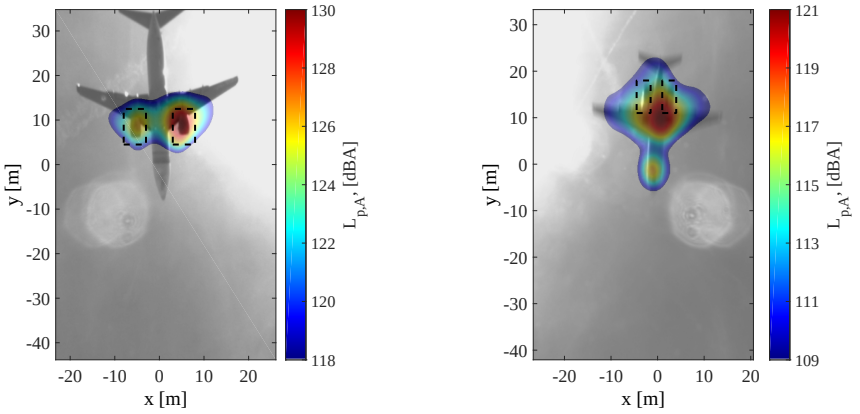

Figure 7.13: Beamforming source plots using functional beamforming with $\nu = 100$ of (a) A Boeing 737–800 flyover. (b) A Fokker 70 flyover. The dashed black rectangles show the ROIs for the variability analysis. Adapted from [2].

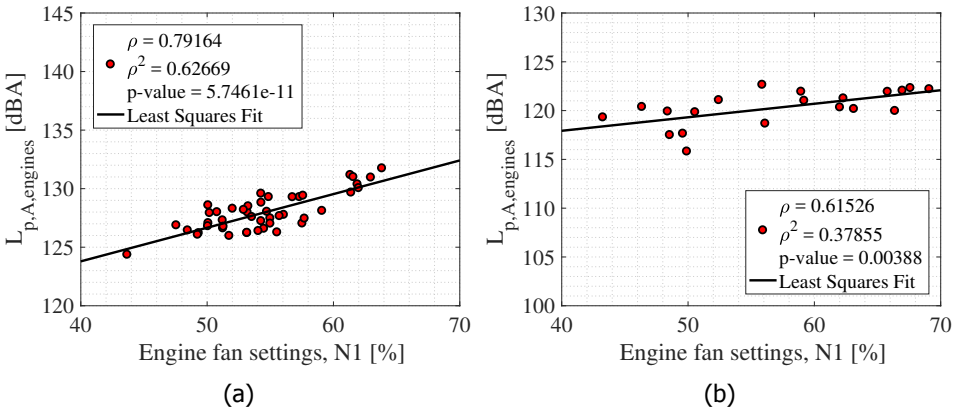

Figure 7.14: Correlation analysis results after applying functional beamforming and considering the engines overall $L_{p,A}$ with respect to $N1\%$ for (a) the Boeing 737 *NG* case and (b) the Fokker 70 case. Adapted from [2].

Figure 7.14 shows the summed overall $L_{p,A}$ integrated in the selected ROIs (black rectangles of Fig. 7.13) plotted with respect to $N1\%$. The increase in the correlation coefficients with respect to $N1\%$ compared to the case without applying beamforming is substantial, where, after beamforming, the engines are found to explain more than 62% of the observed total variation of the $L_{p,A}$ at the engines in the Boeing 737 *NG* case. This can be explained because the contributions from other noise sources are largely eliminated, due to the selection of an appropriate spatial area and frequencies, see section 4.2.2. A comparable study by Simons et al. [11] showed similar results. For the Fokker 70 lower correlations are found. In case that only the $L_{p,A}$ values corresponding to the BPF and its harmonics are considered, the coefficient of determination increases up to $\rho^2 \approx 0.75$ for the Boeing 737 *NG* and $\rho^2 \approx 0.45$ for the Fokker 70 [2].

On the other hand, it was found that the correlation of the engine noise levels with the aircraft velocity is now lower than for the case without beamforming, even being non–significant for the Fokker 70 engine BPF harmonics case (p–value > 0.05) [2]. This is because an increase in aircraft velocity is expected to mostly increase the airframe noise [22–24], and because the main contributors of the airframe noise are the landing gear system and the high-lift devices, engine noise is affected to a lesser extent by aircraft velocity. With this reasoning in mind, the larger correlation of the overall $L_{p,A}$ of the Fokker 70 with the aircraft velocity shown in Fig. 7.12b can be explained, because airframe noise is expected to be more significant for this aircraft type [2]. This is further investigated below.

Airframe noise

A correlation study between the NLG noise emissions and the aircraft velocity was already performed in Chapter 5 for Airbus A320 and regional aircraft, showing very strong and significant correlations ($\rho^2 \approx 0.8$) and a clear agreement with the

expected 6^{th} power law with the flow velocity expected for NLG noise [23–25]. More information about the correlation study for the NLG emissions of the Fokker 70 can be found in [2].

Even if airframe noise is less dominant for the Boeing 737 *NG* case, a similar correlation study was performed for the noise coming from the NLG and the Trailing–Edge Devices (TED), with respect to the aircraft velocity. These two sources were selected because they were distinguishable in most flyover source plots, unlike the main landing gear, which was often masked by the engine noise [2]. The same integration technique for the source maps employed in section 5.2.2 was employed. Unfortunately, there was no information available about the deflection angles of the TED for the flyovers in this research, but, during approach, similar values can be expected [14]. It was confirmed that the TED followed a 5^{th} power law with the flow velocity, as it expected for non–compact sources [26, 27] and that the NLG followed the aforementioned 6^{th} power law [2]. The correlation coefficients obtained for the noise levels with respect to the aircraft velocity ($\rho \approx 0.80$) are similar to the ones obtained for the NLG of the Fokker 70. However, the airframe contribution to the total noise is lower for the Boeing 737 *NG* case.

Relative contribution and variability of the aircraft noise sources

To visualize the relative contributions of the analyzed noise sources on the aircraft and their variability at the same time, the box plots in Fig. 7.15 are presented for the Boeing 737 *NG* and the Fokker 70, respectively.

In the first case (Fig. 7.15a), the engines are the main noise source, with an average overall $L_{\text{p,A}}$ around 4 dBA under the average total overall $L_{\text{p,A}}$. On the other hand, the NLG presents an average overall $L_{\text{p,A}}$ approximately 12 dBA lower than the total. The total overall $L_{\text{p,A}}$ variability (6.9 dBA) is comparable to that of the dominant noise source, i.e., the engine (7.4 dBA). The variability of the NLG is slightly higher (8.7 dBA). However, it has a limited contribution to the total noise level.

For the Fokker 70 (Fig. 7.15b), it was shown that the NLG and the engines present similar contributions to the noise levels with average values about 8 dB lower than the total. The variability of the total overall $L_{\text{p,A}}$ (7.5 dBA) is now slightly larger than the overall $L_{\text{p,A}}$ variabilities of the different sources: engines (6.8 dBA) and NLG (6.2 dBA). It can be observed that the variabilities for both aircraft types are of the same order of magnitude.

Apart from the considerably lower thrust provided, one of the reasons why the engine noise from the Fokker 70 is relatively less dominant than the one from the Boeing 737 *NG* can be the engines location. Figure 7.16 presents one picture of each aircraft type during operating conditions [28, 29]. It can be observed that, whereas the engines of the Boeing 737 *NG* are placed directly under the wing, the engines of the Fokker 70 are placed at the back of the fuselage over the wing, allowing for some noise shielding, especially for noise coming from the engine fan. In addition, the average BPF value of the Fokker 70 is higher than the one for the Boeing 737, and because higher frequencies are usually shielded more efficiently [30], this fact may explain as well why the tonal harmonic peaks from the fan were not very clear for the Fokker 70 in Fig. 7.10b.

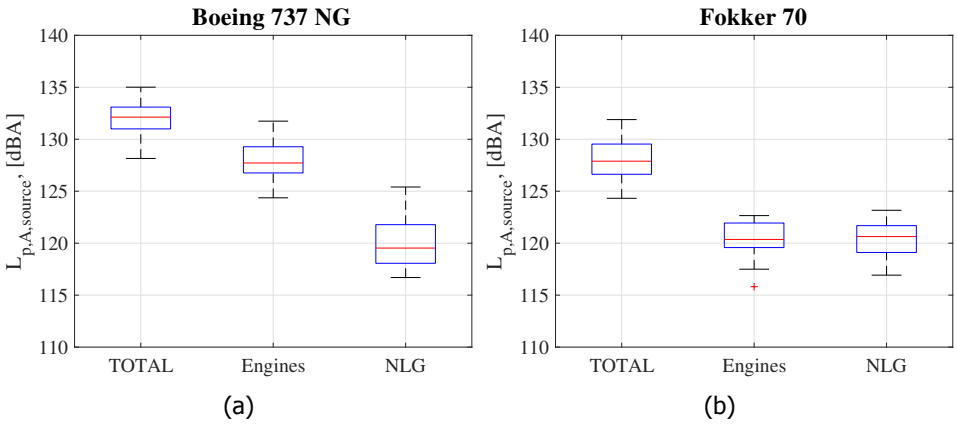

Figure 7.15: Box plot of the total overall $L_{p,A}$ and the overall $L_{p,A}$ at different aircraft components for (a) the Boeing 737 *NG* (b) the Fokker 70. Adapted from [2].

Figure 7.16: (a) A Boeing 737–800 [28]. (b) A Fokker 70. [29]

7.5.2. NOMOS results

For brevity reasons, in the following sections only results of the data recorded by NMT 14 are presented, since that NMT recorded the highest number of flyovers (406 approaches and 329 departures). Moreover, only the Airbus 333 equipped with engines from the CF6–80E1A family and the Boeing 772 aircraft equipped with engines from the GE90 family are considered. These engines were considered to be the most illustrative types because they were the most frequently occurring, see Table 7.4. Data from the other NMTs and engine types showed similar results [4].

Comparison between the measured and modeled engine fan settings

The box plots presented in Fig. 7.17 represent the variability found in several parameters for flyovers recorded by NMT 14. The outliers are plotted individually as red crosses (+). The results are separated depending on the aircraft type (Airbus 333 or Boeing 772) and the operation mode (approach (Ap) or departure (Dep)):

Figure 7.17a shows that both aircraft types present higher $N1\%$ values during departure than during approach, as expected. However, larger variabilities are

found in $N1\%$ during approach, with differences larger than 20%, whereas during departure these differences are roughly 10%. These results indicate that pilots need to adjust the throttle to keep the aircraft on the desired flight path during approach, while for departures the throttle is more fixed. The predicted $N1\%$ values using the data from Fig. 7.1b and Eq. (7.2) for these cases are plotted as black dots on the right of each box plot. Since the recorded aircraft correspond to altitudes within the *plateaus* indicated in Fig. 7.1b, the predicted net thrusts (and hence the $N1\%$) are practically constant per case for the altitude range considered here (see Fig. 7.1b). The default $N1\%$ values for approach fall inside of the box plots obtained experimentally, although they are comparably lower than the average of these. The $N1\%$ values for the departures considered by the NPD tables, on the other hand, are slightly higher the empirical values, i.e., they are slightly overpredicted.

Figure 7.17b contains the variations in true airspeed for the same cases considered above. The mean aircraft true airspeed is practically constant for the four cases and about 68 m/s. The variabilities of this parameter are also similar for the four cases with variations of about 30 m/s.

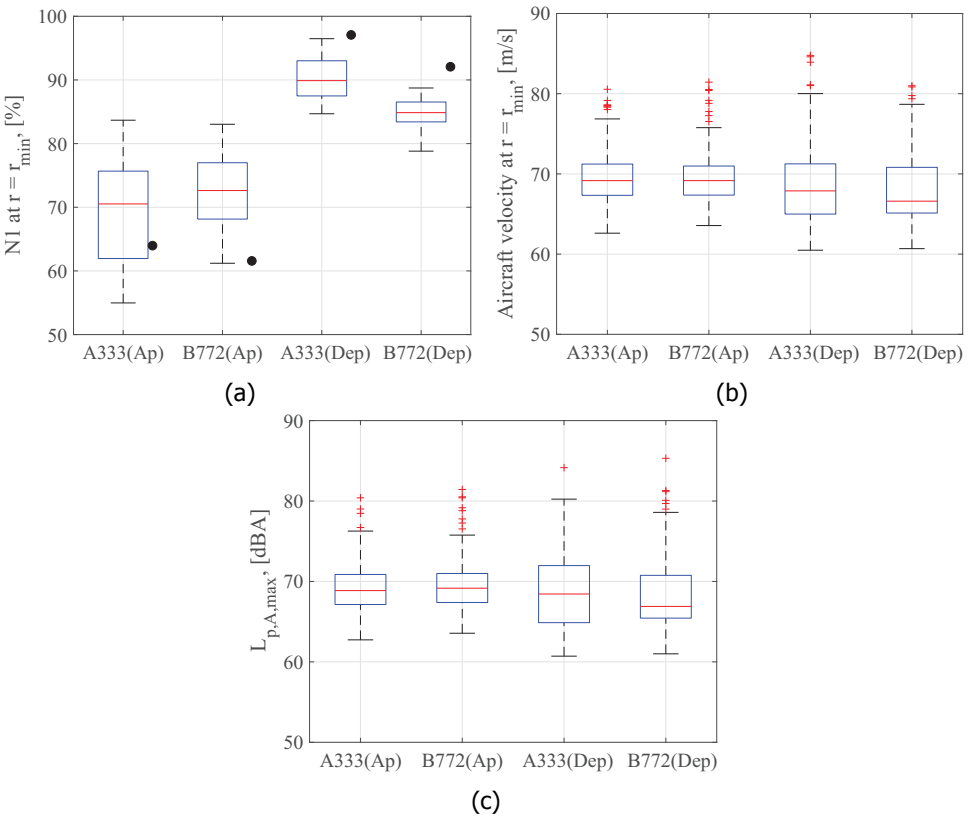

Figure 7.17: Box plots for the flyovers recorded by NMT 14 for the: (a) $N1\%$ at $r = r_{\text{min}}$. (b) True airspeeds at $r = r_{\text{min}}$. (c) $L_{\text{p,A,max}}$ [4].

The box plot in Fig. 7.17c presents the variations in the $L_{p,A,max}$ provided by NOMOS (corrected for distance here, as explained in Eq. (7.1)). The mean values for all four cases are comparable and between 65 and 70 dBA. However, it should be kept in mind that the distance correction explained in Eq. (7.1) is applied to each operation case individually, considering the corresponding mean minimum distance ($\bar{r}_{min}$), but the effect of the higher absolute value of $\bar{r}_{min}$ for departures is not accounted for. Therefore, the reason why departures have comparable $L_{p,A,max}$ values as approaches is because the $\bar{r}_{min}$ values for departures is considerably higher (approximately double) than for approaches for NMT 14, see Fig. 7.3b. In general, variabilities in $L_{p,A,max}$ of about 20 dBA are observed in the four cases. Thus, it is confirmed that the inherent variabilities in the noise levels for the same aircraft and engine type due to manufacturer modifications, as observed in Table 7.4, is negligible compared to the variabilities observed in practice.

Correlation analysis of noise level variations

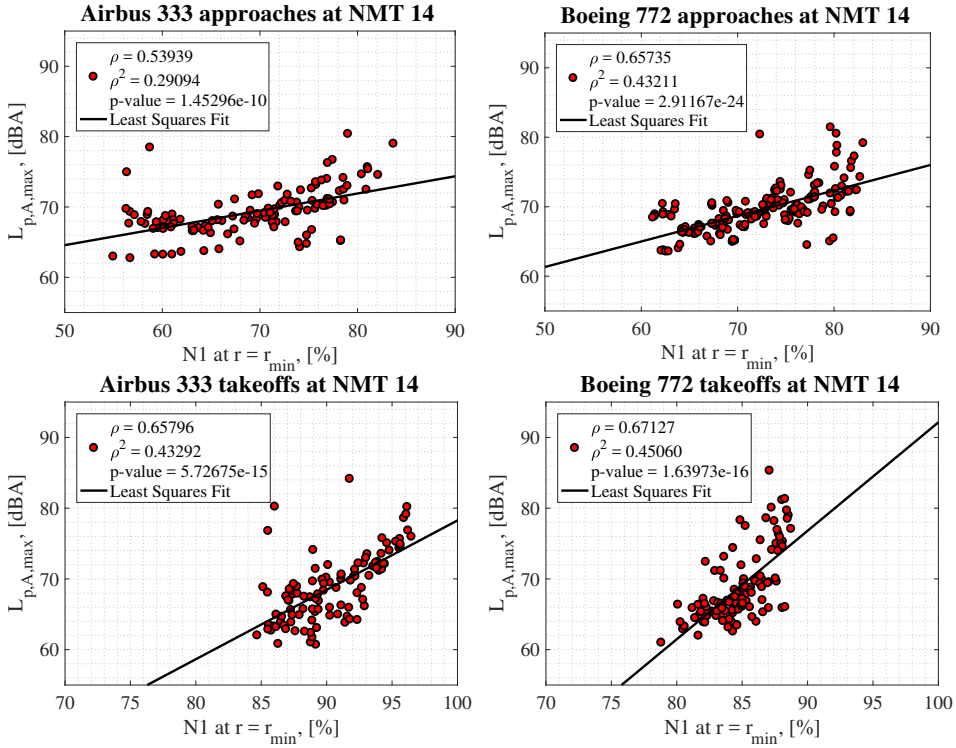

Figure 7.18: Correlation analysis between $L_{p,A,max}$ and $N1\%$ at $r = r_{min}$ recorded by NMT 14 [4].

The results of the correlation analysis between the recorded $L_{p,A,max}$ by the NMT 14 and the calculated engine fan settings ($N1\%$) at $r = r_{min}$ for the Airbus 333 and Boeing 772 flyovers in approaches and departures are presented separately in Fig. 7.18. Following the criterion that the p–value should be lower than 0.05, all

the correlations presented in Fig. 7.18 are deemed as significant. Coefficients of determination between $N1\%$ and $L_{\text{p,A,max}}$ of around 0.3 and 0.4 are found for the approaches of the A333 and B772, respectively. Similar values were obtained in section 7.5.1 for landings of Boeing 737 *NG* and Fokker 70 aircraft. Slightly higher values for ρ^2 (around 0.45) are found for the departure operations of both aircraft in the current study. This is expected because engine noise is supposed to be more dominant during departure than during approach [31], so a stronger correlation with the engine fan settings is justified.

The correlation analysis between the recorded $L_{\text{p,A,max}}$ by the NMT 14 and the aircraft true airspeed at $r = r_{\text{min}}$ showed that none of the correlations found between both variables is significant (if the threshold value of 0.05 is again considered for the p–value). Thus, it is concluded that, in this research, the aircraft velocity at $r = r_{\text{min}}$ does not seem to influence the $L_{\text{p,A,max}}$ experienced on the ground. The fact that jet noise levels decrease with increasing airspeed [12] could explain the lack of significant correlation with the airspeed during departure, where jet noise is a dominant noise source. These results are different to those presented in the research featuring a microphone array, see section 7.5.1. In that study, however, the minimum distances to the aircraft in that study were considerably smaller (around 70 m) and, thus, the engines are supposed to be operating at lower power settings. Therefore, airframe noise, which has a strong correlation with the flow velocity, becomes more relevant [32]. In addition, the noise levels were considered at the source location, instead of on the ground and more sophisticated sound propagation considerations (such as the atmospheric absorption) were taken into account.

Comparison of the recorded noise levels with the modeled ones

In order to assess the importance of including more accurate estimations of the $N1\%$ values obtained with the method explained in section 7.4.2 compared to the ones used in the NPD tables, a comparison with the recorded NOMOS data was made twice:

1. **Case** 1: All the parameters required for Eq. (7.2) were filled in with the experimentally measured values (V_C, $\tilde{h}$, T_0 and θ_T), except for $N1\%$ which was determined according to the NPD estimations, using Eq. (7.2) and Fig. 7.1b, based on the aircraft altitude.

2. **Case** 2: Same conditions as in case 1, but this time the $N1\%$ values used were those found experimentally from the audio recordings as explained in section 7.4.2.

It should be noted that the distance correction explained in Eq. (7.1) was not applied in the $L_{\text{p,A,max}}$ results shown in this subsection, since the NPD tables already account for the effects of the distance to the aircraft (r).

The results of both comparisons with the recorded NOMOS data are gathered in Figs. 7.19 and 7.20 for approaches and departures, respectively. In these figures, the graphs on the left correspond to the comparison for the NPD tables predictions using the default $N1\%$ values and the graphs on the right correspond to the comparison for the NPD tables predictions using the $N1\%$ values obtained experimentally.

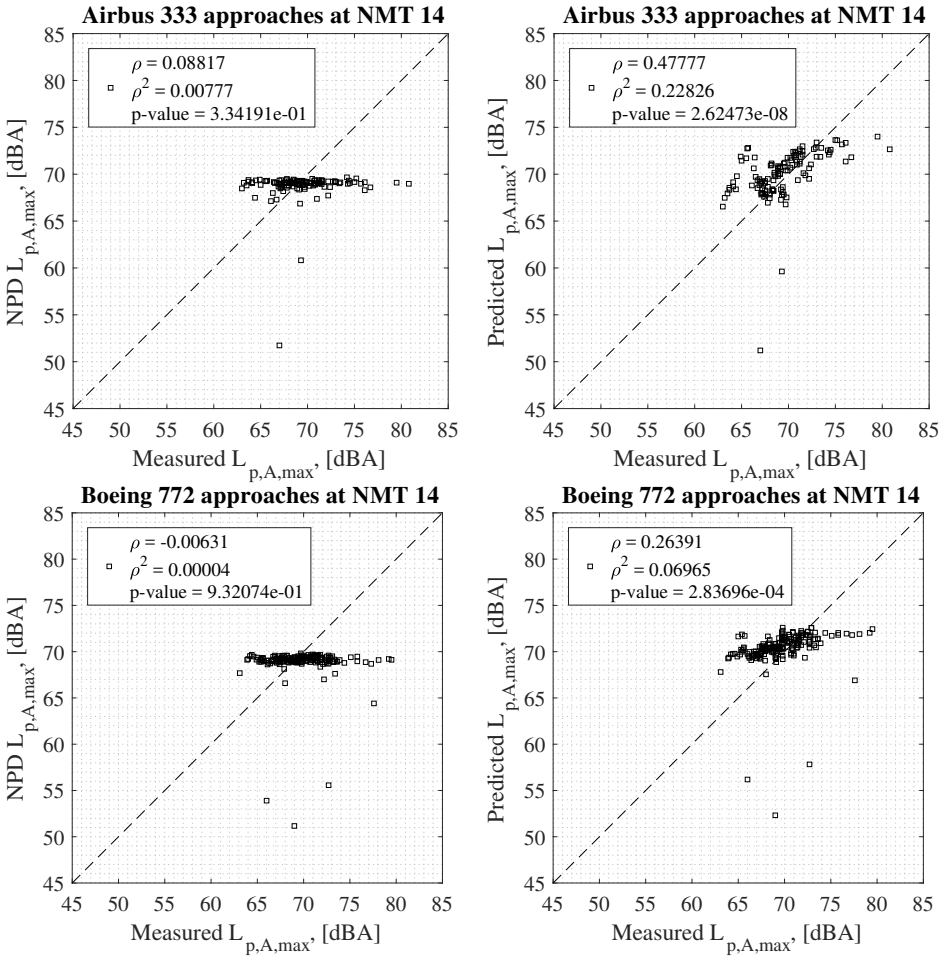

Figure 7.19: Recorded $L_{p,A,max}$ vs. modeled $L_{p,A,max}$ using default (left) or experimental (right) $N1\%$ values for approaches [4].

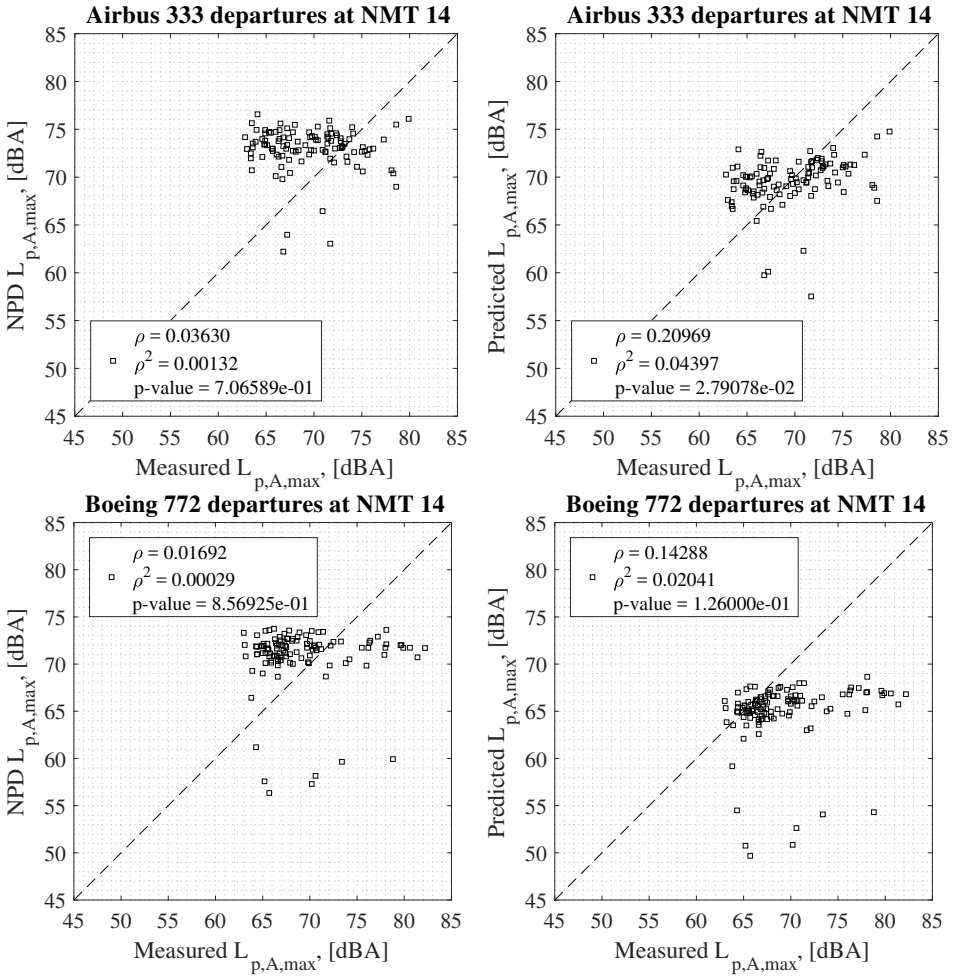

Figure 7.20: Recorded $L_{p,A,max}$ vs. modeled $L_{p,A,max}$ using default (left) or experimental (right) $N1\%$ values for departures [4].

Table 7.5: Average error (ε) and average of the absolute values of the errors (ε_{abs}) for $L_{p,A,max}$ predictions with the NPD tables' default estimations of $N1\%$ and using the $N1\%$ values obtained experimentally [4].

Case	ε_{NPD}, [dBA]	$\varepsilon_{NPD,\ abs}$, [dBA]	ε_{Exp}, [dBA]	$\varepsilon_{Exp,\ abs}$, [dBA]
A333 Ap	1.65	2.65	−0.64	2.18
B772 Ap	1.83	2.62	−0.71	2.26
A333 Dep	−2.97	5.38	0.46	3.78
B772 Dep	−1.62	5.00	1.68	3.85

The statistical parameters (correlation coefficient, coefficient of determination and p–value) are also shown in each graph. The diagonal line (depicted as a black dashed line) in Figs. 7.19 and 7.20 represents a perfect agreement between estimated and measured $L_{p,A,max}$ levels ($\rho = 1$). It can be observed that considering the experimental $N1\%$ values produces a better agreement between the modeled and measured values of $L_{p,A,max}$. This fact is confirmed by the considerably higher correlation coefficient values (and hence higher coefficient of determination values) presented by the graphs that use the experimental $N1\%$ values. The largest improvement is observed for the case of the Airbus 333 approaches (see, Fig. 7.19 top graphs) where ρ increases from a value of 0.088 to a value of 0.478 (more than five times).

The average error (ε) and the average of the absolute values of the errors (ε_{abs}) made by both predictions (using default or calculated $N1\%$ values) for each case are presented in Table 7.5. The error is defined as the difference between the measured and the estimated $L_{p,A,max}$. Hence, $\varepsilon > 0$ means that the model underpredicts the actual noise levels and vice versa. The standard deviations of these errors, $\tilde{s}$, are gathered in Table 7.6. On average, including the experimental estimations of $N1\%$ reduces ε by 1 dBA and ε_{abs} and $\tilde{s}$ by 0.5 dBA. Despite this improvement, there is still a significant discrepancy between the noise measurements and the noise model predictions. Additionally, it can be observed that in all the graphs there are several outliers that are severely underpredicted by both NPD predictions by up to 15 dBA. These recordings were studied and listened manually and it was confirmed that they do correspond to aircraft flyovers, but at higher distances to the observer. Therefore, the investigation of more sophisticated and accurate models is strongly encouraged. However, the rest of aircraft parameters, such as velocity or altitude, are normally not determined for the NPD calculations, and default tabulated values are also used. Thus, the actual NPD estimations for $L_{p,A,max}$ are most probably less accurate than those presented here. Hence, the error reduction obtained by using accurate $N1\%$ values could be even higher in reality. The approach of including the actual aircraft parameters was taken to isolate the influence of the choice of $N1\%$ for NPD predictions.

Moreover, the variabilities of the $L_{p,A,max}$ metric ($\Delta L_{p,A,max}$, i.e., the maximum $L_{p,A,max}$ value minus the minimum $L_{p,A,max}$ value observed) for each dataset (estimations with default or estimated $N1\%$ values or NOMOS recordings) are included in Table 7.7. For the calculation of this parameter, the aforementioned outliers

Table 7.6: Standard deviation ($\tilde{s}$) for $L_{p,A,max}$ predictions with the NPD tables' default estimations of $N1\%$ and using the $N1\%$ values obtained experimentally for each operation case [4].

Case	$\tilde{s}_{NPD}$, [dBA]	$\tilde{s}_{Exp}$, [dBA]
A333 Ap	3.58	3.07
B772 Ap	3.57	3.14
A333 Dep	6.05	5.66
B772 Dep	5.62	5.34

Table 7.7: $\Delta L_{p,A,max}$ in dBA of (left) the predictions with the NPD tables' estimations of $N1\%$, (center) the predictions using the $N1\%$ values obtained experimentally and (right) NOMOS recordings [4].

Case	NPD $\Delta L_{p,A,max}$	Exp. $\Delta L_{p,A,max}$	NOMOS $\Delta L_{p,A,max}$
A333 Ap	2.72	7.47	17.80
B772 Ap	3.27	5.69	16.40
A333 Dep	7.87	9.35	17.10
B772 Dep	5.21	6.55	19.20

present in Figs. 7.19 and 7.20 were excluded. On average, using the experimental estimations of $N1\%$ bring the values of $\Delta L_{p,A,max}$ 2.5 dBA closer to the NOMOS recordings. Once again, despite this improvement, there is still a remaining 10 dBA variability (on average) that remains unexplained. This additional variability is not accounted for by the prediction model suggested in this thesis, and is subject for future investigation.

7.6. Conclusions and outlook

In this chapter, the issue of obtaining accurate predictions of aircraft noise levels was analyzed. The presence of large sound pressure level variations (of several decibels) for the same aircraft type in the same conditions poses a problem when assessing the noise levels around airports and when enforcing environmental laws, since current noise prediction models fail to account for these variations. In this research, the noise variability was assumed to depend mostly on the emitted noise at the source, i.e., the aircraft itself, neglecting the effects of a variable atmosphere. One of the main reasons for these discrepancies in the estimations is the lack of accurate input data for these models. For example, the engine fan settings ($N1\%$) are typically roughly estimated from tabulated default values, because these data are not publicly available for reasons such as pilot privacy and to ensure the operation business strategies of airlines.

Therefore, two different automatic approaches to determine the engine fan settings ($N1\%$) directly from flyover audio recordings were proposed and tested, respectively, on the data from two experimental campaigns around Amsterdam Airport Schiphol: one featuring a microphone array and the other single microphones

from the NOMOS system. Both methods were applied to a large number (more than a thousand) of aircraft flyovers under operational conditions and provided accurate results, even when the audio files had a relatively narrow frequency content. A large spread was found in the values of $N1\%$ obtained experimentally, compared to the default values assumed by the noise models.

It was confirmed that there is a strong and significant correlation between the aircraft noise levels and $N1\%$, especially if only the noise emitted by the engines is considered by applying acoustic imaging. Moreover, some components of the airframe such as the landing gear system and trailing edge devices showed a correlation between their noise levels and the aircraft velocity, in agreement with the theory.

In conclusion, including more accurate estimations for $N1\%$ in the prediction models rather than default tabulated values considerably reduces the error made with respect to the experimental recordings. However, there is still a remaining error in the noise levels unexplained by the noise prediction models.

After observing the limitations of the noise prediction model employed in this chapter, it is recommended to improve such models, especially by using more accurate individual flight parameters or accounting for the influence of $N1\%$ in the noise levels. This recommendation is especially intended for more sophisticated purposes, such as noise abatement studies, rather than studies on the average exposure noise levels over long time periods, where errors in the model estimates can balance out.

Additional research with other aircraft types is encouraged, especially when using signals containing a larger frequency range and when employing microphone arrays which allow the separation of different noise sources on board of the aircraft. Moreover, repeating this study using other noise metrics, such as novel psychoacoustic annoyance metrics [33], see Appendix A.5, is of high interest. Studying the sound radiation directivity pattern is also a topic to be investigated.

In conclusion, an obvious recommendation to reduce the aircraft noise levels perceived in the surroundings of airports is to reduce as much as possible the engine fan settings and the aircraft velocity, while still fulfilling the safety and operational constraints. Investigating low–noise–impact operations is also of interest, such as the continuous descent approach concept [12, 34].

Acknowledgements

The author thanks Dr. Michael Arntzen from Amsterdam Airport Schiphol for providing the NOMOS experimental data and critical thinking. The author also acknowledges Henk Veerbeek from the Netherlands Aerospace Center (NLR) for providing data about the engines for the NOMOS dataset.

Bibliography

[1] M. Snellen, R. Merino-Martinez, and D. G. Simons, *Assessment of aircraft noise sources variability using an acoustic camera,* in *5th CEAS Air & Space Conference. Challenges in European Aerospace. September 7 – 11 2015,*

Delft, Netherlands, Paper 2015–019 (Council of European Aerospace Societies, 2015).

[2] M. Snellen, R. Merino-Martinez, and D. G. Simons, *Assessment of noise level variability on landing aircraft using a phased microphone array,* Journal of Aircraft **54**, 2173 (2017).

[3] R. Merino-Martinez, M. Snellen, and D. G. Simons, *Determination of Aircraft Noise Variability Using an Acoustic Camera,* in *23rd International Congress on Sound and Vibration, July 10 – 14 2016, Athens, Greece* (International Inst. of Acoustics and Vibration (IIAV), Auburn, Alabama, USA., 2016).

[4] R. Merino-Martinez, S. J. Heblij, D. H. T. Bergmans, M. Snellen, and D. G. Simons, *Improving Aircraft Noise Predictions by Considering the Fan Rotational Speed,* Journal of Aircraft (2018), 10.2514/1.C034849, Accepted for publication. DOI: 10.2514/1.C034849.

[5] *Procedure for the Calculation of Airplane Noise in the Vicinity of Airports, Aerospace Information Report AIR 1845*, Tech. Rep. 1845 (Society of Automotive Engineers, Inc. (SAE) - Committee on Aircraft Noise (SAE A-21), 400 Commonwealth Drive, Warrendale, PA 15096, 1986).

[6] *Recommended method for computing noise contours around airports (ICAO Circular 205–AN/1/25)*, Tech. Rep. 9911 (International Civil Aviation Organization (ICAO), Montreal, Canada., 1988).

[7] *CEAC Doc. 29. Report on Standard Method of Computing Noise Contours around Civil Airports. Volume 2: Technical Guide*, Tech. Rep. (European Civil Aviation Conference (ECAC), Neuilly sur Seine Cedex, France, 2016) 4th edition.

[8] B. He, E. Dinges, J. Hemann, D. Rickel, L. Mirsky, C. Roof, E. Boeker, P. Gerbi, and D. Senzig, *Integrated Noise Model (INM) Version 7.0 User's Guide*, Tech. Rep. (Federal Aviation Administration (FAA) – U.S. Department of Transportation, Washington, DC, 2007) report No. FAA-AEE-07-04.

[9] E. Boeker, E. Dinges, B. He, G. Fleming, C. Roof, P. Gerbi, A. Rapoza, and J. Hemann, *Integrated Noise Model (INM) Version 7.0 User's Guide*, Tech. Rep. (Federal Aviation Administration (FAA) – U.S. Department of Transportation, Washington, DC, 2008) report No. FAA-AEE-08-01.

[10] D. Bergmans, M. Arntzen, and W. Lammen, *Noise attenuation in varying atmospheric conditions*, Tech. Rep. NLR–TP–2011–262 (National Aerospace Laboratory (NLR), Anthony Fokkerweg 2, 1059 CM Amsterdam, P.O. Box 90502, 1006 BM Amsterdam, The Netherlands, 2011).

[11] D. G. Simons, M. Snellen, B. Midden, M. Arntzen, and D. H. T. Bergmans, *Assessment of noise level variations of aircraft fly–overs using acoustic arrays,* Journal of Aircraft **52**, 1625 (2015).

[12] C. Zellmann, B. Schäffer, J. M. Wunderli, U. Isermann, and C. O. Paschereit, *Aircraft Noise Emission Model Accounting for Aircraft Flight Parameters,* Journal of Aircraft (2017), 10.2514/1.C034275.

[13] Aircraft Noise and Performance (ANP) database website, *http://www.aircraftnoisemodel.org,* Accessed in June 2017.

[14] R. Merino-Martinez, L. Bertsch, M. Snellen, and D. G. Simons, *Analysis of landing gear noise during approach,* in *22nd AIAA/CEAS Aeroacoustics Conference. May 30 – June 1 2016. Lyon, France* (2016) AIAA paper 2016–2769.

[15] Schiphol Amsterdam Airport NOMOS website, *https://noiselab.casper.aero/ams/,* Accessed in March 2017.

[16] Brüel & Kjær Airport Noise Monitoring and Management System website, *https://www.bksv.com/en/products/environment-management/airport-environment-monitoring/anoms,* Accessed in June 2017.

[17] M. Arntzen, *Aircraft noise calculation and synthesis in a non–standard atmosphere*, Ph.D. thesis, Delft University of Technology (2014), ISBN: 978–94–62594–64–7.

[18] European Aviation Safety Agency (EASA) website, *http://www.easa.europa.eu,* Accessed in August 2013.

[19] Royal Netherlands Meteorological Institute (KNMI) website, *https://www.knmi.nl/nederland-nu/klimatologie/uurgegeven,* Accessed in August 2013.

[20] S. Schlüter and S. Becker, *Determination of aircraft engine speed based on acoustic measurements,* in *45th International Congress and Exposition of Noise Control Engineering, 21–24 August, 2016, Hamburg, Germany* (Institute of Noise Control Engineering, 11130 Sunrive Valley Drive, Suite 350 Reston, VA 20191, USA, 2016).

[21] C. L. Lawson and R. J. Hanson, *Solving least squares problems*, edited by S. for Industrial and A. Mathematics (Prentice–Hall, Inc., Englewood Cliffs, New Jersey, 1974) ISBN: 0–89871–356–0.

[22] W. Dobrzynski and H. Buchholz, *Full–scale noise testing on Airbus landing gears in the German Dutch Wind Tunnel,* in *3rd AIAA/CEAS Aeroacoustics Conference. May 12 – 14 1997, Atlanta GA, USA* (1997) AIAA paper 1997–1597.

[23] M. R. Fink, *Noise component method for airframe noise,* in *4th AIAA Aeroacoustics Conference. October 3 – 5 1977, Atlanta, Georgia, USA* (1977) AIAA paper 1977–1271.

[24] N. Curle, *The influence of solid boundaries upon aerodynamic sound,* Proceedings of Royal Society of London A **231**, 505 (1955).

[25] W. Dobrzynski, *Almost 40 Years of Airframe Noise Research: What Did We Achieve?* Journal of Aircraft **47**, 353 (2010).

[26] J. Delfs, *Basics of Aeroacoustics – Lecture notes at Technische Universität Braunschweig* (Institut für Aerodynamik und Strömungstechnik Abteilung Technische Akustik DLR – Deutsches Zentrum für Luft– und Raumfahrt e.V., Lilienthalplatz 7, 38108 Braunschweig, Germany, 2011).

[27] J. E. Ffowcs Williams and L. H. Hall, *Aerodynamic sound generation by turbulent flow in the vicinity of a scattering half plane,* Journal of Fluid Mechanics **40**, 657 (1970).

[28] Source for Boeing 737–800 picture, *http://www.boeing.com/commercial/737ng/,* Accessed in January 2016.

[29] Source for Fokker 70 picture, *https://commons.wikimedia.org,* Accessed in January 2016.

[30] A. Vieira, M. Snellen, and D. G. Simons, *Assessing the shielding of engine noise by the wings for current aircraft using model predictions and measurements,* Journal of the Acoustical Society of America **143**, 388 (2018).

[31] R. Merino-Martinez, M. Snellen, and D. G. Simons, *Functional beamforming applied to imaging of flyover noise on landing aircraft,* Journal of Aircraft **53**, 1830 (2016).

[32] R. Merino-Martinez, E. Neri, M. Snellen, J. Kennedy, D. Simons, and G. Bennett, *Comparing flyover noise measurements to full–scale nose landing gear wind–tunnel experiments for regional aircraft,* in *23^{rd} AIAA/CEAS Aeroacoustics Conference. June 5 – 9 2017. Denver, Colorado, USA* (2017) AIAA paper 2017–3006.

[33] A. K. Sahai and E. Stumpf, *Incorporating and Minimizing Aircraft Noise Annoyance during Conceptual Aircraft Design,* in *20^{th} AIAA/CEAS Aeroacoustics Conference, June 16 – 20 2014, Atlanta, GA, USA* (2014) AIAA paper 2014–2078.

[34] M. Y. Pereda Albarrán, A. K. Sahai, and E. Stumpf, *Aircraft noise sound quality evaluation of continuous descent approaches,* in *46^{th} International Congress and Exposition of Noise Control Engineering, 27–30 August, 2017, Hong Kong* (2017).

8

Conclusions and outlook

You should bring something into the world that wasn't in the world before. It doesn't matter what that is. It doesn't matter if it's a table or a film or gardening - everyone should create. You should do something, then sit back and say "I did that".

Ricky Dene Gervais

It always seems impossible until it's done.

Nelson Rolihlahla Mandela

8.1. Conclusions

This thesis has investigated the applications of phased microphone arrays for imaging of aerospace noise sources, such as flying aircraft or wind turbine blades. The most common and dominant noise sources to be expected were introduced in Chapter 2. Microphone arrays have become one of the main measurement devices for aeroacoustic noise sources, but the typical experiments (flyover measurements or wind–tunnel tests) present several different challenges, which were summarized in Chapter 3.

It is worthy to revisit the four research objectives stated in Chapter 1 and to assess to what extent they have been fulfilled:

1. **Analyze the state–of–the–art acoustic imaging methods for microphone arrays and assess their performance and applicability to aeroacoustic measurements on typical aerospace noise sources.**

   A detailed analysis of the most widely–used and newest acoustic imaging methods was included in Chapter 4. During the preparation of this thesis,

it was found that functional beamforming seems to be an adequate technique for analyzing aircraft flyover measurements [1, 2]. The integration techniques SPIL and ISPI proved to be the best choices for distributed sound sources, such as trailing–edge noise, even when high background noise levels are present [3, 4]. Lastly, the super–resolution technique HR–CLEAN–SC [5, 6] was introduced and proved to be a better choice than other deconvolution techniques, especially when sound sources are placed very closely (closer than the Rayleigh resolution limit).

2. **Perform experiments with microphone arrays on typical airframe noise sources, such as landing gear noise, and, when possible, compare the results obtained with other aeroacoustic approaches, such as CAA or noise prediction models.**

   The noise emissions of the landing gear system of aircraft under operational conditions were studied in two studies (see Chapter 5): one featuring Airbus A320 flyovers and the other recordings of regional aircraft. This noise source was selected because it is considered to be the dominant airframe noise source on commercial landing aircraft. This fact was confirmed for all the aircraft flyovers analyzed in this thesis, which showed strong tonal noise at a frequency of about 1600 Hz for the Airbus A320 and about 2200 Hz for the regional aircraft. Several findings seem to indicate that these tonal peaks are caused by the presence of open cavities in the landing gear system. The comparison of the flyover measurements with noise prediction models (PANAM, Fink and Guo) showed that these models do not consider these tonal peaks, which leads to considerable differences between the predicted and the measured noise levels. The results for regional aircraft flyovers were compared with wind–tunnel measurements and computational simulations performed within the ALLEGRA project. The wind–tunnel results show similar trends as the flyover measurements and the computational results also show a strong tonal peak at a similar frequency. Recommendations were provided to reduce the noise emissions from this source.

3. **Evaluate the performance of noise reduction measures on airfoil noise for wind turbine applications using wind–tunnel measurements.**

   Two of the main current noise reduction measures for airfoil noise were studied in Chapter 6: trailing–edge serrations and trailing–edge porous inserts.

   Three different experimental campaigns on trailing–edge serrations showed that noise reductions up to 16 dB can be achieved with respect to the baseline case with a straight trailing edge. Special care should be taken when installing serrations on wind turbine blades, because a serration–flow misalignment angle can cause a noise increase after a crossover frequency. General recommendations about the serration design and other parameters influencing the performance of trailing–edge serrations were provided. The use of novel serration geometries can lead to even further noise reductions and it certainly worths future research.

Wind–tunnel experiments showed that inserts of porous materials provide noise reductions of about 10 dB with respect to the solid baseline case, especially at low frequencies, but they cause a noise increase after a threshold frequency (corresponding to a chord–based Strouhal number of $St \approx 14$). It was argued that the physical mechanisms for these phenomena are the cross–flow between both sides of the airfoil (i.e., lower acoustic impedance) and the increased surface roughness, respectively. When porous inserts are employed, the location of the line source causing the trailing–edge noise moves upwind to the permeable–impermeable junction.

4. **Assess the measured variability of aircraft noise flyovers under similar operational conditions, analyze potential causes for this variability, and compare the results with current noise prediction models.**

   Large sound pressure level variations (of more than 6 dB) for the same aircraft type and under the same operational conditions were observed in the experimental campaigns described in Chapter 7, which hinder the accurate prediction of aircraft noise levels around airports. These variations are not accounted for in the *best–practice* noise prediction models due to the lack of accurate input data, such as the engine fan settings ($N1\%$ or relative fan rotational speed). Hence, two approaches were proposed to determine the $N1\%$ of an aircraft flyover using the audio recording. Including the obtained $N1\%$ values in the prediction models (rather than rough tabulated estimations as usual) considerably reduces the errors made with respect to the measured noise levels. The use of a phased microphone array in one of the experimental campaigns allowed for the isolation of certain noise sources on board of the aircraft. Strong and significant correlations were found between the engine noise levels and $N1\%$, and between the airframe noise levels and the aircraft velocity. Therefore, it is highly recommended to update the current models by providing more accurate estimates of parameters such as $N1\%$ or the aircraft velocity. Lastly, it is recommended to reduce as much as possible $N1\%$ and the aircraft velocity, while still fulfilling the safety and operational constraints.

In conclusion, the work presented in this thesis has confirmed the great importance and added value of phased microphone arrays for research in aeroacoustics, in wind–tunnel experiments and in full–scale measurements under operational conditions.

8.2. Outlook

After reviewing the results and statements of this thesis, some recommendations for future work can be made:

- This thesis has confirmed the importance of measuring aircraft flyovers under operational conditions for assessing the noise levels around airports. Therefore, it is highly recommended to perform additional field experiments featuring larger microphone arrays (to achieve better spatial resolution) and to

extend the study to more aircraft types, including aircraft equipped with propeller engines. An interesting approach would be to place a permanent microphone array next to an airport runway, which would continuously record the sound and trajectory of all the flyovers. Issues, such as the protection of the microphones and data acquisition systems against the environmental conditions and data storage should be carefully considered.

- The use of novel sound quality metrics [7–9] (see Appendix A.5) is an interesting approach, since they are believed to express the actual annoyance experienced by the human ear in a better way than the simpler, conventional sound metrics, such as the sound pressure level L_p. This study can be applied to both the sound generated by a whole aircraft or by a certain aircraft component (whose signal would be isolated using acoustic imaging methods). This way, it could be determined which noise sources cause the highest annoyance, rather than just the highest sound pressure levels, and pay special attention to them. This procedure should also be applied to noise reduction measures (see Chapter 6), to ensure that they indeed reduce the annoyance perceived by the population.

- The application of microphone array methods to the results obtained in computational simulations is certainly interesting, since it would allow the use of virtual arrays with large sizes and number of microphones with a considerably lower cost than in actual experiments. In addition, all the emission directions could be, in principle, analyzed non–intrusively, which is practically impossible using the current experimental setups. An hybrid approach as the one presented in Chapter 5 should be performed, if possible.

- After showing the shortcomings of the current aircraft noise prediction models, it is highly recommended to improve their capabilities, such as by considering parasitic noise sources (like open cavities in the landing gear, see Chapter 5) for models considering aircraft components, or by increasing the accuracy of the inputs used, such as the engine fan settings (see Chapter 7).

- Lastly, the investigation of the performance of new noise reduction measures, such as trailing–edge serrations with novel shapes or manufactured in porous materials (see Chapter 6), is of high interest for future research.

Bibliography

[1] R. Merino-Martinez, M. Snellen, and D. G. Simons, *Functional beamforming applied to imaging of flyover noise on landing aircraft,* Journal of Aircraft **53**, 1830 (2016).

[2] R. Merino-Martinez, M. Snellen, and D. G. Simons, *Functional Beamforming Applied to Full Scale Landing Aircraft,* in *6th Berlin Beamforming Conference, February 29 – March 1 2016, Berlin, Germany* (GFaI, e.V., Berlin, 2016) BeBeC–2016–D12.

[3] R. Merino-Martinez, P. Sijtsma, and M. Snellen, *Inverse Integration Method for Distributed Sound Sources,* in 7th Berlin Beamforming Conference, March 5 – 6 2018, Berlin, Germany (GFaI, e.V., Berlin, 2018) BeBeC–2018–S07.

[4] R. Merino-Martinez, P. Sijtsma, A. Rubio Carpio, R. Zamponi, S. Luesutthiviboon, A. M. N. Malgoezar, M. Snellen, N. Van de Wyer, C. Schram, and D. G. Simons, *Integration methods for distributed sound sources,* International Journal of Aeroacoustics (2018), Under review process.

[5] P. Sijtsma, R. Merino-Martinez, A. M. N. Malgoezar, and M. Snellen, *High–Resolution CLEAN–SC: Theory and Experimental Validation,* International Journal of Aeroacoustics **16**, 274 (2017), SAGE Publications Ltd. London, United Kingdom.

[6] S. Luesutthiviboon, A. M. N. Malgoezar, R. Merino-Martinez, M. Snellen, P. Sijtsma, and D. G. Simons, *Adaptive HR–CLEAN–SC for resolving multiple closely–spaced sound sources,* International Journal of Aeroacoustics (2018), Under review process.

[7] W. Aures, *Procedure for calculating the sensory euphony of arbitrary sound signal,* Acustica **59**, 130 (1985).

[8] S. R. More, *Aircraft Noise Characteristics and Metrics*, Ph.D. thesis, Purdue University (2010), report No. PARTNER–COE–2011–004.

[9] A. K. Sahai, *Consideration of Aircraft Noise Annoyance during Conceptual Aircraft Design*, Ph.D. thesis, Rheinisch–Westfälische Technische Hochschule Aachen (2016).

A

Appendix A - Sound metrics for aerospace noise

Several sound metrics have been developed in the past, some of them with the specific aim to quantify the annoyance experienced by the human ear. In this appendix, the most widely used metrics for aerospace noise sources are briefly explained. Additional metrics can be found in the literature [1, 2].

A.1. Sound Pressure Level (SPL or L_p)

Sound waves are generated by small pressure deviations around the barometric ambient pressure of the propagation medium. These pressure deviations are considerably smaller than the ambient pressure, but they can range from 20 μPa (the hearing threshold, $p_{e,0}$, corresponding to 0 dB) to 20 Pa (the pain threshold). Variations outside of this range are of course possible, but lower pressures are not easily detected by humans (and therefore not a cause of annoyance) and higher pressures are not common in practice [1].

Since the variation range of the amplitudes of the acoustic waves is very large (about 6 orders of magnitude), the metric in a logarithmic scale called sound pressure level (SPL or L_p) was introduced with decibel (dB) as its unit. It can be calculated using the following expression

$$L_p = 10 \log_{10} \frac{p_e^2}{p_{e,0}^2} = 20 \log_{10} \frac{p_e}{p_{e,0}}, \tag{A.1}$$

where $p_{e,0}$ is the reference pressure corresponding to the threshold of hearing (typically taken as 20 μPa) and p_e denotes the effective acoustic pressure defined as the root–mean–square (RMS) value of an acoustic wave in a period of time T [1] (see Appendix C.2.3)

$$p_{\mathrm{e}} = \sqrt{\frac{1}{T}\int_0^T p^2 dt}. \tag{A.2}$$

In case K incoherent sound sources are present, the overall sound pressure level (OSPL or $L_{\mathrm{p,overall}}$) can be calculated by summing the contributions $L_{\mathrm{p,k}}$ from each source logarithmically [1]

$$L_{\mathrm{p,overall}} = 10\log_{10}\left(\sum_{k=1}^{K} 10^{L_{\mathrm{p,k}}/10}\right). \tag{A.3}$$

This is also the formula used for calculating the overall sound pressure level in a frequency range, but instead of assuming K sound sources, K frequencies are considered.

A typical human ear is assumed to perceive sound frequencies between 20 Hz and 20 kHz [1]. The hearing threshold is defined as 0 dB and the threshold of pain is normally considered as 120 dB [1].

A.2. A–weighted Sound Pressure Level ($L_{\mathrm{p,A}}$)

Since the human ear perceive a different loudness for sound of different frequencies [1, 3], several weighting functions for the sound pressure level metric have been suggested to take this phenomenon into account. The most commonly used function for aerospace noise sources is the A–weighting, but other functions such as the B, C[1] or D–weighting are also used [1, 2]. The A–weighted sound pressure level $L_{\mathrm{p,A}}$ for a certain frequency f can be calculated by adding a correction factor $\Delta L_{\mathrm{A}}(f)$ for that frequency to the $L_{\mathrm{p}}(f)$

$$\Delta L_{\mathrm{A}}(f) = -145.528 + 98.262\log_{10} f - 19.509(\log_{10} f)^2 + 0.975(\log_{10} f)^3. \tag{A.4}$$

Thus, the $L_{\mathrm{p,A}}$ for a certain frequency can be calculated as

$$L_{\mathrm{p,A}}(f) = L_{\mathrm{p}}(f) + \Delta L_{\mathrm{A}}(f). \tag{A.5}$$

The graphical representation of Eq. (A.4) is illustrated in Fig. A.1. It can be observed that for frequencies between approximately 1 and 6 kHz $\Delta L_{\mathrm{A}} > 0$,i.e., the human ear is more sensitive to these frequencies and a penalty is applied. Outside of this range, the rest of the frequencies are reduced considerably, especially for low frequencies. The unit of $L_{\mathrm{p,A}}$ is referred to as dB(A) or simply dBA.

In case K incoherent sound sources are present, the overall A–weighted sound pressure level (OASPL or $L_{\mathrm{p,A,overall}}$) can be calculated by summing the A–weighted contributions $L_{\mathrm{p,A,k}}$ from each source in the same way as in Eq. (A.3), but using $L_{\mathrm{p,A,k}}$ instead of $L_{\mathrm{p,k}}$ [1].

[1]The C–weighting function focuses on the low frequency noise during takeoff such as jet noise [2].

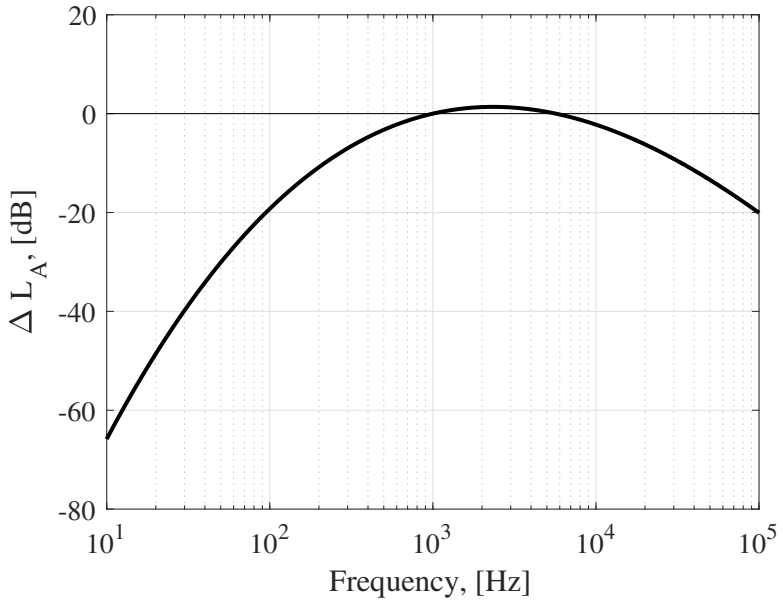

Figure A.1: A–weighting correction factor ΔL_A.

A.3. Sound Exposure Level (SEL or $L_{p,A,e}$)

The sound exposure level (SEL or $L_{p,A,e}$) considers the influence of the duration of the noise in the calculations. This metric integrates all the acoustic energy (described as the $L_{p,A,overall}$) and normalizes it to a one–second interval (i.e., $T = 1$s)

$$L_{p,A,e} = 10 \log_{10} \left(\frac{1}{T} \int_{t_1}^{t2} 10^{L_{p,A,overall}/10} dt \right), \tag{A.6}$$

where the time integration boundaries t_1 and t_2 correspond to the instants where the $L_{p,A,overall}$ is 10 dBA below the maximum $L_{p,A,overall}$, i.e., $L_{p,A,overall,max}$, see Fig. A.2. This metric corresponds to the constant $L_{p,A,overall}$ value (in dBA) that has the same acoustic energy in one second as the noise event in the selected time interval [2].

The $L_{p,A,e}$ metric can also be used for measuring several noise events within a certain period of time, such as a whole day, for law–enforcement and certification purposes. The most common metrics for this purpose are the day–night average L_{DN}, or the day–evening–night average L_{DEN} [1, 2].

A.4. Effective Perceived Noise Level (EPNL)

The Perceived Noise Level (PNL) metric was developed to describe the annoyance experienced by residents living close to airports [2] and to certify aircraft for noise emissions. Using a linear annoyance scale (in the form of equal noisiness curves)

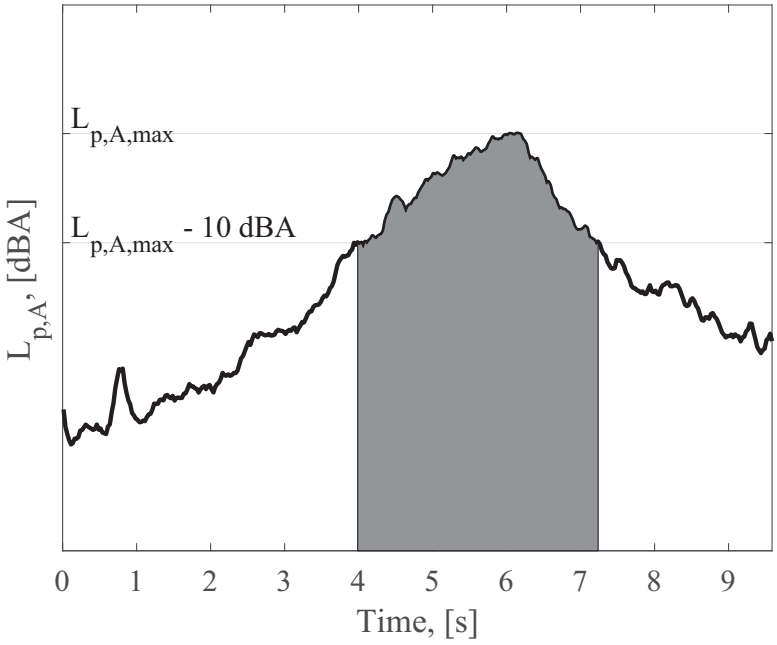

Figure A.2: Calculation of the $L_{\mathrm{p,A,e}}$ metric for an example aircraft flyover.

based on psychoacoustic tests, a certain value in the unit of *noy* is given. Afterwards, the overall noy value can be converted to the logarithmic PNL in PNdB units [1].

The PNL metric was improved to account for the response of the human ear to discrete tones with a higher annoyance. Therefore, a tonal penalty was added to the PNL metric to obtain the Tone–corrected Perceived Noise Level (PNLT), expressed in PNTdB units. The procedure to calculate such tonal penalty is quite complicated and can be found in the literature [1, 2].

If the influence of the duration of noise is included, the Effective Perceived Noise Level (EPNL) is obtained [1]. In a similar way as for for the $L_{\mathrm{p,A,e}}$ metric described before, the PNLT values are integrated between two times t_1 and t_2 corresponding to the instants where the PNLT is 10 PNTdB below the maximum PNLT and normalized for a 10–second interval (i.e., $T = 10$s). The unit of the EPNL is the EPNdB.

A.5. Sound quality metrics

Some state–of–the–art sound quality metrics from the field of psychoacoustics are currently being studied and considered for aircraft noise. These metrics aim to represent the actual annoyance experienced by the human ear by including more elaborated calculations [4].

The most commonly used ones [2] in decreasing order of influence to the experienced annoyance are:

- **Loudness** is the subjective perception of the magnitude of a sound and corresponds to the overall sound intensity [2, 4].
- **Tonality** measures the perceived strength of the unmasked tonal energy within a complex sound [2, 4, 5].
- **Sharpness** describes the high–frequency content of a sound [2, 4].
- **Roughness** refers to the rapid amplitude fluctuations of some sounds in the frequency range between 15 Hz and 300 Hz [2, 4].

Since the ultimate purpose is to obtain a single metric that accurately represents the actual annoyance experienced, combined metrics such as the Psychoacoustic Annoyance (PA) which considers the four metrics listed above have been proposed [2, 4].

Bibliography

[1] G. Ruijgrok, *Elements of aviation acoustics*, Second ed. (VSSD, 2007) ISBN: 1090–6562–155–5.

[2] A. K. Sahai, *Consideration of Aircraft Noise Annoyance during Conceptual Aircraft Design*, Ph.D. thesis, Rheinisch–Westfälische Technische Hochschule Aachen (2016).

[3] M. Arntzen, *Aircraft noise calculation and synthesis in a non–standard atmosphere*, Ph.D. thesis, Delft University of Technology (2014), ISBN: 978–94–62594–64–7.

[4] S. R. More, *Aircraft Noise Characteristics and Metrics*, Ph.D. thesis, Purdue University (2010), report No. PARTNER–COE–2011–004.

[5] W. Aures, *Procedure for calculating the sensory euphony of arbitrary sound signal,* Acustica **59**, 130 (1985).

B

Appendix B - Dimensionless numbers in fluid mechanics

In fluid mechanics several dimensionless quantities are normally used to simplify equations and to perform dimensional analysis and scaling between experiments of different sizes and characteristics. A complete list of all these numbers is out of the scope of this thesis, hence only those used throughout this work are described here.

B.1. Mach number

The Mach number M represents the ratio of the flow velocity V to the local speed of sound in the medium, c [1]:

$$M = \frac{V}{c}. \tag{B.1}$$

Hence, the Mach number depends on the local flow speed and the local temperature, since for ideal gases the speed of sound can be calculated as $c = \sqrt{\gamma R_0 T_0}$, where γ is the ratio of the gas specific heats (approximately 1.4 for air), R_0 is the universal gas constant (approximately 287 m^2/s^{2}K for air), and T_0 is the gas temperature in Kelvin. For dry air at a temperature of 293 K, $c \approx 343$ m/s.

If a three–dimensional flow is considered, the Mach vector $\boldsymbol{M}$ can be used

$$\boldsymbol{M} = \left(M_x, M_y, M_z\right) = \left(\frac{V_x}{c}, \frac{V_y}{c}, \frac{V_z}{c}\right) = \frac{\boldsymbol{V}}{c}. \tag{B.2}$$

In this case, the Mach number M is defined as the Euclidean norm of the Mach vector $\|\boldsymbol{M}\|$.

Using this parameter, different Mach regimes can be defined:

- **Subsonic regime** ($0 < M < 0.8$): In these conditions all the flow velocities within all the airflow present $M < 1$. This is normally the case for wind turbines, propeller aircraft and turbofan aircraft during takeoff and landing. The flow compressibility effects can be neglected and the flow can be considered as incompressible [2].

- **Transonic regime** ($0.8 < M < 1.3$): This regime presents some local flow velocities with $M > 1$. This is the case for most modern turbofan aircraft during cruise operational conditions. Compressibility effects, such as flow choking, become important [1].

- **Supersonic regime** ($1.3 < M < 5$): In this regime, all the airflow presents velocities with $M > 1$. This is the case for some military fighter airplanes at high–speed operational conditions. Shock waves can develop in some regions. The assumptions made for obtaining the linear wave equation (see Eq. (1.1)) do not hold anymore [2].

- **Hypersonic regime** ($M > 5$): In this case the high energy involved in the flow has important effects on the air itself, and the chemical composition of the air can change and the heat transfer to the vehicle becomes an important issue.

Throughout this thesis subsonic conditions are considered, unless the opposite is explicitly stated.

B.2. Reynolds number

The Reynolds number Re is the ratio between the inertial forces and the viscous forces within a fluid with different fluid velocities, which cause fluid friction that develop turbulence [1]. The viscosity of the fluid counteracts this effect by absorbing kinetic energy. Hence, the Reynolds number quantifies the relative importance of these two forces. This quantity is defined as

$$Re = \frac{\rho_0 V l}{\mu}, \tag{B.3}$$

where ρ_0 is the density of the fluid (approximately 1.225 kg/m^3 for air), l is the characteristic dimension (such as the airfoil chord), and μ is the dynamic viscosity of the fluid (approximately 1.81×10^{-5} Pa for air).

Depending on the Reynolds number of a flow, two main regimes can be considered [2]:

- **Laminar regime**: The viscous forces are dominant and the flow is characterized by a smooth and constant motion. For airfoils this is normally the case for $Re < 10^6$.

- **Turbulent regime**: The inertial forces are dominant and the flow becomes more unstable with vortices and eddies developing in a chaotic manner. For

airfoils natural transition to the turbulent regime normally happens for $Re > 10^6$, although it can also be forced by using tripping devices, see section 2.3.

Different Reynolds numbers can cause different sound generation mechanisms, so it is important to match this parameter when comparing two different experiments, see section 3.1.1.

B.3. Strouhal number

The Strouhal number St is normally used to describe oscillating mechanisms or unsteady flow problems, such as vortex shedding [2]. This quantity represents the ratio between the inertial forces because of the local flow unsteadiness and the inertial forces due to the uniform velocity in the flow field. It has the following expression

$$St = \frac{fl}{V}, \tag{B.4}$$

where f is the frequency in Hz and l is again the characteristic length, such as the diameter of a cylinder, the thickness of an airfoil or the thickness of the boundary layer.

B.4. Helmholtz number

The Helmholtz number He is an important parameter in duct acoustics [3]

$$He = \frac{fl}{c}. \tag{B.5}$$

This quantity represents the dimensionless frequency with respect to a characteristic length l, such as the radius of a duct [3] or the aperture of a microphone array [4]. This way the results can be adapted for different sizes and frequencies.

B.5. Pressure coefficient

The pressure coefficient c_p represents the pressures within a flow field [1]. It can be calculated using

$$c_p = \frac{p - p_\infty}{\frac{1}{2}\rho_{0,\infty} V_\infty^2}, \tag{B.6}$$

where p is the static pressure and the subscript ∞ denotes the free–field conditions.

For potential flows (incompressible, inviscid and steady), Eq. (B.6) can be simplified using Bernoulli's equation

$$c_p = 1 - \left(\frac{V}{V_\infty}\right)^2, \tag{B.7}$$

where V represents here the flow speed at the point where c_p is being evaluated. This assumption is considered as valid if $M < 0.3$ [2].

If $c_p = 0$ the pressure is the same as the free–stream pressure. For $c_p = 1$ the pressure is the highest achievable, the stagnation pressure (i.e., an stagnation point). The pressure coefficient can be greater than one for in compressible flows.

B.6. Lift coefficient

The lift coefficient c_L represents the lift force F_L generated by a body with respect to its size and fluid conditions [1]

$$c_L = \frac{F_L}{\frac{1}{2}\rho_0 V^2 S}, \tag{B.8}$$

where F_L is the lift force, and S is the reference surface area. The choice of S is arbitrary but normally it is defined as the wing area or the product of the wing chord and wing span $S = \hat{c}b$. In case a two–dimensional airfoil is considered, the local lift coefficient c_l is employed and instead of using the reference area, the airfoil chord $\hat{c}$ is used. The term $\frac{1}{2}\rho_0 V^2$ is normally referred to as the dynamic pressure of the fluid q.

For a given body, the lift coefficient mostly depends on the angle of attack α, the Reynolds number and the Mach number. In general c_L increases when α is increased until the stall angle (around $15°$ for typical airfoils)

B.7. Drag coefficient

The drag coefficient c_d represents the drag force F_d generated by a body with respect to its size and fluid conditions

$$c_d = \frac{F_d}{\frac{1}{2}\rho_0 V^2 S}, \tag{B.9}$$

where F_d is the drag force, and S is again the reference surface area. The drag coefficient can be divided into parasitic drag (including form drag, skin friction drag and interference drag) and induced drag, wave drag and ram drag. Parasitic drag is not caused by the generation of lift on the body [1].

In aerodynamics, it is common to use the lift–to–drag ratio c_L/c_d (also known as aerodynamic efficiency), which is one of the major goals in aircraft design.

B.8. Coefficient of power

The coefficient of power c_P determines the performance of wind turbines and is one of the most important variables in wind–turbine aerodynamics. It can be calculated using

$$c_P = \frac{W}{\frac{1}{2}\rho_0 S V_\infty^3}, \tag{B.10}$$

where W is the power generated by the wind turbine and S refers here to the wind turbine area.

B.9. Advance ratio

In propeller aerodynamics, the advance ratio J_{prop} is the ratio between the free–stream velocity V to the propeller tip speed

$$J_{prop} = \frac{V}{nd_{prop}}, \tag{B.11}$$

where n is the rotational speed or the propeller in rotations per second and d_{prop} is the diameter of the propeller.

This parameter is the inverse of the tip speed ratio normally used in wind–turbine aerodynamics.

Bibliography

[1] J. D. J. Anderson, *Fundamentals of Aerodynamics*, Third ed. (McGraw–Hill Series in Aeronautical and Aerospace Engineering, 2001) ISBN: 0–07–237335–0.

[2] S. Glegg and W. J. Devenport, *Aeroacoustics of Low Mach Number Flows – Fundamentals, Analysis, and Measurement* (Academic Press, 2017) p. 313, ISBN: 978–0–128–09651–2.

[3] S. W. Rienstra, *Fundamentals of Duct Acoustics*, edited by T. von Karman Institute for Fluid Dynamics (Technische Universiteit Eindhoven, 2015).

[4] E. Sarradj, G. Herold, and S. Jekosch, *Array methods: Which one is the best?* in *7th Berlin Beamforming Conference, March 5 – 6 2018, Berlin, Germany* (GFaI, e.V., Berlin, 2018) BeBeC–2018–S01.

C

Appendix C - Basics of signal processing

This appendix provides a brief overview of the necessary concepts for the signal processing required for microphone–array measurements. Additional explanations can be found in the literature [1, 2].

C.1. Fourier transforms

A Fourier transform $\mathcal{F}$ converts a continuous signal from the time domain $\hat{x}(t)$ to the frequency domain, considering the signal as an infinite sum of individual harmonic components, i.e., sine and cosine waveforms [1]

$$X(f) = \mathcal{F}[\hat{x}(t)] = \int_{-\infty}^{\infty} \hat{x}(t) \exp\big(-2\pi i t\big) dt. \tag{C.1}$$

In practice, signals have to be sampled in a discrete manner $\hat{x}(n) = \hat{x}(n\Delta t)$ with a total of N_{sam} number of samples and with $n = 0, 1, \ldots, N_{\text{sam}} - 1$. For computational analysis, a Discrete Fourier Transform (DFT) or a Fast Fourier Transform (FFT) is considered as

$$X(m) = X(m\Delta f) = \text{DFT}[\hat{x}(n)] = \sum_{n=0}^{N_{\text{sam}}-1} \hat{x}(n) \exp\left(\frac{-2\pi i n m}{N_{\text{sam}}}\right), \tag{C.2}$$

where $m = 0, 1, \ldots, N_{\text{sam}} - 1$, $\hat{x}(n)$ is the n^{th} sample of the signal in the time domain, and N_{sam} is the total number of samples.

In practice, N_{sam} and the sampling frequency f_{sam} are limited by the experimental constraints. Due to the sampling theorem, the maximum frequency of analysis should be limited to half the sampling frequency (i.e., the Nyquist frequency $f_{\text{sam}}/2$) to avoid aliasing [1].

The frequency resolution or frequency step Δf for a DFT depends on the duration of the time signal T used for the analysis as

$$\Delta f = \frac{1}{T} = \frac{f_{\text{sam}}}{N_{\text{sam}}}, \tag{C.3}$$

which shows that a compromise should be made between frequency resolution and time resolution. This has to be made by the user depending on the application. Some applications require a very precise frequency resolution, especially if tonal noise is present, whereas in other experiments the evolution of the sound spectrum with time is of great interest, such as flyover measurements.

The Inverse Discrete Fourier Transform (IDFT) converts the spectrum $X(m)$ to a time signal:

$$\hat{x}(n) = \text{IDFT}[X(m)] = \frac{1}{N_{\text{sam}}} \sum_{m=0}^{N_{\text{sam}}-1} X(m) \exp\left(\frac{2\pi i n m}{N_{\text{sam}}}\right), \tag{C.4}$$

with $m = 0, 1, \ldots, N_{\text{sam}} - 1$.

C.2. Statistical data analysis

Several concepts need to be introduced for performing statistical analysis to a random process. Unless otherwise noted, a random signal sampled in a discrete manner $\hat{x}(n) = \hat{x}(n\Delta t)$ is considered in these explanations.

C.2.1. Expected value

The expected value of a random signal is the mean or average value of a function when infinite samples are employed [1]

$$\text{E}[\hat{x}(n)] = \lim_{N_{\text{sam}} \to \infty} \frac{1}{2N_{\text{sam}} + 1} \sum_{n=-N_{\text{sam}}}^{N_{\text{sam}}} \hat{x}(n). \tag{C.5}$$

For a finite number of samples, the estimator of the mean value is

$$\bar{\hat{x}} = \frac{1}{N_{\text{sam}}} \sum_{n=0}^{N_{\text{sam}}-1} \hat{x}(n). \tag{C.6}$$

C.2.2. Variance and standard deviation

The variance of a random process is defined as [1]

$$\tilde{s}^2 = \frac{1}{N_{\text{sam}} - 1} \sum_{n=0}^{N_{\text{sam}}-1} (\hat{x}(n) - \bar{\hat{x}})^2. \tag{C.7}$$

The standard deviation is defined as the square root of the variance, i.e., $\tilde{s}$.

C.2.3. Root–mean–square (RMS) value

The root–mean–square (RMS) value of a random signal is defined by [1]

$$\hat{x}_{\text{RMS}} = \sqrt{\frac{1}{N_{\text{sam}} - 1} \sum_{n=0}^{N_{\text{sam}}-1} \hat{x}(n)^2}. \tag{C.8}$$

C.2.4. Correlation functions

The autocorrelation function for a stochastic time signal $\hat{x}(t)$ is a measure of the similarity a the signal has with a time–shifted version of itself [1]

$$\tilde{R}_{xx}(\tau) = \text{E}[\hat{x}(t)\hat{x}(t-\tau)], \tag{C.9}$$

where τ is the time shift. For $\tau = 0$, the autocorrelation equals the variance of the signal [1].

The cross–correlation between two different stochastic time signals $\hat{x}(t)$ and $\hat{y}(t)$ can be seen as the mean of the cross product between both signals and is defined as

$$\tilde{R}_{yx}(\tau) = \text{E}[\hat{y}(t)\hat{x}(t-\tau)]. \tag{C.10}$$

If both signals $\hat{x}(t)$ and $\hat{y}(t)$ are zero–mean signals, the cross–correlation between them will reveal whether there is a dependence between $\hat{y}(t)$ and the time–shifted signal $\hat{x}(t-\tau)$. If there is no linear relationship between both signals (i.e., they are uncorrelated) the cross product will have a zero mean, i.e., $\tilde{R}_{yx}(\tau) = 0$. On the other hand, if there is a dependence between both signals, that would lead to a non–zero mean, i.e, $\tilde{R}_{yx}(\tau) \neq 0$.

Correlation coefficients

When analyzing the correlation between two variables, it is common to use the **Pearson correlation coefficient** ρ [3] (also known as Pearson product–moment correlation coefficient or bivariate correlation). This parameter is a measure of the linear correlation between two variables $\hat{x}$ and $\hat{y}$.

$$\rho_{\hat{x},\hat{y}} = \frac{\text{E}[(\hat{x} - \bar{\hat{x}})(\hat{y} - \bar{\hat{y}})]}{\hat{s}_{\hat{x}}\hat{s}_{\hat{y}}}, \tag{C.11}$$

where $\bar{\hat{x}}$ and $\bar{\hat{y}}$ are the mean values of $\hat{x}$ and $\hat{y}$, respectively, see Eq. (C.6). The parameters $\hat{s}_{\hat{x}}$ and $\hat{s}_{\hat{y}}$ are the standard deviations of $\hat{x}$ and $\hat{y}$, respectively, see Eq. (C.7).

The correlation coefficient has a value between -1 and 1, where 1 indicates total positive linear correlation, 0 means no linear correlation and -1 refers to total negative linear correlation.

Another useful parameter in statistical analysis is the **coefficient of determination** [3], which represents the proportion of the variance in the dependent

variable that is predictable from the independent variables. It is defined as the square of the correlation coefficient ρ^2 and, hence, has a value between 0 and 1.

Lastly, the **p–value** is a measure of the significance of the correlation between two variables. It expresses the possibility to obtain that particular correlation coefficient ρ in case the variables are uncorrelated [3]. Therefore, it should be as low as possible. Normally, a p–value threshold value of 0.05 is considered, under which correlations are deemed as significant [3, 4].

C.2.5. Power Spectral Density (PSD)

A frequency spectrum can be defined using its Power Spectral Density (PSD) (also known as autospectral density), which is continuous in frequency and is a density function with units Pa^2/Hz for pressure measurements. It is defined as the Fourier transform (see Eq. (C.1)) of the autocorrelation function [1]

$$\tilde{S}_{xx}(f) = \mathcal{F}[\tilde{R}_{xx}(\tau)] = \int_{-\infty}^{\infty} \tilde{R}_{xx}(\tau) \exp\big(-2\pi i f t\big) d\tau. \tag{C.12}$$

Analogous to the cross–correlation function, the Cross–Spectral Density (CSD) function can be defined as

$$\tilde{S}_{yx}(f) = \mathcal{F}[\tilde{R}_{yx}(\tau)] = \int_{-\infty}^{\infty} \tilde{R}_{yx}(\tau) \exp\big(-2\pi i f t\big) d\tau. \tag{C.13}$$

Equations (C.12) and (C.13) are often called the Wiener–-Khinchine relations [1] and they represent the two–sided frequency spectral densities, i.e., including the negative frequencies in the Fourier transform. The single–sided spectral densities $\tilde{G}$ are normally used, considering only the positive frequency values are defined as

$$\tilde{G}_{xx}(f) = 2\tilde{S}_{xx}(f) \in \mathbb{R} \quad \text{for } f > 0, \tag{C.14}$$

$$\tilde{G}_{xx}(0) = \tilde{S}_{xx}(0), \tag{C.15}$$

$$\tilde{G}_{yx}(f) = 2\tilde{S}_{yx}(f) \in \mathbb{C} \quad \text{for } f > 0, \tag{C.16}$$

$$\tilde{G}_{yx}(0) = \tilde{S}_{yx}(0). \tag{C.17}$$

The elements of the cross–spectral matrix (see chapter 4) correspond to $\tilde{G}_{mn}$, i.e., the cross–correlation between the signals measured by microphones m and n. Section C.3 explains Welch's method to estimate the PSD and CSD functions.

C.2.6. Coherence function

The coherence function between two stochastic time signals $\hat{x}(t)$ and $\hat{y}(t)$ is defined as [1]:

$$\hat{\gamma}_{yx}^2(f) = \frac{|\tilde{G}_{yx}(f)|^2}{\tilde{G}_{xx}(f)\tilde{G}_{yy}(f)}. \tag{C.18}$$

It can be derived that $0 \leq \hat{\gamma}^2_{yx}(f) \leq 1$. If $\hat{\gamma}^2_{yx}(f) = 1$, then $\hat{y}(t)$ derives solely from $\hat{x}(t)$ and there is no extraneous noise. Coherence values lower than one imply that there is contaminating noise on either or both signals.

In measurements with phased microphone arrays featuring incoherent noise between the microphones (such as wind noise, see section 4.2.1), the contribution of the incoherent noise sources to the off–diagonal elements $\tilde{G}_{mn}$ with $m \neq n$ can be reduced by increasing the number of averages H in the time domain [5] (see section C.3)

$$\hat{\gamma}^2_{mn} \approx \frac{1}{H}. \tag{C.19}$$

In practice, H is very large and, hence, it can be considered that incoherent noise sources almost exclusively affect the main diagonal of the CSM, see section 4.2.1.

C.3. Welch's method

One of the most common procedures to calculate the spectral densities of random signals is Welch's method, which is well suited for computer processing [6]. The method works as follows

1. A sampled time signal $\hat{x}(n)$ with a duration T is divided into H segments $\hat{x}_h(n)$, each of them with a duration of T_h, i.e., with an amount $N_{\text{sam},h} = T_h f_{\text{sam}}$ of samples. Normally the mean of the signal $\bar{\hat{x}}$ is subtracted from the signal.

2. Each segment can be weighted using a windowing function $\hat{w}(n)$ and a certain overlap (see Fig. C.1). Different window functions are available, but normally the Hanning window with a 50% data overlap is considered to be the optimal choice [1]. Thus, these parameters have been used throughout this thesis, unless otherwise stated.

3. For the PSD calculation, a DFT (see Eq. (C.2) is calculated for the H windowed segments $\hat{w}(n)\hat{x}_h(n)$, and its squared values $(X_h(f)X_h^*(f))$ are averaged in time for all the H segments for each frequency f, where $X_h(f) = \mathcal{F}(\hat{w}(n)\hat{x}_h(n))$ and $h = 1, \ldots, H$. The same process can be performed for calculating the CSD between two signals $\hat{w}(n)\hat{x}(n)$ and $\hat{w}(n)\hat{y}(n)$ by averaging $(X_h(f)Y_h^*(f))$ for each frequency, where $Y_h(f) = \mathcal{F}(\hat{w}(n)\hat{y}_h(n))$.

4. The averaged result is scaled so that the area under the PSD (or CSD) function is equal to the RMS value of the time function [1]. The following expressions correspond to the case of the PSD calculation using a Hanning windowing function and 50% data overlap

$$\tilde{G}_{xx}(f) = \frac{8}{1.5} \frac{\sum_{h=1}^{H} X_h(f)X_h^*(f)}{N^2_{\text{sam},h} H \Delta f} \quad \text{for } f > 0, \tag{C.20}$$

$$\tilde{G}_{xx}(0) = \frac{4}{1.5} \frac{\sum_{h=1}^{H} X_h(0)X_h^*(0)}{N^2_{\text{sam},h} H \Delta f}, \tag{C.21}$$

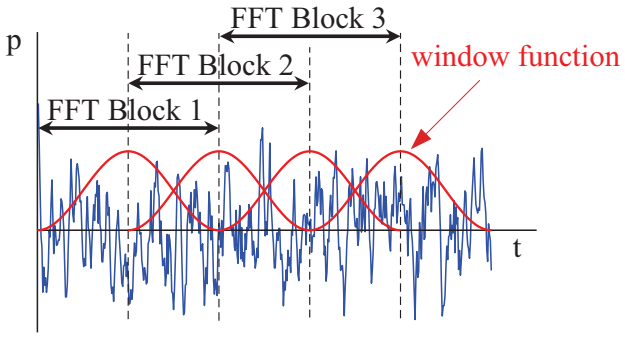

Figure C.1: Illustration of Welch's method for an example signal with several time segments weighted with a Hanning window function (in red) with 50% overlap.

where the expressions are divided by the frequency resolution Δf to obtain a density function. The full derivation of this expression can be found in [1]. For the case of the CSD calculation the variable $X_h^*(f)$ in Eqs. (C.20) and (C.21) needs to be substituted for $Y_h^*(f)$.

In practice, the calculation of the CSM for microphone–array measurements can be performed using Welch's method by substituting the variable $X_h(f)$ in Eqs. (C.20) and (C.21) for $\boldsymbol{p}$. A simple way to compute all the CSMs for a frequency range using the signals of N microphones is to use the spectrogram function, see Fig. 3.10 for an example.

C.3.1. Errors in Welch's estimates

Two main types of errors can be defined when performing a Welch's estimate [1]: the bias error and the random error.

Bias error

The bias error $\varepsilon_{\text{bias}}$ is due to the discretization in frequency for the estimate and the convolution of the true PSD by the squared Fourier transform of the windowing function [1]

$$\varepsilon_{\text{bias}} \approx \frac{(\Delta f)^2 \tilde{G}_{xx}''}{6\tilde{G}_{xx}} + \frac{(\Delta f)^4 \tilde{G}_{xx}^{(4)}}{72\tilde{G}_{xx}}, \tag{C.22}$$

where $\tilde{G}_{xx}''$ and $\tilde{G}_{xx}^{(4)}$ are the second and fourth derivatives of $\tilde{G}_{xx}$ with respect to the frequency, respectively. In essence, the bias error for Welch's estimates depends on the frequency resolution Δf and spectral shape of $\tilde{G}_{xx}$.

Random error

When calculating a single FFT estimate using the periodogram function, the normalized random error $\varepsilon_{\text{rand}}$ has, by definition, a value of one [1]. Hence, if H averages

with no overlap are performed using Welch's method, the normalized random error becomes

$$\varepsilon_{\text{rand}} = \frac{1}{\sqrt{H}}. \tag{C.23}$$

In case overlap is employed for the processing, some of the data values are correlated with each other due to the overlap and the equivalent number of averages H_{eq} needs to be used

$$\varepsilon_{\text{rand}} = \frac{1}{\sqrt{H_{\text{eq}}}}, \tag{C.24}$$

which for a Hanning window with 50% data overlap $H_{\text{eq}} \approx 1.89\,H$. Therefore, when using these parameters, the random error is reduced about 27% with respect to the same dataset in case no overlap is employed.

Assuming a Gaussian distribution for the measurements, the 95% confidence interval for small normalized random errors ($\varepsilon_{\text{rand}} < 0.1$) can be approximated as [1]

$$(1 - 2\varepsilon_{\text{rand}})\tilde{G}_{xx} \leq G_{xx} \leq (1 + 2\varepsilon_{\text{rand}})\tilde{G}_{xx}, \tag{C.25}$$

where G_{xx} and $\tilde{G}_{xx}$ represent the true and estimated values of the PSD, respectively.

C.4. Octave and one–third–octave bands

Frequency bands are defined as a subset of the total frequency spectrum. Two examples of frequency bands are octave bands and one–third–octave bands (terts bands), which are very common in aircraft noise calculations [7]. These bands have constant percentage bandwidths, i.e., the bandwidth increases as the center frequency f_{center} increases. The center frequency is the mean frequency of the band, on a logarithmic scale, of the lower and upper bounds of the frequency band (f_{lower} and f_{upper}). These values for octave bands are defined as

$$f_{\text{lower}} = \frac{f_{\text{center}}}{\sqrt{2}}, \qquad f_{\text{upper}} = \sqrt{2} f_{\text{center}}. \tag{C.26}$$

And for one–third–octave bands as

$$f_{\text{lower}} = \frac{f_{\text{center}}}{\sqrt[6]{2}}, \qquad f_{\text{upper}} = \sqrt[6]{2} f_{\text{center}}. \tag{C.27}$$

Bibliography

[1] A. Brandt, *Noise and vibration analysis: signal analysis and experimental procedures*, Second (John Wiley & Sons, 2011) ISBN: 978-0-470-74644-8.

[2] J. Benesty, J. Chen, and H. Yiteng, *Microphone Array Signal Processing* (Springer Science & Business Media, 2008) ISBN: 978-3-540-78611-5.

C

Table C.1: Center frequencies for the octave bands.

Band number	f_{center}, [Hz]	Band number	f_{center}, [Hz]
1	2	8	250
2	4	9	500
3	8	10	1000
4	16	11	2000
5	31.5	12	4000
6	63	13	8000
7	125	14	16000

Table C.2: Center frequencies for the one–third–octave bands.

Band number	f_{center}, [Hz]	Band number	f_{center}, [Hz]
1	1.25	23	200
2	1.6	24	250
3	2	25	315
4	2.5	26	400
5	3.15	27	500
6	4	28	630
7	5	29	800
8	6.3	30	1000
9	8	31	1250
10	10	32	1600
11	12.5	33	2000
12	16	34	2500
13	20	35	3150
14	25	36	4000
15	31.5	37	5000
16	40	38	6300
17	50	39	8000
18	63	40	10000
19	80	41	12500
20	100	42	16000
21	125	43	20000
22	160		

[3] A. Kozak, R. A. Kozak, C. L. Staudhammer, and S. B. Watts, *Introductory Probability and Statistics – Applications for Forestry and Natural Sciences*, 1st ed. (CAB International, 2008) ISBN: 978–1–84593–275–6.

[4] M. Snellen, R. Merino-Martinez, and D. G. Simons, *Assessment of noise level variability on landing aircraft using a phased microphone array,* Journal of Aircraft **54**, 2173 (2017).

[5] J. Hald, *Removal of incoherent noise from an averaged cross–spectral matrix,* Journal of the Acoustical Society of America **142**, 846 (2017).

[6] P. D. Welch, *The Use of Fast Fourier Transform for the Estimation of Power Spectra: A Method Based on Time Averaging Over Short, Modified Periodograms,* IEEE Transactions on Audio and Electroacoustics **AU–15**, 70 (1967).

[7] G. Ruijgrok, *Elements of aviation acoustics*, Second ed. (VSSD, 2007) ISBN: 1090–6562–155–5.

D

Appendix D - Resolution limit

The resolution limit of a microphone array (or any image–forming device, such as a telescope, a camera or an eye) is defined as the minimum angle at which two (sound) sources can be separated into individual images.

This concept should not be confused with another usual meaning of the word resolution: the *sharpness* of an image (i.e., the number of pixels in an image). For acoustic imaging purposes, this feature is controlled by the user when defining the number of grid points in the scan grid J and the spacing between these Δx, which is typically limited by the computational resources available.

The separation of all the different sound sources in aeroacoustic experiments is of great importance, because, otherwise, multiple sources could be misrepresented as a single source and lead to erroneous results.

In general, any imaging system is limited by the diffraction due to its finite aperture[1]. The diameter of a microphone array (or of a lens in the optics analogy) determines the diffraction pattern. For spherical wavefronts, the waves passing through the imaging system interfere with themselves creating a ring–shape diffraction pattern, normally referred to as the Airy pattern in optics [1].

To calculate the spatial resolution, many authors normally refer to the Rayleigh resolution limit [2], i.e., the theoretical radius of the first null interval around the Airy disk (the first zero of the first order Bessel function). This way, the maximum of the PSF of one source is located at the minimum of the PSF of the other source. If the distance between the two sources is higher than the Rayleigh resolution limit, both sources can be separated and vice versa.

The angular resolution for a planar phased microphone array can be estimated by considering a continuous disk with the same diameter D. The array response a to a plane wave is

[1] For optic imaging systems, aberration phenomena can also have an influence on the achievable resolution.

$$a(\theta_{\text{scan}}) = \frac{2J_1\left[\frac{\|\boldsymbol{k}\|D\sin(\theta_{\text{scan}})}{2}\right]}{\frac{\|\boldsymbol{k}\|D\sin(\theta_{\text{scan}})}{2}} \approx \frac{2J_1\left(\frac{\|\boldsymbol{k}\|D\theta_{\text{scan}}}{2}\right)}{\frac{\|\boldsymbol{k}\|D\theta_{\text{scan}}}{2}}, \tag{D.1}$$

where θ_{scan} is the scan angle with respect to the normal direction to the array plane and J_1 is the first–order Bessel function. The approximation performed in Eq. (D.1) is valid for small scan angles [3].

If the PSF is considered, Eq. (D.1) becomes

$$A(\theta_{\text{scan}}) \approx \left[\frac{2J_1\left(\frac{\|\boldsymbol{k}\|D\theta_{\text{scan}}}{2}\right)}{\frac{\|\boldsymbol{k}\|D\theta_{\text{scan}}}{2}}\right]^2. \tag{D.2}$$

D

The Rayleigh resolution limit ($\theta_{\text{scan},0}$) is defined as the first zero in Eq. (D.2) which provides

$$\theta_{\text{scan},0} \approx 1.2196\frac{c}{Df} = 1.2196\frac{\lambda}{D}. \tag{D.3}$$

For practical applications, it is common to consider the spatial resolution R in meters rather than the angular resolution $\theta_{\text{scan},0}$ in radians [4]. For a scan plane situated at a distance h from the array plane, the minimum distance between two sources for which they can be solved is approximately

$$R \approx 2h\tan\left(\frac{\theta_{\text{scan},0}}{2}\right) \approx h\tan(\theta_{\text{scan},0}). \tag{D.4}$$

The expression of R given by the second term in Eq. (D.4) is more accurate than one given by the third term, which is typically used in the literature [3–5]. The difference between both, however is negligible for small angles $\theta_{\text{scan},0}$. The value of R provides the lower bound for the separation between grid points Δx (and therefore a lower bound for J) in the scan grid for a given frequency. Therefore, higher frequencies require, in general, finer grids than lower frequencies.

The opening angle of the array, and, therefore, the effective array size, decreases when the sound source is not located in front of the array, i.e., with a scan angle $\theta_{\text{scan}} \neq 0$. Hence, the array resolution decreases for oblique source directions [6]. An illustrative example of this can be observed in Fig. D.1, where the cases with $\theta_{\text{scan}} = 0$ (left) and $\theta_{\text{scan}} \neq 0$ (right) are depicted. Whereas $\theta_{\text{scan},0}$ remains the same in both cases, the spatial resolution R is larger for the case with $\theta_{\text{scan}} \neq 0$. Hence, it is highly recommended to place the region of analysis perpendicular to the array center, as much as possible.

Some authors consider the Sparrow resolution limit [7] instead, which is defined as the angular distance for which the sum of the PSF of each source produces a flat profile, whereas for the Rayleigh resolution limit it shows a distinct dip between both sources. The Sparrow resolution limit is defined approximately as $0.95\lambda/D$, i.e., a value about 22% lower than the Rayleigh resolution limit.

However, both criteria are based on the assumption of a continuous disk as a receiver, rather than an array with a finite number of sensors. Hence, both criteria

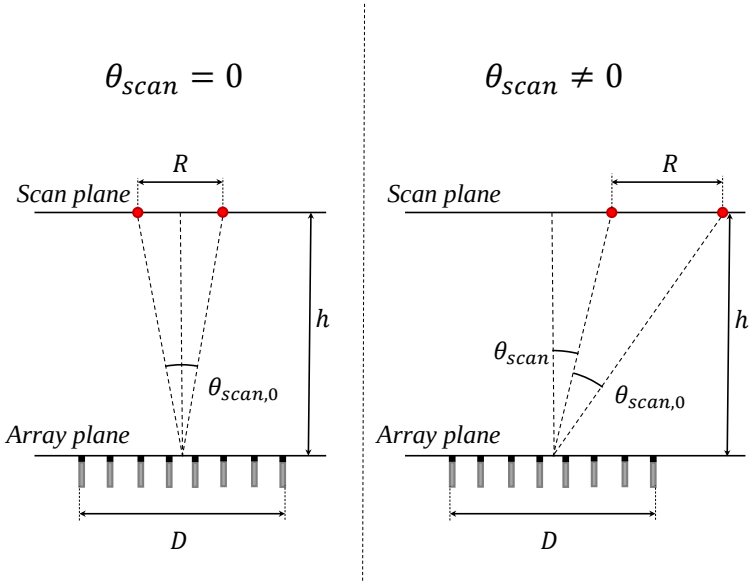

Figure D.1: Diagram explaining the Rayleigh resolution limit for $\theta_{\text{scan}} = 0$ (left) and $\theta_{\text{scan}} \neq 0$ (right).

represent an approximation and a lower bound of the minimum angular resolution achievable for an array. Some acoustic imaging methods, however, have proven to go beyond the Rayleigh resolution limit, see Chapter 4

Bibliography

[1] D. H. Johnson and D. E. Dudgeon, *Array Signal Processing, Concepts and Techniques* (P T R Prentice Hall, Englewood Cliffs, 1993) ISBN: 978–0130485137.

[2] F. R. S. Lord Rayleigh, *XXXI. Investigations in Optics with special reference to the Spectroscope,* The London, Edinburgh and Dublin Philosophical Magazine and Journal of Science **8**, 261 (1879).

[3] P. Sijtsma, R. Merino-Martinez, A. M. N. Malgoezar, and M. Snellen, *High–Resolution CLEAN–SC: Theory and Experimental Validation,* International Journal of Aeroacoustics **16**, 274 (2017), SAGE Publications Ltd. London, United Kingdom.

[4] R. Merino-Martinez, M. Snellen, and D. G. Simons, *Functional beamforming applied to imaging of flyover noise on landing aircraft,* Journal of Aircraft **53**, 1830 (2016).

[5] P. Sijtsma, *Phased array beamforming applied to wind tunnel and fly–over tests*, Tech. Rep. NLR–TP–2010–549 (National Aerospace Laboratory (NLR), Anthony

Fokkerweg 2, 1059 CM Amsterdam, P.O. Box 90502, 1006 BM Amsterdam, The Netherlands, 2010).

[6] S. Oerlemans, *Detection of aeroacoustic sound sources on aircraft and wind turbines*, Ph.D. thesis, University of Twente, Enschede, the Netherlands (2009).

[7] C. Sparrow, *On spectroscopic resolving power,* The Astrophysical Journal **44**, 76 (1916).

E

Appendix E - Acoustic characterization of the A–tunnel

This appendix describes the design of the phased microphone array located at the A–tunnel at Delft University of Technology, as well as the acoustic characterization of the A–tunnel facility. The A–tunnel is the new anechoic version of the V–tunnel described in section 6.1.1. Additional results including the aerodynamic characterization of the flow of the wind tunnel and further explanations of the characteristics of the facility can be found in [1]. Additional modifications to the wind–tunnel facility are expected in the near future which will require the repetition of the characterization.

E.1. Phased microphone array

An acoustic array consisting of 64 G.R.A.S. 40PH analog free–field microphones [2] with integrated constant current power (CCP) amplifiers was installed in the open–jet wind–tunnel. These microphones have a frequency range between 10 Hz and 20 kHz and a sensitivity of 50 mV/Pa at 250 Hz. Each microphone has a diameter of 7 mm and a length of 59.1 mm. All the microphones were calibrated individually using a G.R.A.S. 42AA pistonphone [3]. The DAS consisted of 5 National Instruments (NI) PXIe–4499 sound and vibration data acquisition modules controlled by a NI PXIe–8370 remote control module and a NI RMC–8354 controller. Each microphone is connected to the DAS via a 10–m long G.R.A.S. AA0028 coaxial cable [4].

The design and construction of the structure of the phased microphone array were mostly performed during the M.Sc. thesis work of Vlemmix [5]. After considering different design options for the support structure, a trade–off solution was chosen. It was decided to employ three steel perforated plates with square holes in a regular grid pattern, see Fig. E.1a. Each plate has the dimensions of 1 m $\times$ 2 m

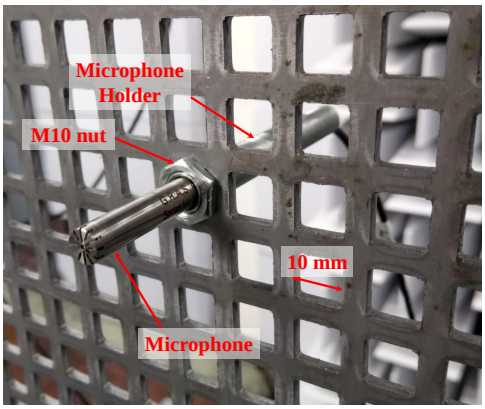

(a)

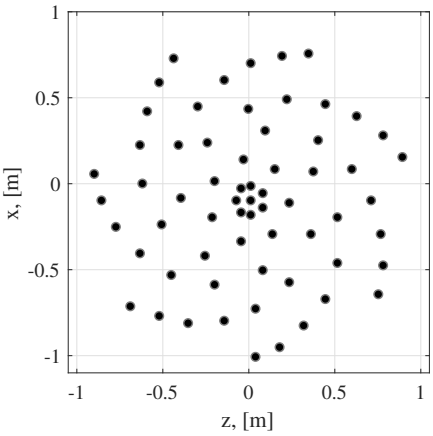

(b)

Figure E.1: (a) Picture showing the microphone holding system and the perforated plate. (b) Microphone array distribution for the A–tunnel measurements.

and has a total of 8450 perforations, i.e., possible microphone positions. This design offers a compromise solution between reduced acoustic reflections, robustness and large number of potential microphone positions.

The size of the perforated holes is 10 mm × 10 mm and the thickness of the metallic border is 2 mm. This provides an open area ratio of approximately 69%. Two structure configurations are available, featuring two or three steel plates, i.e., with sizes of 2 m × 2 m or 3 m × 2 m. For the experiments performed so far, the configuration with just two plates was used. Each microphone is placed inside of a microphone holder consisting of a hollow threaded rod with an outer diameter of 10 mm and an inner diameter of 8 mm, see Fig. E.1a. Thus, there is an almost–perfect fit between the microphone holder outer diameter and the side of the metallic grid square hole and just 1 mm of margin to insert the microphone inside the holder. The holders can be tightly mounted to the array using two M10 nuts, see Fig. E.1a.

All the plates are mounted on a rectangular frame structure manufactured in steel and lifted from the ground using steel support legs, see Fig. E.2, in a way that the center hole is aligned with the model to test. The borders of the metallic frame were covered with acoustic absorbing *Flamex Basic* foam [6] to minimize acoustic reflections [5], see Fig. E.2a. Additional details about the support structure can be found in [5].

The default microphone distribution corresponds to an adapted version of the Underbrink spiral design [7–9] with 7 spiral arms of 9 microphones each and an additional microphone located at the center of the array, see Fig. E.1b. The diameter of the array is approximately 2 m and the distance from the array to the center of the test section is approximately 1.4 m. Different distributions have been used and compared [10].

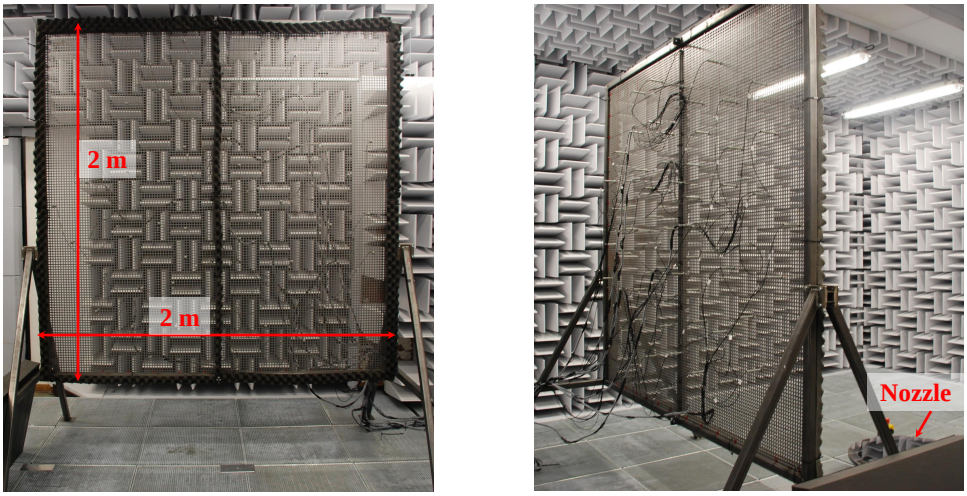

(a) (b)

Figure E.2: Pictures of the microphone array structure setup (a) Front view. (b) Back view.

E.2. Acoustic characterization

E.2.1. Free–field propagation assessment

One of the most important features of an anechoic room is the region of space where the inverse square law spreading [11] hold, i.e., where the free–field conditions are present [12]. The expected sound pressure level L_p at a distance r from the observer can be calculated using the following expression [11], which considers omnidirectional spherical spreading of sound

$$L_p(r) = L_p(r_0) - 20\log\left(\frac{r}{r_0}\right), \tag{E.1}$$

where r_0 is a reference distance to the source, normally considered as 1 m.

Therefore, the measured deviation from the expected free–field decay ΔL_p can be calculated using the following equation

$$\Delta L_p = L_{p,exp} - L_{p,ref}, \tag{E.2}$$

where $L_{p,exp}$ and $L_{p,ref}$ are the measured and expected sound pressure levels, respectively.

The maximum allowable ΔL_p values per third–octave frequency band are given by the standards in ISO3745 [13] and are presented in Table E.1.

In order to assess the free–field conditions a simple setup, following the guidelines in the ISO3745 [12, 13], was used consisting of:

- A sound source, namely a Visaton K50 SQ speaker [14], situated over the wind–tunnel nozzle to simulate a representative experimental setup. This

Table E.1: Maximum allowable difference between measured and modeled free–field L_p depending on the frequency range according to the standards in ISO3745 [13].

One–third–octave–band center frequency f, [Hz]	Allowable ΔL_p, [dB]
$f \leq 630$	± 1.5
$800 \leq f \leq 5000$	± 1
$f \geq 6300$	± 1.5

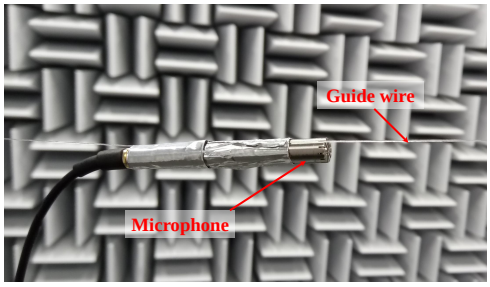

Figure E.3: Microphone on guide wire.

speaker emitted the same broadband white noise signal for each measurement during 60 s.

- A reference G.R.A.S. 40PH microphone [2] next to the speaker ensured the repeatability of the measurements.

- A G.R.A.S. 40PH microphone [2] mounted on a guide wire (see Fig. E.3). For each measurement, the microphone was displaced 0.1 m away from the sound source, starting from an initial distance of 1 m until a distance of 2.2 m. The direction selected was the one pointing at the position where the microphone array is normally placed for the experiments.

The measured ΔL_p values for each third–octave frequency band with respect to the distance to the source r are presented in Fig. E.13. The maximum allowable differences from Table E.1 are plotted as red dashed lines. It can be observed that all the frequency bands above 315 Hz fulfill the standards in ISO3745 [13] for the distance range considered. However, the one–third–octave bands with center frequencies of 250 Hz and 315 Hz show higher deviations than those allowed for distances of 1.1 m and 2 m for the first case and 2.2 m for the second case. These results show that, even if the anechoic room is designed for frequencies higher than 500 Hz, acceptable results can still be achieved for a range of distances below 2 m from the source. It should be noted that, for experiments, the microphone array is typically located at a distance $r = 1.4$ m from the center of the test section.

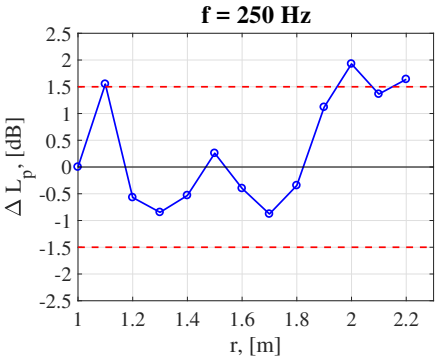
f = 250 Hz
Δ L_p, [dB]
r, [m]

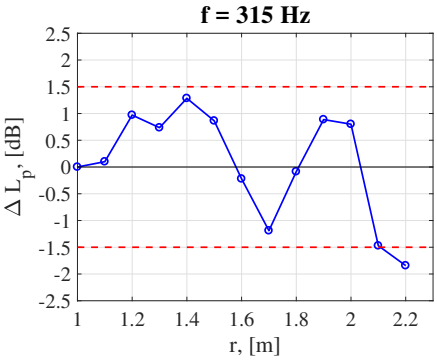
f = 315 Hz
Δ L_p, [dB]
r, [m]

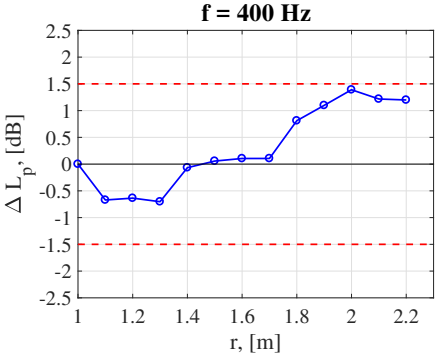
f = 400 Hz
Δ L_p, [dB]
r, [m]

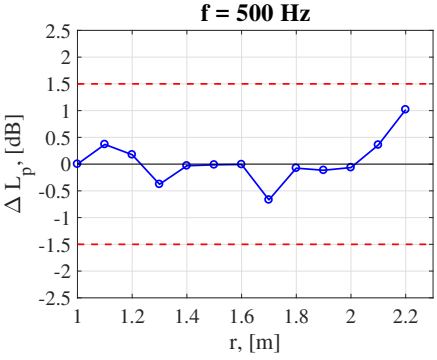
f = 500 Hz
Δ L_p, [dB]
r, [m]

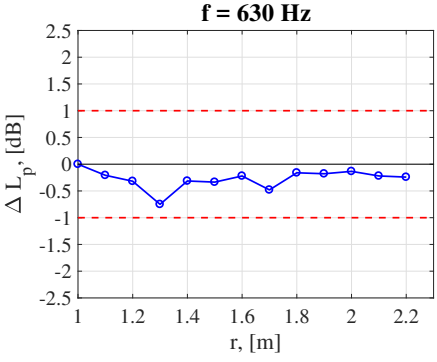
f = 630 Hz
Δ L_p, [dB]
r, [m]

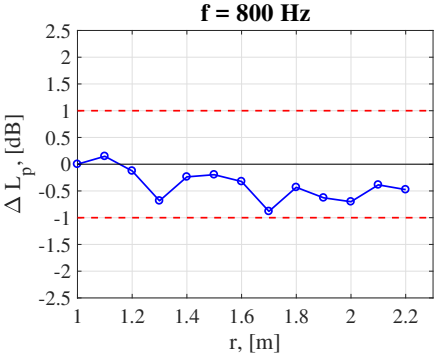
f = 800 Hz
Δ L_p, [dB]
r, [m]

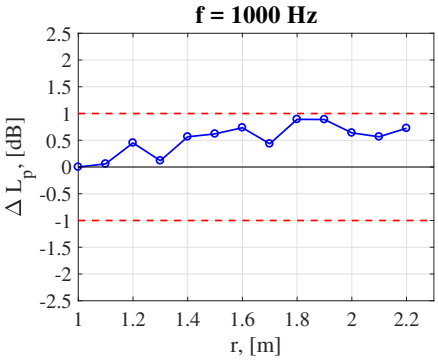
f = 1000 Hz
Δ L_p, [dB]
r, [m]

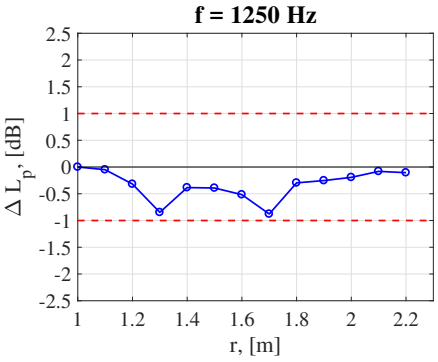
f = 1250 Hz
Δ L_p, [dB]
r, [m]

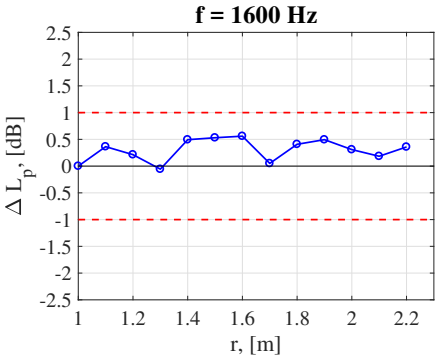
f = 1600 Hz
Δ L_p, [dB]
r, [m]

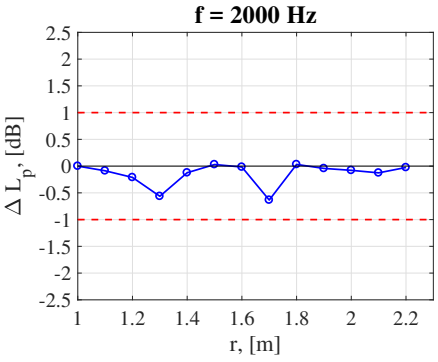
f = 2000 Hz
Δ L_p, [dB]
r, [m]

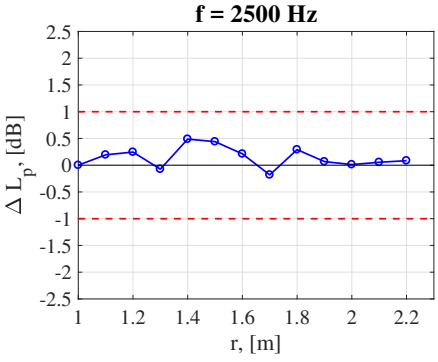
f = 2500 Hz
Δ L_p, [dB]
r, [m]

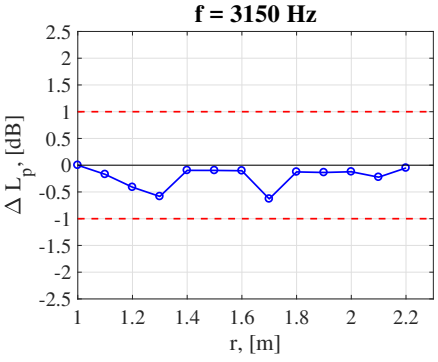
f = 3150 Hz
Δ L_p, [dB]
r, [m]

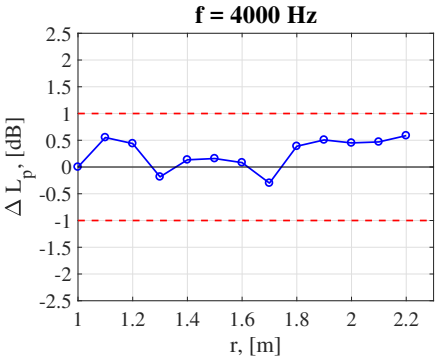
f = 4000 Hz
Δ L_p, [dB]
r, [m]

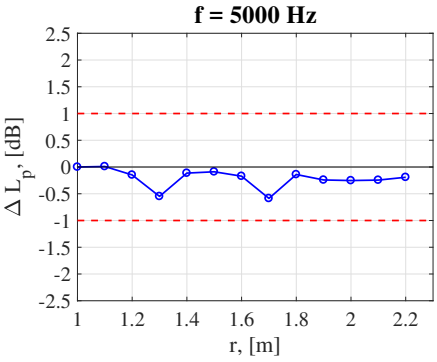
f = 5000 Hz
Δ L_p, [dB]
r, [m]

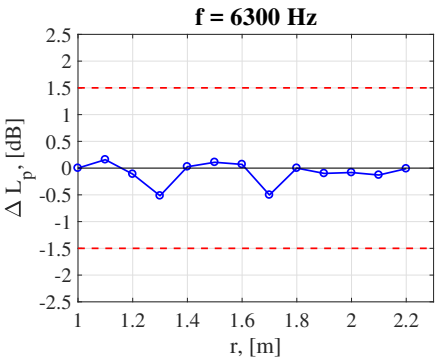
f = 6300 Hz
Δ L_p, [dB]
r, [m]

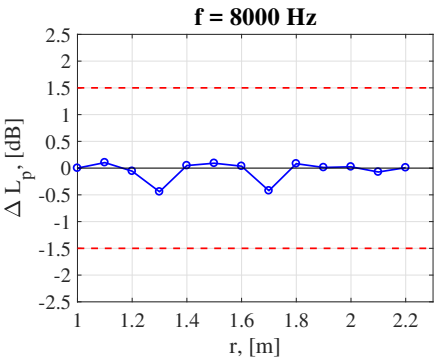
f = 8000 Hz
Δ L_p, [dB]
r, [m]

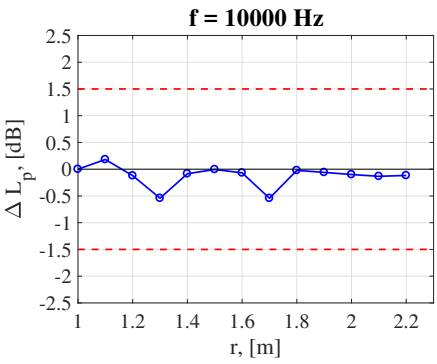
f = 10000 Hz
Δ L_p, [dB]
r, [m]

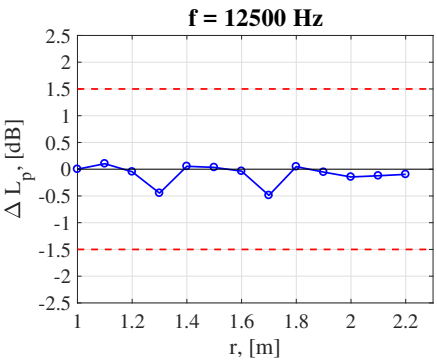
f = 12500 Hz
Δ L_p, [dB]
r, [m]

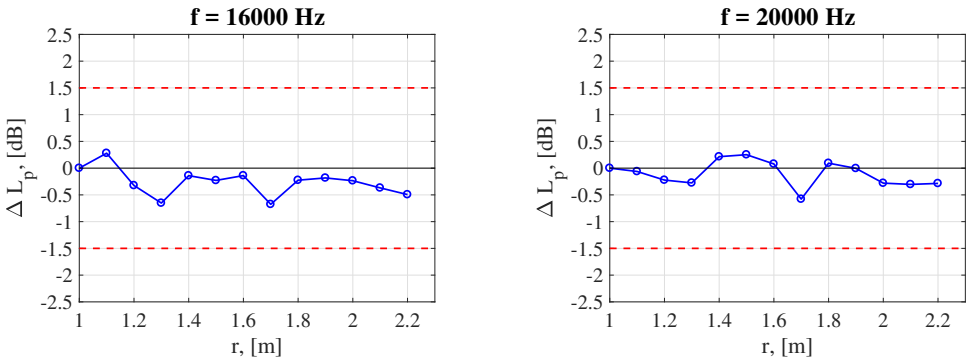

Figure E.13: Deviation from the free–field decay with respect to the distance to the source r. The tolerances according to ISO3745 [13] are depicted as dashed red lines.

E.2.2. Reverberation time

The reverberation time (T_{60}) [11] of the anechoic chamber can be calculated using a single microphone and a pulse signal. In this experiment, a clapping device [15] producing a loud, broadband and short signal was used. The reverberation time is typically defined as the amount of time it takes for the sound pressure level (L_p) of the received signal to decrease by 60 dB. The approximate dimensions of the anechoic chamber of the facility are 6.4 m (length) $\times$ 6.4 m (width) $\times$ 3.2 m (height).

A total of ten measurements were performed with different sound source and receiver positions, especially in locations representative for expected experimental setups. An average T_{60} value of 0.25 s was observed, which corresponds to the anechoic or *acoustically dead* category according to the ISO3382 [16]. It should be noted that, during these experiments, the exit of the wind–tunnel nozzle was not covered to better represent the actual conditions during real testing. For acoustic measurements without flow, it is recommended to cover the nozzle to minimize the reverberation originating from the settling chamber.

E.2.3. Background noise measurements

Typically, the background noise inside of a wind tunnel facility is due to the fan, the jet from the nozzle an the interaction of the jet with the collector [17]. Since some test models can be inherently very quiet, such as noise–reduction measures as trailing–edge serrations [18–21] or trailing–edge porous inserts [22–24], it is desired to have minimal background noise levels. Ideally, a signal to noise ratio of at least 10 dB between the sound signal to be measured and the background noise is desired [17].

The background noise levels of the wind–tunnel facility for different flow speeds were recorded by the whole microphone array located at a distance of 1.43 m from the center of the wind–tunnel nozzle. This array position was chosen since it was the same as in previous experiments [22–24]. Figure E.14a depicts the measured background noise one–third–octave–band spectra averaged over all the microphones for different flow velocities, as well as the background without flow but

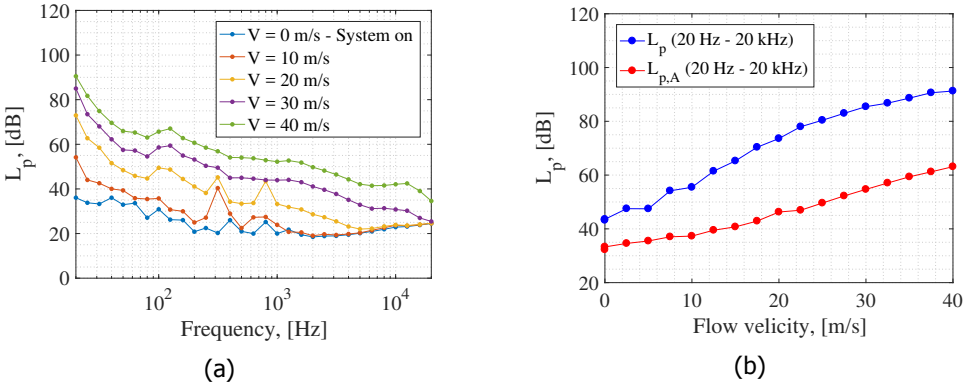

Figure E.14: (a) Background noise spectra for different flow velocities V in one–third–octave frequency bands. (b) Overall L_p and $L_{p,A}$ background noise levels for different flow velocities in the frequency range between 20 Hz and 20 kHz.

with the wind–tunnel system on. As expected, the background noise levels increase with the flow velocity. The spectra corresponding to flow velocities of 10 m/s and 20 m/s present tonal peaks at approximately 315 Hz. Applying acoustic imaging methods to the array data showed that the main noise sources at that frequency are located at the collector in the ceiling followed by the wind–tunnel nozzle. For the 20 m/s case, a peak around 700 Hz is also observed, which corresponded to the cupboard hosting the wind–tunnel controls (mostly due to electronic noise). Both sound sources are located considerably far away from the normal direction of the array, i.e., the test section. Therefore, they are not expected to interfere with the acoustic measurements. The expected modifications of the facility in the near future are expected to reduce these two noise sources.

The overall L_p background noise values and the A–weighted noise levels ($L_{p,A}$, see Appendix A.2) for a frequency range between 20 Hz and 20 kHz are plotted in Fig. E.14b with respect to the flow velocity. This frequency range was selected since it corresponds to the typical audible frequency range of a young person [11]. It can be observed that applying A–weighting considerably reduces the noise levels (up to 25 dB for the higher velocities considered). This indicates the strong content of low–frequency noise of the signal (see Fig. E.14a) because A–weighing considerably reduces the contribution of that part of the spectrum. Another difference between both curves is that the non–A–weighted values seem to follow an logarithmic trend with the flow velocity whereas the A–weighted ones present an almost–linear behavior.

The overall A–weighted background noise levels ($L_{p,A}$) measured at the A–tunnel were compared with the measurements of other aeroacoustic wind tunnels from the literature [17, 25, 26] and scaled using the correction suggested by Sarradj et al. [17] when different nozzle geometries are employed

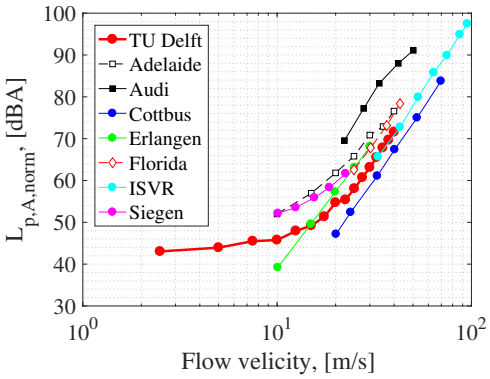

Figure E.15: Comparison of the overall $L_{p,A}$ background noise levels (corrected using Eq.) for different flow velocities with respect to other aeroacoustic wind tunnels: Adelaide University [25], Audi [25], TU Cottbus [17], Erlangen University [17], Florida University [25], ISVR Southampton [26] and Siegen University [17].

$$\Delta L_{p,A,norm} = L_{p,A} - 10\log\left(\frac{S_{nozzle}}{r^2}\right), \tag{E.3}$$

where S_{nozzle} is the exit area of the nozzle.

The compared results are depicted in Fig. E.15. It can be observed that the background noise levels of the A–tunnel are relatively low compared to other wind–tunnel facilities, presenting almost the same values as the aeroacoustic wind tunnel at ISVR Southampton [26]. Only the wind tunnel at TU Cottbus [17] presents lower background noise levels for the range of flow velocities considered.

E.2.4. Point spread function

In order to assess the overall performance of the phased microphone array and the anechoic chamber, the point spread function (PSF) of the array was evaluated. A single sound source (a Visaton K50 SQ speaker [14]) located in the normal direction of the array and over the wind tunnel nozzle was used.

Figure E.16 depicts the PSF obtained experimentally (Fig. E.16a) compared with the theoretical PSF for the same microphone array distribution and source location (Fig. E.16b) for a sound frequency of 4 kHz. It can be observed that the differences between both source plots is negligible, as desired. The theoretical PSF presents a slightly narrower main lobe and slightly lower sidelobes than the experimental one, as expected. This could be because the speaker used is not perfectly omnidirectional and that the free–field conditions in the anechoic chamber are not fulfilled perfectly [10]. Similar results were found for other frequencies and are gathered in [10].

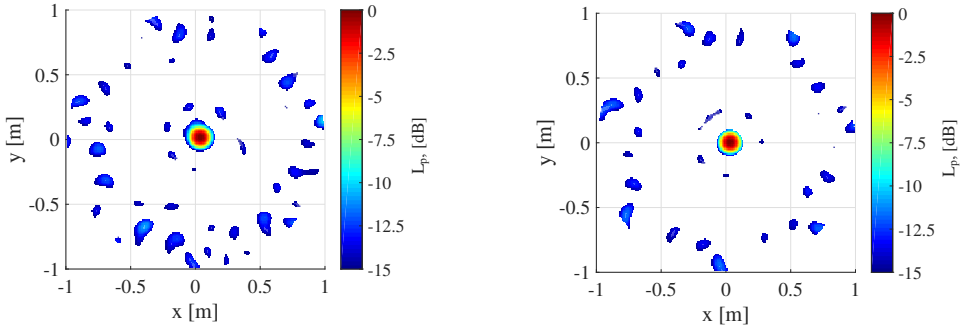

Figure E.16: (a) Experimental and (b) simulated array PSF for a source located at $(x, y) = (0, 0)$ and emitting sound at 4000 Hz. Adapted from [10].

Acknowledgements

The author would like to kindly thank Dr. Daniele Ragni, Dr. Marios Kotsonis and Dr. Francesco Avallone for their huge efforts in refurbishing the previous V–tunnel and converting it into the A–tunnel. Additional thanks go to Christian H. C. Vlemmix for his great help during the design and construction of the microphone array structure.

Bibliography

[1] R. Merino-Martinez, A. Rubio Carpio, C. H. C. Vlemmix, F. Avallone, M. Kotsonis, D. Ragni, M. Snellen, and D. G. Simons, *Aeroacoustic design and characterization of a vertical open–jet anechoic wind tunnel,* AIAA Journal (2018), Manuscript in preparation.

[2] G.R.A.S. Sound & Vibration – 40PH CCP Free–field array microphone, *http://www.gras.dk/products/special-microphone/array-microphones/product/178-40ph,* Accessed in March 2017.

[3] G.R.A.S. Sound & Vibration – 42AA Pistonphone class 1, *https://www.gras.dk/products/calibration-equipment/reference-calibrator/product/255-42aa,* Accessed in March 2017.

[4] G.R.A.S. Sound & Vibration – AA0028 10 m SMB – BNC cable, *https://www.gras.dk/products/cables/product/418-aa0028-extension-cable-for-array-microphones-smb-female-to-bnc,* Accessed in March 2017.

[5] C. H. C. Vlemmix, *Acoustic Array Design – The design of a reconfigurable phased microphone array for aeroacoustic wind tunnel measurements*, Master's thesis, Delft University of Technology (2017).

[6] Flamex Basic – Acoustic Absorbing Foam, *https://www.merford.com/media/202626/flamex-basic.pdf,* Accessed in March 2017.

[7] T. Mueller, *Aeroacoustic Measurements* (Springer Science & Business Media, 2002) p. 313, ISBN: 978–3–642–07514–8.

[8] J. R. Underbrink, *Circularly symmetric, zero redundancy, planar array having broad frequency range applications,* (U.S. Patent number 6,205,224 B1. 2001).

[9] Z. Prime and C. J. Doolan, *A comparison of popular beamforming arrays,* in *Proceedings of ACOUSTICS November 17 – 20 2013. Victor Harbor, Australia*, edited by A. A. Society (2013).

[10] S. Luesutthiviboon, A. Malgoezar, M. Snellen, P. Sijtsma, and D. G. Simons, *Improving Source Discrimination Performance by Using an Optimized Acoustic Array and Adaptive High–Resolution CLEAN–SC Beamforming,* in *7th Berlin Beamforming Conference, March 5 – 6 2018, Berlin, Germany* (GFaI, e.V., Berlin, 2018) BeBeC–2018–D07.

[11] T. D. Rossing, *Handbook of Acoustics*, Second ed. (Springer Science & Business Media, 2007) ISBN: 987–0–387–30446–5.

[12] V. Kopiev, V. Palchikovskiy, Y. Bersenev, S. Makashov, I. Belyaev, I. Korin, E. Sorokin, I. Khramtsov, and O. Kustov, *Design and quantification of an anechoic facility in PNRPU,* Procedia Engineering **176**, 264 (2017).

[13] *ISO norm 3745 – Acoustics – Determination of sound power levels and sound energy levels of noise sources using sound pressure – Precision methods for anechoic rooms and hemi–anechoic rooms*, Tech. Rep. 3 (International Organization for Standardization, 2012).

[14] Visaton – Speaker K 50 SQ – 8 Ohm, *http://www.visaton.de/en/products/fullrange-systems/k-50-sq-8-ohm,* Accessed in March 2017.

[15] Eurofysica – Clapper for acoustic measurements, *https://www.eurofysica.nl/webshop/natuurkunde/golven-licht-geluid/geluid/product/klapper-voor-geluidsmeting,* Accessed in March 2017.

[16] *ISO norm 3382 – Acoustics – Measurement of room acoustic parameters*, Tech. Rep. 1 (International Organization for Standardization, 2012).

[17] E. Sarradj, C. Fritzsche, T. Geyer, and J. Giesler, *Acoustic and aerodynamic design and characterization of a small–scale aeroacoustic wind tunnel,* Applied Acoustics **70**, 1073 (2009).

[18] C. Arce León, R. Merino-Martinez, D. Ragni, F. Avallone, and M. Snellen, *Boundary layer characterization and acoustic measurements of flow–aligned trailing edge serrations,* Experiments in Fluids **57**, 1 (2016).

[19] C. Arce León, R. Merino-Martinez, D. Ragni, F. Avallone, F. Scarano, S. Pröbsting, M. Snellen, D. G. Simons, and J. Madsen, *Effect of trailing edge serration–flow misalignment on airfoil noise emission,* Journal of Sound and Vibration **405**, 19 (2017).

[20] C. Arce León, R. Merino-Martinez, S. Pröbsting, D. Ragni, and F. Avallone, *Acoustic Emissions of Semi–Permeable Trailing Edge Serrations,* Acoustics Australia **46**, 111 (2017).

[21] C. Arce León, R. Merino-Martinez, D. Ragni, S. Pröbsting, F. Avallone, A. Singh, and J. Madsen, *Trailing Edge Serrations – Effect of Their Flap Angle on Flow and Acoustics,* in *7th International Meeting on Wind Turbine Noise, May 2 – 5 2017, Rotterdam, the Netherlands* (2017).

[22] A. Rubio Carpio, R. Merino-Martinez, F. Avallone, D. Ragni, M. Snellen, and S. van der Zwaag, *Broadband Trailing Edge Noise Reduction Using Permeable Metal Foams,* in *46th International Congress and Exposition of Noise Control Engineering, 27–30 August, 2017, Hong Kong* (2017).

[23] A. Rubio Carpio, R. Merino-Martinez, F. Avallone, D. Ragni, M. Snellen, and S. van der Zwaag, *Experimental characterization of the turbulent boundary layer over a porous trailing edge for noise abatement,* Journal of Sound and Vibration (2018), Accepted for publication.

[24] A. Rubio Carpio, F. Avallone, and D. Ragni, *On the Role of the Flow Permeability of Metal Foams on Trailing Edge Noise Reduction,* in *24th AIAA/CEAS Aeroacoustics Conference. June 25 – 29 2018. Atlanta, Georgia, USA* (2018) AIAA paper 2018–2964.

[25] E. Duell, J. Walter, S. Arnette, and Y. J., *Recent Advances in Large–Scale Aeroacoustic Wind Tunnels,* in *8th AIAA/CEAS Aeroacoustics Conference, 17 – 19 June 2002, Breckenridge, Co, USA* (2002) AIAA paper 2002–2503.

[26] T. P. Chong, P. F. Joseph, and P. O. A. L. Davies, *Design and performance of an open jet wind tunnel for aero–acoustic measurement,* Applied Acoustics **70**, 605 (2009).

Acknowledgements

After spending the last four years in this Ph.D. project, there is a long list of people that I would like to thank. I am aware that I am forgetting many names, so my apologies in advance for that.

First of all, I would like to kindly thank my promotor Prof. Dr. Dick G. Simons for offering me the opportunity to work in this project. From the very beginning you believed in me and trusted my abilities. I greatly value your critical feedback and your physicist point of view. Thanks very much for all your help and advice during these years.

I also want to express my sincere gratitude to my supervisor Dr. Mirjam Snellen for the uncountable technical conversations we had about my work. You always motivated and encouraged me to begin all the new projects I was interested in, and I very much like one of your main drivers for work is achieving a strong scientific value. Lastly, you have greatly improved the quality of all our publications with your detailed comments and reviews.

I would like to kindly acknowledge the efforts of all the committee members of my Ph.D. defense. Thank you very much for taking the time for reading this thesis and for attending my defense.

I especially thank Dr. Pieter Sijtsma for all the interesting conversations we had about acoustic imaging during the last years. I feel very lucky to have met one of the *fathers of beamforming* and to have him available to discuss next door. With your mathematician point of view, you often solved many of the questions I have been struggling for days in few minutes.

Working in a group as ANCE has proved to be a very satisfying experience, especially for having a team of great colleagues around me. First, I would like to thank Anwar because we have been working together since we started our Ph.D.s and, since then, we have had lots of interesting conversations and fun moments. Thanks a lot for your Dutch translations as well! My office mate Timo should get a medal for bearing with me for the last years also. I greatly enjoyed our talks (and beers) together. It was certainly great to have another Spaniard in the team, especially if he is as friendly and funny as Alejandro. It was a pleasure to work together in the wind tunnel and I really enjoyed our road trip in the U.S. Additional thanks to Abhi, Ana, Afrizal, Colin, Feijia, Leo, Lothar, Salil, Tannaz and Thijs for all your support and funny moments. Last but not least, I would like to thank our secretaries, Geeta and Lisette for all their help and kindness during the last years.

Another outstanding team I have worked with is the one formed by Daniele Ragni, Francesco Avallone, Carlos Arce León and Wouter van der Velden. What started as a simple collaboration about trailing–edge serrations became a strong friendship with each of you. You all have a great technical expertise in your fields but, most importantly, a great sense of humor. Working with you was definitely a

very pleasant experience. I wish all the best to Dani and Fra and their new Aeroacoustics group. Hopefully we will keep collaborating in many successful projects in the future!

I would like to thank Eleonora Neri and her team in Trinity College Dublin for collaborating in an interesting study about landing gear noise. It is always nice to meet you somewhere in Europe! Kind gratitude also goes to the aeroacoustics team in the University of Twente (Leandro Dantas de Santana, Marijn Sanders, Luciano Caldas and Kees Venner) for hosting me during our experimental campaign.

The last acknowledgements regarding work go to all the students I have supervised in any way in the last years. I hope that you have learnt something useful from me, because I certainly obtained new ideas and enjoyed your enthusiasm. Special mention goes to Christian Vlemmix for all his help in designing and constructing the new microphone array of the A–tunnel.

During the last four years in Delft, I have made many good friends that I would like to thank, even if their contribution was not technical. Fabricio and Johan (el patrón), I met you during my first days in Delft and, since then, we have been close friends and shared a lot of moments (and beers). Special thanks to Clara for all her support and our hilarious dinners with *morcillas*. For my first two years, I was part of the Ph.D. board of the Aerospace Engineering Faculty from which I keep very good memories, especially with Tomas and Maurice. During the last year, I greatly enjoyed the friendship of Pavlo: we met randomly in a course in Italy and, since then, we have found a large number of similarities between both of us. Many thanks to Anete for her great support and understanding during tough times and all the good moments. Finally, thanks to the Atmosfeer gang (Víctor, Reynard, Hermes, Marsil, Daduí, Pedro, Bruce, Dirk, Vis, etc.) for all the fun evenings spent there.

Throughout my Ph.D. I was also a proud member of the Board of European Students of Technology (BEST) in the local group in Delft. Thanks to this organization I got to know some of my best friends. You are way too many to list here, so I will simply drop the names of Jason, Leon, Luca, Jason, Rak, Remi, Shakthi, Sharath, Vicente, and the *Aluminati* as a whole. I really enjoyed all our random trips and parties during these years. Special thanks to Santi for all his support during hard times and all his inappropriate jokes. All the best for everyone! And remember that Roberto provides.

I would like to kindly thank Lenka for her caring and supportive attitude and all the good moments spent.

Despite the distance, I really value all my good friends in Burgos and Madrid. Once again, you are too many to list here, but I want to particularly thank Luis, Elena, Álvar and Raúl for your support and care. Special thanks for those of you who came to visit me during these years (Aarón, Adriano, Alberto, Cris, Diego, Gustavo, Irene, Lara, Miguel, Natalia, Pedro and Raúl), it is always great to meet you anywhere.

My kindest gratitude goes to my lovely girlfriend Ligaya, who constantly believed in me and supported me. I never thought that I would find someone with my same stupid sense of humor, but it seems that I was wrong. Thank you so much for being as you are and for all the amazing moments and trips together. Words cannot really

express how lucky I feel to have you in my life. I am really looking forward to future challenges in common and traveling together. I love you a lot.

Last, but definitely not least, I would like to thank all my family for their love, support and understanding. I would not be who I am without you and I would certainly not have achieved this without all your unrelenting support and encouragement. I feel really lucky to have such wonderful and loving parents (Roberto and Carmen), most probably the kindest people I have ever known, and such an intelligent, funny and caring brother (Mario). You have always been my role models and you will always be. I feel especially happy that both my grandmothers got to see their (second) grandson becoming a doctor. Thank you all, I love you a lot.

Por último, y definitivamente no por ello menos importante, me gustaría dar las gracias a toda mi familia por su amor, apoyo y comprensión. No sería quién soy sin vosotros y seguro que no hubiera conseguido esto sin vuestros inexorable apoyo y ánimos. Me siento muy afortunado de tener unos padres (Roberto y Carmen) tan maravillosos y cariñosos, seguramente las mejores personas que he conocido, y un hermano (Mario) tan inteligente, gracioso y bondadoso. Siempre habéis sido y seréis mis modelos a seguir. Me siento especialmente contento de que mis dos abuelas hayan podido ver como su (segundo) nieto se convierte en doctor. Gracias a todos, os quiero mucho.

Curriculum Vitæ

Roberto Merino–Martínez

11-05-1991 Born in Burgos, Spain.

Education

2006–2008 International Baccalaureate (IB),
I.E.S. Cardenal López de Mendoza, Burgos, Spain.
Graduated with honors.

2008–2014 Bachelor and Master of Science in Aerospace Engineering,
Madrid Polytechnic Univeristy (UPM), Madrid, Spain.

2013–2014 Master of Science (M.Sc.) Thesis in Aerospace Engineering,
Royal Institute of Technology (KTH), Stockholm, Sweden.
Within an Erasmus scholarship.
Thesis: Design and analysis of the control and stability of a Blended Wing Body aircraft.

2014–2018 Doctor of Philosophy (Ph.D.) in Aeroacoustics,
Faculty of Aerospace Engineering,
Delft University of Technology, Delft, the Netherlands.
Thesis: Microphone arrays for imaging of aerospace noise sources.
Promotor: Prof. dr. D.G. Simons.

2018–Present Postdoctoral researcher in Aerospace Engineering,
Delft University of Technology, Delft, the Netherlands.

List of Publications

Journal papers

15. **R. Merino–Martínez**, S. Luesutthiviboon, A. Rubio Carpio, R. Zamponi, D. Ragni, N. Van de Wyer, and M. Snellen, *Assessment of the accuracy of microphone array methods*, Manuscript in preparation.

14. **R. Merino–Martínez**, A. Rubio Carpio, C.H.C. Vlemmix, F. Avallone, M. Kotsonis, D. Ragni, M. Snellen, and D.G. Simons, *Aeroacoustic design and characterization of a vertical open–jet anechoic wind tunnel*, Manuscript in preparation.

13. **R. Merino–Martínez**, P. Sijtsma, A. Rubio Carpio, R. Zamponi, S. Luesutthiviboon, A.M.N. Malgoezar, M. Snellen, N. Van de Wyer, C. Schram, and D.G. Simons, *Integration methods for distributed sound sources*, International Journal of Aeroacoustics, (2018). Under review process.

12. S. Luesutthiviboon, A.M.N. Malgoezar, **R. Merino–Martínez**, M. Snellen, P. Sijtsma and D.G. Simons, *Adaptive high-resolution CLEAN-SC for resolving multiple closely-spaced sound sources*, International Journal of Aeroacoustics, (2018). Under review process.

11. A. Rubio Carpio, **R. Merino–Martínez**, F. Avallone, D. Ragni, M. Snellen and S. van der Zwaag, *Experimental characterization of the turbulent boundary layer over a porous trailing edge for noise abatement*, Journal of Sound and Vibration, (2018). Accepted for publication.

10. T. Sinnige, B. Della Corte, R. de Vries, F. Avallone, **R. Merino–Martínez**, D. Ragni, G. Eitelberg and L. L. M. Veldhuis, *Alleviation of unsteady loading due to propeller-slipstream impingement by flow–pearmeable leading edges*, Journal of Aircraft, (2018). Accepted for publication.

9. **R. Merino–Martínez**, P. Sijtsma, M. Snellen, T. Ahlefeldt, J. Antoni, C.J. Bahr, D. Blacodon, D. Ernst, A. Finez, S. Funke, T.F. Geyer, S. Haxter, G. Herold, X. Huang, W.M. Humphreys, Q. Leclère, A. Malgoezar, U. Michel, T. Padois, A. Pereira, C. Picard, E. Sarradj, H. Siller, D. G. Simons and C. Spehr, *A review of acoustic imaging methods using phased microphone arrays. (Part of the "Aircraft Noise Generation and Assessment" Special Issue)*, CEAS Aeronautical Journal, (2018). Accepted for publication.

8. **R. Merino–Martínez**, S. J. Heblij, D. H. T. Bergmans, M. Snellen and D. G. Simons, *Improving aircraft noise prediction models by calculating turbofan engine fan settings from flyover recordings*, Journal of Aircraft, (2018). In press.

7. C. Arce León, **R. Merino–Martínez**, S. Pröbsting, D. Ragni and F. Avallone, *Acoustic emissions of semi-permeable trailing edge serrations*, Acoustics Australia **46**, 1, pp. 111–117 (2017).

6. P. Sijtsma, **R. Merino–Martínez**, A.M.N. Malgoezar and M. Snellen *High-resolution CLEAN-SC: Theory and experimental validation*, International Journal of Aeroacoustics **16**, 4–5, pp. 274–298 (2017).

5. C. Arce León, **R. Merino–Martínez**, D. Ragni, F. Avallone, F. Scarano, S. Pröbsting, M. Snellen, D.G. Simons and J. Madsen, *Effect of trailing edge serration-flow misalignment on airfoil noise emissions*, Journal of Sound and Vibration **405**, pp. 19–33, (2017).

4. M. Snellen, **R. Merino–Martínez** and D.G. Simons, *Assessment of noise variability on landing aircraft using phased microphone array*, Journal of Aircraft **54**, 6, pp. 2173–2183, (2017).

3. A.M.N. Malgoezar, M.Snellen, **R. Merino–Martínez**, D.G. Simons and P. Sijstma, *On the use of global optimization methods for acoustic source mapping*, Journal of the Acoustical Society of America **141**, 1, pp. 453–465, (2017).

2. C. Arce León, **R. Merino–Martínez**, D. Ragni, F. Avallone, and M. Snellen *Boundary layer characterization and acoustic measurements of flow-aligned trailing edge serrations*, Experiments in Fluids **57**, 182, pp. 1–22 (2016).

1. **R. Merino–Martínez**, M. Snellen and D.G. Simons, *Functional beamforming applied to imaging of flyover noise on landing aircraft*, Journal of Aircraft **53**, 6, pp. 1830–1843, (2016).

Conference papers

20. A, Rubio Carpio, S. Luesutthiviboon, **R. Merino–Martínez**, F. Avallone, D. Ragni, M. Snellen and S. van der Zwaag, *3D–printed permeable materials for trailing edge noise reduction*, 25th AIAA/CEAS Aeroacoustics Conference, Delft, the Netherlands, (2019).

19. A, Vieira, U. Mehmood, **R. Merino–Martínez**, M. Snellen and D.G. Simons, *Variability of sound quality metrics for different aircraft types during landing and takeoff*, 25th AIAA/CEAS Aeroacoustics Conference, Delft, the Netherlands, (2019).

18. **R. Merino–Martínez**, A. Vieira, M. Snellen and D.G. Simons, *Sound quality metrics applied to aircraft components under operational conditions using a microphone array*, 25th AIAA/CEAS Aeroacoustics Conference, Delft, the Netherlands, (2019).

17. **R. Merino–Martínez**, M.P.J. Sanders, L.C. Caldas, F. Avallone, D. Ragni, L.D. de Santana, M. Snellen and D.G. Simons, *Comparison between analog and digital microphone phased arrays for aeroacoustic measurements*, 24th AIAA/CEAS Aeroacoustics Conference, Atlanta, Georgia, USA, (2018).

16. **R. Merino–Martínez**, E. Neri, M. Snellen, J. Kennedy, D.G. Simons and G. Benneth, *Analysis of nose landing gear noise comparing numerical computations, prediction models and flyover and wind–tunnel measurements*, 24th AIAA/CEAS Aeroacoustics Conference, Atlanta, Georgia, USA, (2018).

15. **R. Merino–Martínez**, P. Sijstma and M. Snellen, *Inverse integration method for distributed sound sources*, 7th Berlin Beamforming Conference (BeBeC), Berlin, Germany, (2018).

14. A. Rubio Carpio, **R. Merino–Martínez**, F. Avallone, D. Ragni, M. Snellen and S. van der Zwaag, *Broadband trailing edge noise reduction using permeable metal foams*, 46th International Congress and Exposition of Noise Control Engineering, Hong Kong, (2017).

13. D.G. Simons, M. Snellen, **R. Merino–Martínez** and A.M.N. Malgoezar, *Noise breakdown of landing aircraft using a microphone array and an airframe noise model*, 46th International Congress and Exposition of Noise Control Engineering, Hong Kong, (2017).

12. F. Avallone, W. van der Velden, **R. Merino–Martínez** and D. Ragni, *Hydrodynamic effects of serration length on trailing-edge noise reduction*, 23rd AIAA/CEAS Aeroacoustics Conference, Denver, Colorado, USA, (2017).

11. P. Sijtsma, **R. Merino–Martínez**, A.M.N. Malgoezar and M. Snellen, *High-resolution CLEAN-SC: Theory and experimental validation*, 23rd AIAA/CEAS Aeroacoustics Conference, Denver, Colorado, USA, (2017).

10. E. Sarradj, G. Herold, P. Sijtsma, **R. Merino–Martínez**, A.M.N. Malgoezar, M. Snellen, T.F. Geyer, C.J. Bahr, R. Porteus, D. Moreau and C. Doolan, *A microphone array method benchmarking exercise using synthesized input data*, 23rd AIAA/CEAS Aeroacoustics Conference, Denver, Colorado, USA, (2017).

9. **R. Merino–Martínez**, E. Neri, M. Snellen, J. Kennedy, D.G. Simons and G. Benneth, *Comparing flyover noise measurements to full-scale nose landing gear wind-tunnel experiments for regional aircraft*, 23rd AIAA/CEAS Aeroacoustics Conference, Denver, Colorado, USA, (2017).

8. C. Arce León, **R. Merino–Martínez**, S. Pröbsting, D. Ragni, F. Avallone, A. Singh and J. Madsen, *Trailing edge serrations – Effect of their flap angle on flow and acoustics*, 7th International Conference on Wind Turbine Noise, Rotterdam, the Netherlands, (2017).

7. **R. Merino–Martínez**, W. van der Velden, F. Avallone and D. Ragni, *Acoustic measurements of a DU96-W-180 airfoil with flow-misaligned serrations at a high Reynolds number in a closed-section wind tunnel*, 7th International Conference on Wind Turbine Noise, Rotterdam, the Netherlands, (2017).

6. **R. Merino–Martínez**, M. Snellen and D.G. Simons, *Determination of aircraft noise variability using an acoustic camera*, 23rd International Congress on Sound and Vibration, Athens, Greece, (2016).

5. **R. Merino–Martínez**, L. Bertsch, M. Snellen and D.G. Simons, *Analysis of landing gear noise during approach*, 22nd AIAA/CEAS Aeroacoustics Conference, Lyon, France, (2016).

4. **R. Merino–Martínez**, M. Snellen and D.G. Simons, *Functional Beamforming applied to full scale landing aircraft*, 6th Berlin Beamforming Conference (BeBeC), Berlin, Germany, (2016).

3. M. Snellen, **R. Merino–Martínez** and D.G. Simons, *Assessment of aircraft noise sources variability using an acoustic camera*, 5th CEAS Air & Space Conference. Challenges in European Aerospace, Delft, the Netherlands, (2015).

2. **R. Merino–Martínez**, *Design and analysis of the control and stability of a Blended Wing Body aircraft*, 5th CEAS Air & Space Conference. Challenges in European Aerospace, Delft, the Netherlands, (2015).

1. **R. Merino–Martínez**, *Design and analysis of the control and stability of a Blended Wing Body aircraft*, 11th Pegasus-AIAA Student Conference, Salon de Provence, France, (2015).

Other contributions

2. P. Bazilinskyy, C. Beretta and **R. Merino–Martínez**, *Towards a sustainable transport system*, Angle Journal, (15th October 2018).

1. Contribution titled **Noise reduction mechanism of serrated-trailing-edge devices** published in A. G. Wilson, *Aeroacoustics research in Europe: The CEAS–ASC report on 2016 highlights*, Journal of Sound and Vibration **427**, (2018).